

Controlled Synthesis of Polymer Micro- and Nanoparticles Stained with Luminophores and Analysis of the Resulting Particle Surface Functionalities and Luminescence Properties

**Inaugural-Dissertation**

to obtain the academic degree

Doctor rerum naturalium (Dr. rer. nat.)

submitted to the Department of Biology, Chemistry, Pharmacy  
of Freie Universität Berlin

by

**Lena Scholtz**

Berlin, 2023

The work presented in this thesis was carried out from January 2020 to December 2023 at the Bundesanstalt für Materialforschung und -prüfung (BAM), 12489 Berlin under the supervision of Dr. Ute Resch-Genger in the Department 1.2 *Biophotonics*.

**1<sup>st</sup> reviewer:** Dr. Ute Resch-Genger  
**2<sup>nd</sup> reviewer:** Prof. Dr. Siegfried Eigler

Date of defense: 29.04.2024

*"I am among those who think that science has great beauty. A scientist in his laboratory is not only a technician: he is also a child placed before natural phenomena which impress him like a fairy tale."*

**Marie Skłodowska-Curie**

---

*To everyone who supported me - and myself.*

---

I owe immense gratitude to all people who accompanied and supported me during my doctoral studies and university - without you, a lot would not have been possible.

First, I want to thank Dr. Ute Resch-Genger for the possibility to broaden my horizon with this research topic under her supervision and in her division, but also for the trust and support that I experienced from the beginning. I always felt that my work and I as a person were appreciated and am thankful to have learned so much, regarding scientific practice, but also independent management and supervisory tasks. In addition, thank you for the possibility to present my work in the form of poster presentation and talks at several conferences, and the constructive support of all my projects.

I want to thank Prof. Dr. Siegfried Eigler for agreeing to be my second reviewer, but also for the great support with writing this work and the opportunity to present and discuss my results to gain a new perspective.

Special thanks are directed towards my (former) colleagues from the division Biophotonics, in particular Dr. Nithiya Nirmalananthan-Budau for the friendly welcome and support in the first weeks and months. I also want to thank Dr. Karl-David Wegner and the participants of the nanoparticle seminar for the professional discussions, constructive criticism and new insights, as well as the responsible colleagues for the introduction to several measurement devices (Dr. Jutta Pauli, Arne Güttler). A special thanks goes to Maria Richter for the quality management, organization of the ordering and so much more. I also want to thank the other doctoral students Lisa-Marie, Alexander, Philipp, Viktoriia, Abdel and Anna as well as the postdocs for the many nice talks during the weekly lunch, at the conferences/summer schools and on Girls' Day, the exchange and encouragement you provided during my time at BAM. Thank you to the students I had the opportunity to supervise - Toufiq, Alexandra and Philipp. They really helped me with their scientific contributions, but also taught me a lot outside of this.

Without cooperation, science would not be possible, so I want to thank my cooperation partners inside and outside BAM. These include Dr. Daniel Geißler, Dr. Nithiya Nirmalananthan-Budau, Dr. Isabella Tavernaro, Oskar Hübner, Dr. Priyanka Srivastava, Marc Lutowski,

Dr. Andreas Hertwig and Gundula Hidde (all BAM), as well as Gerrit Eckert, Franziska Lübke-Warwas, Rebecca Graf and Prof. Dr. Nadja Bigall from Leibniz Universität Hannover (AG Bigall), and Yalei Hu from Freie Universität Berlin (AG Eigler). A special thanks goes to Thomas Thiele and Maiko Schulze from PolyAn, who provided me with their vast knowledge about polymers when writing my publications and this thesis. I also owe thanks to all project partners and funding agencies of the EMPIR project 18HLT02 AeroTox and the SAFERA project ANOPSA, as well as BAM for providing me with the financial means to finish this work.

Very big thanks of course also go towards my family - my parents Sonja and Martin, my brothers Henrik and Simon, but also my grandparents Erna and Werner as well as my uncle Rolf - who supported me financially and stood behind me. I was always curious as a child, and especially my parents supported my search for knowledge and provided me with the answers to my never-ending questions of "Why?". I will be eternally grateful for that. You all believed I would one day be "Frau Doktor", and especially because of this, this work is also dedicated to you.

I am so grateful to have had my best friends Anne, Gerrit and Timon with me during this time, if directly or emotionally. You have been by my side for so long now, through good and bad times, you understand me - and what this work means to me, what I invested and had to go through to get here. Without your support, encouragement, all the shared experiences, the distraction from everyday life and the problem solving, I would not have made it this far. At last, to the most important person: My boyfriend and soon to be husband Torben. The one who was present from the beginning, experienced everything with me and always believed in me, without ever taking anything for granted. Thank you so much for all the talks, practice presentations and your willingness to not only support my passion for science, but to help carry it. Thank you for growing with and alongside me, for sticking with me, and for your unwavering trust. You have always been my backup, and not least because of you, this work now exists.

THANK YOU!



## **Declaration of Independence**

Herewith I certify that I have prepared and written my thesis independently and that I have not used any sources and aids other than those indicated by me. This dissertation has not yet been presented to any other examination authority in the same or a similar form and has not yet been published.

Berlin, May 2024

---

Lena Scholtz



# Contents

<b>List of Abbreviations</b>	<b>iii</b>
<b>1. Abstract</b>	<b>1</b>
<b>2. Kurzzusammenfassung</b>	<b>5</b>
<b>3. Introduction</b>	<b>9</b>
3.1. Organic Polymer Microparticles (PMPs) and Polymerization Techniques . . .	9
3.1.1. Introduction to PMPs . . . . .	9
3.1.1.1. Definition . . . . .	9
3.1.1.2. Applications . . . . .	10
3.1.1.3. Properties . . . . .	10
3.1.1.4. Analytics . . . . .	12
3.1.2. Overview of Polymerization Procedures . . . . .	12
3.1.3. Emulsion Polymerization . . . . .	15
3.1.4. Suspension Polymerization . . . . .	17
3.1.5. Dispersion Polymerization . . . . .	18
3.1.6. Microfluidic Approaches . . . . .	20
3.1.7. Comparison of Polymerization Procedures . . . . .	20
3.2. Luminescent Semiconductor Nanoparticles (NPs) . . . . .	22
3.2.1. Semiconductor NP Architectures . . . . .	24
3.2.1.1. Quantum Dots (QDs) . . . . .	25
3.2.1.2. Quantum Rods (QRs) . . . . .	28
3.2.1.3. Nanoplatelets (NPLs) . . . . .	29
3.3. Luminescent PMPs . . . . .	31
3.3.1. Applications and Properties . . . . .	31
3.3.2. Luminophore Staining Methods . . . . .	32
3.3.2.1. Staining During Polymerization . . . . .	32
3.3.2.2. Post-synthetic Swelling . . . . .	33

3.3.2.3.	Layer-by-layer Technique . . . . .	33
3.3.2.4.	Comparison of Staining Methods . . . . .	34
3.3.3.	Inorganic Semiconductor NPs vs Organic Dyes as Luminophores for PMP Staining . . . . .	36
3.3.4.	PMP Surface Chemistry . . . . .	37
3.4.	Motivation and Objectives . . . . .	38
<b>4.</b>	<b>Methods for Luminescent PSMP Synthesis and Characterization</b>	<b>41</b>
4.1.	Synthesis Procedures . . . . .	41
4.1.1.	Synthesis of Luminescent Semiconductor NPs . . . . .	41
4.1.1.1.	Semiconductor Core/shell-QDs with Different Shell Thicknesses and Composition . . . . .	41
4.1.1.2.	Semiconductor Dot-in-rod-QRs . . . . .	42
4.1.1.3.	Semiconductor Core/shell-NPLs . . . . .	42
4.1.2.	Synthesis of Polystyrene Microparticles (PSMPs) Stained with Lumi- nescent Semiconductor NPs . . . . .	43
4.1.2.1.	Pretreatment of NPs with a Polymer-compatible Ligand . . . . .	43
4.1.2.2.	Synthesis of PSMPs with and without Surface Functionalization	43
4.2.	Characterization of NPs and PSMPs . . . . .	44
4.2.1.	Size, Size Distribution and Particle Morphology . . . . .	44
4.2.1.1.	Dynamic Light Scattering (DLS) . . . . .	44
4.2.1.2.	Scanning Electron Microscopy (SEM) . . . . .	45
4.2.1.3.	Transmission Electron Microscopy (TEM) . . . . .	46
4.2.1.4.	Confocal Laser Scanning Microscopy (CLSM) . . . . .	47
4.2.2.	Optical Properties . . . . .	48
4.2.2.1.	Absorption . . . . .	48
4.2.2.2.	Emission . . . . .	49
4.2.2.3.	Photoluminescence Quantum Yield (PLQY) . . . . .	50
4.2.2.4.	Fluorescence Lifetime (FLT) and Decay Kinetics . . . . .	51
4.2.3.	Chemical Composition . . . . .	52
4.2.3.1.	Nuclear Magnetic Resonance Spectroscopy (NMR) . . . . .	52
4.2.3.2.	Atomic Absorption Spectroscopy (AAS) . . . . .	54
4.2.3.3.	Fourier Transform Infrared Spectroscopy (FTIR) . . . . .	54

4.2.4.	Surface Charge . . . . .	55
4.2.4.1.	Zeta Potential . . . . .	55
4.2.5.	Quantification of Acidic Surface Functional Groups (FGs) . . . . .	56
4.2.5.1.	Conductometry . . . . .	56
4.2.5.2.	Optical Assays . . . . .	58
<b>5.</b>	<b>Results: Publications and Submitted Manuscripts</b>	<b>61</b>
5.1.	Major Contributions . . . . .	61
5.1.1.	Luminescence Encoding of Polymer Microbeads With Organic Dyes and Semiconductor Quantum Dots During Polymerization . . . . .	61
5.1.2.	Influence of Nanoparticle Encapsulation and Encoding on the Surface Chemistry of Polymer Carrier Beads . . . . .	88
5.1.3.	Correlating Semiconductor Nanoparticle Architecture and Applicability for the Controlled Encoding of Luminescent Polymer Microparticles . . . . .	113
5.2.	Minor Contributions . . . . .	173
5.2.1.	Analyzing the Surface of Functional Nanomaterials - How to Quantify the Total and Derivatizable Number of Functional Groups and Ligands (Review Article) . . . . .	173
5.2.2.	Dual Color pH Probes Made From Silica and Polystyrene Nanoparticles and Their Performance in Cell Studies . . . . .	203
<b>6.</b>	<b>Synopsis of Results</b>	<b>249</b>
6.1.	Optimized Synthesis of PSMPs Stained with Luminophores . . . . .	249
6.2.	Influence of Synthesis Routes on the Preparation of QD-stained PSMPs and Their Surface FGs . . . . .	251
6.3.	Correlation Between NP Architecture and Their Applicability for Controlled PSMP Staining . . . . .	253
6.4.	Synthesis of pH-responsive PSNPs Stained with NR and Their Application as Ratiometric Sensors . . . . .	254
6.5.	Summary of Generated Knowledge and Outlook . . . . .	254
	<b>References</b>	<b>257</b>

**A. Appendix** **281**

A.1. List of Publications . . . . . 281

A.2. Conference Contributions . . . . . 282

---

# List of Abbreviations

<b>AA</b>	acrylic acid
<b>AAS</b>	atomic absorption spectroscopy
<b>AIBN</b>	azobisisobutyronitrile
<b>APTES</b>	(3-aminopropyl)triethoxysilane
<b>BET</b>	Brunauer–Emmett–Teller
<b>BODIPY</b>	dipyrometheneboron difluoride
<b>BSE</b>	backscattered electron
<b>CLSM</b>	confocal laser scanning microscopy
<b>CMC</b>	critical micelle concentration
<b>DAPI</b>	4,6-diamidino-2-phenylindole
<b>DCM</b>	dichloromethane
<b>DLS</b>	dynamic light scattering
<b>DMEM</b>	Dulbecco's Modified Eagle's Medium
<b>DMF</b>	<i>N,N'</i> -dimethylformamide
<b>DMSO</b>	dimethyl sulfoxide
<b>DNA</b>	deoxyribonucleic acid
<b>DVB</b>	divinylbenzene
<b>EDC</b>	<i>N</i> -(3-dimethylaminopropyl)- <i>N'</i> -ethylcarbodiimid
<b>EDXS</b>	energy-dispersive X-ray spectroscopy
<b>ESEM</b>	environmental scanning electron microscope

---

<b>FCM</b>	flow cytometry
<b>FDA</b>	U.S. Food and Drug Administration
<b>FG</b>	functional group
<b>FID</b>	free induction decay
<b>FLT</b>	fluorescence lifetime
<b>FTIR</b>	Fourier transform infrared
<b>FWHM</b>	full width at half maximum
<b>GPC/SEC</b>	gel permeation chromatography/size exclusion chromatography
<b>HAADF-STEM</b>	high-angle annular dark-field scanning transmission electron microscopy
<b>HLB</b>	hydrophilic-lipophilic balance
<b>HOMO</b>	highest occupied molecular orbital
<b>IC</b>	internal conversion
<b>ICT</b>	intramolecular charge transfer
<b>IR</b>	infrared
<b>ISC</b>	intersystem crossing
<b>LbL</b>	layer-by-layer
<b>LED</b>	light-emitting diode
<b>LUMO</b>	lowest unoccupied molecular orbital
<b>MALDI-TOF MS</b>	matrix-assisted laser desorption/ionization time-of-flight mass spectrometry
<b>MCP</b>	microchannel plate
<b>ML</b>	monolayer
<b>MP</b>	microparticle

---

<b>N-APPA</b>	<i>N</i> -(aminoethyl)-3-(pyridin-2-yl)disulfanyl-propanamide trifluoroacetate
<b>NMR</b>	nuclear magnetic resonance
<b>NP</b>	nanoparticle
<b>NPL</b>	nanoplatelet
<b>NR</b>	Nile Red
<b>OA</b>	oleic acid
<b>OBDAC</b>	benzyltrimethylammonium chloride
<b>ODE</b>	1-octadecene
<b>ODPA</b>	<i>n</i> -octadecylphosphonic acid
<b>OIA</b>	oleylamine
<b>PBS</b>	phosphate-buffered saline solution
<b>PEG</b>	poly(ethylene glycol)
<b>PEG-<i>b</i>-PCL</b>	poly(ethylene glycol)- <i>block</i> -poly( $\epsilon$ -caprolactone)
<b>PET</b>	photoinduced electron transfer
<b>PL</b>	photoluminescence
<b>PLQY</b>	photoluminescence quantum yield
<b>PMMA</b>	poly(methyl methacrylate)
<b>PPS</b>	potassium persulfate
<b>PS</b>	polystyrene
<b>PMP</b>	polymer microparticle
<b>PNP</b>	polymer nanoparticle
<b>PSMP</b>	polystyrene microparticle
<b>PSNP</b>	polystyrene nanoparticle

---

<b>PVA</b>	poly(vinyl alcohol)
<b>PVC</b>	poly(vinyl chloride)
<b>PVP</b>	polyvinylpyrrolidone
<b>QD</b>	quantum dot
<b>QR</b>	quantum rod
<b>RAFT</b>	reversible addition-fragmentation chain-transfer
<b>RhB</b>	Rhodamine B
<b>RITC</b>	Rhodamine B isothiocyanate
<b>RNA</b>	ribonucleic acid
<b>SDS</b>	sodium dodecyl sulfate
<b>SE</b>	secondary electron
<b>SEM</b>	scanning electron microscopy
<b>SI</b>	supplementary information
<b>SPDP</b>	<i>N</i> -succinimidyl-3-(2-pyridyldithio) propionate
<b>STEM</b>	scanning transmission electron microscopy
<b>sulfo-NHS</b>	<i>N</i> -hydroxy-sulfosuccinimide sodium salt
<b>TBO</b>	toluidine blue
<b>TCEP</b>	tris(2-carboxyethyl) phosphine hydrochloride
<b>TCSPC</b>	time-correlated single photon counting
<b>TEM</b>	transmission electron microscopy
<b>TEOS</b>	tetraethoxysilane
<b>TGA</b>	thermogravimetric analysis
<b>THF</b>	tetrahydrofuran

---

<b>TOP</b>	trioctylphosphine
<b>TOPO</b>	trioctylphosphine oxide
<b>UCNP</b>	upconversion nanoparticle
<b>UV</b>	ultraviolet



# 1 | Abstract

This work is focused on systematic studies of the correlation between the morphology of semiconductor nanoparticles (NPs), their luminescence properties and the application relevant features of polymer microparticles (PMPs) stained with these NPs. These PMPs are of considerable importance for various fields of life science, as they can be applied as sensors/reporters or carriers for medical/diagnostic purposes as well as for instrument calibration and bead-based assays. The luminescence is introduced in the form of different inorganic, semiconductor NPs and can be utilized for the identification and readout (e.g., quantification or localization) of the resulting PMPs. This is performed with optical methods such as fluorescence microscopy, flow cytometry (FCM) and fluorescence spectroscopy, enabling the PMPs to act as a marker or carrier for barcodes. For these applications, the precise control of the luminescence properties and surface chemistry of the PMPs, and hence of the spectral characteristics of the employed NPs, is of high importance. Both luminescence and surface chemistry of the PMPs directly influence their suitability for specific use, e.g. via the interaction with their environment or sufficient signal intensity for fluorescence readout. The synthesis of PMPs, with or without luminophore, can be performed by different methods. Common synthesis approaches include (mini)emulsion and suspension polymerization, microfluidic approaches and dispersion polymerization, with the latter being employed in this work because of its simplicity, low cost and good reproducibility.

The synthesis of luminescent, quantum dot (QD)-stained polystyrene microparticles (PSMPs) was first developed and optimized for CdSe/CdS-QDs (see Scholtz *et al.*, Luminescence encoding of polymer microbeads with organic dyes and semiconductor quantum dots during polymerization, *Scientific Reports* **12.1** (2022), p. 12061). Apart from nanoscale luminophores such as QDs, molecular luminophores such as organic dyes have been long employed for the synthesis of PMPs. While the incorporation of dyes is comparatively easy and well studied, the use of luminescent NPs such as QDs often goes along with challenges such as NP aggregation or excessive loss of fluorescence intensity. However, they also present significant advantages over dyes, such as a much better photostability or their very symmetric and narrow

emission spectra. Semiconductor NPs typically can be excited by a wide range of irradiation, as their absorbance spectra are very broad. This enables the simultaneous excitation of NPs of different colors/sizes, composition or shape. These factors prompted the development of a simple, but efficient and optimized synthesis of NP-stained PSMPs, overcoming the presenting challenges and ensuring sufficient luminescence in the finished particles for future applications. Challenges that were encountered and addressed include the significant loss of NP fluorescence, NP aggregation/separation during the synthesis combined with insufficient incorporation into the polymer matrix, leakage of the NPs from the finished beads and a very broad PSMP size distribution.

The incorporation of both molecular luminophores such as organic dyes, and nanoscale luminophores such as semiconductor QDs into polymer beads can be performed by different means. These include post-synthetic swelling, the layer-by-layer (LbL) method, and addition before/during the polymerization procedure. The latter was employed in this work, as it often enables better NP homogeneity and sterical incorporation into the beads, as well as the simultaneous synthesis of a large amount of PSMPs with a high variability in bead size. An adaptation of the synthesis for different kinds of NPs is possible. In addition, the synthesis route can play a huge role for the luminescence properties and location in the beads of the employed NPs, which was investigated and confirmed in this work.

The influence of the polymerization reaction on NPs such as QDs, or even more so nanoplatelets (NPLs), is generally much more significant than on dye molecules. This triggered the systematic investigation of nanoscale, core/shell-type luminophores of different shell thicknesses, materials/composition and shapes before, during and after the PSMP synthesis (see Scholtz *et al.*, Correlating Semiconductor Nanoparticle Architecture and Applicability for the Controlled Encoding of Luminescent Polymer Microparticles, submitted to *Chemistry of Materials* (2023)). This investigation yielded important insights into the suitability of individual NPs for this synthesis, including the influence of NP anisotropy. The utilized characterization methods include fluorescence spectroscopy (emission intensity, fluorescence lifetime (FLT)), integrating sphere spectroscopy (photoluminescence quantum yield (PLQY)) and confocal laser scanning microscopy (CLSM). Luminescent NPs employed include CdSe/CdS-QDs, CdSe/ZnS-QDs, CdSe/CdS-quantum rod (QR), and CdSe/CdS-NPLs to cover a variety of

particle morphologies, while still ensuring sufficient comparability through choosing the same particle architecture (core/shell) and the same core material for all NPs.

The synthetic influence of PSMP surface functional groups (FGs) is also explored in this work (see Scholtz *et al.*, Influence of nanoparticle encapsulation and encoding on the surface chemistry of polymer carrier beads, *Scientific Reports* **13.1** (2023), p. 11957). To enable applications that require specific moieties binding to the PSMP surface, FGs such as carboxy groups must first be introduced. These FGs control the surface charge of the beads, thus also directly influencing their colloidal stability. The interaction with their environment, and accordingly with biological systems, depends significantly on the number and type of surface FG, which makes the synthetic control of this factor application relevant. The total and accessible amount of surface FGs can be influenced significantly by the exact synthesis route, directly influencing the PSMP suitability for potential applications.

The nanoscale equivalents of PSMPs, namely polystyrene nanoparticles (PSNPs), are also commonly employed, and are included in this work (see Srivastava *et al.*, Dual color pH probes made from silica and polystyrene nanoparticles and their performance in cell studies, *Scientific Reports* **13.1** (2023), p. 1321). Because of their smaller size, they are predominantly used for biochemical applications, e.g. in cell studies, as markers and sensor particles, for drug delivery, and as reporters in immuno assays. These particles can also be surface modified and provided with additional moieties, e.g. sensor dyes that detect changes in temperature, oxygen or pH. Thus, they can help with imaging different cell regions, or the monitoring of changes in the particle environment. This work includes the synthesis of PSNPs stained with the organic dye Nile Red (NR) and provided with a second, pH sensitive dye on the particle surface. The resulting PSNPs were employed for the selective staining and imaging of lysosomes in lung cancer cells with CLSM.



## 2 | Kurzzusammenfassung

Diese Arbeit konzentriert sich auf die systematische Untersuchung des Zusammenhangs zwischen der Morphologie von Halbleiter-Nanopartikeln (NPs), ihrer Lumineszenzeigenschaften und den anwendungsrelevanten Charakteristika von Polystyrol-Mikropartikeln (PMPs), die mit diesen NPs gefärbt wurden. Diese PMPs sind von großer Bedeutung für verschiedene Bereiche der Naturwissenschaften, da sie sowohl als Sensoren/Reporter oder Trägermaterialien zu medizinischen/diagnostischen Zwecken, als auch für Instrumentkalibrierungen und partikelbasierte Tests verwendet werden können. Die Lumineszenz wird dabei in Form von verschiedenen, anorganischen Halbleiter-NPs eingeführt und kann genutzt werden, um die resultierenden PMPs zu identifizieren und auszulesen (z.B. für Quantifizierung oder Lokalisierung). Dies wird mit optischen Methoden wie Fluoreszenzmikroskopie, Durchflusszytometrie und Fluoreszenzspektroskopie durchgeführt, was dazu führt, dass die PMPs als Kennzeichnung oder Träger für Barcodes verwendet werden können. Für diese Anwendungen ist es wichtig, präzise Kontrolle über die Lumineszenzeigenschaften und Oberflächenchemie der PMPs, und damit auch über die spektralen Eigenschaften der verwendeten NPs, zu haben. Sowohl die Lumineszenz als auch die Oberflächenchemie der PMPs beeinflussen direkt ihre Eignung für die spezifische Nutzung, z.B. über die Interaktion mit ihrer Umgebung oder ausreichende Signalintensität für das Auslesen der Fluoreszenz. Die Synthese von PMPs, mit oder ohne Luminophor, kann mit verschiedenen Methoden erreicht werden. Zu den üblichen Synthesansätzen zählen (Mini)Emulsions- und Suspensionspolymerisation, Mikrofluidik und Dispersionspolymerisation. Der letzte Ansatz wurde aufgrund der einfachen Durchführbarkeit, geringer Kosten und guter Reproduzierbarkeit für diese Arbeit gewählt.

Die Synthese von Quantenpunkt (QD)-gefärbten Polystyrol-Mikropartikeln (PSMPs) wurde zuerst für CdSe/CdS-QDs entwickelt und optimiert (siehe Scholtz *et al.*, Luminescence encoding of polymer microbeads with organic dyes and semiconductor quantum dots during polymerization, *Scientific Reports* **12.1** (2022), p. 12061). Neben nanoskaligen Luminophoren wie QDs werden auch molekulare Luminophore wie organische Farbstoffe bereits seit langem für die Synthese von PMPs verwendet. Während die Einbringung von Farbstoffen

vergleichsweise einfach und gut untersucht ist, treten bei der Verwendung von lumineszenten NPs Herausforderungen wie NP-Aggregation oder exzessiver Verlust der Fluoreszenzintensität auf. Allerdings bieten sie auch deutliche Vorteile gegenüber Farbstoffen, wie deutlich bessere Photostabilität oder ihre symmetrischen und schmalen Emissionsspektren. Halbleiter-NPs können üblicherweise von einem breiten Spektrum an Strahlung angeregt werden, da ihre Absorptionsspektren sehr breit sind. Dies ermöglicht die gleichzeitige Anregung von NPs mit unterschiedlichen Farben/Größen, Zusammensetzungen oder Formen. Diese Faktoren veranlassten die Entwicklung einer einfachen, aber effizienten und optimierten Synthese von NP-beladenen PSMPs, wobei die auftretenden Herausforderungen überwunden und eine ausreichende Lumineszenz der resultierenden Partikel für zukünftige Anwendungen erreicht wurden. Aufgetretene Herausforderungen beinhalten die signifikante Minderung der NP-Fluoreszenz, NP-Aggregation/Separierung während der Synthese kombiniert mit unzureichendem Einbau in die Polymermatrix, Ausbluten der NPs aus den fertigen Partikeln und eine sehr breite Größenverteilung der PSMPs.

Der Einbau von sowohl molekularen Luminophoren wie organischen Farbstoffen, als auch nanoskaligen Luminophoren wie QDs in Polymerpartikel kann über verschiedene Ansätze erreicht werden. Diese beinhalten eine Quellprozedur im Anschluss an die Synthese, die Schicht-für-Schicht-Methode (auch layer-by-layer (LbL)), und Zugabe vor/während der Polymerisationsprozedur. Die letzte Methode wurde in dieser Arbeit angewandt, da sie häufig bessere NP-Homogenität und sterischen Einbau in die Polymerpartikel ermöglicht, sowie die simultane Synthese einer großen Menge an PSMPs mit einer hohen Variabilität bezüglich Partikelgröße. Für verschiedene Arten von NPs ist eine Anpassung der Synthese möglich. Zudem kann der Syntheseweg eine sehr große Rolle für die Lumineszenzeigenschaften und Lage der NPs in den PMPs spielen, was in dieser Arbeit untersucht und bestätigt wurde.

Der Einfluss der Polymerisationsreaktion auf NPs wie QDs, oder noch mehr auf Nanoplättchen (NPLs), ist im Allgemeinen sehr viel signifikanter als auf Farbstoffmoleküle. Dies stieß eine systematische Untersuchung an, die sich mit nanoskaligen Kern/Schale-Luminophoren verschiedener Schalendicken, Materialien/Zusammensetzung und Form vor, während und nach der Synthese beschäftigt (siehe auch Scholtz *et al.*, Correlating Semiconductor Nanoparticle Architecture and Applicability for the Controlled Encoding of Luminescent Polymer Microparticles, eingereicht in *Chemistry of Materials* (2023)). Diese Untersuchung ergab wichtige Einsichten

in die Eignung von individuellen NPs für diese Synthese, auch bezüglich des Einflusses von NP-Anisotropie. Die angewandten Charakterisationsmethoden beinhalten Methoden wie Fluoreszenzspektroskopie (Emissionsintensität, Fluoreszenzlebensdauer (FLT)), Ulbricht-Kugelspektroskopie (Photolumineszenz-Quantenausbeute (PLQY)), und Konfokale Laser-Raster-Mikroskopie (CLSM). Verwendete, lumineszente NPs beinhalten CdSe/CdS-QDs, CdSe/ZnS-QDs, CdSe/CdS-QRs und CdSe/CdS-NPLs um eine breite Palette an Partikelmorphologien abzubilden, während die Vergleichbarkeit durch die gemeinsame Kern/Schale-Architektur und das gleiche Kernmaterial gewährleistet bleibt.

Der synthetische Einfluss von funktionellen Gruppen (FGs) auf der PSMP-Oberfläche wurde ebenfalls in dieser Arbeit untersucht (siehe auch Scholtz *et al.*, Influence of nanoparticle encapsulation and encoding on the surface chemistry of polymer carrier beads, *Scientific Reports* **13.1** (2023), p. 11957). Um Anwendungen zu ermöglichen, die die Anbindung von verschiedenen Einheiten an die Partikeloberfläche erfordern, müssen FGs wie Carboxylgruppen auf der Oberfläche der PSMPs angebracht werden. Diese FGs kontrollieren die Oberflächenladung der Partikel, und beeinflussen damit auch direkt ihre kolloidale Stabilität. Die Interaktion mit der Umgebung, und deshalb auch mit biologischen Systemen, hängt stark von der Anzahl und Art der FGs auf der Partikeloberfläche ab, weshalb synthetische Kontrolle über diesen Faktor von großer Bedeutung ist. Die totale und zugängliche Menge an FGs kann stark durch die exakte Syntheseroute beeinflusst werden, was wiederum direkten Einfluss auf die Eignung der PSMPs für potentielle Anwendungen hat.

Die nanoskaligen Äquivalente der PSMPs, genannt Polystyrolnanopartikel (PSNPs), werden ebenfalls allgemein verwendet und sind Teil dieser Arbeit (siehe auch Srivastava *et al.*, Dual color pH probes made from silica and polystyrene nanoparticles and their performance in cell studies, *Scientific Reports* **13.1** (2023), p. 1321). Durch ihre geringere Größe werden sie vorwiegend für biochemische Anwendungen genutzt, z.B. in Zellstudien, als Markierung und Sensorpartikel, zum Wirkstofftransport, und als Reporter in Immuntests. Diese Partikel können ebenfalls oberflächenmodifiziert und mit weiteren Gruppen/Einheiten versehen werden, z.B. Sensorfarbstoffe, die Unterschiede in Temperatur, Sauerstoff oder pH detektieren. Damit können sie helfen, verschiedene Zellregionen sichtbar zu machen, oder auch die Verfolgung von Änderungen im Umfeld der Partikel. Diese Arbeit beinhaltet die Synthese von

PSNPs beladen mit dem organischen Farbstoff Nilrot (NR) und versehen mit einem weiteren, pH-sensitiven Farbstoff auf der Partikeloberfläche. Die resultierenden PSNPs wurden für die selektive Einfärbung und das Sichtbarmachen von Lysosomen in Lungenkrebszellen mittels CLSM eingesetzt.

## 3 | Introduction

The theoretical chapter of this work is divided into three main topics. First, section 3.1 introduces PMPs and polymer nanoparticles (PNPs) with their intended applications and properties, as well as their possible synthesis procedures. The following section 3.2 is dedicated to luminescent semiconductor NPs, providing insights into semiconductor fundamentals and different particle compositions and shapes. Alongside the properties, applications and syntheses of the different NPs, a comparison with organic dyes as luminophores is provided. The last section 3.3 brings together the two preceding sections by addressing luminescent PMPs, comparing different synthesis routes and stating relevant properties for subsequent applications. Finally, section 3.4 combines all addressed topics to highlight the motivation for this work and the objectives resulting from it.

### 3.1 | Organic Polymer Microparticles (PMPs) and Polymerization Techniques

#### 3.1.1 | Introduction to PMPs

##### **Definition**

Synthetic microparticles generally cover a wide range of materials, including not only various polymers and silica, but also metals, glass and ceramics. By definition, they have sizes of 0.5–1000  $\mu\text{m}$ . Polymer microspheres are among the most commonly produced microparticles, and in addition to the "solid" polymer microspheres, there are also microcapsules with a "hollow core" in which solids, liquids or gases are encapsulated.<sup>[1]</sup>

The PMPs synthesized in this work have a spherical shape and consist of polystyrene, sometimes copolymerized with divinylbenzene (DVB), with a size of about 0.5–3  $\mu\text{m}$ . There are several possible approaches to the synthesis of such PMPs, which will be presented in the following subsections. This section focuses on PMPs as a class of materials, while specifically luminescent PSMPs will be discussed in section 3.3.

## **Applications**

PMPs are widely used materials in the life sciences. They are highly versatile in their own right and also offer the possibility of incorporating smaller entities such as luminophores or magnetic particles into the polymer matrices. This can present a number of advantages, such as protecting the incorporated material from environmental factors such as heat, UV irradiation, oxidation and extreme pH conditions.<sup>[1]</sup> It can also help to improve the general handling of the incorporated material, especially if it is (cyto)toxic. Most importantly, the addition of optically active components allows PMPs to be tracked with optical methods such as spectroscopy or microscopy. Luminescent PMPs, e.g., are valuable assets for sensing, imaging and labelling applications.<sup>[2-5]</sup> Luminescent NPs or molecular luminophores such as dyes can introduce identifiable labels such as barcodes to the PMPs, making them useful for bioanalytical and diagnostic studies. This topic will be discussed in more detail, specifically for luminescent PMPs, in section 3.3. The controlled release of drugs or other compounds from the polymer matrix is also possible with stained PMPs.<sup>[1]</sup> In addition, PMPs are industrially produced for use as texturing elements in coatings or paints, in adhesives, toners and cosmetics, for instrument calibration and for the production of packaging.<sup>[1,6]</sup>

PMPs differ in their design, which can be tuned to best suit a specific application. The reproducibility of the PMP synthesis is generally of high importance, particularly in terms of both particle composition and size distribution, as the application of the particles is only possible with defined properties.

## **Properties**

A major challenge of PMP synthesis is the reproducible production of particles with the same surface chemistry. Surface FGs influence the interaction of the PMPs with their environment, resulting in the surface charge, and together with particle size and concentration, determining the (colloidal) stability of PMPs.<sup>[7,8]</sup> Apart from the distance between individual particles in a dispersion, which can be influenced by changing the concentration, Coulomb and van der Waals forces play a critical role in colloidal particle stability.<sup>[7]</sup> Thus, the PMPs experience attractive and repulsive forces, which can be artificially influenced by introducing changes to the particle surface. If the attractive forces become too strong, this leads to particle aggregation, and sometimes accelerated sedimentation. To prevent (in the case of PNPs) or decelerate this process, the PMPs can be stabilized by introducing charged FGs (e.g., carboxy or amino

groups) to the particle surface, which leads to electrostatic repulsion. Another approach is to add long-chain ligands to the surface of the PMPs to create steric repulsion, which occurs when the electron clouds of the ligand atoms overlap due to close proximity. A combination of both methods for electrosteric stabilization is also possible.<sup>[8]</sup> Irrespective of surface modifications, very large PMPs will always experience sedimentation over time, depending on the dispersant, simply due to their size and mass. The surface chemistry and charge of the particles not only influence their colloidal stability, but also to a large extent their reactivity, biocompatibility and -particle distribution.<sup>[9]</sup> This is particularly important for biochemical applications, where surface FGs are required for the attachment of various moieties to the particle surface. Examples include dyes/sensors,<sup>[10,11]</sup> linker molecules,<sup>[12]</sup> biomolecules such as proteins,<sup>[13,14]</sup> probes such as ribonucleic acid (RNA) and deoxyribonucleic acid (DNA),<sup>[15]</sup> or even antifouling reagents.<sup>[16]</sup> This topic is discussed in more detail in subsection 3.3.4, including the introduction of the FGs to the particle surface.

As mentioned above, another important factor is the particle composition, e.g. the choice of the polymer matrix. PMPs made from natural polymers such as alginate, gelatin, cellulose or chitosan typically show varying degrees of synthesis reproducibility in terms of particle size and properties. Synthetic PMPs have a much better batch-to-batch reproducibility and purity, making them promising candidates for applications where bead uniformity is essential.<sup>[17]</sup> The polymers that form the PMPs can have a carbon-only main chain with possible heteroatoms in the side chains, including materials such as polystyrene (PS), poly(methyl methacrylate) (PMMA), polyacrylates or polyacrylamide.<sup>[17]</sup> A heteroatomic main chain is also possible with materials such as poly(lactides), poly(amino acids), and poly(caprolactones). Polymers with carbon-only main chains are generally more stable and do not degrade as easily.<sup>[18]</sup>

In addition to particle composition and surface chemistry/charge, size/size distribution, shape, number of particles per batch and optical properties are important factors to consider for potential applications of PMPs. As the particle size has a major influence on the physicochemical properties and biological behaviour of the PMPs, it is an aspect that needs to be controlled very precisely. This can be done by choosing a suitable synthesis method and polymer matrix, as described in section 3.1 (see also Table 1). The size not only has a direct influence on particle sedimentation rates and surface area, but also determines cell uptake efficiency and,

in general, how the particles interact with their environment.<sup>[9,19]</sup> Size distribution is similarly important, as many PMP properties are dependent on the particle size. For example, polydisperse PMP batches exhibit broadened emission bands, making it difficult to read out barcoded particles. In addition, the interaction with the particle environment, such as cell uptake, differs in polydisperse samples.

While most PMPs are spherical, it is also possible to synthesize them in different shapes such as rods, discs or fibres.<sup>[20,21]</sup> Like the particle size, the shape and porosity of PMPs also influence cell uptake and behaviour in biological systems.<sup>[20]</sup> The synthesis of non-spherical PMPs typically requires more complex approaches and/or templates for particle formation. The reproducibility of the PMP synthesis, taking into account all the aforementioned properties, is the most important characteristic to consider. This is particularly important for industrial production, and to provide reliable results in all areas of application. The application relevant optical properties of the PMPs are highly dependent on other particles and/or molecules added to the polymer, e.g. dyes or luminescent NPs bound to the PMP surface or embedded in the matrix. This topic is discussed in section 3.3.

## **Analytcs**

Typical analytical techniques used to investigate polymer particle size, size distribution and shape include dynamic light scattering (DLS),<sup>[22,23]</sup> FCM<sup>[24,25]</sup> and scanning electron microscopy (SEM)/transmission electron microscopy (TEM).<sup>[26,27]</sup> The Brunauer–Emmett–Teller (BET) method, size exclusion chromatography (also used for size selection), different porosimetry and porometry approaches, and even electron microscopy image analysis are commonly used for porosity determination.<sup>[28,29]</sup> For molecular weight determination, gel permeation chromatography/size exclusion chromatography (GPC/SEC),<sup>[30]</sup> matrix-assisted laser desorption/ionization time-of-flight mass spectrometry (MALDI-TOF MS),<sup>[31]</sup> viscometry<sup>[32]</sup> and <sup>1</sup>H-nuclear magnetic resonance (NMR) spectroscopy<sup>[33]</sup> are used. Examples of the methods used to analyze PMPs in this work are given in section 4.2.

### **3.1.2 | Overview of Polymerization Procedures**

Generally, heterogeneous/particle yielding polymerization procedures are carried out in two-phase systems, consisting at least of the chosen monomer or the formed polymer as one phase,

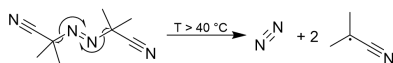
and an immiscible liquid (called polymerization medium in the following paragraphs) as the second phase.<sup>[34]</sup> The additionally needed initiator, often a free radical generator, can be soluble either in the monomer or the liquid polymerization medium, depending on the type of polymerization. This will be explained in more detail in the next subsections for the individual polymerization procedures. Apart from free-radical initiators, polymerizations can also be initiated thermally, or by irradiation (photopolymerization) or high pressure, depending on the monomer(s) and desired outcome. This work is focused on free radical polymerization, which will be explained in detail in the next paragraph. Normally, at least one surfactant is added to the mixture to emulsify the monomer and/or stabilize the forming polymer particles or monomer droplets.<sup>[34]</sup> Surfactant-free polymerization reactions are possible, but less common, e.g. for surfactant-free emulsion polymerization.<sup>[35]</sup>

The mechanism of a free-radical polymerization is depicted in Figure 1. This approach is widely applied and well studied. It can be used for a broad range of monomers and reaction conditions, with simple implementation and low costs compared to other, competing processes. It does, however, show limitations regarding the control over the molar weight distribution and macromolecular architecture of the generated polymer, as well as over copolymer composition.<sup>[36]</sup> The traditional free-radical mechanism can, however, be influenced, e.g., by addition of a chain-transfer agent to gain more control over the mentioned factors. Therefore, the so-called reversible addition-fragmentation chain-transfer (RAFT)-polymerization has been developed, with a thiocarbonylthio compound (e.g., thiocarbamates or dithioesters) as the chain-transfer, or RAFT, agent.<sup>[36,37]</sup> This is a robust and versatile process with the possibility of activation and deactivation of the polymer chain radicals, which enables good control over the molar ratio of copolymer components.

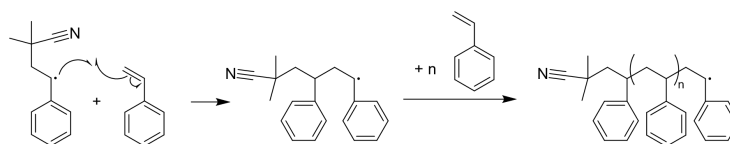
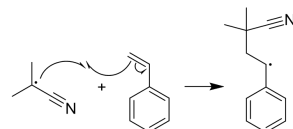
The three main variations of particle producing polymerization reactions are called emulsion, suspension and dispersion polymerization and will be described in the following subsections. They are distinguished by the particle formation mechanism, which largely depends on the solubility of the monomer(s), the radical starter, and the surfactant(s) employed in the synthesis. The accessible size range for polymer particles produced from these syntheses ranges from only 10 nm to several mm. The size and shape of the PMPs is influenced by different factors such as reaction temperature, stirring speed, and the amount of monomer(s), radical

starter and surfactant. The influence and its extent are different for the individual procedures and were investigated in more detail for the dispersion polymerization in this work .

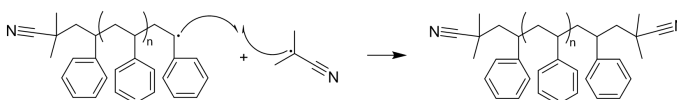
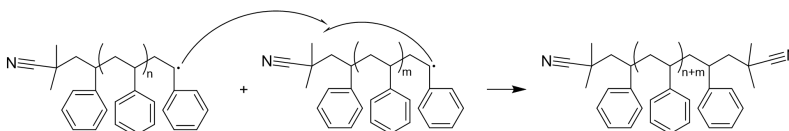
### a) Initiation



### b) Propagation



### c) Termination



### d) Chain Transfer



+ · monomer/polymer/solvent

Figure 1: Depiction of the mechanism of a free-radical polymerization, exemplary for the radical initiator azobisisobutyronitrile (AIBN) and the monomer styrene, with a) heat-induced initiation of the formation of two radicals from AIBN with the generation of nitrogen gas; b) polymer chain propagation and formation of a PS chain; c) termination by recombination of two PS chain radicals or a polymer chain and an AIBN radical; and d) transfer of the polymer chain reactivity to a monomer, polymer or solvent molecule.

To introduce surface FGs to the formed PMPs, an additional monomer with the desired functionality can be added when most of the initial polymer is depleted, usually toward the end of the polymerization reaction. The new monomer can now take part in the polymerization reaction, and is thus mostly found on the surface of the particles. This can significantly influence their surface chemistry and later ability to form bonds with different moieties. In addition, it is possible to add another monomer such as DVB to the reaction mixture to achieve crosslinking of the polymer network.

### 3.1.3 | Emulsion Polymerization

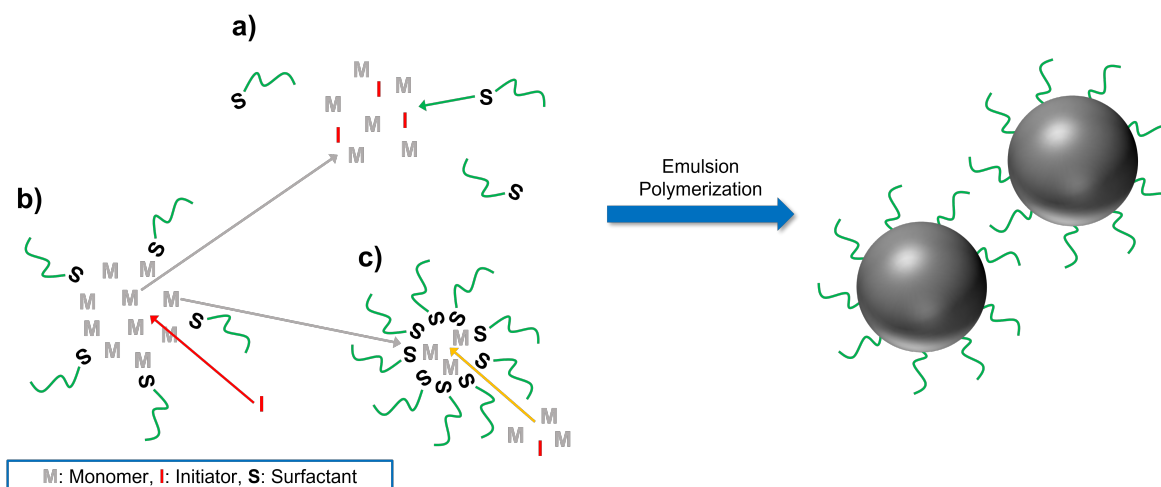


Figure 2: Schematic depiction of the emulsion polymerization process with monomer(s) insoluble and the initiator soluble in the polymerization medium, with a) primary particle nucleation directly from the polymerization medium; b) monomer droplets stabilized by surfactant molecules, acting mostly as suppliers of monomer; and c) surfactant micelles swollen with monomer as nucleation centers.

The most popular way to synthesize PMPs and PNPs is the radically initiated emulsion polymerization reaction. Here, the monomers are insoluble or poorly soluble in the employed polymerization medium, and monomer droplets are emulsified, usually into an aqueous solution of a surfactant, by applying shear forces (e.g., through stirring).<sup>[38]</sup> This yields an oil-in-water emulsion, with the monomer forming droplets with sizes of about 10  $\mu\text{m}$  that are stabilized by adsorbed surfactant molecules. In addition, surfactant micelles are formed with aggregates of around 50–100 molecules when the surfactant concentration is above the critical micelle concentration (CMC).<sup>[38]</sup> These micelles swell through absorption of monomer molecules to a size of about 10 nm. The monomer droplets and monomer-swollen micelles both serve as starting points for nucleation and polymer particle growth upon addition and activation of the water-soluble free-radical starter. In addition, polymer particles of about 50–500 nm are formed as intermediates through homogeneous nucleation from the residual monomer molecules in the aqueous phase.<sup>[38]</sup> Both the swollen micelles (if the concentration of surfactant is above the CMC) and the polymer particles contribute to the formation of the final polymer particles, while the initially formed monomer droplets play a minor role and mostly act as suppliers of monomer molecules.<sup>[38]</sup> The segregation of the polymer chains in

the small particles allows for high polymerization rates with simultaneously high molecular weight.<sup>[38]</sup> The emulsion polymerization process is schematically depicted in Figure 2.

The size and shape of the polymer particles are partly determined by the hydrophilic-lipophilic balance (HLB) value of the surfactant.<sup>[39]</sup> The HLB is defined as a measure for the balance of hydrophilic and lipophilic moieties of a surfactant molecule, which takes into account their size and strength. By increasing the surfactant concentration, the size of the micelles and thus, the size and number of formed particles can be influenced. Commonly produced polymers via this procedure include PS and PMMA, with mostly water-soluble initiators such as potassium persulfate (PPS). Emulsion polymerization is used for the synthesis of nonporous PMPs, as porosity is not readily achievable with this procedure. This is a result of the polymerization mechanism, where the initiation, chain growth and main monomer presence are all located at different places.<sup>[28]</sup>

There are two popular subtypes of the emulsion polymerization procedure. The first is the so-called miniemulsion polymerization, where the monomers are dispersed by strong mechanical agitation or homogenization into droplets of less than 0.5  $\mu\text{m}$  in size.<sup>[40]</sup> In addition to the usual ionic surfactant, a strongly hydrophobic co-surfactant/-stabilizer (e.g., a long-chain fatty alcohol such as cetyl alcohol) is introduced.<sup>[41]</sup> The large interfacial area between monomer droplets and polymerization medium, combined with a low concentration of surfactant (well below the CMC), leads to nearly complete adsorption of the surfactant to the monomer droplets. This prevents the formation of micelles.<sup>[38]</sup> Particles formed by homogeneous nucleation in the polymerization medium cannot be stabilized because of the low surfactant concentration, so they simply enter the monomer droplets and there, further take part in the polymerization reaction.<sup>[38]</sup> Therefore, the monomer droplets are the only source of particle nucleation. The nucleation occurs by a free radical migrating into the droplets. As usually only one free radical is present in each droplet, this segregation of propagating polymer chains from each other during the reaction enables very high molecular weights of over 1,000,000 g/mol.<sup>[38,40]</sup> In addition, the formed polymer beads are almost identical in size to the initial monomer droplets, enabling the synthesis of very small particles of 50-500 nm in size.<sup>[40]</sup> The size distribution of particles produced with emulsion polymerization is mostly influenced by the employed amount of initiator and stabilizer, with a higher amount of initiator and a lower amount of stabilizer leading to narrower distributions.<sup>[42]</sup> Diameters have been

reported to deviate between  $<1\%$  up to nearly 10%, which additionally depends on the reaction time.<sup>[43]</sup> Apart from free radical polymerization, also polycondensation and polyaddition procedures are possible with this method.<sup>[38]</sup>

The second popular subtype of emulsion polymerization is called microemulsion polymerization. It is performed by strongly increasing the amount of surfactant past the CMC to create micelles.<sup>[38]</sup> The thus formed microemulsion is thermodynamically stable, and all monomers are included in the formed micelles. The resulting particles are 10–100 nm in size, with the initiator being either soluble in the monomer or in the polymerization medium. This method is employed much less frequently than the miniemulsion polymerization, partly because the surfactant concentration has to be carefully adjusted to avoid the formation of a continuous network instead of discrete micelles.<sup>[38]</sup>

### 3.1.4 | Suspension Polymerization

Suspension polymerization is a procedure where the initiator is soluble in the monomer, and both the initiator and monomer are insoluble in the polymerization medium (often water). By adding a suitable surfactant and applying a mechanical shear force such as stirring, the monomer is dispersed in the polymerization medium in the form of small droplets.<sup>[34,38]</sup> This is schematically depicted in Figure 3.

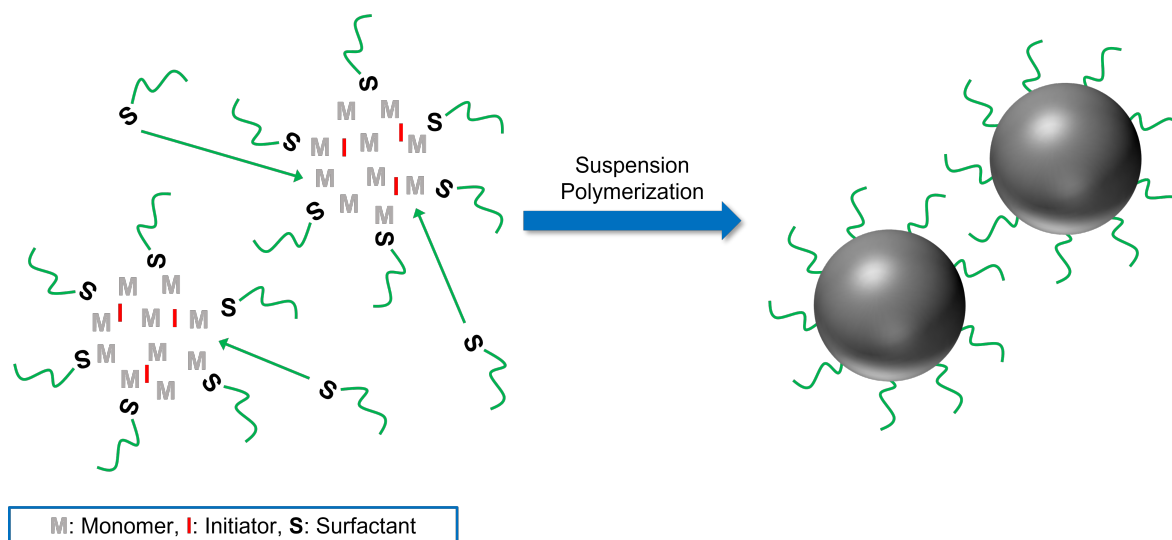


Figure 3: Schematic depiction of the suspension polymerization process, with the initiator soluble in the monomer, and both insoluble in the polymerization medium.

The shear forces, often assisted by a small amount of surfactant, lead to the formation of an emulsion that can either be oil-in-water or water-in-oil, depending on the chosen monomer/polymer. The suspension only forms when the reaction is initiated, with the monomer droplets acting as points of nucleation and PMP growth, the forming polymer being insoluble in the reaction medium and suspended in it with the help of surfactant molecules. The monomer soluble initiator is what separates suspension from emulsion polymerization, effectively changing the place of initiation, and thus the whole mechanism of the polymerization.<sup>[28]</sup> The reaction kinetics are assumed to be similar to bulk or solution polymerization. The monomer droplets act as individual microreactors with little to no exchange of monomer and no solvent present at the site of polymerization.<sup>[34,38]</sup> Like for the miniemulsion polymerization, the monomer droplet size is almost identical to that of the formed polymer particles, producing beads with sizes of about 10  $\mu\text{m}$  to 2 mm.<sup>[34,38]</sup> This leads to very high conversion rates of monomer to polymer up to roughly 100 %. By lowering the amount of surfactant, the interfacial tension and thus, the size of the monomer droplets (and the resulting polymer particles) can be decreased.<sup>[38,44]</sup>

A variety of monomers can be converted to PMPs with a suspension polymerization. Industrially important materials include PS, poly(vinyl chloride) (PVC), polyacrylates and polyacetates, polyacrylamide, but also natural gums.<sup>[34]</sup> A typical initiator for oil-in-water suspension is AIBN, enabling the performance of the reaction between 50 °C–100 °C. As a surfactant, polyvinylpyrrolidone (PVP) is commonly employed. In contrast, water-in-oil suspensions are performed at 20 °C–50 °C with a water-soluble initiator such as PPS, and cellulose or amphiphilic oligomer surfactants.<sup>[34]</sup> Classic suspension polymerization yields nonporous PMPs, but the procedure can readily be modified with the addition of a porogen (e.g., crosslinkers, a nonsolvent or linear polymers) to create beads with differing porosity.<sup>[28]</sup>

### 3.1.5 | Dispersion Polymerization

The dispersion polymerization, which was employed in this work, is a common method for the synthesis of polymer microspheres in a single batch process.<sup>[6]</sup> Monodisperse polymer particles in the low micrometer size range were originally difficult to produce, as conventional emulsion polymerization only produces polymer spheres with sizes of  $<1 \mu\text{m}$ , and suspension polymerization yields particles with sizes of  $>5 \mu\text{m}$ . While it is possible to use emulsion polymerization in a seeded growth approach to produce polymer beads of a few micrometers in

size, this is much more time-consuming than a single batch synthesis.<sup>[6]</sup> This prompted the investigation of dispersion polymerization reactions as an alternative. Also, the monodispersity of particles produced with a dispersion polymerization is typically much better than that of particles synthesized by classical emulsion and suspension polymerization procedures.<sup>[45]</sup>

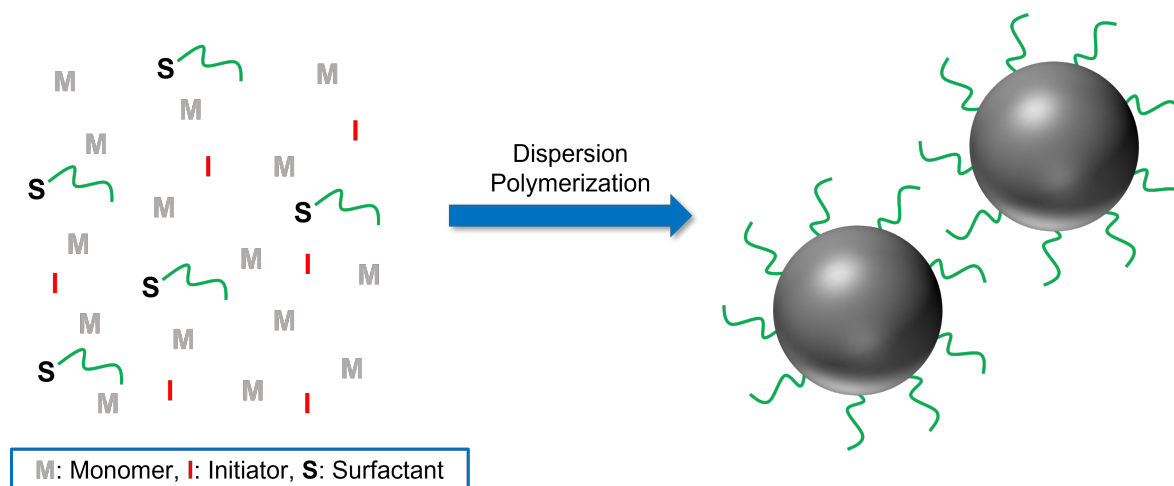


Figure 4: Schematic depiction of the dispersion polymerization process, with both initiator and monomer soluble in the polymerization medium.

The dispersion polymerization starts from a homogeneous solution of the monomer(s), the initiator and surfactant(s) in the polymerization medium. It can be distinguished from an emulsion and a suspension polymerization through the good solubility of the monomer in the employed polymerization medium, which changes to insolubility and precipitation of the formed polymer particles. Because of this, dispersion polymerization is considered a variety of precipitation polymerization. The growing, insoluble polymer beads are then stabilized by the surfactant(s), as depicted in Figure 4. The amount of surfactant has to be carefully adjusted to enable sufficient particle stabilization, but avoid micelle formation to prevent the development of an emulsion when exceeding the CMC. Typical polymer matrices produced with this method include PS, PMMA and polymethacrylates, the resulting PMPs and PNPs often being stabilized with PVP.<sup>[6]</sup> The reaction is performed between 50 °C–100 °C, similar to a suspension polymerization, and depends on the employed initiator (often AIBN). Dispersion polymerization yields mostly nonporous and non-crosslinked PMPs, although crosslinking, and thus porosity, is possible to a limited degree.<sup>[28]</sup>

### **3.1.6 | Microfluidic Approaches**

For certain applications, it is of high importance that the synthesized PMPs have a high reproducibility in terms of size, structure and staining efficiency.<sup>[46,47]</sup> For this reason, droplet microfluidic approaches have been developed for the emulsion-based synthesis of highly uniform PMPs. The microfluidic devices create monomer droplet emulsions from streams of immiscible fluids, which can be tuned by factors such as fluid ratios, flow speed, and order of emulsion (e.g., oil-in-water-in-oil is considered a double emulsion/second order).<sup>[46]</sup> This method is very versatile and offers a high degree of control over particle size, shape and porosity, enabling the synthesis of complex particle architectures, also of non-spherical shape.<sup>[47]</sup> Drawbacks include very low production rates, which are difficult to increase because of the reactor setups.<sup>[46]</sup> It is also quite complex, time-consuming and takes specific expertise to develop a working and calibrated droplet-based microfluidic system. Microfluidic devices are available commercially, but require a high degree of customization and research to create working systems for the synthesis of PMPs. This is why, up until now, this method is mainly used for the laboratory-scale synthesis of highly monodisperse and complex PMPs, e.g. for the use as drug delivery agents with controlled release properties, or for non-spherical particles.<sup>[46]</sup>

### **3.1.7 | Comparison of Polymerization Procedures**

In Table 1, the properties of the PMPs resulting from the above described polymerization procedures are summarized and compared to give an overview of the achievable results.

Table 1.: Comparison of commonly employed polymerization techniques, created with data from Chaudhary *et al.* and Dendukuri *et al.*, [45,47]

Polymerization procedure	Emulsion	Suspension	Dispersion	Droplet-based microfluidics
Solubility in polymerization medium	Monomer insoluble, initiator soluble	Monomer and initiator insoluble	Monomer and initiator soluble	Monomer insoluble, initiator soluble
Use of surfactant	Typically above the CMC; well below CMC for mini	Little to no surfactant, to prevent formation of emulsion	Little surfactant, to stabilize particles but not form emulsion	High amount to form emulsion
Particle size / $\mu\text{m}$	0.06–0.8; 0.05–0.5 for mini	10–2000	0.1–20	7–1000
Particle size dispersion	Polydisperse	Polydisperse	Monodisperse	Very monodisperse
Porosity	Mostly nonporous	Varying degrees of porosity	Mostly nonporous	Highly porous to nonporous
Molecular weight	High; very high (>1,000,000) for mini	Very high	Medium-high	Usually high, variable
Example materials	PS, PMMA	PS, PVC, poly(vinyl alcohol) (PVA)	PS, PMMA	PS, polyacrylates
Complexity	Facile	Facile	Facile	Complex
Cost	Typically low, but can be high	Low	Low	Low to moderate

## 3.2 | Luminescent Semiconductor Nanoparticles (NPs)

If at least one dimension of a material is between 1–100 nm in size, it is considered a nanomaterial. This is consistent with the updated definition of a nanomaterial recommended by the European Commission.<sup>[48]</sup> Based upon the matrix material, nanomaterials (referred to here as NPs) are divided into different classes such as inorganic (e.g., semiconductors or metals), organic (e.g., polymers, carbon structures and liposomes) and hybrid materials. NPs can be synthesized in various shapes, e.g., from spherical, over rod-shaped, to cubic, triangle, and hexagonal shapes, as well as core and core/shell materials, consisting of a single material or presenting heterostructures consisting of different materials. This will be exemplarily discussed for thesis-relevant semiconductor NPs in subsection 3.2.1, including an introduction of different semiconductor NP heterostructures such as semiconductor core/shell QDs, QRs, and NPLs. Due to their small size, NPs exhibit properties that are not displayed by the respective bulk materials. They have an exceptionally high surface-to-volume-ratio, which can contribute to a higher reactivity, and can display unique optical and electrical, but also thermal, magnetic and mechanical properties, depending on the NP material.<sup>[49]</sup> The versatility concerning material(s), chemical composition, particle architectures, and functional properties renders NPs a very attractive class of materials for a broad range of (potential) applications in life and material sciences.<sup>[50]</sup> Examples for specific applications will be discussed in subsection 3.2.1 for semiconductor NPs.

For a nanomaterial such as a semiconductor QDs, size effects can arise that result purely from quantum mechanical effects (so-called quantum size effects), yielding optical, electronic, and catalytic properties that are distinctly different from those of the respective bulk material.<sup>[51]</sup> In semiconductor NPs, confinement of the charge carriers (electrons and holes) occurs if at least one particle dimension is less than 10 nm in size, leading to a change in, e.g., the optical properties and band structure, which opens up new features, functionalities, and applications for the resulting nanomaterials.<sup>[52]</sup> To explain this effect, the surface of a NP can be regarded as a potential barrier that effectively confines charge carriers, generated e.g., upon light absorption by the material in the NP. According to the model of the particle in the box, the energy of such a confined electron increases with decreasing size of the box, which is equivalent to the particle diameter in this case. With decreasing particle size, the energy levels start to split and become increasingly more discrete. Hence, the importance of quantum

size effects increases for smaller particles, revealing larger bandgaps.<sup>[52]</sup> This effect is called size quantization and is depicted schematically in Figure 5. The displayed energy diagram shows the valence and conduction band of a semiconductor with decreasing size, including the decrease in energy level density and the simultaneously increased bandgap. This quantum size effect accounts for the unique properties of semiconductor NPs that are distinct from those of the bulk material as well as from the respective molecules or atoms.<sup>[53,54]</sup> The size of the bandgap and the energetic positions of the valence and conduction band are very important for the optical, electrochemical, and catalytic properties of the NPs, as this defines the chemical potential of a semiconductor and determines the energy that can be absorbed or released by the material.

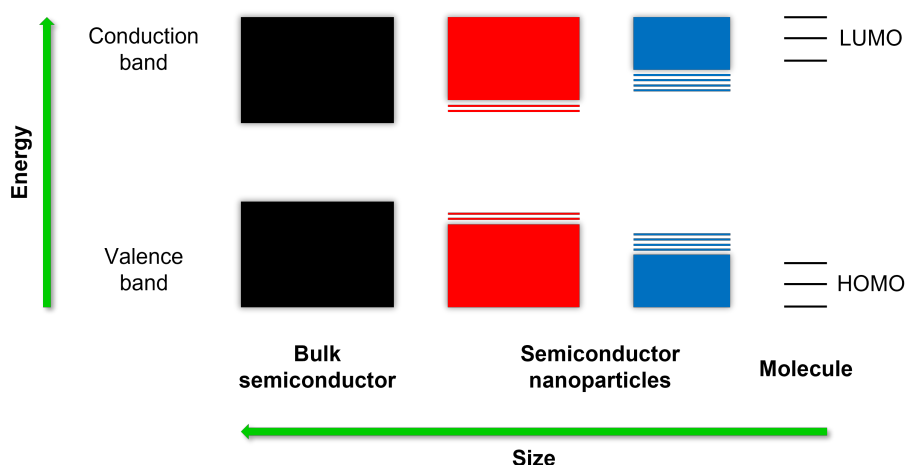


Figure 5: Size quantization effect, displayed schematically for the band structure of a semiconductor. Included are also the highest occupied molecular orbital (HOMO) and lowest unoccupied molecular orbital (LUMO) of a molecular system.

In the case of semiconductor NPs, the illumination with light of a higher energy than the respective bandgap leads to the excitation of an electron ( $e^-$ , negative) from the valence to the conduction band, creating a respective hole ( $h^+$ , positive) in the valence band. Both charge carriers are attracted by Coulomb forces, which leads to a bound state of electron and hole. This electrically neutral quasiparticle with a (restricted) mobility is called exciton. The distance between both charge carriers of an exciton is referred to as the Bohr radius. The effective masses of both electron and hole are influenced by the type and size of the semiconductor material.

The radiative recombination of the excited electron and hole pair, leading to the emission of a photon, is called photoluminescence. Due to the size quantization effect, not only the optical

bandgap and the onset of absorption are shifted to higher energies for smaller particles/a larger bandgap, but also the emission is hypsochromically shifted. This demonstrates how the optical properties of such semiconductor NPs can be tuned by changing their size and shape through synthetic strategies providing control over these properties. Such strategies have been developed for different NPs consisting of, e.g., II/VI, III/V and IV/VI semiconductors.<sup>[52]</sup> The wavelength of the emitted photons, and thus the emission color, are not only influenced by particle size, but also by the NP shape and environment. The NP core material and the material and thickness of the inorganic surface passivation shell also play a major role for the NP luminescence. Such shells are commonly utilized to block trap sites on the core surface for charge carriers, they are described in the following subsections.

The lifetime of the exciton is dependent on the material and the presence of trap sites within the NP bandgap, that can act as binding sites for electrons and/or holes. Such trap or defect states can delay the radiative recombination of the charge carriers and its probability. Trap states are typically created through defects in the semiconductor material, like lattice vacancies or inclusions, especially at the particle surface.<sup>[55]</sup> To prevent or at least minimize the number of defect states at the NP surface, semiconductor NPs are commonly surface passivated. A surface passivation is achieved by forming an inorganic shell of a different semiconductor material with larger bandgap around the particles. This can effectively saturate a high number of interface trap states and improve the photoluminescence (PL) properties of the NPs, reducing or blocking a long lived broad defect state emission and giving rise to the desired narrow and symmetric bandgap luminescence of high PLQY.<sup>[56]</sup> Additionally, a layer of organic surface ligands is coordinatively bound to the particle surface to ensure a good dispersibility and colloidal stability of the core and core/shell NPs. As detailed in the next subsection, the surface passivation and the ligand shell have a significant influence on the optical properties of the NPs by decreasing the influence of the particle environment. In the following subsection, the optical properties of different semiconductor (hetero)structures will also be discussed.

### **3.2.1 | Semiconductor NP Architectures**

Depending on the number of confined dimensions, different NPs are distinguished: QDs are spherical, and thus confined in three dimensions, while QRs are confined in two and quantum wells only in one dimension. The colloidal equivalent of quantum wells are called NPLs. Here,

the exciton Bohr radius comes into play, which is between 1–10 nm for most materials. In this subsection, three different variants of semiconductor NPs with varying dimensionality are discussed in more detail to highlight their differences and importance. In Figure 6, the QDs, QRs and NPLs that were employed in this work are displayed to highlight their different structures and compositions.

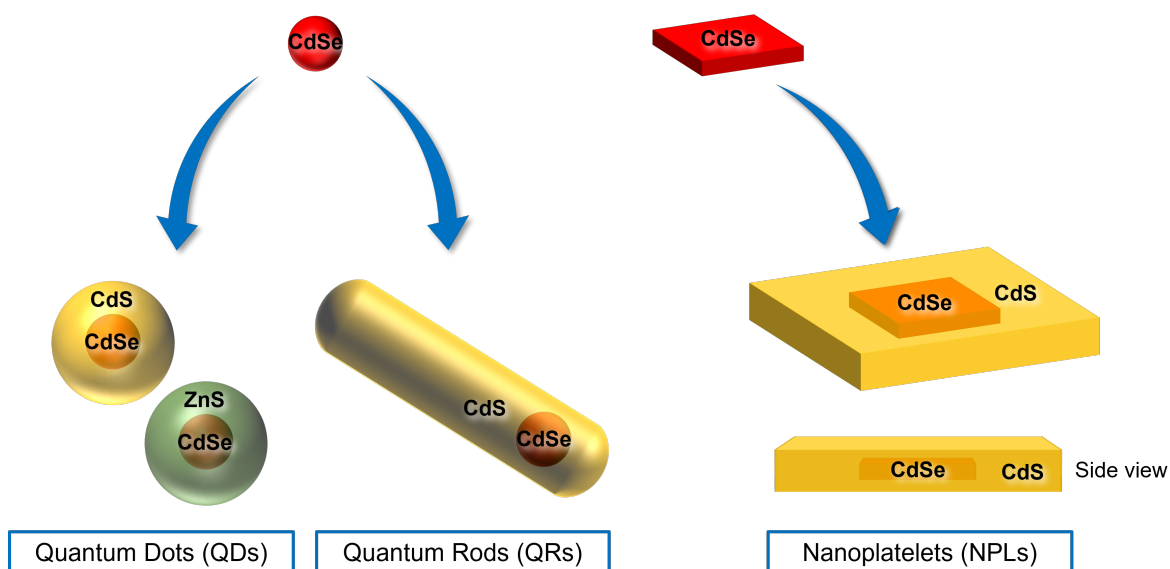


Figure 6: Different NP shapes and compositions, with core/shell-QDs, dot-in-rod-QRs and core/shell-NPLs, schematically displayed for the particle compositions employed in this work.

While the size quantization effect comes into effect for all three dimensions concerning QDs, this is not the case for the other NPs. As QRs are elongated in one dimension, the size quantization only comes into effect for the other two dimension, and the 2D-NPLs are only affected in one dimension. The specific (optical) properties of the individual NPs, which are affected significantly by their shape, are discussed in the following paragraphs.

## Quantum Dots (QDs)

### Optical Properties and Applications

Typically, spherical semiconductor nanocrystals with sizes of <10 nm are called QDs. They often have a core/shell particle architecture (see Figure 6) and are stabilized with an (organic) ligand layer. Commonly employed materials for QD synthesis are II/VI, III/V and IV/VI semiconductors. They exhibit broad absorption spectra and narrow, symmetric emission bands with a low full width at half maximum (FWHM). Together with a relatively

high photostability exhibited by most of these materials, these properties have led to their employment in various fields of application over the last decades. To name some of their many applications, QDs are used for bioanalytical and bioimaging studies (e.g., labeling and imaging, particle-based assays),<sup>[3,4,57–61]</sup> in photonic and electronic applications such as light-emitting diodes (LEDs)<sup>[62]</sup> and photovoltaics,<sup>[63]</sup> and as photocatalysts.<sup>[61,64]</sup> While the first QDs were composed of Cd-based semiconductors such as CdSe and/or CdS, the recent development focuses on less toxic, heavy-metal free materials such as InP,<sup>[65]</sup> Ag<sub>2</sub>S<sup>[66]</sup> and ternary QDs,<sup>[60]</sup> but also carbon- and silicon-based particles.<sup>[61,67,68]</sup> However, Cd-based QDs are still widely employed, e.g., due to their good PL properties, including a high PLQY. As the synthesis of these QDs is well researched, it is easily reproducible and a precise and extensive tunability regarding size and optical/electronic properties is possible.<sup>[69]</sup>

### **QD Heterostructures**

The combination of different semiconductor materials to create a heterostructure in one particle is very common to optimize NP functional properties, such as their PL and performance in applications. Three types of QDs can be distinguished, depending on the band structure of the employed materials, and thus the (de)localization of the charge carriers created upon energy input (exciton) throughout the heterostructure.<sup>[54]</sup> In the case of two-material QDs such as depicted in Figure 7, type I heterostructures consist of a core material with a smaller bandgap than that of the shell material. The band edges of the core material are located in the bandgap of the shell material, which leads to electron and hole localization in the core. For type II structures, the bandgaps of core and shell are aligned in such a way that it is energetically favorable for one of the charge carriers to remain in the core, and for the other in the shell material. The quasi-type II can be considered as a combination of type I and II, as only one charge carrier is localized either in the core or in the shell, depending on the combined semiconductor materials. For CdSe/CdS-QDs, this means the hole is localized in the CdSe core.<sup>[70]</sup> The energetic difference between a localization in the core or shell is very low for the other charge carrier. Thus, it is delocalized over the whole core/shell-structure. While type I and quasi-type II heterostructures generally exhibit better PL properties, the charge separation in type II heterostructures is favorable for applications such as (photo)catalysis and photovoltaics.<sup>[71,72]</sup>

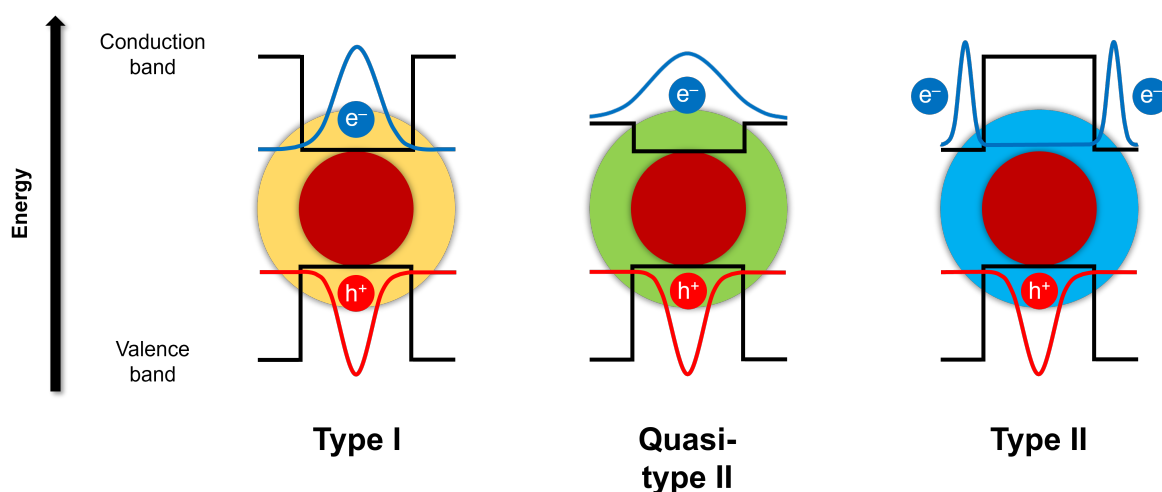


Figure 7: Schematic representation of the three semiconductor heterostructure types with band structures and charge carrier probability densities, exemplarily shown for QDs. The localization for type II can be reversed, i.e. the hole can be localized in the shell and the electron in the core, depending on the respective materials.

### Synthesis Approaches

Semiconductor QDs are commonly synthesized by wet-chemical processes such as colloidal, hydrothermal or microwave-assisted syntheses.<sup>[71]</sup> Other possible synthesis methods include self-assembly (e.g., through application of strain or external electrodes), selective area epitaxy or growth on vicinal substrates.<sup>[72]</sup> In this work, the focus is set on colloidal QD synthesis.

Two of the most commonly employed colloidal synthesis approaches for QDs are the *hot-injection* method and the *heat-up* method. The *hot-injection* method was first published by Murray *et al.* in 1993,<sup>[73]</sup> and exploits the principle of supersaturation: Only one precursor is present during the heating period, and the other is added at high temperatures. This rapidly cools down the reaction mixture, which leads to critical supersaturation and formation of seed crystals, which are created as long as the supersaturation is critical. Then, the seed crystals grow until the solution has reached the saturation concentration.<sup>[74]</sup> As this leads to very monodisperse particles if the nucleation period is kept short, this method has evolved to be the most popular one for QDs. The *heat-up* method is often more straightforward, as usually all reactands are combined before the synthesis, before the mixture is heated and the precursors start to decompose. The resulting monomers form seed crystals, and eventually grow to the final QD size. To colloiddally stabilize the forming QDs, organic ligand molecules are present during both types of reactions, sometimes simultaneously acting as solvents.

For the typically performed shelling of the semiconductor core particle with a surface passivation consisting of another semiconductor, different approaches can be utilized that vary in complexity. For dispersed QDs, it is possible to add a new precursor to a heated dispersion of the core particles. This is either performed via a step-by-step addition of the precursor for a layer-by-layer buildup of the shell, or continuously, slow and highly diluted. In both approaches, the precursors are decomposed and form the shell around the core particles. The step-by-step addition offers precise control over the thickness and its size distribution, but the added amount of precursor for a new shell layer has to be calculated and the shell growth performed individually, which can be quite time-consuming.<sup>[75]</sup> The continuous, slow addition over a longer time frame at low precursor concentration enable the synthesis of thicker shells in only one step, but a subsequent tempering step is needed. During the tempering, the crystal structure of the shell material is reorganized, leading to spherical QDs. The formation of an alloy between core and shell material through intramolecular diffusion is possible with this method. This can be an advantage, as it helps to anneal crystal defects and can significantly improve the luminescence properties of the QDs.<sup>[76]</sup>

The thickness of the QD shell has a significant impact on their optical properties, as the charge carrier transfer rates increase with increasing shell thickness.<sup>[77]</sup> In addition, the strain put on the QD core increases with increasing shell thickness, causing stress and the formation of crystal defects that act as trap sites. Combined, these phenomena lead to longer exciton lifetimes, and thus slower decay kinetics for QDs with a large shell, but also to a reduced PLQY because of an increase in nonradiative relaxation. Due to this, the shell thickness of a QD is typically chosen and adjusted specifically for an intended applications to meet its specific needs.

### **Quantum Rods (QRs)**

QRs, also called nanorods, are an example of anisotropic (semiconductor) nanoparticles with unique optical properties that gained interest in the 1990s.<sup>[78]</sup> They can easily be assembled into (macro)structures, and often even show self-assembly, which makes them promising candidates for the formation of, e.g. macroscopic aerogels with the optical properties of the nanomaterial retained.<sup>[79]</sup> Similar to QDs, there are different types of band alignments depending on the QR composition, which are displayed schematically in Figure 8.

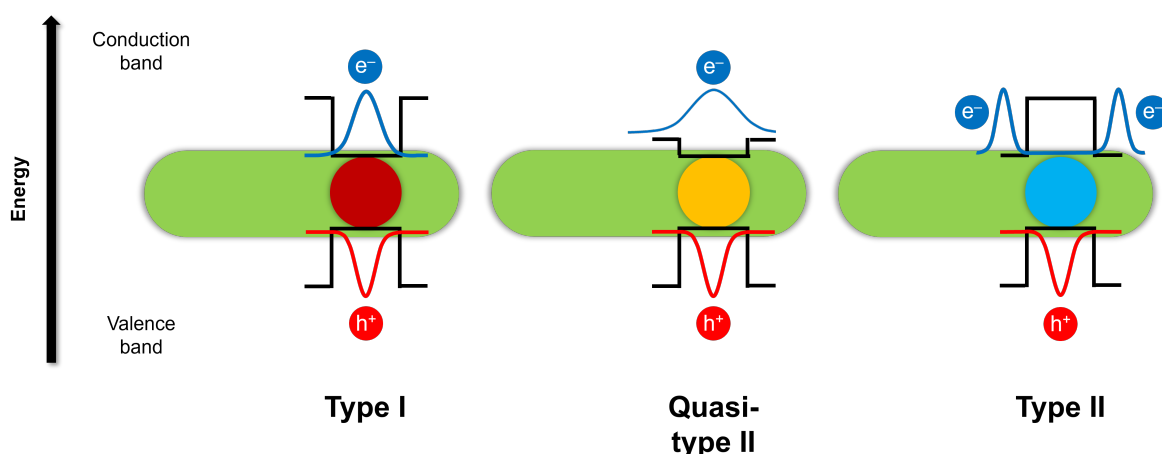


Figure 8: Schematic representation of the semiconductor QR heterostructure types with band structures and charge carrier probability densities.

Semiconductor QRs are commonly prepared by synthesizing a QD as the core, and then growing the cylindrical shell around it in a so-called seeded growth approach. The choice of surfactants/ligands is of utmost importance for the anisotropic growth of the particles.<sup>[79]</sup> The anisotropy is, in this case, mainly controlled by the chosen surfactants present during the synthesis, which show varying binding energies to the different crystal faces of the forming nanoparticle. This encourages growth in the direction of crystal faces with a weaker bond to the surfactant molecules, allowing for shape tunability through the choice of surfactant.

A common property of all heterostructures with a rod-shaped shell is the difference in dimensions between the core and the surrounding rod, which exhibits a much larger volume than the core. This leads to the optoelectronic properties largely depending on the rod/shell material, with the aspect ratio (length divided by width) of the QR being used as a measure for this influence.<sup>[80]</sup> As the length of the rod can be tuned by changing synthesis parameters, there is a high variability regarding QR emission maxima. Anisotropic semiconductor NPs such as QRs are particularly useful for applications such as lasers, LEDs and solar cells, where polarized emission is needed.<sup>[80]</sup> Combined with their high extinction coefficient, this makes them promising candidates for non-linear optical applications.

### Nanoplatelets (NPLs)

Luminescent nanoplatelets (NPLs) are a relatively new class of luminescent semiconductor NPs, and can be produced in their colloidal form since 2008.<sup>[81]</sup> As the thickness can be controlled atomically precise in the range of a few nm, the quantum confinement in this direction

is strong. This leads to very narrow emission bands that are only marginally influenced by the lateral dimensions of the NPL.<sup>[81,82]</sup> Due to the very high tunability of their thickness, NPLs offer unique electrical and optical properties and have gained a lot of interest over the last two decades.<sup>[82]</sup> As for QDs, the introduction of an additional semiconductor material, e.g., as a shell or crown around the particle core, can strongly influence and enhance the NPL optical properties. If the second material is only added laterally, core/crown-NPLs are created without affecting the particle thickness. If the growth is proceeding in all directions, this results in the formation of core/shell-NPLs. The type of shell growth can significantly influence the type of heterostructure created. For example, in the case of CdSe/CdS heterostructures, core/crown-NPLs present type I structures (due to the high electron binding energy),<sup>[83]</sup> while core/shell-NPLs present as quasi-type II (reduced confinement; comparable to CdSe/CdS-QDs).<sup>[84]</sup> This opens up even more opportunities for the tuning of the optical properties than QD structures. Examples for NPL heterostructures are exemplarily displayed in Figure 9.

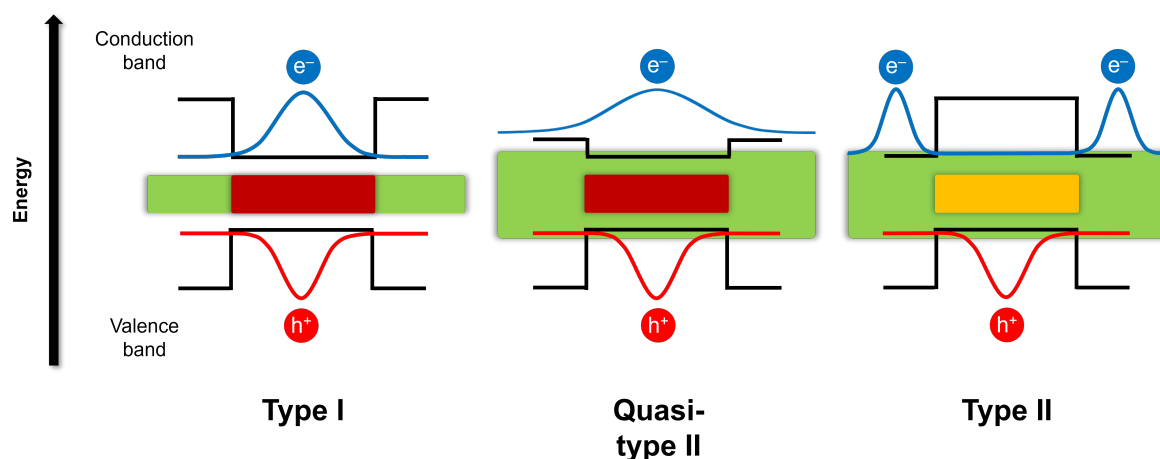


Figure 9: Schematic representation of the three semiconductor NPL heterostructure types with band structures and charge carrier probability densities, type I and quasi-type II exemplarily displayed for CdSe/CdS-NPLs.

Additionally, the type of heterostructure has a significant influence on the NPL stability against changes in particle environment. This is why a core/crown-architecture, where the CdSe core is better protected, was chosen for this work. Also, the surface ligands are highly important for the NPL properties because of the high surface-to-volume ratio.<sup>[85]</sup> The influence of the ligand shell is even more pronounced than for QDs. Like QRs, NPLs tend to self-

---

assemble and can form stacked (macro)structures,<sup>[86]</sup> and as another class of anisotropic NPs with polarized emission, can similarly be employed for non-linear optics.

## 3.3 | Luminescent PMPs

### 3.3.1 | Applications and Properties

Luminescent PMPs, like PNPs, are widely employed and well studied materials. The particles are stained with different luminophores, which can be molecular such as organic dyes, or nanoscale such as semiconductor or lanthanide-based NPs.<sup>[26]</sup> They are frequently used for instrument calibration, but also as sensor/reporter particles,<sup>[2]</sup> e.g. for bioimaging,<sup>[3]</sup> and as labels in bioanalytical and medical/diagnostic applications.<sup>[4,5]</sup> This includes the usage as carriers for bead-based assays, e.g. for biomarker detection or DNA sequencing,<sup>[15]</sup> but also sensing of biomolecular interactions<sup>[87,88]</sup> or as drug carriers. With their ability to be encoded with several luminophores in specific ratios,<sup>[89,90]</sup> PMPs can be employed for color multiplexing and, e.g. be read out by a flow cytometer or with fluorescence spectroscopy/microscopy.<sup>[24,91–93]</sup> When combined with magnetic NPs (e.g. iron oxide), the (luminescent) PMPs can be employed for immuno-separation.<sup>[92,94,95]</sup> In addition, both PMPs and PNPs can be used for anti-counterfeiting and as security/authentication labels.<sup>[89,90,96]</sup> For all applications, the surface chemistry of the beads is of high importance for the binding of antibodies, proteins or analyte-responsive dyes to the PMP surface.

Especially for luminescent PMPs, the optical properties of the particles are of high importance. Luminescence properties such as emission intensity, maximum ( $\lambda_m$ ) and the FWHM of the band, but also fluorescence lifetime and the corresponding PL decay kinetics, or the PLQY can serve as easily detectable particle characteristics. This enables the study of biological interactions when the PMPs are stained with organic dyes or luminescent NPs. Through the choice of the luminophore and staining procedure, these properties can be tuned to a certain degree, which is explained in the following subsection in more detail.

### 3.3.2 | Luminophore Staining Methods

#### Staining During Polymerization

The staining procedure during the polymerization reaction, which was utilized in this work, is among the most common preparation routes for luminophore-stained PMPs. It is suitable for both organic dyes<sup>[97–100]</sup> and luminescent NPs,<sup>[22,101–108]</sup> with the luminophore dissolved or dispersed in the monomer and the incorporation performed during the polymerization procedure. It can provide a homogeneous luminophore distribution, especially for larger PMP, but requires luminophore stability against the reaction conditions (presence of radicals, elevated temperature etc.) and a sufficient solubility/dispersibility in the polymerization mixture.<sup>[109]</sup> This approach enables a comparatively simple, one-step synthesis for PMP staining, but often goes along with a loss in fluorescence intensity and PLQY for the staining with semiconductor NPs.<sup>[22]</sup> Despite its limitations, this approach has been employed for a large variety of hydrophobic dyes and different NPs.<sup>[22,27]</sup> Mostly, Cd-based NPs such as CdSe-, CdTe- or CdSe/ZnS-QDs stabilized with trioctylphosphine (TOP)/trioctylphosphine oxide (TOPO) ligands are employed and stained into PMPs of different compositions. Commonly used materials include PS, with or without crosslinking, e.g. with DVB or PMMA,<sup>[13,22,26,27,101–108,110–115]</sup> poly(lactic-co-glycolic acid) and polyisoprene.<sup>[116–119]</sup> The beads are often synthesized by (mini)emulsion, dispersion or suspension polymerization,<sup>[13,101–108,111,113,114,120]</sup> mostly depending on the desired bead size, with more complex microfluidic approaches increasing in importance.<sup>[121–125]</sup> A polymerizable ligand is occasionally added onto the NP surface to enhance the polymer compatibility and improve incorporation into the PMPs.<sup>[22,26,27,110,112]</sup> However, no systematic studies have been performed yet to correlate the PL of the initial semiconductor NPs with those of the bead-encapsulated NPs. This is crucial to identify optimal NP structures and reaction parameters to preserve the initial luminescence features of the NPs. In this work, the utilized NPs for the staining of PMPs were successfully expanded from spherical QDs to other NP shapes, namely QRs and NPLs. Apart from the different shapes, the NP composition was also varied by introducing two different shell materials for the core/shell-QDs (CdSe and ZnS, respectively - see subsection 5.1.3).<sup>[27]</sup> This opens up new possibilities regarding potential applications of luminescent PMPs, as NPs with different composition and shape can introduce additional or improved (optical) features to this material class. Those include even narrower emission bands, more efficient energy transfer and the access to more colors with a high brightness.<sup>[126]</sup>

## Post-synthetic Swelling

The post-synthetic swelling approach to PMP staining with dyes or NPs is relatively straightforward and well established, and commercial beads can be employed.<sup>[93,127–129]</sup> In this procedure, the premanufactured PMPs, commonly made from PS or PMMA, are swelled through the addition of an apolar organic solvent containing the luminophores, such as tetrahydrofuran (THF). This allows the luminophores to penetrate the PMP matrix and diffuse into the beads. PMPs are available in a variety of sizes and surface functionalities, making this procedure quite versatile. However, the process can still be quite challenging, as the choice of solvent for a specific luminophore influences not only their luminescence properties, but especially in the case of NPs also their size and colloidal stability. An unwisely chosen solvent can lead to luminescence quenching and aggregation/agglomeration of the NPs.<sup>[88,93,129,130]</sup> In addition, the pore size distribution inside the PMPs can influence the NP size distribution, which can turn out to be inhomogeneous. Poor reproducibility, a generally low staining density, and a possible NP leakage from the PMPs can be the results.<sup>[120]</sup> Therefore, post-synthetic swelling is more common for molecular luminophores such as organic dyes than for luminescent NPs. If surface FGs are present on the PMPs during the swelling procedure, this can lead to NP accumulation on the bead surface, as shown in this work (see subsection 5.1.2). Here, it was demonstrated that the CdSe/CdS-QDs accumulated on the PSMP surface, most likely because of their affinity to bind to the COOH FGs.<sup>[26]</sup>

## Layer-by-layer Technique

Another popular approach to fabricate luminophore-stained PMPs is the layer-by-layer deposition onto smaller particles.<sup>[25,95,131–133]</sup> It is less commonly used than the procedures described above, but provides an interesting alternative when luminophore staining only at the particle surface, or in a defined area of the bead, is desired or compatible with the intended application. This can be the case if the luminophore is supposed to directly interact with the particle environment, or to spatially separate different luminophores. The procedure involves the subsequent deposition of layers of oppositely charged polyelectrolytes, at least one of which contains the luminophore, onto preformed PMPs as templates.<sup>[131]</sup> Here, premanufactured/commercially available particles can be employed as templates. The method is limited to surface staining due to its nature. This can later lead to difficulties with bioconjugation, as the surface chemistry of the PMPs is significantly altered and may have to be modified

again for the attachment of specific moieties. The method is still relevant for bioanalytical applications, e.g. as drug-release layers can be included.<sup>[134]</sup> While layer-by-layer deposition is reasonably precise in terms of layer thickness, it can still lead to a broadening of the PMP size distribution when distributing several layers, and a number of purification steps have to be performed.<sup>[25,131,134]</sup> This can result in a loss of material and makes the whole procedure quite time-consuming and tedious, although it is still very versatile regarding layer thickness and choice of luminophore. With this procedure, the incorporation of different luminophores, or NPs in general, that are spatially separated from each other can be realized, e.g. by adding an unstained layer in-between the luminophore-stained layers.<sup>[135]</sup>

This procedure has been reported both for molecular luminophores such as organic dyes and different luminescent NPs, but its influence on the PL properties of NPs has not yet been evaluated systematically.

### **Comparison of Staining Methods**

Each of the previously described PMP staining methods has its distinct advantages and drawbacks, which are summarized in Table 2. For this work, the incorporation during the polymerization reaction was chosen mainly because of its high versatility and accessibility. After optimization, this procedure allows for the performance of a straightforward, accessible and reproducible synthesis with high yield and versatility regarding PMP size and crosslinking of the polymer matrix. The layer-by-layer distribution is significantly more time consuming, and the well-established swelling procedure was ruled out because of its limits regarding PMP size, significantly lower yield per batch and often insufficient homogeneity of the NP distribution in the beads.

Table 2.: Comparison of different routes to preparing NP-stained PSMPs - with the luminophore incorporated during the polymerization, via post-synthetic swelling or with layer-by-layer-deposition.

Incorporation procedure	During polymerization	Post-synthetic swelling	Layer-by-layer deposition
Advantages	Size easily adjustable	Use of commercial PSMPs	Use of commercial PSMPs
	Simple one-step synthesis	Simple and straightforward	Spatial separation of luminophores <sup>[135]</sup>
	Versatile: size, crosslinking	Versatile: good transferability to other polymers/NPs	Versatile: layer thickness/structure <sup>[134]</sup>
	High yield	Less time consuming	
	Good luminophore distribution <sup>[22]</sup>	Monodisperse PSMPs (commercial)	
Disadvantages	Time-consuming	Lower yield	Tedious and time-consuming
	Possible loss of PL: reaction conditions <sup>[22]</sup> need to be optimized	Possible loss of PL: choice of solvent <sup>[130]</sup> needs to be optimized	Loss of material due to purification
	Less monodisperse	Possible leakage <sup>[120]</sup>	Less monodisperse <sup>[25]</sup>
	Dispersibility of luminophore in monomer(s) <sup>[109]</sup>	Choice of size limited (commercial PSMPs)	Limited to surface staining
		Possible accumulation of NPs on PSMP surface <sup>[26]</sup>	Surface chemistry is modified
	Possibility of inhomogeneous distribution		

### 3.3.3 | Inorganic Semiconductor NPs vs Organic Dyes as Lumino- phores for PMP Staining

Although luminescent NPs have been used for the staining of PMPs or PNPs for quite some time now, it is still far more common to use organic dyes.<sup>[97,98,127,136]</sup> The staining procedures for polymer particles with dyes are relatively well established and mostly lead to homogeneously stained beads.<sup>[127]</sup> In contrast to this, the (homogeneous) staining of PMPs with NPs is far more complex. The luminescence properties of NPs considerably depend on their composition and surface chemistry, which is why exposure to harsher conditions during the staining procedure often leads to a loss in luminescence intensity.<sup>[119,128]</sup> Due to their colloidal nature and significantly larger size compared to dye molecules, and/or due to their surface properties, a less homogeneous particle staining can occur. Aggregation of the NPs during the staining process is also quite common, which can lead to only partial incorporation into the PMPs, and again a loss in luminescence intensity.<sup>[26]</sup> This can happen when the number of NP surface ligands is modified during the staining process, e.g., by ligand removal through the solvent, and this introduces additional trap states on the NP surface. Because of this, it is important to ensure a good colloidal stability and polymer compatibility of the employed NPs, e.g. by introducing an additional ligand or exchanging the existing ones.<sup>[22,93]</sup> In addition, conventional semiconductor NPs, especially those based on heavy metals such as Cd, can be more toxic for biological systems than most dyes.<sup>[127,136,137]</sup>

Apart from these difficulties, many NPs have significant advantages over organic dyes. An important point is the often much better photostability and brightness of, e.g., semiconductor NPs such as QDs, which enables longer usability and illumination times of the luminescent PMPs.<sup>[119,137]</sup> This can be important, e.g. for microscopically tracking the luminescent beads within cells or in an assay, or for the long-time use of a device operating with luminescent PMPs. The optical properties of semiconductor NPs enable the simultaneous excitation and spectral discrimination of different NPs in one sample or bead. This is ideal for barcoding of the synthesized particles with a library of complex patterns.<sup>[128]</sup> In the case of organic dyes, a spectral discrimination is complicated by their broader emission spectra, and the spectral overlap between absorption and emission favoring spectral crosstalk.<sup>[138]</sup>

To highlight the differences for dyes and semiconductor NPs as potential luminophores for PMP and PNP staining, their respective properties are summarized in Table 3.

Table 3.: Comparison of organic dye and NP properties relevant to their employment as luminophores for polymer particle staining. Information partly obtained from Resch-Genger *et al.*,<sup>[58]</sup> and the preceding paragraphs.

Property	Organic dyes	Semiconductor NPs
Size	Molecules (ca. 0.5 nm)	Depending on dimensionality, between <10 and about 100 nm
Absorption	Discrete bands	Increase towards ultraviolet (UV) wavelengths, broad
Emission	Asymmetric bands with high FWHM	Symmetric bands with small FWHM
FLT	1–10 ns, mono-exponential decay	10–150 ns, typically multi-exponential decay kinetics
PLQY	5–100%	10–100%
Spectral multiplexing	Possible, but only for specific dyes, up to 4	Ideally suited, easy combination of up to 5 colors
Photostability	Relatively low, sufficient for some applications	Typically high for most materials
Polymer compatibility	Very high for hydrophobic dyes, low for hydrophilic	Depends on surface chemistry, from not to highly compatible
Toxicity	Depends on dye, very low to high	Depends on NP, typically high (due to heavy metal leakage)

### 3.3.4 | PMP Surface Chemistry

The surface chemistry of PMPs is of utmost importance for their application. FGs on the bead surface provide anchors for different (recognition) moieties, such as sensor molecules, proteins, poly(ethylene glycol) (PEG) or antibodies, and generally play a major role in how the PMPs interact with their environment. Colloidal stability and reactivity, but also cellular uptake and general biocompatibility and -distribution are determined by particle surface chemistry and size.<sup>[9]</sup> Charged surface FGs can be introduced to ensure the colloidal stability of PMPs, as electrostatic repulsion between individual particles is elicited by the formation of a double-layer of counterions around the charged FGs. This was discussed in detail in section 3.1.

For biochemical applications, it is often necessary that the PMPs are biocompatible. As the surface of the PMPs is what interacts with the environment, controlled surface functionalization is a useful tool to enable or enhance biocompatibility of (luminescent) PMPs. As a lot of biomolecules have both primary amines and carboxy groups, the choice of PMP surface FGs can be used to control which of the biomolecule FGs bind to the particles, and which are left unbound, e.g. for further reactions. Such controlled functionalization of the PMPs

can help to improve hydrophilicity and biocompatibility, but also influences biological transport/biodistribution and cell uptake mechanisms.<sup>[139]</sup> A prominent example is PEG, which is hydrophilic and biologically inert, and can act as a stabilizing agent in biological systems when attached to PMPs by so-called PEGylation.<sup>[140,141]</sup> It not only makes the PMPs inert to their environment, but also prevents aggregation and hinders non-specific cell interactions, and as such has been approved by the U.S. Food and Drug Administration (FDA) for internal use, e.g. as a stabilizing agent.<sup>[142]</sup> Hydrophobic PMPs with highly positive surface charge are especially prone to interact with anions on cellular membranes. The use of hydrophilic, anionic or even neutral FGs can not only greatly improve biocompatibility, but also significantly reduce or even prevent cyto- or systemic toxicity.<sup>[139,143,144]</sup>

The introduction of surface FGs is commonly performed by choosing a suitable co-monomer which bears the desired functionalities.<sup>[26,145]</sup> Commonly chosen FGs include carboxy and amino functionalities, as they provide anchor points for post-synthetic functionalization with more complex groups or larger molecules. These can then be attached, e.g. covalently by organic chemistry reactions.<sup>[145,146]</sup> Both carboxy and amino groups are widely employed for PMP surface functionalization, as a variety of moieties can be attached to them and they offer negative (carboxy) or positive (amino) surface charge. The attachment of (bio)molecules and/or dyes with amino functionality to the PMPs can be performed by formation of an amide bond,<sup>[147–149]</sup> and moieties with carboxy or ester groups can bind to amino-functionalized PMPs.<sup>[150–152]</sup> There are other FGs that can be utilized as PMP surface FGs, e.g. thiol,<sup>[153,154]</sup> aldehyde,<sup>[155,156]</sup> or azide groups,<sup>[157]</sup> to enable a variety of possible reactions and attachment of different moieties.

### 3.4 | Motivation and Objectives

As luminophore-stained and encoded PMPs are widely applied in a plethora of fields, it is essential to have procedures at hand that enable the controlled, simple, and cost-effective synthesis of such particles. This requires knowledge about the influence of different reaction parameters, and in turn enables control and tuning of the PMP size. This makes the synthesis more versatile and adaptable. Although a range of publications addressing the synthesis of luminescent PMPs exists, there has been a significant lack of systematic assessments of the employed procedures, which was performed in this work.

In addition, it is important to know how the synthesis conditions and the staining into the polymer matrix affect the employed NPs, especially regarding their PL properties. A systematic study linking the changes in NP properties induced by the polymerization reaction, e.g. regarding the PLQY value, to NP composition and shape has not been published before. However, such an insight helps to predict the behaviour of newly employed NPs for the staining, and to choose suitable NPs for the desired outcome. This is an important and new aspect of luminescent PMP synthesis addressed in this work.

Another important point is the surface chemistry of the synthesized PMPs, which plays a major role in the particle interaction with its environment, and also the ability to attach specific moieties to the PMPs surface. Consequently, the introduction of suitable FGs to the surface of luminescent PMPs was also explored.

To summarize, this work targeted the following goals:

- The development of a synthetic procedure to obtain QD-stained, luminescent PSMPs with a facile, reproducible and tunable dispersion polymerization procedure - with QDs present during the reaction. Optimization of the PL features of the bead-incorporated QDs.
- Surface functionalization with carboxy groups of QD-stained, luminescent PSMPs. Analysis and comparison of the surface FG amount and PL properties of comparable beads prepared by different synthesis routes.
- Systematic study of the influence of the dispersion polymerization procedure on the PL properties of NPs with different composition, shell thicknesses, shape and surface chemistry.

These three main goals are closely linked to one another, and are each addressed and examined in individual publications.<sup>[22,26,27]</sup> This work overcomes existing challenges connected with the synthesis of luminescent PMPs, such as the significant quenching of luminophore PL, while simultaneously introducing new materials such as NPLs to the optimized, reproducibly fabricable PMPs. With knowledge and control over all these factors, the synthesis parameters and employed NPs can be adjusted to individual needs, and highly versatile and tunable, luminescent PMPs are the outcome.



## 4 | Methods for Luminescent PSMP Synthesis and Characterization

### 4.1 | Synthesis Procedures

#### 4.1.1 | Synthesis of Luminescent Semiconductor NPs

##### Semiconductor Core/shell-QDs with Different Shell Thicknesses and Composition

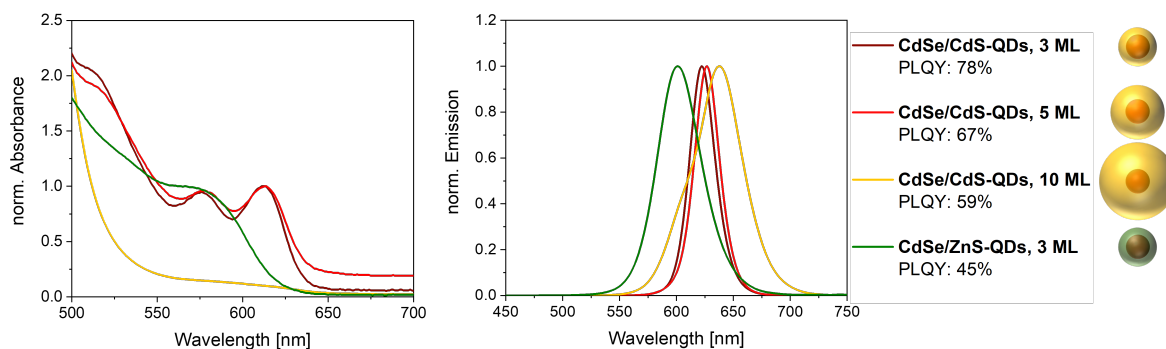


Figure 10: Normalized absorbance and emission spectra with PLQY values of all employed core/shell-QDs in hexane, with schematic depictions of the QD structure. The image was adapted from Scholtz *et al.* (2023).<sup>[27]</sup>

The syntheses of CdSe/CdS- and CdSe/ZnS-core/shell-QDs were performed by J. Gerrit Eckert (Leibniz Universität Hannover) according to a modified procedure established from Carbone *et al.*, Nightingale *et al.* and Chen *et al.*<sup>[76,158,159]</sup> The synthesis procedures for the employed QDs are described in detail in the supplementary information (SI) of Scholtz *et al.* (2022)<sup>[22]</sup> and Scholtz *et al.* (2023).<sup>[26,27]</sup> In short, the CdSe core particles were synthesized with a *hot-injection* approach, with CdO and Se as precursors. The CdS shell growth was initiated by simultaneous addition of diluted solutions of the precursors Cd(oleate)<sub>2</sub> and 1-octanethiol to the heated core particle dispersion over two hours. To synthesize QDs with different shell thicknesses, the amount of added precursors was varied, and for ZnS shell growth, the precursor Cd(oleate)<sub>2</sub> was exchanged with Zn(oleate)<sub>2</sub>. In Figure 10, the absorbance and emission spectra, and the PLQY values of all synthesized QDs are illustrated.

### Semiconductor Dot-in-rod-QRs

The CdSe/CdS-dot-in-rod-QRs employed in this work were purchased from ABCR GmbH (CANdot quantum rods, product number AB391053; surface ligands: octadecylphosphonic acid/hexylphosphonic acid). The particle absorbance and emission spectra, and the PLQY value are shown in Figure 11.

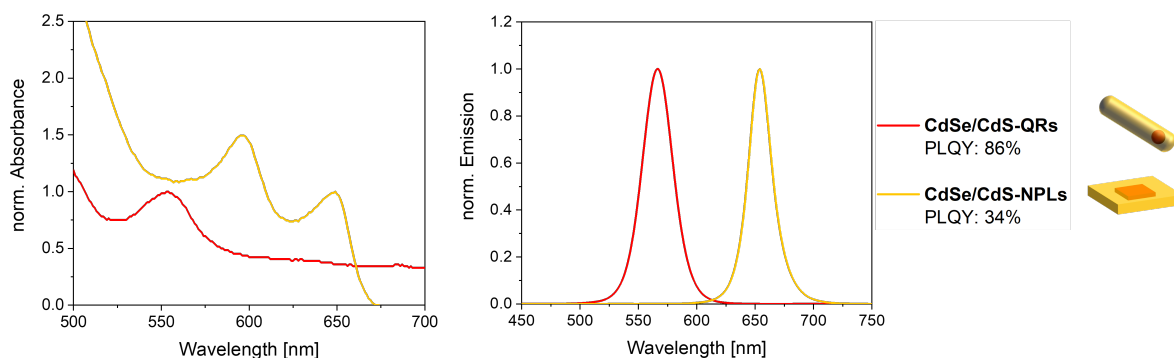


Figure 11: Normalized absorbance and emission spectra with PLQY values of the employed core/shell-NPLs and dot-in-rod-QRs in hexane, with schematic depictions of the NP structure. The image was adapted from Scholtz *et al.* (2023).<sup>[27]</sup>

### Semiconductor Core/shell-NPLs

The syntheses of the CdSe/CdS-NPLs were performed by Rebecca Graf (Leibniz Universität Hannover), according to Graf *et al.*<sup>[86]</sup> The synthesis procedure for the employed NPLs is described in detail in the SI of Scholtz *et al.* (2023).<sup>[27]</sup> In short, a *hot-injection* method with Cd(myr)<sub>2</sub> and Se as precursors was performed to produce the CdSe core NPLs. Similarly to the CdSe/CdS-QDs, oleylamine (OIA) and 1-octanethiol were added slowly to the core particles in 1-octadecene (ODE) and Cd(oleate)<sub>2</sub> at 300 °C to create monodisperse CdSe/CdS-core/shell-NPLs. The earlier addition of Cd(oleate)<sub>2</sub> was chosen to reduce core NPL etching during the synthesis. In Figure 11, the absorbance and emission spectra, and the PLQY value of the NPLs are illustrated.

## 4.1.2 | Synthesis of Polystyrene Microparticles (PSMPs) Stained with Luminescent Semiconductor NPs

### Pretreatment of NPs with a Polymer-compatible Ligand

The employed, luminescent NPs mostly have a ligand layer consisting of oleic acid (OA) and oleylamine on the particle surface. When the NPs are employed as-is and dispersed in styrene, this results in insufficient incorporation into the PSMPs, and thus to a very high loss in NP luminescence intensity.<sup>[22]</sup> As this method apparently leads to poor compatibility of the polymer matrix with the NP surface, a modification of the particle was necessary. For better polymer compatibility, the additional ligand benzyldimethyloctadecylammonium chloride (OBDAC) was introduced to the NP surface. A small amount of OBDAC was added to the respective NP dispersions, along with ethanol to precipitate the particles. After shaking the mixture, it was centrifuged, washed once with ethanol and redispersed in styrene (see Scholtz *et al.* (2022)<sup>[22]</sup> for detailed procedure). It is believed that the OBDAC molecule intercalates with the existing ligands (OA and OIA) and forms a polymer-compatible coating around the NPs. The OBDAC coating significantly improved NP incorporation and preservation of the NP luminescence intensity.<sup>[22]</sup>

### Synthesis of PSMPs with and without Surface Functionalization

The pretreated, OBDAC-coated NPs were employed for the production of luminescent PSMPs. The synthesis was performed via a dispersion polymerization reaction, with the NPs present during the polymerization. The pretreated NPs (as described above) were dispersed in styrene and DVB and added to the reaction mixture, consisting of ethanol, AIBN, PVP, polyethylene glycol-*block*-poly( $\epsilon$ -caprolactone) (PEG-*b*-PCL) in toluene. The amphiphilic copolymer PEG-*b*-PCL was added to improve the PSMP size distribution by preventing particle aggregation and secondary nucleation through sterical stabilization of the growing PSMPs. The synthesis was performed under argon at low stirring speeds (70–100 rpm), with temperatures between 60 °C–80 °C. The PSMP synthesis procedure is described in detail for CdSe/CdS-QD-stained PSMPs in Scholtz *et al.* (2022),<sup>[22]</sup> and for different NPs (including CdSe/CdS- and CdSe/ZnS-QDs, CdSe/CdS-QRs, and CdSe/CdS-NPLs) in Scholtz *et al.* (2023).<sup>[27]</sup>

To enable functionalization of the PSMP surface, acrylic acid (AA) was added to the mixture after 3/4 of the reaction time to enable its copolymerization at the outside of the polymer beads. To properly dissolve the AA, water had to be added to the reaction mixture in a 1:9 ratio with ethanol. The procedure is described in detail in Scholtz *et al.* (2023).<sup>[26]</sup>

## 4.2 | Characterization of NPs and PSMPs

### 4.2.1 | Size, Size Distribution and Particle Morphology

#### Dynamic Light Scattering (DLS)

DLS is a widely employed method for the determination of NP and microparticle (MP) size, although it is limited to particles ranging from 1–10,000 nm. It is a simple and fast method that delivers the hydrodynamic diameter of particles in dispersion, which includes the solvent layer attached to the particle surface. Consequently, it is larger than the particle size determined from TEM or SEM images. Due to Brownian motion, the dispersed particles constantly move, and as particle distances change, so do destructive and constructive interferences of light scattered by the particles. When irradiated with a monochromatic, coherent laser source, this motion consequently has an influence on the transmitted light. This changes the intensity of the detected light and allows for the determination of the diameter through the Stokes-Einstein equation:<sup>[160,161]</sup>

$$D = \frac{k_{\text{B}}T}{6\pi\eta r_{\text{h}}} \quad (1)$$

This equation enables the determination of the hydrodynamic radius  $r_{\text{h}}$ , from which the diameter can easily be derived. The diffusion coefficient  $D$  is determined through the observation of light interference changes, and will be higher for bigger particles as their movement is slower, which means the fluctuations in detected laser light intensity change slower than for small particles.<sup>[23]</sup> Through knowledge of  $D$ , the dispersant viscosity  $\eta$  and the Boltzmann constant  $k_{\text{B}}$ ,  $r_{\text{h}}$  can be determined for a constant temperature  $T$ . Consequently, the hydrodynamic radius/diameter changes for different temperatures and solvents/solvent viscosities. The concentration of particle dispersions measured by DLS has to be adjusted, as it has a direct influence on the outcome of the measurement. If the concentration is too low, the light scattered by the particles can be too weak, and thus the results include a high background

noise. If the concentration is too high, particle-particle interactions can contort the results. DLS measurement data are typically displayed as size distribution graphs with a mean size value, including the calculated standard deviation. Figure 12 shows a fitted size distribution graph exemplarily for PMPs.

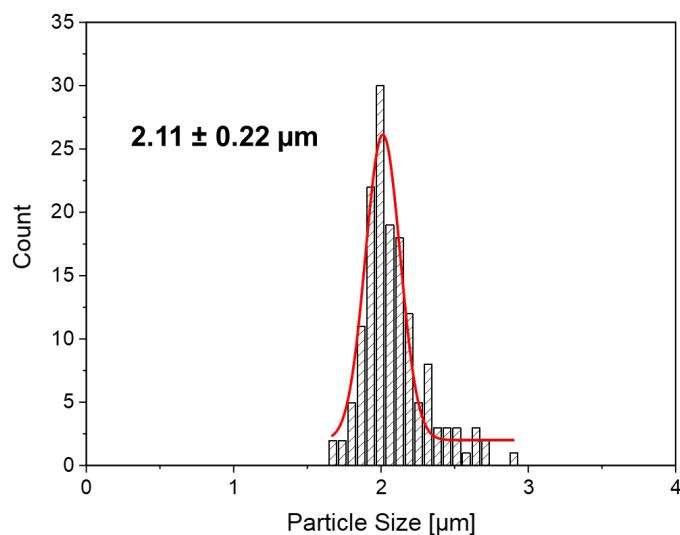


Figure 12: Size distribution graph with mean size and standard deviation of a PSMP sample, determined by DLS.

### Scanning Electron Microscopy (SEM)

SEM is an imaging technique that is commonly used for the visualization of NPs and MPs, but also a wide variety of other nano- and microstructures. From the recorded images, particle size, size distribution and shape can be identified, and valuable insights into the particle surface structure, or more broadly the sample topography, can be derived. Depending on the used instrumentation, this method can have a resolution better than one nm, which enables extensive studies of the sample surface structure and even the determination of nanoscale porosity.

SEM works by scanning the sample surface with a focused electron beam that is typically created thermionically with an electron gun, which is equipped with a tungsten cathode. The beam is focused by condenser lenses, passes through deflector plates or scanning coils and finally reaches the sample, with which it interacts. The teardrop-shaped area of interaction is known as the interaction volume. When the primary beam now interacts with the sample surface, various processes occur. Some of the electrons are scattered elastically, creating

high-energy backscattered electrons (BSEs), and lower-energy secondary electrons (SEs) are released from the sample due to inelastic scattering. Both kinds of electrons can be detected by specialized detectors and carry different types of information. SEM measurements require the sample to be placed in vacuo to eliminate interaction of the electron beam with anything other than the sample. In conventional SEM, the measurements are conducted in high vacuum, but low vacuum, even under wet conditions, is also possible with some instruments such as an environmental scanning electron microscope (ESEM), admittedly with a lower resolution.<sup>[162]</sup> Typically, the samples are dried and fixated on a suitable substrate, and samples with a low conductivity have to be coated with a very thin layer of a conductive material such as gold to prevent sample charging effects. In Figure 13, SEM images of two different PSMP samples are displayed to highlight the visibility of the different surface structures.

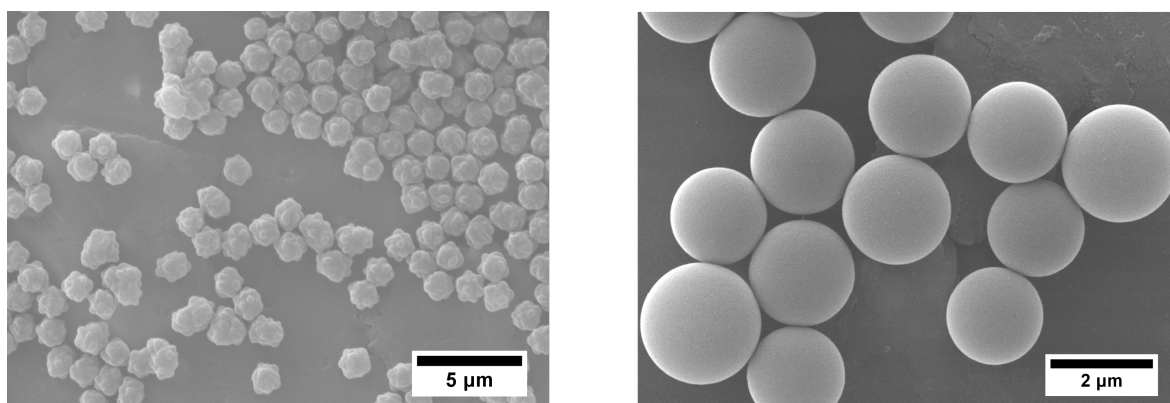


Figure 13: ESEM images of two PSMP samples with different surface structures.

### Transmission Electron Microscopy (TEM)

Like SEM, TEM is used to visualize nano- and microscopic materials. The difference is that when using TEM, the electron beam passes through the sample, and the transmitted electrons are detected. This requires very thin samples to enable electron transmission, but in turn can give valuable insights into the interior of the examined sample.

When using TEM, the electrons are emitted from an electron gun, either by thermionic (tungsten filament or LaB<sub>6</sub> single crystal) or field electron (field emission gun) emission, and the measurement is conducted in high vacuum.<sup>[163]</sup> The initial electron beam is typically accelerated and condensed by a lens system to focus it before hitting the sample and interacting with it. The resolution of TEM measurements can be in the dimension of singular atoms, which makes crystallographic studies (e.g. visualization of crystal lattice structures) possible.<sup>[164]</sup>

Theoretically, the resolution is only limited by the electron energy/wavelength, but practically small intrinsic defects of the lenses are the limiting factor. These can cause spherical and chromatic aberrations and have to be corrected by aberration correctors (lenses and/or energy filtering of the electron beam).<sup>[165]</sup> With an objective aperture, either the central beam can be selected for a bright-field image, or if a diffracted beam is chosen, this allows for dark-field images. Apart from the conventional measurement, there are different possible operating modes such as scanning transmission electron microscopy (STEM). For example, high-angle annular dark-field scanning transmission electron microscopy (HAADF-STEM) is employed to image variations in atomic numbers of different atoms in the sample with a high sensitivity. When using this method, the scattered electrons are collected with an annular dark-field detector, while in regular TEM dark-field imaging, an objective aperture is used to collect the scattered electrons.<sup>[166]</sup> In Figure 14, a conventional TEM image and an image collected with HAADF-STEM are displayed to highlight the advantages of both imaging techniques.

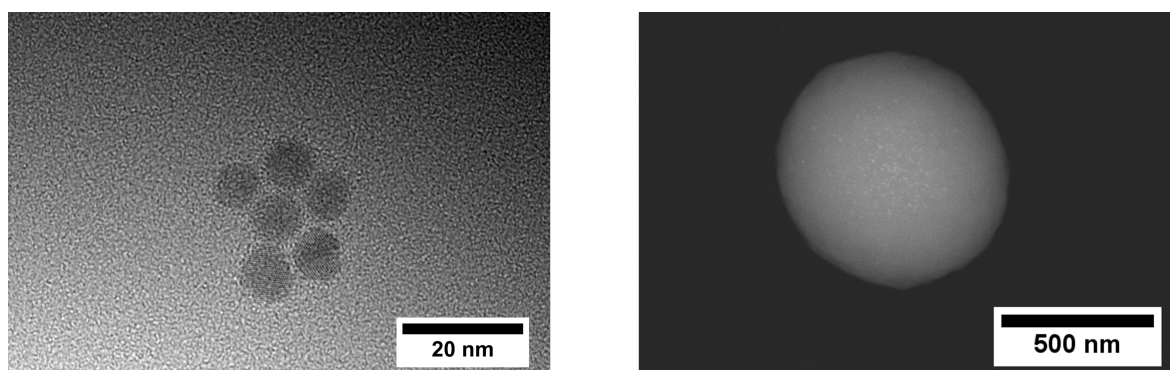


Figure 14: TEM image of CdSe/CdS-QDs with crystal lattices visible (left), and HAADF-STEM image of CdSe/CdS-QDs inside of a PSMP (right).

### **Confocal Laser Scanning Microscopy (CLSM)**

CLSM is a common imaging method that is predominantly used for bioanalytical studies. A focused, concentrated laser beam scans the sample, which consists of nano- or microstructures that can be embedded, e.g. in cell systems, and the sample signal intensity (often fluorescence) is detected. This method implies a point illumination of the sample with a focused laser beam, which is directed onto the sample with a system of lenses and mirrors.<sup>[167]</sup> The microscope also has an optically conjugate plane with a very small hole in front of the detector to eliminate signal that is out of focus.<sup>[168]</sup> In contrast, traditional fluorescence microscopy uses wide-field illumination that excites all parts of the sample simultaneously. These differences lead to much

better resolution, but also reduced intensity when measuring with CLSM. To still record an adequate intensity from the sample, exposure times are extended and sensitive detectors with photomultipliers are used.<sup>[167]</sup> The resolution of CLSM is limited by diffraction, as it is a type of light microscopy, which means it is dependent on the employed excitation wavelength in addition to instrument limitations. Figure 15 shows images recorded with CLSM, both with the fluorescence signal and the laser light transmitted through the sample. The comparison of such images can enable valuable insights into the location of fluorescent components inside of superordinate structures.

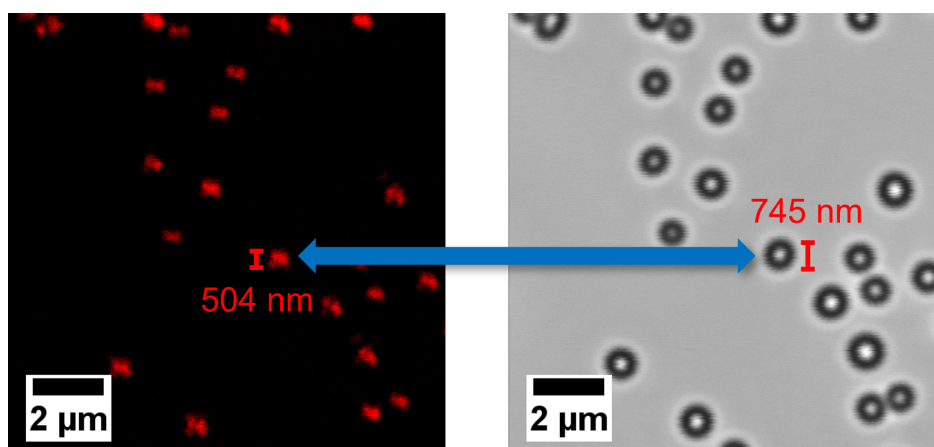


Figure 15: CLSM images of QD-stained PSMPs, with sample fluorescence (left) and transmission (right). Image adapted with permission from Scholtz *et al.*, copyright 2022 Scientific Reports.<sup>[22]</sup>

## 4.2.2 | Optical Properties

### Absorption

The interaction of electromagnetic irradiation with a sample includes the absorption of light, but also reflection or scattering. When a molecule or particle in the sample absorbs incident photons, this leads to an excitation of an electron from the electronic ground state to electronic and vibronic states of higher energy. The sample absorbance  $A$  is then determined by comparing the incident irradiation intensity  $I_0$  to the transmitted irradiation  $I$  that passes through the sample and is registered by a detector. The Beer-Lambert law shows the dependence of  $A(\lambda)$ , the absorbance at a certain wavelength, on the optical pathlength  $d$  (e.g., the width of the used cuvette), the concentration of the sample  $c$ , and the absorption coefficient  $\epsilon_\lambda$  which is specific for the material and the wavelength.<sup>[169]</sup>

$$A(\lambda) = \log \frac{I_0}{I} = \epsilon_\lambda cd \quad (2)$$

This also means that the change of  $A(\lambda)$  is directly proportional to the change of  $c$  when  $d$  is constant and  $\epsilon_\lambda$  is known. This only applies to dilute, transparent samples with an absorbance value  $\leq 1$  and a particle size of less than about 50 nm, where the influence of scattering and reflection effects is negligible.<sup>[169]</sup> The experimentally determined absorbance value includes not only absorption, but also scattering, reflection and diffraction effects, which become relevant for large particles and/or highly scattering samples.<sup>[170]</sup> When the "true" absorption of such samples is wanted, an integrating sphere has to be used, so that scattered/reflected photons are directed back by scattering on the coating of the sphere and can interact again with the sample.

### Emission

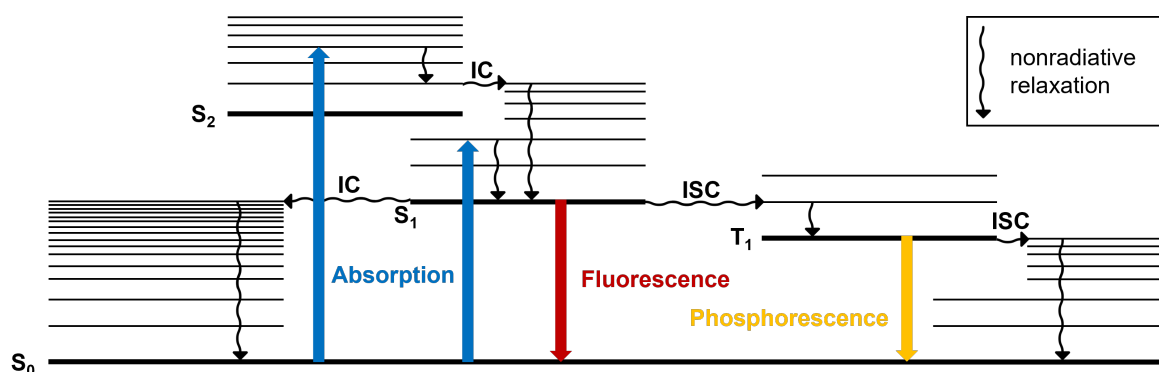


Figure 16: Jablonski diagram with absorption, fluorescence and phosphorescence processes illustrated for molecular luminophores.

The emission of photons can occur after the absorption of light by an emitter. The electrons that are excited by absorption of a photon are elevated to an electronically as well as vibronically excited state. In the case of molecular luminophores such as dyes, after the excitation of an electron, what occurs first is vibronic, nonradiative relaxation to the lowest level of the electronically excited state  $S_1$ .<sup>[171]</sup> When the electron was excited to an electronically higher state  $S_2$ , this first occurs by internal conversion (IC) and subsequent, nonradiative relaxation to the vibronic ground state of  $S_1$ .<sup>[172]</sup> The emission of a photon results from the radiative relaxation of the excited electron back into the electronic ground state  $S_0$ . The emitted photons normally have less energy than the initially absorbed photon, as the preceding vibronic

relaxation to the energetically lowest state of the conduction band occurs nonradiatively, accounting for the so-called Stokes shift. This term refers to the bathochromic shift of the sample emission spectrum compared to its absorbance spectrum.<sup>[172]</sup> In some systems, a change of the excited electron from the singlet electronic state to a triplet state ( $T_1$ ) is possible through intersystem crossing (ISC).<sup>[171]</sup> The radiative relaxation of an electron from an excited triplet state to the ground state after ISC is spin-forbidden and called phosphorescence, a nonradiative relaxation is also possible after another ISC.<sup>[172]</sup> These processes are summarized in the Jablonski diagram in Figure 16.

In the case of semiconductor NPs, electrons are excited from the valence band to the conduction band. Fluorescence occurs when the excited electron relaxes back to the valence band, releasing the absorbed energy by emission of a photon. A nonradiative relaxation into the ground state is possible for semiconductor NPs, e.g. through lattice vibrations (phonons). The non-emissive dark states act as electron traps and do not offer the pathway of radiative relaxation. All of these processes are summarized in the energy level diagram in Figure 17. As the exact relaxation routes of semiconductor NP are not yet fully understood, the energy level diagram is intentionally kept simple.

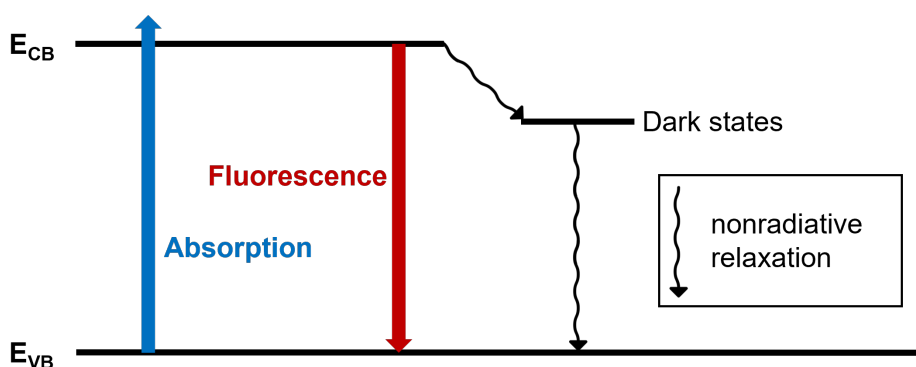


Figure 17: Simplified energy level diagram for semiconductor NPs, with absorption and fluorescence processes illustrated, including the energy levels of the valence band ( $E_{VB}$ ) and the conduction band ( $E_{CB}$ ).

### Photoluminescence Quantum Yield (PLQY)

The PLQY is defined as the ratio of the number of emitted photons  $N_{em}$  to the number of absorbed photons  $N_{abs}$ , and consequently is a measure for the percentage of radiative relaxation. Thus, it contributes to the brightness of an emitter (along with the absorption coefficient).

Alongside the fluorescence decay kinetics and lifetime, it is one of the most important characteristics of a luminophore and can be expressed with the following equation:<sup>[172]</sup>

$$\Phi = \frac{N_{\text{em}}}{N_{\text{abs}}} = \frac{\Gamma}{\Gamma + k_{\text{nr}}} \quad (3)$$

It includes the rate constants  $\Gamma$  for radiative relaxation (emission of photons) and  $k_{\text{nr}}$  for all nonradiative relaxation processes of the excited electron. The PLQY can be close to 100% if the nonradiative decay is negligible, but will never reach 100% due to Stokes losses (see also Stokes shift in the preceding subsection about emission).<sup>[172]</sup> The PLQY can be determined relatively through comparing the sample emission intensity with that of a reference luminophore with known PLQY, commonly an organic dye, while keeping the measurement conditions identical. Another possibility is the absolute determination, where the sample emission and absorption are measured in an integrating sphere setup to determine  $N_{\text{em}}$  as well as  $N_{\text{abs}}$  directly.<sup>[173]</sup> For scattering samples such as PMPs, but also for solid and powder samples, films and other NP and MP dispersions, the PLQY can only be reliably determined absolutely by integrating sphere spectroscopy.<sup>[172,173]</sup>

### **Fluorescence Lifetime (FLT) and Decay Kinetics**

The FLT is defined as the average time an electron of a luminophore spends an excited state before relaxation back to the ground state. This includes the emission of photons (radiative relaxation) as well as nonradiative relaxation processes such as lattice vibrations. It can be expressed by the following equation, including the rate constants  $\Gamma$  and  $k_{\text{nr}}$  for radiative and nonradiative relaxation, respectively:<sup>[172]</sup>

$$\tau = \frac{1}{\Gamma + k_{\text{nr}}} \quad (4)$$

The PL decay kinetics are commonly measured after periodic excitation with a pulsed light source, e.g. a laser, with a process called time-correlated single photon counting (TCSPC). This yields multi- or single exponential fluorescence decay curves, depending on the luminophore, from which the FLT can be determined:<sup>[174,175]</sup>

$$\text{FLT}(t, \lambda) = I(\lambda) \sum_{i=1}^n a_i e^{-\frac{t}{\tau_i}} \quad (5)$$

Here,  $a_i$  is the amplitude fraction of the lifetime component  $i$ ,  $I(\lambda)$  is the total amplitude,  $t$  the time and  $\lambda$  the wavelength. Commonly employed excitation light sources for PL decay measurements, that were also used in this work, include picosecond pulsed LEDs that provide light of a fixed wavelength. These LEDs are available for the UV/Vis range, bridging the gap between nanosecond flashlight excitation and femtosecond lasers. The detection was performed with a microchannel plate (MCP) to amplify the emitted photons by the multiplication of electrons via secondary emission.

The determination of the FLT from the generated decay curves can be performed with different fitting models, e.g., weighted either on the intensity ( $\tau_{\text{int}}$ ) or the amplitude ( $\tau_{\text{amp}}$ ):<sup>[175]</sup>

$$\langle \tau_{\text{int}} \rangle = \frac{\sum_{i=1}^n a_i \tau_i^2}{\sum_{i=1}^n a_i \tau_i} \quad (6)$$

$$\langle \tau_{\text{amp}} \rangle = \frac{\sum_{i=1}^n a_i \tau_i}{\sum_{i=1}^n a_i} \quad \text{with} \quad \sum_{i=1}^n a_i = 1 \quad (7)$$

The amplitude average FLT is commonly employed for systems with energy transfer between the luminophores, which leads to multiexponential decay curves. When employing the intensity average FLT, the focus is set on the ensemble of emitters present in the sample. Here, more weight is placed on the longer lifetimes, thus reducing the visibility of changes for shorter components.

### 4.2.3 | Chemical Composition

#### Nuclear Magnetic Resonance Spectroscopy (NMR)

NMR spectroscopy is a very commonly employed characterization method for a wide variety of (organic) compounds. It primarily enables access to structural information on the analyzed molecules, but can also help to assess purity and even quantitative data.<sup>[176,177]</sup> NMR works by observing local magnetic fields around certain atomic nuclei, e.g. the common elemental isotopes  $^1\text{H}$ ,  $^{13}\text{C}$ ,  $^{31}\text{P}$ ,  $^{19}\text{F}$  or  $^{15}\text{N}$ . To be suitable, the isotopes must have a nuclear spin deviating from zero, and thus a magnetic moment, and a high enough occurrence (in nature). As the magnetic fields are unique or at least highly characteristic to specific compounds and/or chemical entities/groups, NMR is the most common method for organic compound structure determination, and also very popular for protein analysis.<sup>[176]</sup>

During the measurement, the magnetic nuclear spins of the investigated compound are polarized in a constant magnetic field that is applied by the instrument. This spin alignment is disrupted by an oscillating magnetic field in the form of a pulse, and the electromagnetic waves emitted by the sample upon this perturbation are detected as a free induction decay (FID), which is the return of the magnetization to the equilibrium. After Fourier transformation, a frequency spectrum is obtained. The chemical shifts of resonances, and thus the peaks displayed in NMR spectra, are dependent on the local magnetic field of the investigated nuclei, which is in turn dependent on the chemical environment of the nuclei.<sup>[176,177]</sup> The chemical shift is converted from MHz to ppm through dividing the shift in Hz by the reference frequency of the spectrometer, and multiplying it by one million. The peak intensity typically depends proportionally on the number of nuclei involved in creating the signal. Figure 18 shows a <sup>1</sup>H-NMR spectrum of a copolymer with assignment of all signals to the respective atoms of the molecule to illustrate the information gained by NMR spectroscopy. From the spectrum, the ratio of the two polymer components (n/m) can be determined directly, but not to the molecular weight or molar mass of the copolymer.

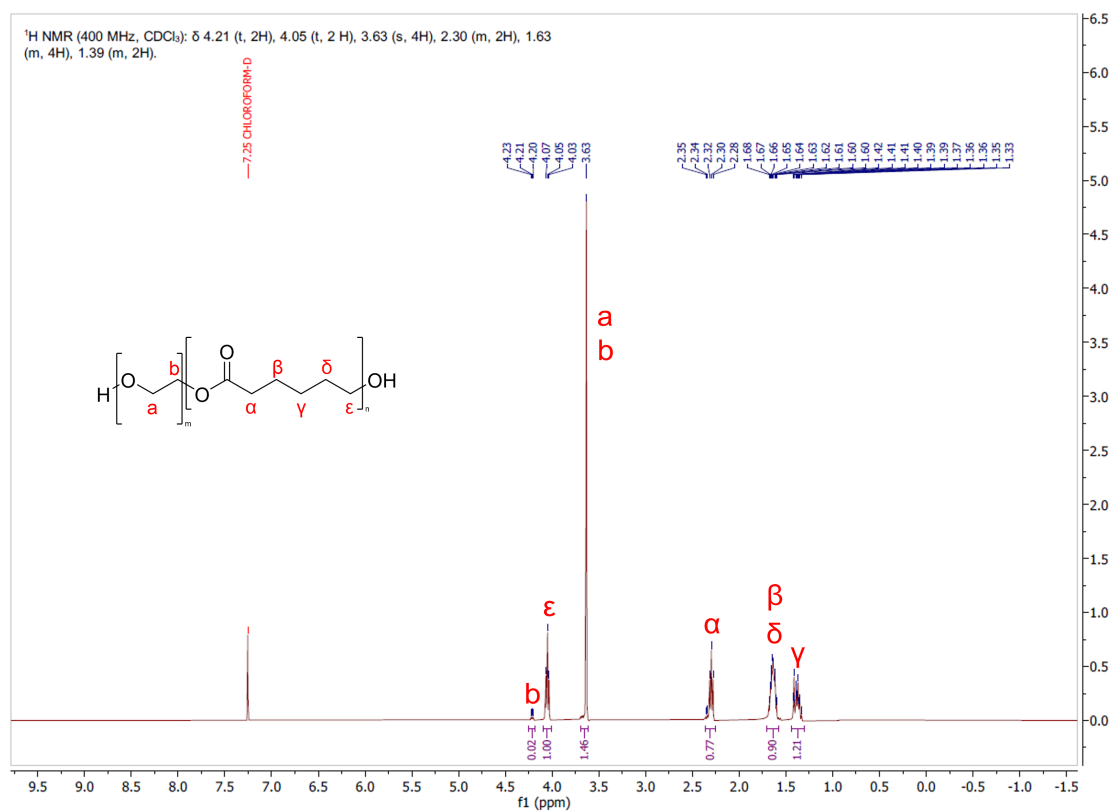


Figure 18: <sup>1</sup>H-NMR spectrum of the copolymer PEG-*b*-PCL with chemical shifts assigned to the respective atoms/parts of the molecule, measured at 400 MHz in CDCl<sub>3</sub>.

### **Atomic Absorption Spectroscopy (AAS)**

Atomic absorption spectroscopy (AAS) is a common method for quantification of chemical elements in a sample. To analyze a sample, either in solution or solid, it has to be atomized to enable the measurement of the atomic absorption spectrum. This is most commonly done by either flame or electrothermal atomizers.<sup>[178–180]</sup> Flame atomizers, which are used for liquid samples, utilize air-acetylene or nitrous oxide gas mixtures that burn with flames of 2300 °C and 2700 °C, respectively.<sup>[180]</sup> The sample is aerosolized with a nebulizer, mixes with the flame gases and is atomized in the flame. With an electrothermal atomizer, the sample is heated rapidly and promptly in an electrically heated graphite tube. A light source now directs irradiation at and through the atomized sample, which causes absorption of photons by the atoms and attenuates the intensity of the irradiation. The detected intensity after passing through the sample and the initial intensity are compared, which yields information on the absorption through the analyte atoms.<sup>[178,179]</sup> Often, element-specific line radiation sources are employed, as in the case of this work for Cd. The use of a continuum irradiation source is also possible. To be able to determine the elemental concentration from the atomic absorption lines, a calibration series with known concentrations of the analyte has to be measured in advance. Signal comparison with the calibration line then yields the analyte concentration in the sample.

### **Fourier Transform Infrared Spectroscopy (FTIR)**

Fourier transform infrared (FTIR) spectroscopy is the most common variation of infrared (IR) spectroscopy. It utilizes IR irradiation that passes through the sample, which can be in solid, liquid or gaseous form. When the frequency of the irradiation is the same as the vibrational frequency of a bond (or group of bonds) in the sample, a photon is absorbed and the vibrational mode is excited.<sup>[181,182]</sup> The transmitted light is detected, and in the case of FTIR spectroscopy an interferogram is created with an interferometer. The interferogram is then Fourier transformed into an IR spectrum with the sample absorbance at different wave numbers.<sup>[181]</sup> Typically, a reference spectrum is recorded to account for and eliminate instrument influences. An example FTIR spectrum is displayed in Figure 19 for QD-stained and unstained PSMPs, the first functionalized with COOH surface FGs. This method is commonly used for samples with covalent bonds, and the created spectra increase in complexity with the number of IR active bonds in a sample. The bands in the IR spectrum are characteristic for

particular bonds, which enables the identification of bonds/bond groups present in the sample, and thus of the measured material. FTIR spectra can even allow for (semi)quantification of certain bonds/moieties.<sup>[181,182]</sup> In the case of COOH surface groups on PSMPs, e.g., the carbonyl peak at about 1745 cm<sup>-1</sup> can be used to monitor the amount of COOH groups.

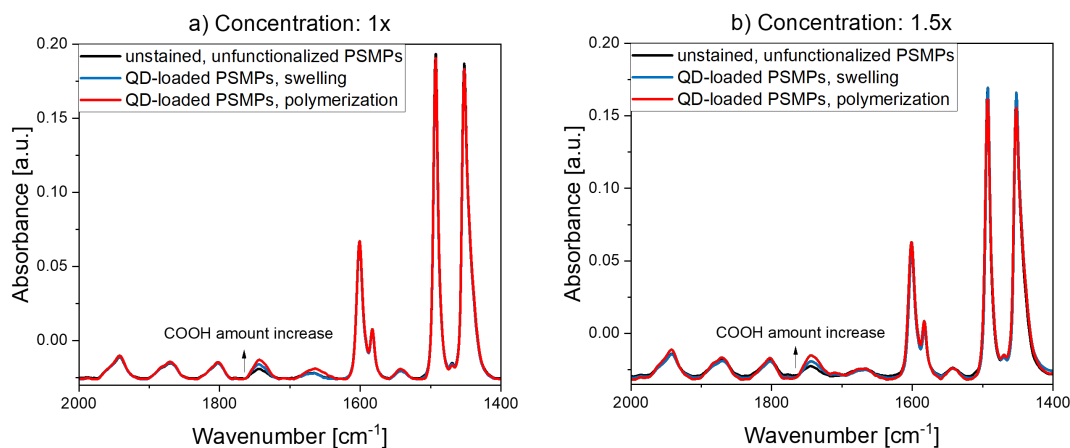


Figure 19: FTIR spectra (sectioned) of QD-stained and unstained PSMPs, the first functionalized with COOH surface FGs, at two different concentrations. Changes in the intensity of the carbonyl peak at 1744 cm<sup>-1</sup> indicate a difference in COOH amount for the different PSMP preparation methods (QDs present during polymerization or post-synthetic swelling). The other visible peaks can be ascribed to aromatic benzene vibrations. All samples were measured in solid form (KBr tablets, pure KBr as reference), and the offset of the IR spectra (baseline value below 0) is caused by the normalization procedure. Image adapted with permission from Scholtz *et al.*, copyright 2023 Scientific Reports.<sup>[26]</sup>

#### 4.2.4 | Surface Charge

##### Zeta Potential

As explained in subsection 3.3.4, the surface charge of MPs and NPs is of high importance for their interaction with the environment, including their colloidal stability. It is commonly measured with electrophoretic light scattering to determine the electrophoretic mobility  $U_e$  of the dispersed particles, from which the surface charge can be conveyed by the following formula:<sup>[183]</sup>

$$\zeta = \frac{3}{2} \frac{U_e \eta}{\epsilon f(ka)} \quad (8)$$

The such determined variable is called zeta potential  $\zeta$ , with the dynamic viscosity of the liquid  $\eta$ , the dielectric constant of the sample  $\epsilon$  and the Henry function  $f(ka)$ . The zeta potential is a term used for the electrokinetic potential of a colloidal dispersion. A particle with surface charge attracts ions of the opposite charge, and as a result, an ionic, interfacial double layer is formed. This double layer includes the surface charge (first layer) and the oppositely charged Stern layer (second layer). The  $\zeta$  potential is defined as the charge (or potential difference) at the slipping plane separating the particle, including the interfacial double layer, and the surrounding dispersion medium.<sup>[142]</sup> It can depend on the pH if (de)protonable FGs are present on the particle surface, the dielectric constant and composition of the dispersion medium, and the ionic strength. Usually, a sample is considered colloidally stable with a  $\zeta$  potential below -20 mV or above 20 mV, as the electrostatic repulsion at these values is high enough to prevent rapid agglomeration.<sup>[183]</sup>

## 4.2.5 | Quantification of Acidic Surface Functional Groups (FGs)

### Conductometry

Electrochemical titrations, such as conductometry, are commonly employed quantification methods for (de)protonable surface FGs such as amines, carboxy and thiol groups on a wide variety of different nano- and micromaterials. The FG quantification with electrochemical titrations is generally precise, relatively fast, inexpensive and requires no specialized instrumentation, but requires a relatively large amount of sample (about 10–20 mg/mL of material).<sup>[184]</sup> When performing an electrochemical titration, defined amounts of an acid or base are added to the sample as a titrant while observing changes in the electrochemical properties. In the case of conductometry, the observed parameter is the conductivity of the sample, which changes as a function of the added amount of titrant.<sup>[184]</sup> This method is commonly used for the determination of carboxy or amino groups on PNPs and PMPs, and the suitability has been validated, e.g. for carboxy groups on PMMA and PS particles by comparison with other quantification methods.<sup>[185,186]</sup> As all (de)protonable FGs and species with a  $pK_a$  value (negative base 10 logarithm of the acid dissociation constant  $K_a$ ) similar to the investigated FGs are detected during the measurement, e.g. residue molecules from the synthesis or excess ligands, this method can lack selectivity and specificity for certain particles/systems. Because of this, adequate purification, e.g. through washing steps, of the sample prior to the titration are of high importance. The execution of the titration under

inert atmosphere is also beneficial, as the formation of carbonic acid from dissolved CO<sub>2</sub> can be prevented.<sup>[187]</sup> In addition, the investigated samples have to be stable in the monitored pH range, which is often quite broad.

When performing a conductometric titration, the addition of the acid or base leads to a (de)protonation or neutralization in the sample dispersion/solution. The sample conductivity is determined by the concentrations of the highly conductive protons (H<sup>+</sup>) and hydroxyl ions (OH<sup>-</sup>), which change in concentration during the course of the titration.<sup>[188]</sup> An exemplary titration curve is displayed in Figure 20.

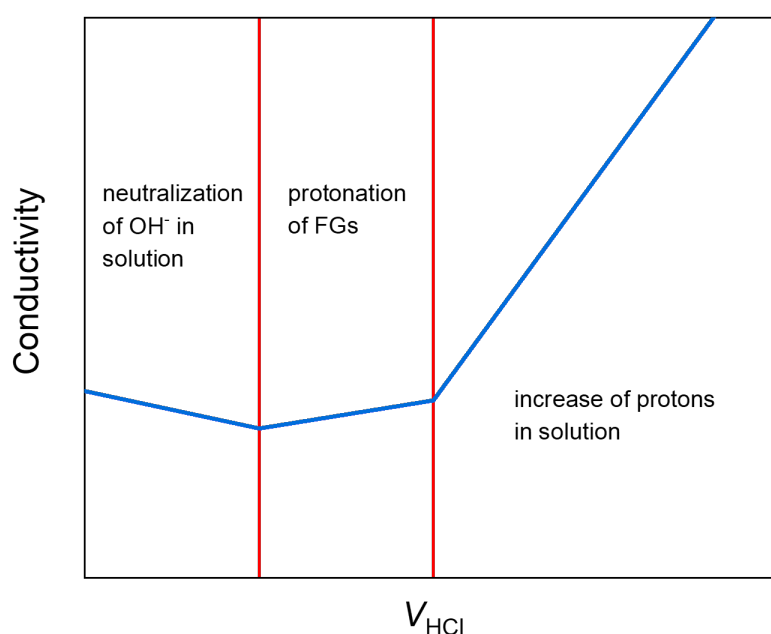


Figure 20: Schematic, simplified conductometric curve of PNP or PMP titration with HCl, displaying the change in sample conductivity with increasing titrant volume, with the three occurring phases indicated.

As illustrated, a typical conductometric titration of PNPs or PMPs with an acid such as HCl first leads to neutralization of the hydroxyl ions in solution. When this is completed, the FGs are protonated by the HCl, and finally the concentration of protons in solution increases. Here, the change of slope between the first and second phase indicates the start, and between the second and third phase the end of FG protonation. The two intersections between the linear parts of this curve are called equivalence points, and from the titrated volume between them, the amount of FGs can be determined with the following equation:

$$\text{amount of FGs} = \frac{c_{\text{titrant}} V_{\text{titrant}}}{m_{\text{analyte}}} \quad (9)$$

This equation can be formulated because  $V_{\text{titrant}}$  is proportional to the amount of (de)protonatable FGs in the sample.<sup>[142,189]</sup> After the titration with an acid such as HCl, a back titration with a base such as NaOH is commonly performed as a method of validation. The thus determined FG amounts should be the same. With conductometry, and electrochemical titrations in general, the total amount of FGs can be determined if the employed ions are sufficiently small. Not all FGs are accessible for the connection to other molecules/particles larger than a proton/oxonium ion, e.g. as they can be sterically hindered. Bulkier titrants (e.g. ammonium chloride) can be employed for conductometric titrations, but are less frequently used and do not always provide the total amount of FGs. To determine the accessible amount of FGs, commonly other methods such as optical assays with dye molecules are employed.

### Optical Assays

Optical assays are a fast, inexpensive and simple method for the quantification of surface FGs. They can be performed with commonly used laboratory equipment and instrumentation, and can be used to determine the accessible amount of FGs such as carboxy or amino groups on nano- or micromaterials. A fluorometric or spectrophotometric label, e.g. an organic dye, is needed for this method, which is attached to the sample material surface covalently or electrostatically. With the dye or another label absorbing or emitting photons in the visible, UV or NIR region, the readout can be performed with standard emission or UV-Vis spectrometers after separating unbound and sample-bound dye, as they can not be distinguished spectroscopically. This can be done by washing the particles and removing the excess dye. While this method is quite simple and straightforward, the use of organic solvents for the labelling can lead to the swelling of particles, especially in the case of PNPs or PMPs.<sup>[142]</sup> This can then further lead to incorporation of the label into the polymer matrix, which can falsify the results. In addition, the impact of particle scattering is significant for polymer particles. These are reasons that suggest the employment of an indirect quantification method, which is done by performing the optical measurement not with the dye-labeled particles, but with the unbound dye molecules in the supernatant. Commonly used dyes for optical assays include toluidine blue (TBO), *N*-(aminoethyl)-3-(pyridin-2-yl)disulfanyl)-propanamide trifluoroacetate (*N*-APPA), fluorescein- and dipyrrometheneboron difluoride (BODIPY)-derivatives.<sup>[26,184,185]</sup>

Apart from these "always on" dyes, activatable labels that turn emissive or absorptive upon attachment to the sample,<sup>[151]</sup> or chameleon dyes that change color upon attachment can also be employed.<sup>[190]</sup> These do however require calibration with a model system. The sample labeling can also be performed with multimodal cleavable linkers.<sup>[191,192]</sup> These molecules have a part that can bind to the sample, as well as a cleavable and a reporter part, which can be an organic dye. After attaching the linker to the sample, it is cleaved. The reporter can then be detected directly in solution, without need for particle dissolution.<sup>[142]</sup>



## 5 | Results: Publications and Submitted Manuscripts

### 5.1 | Major Contributions

#### 5.1.1 | Luminescence Encoding of Polymer Microbeads With Organic Dyes and Semiconductor Quantum Dots During Polymerization

Authors: **Lena Scholtz**, J. Gerrit Eckert, Toufiq Elahi, Franziska Lübke, Oskar Hübner, Nadja C. Bigall, Ute Resch-Genger\*

To this work, L. Scholtz contributed with the planning and execution of the syntheses of QD-stained PSMPs, with exception of the investigation of the polymerization reaction conditions (see Figure 7 of the manuscript, work performed by T. Elahi). Characterization of the PSMPs were also planned by L. Scholtz, with all fluorescence, integrating sphere and absorption spectroscopy as well as DLS and zeta potential measurements performed by L. Scholtz. Other authors contributed with SEM and AAS measurements of the PSMPs and QDs, respectively (J. G. Eckert), STEM of the QD-stained PSMPs (F. Lübke) and CLSM measurements of the same PSMPs (O. Hübner). L. Scholtz coordinated and carried out the data interpretation of these measurements, with significant help of the aforementioned contributors. The manuscript was mainly written by L. Scholtz, with significant help from U. Resch-Genger and N. C. Bigall.

**Estimated Contribution: 70%**

Work published in journal: Scientific Reports, 2022

See online here: <https://www.nature.com/articles/s41598-022-16065-x>

DOI: <https://doi.org/10.1038/s41598-022-16065-x>

This article is licensed under a Creative Commons Attribution 4.0 International (CC BY 4.0, <https://creativecommons.org/licenses/by/4.0/>).

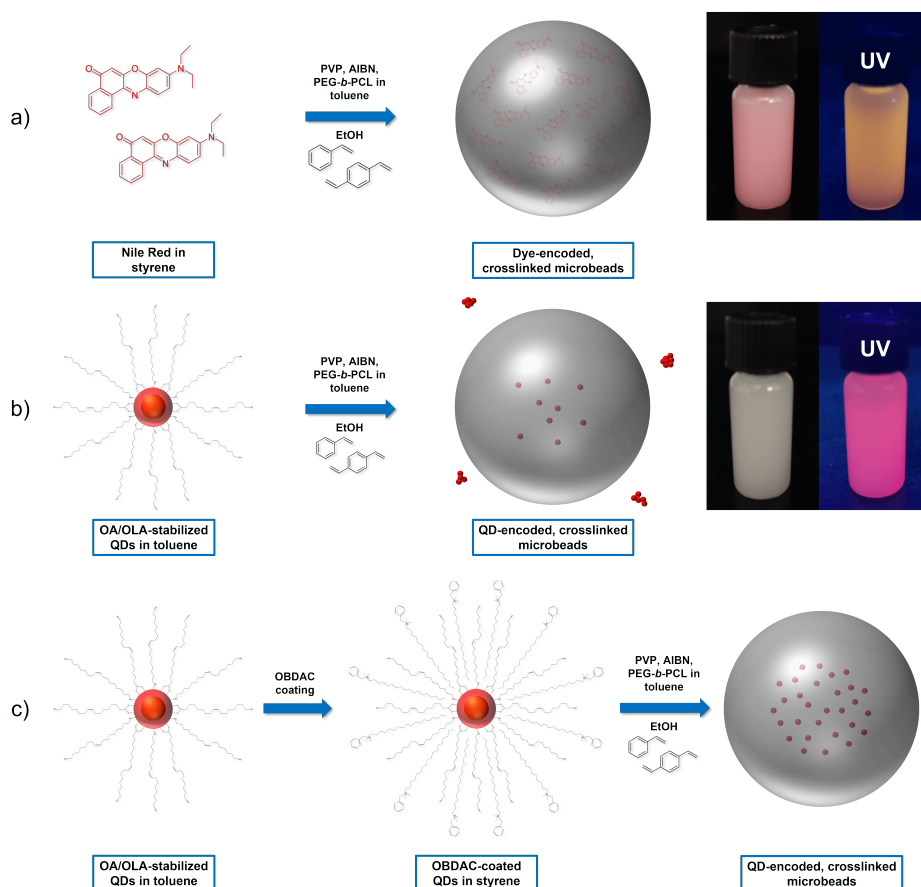


Figure 21: Schematic depiction of luminophore-stained PSMP production, with a) synthesis of NR-stained PSMPs, b) synthesis of QD-stained PSMPs without pretreatment of QDs, and c) synthesis of QD-stained PSMPs including pretreatment of QDs with the polymer-compatible ligand OBDAc. Image taken with permission from L. Scholtz *et al.*, copyright 2022 Scientific Reports.<sup>[22]</sup>



OPEN

# Luminescence encoding of polymer microbeads with organic dyes and semiconductor quantum dots during polymerization

Lena Scholtz<sup>1,2</sup>, J. Gerrit Eckert<sup>3</sup>, Toufiq Elahi<sup>2</sup>, Franziska Lübke<sup>3,4</sup>, Oskar Hübner<sup>1,2</sup>, Nadja C. Bigall<sup>3,4</sup> & Ute Resch-Genger<sup>1,5</sup>✉

Luminescence-encoded microbeads are important tools for many applications in the life and material sciences that utilize luminescence detection as well as multiplexing and barcoding strategies. The preparation of such beads often involves the staining of premanufactured beads with molecular luminophores using simple swelling procedures or surface functionalization with layer-by-layer (LbL) techniques. Alternatively, these luminophores are sterically incorporated during the polymerization reaction yielding the polymer beads. The favorable optical properties of semiconductor quantum dots (QDs), which present broadly excitable, size-tunable, narrow emission bands and low photobleaching sensitivity, triggered the preparation of beads stained with QDs. However, the colloidal nature and the surface chemistry of these QDs, which largely controls their luminescence properties, introduce new challenges to bead encoding that have been barely systematically assessed. To establish a straightforward approach for the bead encoding with QDs with minimized loss in luminescence, we systematically assessed the incorporation of oleic acid/oleylamine-stabilized CdSe/CdS-core/shell-QDs into 0.5–2.5  $\mu\text{m}$ -sized polystyrene (PS) microspheres by a simple dispersion polymerization synthesis that was first optimized with the organic dye Nile Red. Parameters addressed for the preparation of luminophore-encoded beads include the use of a polymer-compatible ligand such as benzyltrimethyloctadecylammonium chloride (OBDAC) for the QDs, and crosslinking to prevent luminophore leakage. The physico-chemical and optical properties of the resulting beads were investigated with electron microscopy, dynamic light scattering, optical spectroscopy, and fluorescence microscopy. Particle size distribution, fluorescence quantum yield of the encapsulated QDs, and QD leaking stability were used as measures for bead quality. The derived optimized bead encoding procedure enables the reproducible preparation of bright PS microbeads encoded with organic dyes as well as with CdSe/CdS-QDs. Although these beads show a reduced photoluminescence quantum yield compared to the initially very strongly luminescent QDs, with values of about 35%, their photoluminescence quantum yield is nevertheless still moderate.

Luminescent polymer beads, encoded either with molecular or nanoscale luminophores, have been increasingly employed in the life and material sciences in the last decades in conjunction with fluorescence spectroscopy, microfluorometry, fluorescence microscopy, and flow cytometry. Such particles are often equipped with surface functional groups to which recognition moieties like proteins and antibodies or analyte-responsive dyes can be attached<sup>1,2</sup>. This opens up many different applications including (bio)imaging, biomedical assays, and chemical sensing<sup>3–8</sup>. While luminescent polymer nanobeads are often employed for cell labeling and assay platforms, commonly larger microbeads are used for bead-based bioassays and spectral multiplexing schemes<sup>8–21</sup>, utilizing either color encoding or recently also lifetime encoding<sup>22</sup>, in conjunction with flow cytometry or fluorescence microscopy. Here, the luminescence color or lifetime of the encoded carrier beads is utilized as an identifying code for the bead surface chemistry and the subsequently bead-bound captured target is then quantified with

<sup>1</sup>Division 1.2 Biophotonics, Federal Institute for Materials Research and Testing (BAM), Richard-Willstätter-Str. 11, 12489 Berlin, Germany. <sup>2</sup>Institute for Chemistry and Biochemistry, Free University Berlin, Takustr. 3, 14195 Berlin, Germany. <sup>3</sup>Institute of Physical Chemistry and Electrochemistry, Leibniz Universität Hannover, Callinstraße 3A, 30167 Hannover, Germany. <sup>4</sup>Cluster of Excellence PhoenixD (Photonics, Optics, and Engineering-Innovation Across Disciplines), 30167 Hannover, Germany. ✉email: ute.resch@bam.de

the aid of an additional spectrally distinguishable fluorescent label. Nano- and micrometer-sized encoded beads can both also be utilized for security, anti-counterfeiting, and authentication applications and printed codes<sup>23–25</sup>.

A common approach to the luminescence encoding of polymer beads presents the swelling of premanufactured polystyrene (PS) or polymethylmethacrylate (PMMA) beads by addition of an apolar organic solvent containing luminophores, which allows the luminophores to permeate the bead matrix<sup>26–28</sup>. Such procedures have been used, e.g., for the fabrication of beads bearing different surface functionalities, which are applied as carriers for bead-based platforms<sup>5</sup>. Alternatively, layer-by-layer coating of premanufactured beads can be performed. This versatile approach involves the step-by-step deposition of layers of oppositely charged polyelectrolytes containing nanocrystals such as colloidal semiconductor quantum dots (QDs) or organic dyes<sup>29–32</sup>. Thereby, only surface staining is achieved and the accordingly altered bead surface chemistry can impose challenges on subsequent bioconjugation steps. Another method is the incorporation of the luminophore during the polymerization reaction, both for organic dyes<sup>33–36</sup> and different nanocrystals<sup>13,37–43</sup>. Here, the luminescent compound is dissolved or dispersed in the monomer solution or added to the reaction mixture. This procedure can provide a homogeneous luminophore distribution within the beads but requires sufficiently stable emitters with a suitable solubility or dispersibility that can survive the occasionally harsh polymerization conditions<sup>44</sup>.

While procedures for the incorporation of organic dye molecules into polymer beads of different chemical composition, size, and surface chemistry are relatively well established, bead encoding with nanoscale luminophores like QDs with their very broad absorption spectra, narrow emission bands, and high photostability is far more complex<sup>3,17,45</sup>. These luminescent nanocrystals with sizes < 10 nm commonly have a core/shell particle architecture consisting of an inorganic core, an inorganic surface passivation shell, and a stabilizing organic ligand shell, which ensures dispersibility and colloidal stability<sup>46</sup>. As the surface chemistry of the QDs is not only very important for their colloidal stability but also largely controls their photoluminescence (PL) properties, particularly their photoluminescence quantum yield, this introduces considerable challenges for the encoding of polymer beads without risking QD aggregation and a significant loss in QD luminescence<sup>4,38,41,47–49</sup>. This is related to the fact that the bead incorporation process can modify the number of ligands on the QD surface, thereby introducing additional trap states by ligand removal, or require a ligand exchange first to ensure the compatibility of the QD surface chemistry with the monomer/polymer phase, that can also result in luminescence quenching<sup>47</sup>.

The reproducible encoding with nanocrystals like QDs calls for the careful consideration of all parameters controlling their colloidal stability and functionality and hence commonly an adaptation of the encoding procedures established for molecular luminophores. Utilization of a swelling procedure, which has been reported for different types of polymer beads<sup>17,20,47,50</sup>, requires careful control of the pore size distribution within the beads and can lead to inhomogeneous bead staining, a low QD loading density, lack of reproducibility, and subsequent QD leakage<sup>47</sup>. In addition, the swelling procedure and solvents can considerably affect the luminescence properties of the QDs and result in luminescence quenching. Layer-by-layer coating of premanufactured particles of different chemical composition for QDs is time-consuming, can lead to a broadening of the initial bead size distribution, and requires different purification steps resulting in material loss<sup>51–55</sup>. Also, the influence of this encoding procedure on the PL properties of the incorporated QDs has not been yet systematically assessed. The most frequently used procedure for the fabrication of QD-encoded beads presents the incorporation of the QDs during the polymerization reaction, e.g., for the preparation of PS microparticles, or PS beads containing divinylbenzene (DVB) or PMMA<sup>4,13,37–43,48,56–60</sup> and polyisoprene as well as poly(lactic-co-glycolic acid) beads<sup>52,3,45,61</sup>. Employed polymerization techniques include (mini)emulsion and suspension polymerization<sup>4,13,37–43,47,56,58,59</sup> as well as more complicated microfluidic approaches<sup>9,10,14,16,62</sup>. Nearly all of these procedures utilize Cd-based QDs such as CdSe, CdSe/ZnS or CdTe, which are commonly stabilized with a combination of trioctylphosphine (TOP)/trioctylphosphine oxide (TOPO) ligands. Occasionally, a polymerizable ligand was introduced to the QD surface for better compatibility of the QDs with the reaction mixture and improved bead incorporation<sup>48,57</sup>.

Despite many reports on QD-encoded polymer beads, up to now, the influence of bead incorporation on the PL properties of QDs has not been systematically studied and commonly the PL features of the initial QDs are not or only very roughly compared with those of the resulting QD-stained beads. Particularly, changes in the photoluminescence (PL) quantum yield (PLQY) have not been thoroughly examined, although this property, which equals the number of emitted per number of absorbed photons, largely determines the intensity of the PL signal and bead brightness. Moreover, PLQY provides a direct measure for the quality and tightness of QD surface passivation shells and enables insights into changes in the ligand shell<sup>49,63,64</sup>. This encouraged us to develop a simple procedure to synthesize luminescent PS microbeads with sizes of about 1  $\mu\text{m}$  encoded with hydrophobic organic dyes and ligand-stabilized core/shell QDs via a dispersion polymerization of styrene with minimized loss in initial luminescence. Therefore, representatively for Nile Red (NR) and oleic acid (OA)/oleylamine (OLA)-stabilized CdSe/CdS-core/shell-QDs, different polymerization conditions were systematically examined such as temperature, stirring speed, amount of initiator, reaction time, and the addition of the crosslinker divinylbenzene (DVB) as well as QD surface chemistry and the use of a polymer-compatible QD surface ligand. The characterization of the encoded microbeads comprised the determination of the particle size and size distribution with dynamic light scattering (DLS) and electron microscopy as well as elemental mapping of the QD-encoded beads by energy-dispersive X-ray spectroscopy (EDXS) for QD localization within the beads. In addition, the fluorescence properties of the luminophores before the polymerization reaction and in the beads were determined by PL and integrating sphere spectroscopy as well as confocal laser scanning microscopy (CLSM) in the case of the luminophore-stained beads. Thereby, we could identify parameters that provide strongly luminescent PS microbeads with a narrow size distribution and a minimized, albeit still noticeable loss in PLQY of the bead-incorporated QDs.

## Materials and methods

**Materials.** Styrene ( $\geq 99.0\%$ ), divinylbenzene (DVB, 80%), azobisisobutyronitrile (AIBN, 98%), tin(II) 2-ethylhexanoate (92.5–100%),  $\epsilon$ -caprolactone (97%), poly(ethylene glycol) (PEG,  $M_w$  2,500), triethylphosphine oxide (TOPO, 99%), 1-octadecene (ODE, 90%), toluene ( $\geq 99.7\%$ ), methanol ( $\geq 99.8\%$ ), isopropanol ( $\geq 99.8\%$ ), oleylamine (OLA, 70–80%), 1-octanethiol (98.5%) and acetone ( $\geq 99.5\%$ ) were obtained from Sigma Aldrich Co. Polyvinylpyrrolidone (PVP,  $M_w$  40,000), cadmium oxide (CdO, 99.998%), selenium powder (200 mesh, 99.999%) and oleic acid (OA, 90%) were purchased from Alfa Aesar. Toluene, ethanol and *n*-heptane (all spectr. grade) as well as *n*-hexane ( $\geq 99\%$ ) were obtained from Merck KGaA. Ethanol (abs., 99.9%) and dichloromethane (HPLC grade) were obtained from Chemsolute. Benzyltrimethylammonium chloride (OBDAC, 98.9%) was purchased from HPC Standards GmbH, Nile red (NR) from Fluka Analytical, *n*-octadecylphosphonic acid (ODPA,  $>99\%$ ) from PCI Synthesis and tri-*n*-octylphosphine (TOP, 99.7%) as well as deuterated chloroform (99.8 atom%) from ABCR. All solvents used for the optical measurements were of spectroscopic grade and all chemicals were employed as received without further purification.

**Synthesis of CdSe/CdS quantum dots.** The oleic acid (OA)/oleylamine (OLA)-stabilized CdSe/CdS-core/shell-QDs were synthesized according to a modified synthesis described by Carbone et al., Nightingale et al. and Chen et al.<sup>65–67</sup> which is described in detail in the Supplementary Information (SI).

**Synthesis of polyethylene glycol-block-poly( $\epsilon$ -caprolactone).** The block-copolymer polyethylene glycol-block-poly( $\epsilon$ -caprolactone) (PEG-*b*-PCL) was synthesized according to an adapted procedure by Meier et al.<sup>68</sup> and is described in detail in the SI.

**Coating of QDs with OBDAC.** For the coating of the OA/OLA-stabilized QDs, a spatula tip of OBDAC was added to 100  $\mu$ L of the QD solution in toluene in a vial. Then, ethanol was added to reach a volume of 1 mL and the mixture was placed on a shaker at 200 rpm for 5 min. The precipitated QDs were then centrifuged with an Eppendorf Microcentrifuge 5415 D at 8000 rpm for 5 min and washed one time with ethanol. The OBDAC-coated QDs were redispersed in 1 mL styrene, sealed, and stored in the refrigerator until further use.

**Synthesis of crosslinked, dye- or QD-encoded polystyrene microbeads.** The synthesis of the encoded PS microbeads was performed according to a modified procedure described by Acter et al.<sup>69</sup> and the crosslinking of the beads was implemented following a procedure from Li et al.<sup>70</sup>. First, 36.6 mg of PEG-*b*-PCL were dissolved in 403  $\mu$ L toluene. The mixture was placed on a shaker at 200 rpm for 30 min to dissolve the copolymer. In the meantime, 1.465 g PVP and 36.6 mg AIBN were sequentially dissolved in 40 mL of ethanol.

For the dye encoding of the polymer beads, 4 mg of Nile Red were dissolved in 4 mL styrene and 200  $\mu$ L DVB and the mixture was then briefly sonicated. The ethanolic mixture, the dye-monomer mixture, and PEG-*b*-PCL dissolved in toluene were added to a 100 mL two-neck round-bottom flask in this order. Typically, the flask was sealed under argon and heated to 70 °C in an oil bath. The reaction was stirred at 70 rpm for 24 h before cooling to RT. In case any parameter was varied for the bead synthesis, this is explicitly stated in the following section. The resulting particle dispersion was centrifuged with 2000 rcf for 10 min, the supernatant was discarded, and the remaining particles were washed once with ethanol at 1600 rcf for 10 min. For these washing steps, a Multifuge X1R from Thermo Fisher Scientific Inc. was used. The polymer microbeads were then redispersed in ethanol and stored at room temperature in the dark. For the analytical characterization, the particle stock solution was washed additionally three times with ethanol and each time centrifuged for 10 min at 700 rcf to separate smaller beads and remove any remaining synthesis residuals like styrene or AIBN. These washing steps were performed with an Eppendorf Microcentrifuge 5415 D.

For the QD encoding of the polymer beads, 1 mL of a dispersion of OBDAC-coated, oleic acid/oleylamine-stabilized CdSe/CdS-QDs in styrene, prepared as described in the previous section, were added to 3 mL styrene. For the crosslinking of the beads, 50–200  $\mu$ L DVB were added and the mixture was briefly sonicated. The ethanolic mixture as well as the PEG-*b*-PCL solution in toluene were prepared as described above and added to the flask together with the QD-monomer mixture. The reaction procedure was otherwise performed under the same conditions as employed for the preparation of the dye-encoded microparticles.

**Nuclear magnetic resonance (NMR).** A solution <sup>1</sup>H-NMR spectrum of the synthesized PEG-*b*-PCL was recorded at RT with a 400 MHz JEOL JNM-ECX400 spectrometer at Free University Berlin. The PEG-*b*-PCL sample was prepared by dissolving 6 mg PEG-*b*-PCL in 700  $\mu$ L CDCl<sub>3</sub>. The corresponding spectrum, confirming the chemical identity of the copolymer, is displayed in the SI (Fig. S1).

<sup>1</sup>H-NMR (CDCl<sub>3</sub>, 400 MHz):  $\delta$  = 1.38 (m, 2H,  $\gamma$ ), 1.63 (m, 4H,  $\beta$  &  $\delta$ ), 2.30 (m, 2H,  $\alpha$ ), 3.64 (s, 4H, a & b), 4.05 (t, 2H,  $\epsilon$ ), 4.21 (t, 2H, b).

The number-average molecular weight  $M_n$  of the synthesized PEG-*b*-PCL was calculated from the ratio of protons of the PEG and PCL signals according to Meier et al.<sup>68</sup> to be roughly 4840 g/mol.

**Dynamic light scattering (DLS) and zeta potential measurements.** DLS and zeta potential measurements of the different microparticles were carried out with a Zetasizer Nano ZS from Malvern Panalytical Ltd. at T = 25 °C in disposable folded capillary cells (DTS1070), also from Malvern Panalytical Ltd. All particles were dispersed in Milli-Q water (Millipore) for these measurements.

**High-angle annular dark-field scanning transmission electron microscopy (HAADF-STEM).** HAADF-STEM measurements were performed using a 200 kV JEOL JEM-2100F-UHR operated at 200 kV and equipped with a field emission gun as well as an Oxford Instruments INCA 200 for energy-dispersive X-ray spectroscopy (EDXS) enabling elemental mapping. The samples were prepared on carbon-coated copper grids (Quantifoil) via drop-casting of the ethanolic microbead dispersion.

**Scanning electron microscopy (SEM).** Scanning electron micrographs were captured with a JEOL JSM-6700F. The samples taken from the ethanolic microbead dispersions were drop-casted on brass holders. The measurements were performed using low acceleration voltage and current (1 kV and 2  $\mu$ A).

**Atomic absorption spectroscopy (AAS).** AAS measurements were carried out with an AA140 instrument from Varian Inc. with an oxygen/acetylene flame atomizer to determine the Cd(II) concentration in the QD dispersion. Samples of the QD dispersions were prepared by dissolution of the particles with *aqua regia*. Six standard solutions with different Cd(II) concentrations were used to obtain a calibration curve for the quantification of the Cd(II) concentration.

**Absorption spectroscopy.** Absorption spectra of the CdSe/CdS-QDs and Nile Red in toluene/styrene and the respective encoded microbeads in ethanol were recorded with a Specord 210plus spectrophotometer from Analytik Jena at RT in (10  $\times$  10) mm quartz glass cuvettes from Hellma GmbH. The different QD and dye-encoded beads for the leaking experiments were dispersed in MilliQ water and measured using the same conditions and instrument settings.

**Fluorescence spectroscopy.** Emission spectra of the CdSe/CdS-QDs and Nile Red in toluene/styrene and the respective encoded microbeads in ethanol were recorded with a FSP920 fluorescence spectrometer from Edinburgh Instruments Ltd. at RT in (10  $\times$  10) mm quartz glass cuvettes from Hellma GmbH. The excitation wavelength was set at 350 nm.

**Integrating sphere spectroscopy.** The photoluminescence quantum yields (PLQY) of solutions of the luminophores in styrene/toluene and the luminophore-encoded microparticles in ethanol were determined absolutely with a stand-alone Quantaaurus integrating sphere setup from Hamamatsu Photonics K.K. The measurements were performed at 25  $^{\circ}$ C in (10  $\times$  10) mm, long-neck quartz glass cuvettes from Hamamatsu Photonics K. K with an excitation wavelength of 350 nm. For PLQY measurements of transparent luminophore solutions, the respective solvent was used as a blank. For all encoded microbead dispersions, dispersions of unstained plain microparticles of similar size and bead concentration were employed as blank.

**Confocal laser scanning microscopy (CLSM).** CLSM measurements were performed using the confocal laser scanning microscope Olympus FV1000 (Olympus, Germany) based on the motorized inverted microscope Olympus IX81 (Olympus, Germany) and a 60  $\times$  water immersion objective ( $A_N = 1.2$ ). Transmission images were measured at 488 nm. For the recording of the fluorescence images, for optimal signal intensity, excitation with a 458 nm (87% laser power) and a 355 nm (99% laser power) laser was employed and the fluorescence emission was recorded in the range of 560–660 nm. For these experiments, the microbead stock solutions were washed three times with MilliQ water, redispersed in MilliQ water and diluted to a concentration of 0.2 mg/mL. 1  $\mu$ L of the sample was applied onto a 0.17 mm glass slide.

**Photostability tests.** The short-term photostability of the NR- and QD-encoded beads was examined with the confocal laser scanning microscope Olympus FV1000 from Olympus, Germany based upon the motorized inverted microscope Olympus IX81 from Olympus, Germany, and a 60  $\times$  water immersion objective ( $A_N = 1.2$ ). Fluorescence images with a dedicated region of interest (ROI) were recorded with a 458 nm laser for the QD-encoded beads (emission range 580–680 nm) and a 514 nm laser for the NR-encoded beads (emission range 560–660 nm). The image size was set to 512  $\times$  512 px and a scanning speed of 8  $\mu$ s/px was employed, resulting in an image acquisition time of 2.1 s. The excitation power was determined to be 1 mW in the beam path for the two excitation light sources. For the sample preparation, the microbead stock solutions were washed three times with MilliQ water, redispersed in MilliQ water and diluted to a concentration of 0.2 mg/mL. 1  $\mu$ L of the sample were applied onto a 0.17 mm glass slide and left to dry before the measurements.

The long-term stability of the dye NR, the QDs as well as NR- and QD-encoded beads against sunlight was tested with a SUNTEST CPS + setup from Atlas Material Testing Technology GmbH. The dried samples were illuminated for seven days with a power density of 650 W/m<sup>2</sup> and a maximum chamber temperature of 60  $^{\circ}$ C. The PL intensity of the dried solid samples of NR, QDs and the NR- and QD-encoded polymer beads was measured in intervals of 24 h using a spectrofluorometer Dual-FL equipped with a Quanta-Phi integrating sphere, both from Horiba Scientific.

## Results and discussion

The versatility of dispersion polymerizations, which can be performed in solvents like water or ethanol, in combination with their good reproducibility and high yields render this approach very attractive for the synthesis of luminophore-encoded polymer nanoparticles and microparticles. Polymer nanoparticles with sizes of about 50–200 nm and a narrow size distribution can be synthesized with this classical approach using a monomer, a surfactant, and a radical starter<sup>3,4,35,39,40,43,45,48,56–59,61</sup>. For bead encoding with hydrophobic organic dyes,

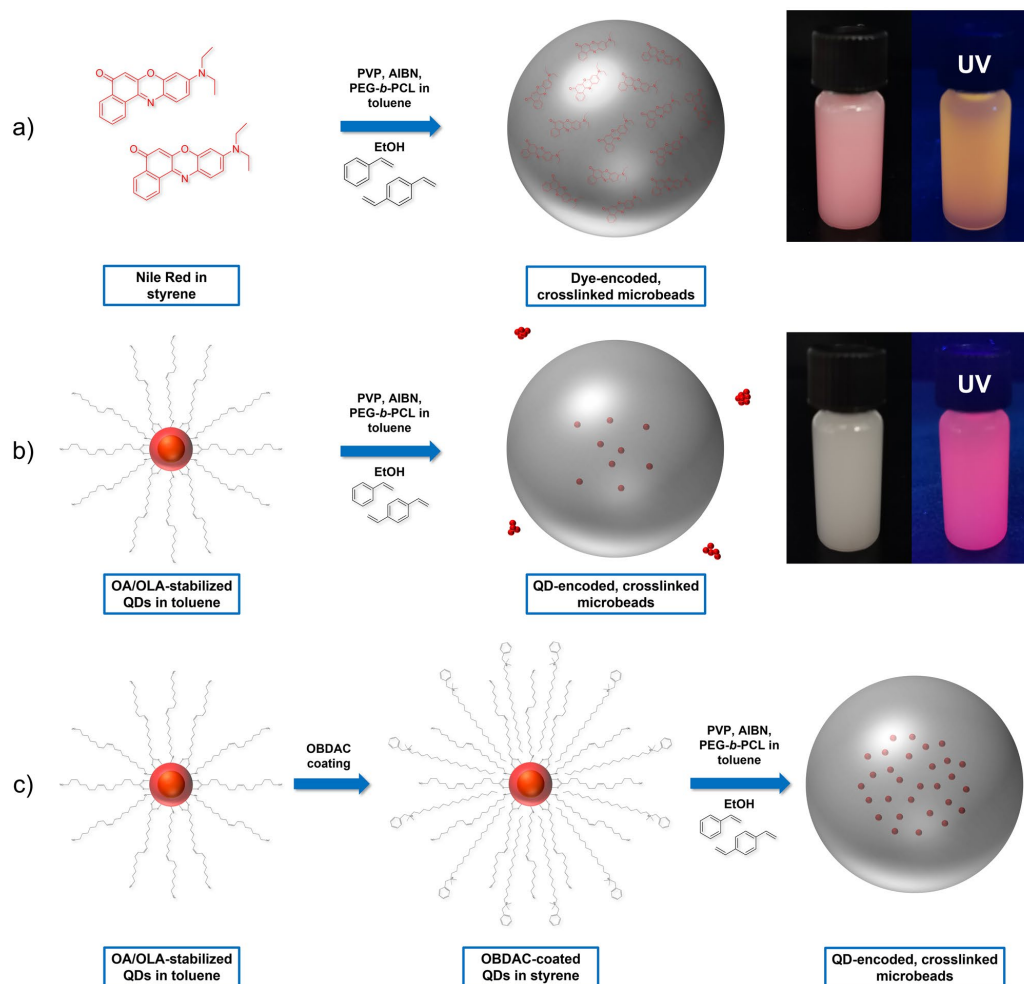


**Figure 1.** Schematic presentation of the synthesis routes employed for the preparation of the luminescent polystyrene (PS) microbeads, encoded with (a) Nile Red, (b) OA/OLA-stabilized CdSe/CdS-QDs without pretreatment, and (c) OA/OLA-stabilized CdSe/CdS-QDs, synthesized with the developed and optimized procedure, including the pretreatment of the QDs with the polymer-compatible ligand OBDAc. The photographs of the respective ethanolic bead dispersions were taken under day and UV light.

which are sufficiently stable to survive the polymerization conditions, the luminophore is commonly dissolved directly in the liquid monomer. The synthesis of microparticles with sizes of about 500 nm up to several hundred  $\mu\text{m}$  calls for some modifications of this procedure, especially for the incorporation of small nanocrystals like QDs<sup>2,8,10–14,37,38,40–43,47,48,62</sup>. In the following work, the optimization of this procedure is done exemplarily for the solvatochromic, hydrophobic, and sufficiently stable dye Nile Red (NR), which has been utilized by us before to assess and optimize the loading of premanufactured PS nanoparticles and microparticles with a swelling procedure<sup>26,27</sup>. This was done to establish the bead synthesis for the simplest case, a small molecular fluorophore, and show its general suitability for the preparation of homogeneously stained beads. Subsequently, we determined the optimum conditions for the preparation of bright and stable QD-encoded PS microparticles. For this, only one parameter at a time is varied. Thereby, the influence of the copolymer PEG-*b*-PCL, QD coating with OBDAc, and the crosslinking with DVB can be consecutively assessed. The optimized reaction procedure derived for dye and QD encoding of PS microbeads with sizes of 0.5–2.5  $\mu\text{m}$  is schematically displayed in Fig. 1.

**Preparation of polymer microparticles with a narrow size distribution.** PS microbeads prepared by a dispersion polymerization tend to display a broad size distribution. This is mostly caused by the secondary

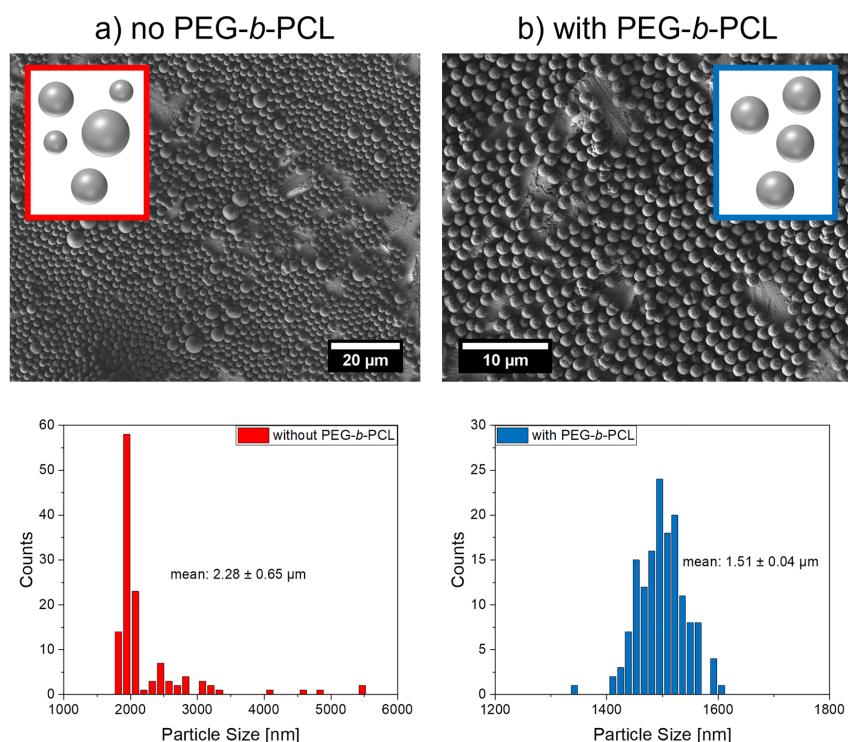


**Figure 2.** SEM images and particle size distributions of the different PS microbeads prepared: (a) without addition of PEG-*b*-PCL (toluene added without PEG-*b*-PCL; synthesis with 500 mg AIBN, no crosslinker) and (b) with addition of 36.6 mg PEG-*b*-PCL in toluene (synthesis with 100 mg AIBN, crosslinked with 200  $\mu$ L DVB). Conditions used for the preparation of both bead types: 75  $^{\circ}$ C, 70 rpm stirring speed, 24 h reaction time.

nucleation occurring during the long growth times which leads to differently sized polymer particles. To tackle this challenge, we added the *block*-copolymer PEG-*b*-PCL to the reaction mixture as described by Acter et al.<sup>69</sup>. The addition of this amphiphilic copolymer prevents secondary nucleation and aggregation during bead synthesis by sterically stabilizing the growing particles. The effect of PEG-*b*-PCL on the size distribution of the resulting PS microbeads is visualized in Fig. 2. The SEM images and the derived histograms of the size distribution show a significantly narrower and more regular size distribution with a smaller standard deviation in the presence of PEG-*b*-PCL. While the particles without PEG-*b*-PCL are generally larger because of the higher amount of AIBN, this influence is still clearly visible. This confirms the beneficial influence of PEG-*b*-PCL on the particle features. Because of these findings, PEG-*b*-PCL was employed in all following syntheses for dye and QD encoded beads to ensure a narrow size distribution of the formed beads.

**Nile Red-encoded microparticles.** The optical properties of NR were determined in styrene before particle synthesis. The corresponding absorption and emission spectra are displayed in Fig. 3. The PLQY of NR in styrene was determined to be 86%.

To evaluate the influence of crosslinking on the PL properties of the beads, NR-encoded microbeads were synthesized without and with the crosslinker DVB using the same amount of dye (1 mg/mL monomer). As derived from SEM images, with a size of  $1262 \pm 120$  nm, the crosslinked beads are larger than the non-crosslinked ones revealing a size of  $945 \pm 166$  nm. The standard deviation of the particle size of both beads is similar, yet slightly higher than for the plain particles without luminophore encoding previously introduced and discussed.

The emission spectra of the polarity probe NR in the initial reaction mixture before polymerization, after 24 h, and after five washing steps are displayed in Fig. 3. The bathochromic shift of the emission band of NR in the polymerization cocktails is ascribed to an increased polarity of the dye environment. Upon polymerization, the NR emission maximum shifts from 637 to 610 nm for both types of microparticles. The PLQY of the reaction mixtures before the synthesis was 47% in both cases. After a reaction time of 24 h, however, PLQY values of 23% and 55% were obtained for the non-crosslinked and crosslinked microparticles. After five washing steps, the PLQY of both bead types amounted to 74%. The decrease in PLQY compared to NR in styrene (86%) is

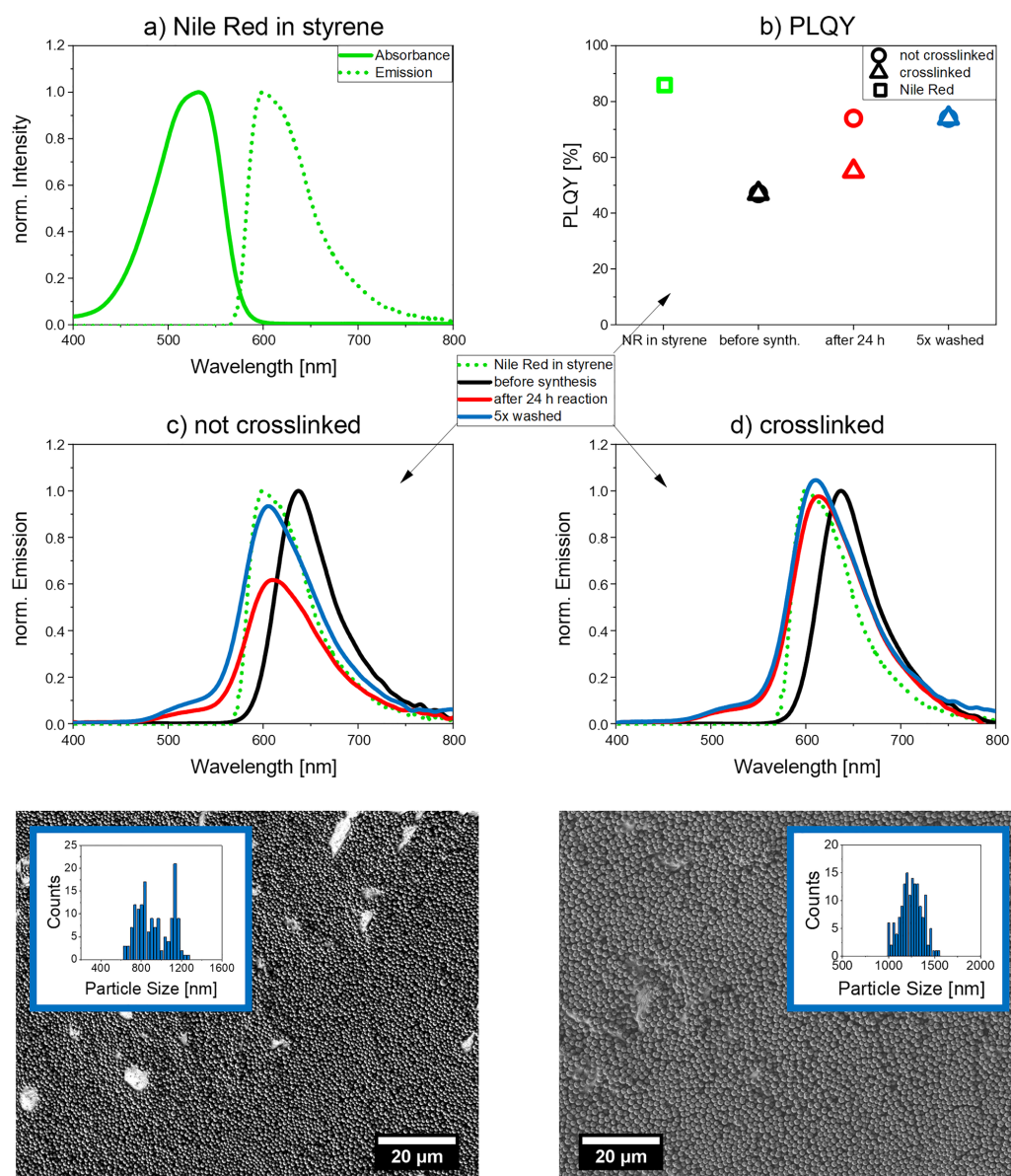


**Figure 3.** Luminescence properties of NR and NR-encoded PS microbeads. (a) Normalized absorbance and emission spectra ( $\lambda_{\text{exc}} = 350 \text{ nm}$ ) of NR in styrene; (b) PLQY of NR in styrene and in the resulting microbeads in ethanol at different stages; emission spectra ( $\lambda_{\text{exc}} = 350 \text{ nm}$ ) of NR-encoded PS microbeads in ethanol prepared (c) without and (d) with addition of 200  $\mu\text{L}$  of the crosslinker DVB. The emission spectra were normalized to the black emission spectra of the dye NR recorded in the initial reaction mixture prior to polymerization to visualize polymerization-induced changes in fluorescence. For the preparation of the dye-encoded microbeads, the following conditions were used: 65  $^{\circ}\text{C}$ , 100 mg AIBN, 36.6 mg PEG-*b*-PCL, 100 rpm stirring speed, and 24 h reaction time.

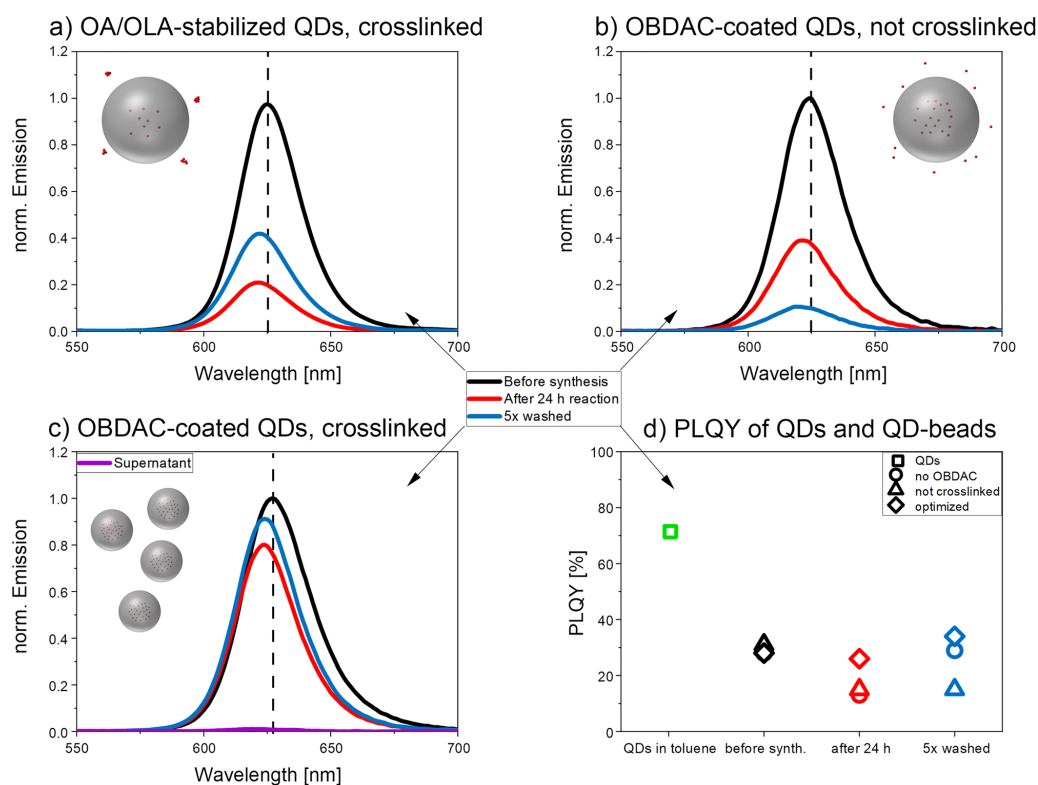


**Figure 4.** Emission spectra ( $\lambda_{exc} = 350$  nm) of CdSe/CdS-QDs in the reaction mixture before the polymerization reaction and the resulting QD-encoded PS microbeads in ethanol, obtained for (a) OA/OLA-stabilized QDs, crosslinked with DVB, (b) OBDAc-coated, OA/OLA-stabilized QDs without crosslinking, with PEG-*b*-PCL, (c) for optimized conditions, i.e., OBDAc-coated, OA/OLA-stabilized QDs, addition of PEG-*b*-PCL, and crosslinking with DVB, and (d) the corresponding PLQY values obtained at different reaction stages and for the initial QDs. Conditions used for the preparation of the QD-encoded PS beads: 75 °C, 36.6 mg AIBN, 36.6 mg PEG-*b*-PCL, 70 rpm stirring speed, and 24 h reaction time. For the comparison of the PL spectra, the emission intensity of the QDs in the initial reaction mixture was always set to one and the other spectra were scaled accordingly. The observed shift of the emission maxima is attributed to the change in QD environment from initially styrene/ethanol to polystyrene after the polymerization reaction. The increase in PL intensity of the beads in panels (a,c) washed 5 times with ethanol compared to the PL of the beads after a reaction time of 24 h is attributed to a slight change in bead concentration and bead loss during the washing steps as revealed by the corresponding absorption spectra displayed in the SI (Fig. S4).

attributed to a slightly increased polarity of the dye environment in the PS beads which is known to reduce the PLQY of NR<sup>26,71</sup>. This is supported by the slight bathochromic shifts of the emission spectra shown in panels c and d of Fig. 3.

#### QD-encoded microbeads with fluorescence preservation—influence of QD surface chemistry and crosslinking.

Although there are several reports on the preparation of QD-encoded beads, as stated earlier, the influence of the polymerization reaction and the bead matrix on the optical properties of QDs have been only rarely assessed systematically, mostly just by comparison of the emission maxima before and after the reaction<sup>3,4,11–13,35,38–43,48,56,57,60–62</sup>. Up to now, there exist only two examples for PLQY studies of QDs prior to and after bead incorporation, one from Yang et al.<sup>41</sup> on 3-mercaptopropionic acid-stabilized CdTe in polystyrene and one from Sheng et al.<sup>48</sup> on TOP/TPO-stabilized, additionally oligomeric phosphine-coated CdSe/ZnCdS/ZnS in polystyrene. In both cases, a significant loss in PLQY upon QD incorporation into the microbeads was reported<sup>41,48</sup>.

Aiming for bright QD-encoded beads with minimum loss in QD fluorescence and no QD leaking, we assessed and optimized the conditions of the polymerization reaction utilizing DLS, SEM, and PL measurements for bead quality control. The results are summarized in Figs. 4 and 5. Before the synthesis, the structure-analytical and

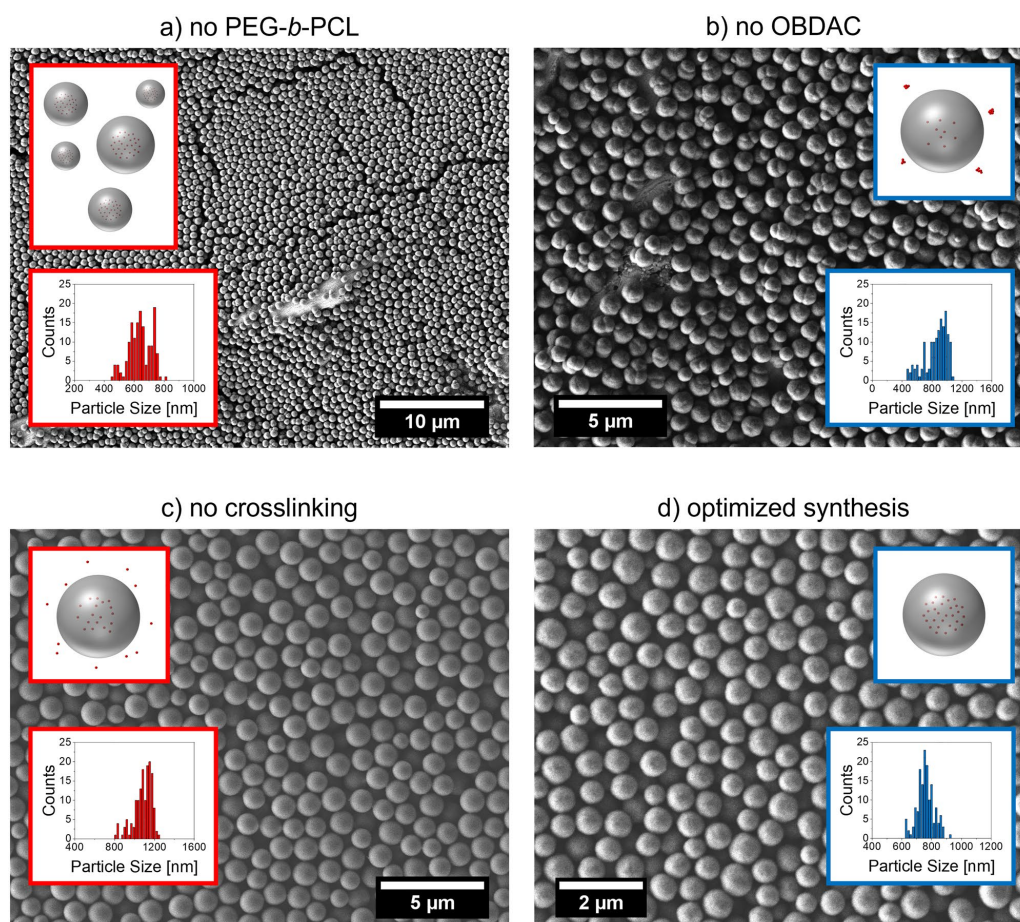


**Figure 5.** SEM images with the schematic presentation of the CdSe/CdS-encoded microbeads and the size distribution, synthesized from (a) OBDAC-coated, OA/OLA-stabilized CdSe/CdS-QDs and styrene (36.6 mg AIBN, toluene added without PEG-*b*-PCL, 200  $\mu$ L DVB), (b) OA/OLA-stabilized CdSe/CdS-QDs and styrene in the presence of the copolymer PEG-*b*-PCL (36.6 mg AIBN, 36.6 mg PEG-*b*-PCL, 200  $\mu$ L DVB), (c) OBDAC-coated, OA/OLA-stabilized CdSe/CdS-QDs and styrene in the presence of PEG-*b*-PCL without the crosslinker DVB (100 mg AIBN, 36.6 mg PEG-*b*-PCL), and (d) OBDAC-coated, OA/OLA-stabilized CdSe/CdS-QDs and styrene with the optimized procedure (36.6 mg AIBN, 36.6 mg PEG-*b*-PCL, 200  $\mu$ L DVB). Reaction conditions for all: 75  $^{\circ}$ C, 70 rpm stirring speed, 24 h reaction time.

optical properties of the oleic acid (OA)/oleylamine (OLA)-stabilized CdSe/CdS-QDs were examined by TEM as well as absorption and PL spectroscopy and the QD concentration of the dispersion used was determined by AAS (for both see SI, Fig. S2). As a tool for bead quality, we focused here first on the PL properties of the QD-encoded beads with special emphasis on the spectral position and spectral width (FWHM: full width at half maximum) of the QD emission band, which correlate with QD size and size distribution, and PLQY which is independent of bead size and the number of incorporated QDs. The structure-analytical characterization of the different types of QD-encoded beads obtained from QDs with different surface chemistries and without and in the presence of a crosslinker are detailed in the following section, thereby assessing features such as bead size, size distribution, and surface morphology as well as QD distribution within the beads.

**Bead-encoding with OA/OLA-stabilized CdSe/CdS-QDs.** In a first attempt to produce QD-encoded beads, OA/OLA-stabilized CdSe/CdS-QDs dispersed in toluene were precipitated by addition of ethanol, separated by centrifugation (5 min at 8000 rpm with an Eppendorf Microcentrifuge 5415 D), and redispersed in styrene. As depicted in Fig. 4a, the QD emission maximum shifts only slightly from 625 to 622 nm due to the change in QD environment and the FWHM of the PL spectra barely changes for bead incorporated QDs. This indicates that the

QD size and size distribution are not altered during the polymerization reaction. The formed QD-encoded beads crosslinked with DVB and dispersed in ethanol show a decrease of 80% compared to the initial intensity before the synthesis and PLQY decreased from 28 to 13% (Fig. 4b). After bead purification by washing with ethanol (5 washing-centrifugation cycles), PLQY increased by about 16% reaching a value of 29%. This is ascribed to the presence of free, possibly damaged QDs after bead preparation, which exhibit a low PLQY or are even dark, i.e., non-emissive and contribute only to the absorption of the dispersion, thereby distorting the resulting PLQY of the bead dispersion. These results indicate that under these conditions, the compatibility of the QD surface chemistry with the polymer matrix is poor, as many QDs are obviously not included in the PS particles formed. Also, the polymerization conditions clearly affect QD fluorescence, possibly by modifying the ligand shell. The PL properties of the synthesized beads (emission maxima, FWHM, PLQY) encoded with QDs as well as those encoded with NR are also summarized in the SI (Table S3).

**Bead-encoding with OBDAC-coated, OA/OLA-stabilized CdSe/CdS-QDs.** To better shield and anchor the QDs in the bead matrix, we examined the influence of an additional, polymer-compatible surface ligand, here OBDAC, on the reaction outcome. OBDAC supposedly intercalates with the initially present OA/OLA ligand shell, acting as an additional organic coating wrapped around the QDs. Thereby, ligand exchange and removal are being avoided which can introduce defect and trap states at the QD surface leading to a reduction in PL intensity and PLQY<sup>72</sup>. A comparison of the PL spectra and PLQY of the OBDAC-coated OA/OLA-stabilized and the uncoated QDs shown in the SI (Fig. S2) reveals the absence of spectral shifts and changes in the spectral width of the QD luminescence band. PLQY drops from 72% observed for the as-prepared, OA/OLA-stabilized CdSe/CdS-QDs in toluene to 68% for the OBDAC-coated QDs by only 4%. As observed for the OA/OLA-stabilized QD, the QD emission maximum shifts from 627 to 624 nm for the microbeads containing OBDAC-coated QDs and FWHM was barely affected, suggesting no change in QD size and size distribution during polymerization (Fig. 4c). As shown in Fig. 4b, the PLQY values of the QDs in the reaction mixture before the start of the polymerization reaction was about 28% for both OA/OLA-stabilized QDs and QDs additionally coated with OBDAC. However, in the latter case, PLQY of the resulting QD-encoded microbeads reached 26% after 24 h for the OBDAC-coated, OA/OLA-stabilized QDs, which exceeds the PLQY value resulting for the former (13%) by a factor of 2. For the washed microbeads encoded with OBDAC-coated, OA/OLA-stabilized QDs, a PLQY of 34% was obtained, which is slightly higher (by 5%) than the PLQY of the microbeads containing OA/OLA-stabilized QDs.

**Crosslinking of QD-encoded beads.** A well-known challenge luminophore-encoded beads have to master is the prevention of luminophore leaking under application relevant conditions like washing steps mandatory for bead purification or the presence of proteins or surfactants like streptavidin often used for bioconjugation reactions. As washing of the QD-encoded PS microparticles with ethanol leads to QD leakage even for the OBDAC-coated, OA/OLA-stabilized QDs indicated by a loss in PL intensity, therefore, up to 5% DVB (referring to the amount of styrene used) was added to the polymerization cocktail as a second monomer to crosslink the PS matrix. Subsequently, we examined the influence of bead crosslinking on QD PL features. The emission spectra of the reaction mixture before the polymerization as well as after a reaction time of 24 h and after five consecutive washing steps with ethanol displayed in Fig. 4d clearly demonstrate the beneficial effect of the crosslinker. As shown in this figure, the QD emission maximum shifts from 627 to 624 nm due to the change in QD environment for OBDAC-coated, OA/OLA-stabilized QDs in the presence of DVB. Particles without DVB suffer from a significant loss in PL intensity during bead formation, inhibiting only about 40% of the initial PL intensity and during the washing steps, it even decreases to about 10% of the initial PL intensity. Crosslinking considerably reduces the diminution in PL intensity and helps to prevent QD leaking during bead purification (see also forthcoming section). The latter is indicated by the minimum PL detectable in the supernatant of the washed, crosslinked QD-encoded PS beads (optimized procedure). As shown in Fig. 4, DVB also affects the PLQY of the bead incorporated QDs. While with values of 31% and 28%, the PLQY of the QDs in the polymerization cocktail were very similar without and with crosslinker, the beneficial influence of DVB became apparent after bead formation. PLQY of the crosslinked beads reached a value of 26% exceeding PLQY of the non-crosslinked ones of 15% by a factor of almost 2. The favorable influence of the crosslinker became even more pronounced after five washing steps with PLQY values of 34% for the crosslinked and 15% for the non-crosslinked beads. Apparently, by tightly encapsulating the QDs during bead formation at an early stage of the reaction, DVB cannot only circumvent QD leaking, yet also prevent damage to the OBDAC-coated, OA/OLA-stabilized CdSe/CdS-QDs and shields them from ethanol, which can induce PL quenching, e.g., by irreversible aggregation of the QDs or removal of surface ligands.

**Structure analytical characterization of QD-encoded beads.** *Bead size.* Characterization of the QD-encoded beads obtained with OA/OLA-stabilized and OBDAC-coated, OA/OLA-stabilized QDs under identical reaction conditions (75 °C, 36.6 mg AIBN, 70 rpm stirring speed) using DLS and electron microscopy revealed considerable differences in bead size. While in the presence of the former, the bead size amounted to  $872 \pm 150$  nm, for the latter, a bead size of  $768 \pm 57$  nm is obtained (sizes determined from SEM images). The corresponding SEM images with the bead size distributions are shown in Fig. 5.

A comparison of the SEM images of not crosslinked and crosslinked PS particles displayed in Fig. 5 reveals a slightly rougher surface of the crosslinked beads compared to the smoother bead surface obtained without DVB. Also, the presence of DVB increases the bead size. While the crosslinked beads (prepared with 36.6 mg AIBN) have a size of  $768 \pm 57$  nm, the size of the beads without DVB, yet with 100 mg AIBN, amounts to  $1097 \pm 91$  nm as determined from SEM images. The larger size of the latter is partly attributed to the higher amount of AIBN. Crosslinked particles often tend to be larger than their non-crosslinked counterparts, even for otherwise equal

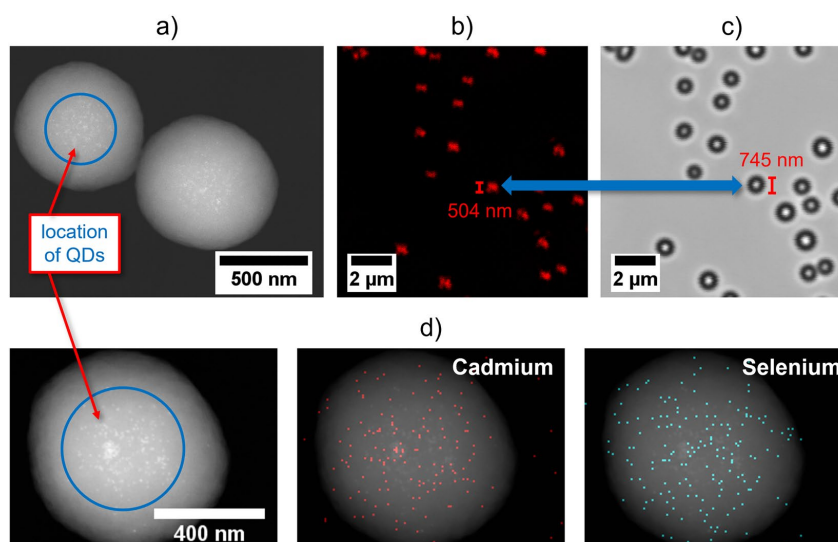


**Figure 6.** Localization of the QDs inside the PS microbeads, determined (a) with a STEM image of DVB-crosslinked PS microbeads encoded with OBDAC-coated, OA/OLA-stabilized CdSe/CdS-QDs, revealing the location of the QDs in the microbead core region; with CLSM images of the same particles measured (b) in fluorescence and (c) in transmission, including a size comparison of the fluorescent area and the particle diameter derived from the transmission image and (d) with EDXS analysis of the same DVB-crosslinked PS microbeads encoded with OBDAC-coated, OA/OLA-stabilized CdSe/CdS-QDs. Reaction conditions of particles in all images: 75 °C, 36.6 mg AIBN, 36.6 mg PEG-*b*-PCL, 70 rpm stirring speed, 24 h reaction time.

reaction conditions (see Fig. 3 for NR-encoded microbeads). This difference can be attributed to changed reaction dynamics introduced by the crosslinker, e.g., by interfering with the particle nucleation<sup>73</sup>. The size distribution of the optimized, QD-encoded beads is very similar to that of the plain beads with a relatively small standard deviation. However, as the focus of our study was on the preservation of a high PLQY of the encapsulated QDs and the prevention of QD leaking, this increase in bead size was not relevant here. Also, for most applications of such QD-encoded beads, this increase in particle size by about 25% is not important.

**QD distribution within the polymer beads.** The QD distribution within the PS microparticles, which can be relevant, e.g., for all types of applications relying on energy transfer from the encoding fluorophores to surface-bound fluorophores, was exemplarily assessed for selected beads encoded with OBDAC-coated, OA/OLA-stabilized CdSe/CdS-QDs utilizing STEM with EDXS and CLSM. To obtain a detailed insight into the QD distribution in a single microbead, STEM images were taken with an acceleration voltage of 200 kV while the distribution of Cd, Se, and S constituting the core/shell QDs within the microbead was derived from EDXS measurements. The obtained images are displayed in Fig. 6. The STEM image indicates the localization of the QDs in the bead core region. This also reveals only very little agglomeration or aggregation of the single QDs within the bead. The EDXS maps shown in Fig. 6d indicate the presence of Cd and Se in the encoded microbeads, which confirms the successful incorporation of the CdSe/CdS-QDs into the beads. Additional EDXS maps of C and S are included in the SI (Fig. S5). As can be seen in Fig. 6b,c, the CLSM images of the QD-encoded beads support that the origin of PL mainly originates from the bead core. This becomes obvious by comparing the fluorescence with the transmission image, with the latter showing larger particles than the bright areas in the fluorescence image. The QD accumulation in the core region is ascribed to the hydrophobicity of the OBDAC-coated, OA/OLA-stabilized QDs that, together with the crosslinking with DVB, favors QD incorporation in the first bead seeds formed from the start of the nucleation reaction, thereby removing them as far as possible from the ethanolic part of the reaction mixture.

**Stability and leaking studies with encoded beads.** To further investigate the stability of dye and QD encoding, the differently prepared and purified encoded beads were incubated in different media (MilliQ water, phosphate-buffered saline solution (PBS), Dulbecco's Modified Eagle's Medium (DMEM)) for one hour at 37 °C. Then, the beads were separated with centrifugal filter units (10 kDa, Amicon Ultra, Merck Millipore) and the amount of released dye molecules or QDs in the supernatant was photometrically determined. The results of the leaking studies are displayed in the SI (Fig. S6). These experiments revealed high leaking stability of NR molecules and QDs in the microbeads, as the detected amount of luminescent compound was far below 1% in most

cases. For DVB crosslinked microbeads with OBDAC-coated, OA/OLA-stabilized CdSe/CdS-QDs, the amount of free QDs was below 1% for MilliQ water and PBS, and below 2% for DMEM. The same applies to the amount of free dye for DVB crosslinked microbeads with NR. For the NR-encoded beads without crosslinking, less than 1% of free dye could be detected for all three media. For OBDAC-coated, OA/OLA-stabilized CdSe/CdS-QDs, QD release from microbeads prepared without DVB was below 1% in MilliQ water and DMEM, and about 1% for PSB. These results confirm the excellent leaking stability of our NR- and QD-encoded beads.

**Photostability studies of the NR- and QD-encoded beads.** The short-term photostability of the NR- and QD-encoded microbeads was assessed with the CLSM. The long-term stability was estimated with a sunlight simulator, here also in comparison to the dye NR and the QDs. The corresponding data are displayed in the SI (see Fig. S7).

The short-term CLSM measurements revealed a roughly exponential decay of the luminescence intensity of the NR-encoded beads and a nearly linear decay for the QD-encoded beads. After 20 scans, corresponding to about 42 s, the NR-encoded beads were left with about 48% of their initial luminescence intensity, while the QD-encoded beads preserved 67% of their initial luminescence.

As expected, the NR-encoded beads showed a very limited photostability with a significant loss in luminescence even after short intervals of light exposure. The NR-encoded beads, however, still show a luminescence after 24 h of illumination at a power density of 650 W/m<sup>2</sup> in the sunlight simulator, albeit a much smaller remaining luminescence than the QD-encoded beads. After illumination for 72 h, the NR-encoded beads show a more or less complete loss in luminescence after 72 h while the QD-encoded beads are still luminescent after 120 h of light exposure.

**Optimization of the polymerization conditions and assessing the tunability of bead size.** Subsequently, we performed screening studies of the size tunability of the polymer microbeads encoded with OBDAC-coated, OA/OLA-stabilized CdSe/CdS-QDs utilizing our polymerization procedure to assess its flexibility and identify the most relevant parameters for bead size control. Therefore, different parameters of the previously optimized polymerization reaction were varied, and the size of the resulting beads was determined with DLS. Assessed parameters included temperature (varied between 60 and 80 °C), stirring speed (50–250 rpm), reaction time (0.5–24 h), and AIBN amount (36.6–200 mg), which were modified while keeping other synthesis conditions constant. As shown in Fig. 7, panel a, an important factor with a considerable influence on particle size is the reaction temperature, the increase of which leads to a decrease in bead size. This is attributed to an increased number of seeds formed simultaneously at high temperatures which then automatically results in a smaller particle size. The microbeads formed at a reaction temperature of 60 °C are relatively small and the resulting bead dispersion has a low bead concentration, indicating that the polymerization reaction is significantly slowed down and incomplete at this temperature. As depicted in panel b of Fig. 7, an increase in stirring speed favors the formation of smaller microbeads by decreasing the size of the PVP micelles in which the polymer beads grow. The time dependence of the bead growth behavior shown in Fig. 7c indicates that for reaction times of up to four hours, the particle size increases fast and almost linearly. Then, the growth speed significantly slows down. Also, the amount of the radical initiator AIBN can affect microbead size (Fig. 7d). As to be expected, usage of an increased amount of AIBN, and thus the presence of a larger number of radicals, speeds up the polymerization reaction and provides larger beads. An AIBN amount exceeding 200 mg, however, causes microbead aggregation during the polymerization reaction.

### Conclusion and outlook

In this work, we developed optimized procedures for the encoding of polymer microbeads with hydrophobic, organic dyes and semiconductor quantum dots (QDs) added during the polymerization representatively for Nile Red (NR) and CdSe/CdS QDs stabilized with oleic acid (OA) and oleylamine (OLA). Special emphasis was dedicated to the preservation of the initial photoluminescence (PL) of the QD during bead synthesis and used to optimize the preparation of the QD-encoded beads which has been rarely systematically assessed before. This also provides a deeper insight into how the bead formation reaction and some of its parameters influence QD luminescence. By careful parameter adjustment, the synthesis of luminescent microbeads with narrow size distribution and stable emission properties as well as a relatively high photoluminescence quantum yield (PLQY) could be realized, although the PLQY is still reduced compared to the initial PLQY of the QDs. A minimization of PLQY loss for the bead-incorporated QDs was achieved by using the ligand benzyldimethyloctadecylammonium chloride, that was wrapped around the QDs, making the QD surface chemistry better compatible with the polymer matrix, and the crosslinker divinylbenzene (DVB) to prevent QD leakage.

The developed optimized dispersion polymerization approach is simple and paves the road for the facile usage and combination of different materials such as QDs with varying compositions, dyes or other luminescent nanocrystals as encoding materials for the microbeads which can then be employed for optical multiplexing and the combination with magnetic nanoparticles, e.g., for immuno-separation. By introducing functional groups to the microbead surface during bead synthesis, particles with different surface chemistries can be made enabling further processing steps like bioconjugation reactions. In the future, we plan to expand these studies on the influence of the polymerization reaction and bead incorporation on the luminescence properties of nanocrystals to QDs with systematically varied surface chemistries including the chemical nature and thickness of the surface passivation shell, QD surface chemistry, and morphology. These encoded beads will then be employed for follow-up studies regarding possible applications such as multiplexed bioassays.

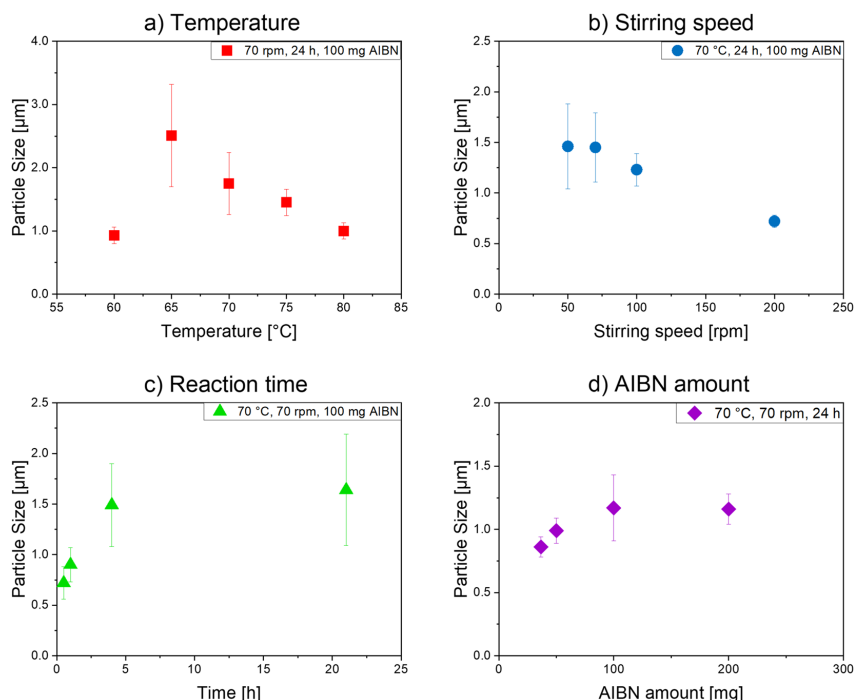


**Figure 7.** Particle size of DVB-crosslinked PS microbeads encoded with OBDAC-coated, OA/OLA-stabilized CdSe/CdS-QDs, as determined by DLS, obtained as a function of systematically varied (a) reaction temperature, (b) stirring speed, (c) reaction time (samples not purified), and (d) amount of AIBN. In all cases, 36.6 mg PEG-*b*-PCL in toluene and the same amount of OBDAC-coated, OA/OLA-stabilized CdSe/CdS-QDs were used.

#### Data availability

All data generated or analyzed during this study are included in this published article (and its Supplementary Information files) or are available upon request.

Received: 18 April 2022; Accepted: 4 July 2022

Published online: 14 July 2022

#### References

- Sun, L. *et al.* Preparation of quantum dots encoded microspheres by electrospray for the detection of biomolecules. *J. Colloid Interface Sci.* **358**, 73–80. <https://doi.org/10.1016/j.jcis.2011.02.047> (2011).
- Yu, X., Cheng, G., Zhou, M.-D. & Zheng, S.-Y. On-demand one-step synthesis of monodisperse functional polymeric microspheres with droplet microfluidics. *Langmuir* **31**, 3982–3992. <https://doi.org/10.1021/acs.langmuir.5b00617> (2015).
- Kim, J. S. *et al.* In vivo NIR imaging with CdTe/CdSe quantum dots entrapped in PLGA nanospheres. *J. Colloid Interface Sci.* **353**, 363–371. <https://doi.org/10.1016/j.jcis.2010.08.053> (2011).
- Zhou, C. *et al.* Fluorescent QDs-polystyrene composite nanospheres for highly efficient and rapid protein antigen detection. *J. Nanoparticle Res.* **15**, 1–11. <https://doi.org/10.1007/s11051-013-1901-1> (2013).
- Rödiger, S. *et al.* Nucleic acid detection based on the use of microbeads: A review. *Microchim. Acta* **181**, 1151–1168. <https://doi.org/10.1007/s00604-014-1243-4> (2014).
- Wen, C.-Y. *et al.* Fluorescent/magnetic micro/nano-spheres based on quantum dots and/or magnetic nanoparticles: Preparation, properties, and their applications in cancer studies. *Nanoscale* **8**, 12406–12429. <https://doi.org/10.1039/C5NR08534A> (2016).
- Zhang, J., Shikha, S., Mei, Q., Liu, J. & Zhang, Y. Fluorescent microbeads for point-of-care testing: A review. *Microchim. Acta* **186**, 1–21. <https://doi.org/10.1007/s00604-019-3449-y> (2019).
- Wang, G. *et al.* Highly efficient preparation of multiscaled quantum dot barcodes for multiplexed hepatitis B detection. *ACS Nano* **7**, 471–481. <https://doi.org/10.1021/nn3045215> (2013).
- Bian, F., Wang, H., Sun, L., Liu, Y. & Zhao, Y. Quantum-dot-encapsulated core-shell barcode particles from droplet microfluidics. *J. Mater. Chem. B* **6**, 7257–7262. <https://doi.org/10.1039/C8TB00946E> (2018).
- Chen, Y., Dong, P.-F., Xu, J.-H. & Luo, G.-S. Microfluidic generation of multicolor quantum-dot-encoded core-shell microparticles with precise coding and enhanced stability. *Langmuir* **30**, 8538–8542. <https://doi.org/10.1021/la501692h> (2014).
- Leng, Y. *et al.* Magnetic/fluorescent barcodes based on cadmium-free near-infrared-emitting quantum dots for multiplexed detection. *Adv. Funct. Mater.* **26**, 7581–7589. <https://doi.org/10.1002/adfm.201602900> (2016).
- Vaidya, S. V., Gilchrist, M. L., Maldarelli, C. & Couzis, A. Spectral bar coding of polystyrene microbeads using multicolored quantum dots. *Anal. Chem.* **79**, 8520–8530. <https://doi.org/10.1021/ac0710533> (2007).

13. Vaidya, S. V., Couzis, A. & Maldarelli, C. Reduction in aggregation and energy transfer of quantum dots incorporated in polystyrene beads by kinetic entrapment due to cross-linking during polymerization. *Langmuir* **31**, 3167–3179. <https://doi.org/10.1021/la503251s> (2015).
14. Zhao, Y. *et al.* Microfluidic generation of multifunctional quantum dot barcode particles. *J. Am. Chem. Soc.* **133**, 8790–8793. <https://doi.org/10.1021/ja200729w> (2011).
15. Leng, Y., Sun, K., Chen, X. & Li, W. Suspension arrays based on nanoparticle-encoded microspheres for high-throughput multiplexed detection. *Chem. Soc. Rev.* **44**, 5552–5595. <https://doi.org/10.1039/C4CS00382A> (2015).
16. Zhao, Y. *et al.* Microfluidic synthesis of barcode particles for multiplex assays. *Small* **11**, 151–174. <https://doi.org/10.1002/sml.201401600> (2015).
17. Han, M., Gao, X., Su, J. Z. & Nie, S. Quantum-dot-tagged microbeads for multiplexed optical coding of biomolecules. *Nat. Biotechnol.* **19**, 631–635. <https://doi.org/10.1038/90228> (2001).
18. Wilson, R., Cossins, A. R. & Spiller, D. G. Encoded microcarriers for high-throughput multiplexed detection. *Angew. Chem. Int. Ed.* **45**, 6104–6117. <https://doi.org/10.1002/anie.200600288> (2006).
19. Nolan, J. P. & Sklar, L. A. Suspension array technology: Evolution of the flat-array paradigm. *Trends Biotechnol.* **20**, 9–12. [https://doi.org/10.1016/S0167-7799\(01\)01844-3](https://doi.org/10.1016/S0167-7799(01)01844-3) (2002).
20. Gao, X. & Nie, S. Quantum dot-encoded mesoporous beads with high brightness and uniformity: Rapid readout using flow cytometry. *Anal. Chem.* **76**, 2406–2410. <https://doi.org/10.1021/ac0354600> (2004).
21. Mulvaney, S. P., Mattoussi, H. & Whitman, L. J. Incorporating fluorescent dyes and quantum dots into magnetic microbeads for immunoassays. *Biotechniques* **36**, 602–609. <https://doi.org/10.2144/04364B101> (2004).
22. Kage, D., Hoffmann, K., Borcherdig, H., Schedler, U. & Resch-Genger, U. Lifetime encoding in flow cytometry for bead-based sensing of biomolecular interaction. *Sci. Rep.* **10**, 19477. <https://doi.org/10.1038/s41598-020-76150-x> (2020).
23. Sonawane, S. L. & Asha, S. K. Fluorescent polystyrene microbeads as invisible security ink and optical vapor sensor for 4-nitrotoluene. *ACS Appl. Mater. Interfaces* **8**, 10590–10599. <https://doi.org/10.1021/acami.5b12325> (2016).
24. White, K. A. *et al.* Near-infrared luminescent lanthanide MOF barcodes. *J. Am. Chem. Soc.* **131**, 18069–18071. <https://doi.org/10.1021/ja907885m> (2009).
25. Shikha, S., Salafi, T., Cheng, J. T. & Zhang, Y. Versatile design and synthesis of nano-barcodes. *Chem. Soc. Rev.* **46**, 7054–7093. <https://doi.org/10.1039/c7cs00271h> (2017).
26. Behnke, T. *et al.* Encapsulation of hydrophobic dyes in polystyrene micro- and nanoparticles via swelling procedures. *J. Fluoresc.* **21**, 937–944. <https://doi.org/10.1007/s10895-010-0632-2> (2011).
27. Behnke, T., Würth, C., Laux, E.-M., Hoffmann, K. & Resch-Genger, U. Simple strategies towards bright polymer particles via one-step staining procedures. *Dyes Pigm.* **94**, 247–257. <https://doi.org/10.1016/j.dyepig.2012.01.021> (2012).
28. Huber, A., Behnke, T., Würth, C., Jaeger, C. & Resch-Genger, U. Spectroscopic characterization of Coumarin-stained beads: Quantification of the number of fluorophores Per particle with solid-state 19F-NMR and measurement of absolute fluorescence quantum yields. *Anal. Chem.* **84**, 3654–3661. <https://doi.org/10.1021/ac3000682> (2012).
29. Sukhorukov, G. B. *et al.* Layer-by-layer self-assembly of polyelectrolytes on colloidal particles. *Colloids Surf. A Physicochem. Eng. Aspects* **137**, 253–266. [https://doi.org/10.1016/S0927-7757\(98\)00213-1](https://doi.org/10.1016/S0927-7757(98)00213-1) (1998).
30. Schnäckel, A., Hiller, S., Reibetanz, U. & Donath, E. Fluorescent bead arrays by means of layer-by-layer polyelectrolyte adsorption. *Soft Matter* **3**, 200–206. <https://doi.org/10.1039/B612117A> (2007).
31. McNamara, K. P. *et al.* Synthesis, characterization, and application of fluorescence sensing lipobeads for intracellular pH measurements. *Anal. Chem.* **73**, 3240–3246. <https://doi.org/10.1021/ac0102314> (2001).
32. Stein, E. W., Singh, S. & McShane, M. J. Microscale enzymatic optical biosensors using mass transport limiting nanofilms. 2. Response modulation by varying analyte transport properties. *Anal. Chem.* **80**, 1408–1417. <https://doi.org/10.1021/ac701738e> (2008).
33. Kimura, F. *et al.* Dual luminophore polystyrene microspheres for pressure-sensitive luminescent imaging. *Meas. Sci. Technol.* **17**, 1254–1260. <https://doi.org/10.1088/0957-0233/17/6/s04> (2006).
34. Wang, X., Xu, S. & Xu, W. Luminescent properties of dye-PMMA composite nanospheres. *Phys. Chem. Chem. Phys.* **13**, 1560–1567. <https://doi.org/10.1039/C0CP00929F> (2011).
35. Zhang, X. *et al.* Fabrication of aggregation induced emission dye-based fluorescent organic nanoparticles via emulsion polymerization and their cell imaging applications. *Polym. Chem.* **5**, 399–404. <https://doi.org/10.1039/C3PY00984J> (2014).
36. Chen, J. *et al.* Design and synthesis of FRET-mediated multicolor and photoswitchable fluorescent polymer nanoparticles with tunable emission properties. *J. Phys. Chem. B* **116**, 4354–4362. <https://doi.org/10.1021/jp2110659> (2012).
37. Yang, X. & Zhang, Y. Encapsulation of quantum nanodots in polystyrene and silica micro-/nanoparticles. *Langmuir* **20**, 6071–6073. <https://doi.org/10.1021/la049610t> (2004).
38. O'Brien, P. *et al.* Quantum dot-labelled polymer beads by suspension polymerisation. *Chem. Commun.* **25**, 2532–2533. <https://doi.org/10.1039/B307500A> (2003).
39. Esteves, A., Barros-Timmons, A., Monteiro, T. & Trindade, T. Polymer encapsulation of CdE (E = S, Se) quantum dot ensembles via in-situ radical polymerization in miniemulsion. *J. Nanosci. Nanotechnol.* **5**, 766–771. <https://doi.org/10.1166/jnn.2005.090> (2005).
40. Li, Y. *et al.* Synthesis and characterization of CdS quantum dots in polystyrene microbeads. *J. Mater. Chem.* **15**, 1238–1243. <https://doi.org/10.1039/B412317D> (2005).
41. Yang, Y., Wen, Z., Dong, Y. & Gao, M. Incorporating CdTe nanocrystals into polystyrene microspheres: Towards robust fluorescent beads. *Small* **2**, 898–901. <https://doi.org/10.1002/sml.200600086> (2006).
42. Yang, Y., Tu, C. & Gao, M. A general approach for encapsulating aqueous colloidal particles into polymeric microbeads. *J. Mater. Chem.* **17**, 2930–2935. <https://doi.org/10.1039/B703060F> (2007).
43. Tu, C., Yang, Y. & Gao, M. Preparations of bifunctional polymeric beads simultaneously incorporated with fluorescent quantum dots and magnetic nanocrystals. *Nanotechnology* **19**, 105601. <https://doi.org/10.1088/0957-4484/19/10/105601> (2008).
44. Kage, D. *et al.* Close spectroscopic look at dye-stained polymer microbeads. *J. Phys. Chem. C* **122**, 12782–12791. <https://doi.org/10.1021/acs.jpcc.8b02546> (2018).
45. Abdel-Mottaleb, M. M., Beduneau, A., Pellequer, Y. & Lamprecht, A. Stability of fluorescent labels in PLGA polymeric nanoparticles: Quantum dots versus organic dyes. *Int. J. Pharm.* **494**, 471–478. <https://doi.org/10.1016/j.ijpharm.2015.08.050> (2015).
46. Resch-Genger, U., Grabolle, M., Cavaliere-Jaricot, S., Nitschke, R. & Nann, T. Quantum dots versus organic dyes as fluorescent labels. *Nat. Methods* **5**, 763–775. <https://doi.org/10.1038/NMETH.1248> (2008).
47. Bradley, M., Bruno, N. & Vincent, B. Distribution of CdSe quantum dots within swollen polystyrene microgel particles using confocal microscopy. *Langmuir* **21**, 2750–2753. <https://doi.org/10.1021/la047322r> (2005).
48. Sheng, W. *et al.* In-situ encapsulation of quantum dots into polymer microspheres. *Langmuir* **22**, 3782–3790. <https://doi.org/10.1021/la051973j> (2006).
49. Grabolle, M. *et al.* Determination of the fluorescence quantum yield of quantum dots: Suitable procedures and achievable uncertainties. *Anal. Chem.* **81**, 6285–6294. <https://doi.org/10.1021/ac900308v> (2009).
50. Stsiapura, V. *et al.* Functionalized nanocrystal-tagged fluorescent polymer beads: Synthesis, physicochemical characterization, and immunolabeling application. *Anal. Biochem.* **334**, 257–265. <https://doi.org/10.1016/j.ab.2004.07.006> (2004).

51. Sukhanova, A. *et al.* Nanocrystal-encoded fluorescent microbeads for proteomics: Antibody profiling and diagnostics of autoimmune diseases. *Nano Lett.* **7**, 2322–2327. <https://doi.org/10.1021/nl070966+> (2007).
52. Rogach, A. *et al.* Nano- and microengineering: Three-dimensional colloidal photonic crystals prepared from submicrometer-sized polystyrene latex spheres pre-coated with luminescent polyelectrolyte/nanocrystal shells. *Adv. Mater.* **12**, 333–337. [https://doi.org/10.1002/\(SICI\)1521-4095\(200003\)12:5%3c333::AID-ADMA333%3e3.0.CO;2-X](https://doi.org/10.1002/(SICI)1521-4095(200003)12:5%3c333::AID-ADMA333%3e3.0.CO;2-X) (2000).
53. Radtchenko, I. L. *et al.* Core-shell structures formed by the solvent-controlled precipitation of luminescent CdTe nanocrystals on latex spheres. *Adv. Mater.* **13**, 1684–1687. [https://doi.org/10.1002/1521-4095\(200111\)13:22%3c1684::AID-ADMA1684%3e3.0.CO;2-Z](https://doi.org/10.1002/1521-4095(200111)13:22%3c1684::AID-ADMA1684%3e3.0.CO;2-Z) (2001).
54. Martynenko, I. V. *et al.* Magneto-fluorescent microbeads for bacteria detection constructed from superparamagnetic Fe<sub>3</sub>O<sub>4</sub> nanoparticles and AlS/ZnS quantum dots. *Anal. Chem.* **91**, 12661–12669. <https://doi.org/10.1021/acs.analchem.9b01812> (2019).
55. Kage, D. *et al.* Tempo-spectral multiplexing in flow cytometry with lifetime detection using QD-encoded polymer beads. *Sci. Rep.* **10**, 653. <https://doi.org/10.1038/s41598-019-56938-2> (2020).
56. Joumaa, N. *et al.* Synthesis of quantum dot-tagged submicrometer polystyrene particles by miniemulsion polymerization. *Langmuir* **22**, 1810–1816. <https://doi.org/10.1021/la052197k> (2006).
57. Sherman, R. L. & Ford, W. T. Semiconductor nanoparticle/polystyrene latex composite materials. *Langmuir* **21**, 5218–5222. <https://doi.org/10.1021/la0468139> (2005).
58. Fleischhaker, F. & Zentel, R. Photonic crystals from core-shell colloids with incorporated highly fluorescent quantum dots. *Chem. Mater.* **17**, 1346–1351. <https://doi.org/10.1021/cm0481022> (2005).
59. Rubio-Rios, A. *et al.* Effect of synthesis variables on the fluorescence properties of CdSe-polystyrene latexes. *J. Polym. Res.* **19**, 1–7. <https://doi.org/10.1007/s10965-012-9833-5> (2012).
60. Zhang, H. *et al.* Fluorescent nanocrystal-polymer composites from aqueous nanocrystals: Methods without ligand exchange. *Chem. Mater.* **17**, 4783–4788. <https://doi.org/10.1021/cm050260l> (2005).
61. Yin, W. *et al.* Fluorescent quantum dot-polymer nanocomposite particles by emulsification/solvent evaporation. *Chem. Mater.* **19**, 2930–2936. <https://doi.org/10.1021/cm070214g> (2007).
62. Liu, H. *et al.* Microfluidic synthesis of QD-encoded PEGDA microspheres for suspension assay. *J. Mater. Chem. B* **4**, 482–488. <https://doi.org/10.1039/C5TB02209F> (2016).
63. Poselt, E., Fischer, S., Foerster, S. & Weller, H. Highly stable biocompatible inorganic nanoparticles by self-assembly of triblock-copolymer ligands. *Langmuir* **25**, 13906–13913. <https://doi.org/10.1021/la901876b> (2009).
64. Ostermann, J. *et al.* Controlling the physical and biological properties of highly fluorescent aqueous quantum dots using block copolymers of different size and shape. *ACS Nano* **7**, 9156–9167. <https://doi.org/10.1021/nn4037859> (2013).
65. Carbone, L. *et al.* Synthesis and micrometer-scale assembly of colloidal CdSe/CdS nanorods prepared by a seeded growth approach. *Nano Lett.* **7**, 2942–2950. <https://doi.org/10.1021/nl0717661> (2007).
66. Nightingale, A. M. *et al.* Large-scale synthesis of nanocrystals in a multichannel droplet reactor. *J. Mater. Chem. A* **1**, 4067–4076. <https://doi.org/10.1039/C3TA10458C> (2013).
67. Chen, O. *et al.* Compact high-quality CdSe–CdS core-shell nanocrystals with narrow emission linewidths and suppressed blinking. *Nat. Mater.* **12**, 445–451. <https://doi.org/10.1038/nmat3539> (2013).
68. Meier, M. A., Aerts, S. N., Staal, B. B., Rasa, M. & Schubert, U. S. PEO-b-PCL block copolymers: Synthesis, detailed characterization, and selected micellar drug encapsulation behavior. *Macromol. Rapid Commun.* **26**, 1918–1924. <https://doi.org/10.1002/marc.200500591> (2005).
69. Acter, S. *et al.* Synthesis and shape control of uniform polymer microparticles by tailored adsorption of poly(ethylene oxide)-b-poly( $\epsilon$ -caprolactone) copolymer. *Bull. Korean Chem. Soc.* **36**, 1467–1473. <https://doi.org/10.1002/bkcs.10288> (2015).
70. Li, K. & Stöver, H. D. H. Highly crosslinked micron-range polymer microspheres by dispersion polymerization of divinylbenzene. *J. Polym. Sci. A Polym. Chem.* **31**, 2473–2479. <https://doi.org/10.1002/pola.1993.080311007> (1993).
71. Fleige, E., Ziem, B., Grabolle, M., Haag, R. & Resch-Genger, U. Aggregation phenomena of host and guest upon the loading of dendritic core-multishell nanoparticles with solvatochromic dyes. *Macromolecules* **45**, 9452–9459. <https://doi.org/10.1021/ma301977r> (2012).
72. Shen, Y., Tan, R., Gee, M. Y. & Greytak, A. B. Quantum yield regeneration: Influence of neutral ligand binding on photophysical properties in colloidal core/shell quantum dots. *ACS Nano* **9**, 3345–3359. <https://doi.org/10.1021/acsnano.5b00671> (2015).
73. Song, J.-S. & Winnik, M. A. Cross-linked, monodisperse, micron-sized polystyrene particles by two-stage dispersion polymerization. *Macromolecules* **38**, 8300–8307. <https://doi.org/10.1021/ma050992z> (2005).

### Acknowledgements

We thank A. Feldhoff from the Institute of Physical Chemistry and Electrochemistry, Leibniz University Hannover for providing the TEM facilities and Dr. A. Schaefer from the Institute for Chemistry and Biochemistry, Free University Berlin for providing the NMR facilities supported by DFG. In addition, we thank Dr. K. D. Wegner from Division *Biophotonics* of the BAM for fruitful discussions and Dr. Thomas Thiele, PolyAn GmbH Berlin for the critical reading of the manuscript.

### Author contributions

L.S. planned and carried out the syntheses, except for the experiments contributing to the screening of the reaction conditions of the polymerization reaction and bead size tunability in the ms (Fig. 7) which were carried out by T.E. Measurements were planned by L.S. and performed by J.G.E. (SEM, AAS), F.L. (STEM), O.H. (CLSM) and L.S. (DLS, all fluorescence & absorption spectroscopy), every listed author also helped to interpret the data. L.S. wrote the manuscript with significant help from U.R.-G. and N.C.B. All authors were involved in discussing the results as well as proofreading, reviewing, and editing, and approved the final manuscript.

### Funding

Open Access funding enabled and organized by Projekt DEAL. L. Scholtz acknowledges funding by the European Metrology Programme for Innovation and Research (EMPIR) as part of the project “AeroTox” from the health call (18HLT02). The EMPIR initiative is co-funded by the European Union’s Horizon 2020 research and innovation programme and by the EMPIR participating states. J. G. Eckert acknowledges funding by the MWK—School for Additive Manufacturing SAM. N. C. Bigall and F. Lübke acknowledge funding by the Deutsche Forschungsgemeinschaft (DFG, German Research Foundation) under Germany’s Excellence Strategy within the Cluster of Excellence PhoenixD (EXC 2122, Project ID 390833453). O. Hübner acknowledges funding by ERA.Net Rus project TARQUS.

www.nature.com/scientificreports/

### Competing interests

The authors declare no competing interests.

### Additional information

**Supplementary Information** The online version contains supplementary material available at <https://doi.org/10.1038/s41598-022-16065-x>.

**Correspondence** and requests for materials should be addressed to U.R.-G.

**Reprints and permissions information** is available at [www.nature.com/reprints](http://www.nature.com/reprints).

**Publisher's note** Springer Nature remains neutral with regard to jurisdictional claims in published maps and institutional affiliations.



**Open Access** This article is licensed under a Creative Commons Attribution 4.0 International License, which permits use, sharing, adaptation, distribution and reproduction in any medium or format, as long as you give appropriate credit to the original author(s) and the source, provide a link to the Creative Commons licence, and indicate if changes were made. The images or other third party material in this article are included in the article's Creative Commons licence, unless indicated otherwise in a credit line to the material. If material is not included in the article's Creative Commons licence and your intended use is not permitted by statutory regulation or exceeds the permitted use, you will need to obtain permission directly from the copyright holder. To view a copy of this licence, visit <http://creativecommons.org/licenses/by/4.0/>.

© The Author(s) 2022

Supplementary Information for:

## Luminescence Encoding of Polymer Microbeads with Organic Dyes or Semiconductor Quantum Dots during Polymerization

Lena Scholtz<sup>1,2</sup>, J. Gerrit Eckert<sup>3</sup>, Toufiq Elahi<sup>2</sup>, Franziska Lübke<sup>3,4</sup>, Oskar Hübner<sup>1,2</sup>, Nadja C. Bigall<sup>3,4</sup>, Ute Resch-Genger<sup>1,\*</sup>

<sup>1</sup>Bundesanstalt für Materialforschung und -prüfung (BAM), Division 1.2 Biophotonics, Richard-Willstätter-Str. 11, 12489 Berlin, Germany.

<sup>2</sup>Institute for Chemistry and Biochemistry, Free University Berlin, Takustr. 3, 14195 Berlin, Germany.

<sup>3</sup>Institute of Physical Chemistry and Electrochemistry, Leibniz Universität Hannover, Callinstraße 3A, 30167 Hannover, Germany.

<sup>4</sup>Cluster of Excellence PhoenixD (Photonics, Optics, and Engineering – Innovation Across Disciplines), 30167 Hannover, Germany.

\* ute.resch@bam.de, Phone: +49 (0)30 8104 1134

### 1. Synthesis of CdSe/CdS-core/shell-QDs

The oleic acid (OA)/oleylamine (OLA)-stabilized CdSe/CdS-core/shell-QDs were synthesized according to a modified synthesis described by Carbone *et al.*, Nightingale *et al.* and Chen *et al.*<sup>65-67</sup>

**Synthesis of CdSe cores.** In the first step, wurtzite CdSe cores were synthesised according to Carbone *et al.*<sup>65</sup> For the synthesis, 120 mg CdO, 560 mg ODPa and 6 g TOPO were degassed for 1 h at 150 °C. The mixture was heated under argon flow at 300 °C and 2 mL TOP were injected. After heating to 380 °C and a retention period of 10 min, 3.6 mL of a previously prepared TOP/Se solution (120 mg/3.6 mL) was swiftly injected. The temperature was allowed to rise to 380 °C again before the reaction was quenched by adding 5 mL ODE and cooled down to 70 °C. At this point, 5 mL toluene was added. The resulting particles were precipitated by methanol/isopropanol (1:2) and redispersed in 2 mL hexane.

**Synthesis of Cd(oleate)<sub>2</sub>.** The Cd(oleate)<sub>2</sub> precursor solution was synthesised according to Nightingale *et al.*<sup>66</sup> For the synthesis of a 0.5 M Cd(oleate)<sub>2</sub> solution, a mixture of 1.284 g CdO, 12.94 mL oleic acid and 7.04 mL ODE were degassed for 10 min at 100 °C. Under argon flow, the dispersion was heated to 180 °C and kept there for 60 min under vigorous stirring. To remove water as a side product, the mixture was cooled to 120 °C and degassed for 45 min. The solution was then used as prepared.

**Synthesis of CdS shells.** The growth of the CdS surface passivation shell was performed according to an adapted synthesis by Chen *et al.*<sup>67</sup> 100 nmol of the CdSe cores (90–100 µL) were dispersed in 3 mL OLA and ODE, respectively and degassed for 30 min at 90 °C. In the meantime, the S and Cd precursor solutions were prepared. For the desired shell thickness of 5 monolayers, 758 µL Cd(oleate)<sub>2</sub> and 68 µL 1-octanethiol were diluted to 7 mL with ODE. Under argon flow, the flask was heated in two steps to 310 °C. At 240 °C, the injection of the previously prepared Cd(oleate)<sub>2</sub> and 1-octanethiol solution via syringe pump (6 mL, 3 mL/h) was started. After two hours, 1 mL oleic acid was injected, and the temperature was maintained at 310 °C for another hour. Finally, the reaction mixture was cooled down to room temperature, and the particles were precipitated by addition of acetone, centrifuged, and redispersed in toluene.

### 2. Synthesis and <sup>1</sup>H NMR of polyethylene glycol-block-poly(ε-caprolactone)

The block-copolymer polyethylene glycol-block-poly(ε-caprolactone) (PEG-*b*-PCL) was synthesized according to an adapted procedure by Meier *et al.*<sup>68</sup>

In short, 800 mg of poly(ethylene glycol) was placed in a dry flask and 1536 µL of ε-caprolactone was added. The mixture was then stirred in a preheated oil bath at 130 °C for 5 min followed by addition of one drop of Sn(II) 2-ethylhexanoate to initiate and catalyze the reaction. The reaction temperature was kept at 130 °C for 3 h before the reaction mixture was rapidly cooled with the aid of an ice bath leading to the precipitation of a solid product. The solid product was then dissolved in a small amount of dichloromethane and precipitated by addition of *n*-heptane.

The recrystallized polymer was filtered and washed several times with *n*-heptane before drying and subsequently characterized by nuclear magnetic resonance spectroscopy (solution  $^1\text{H-NMR}$ ) from which the number-averaged molecular weight was calculated.

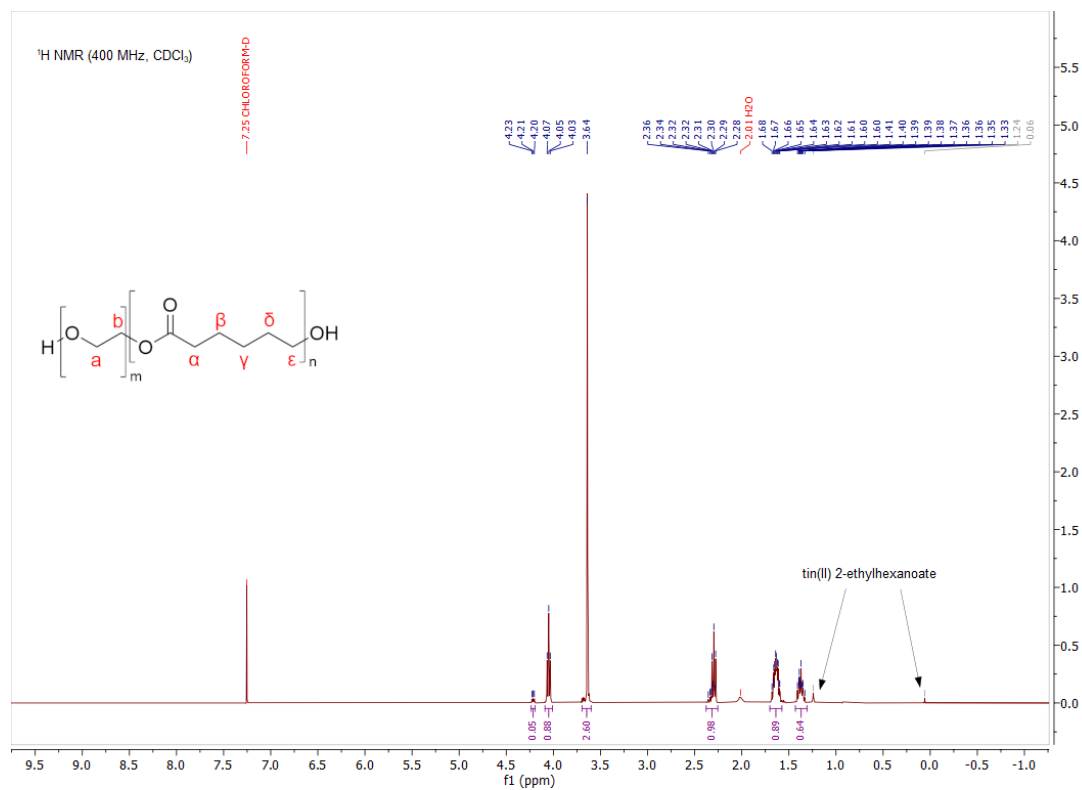


**Figure S1:**  $^1\text{H-NMR}$  spectrum (400 MHz,  $\text{CDCl}_3$ ) with structural formula of the synthesized poly(ethylene glycol)-*block*-poly( $\epsilon$ -caprolactone) (PEG-*b*-PCL) with all compound peaks, two solvent peaks and two impurity peaks that can be attributed to the used catalyst tin(II) 2-ethylhexanoate.

### 3. Electron microscopy and optical properties of CdSe/CdS-QDs

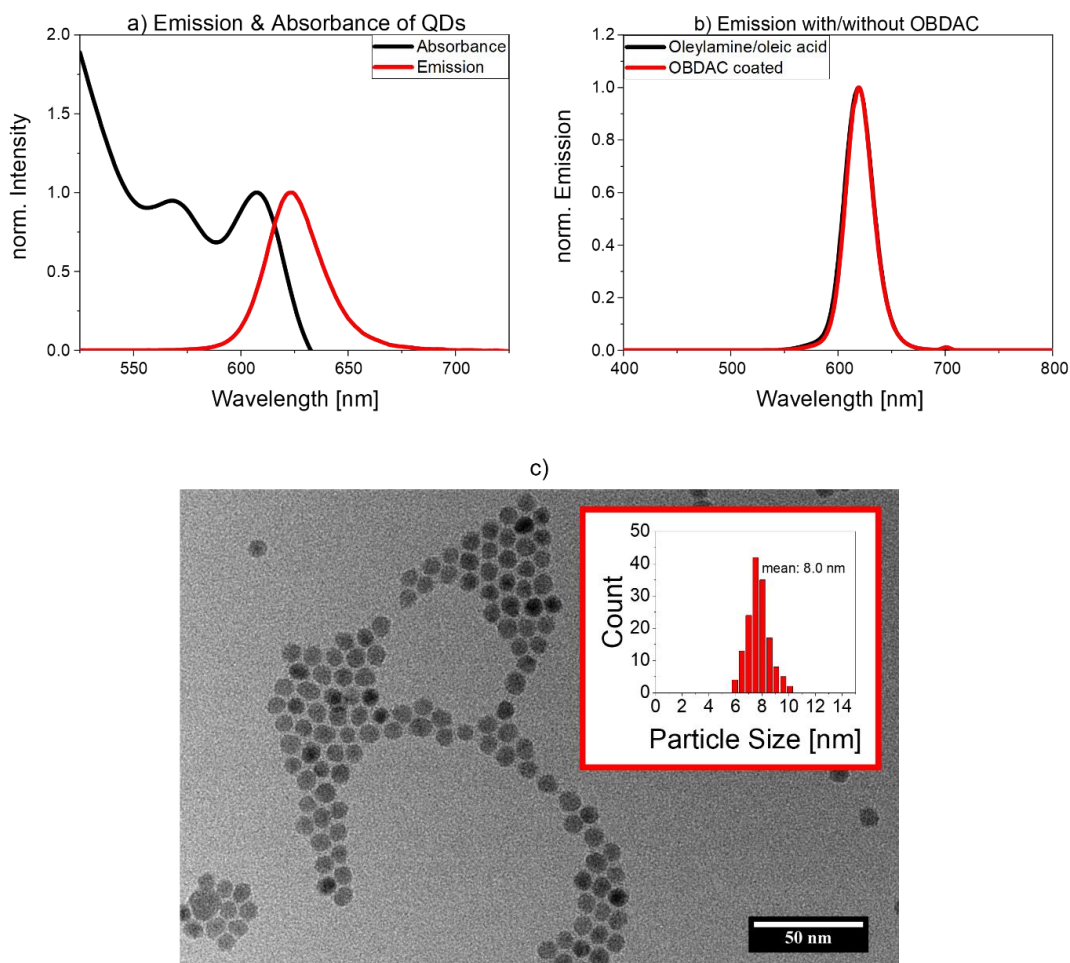


**Figure S2:** a) Emission ( $\lambda_{exc} = 350$  nm) and absorbance spectra of OA/OLA-stabilized CdSe/CdS semiconductor quantum dots (QDs) in toluene, b) Emission spectra ( $\lambda_{exc} = 350$  nm) of as-prepared CdSe/CdS-QDs with OA/OLA ligands and OBDAC-coated, OA/OLA-stabilized CdSe/CdS-QDs, both in toluene and c) TEM image of OA/OLA-stabilized CdSe/CdS-core/shell-QDs with size distribution.

The Cd concentration of the CdSe/CdS semiconductor quantum dot (QD) dispersion was determined to be 129 mmol/L by atomic absorption spectroscopy (AAS), the mean size of the particles was calculated from the TEM images to 8.0 nm (standard deviation 0.8 nm). For the OBDAC-coated, OA/OLA-stabilized QDs, the photoluminescence quantum yield (PLQY) decreased slightly to 68 % compared to the initial OA/OLA stabilized QDs with a value of 72 %.

#### 4. Photoluminescence properties of Nile Red- and QD-encoded PS microbeads

**Table S3:** Summary of the PL properties of Nile Red (NR), CdSe/CdS-QDs and the resulting encoded PS microbeads.

Sample	Emission Maximum / nm	FWHM / nm	PLQY / %
NR in styrene	599	68.7	86
NR-encoded beads, crosslinked	610	89.0	74
NR-encoded beads, not crosslinked	606	91.6	74
OA/OLA stabilized QDs in toluene	619	32.0	72
OBDAC coated, OA/OLA stabilized QDs in toluene	619	30.4	68
Microbeads encoded with OA/OLA stabilized QDs, crosslinked	622	28.6	29
Microbeads encoded with OBDAC coated, OA/OLA stabilized QDs, not crosslinked	622	26.9	15
Microbeads encoded with OBDAC coated, OA/OLA stabilized QDs, crosslinked (optimized)	624	30.9	34

Table S3 shows that the spectral width or Full Width at Half Maximum (FWHM) values of the optimized, QD-encoded bead emission band are very similar to those of the initial QDs. This indicates that QD size and size distribution did not change during the polymerization reaction.

5. Absorbance spectra of polymer microbeads encoded with OBDAC-coated, OA/OLA-stabilized CdSe/CdS-QDs

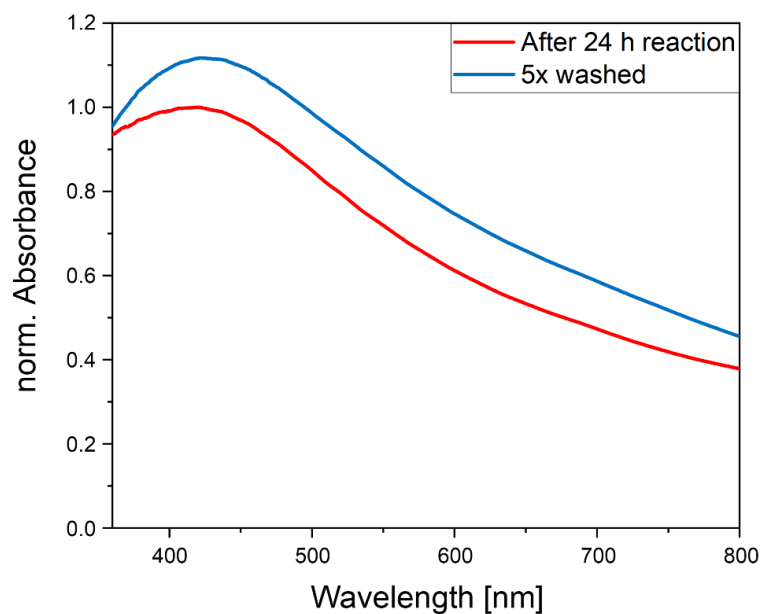


**Figure S4:** Absorbance spectra of DVB-crosslinked PS microbeads encoded with OBDAC-coated, OA/OLA-stabilized CdSe/CdS-QDs, directly and without purification after 24 h reaction time, and after five consecutive washing steps. Synthesis conditions: 70 °C, 100 mg AIBN, 36.6 mg PEG-b-PCL, 70 rpm stirring speed, 24 h reaction time.

The absorbance spectra of QD-encoded microbeads in Figure S4 show a higher absorbance for the washed beads (blue line) compared to those measured directly after the synthesis (red line). This can be attributed to an increase in the concentration of the bead solution caused by the loss of solvent (ethanol) during the washing steps.

6. EDXS mapping of QD-encoded PS microbeads

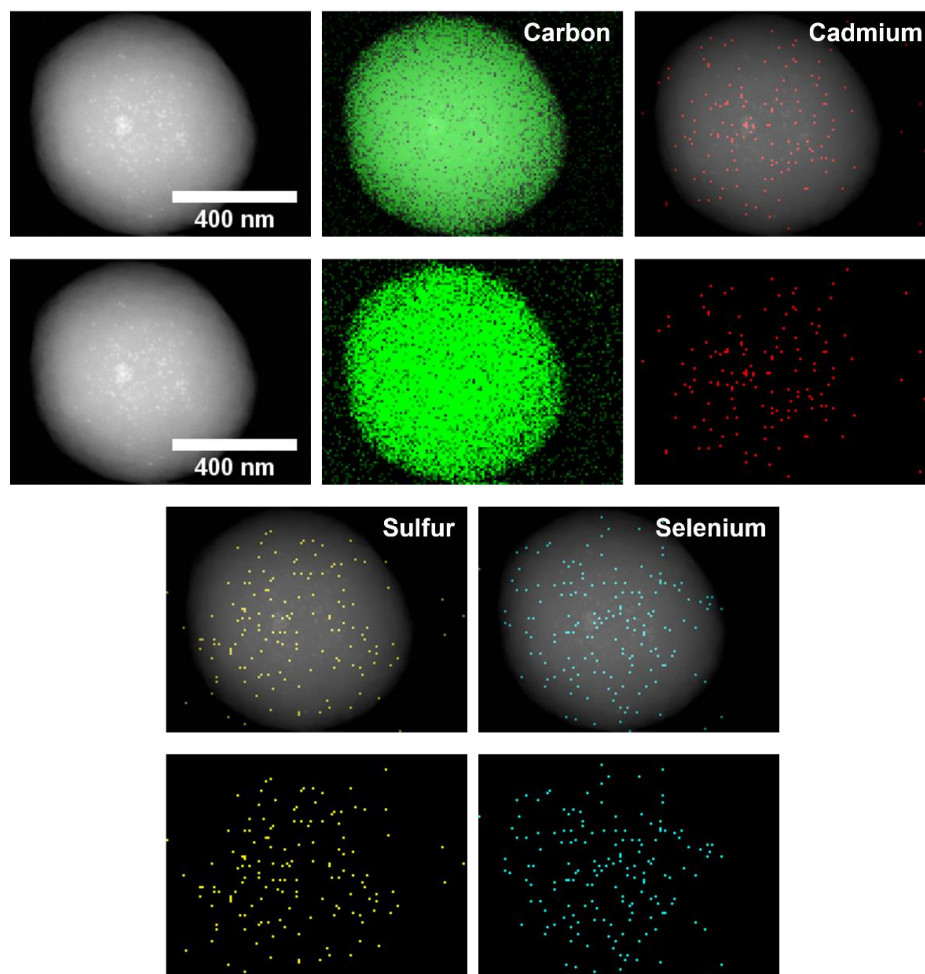


**Figure S5:** EDXS maps for different elements contained in a DVB crosslinked microbead encoded with OBDAC-coated, OA/OLA-stabilized CdSe/CdS-QDs. Reaction conditions for microbeads: 75 °C, 36.6 mg AIBN, 36.6 mg PEG-b-PCL, 70 rpm stirring speed, 24 h reaction time.

The EDXS maps of the different elements that are part of the OBDAC-coated, OA/OLA-stabilized CdSe/CdS-QDs show a clear location inside of the microbead. This confirms the presence of the QDs in the beads.

## 7. Stability studies with NR- and QD-encoded PS microbeads

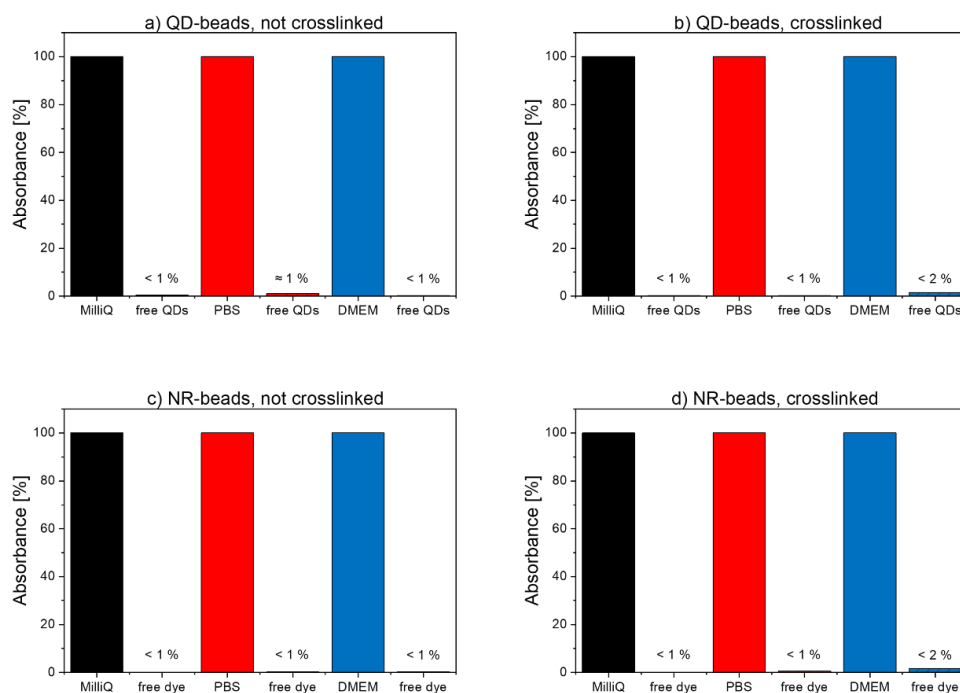


**Figure S6:** Comparison of the absorbance of purified, encoded microbeads incubated in different media (MilliQ water, phosphate-buffered saline solution (PBS), Dulbecco's Modified Eagle's Medium (DMEM)) for one hour at 37 °C and the respective supernatants after centrifugation at 12000 rcf for 10 min (Eppendorf Microcentrifuge 5415 D) with centrifugal filter units (10 kDa, Amicon Ultra, Merck Millipore) for a) microbeads without crosslinking, encoded with OBDAC-coated, OA/OLA-stabilized CdSe/CdS-QDs; b) DVB-crosslinked microbeads encoded with OBDAC-coated, OA/OLA-stabilized CdSe/CdS-QDs; c) microbeads without crosslinker, encoded with NR, and d) DVB crosslinked microbeads encoded with NR.

## 8. Photostability of NR- and QD-encoded PS microbeads

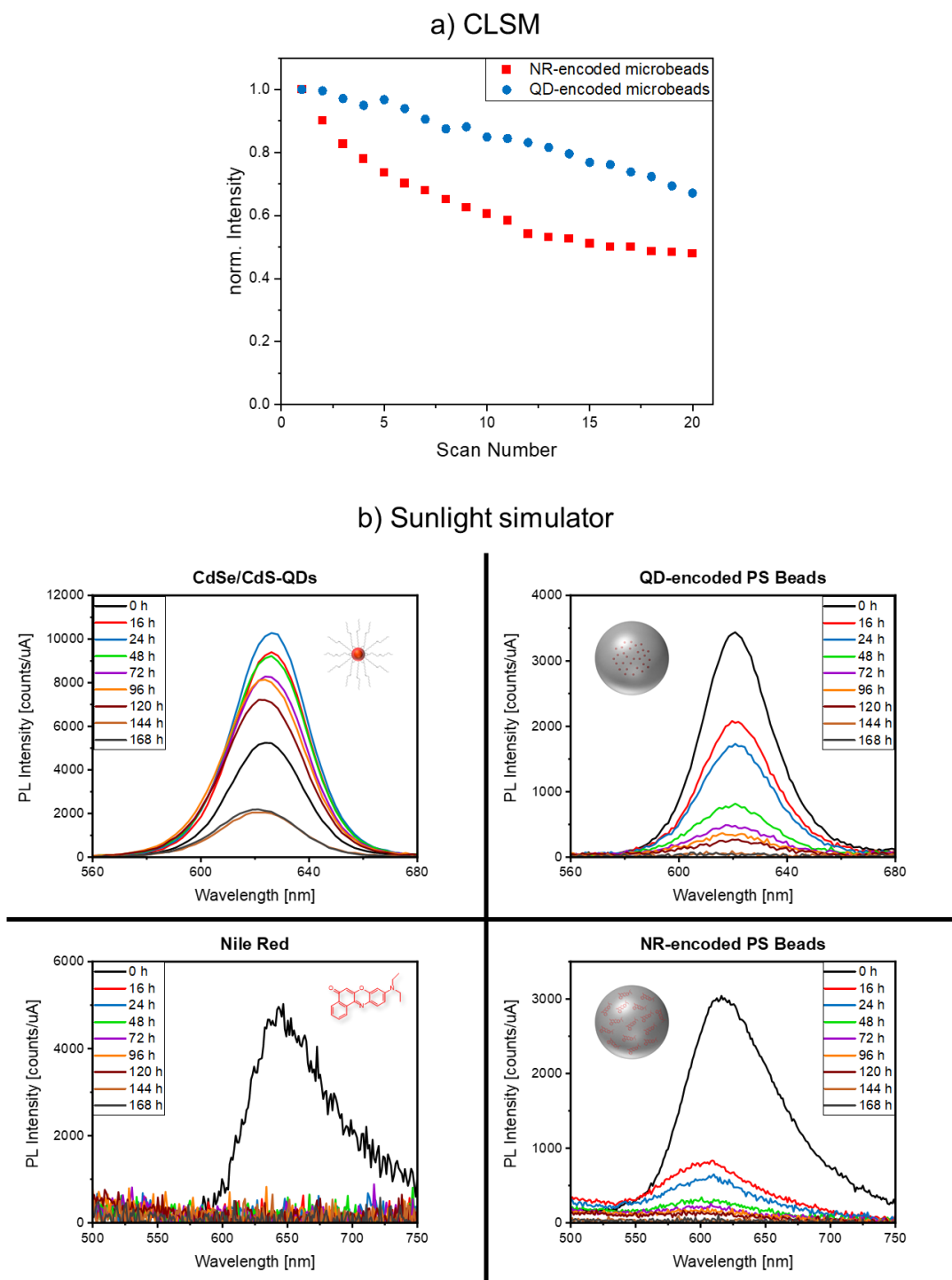


**Figure S7:** Short-term and long-term photostability studies of NR- and QD-encoded PS microbeads, a) Short-term light exposure utilizing a CLSM (time per scan 2.1 s, 1 mW excitation power in the beam path) and b) long-term exposure with a sunlight simulator (650 W/m<sup>2</sup> illumination), here in comparison to the dye NR and the initial QDs. In the case of the CLSM measurements, the luminescence intensities and their changes were calculated by integrating the intensity of the region of interest (ROI) and normalizing the intensities by setting the start values to one. The spectra recorded after exposure with the sunlight simulator were also normalized by setting the start value to one.

As can be seen in Figure S7, the luminescence intensity of the QDs illuminated with the sunlight simulator initially increased (photobrightening) and then started to decrease after 24 h. We attribute the initial photobrightening to a healing of defects on the QD surface. In contrast, the luminescence of the QD-encoded beads did not undergo photobrightening yet revealed a slow decrease in luminescence. In the case of the bead-incorporated QDs, surface defect healing apparently occurred already during microbead synthesis. The light-induced blue shift in QD luminescence is ascribed to a decrease in QD size. In all cases, the QD systems revealed an improved photostability compared to the dye systems.

### 5.1.2 | Influence of Nanoparticle Encapsulation and Encoding on the Surface Chemistry of Polymer Carrier Beads

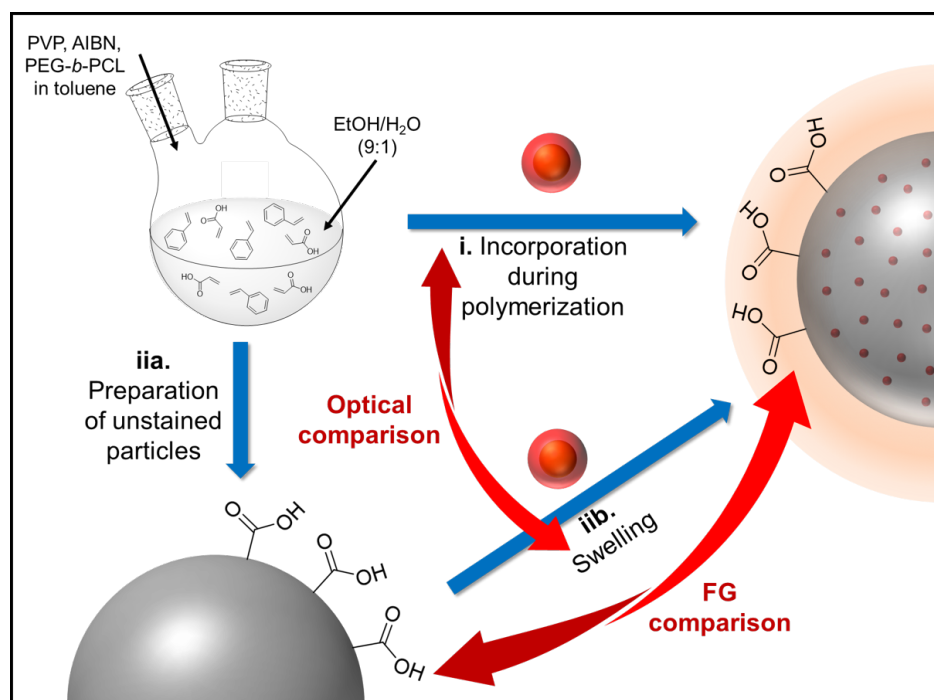


Figure 22: Schematic depiction of different routes for the synthesis of carboxylated, QD-stained PSMPs, taken with permission from L. Scholtz *et al.*, copyright 2023 Scientific Reports.<sup>[26]</sup>

Authors: **Lena Scholtz**, Isabella Tavernaro, J. Gerrit Eckert, Marc Lutowski, Daniel Geißler, Andreas Hertwig, Gundula Hidde, Nadja C. Bigall, Ute Resch-Genger\*

To this work, L. Scholtz contributed by planning and performing the PSMP and PEG-*b*-PCL syntheses, as well as all fluorescence and integrating sphere spectroscopy, DLS and zeta potential measurements and interpreting the resulting data. L. Scholtz planned the study together with I. Tavernaro and D. Geißler. I. Tavernaro also contributed with planning and executing the the post-synthetic swelling procedures with QDs/dyes and the optical assays for FG quantification, including data analysis. Further contributions include QD synthesis and AAS measurements by J. G. Eckert, conductometry including data analysis by M. Lutowski, and FTIR measurements with data interpretation by A. Hertwig, G. Hidde and L. Scholtz. The manuscript was mainly written by L. Scholtz and I. Tavernaro, with significant help from U. Resch-Genger and N. C. Bigall.

**Estimated Contribution: 60%**

Work published in journal: Scientific Reports, 2023

See online here: <https://www.nature.com/articles/s41598-023-38518-7>

DOI: <https://doi.org/10.1038/s41598-023-38518-7>

This article is licensed under a Creative Commons Attribution 4.0 International (CC BY 4.0, <https://creativecommons.org/licenses/by/4.0/>).

## scientific reports

**OPEN** Influence of nanoparticle encapsulation and encoding on the surface chemistry of polymer carrier beadsLena Scholtz<sup>1,2</sup>, Isabella Tavernaro<sup>1</sup>, J. Gerrit Eckert<sup>3</sup>, Marc Lutowski<sup>1</sup>, Daniel Geißler<sup>1,6</sup>, Andreas Hertwig<sup>4</sup>, Gundula Hidde<sup>4</sup>, Nadja C. Bigall<sup>3,5</sup> & Ute Resch-Genger<sup>1,5</sup>

Surface-functionalized polymer beads encoded with molecular luminophores and nanocrystalline emitters such as semiconductor nanocrystals, often referred to as quantum dots (QDs), or magnetic nanoparticles are broadly used in the life sciences as reporters and carrier beads. Many of these applications require a profound knowledge of the chemical nature and total number of their surface functional groups (FGs), that control bead charge, colloidal stability, hydrophobicity, and the interaction with the environment and biological systems. For bioanalytical applications, also the number of groups accessible for the subsequent functionalization with, e.g., biomolecules or targeting ligands is relevant. In this study, we explore the influence of QD encoding on the amount of carboxylic acid (COOH) surface FGs of 2 µm polystyrene microparticles (PSMPs). This is done for frequently employed oleic acid and oleylamine stabilized, luminescent core/shell CdSe QDs and two commonly used encoding procedures. This included QD addition during bead formation by a thermally induced polymerization reaction and a post synthetic swelling procedure. The accessible number of COOH groups on the surface of QD-encoded and pristine beads was quantified by two colorimetric assays, utilizing differently sized reporters and electrostatic and covalent interactions. The results were compared to the total number of FGs obtained by a conductometric titration and Fourier transform infrared spectroscopy (FTIR). In addition, a comparison of the impact of QD and dye encoding on the bead surface chemistry was performed. Our results demonstrate the influence of QD encoding and the QD-encoding strategy on the number of surface FG that is ascribed to an interaction of the QDs with the carboxylic acid groups on the bead surface. These findings are of considerable relevance for applications of nanoparticle-encoded beads and safe-by-design concepts for nanomaterials.

Surface-functionalized polymeric microparticles (MPs) are increasingly utilized in the life sciences. They are stained with different types of molecular and nanoscale luminophores such as organic dyes, semiconductor quantum dots (QDs), and lanthanide-based nanocrystals, or magnetic nanoparticles. Typical applications are as carrier beads for bead-based assay platforms and immune-separation, read out with fluorescence microscopy and flow cytometry<sup>1-4</sup>, drug carriers, conventional and multimodal labels, and fluorescent sensors<sup>5-11</sup>. Hydrophobic, organic dyes and nanoparticles are typically surface-capped with coordinatively bound, apolar surface ligands utilized for the initial nanomaterial synthesis. The encapsulation into organic, inorganic or hybrid particles presents an efficient and versatile strategy to render them water-dispersible and protect them from the environment<sup>12</sup>. This can also reduce the potential toxicity of semiconductor nanocrystals<sup>13-16</sup>. Particularly interesting for optical encoding and multiplexing schemes are II-VI, III-V, and IV-VI as well as doped, ternary/quaternary, and alloyed QDs<sup>17-20</sup> with their unique size- and composition-dependent optical properties and high photostability<sup>21-24</sup>. This

<sup>1</sup>Division 1.2 Biophotonics, Federal Institute for Materials Research and Testing (BAM), Richard-Willstätter-Str. 11, 12489 Berlin, Germany. <sup>2</sup>Institute for Chemistry and Biochemistry, Free University Berlin, Takustraße 3, 14195 Berlin, Germany. <sup>3</sup>Institute of Physical Chemistry and Electrochemistry, Leibniz University Hannover, Callinstraße 3A, 30167 Hannover, Germany. <sup>4</sup>Division 6.1 Surface Analysis and Interfacial Chemistry, Federal Institute for Materials Research and Testing (BAM), Unter den Eichen 87, 12205 Berlin, Germany. <sup>5</sup>Cluster of Excellence PhoenixD (Photonics, Optics, and Engineering – Innovation Across Disciplines), 30167 Hannover, Germany. <sup>6</sup>Present address: PolyAn GmbH, Schkopauer Ring 6, 12681 Berlin, Germany. ✉email: ute.resch@bam.de

enables the free choice of the excitation wavelength and the simultaneous excitation of several QDs with different emission colors with a single excitation source<sup>25–27</sup>.

Nanoparticle (NP)-stained MPs bear functional groups (FGs) such as carboxylic acid (COOH) at their surface, which can be used for the covalent attachment of polyethylene glycol (PEG) or targeting ligands and biomolecules using, e.g., EDC/NHS chemistry, click chemistry or heterobifunctional cross-linkers<sup>28–30</sup>. Their fabrication requires simple procedures for bead encoding and surface functionalization. In addition, simple and cost-efficient analytical methods are needed for the characterization of their application-relevant properties and process control. Three strategies are commonly applied for the preparation of surface functionalized encoded or stained beads: (i) The addition of the staining agent before or during bead formation followed by the introduction of suitable FGs, i.e., by a grafting step, (ii) the utilization of premanufactured, surface-functionalized MPs together with a post synthetic swelling procedure, and (iii) the wrapping of beads by alternating shells of oppositely charged polyelectrolytes incorporating the staining agent (layer-by-layer (LbL) method). Procedure (i) requires NPs that survive the sometimes harsh polymerization conditions and do not undergo a loss of their functional properties such as photoluminescence<sup>31–33</sup>. Procedure (ii) often exploits commercial polymer beads made from, e.g., polystyrene (PS) and polymethylmethacrylate (PMMA) available in different sizes with different FGs. Challenges to be tackled particularly for the encoding with NPs like QDs include the choice of a solvent mixture for bead swelling, that does not induce the quenching of the QD photoluminescence and QD agglomeration or aggregation and prevents QD leaking. The LbL method (iii), that is not employed in this study, utilizes premanufactured polymer beads as templates coated with a NP-stained polyelectrolyte shell of varying thickness. This method is versatile, yet tedious and limited to surface staining, which can make further bioconjugation steps challenging<sup>34–36</sup>.

The broad application of surface-functionalized, stained MPs encouraged us to explore the influence of the particle staining procedure on the number of surface FGs by procedures (i) and (ii), exemplarily for unstained polystyrene microparticles (PSMPs) and carboxylated beads. The latter were chosen because of the frequent use of carboxylate polymer microparticles in the life sciences, e.g., for bead-based assays and DNA sequencing platforms. Aiming for a better understanding of the impact of this encoding step on the application relevant properties of such QD-stained polymer particles, we evaluated and compared both QD-staining methods in terms of the size, surface charge, amount of total and accessible FG, and luminescence properties of the resulting QD-encoded PSMPs. As representative QDs, we focused on oleic acid and oleylamine stabilized CdSe/CdS QDs with a mean particle size of  $10.3 \pm 1.2$  nm and a strong red luminescence. Such QDs have been broadly used in many different applications. Based upon previously examined and validated protocols for FG quantification<sup>37–40</sup>, the total amount of (de)protonable COOH groups was determined by a conductometric titration. In addition, Fourier transform infrared (FTIR) spectroscopy was used as a semiquantitative method for the determination of the number of total COOH acid groups. The number of accessible COOH groups was obtained with an adsorption/desorption-based assay, relying on electrostatic interactions between the negatively charged beads and the relatively large, positively charged dye toluidine blue (TBO). Also, a catch-and-release assay using the small, cleavable, COOH-reactive reporter *N*-(aminoethyl)-3-(pyridin-2-yl)disulfanyl-propanamide trifluoroacetate (*N*-APPA) was performed. This involved the covalent binding of the reporter to the bead surface FGs. As control samples, we used pristine carboxylated beads as well as carboxylated beads which were encoded with rhodamine B isothiocyanate (RITC) and the neutral polarity probe Nile Red (NR) with our post synthetic swelling procedure, previously optimized for different dye classes. In addition to the quantification of the number of surface FGs, also the impact of the encoding procedure on QD luminescence was examined.

## Materials and methods

The experimental procedures employed for the synthesis of the CdSe/CdS-QDs, polyethylene glycol-*block*-poly( $\epsilon$ -caprolactone), the post-synthetic swelling procedures for dyes and the QD-loaded PSMPs, as well as for the fluorescence and integrating sphere spectroscopy, atomic absorption spectrometry, dynamic light scattering/zeta potential and both assays (TBO and *N*-APPA) have been partly previously employed and reported by us<sup>31,37,38,40,41</sup>.

**Materials.** Hydrochloric acid (HCl), sodium hydroxide (NaOH), sodium dihydrogen phosphate ( $\text{NaH}_2\text{PO}_4$ ), dimethyl sulfoxide (DMSO), acetone ( $\geq 99.5\%$ ), styrene ( $\geq 99.0\%$ ), tin(II) 2-ethylhexanoate (92.5–100%),  $\epsilon$ -caprolactone (97%), poly(ethylene glycol) (PEG,  $M_w$  2500), trioctylphosphine oxide (TOPO, 99%), 1-octadecene (ODE, 90%), toluene ( $\geq 99.7\%$ ), methanol ( $\geq 99.8\%$ ), isopropanol ( $\geq 99.8\%$ ), oleylamine (OLA, 70–80%), 1-octanethiol (98.5%), acrylic acid (AA, 99%, anh.), azobisisobutyronitrile (AIBN, 98%), *N*-(3-dimethylaminopropyl)-*N'*-ethylcarbodiimid hydrochloride (EDC,  $\geq 98\%$ ), hydroxy-2,5-dioxopyrrolidine-3-sulfonic acid sodium salt (sulfo-NHS, 98%), Rhodamine B isothiocyanate (RITC) and Toluidine Blue O (TBO) were purchased from Sigma Aldrich. Polyvinylpyrrolidone (PVP,  $M_w$  58,000), potassium bromide (KBr, p. A.), selenium powder (200 mesh, 99.999%), oleic acid (OA, 90%) and cadmium oxide (CdO, 99.998%) were obtained from Alfa Aesar. Ethanol, toluene and *n*-heptane (all spectr. grade) as well as *n*-hexane ( $\geq 99\%$ ) were purchased from Merck KGaA. *N*-succinimidyl-3-(2-pyridyldithio) propionate (SPDP) and tris(2-carboxyethyl) phosphine hydrochloride (TCEP) were obtained from Thermo Fisher Scientific, benzyltrimethyloctadecylammonium chloride (OBDAC, 98.9%) from HPC Standards GmbH, tri-*n*-octylphosphine (TOP, 99.7%) and deuterated chloroform (99.8 atom%) were obtained from abcr GmbH, *n*-octadecylphosphonic acid (ODPA,  $>99\%$ ) from PCI Synthesis, Nile Red (NR) from Fluka and 1-butanol ( $>99.5\%$ ), tetrahydrofuran (THF,  $>99.9\%$ ), *N,N*-dimethylformamide (DMF,  $>99.9\%$ ), and chloroform from Chemsolute. All solvents used for the spectroscopy measurements and optical assays were of spectroscopic grade and all chemicals were employed without further purification. All aqueous solutions, buffers, and microparticles were prepared with deionized water ( $0.05 \mu\text{S m}^{-1}$ ; Milli-Q water, Millipore).

**Synthesis of CdSe/CdS-core/shell-QDs.** The CdSe/CdS-QDs with a core/shell-architecture in hexane were prepared according to a previously described procedure<sup>31</sup> adapted from Carbone et al., Nightingale et al. and Chen et al.<sup>21–23</sup> The synthesis is described in detail in the Supplementary Information (SI).

**Synthesis of polyethylene glycol-*block*-poly( $\epsilon$ -caprolactone).** The synthesis of the *block*-copolymer polyethylene glycol-*block*-poly( $\epsilon$ -caprolactone) (PEG-*b*-PCL) was performed following a previously reported procedure<sup>31</sup> adapted from Meier et al.<sup>42</sup> which is described in more detail in the SI. The chemical identity of the synthesized PEG-*b*-PCL was confirmed by solution <sup>1</sup>H-NMR spectroscopy (see SI, Figure S1).

**Synthesis of unstained and QD-encoded PSMPs via a polymerization procedure (route i).** The PSMPs were synthesized following a previously described polymerization procedure<sup>31</sup>, modified considering two other procedures reported by Kimura et al.<sup>43</sup> and Nirmalanathan-Budau et al. (regarding COOH functionalization)<sup>38</sup>.

Typically, 400 mg of PVP were dissolved in 45 mL of a mixture of ethanol and water (9:1). Additionally, 45.75 mg of PEG-*b*-PCL were dissolved in 504  $\mu$ L of toluene and placed on a shaker for 30 min. Both solutions were combined under argon atmosphere. The mixture was heated to 80 °C and stirred at 100 rpm for 30 min, before 5 mL of styrene (with or without QDs) and 180 mg AIBN dissolved in 5 mL of ethanol/water (9:1) were sequentially added. The reaction mixture was stirred at 80 °C for 3 h. Then, 150  $\mu$ L of AA dissolved in 1.78 mL of ethanol/water mixture (9:1) were added dropwise to the reaction mixture. The reaction was continued for one hour before the mixture was cooled to room temperature (RT). The resulting particles were centrifuged at 1500 rcf for 2 min, the supernatant was discarded, and the particles were redispersed in 30 mL ethanol. They were again centrifuged (1500 rcf/2 min) and redispersed in 45 mL ethanol to create a stock solution. Prior to further investigation, the particles were washed three times with ethanol (also 1500 rcf/2 min) by discarding the supernatant after every step and redispersing the PSMPs in ethanol. The PSMPs were stored in ethanolic dispersion at RT.

For the QD incorporation during bead formation (polymerization), the CdSe/CdS-QDs were pretreated as follows: A spatula tip of OBDAC (approximately 2 mg) and 900  $\mu$ L of ethanol were added to 100  $\mu$ L of the QD dispersion in a vial. The mixture was homogenized on a shaker for 5 min, centrifuged at 6000 rcf for 5 min, and washed once with ethanol. The coated QDs were redispersed in 1 mL of styrene, sealed, and stored in the refrigerator. The polymerization procedure was performed as described above for the unstained PSMPs.

**Post-synthetic swelling procedure for QD loading (route ii).** 2 mg of unstained PSMPs were dispersed in 1 mL of MilliQ water, washed twice with butanol, and finally redispersed in 500  $\mu$ L of butanol. 5  $\mu$ L of QDs (in hexane, 32.9 mg/mL (Cd content, determined by AAS)) were mixed with 95  $\mu$ L of chloroform and added dropwise to the particle suspension under stirring. The reaction mixture was stirred for additional 30 min at RT, before it was centrifuged at 18,000 rcf for 15 min. The separated particles were washed twice with ethanol and once with MilliQ-water (centrifugation 18,000 rcf/15 min, supernatant discarded each time and particles redispersed in the respective solvent), followed by redispersion in 1 mL of MilliQ-water or ethanol.

**Post-synthetic swelling procedure for dye loading.** Loading of the unstained PSMPs with RITC and NR were performed following a previously described swelling procedure<sup>41</sup>. In a typical experiment, 12 mg of the unstained PSMPs were dispersed in 4 mL of MilliQ-water. In parallel, 0.54 mg (1.0  $\mu$ mol) of RITC or 0.32 mg (1.0  $\mu$ mol) of NR were dissolved in 0.4 mL of a THF:DMF (50:50 w%) mixture. The dye solution was added to the particle dispersion and the mixture was vigorously shaken at RT for 1 h. During the incubation, the particles were ultrasonicated four times (2 min, ultrasonic bath). After 1 h, 0.6 mL of MilliQ-water were added before the particle dispersion was centrifuged at 10,000 rcf for 30 min. The separated particles were washed three times with MilliQ-water (centrifugation 10,000 rcf/30 min, discarding of supernatant, and redispersion of particles each time), followed by redispersion in MilliQ-water.

**Scanning electron microscopy (SEM).** For the SEM micrographs of the PSMPs, obtained with a Philips XL30 ESEM using an acceleration voltage of 20/25 kV, the samples were drop-casted onto aluminum holders from diluted PSMP dispersions and dried under ambient conditions. The mean particle sizes and the corresponding size distribution were determined using the software ImageJ (Version: 1.52e, <https://imagej.nih.gov/ij/>).

**Transmission electron microscopy (TEM).** TEM measurements of the QD dispersion were performed using a JEOL JEM-2100F-UHR equipped with a field emission gun and operated at 200 kV. The QD samples were prepared on carbon-coated copper grids (Quantifoil, 400 mesh) via drop casting and drying under ambient conditions. The mean particle size and the size distribution were determined with ImageJ as described for the SEM samples.

**High-angle annular dark-field scanning transmission electron microscopy (HAADF-STEM).** The HAADF-STEM measurements of both QD-loaded PSMPs were carried out with a ThermoFisher Scientific Talos F200S TEM at 200 kV. The samples were prepared by drop-casting diluted dispersions of the respective PSMPs in ethanol onto lacey, carbon-coated copper grids (PELCO by Ted Pella, Inc., 400 mesh).

**Dynamic light scattering (DLS) and zeta potential measurements.** DLS and zeta potential measurements of the unstained and QD-stained PSMPs dispersed in MilliQ-water were carried out with a Zetasizer Nano ZS from Malvern Panalytical Ltd. (back scattering angle 173°), equipped with a 633 nm laser, at T = 25 °C in dispo-

able folded capillary cells (DTS1070, Malvern Panalytical). For each sample, three independent measurements including several sub-runs were performed. For the DLS measurements, the hydrodynamic diameter based on the  $z$ -average and number distribution was used. The zeta potential was calculated from the particle electrophoretic mobility using the Einstein–Smoluchowski theory, with a refractive index of 1.46 assumed for polystyrene for both studies.

**Atomic absorption spectroscopy (AAS).** The Cd(II) concentration of the QD dispersions was determined with an AA140 instrument from Varian Inc. with an oxygen/acetylene flame atomizer after dissolving the QDs in *aqua regia* overnight. Six standard solutions with varying Cd(II) concentrations were employed to create a calibration curve.

**Fluorescence spectroscopy.** The emission spectra of the CdSe/CdS-QDs in toluene and the QD-loaded PSMPs in ethanol were recorded at 350 nm excitation with a calibrated FSP920 fluorescence spectrometer from Edinburgh Instruments Ltd. in (10 × 10) mm quartz glass cuvettes (Hellma GmbH) at RT.

**Integrating sphere spectroscopy.** The photoluminescence quantum yield (PLQY) values for the QD-loaded PSMPs in ethanol and the QD dispersion in toluene were determined with a stand-alone Quantaurus integrating sphere setup (Hamamatsu Photonics K.K., absolute determination). The measurements were conducted in (10 × 10) mm long-neck quartz glass cuvettes (Hamamatsu Photonics K. K) using an excitation wavelength of 350 nm at 25 °C. The respective solvent was used as a blank for the QD dispersion, while for both QD-loaded PSMPs, a dispersion of the unstained PSMPs with similar bead concentration was employed as a blank.

**Fourier-transform infrared (FTIR) spectroscopy.** FTIR spectroscopy was performed in the transmission mode with a Vertex 70 FTIR spectrometer from Bruker. The dried PSMPs were pestled together with 100 mg dry KBr (dried for four hours at 110 °C, then stored in a desiccator until use) in two different concentrations and pressed into tablets. The particle amounts used for this procedure were 3.0/4.6 mg ( $6.76 \times 10^8/1.04 \times 10^9$  particles) for unstained, unfunctionalized PSMPs, 4.5/6.6 mg ( $4.12 \times 10^8/6.04 \times 10^8$  particles) for QD-loaded PSMPs prepared via the post-synthetic swelling procedure, and 2.9/5.3 mg ( $3.51 \times 10^8/6.42 \times 10^8$  particles) for QD-loaded PSMPs prepared via the polymerization procedure. A pure KBr tablet was employed to record a blank or background spectrum. After an atmospheric compensation ( $H_2O$ ,  $CO_2$ ) and background correction (concave rubber band correction with 10 iterations and 64 baseline points), the spectra were normalized (vector normalization) to the CH bands from 2655.1 to 3216.6  $cm^{-1}$ .

**Conductometric titration.** Conductivity measurements providing the maximum (total) number of (de)protonable COOH groups were carried out with a Modul 856 conductometer (Methrom). Prior to the measurements, the PSMPs were dialyzed against Milli-Q water to remove contaminations from the particle synthesis. For the measurement, samples containing either 20 mg of unstained PSMPs or 20 mg of QD-loaded PSMPs in 80 mL of Milli-Q water were employed. For the complete protonation/deprotonation of the FGs, the conductivity of the samples was adjusted to 100  $\mu S/cm$  with either HCl (10 mM) or NaOH (10 mM) as a starting point. Titration with the base or the acid was performed in 20  $\mu L$  steps at RT under argon atmosphere to exclude  $CO_2$ .

**TBO assay.** The colorimetric TBO adsorption/desorption assay previously reported by us<sup>40</sup> was performed with some modifications. 5 mg ( $1 \times 10^{11}$  particles) of unstained and QD-loaded PSMPs were washed twice with MilliQ-water and redispersed in 0.8 mL of MilliQ-water. The pH of the particle suspensions was set to 8 and a solution of 0.2 mL of TBO (3.2  $\mu mol$ ) in MilliQ-water was added and incubated under gentle shaking for 20 min at RT. Subsequently, the particles were washed by several cycles of centrifugation, removal of supernatant, and addition of MilliQ-water. When the supernatant was clear, 1 mL of 1% SDS was added, and the particles were additionally incubated for 30 min under gentle shaking at RT. After separation of the supernatant from the particles, an absorption spectrum of the supernatant was measured and the absorbance at 632 nm ( $\epsilon = 50,000 L mol^{-1} cm^{-1}$ ) was utilized to determine the amount of desorbed TBO, assuming one TBO molecule react with one COOH group. Finally, the particles were extensively washed to remove SDS, dried *in vacuo*, and the weight of the remaining particles was determined. This final step of particle drying and weighing accounts for partial loss of material during the excessive washing steps and reduces the variation coefficient to around 15%<sup>40,44</sup>.

**N-APPA assay.** N-APPA was freshly prepared as described in the literature<sup>37,38</sup>, and used for the catch-and-release assay. 5 mg (0.002 nmol/L) of unstained PSMPs, 5 mg (0.002 nmol/L) of QDs-loaded PSMPs (polymerization procedure), and 1 mg (0.0004 nmol/L) of QDs-loaded PSMPs (swelling procedure) were dispersed in 0.8 mL of MES buffer (pH 5.0), respectively. An excess of EDC ( $3 \times 10^{-11}$  mol in 500  $\mu L$  of MES buffer (pH 5.0)) and sulfo-NHS ( $3 \times 10^{-11}$  mol in 500  $\mu L$  of MES buffer (pH 5.0)) was added to each particle suspension and stirred at RT for 1 h. The activated particles were centrifuged and redispersed in 950  $\mu L$  of phosphate buffer (pH 8.0), before 50  $\mu L$  (0.2  $\mu mol$  in MeOH) of N-APPA were added. The reaction mixture was shaken (600 rpm) overnight at RT, followed by centrifugation at 5000 rcf for 10 min, separation of the supernatant, and washing of the particles with 500  $\mu L$  of phosphate buffer (pH 8) twice. The washed particles were redispersed in 450  $\mu L$  of phosphate buffer and 50  $\mu L$  (2  $\mu mol$ ) of a prepared TCEP solution in phosphate puffer were added, before the mixture was incubated for 45 min at RT. To separate the formed 2-thiopyridone (2-TP) from the particles, the mixture was centrifuged at 5000 rcf for 10 min and washed twice with 500  $\mu L$  phosphate buffer (pH 8). The

amount of 2-TP in the merged supernatants was photometrically quantified at 343 nm ( $\epsilon = 8000 \text{ L mol}^{-1} \text{ cm}^{-1}$ ) as previously described<sup>37</sup>.

### Results and discussion

For the incorporation of the oleic acid and oleylamine stabilized CdSe/CdS-QDs into the COOH functionalized PSMPs, two different synthesis routes were utilized and compared. As schematically depicted in Fig. 1, this included i) QD addition during polymerization/bead formation (called polymerization procedure) and ii) a post-synthetic swelling procedure. For QD incorporation during bead formation, the QDs were dispersed in styrene and added during the polymerization procedure<sup>31</sup>. Thereby, the QDs are exposed to harsh reaction conditions, such as an elevated temperature and the presence of radicals, which can also affect their fluorescence properties. For the bead swelling procedure, first unstained, carboxylated microbeads were synthesized with a polymerization procedure previously established and adapted for the surface functionalization with COOH groups<sup>31</sup>. These unstained, pristine beads were also employed as control or blank to determine the influence of QD staining on the bead surface FGs. Bead encoding by a swelling and shrinking step was utilized by us before to encode differently sized and surface functionalized polymer beads with organic luminophores and sensor dyes<sup>45–47</sup>. This approach has been also pursued by other research groups to fabricate polymer particles, encoded with QDs<sup>48–50</sup>, other luminescent nanocrystals such as lanthanide-based nanomaterials<sup>51,52</sup> or magnetic nanoparticles<sup>53</sup> for use as carrier beads for bead-based assays, immune-separation or particle reporters for immunoassays. For QDs, particularly the organic solvent used for bead swelling must be carefully chosen as the solvent can induce quenching of QD luminescence.

Subsequently, we examined the influence of these two widely applied fabrication procedures of NP-encoded beads on the number or density of the surface FGs of the resulting QD-stained, COOH-functionalized PSMPs, as well as on the luminescence properties of the QDs incorporated into these PSMPs. We compared them to the respective pristine, carboxylated PSMPs and dye-stained, carboxylated PSMPs (utilizing RITC and the neutral polarity probe NR and the post-synthetic swelling procedure).

**Physico-chemical characterization of the (free) QDs.** The CdSe/CdS-QDs were analyzed by TEM regarding their size (particle diameter:  $d_{\text{TEM}} = 10.3 \pm 1.2 \text{ nm}$ ) and by AAS regarding their Cd(II) concentration (AAS: 32.9 mg/mL). Moreover, spectroscopic measurements were carried out ( $\lambda_{\text{em}} = 638 \text{ nm}$ , PLQY = 58%).

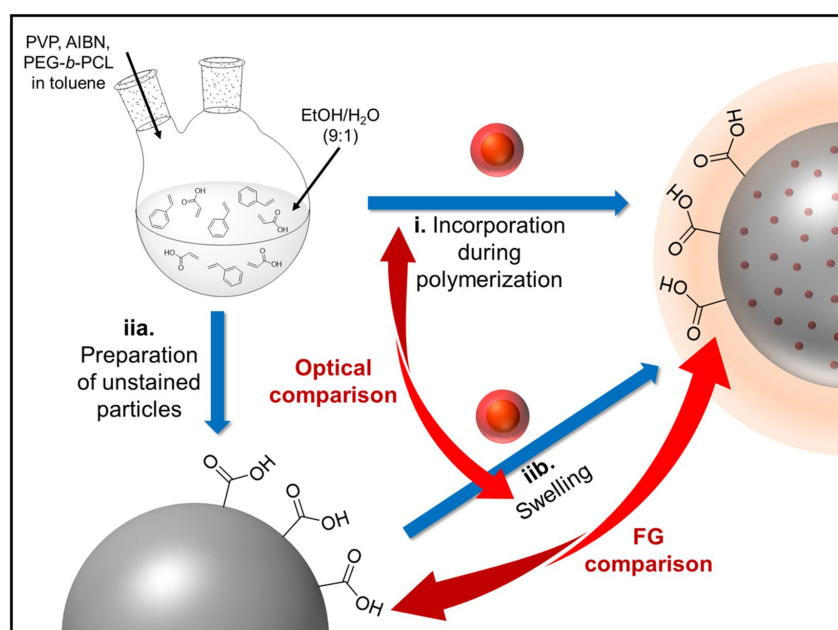


**Figure 1.** Schematic presentation of the synthesis routes used for the fabrication of carboxylated, QD-loaded polystyrene microparticles (PSMPs). (i) QD incorporation during the polymerization reaction (polymerization procedure) and (ii) preparation of unstained PSMPs followed by (iib) QD staining via a post-synthetic swelling procedure of the beads through addition of an organic solvent like butanol in presence of the QDs.

**Physico-chemical characterization of the PSMPs.** Subsequently, we compared and evaluated the properties of the QDs-loaded PSMPs prepared by the two different synthesis routes as well as the unstained PSMPs. For this reason, the size of all particles was first determined by DLS and SEM measurements. The corresponding results are displayed in Fig. 2, and the size distribution histograms are presented in the SI (see Figure S3).

The bead sizes obtained by DLS, corresponding to the intensity-based hydrodynamic diameter of the particles, differ between the three PSMP samples. This is most likely caused by the organic shell and hydration layer around the PSMPs changing through loading the particles with the QDs, and possibly also by a slightly changed refractive index also caused by the QD presence. The SEM micrographs show that all beads are nearly identical in size and have a spherical shape with slightly rough surfaces. Both particle size and morphology are barely influenced by the QD loading procedure. For the PSMPs prepared by the post-synthetic swelling procedure, some cases of particle fusion could be observed, as well as a rougher particle surface. These particles also showed a slightly larger size and size distribution than the other PSMPs, which can be attributed to the swelling process. The zeta potentials of the unstained and the QD-loaded polymer particles obtained by the polymerization procedure closely match with values of  $-48$  mV and  $-49$  mV. In contrast, the swelling procedure affects the zeta potential of the resulting QD-loaded PSMPs, which revealed a zeta potential of  $-22$  mV. A change in zeta potential is in good agreement with previous results obtained with dye-loaded polystyrene NPs and MPs using a similar swelling procedure, that also indicated an increase of the zeta potential after the dye-loading of around  $10$  mV (used dyes/particles: a dyad dye and a rhodamine-B derivate with self-manufactured polystyrene NPs and MPs, as well as NR with commercially available polystyrene NPs)<sup>41,54</sup>.

To determine the influence of the QDs on PSMP loading, similar studies were performed with the amphoteric dye RITC and the neutral polarity probe NR using our post-synthetic swelling procedure previously optimized for different classes of organic dyes (see also SI for more details)<sup>46</sup>. The resulting RITC- and NR-loaded PSMPs showed zeta potentials of  $-39$  mV and  $-40$  mV, respectively. These values are slightly higher than the zeta potential of  $-48$  mV of the unstained PSMPs. NR staining of commercial  $2$   $\mu\text{m}$ -sized PSMPs, revealing a zeta potential of  $-36$  mV, resulted in dye-stained PSMPs with a zeta potential of  $-33$  mV. This shows that the large

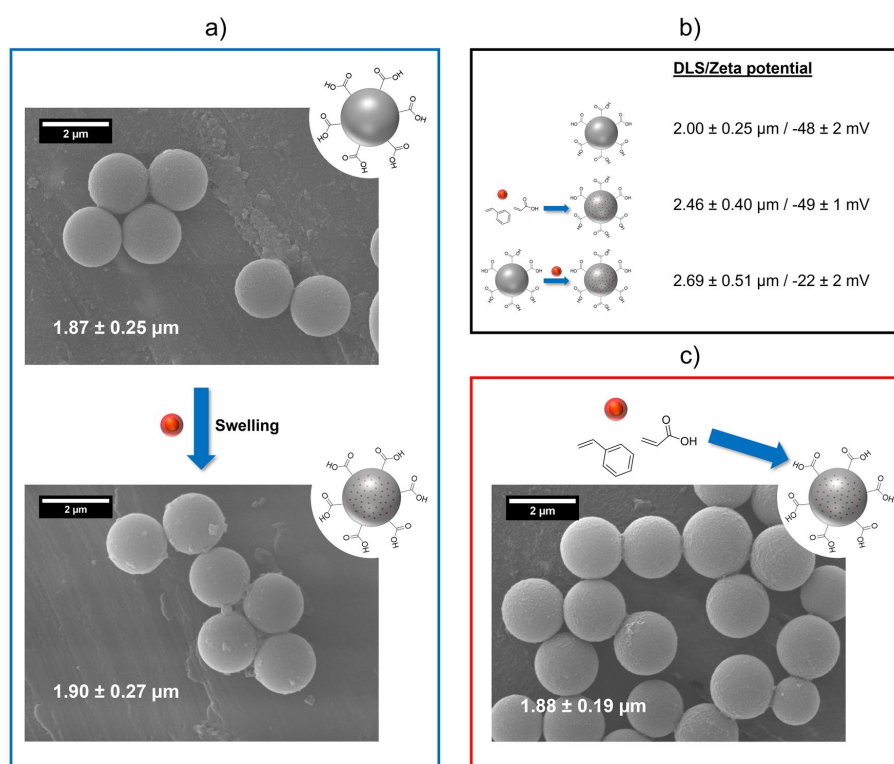


**Figure 2.** SEM images of the synthesized PSMPs, with (a) unstained PSMPs and QD-loaded PSMPs prepared from the former via the post-synthetic swelling procedure, and (c) QD-loaded PSMPs prepared via the polymerization procedure; (b) PSMP sizes determined by DLS and their zeta potential values, illustrated with schematic displays of the particle synthesis routes.

increase of the zeta potential in the case of the QD-loaded PSMPs cannot solely be explained by the swelling procedure. Apparently, also the presence of the QDs contributes to this effect. Reasons for this are discussed in later sections considering the location of the QDs in/on the PSMPs.

**Luminescence Properties of QD-loaded PSMPs.** The luminescence properties of the QDs in the differently prepared PSMPs were compared by assessing their emission spectra and their photoluminescence quantum yields (PLQY), which is a measure for their photoluminescence efficiency. The former provides the spectral position and full width at half maximum (FWHM) of the QDs in the beads, which provide information on changes in QD size and size distribution. The latter indicates changes in QD surface chemistry, i.e., the formation of additional trap states during bead incorporation, favoring the non-radiative recombination of charge carriers. The corresponding spectra and PLQY values are displayed in Fig. 3. Apparently, the emission spectra of the QDs added during the polymerization procedure are hypsochromically shifted by about 4 nm compared to the emission spectra of the parent QDs dispersed in hexane. The swelling procedure only slightly affects the QD emission spectrum. Interestingly, the FWHM of the emission band of the QDs dispersed in hexane slightly exceeds the spectral bandwidths of the QD emission bands of the QD-loaded PSMPs. The refractive indices of hexane and polystyrene are slightly different (1.37 and 1.59, respectively), and their dielectric constants also differ (2.4–3 and 1.9). This can influence the QD emission features, as a change in QD environment can change, e.g., the emission maximum. The slight shift of the emission maximum that occurs only for the QDs added during the polymerization procedure, points to a slightly stronger interaction of the QDs with the polystyrene matrix as observed for the QDs incorporated with the swelling procedure. The narrowing of the FWHM in case of the QD-loaded PSMPs, compared to the free QDs, indicates a quenching of the smaller QDs during the preparation of these particles, leading to a narrowing in the energetically higher range of the emission spectrum. This can be explained by the reaction conditions to which the QDs are exposed in both loading procedures, which seem to affect and quench particularly the slightly smaller QDs.

For both staining procedures, the PLQY of the QDs decreases after PSMP incorporation. The decrease is more pronounced for the QDs present during the polymerization procedure. This diminution in PLQY is attributed to the elevated temperature and the presence of radicals during the polymerization reaction as well as to the presence of ethanol and water molecules. An ethanolic/aqueous environment is known to have a negative effect on the PL properties of some luminescent QDs by decreasing their stability e.g., by the removal of surface ligands or inducing irreversible aggregation and quenching<sup>55</sup>. However, the PLQY values of the QDs in both types of QD-loaded beads are sufficiently high for typical applications of such QD-encoded particles.

Subsequently, the QD location and spatial distribution within the PSMPs prepared by the two different staining methods were explored by STEM measurements. The corresponding images are displayed in Fig. 4. These images reveal a QD accumulation at the PSMP surface, especially for the particles prepared by the post-synthetic bead swelling procedure. These findings are attributed to the direct binding of the ligand, i.e., oleic acid and oleylamine, stabilized QDs to the COOH groups on the PSMP surface. This seems to prevent QD penetration into the bead cores for the swelling procedure. In addition, we cannot exclude that the PSMPs do not swell enough to allow the QDs to properly and deeply penetrate the particles. The stabilization of the QDs with

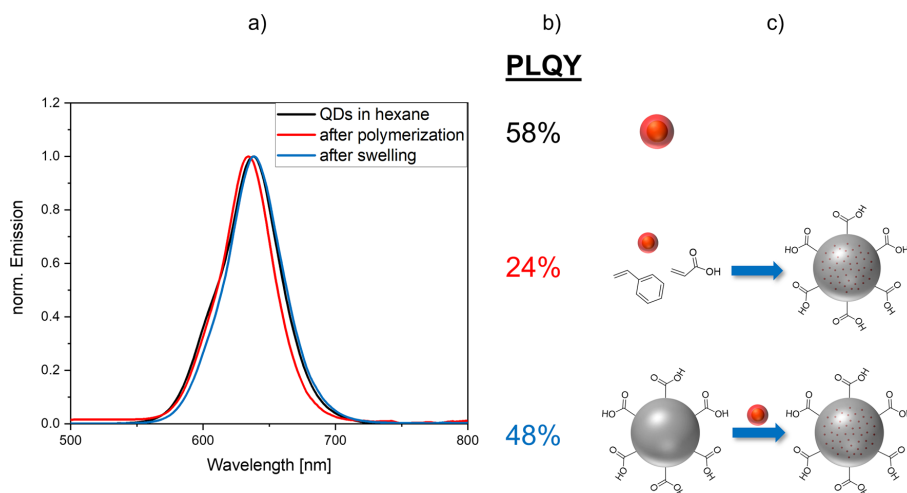


**Figure 3.** Optical characterization of the QD-loaded PSMPs. (a) Emission spectra of the CdSe/CdS-QDs dispersed in hexane and the QD-loaded PSMPs obtained by the polymerization and swelling procedures, respectively; (b) PLQY and (c) Schematic display of the synthesis routes leading to the respective PSMPs. The offset from zero of the red spectrum can be explained by scattering effects.

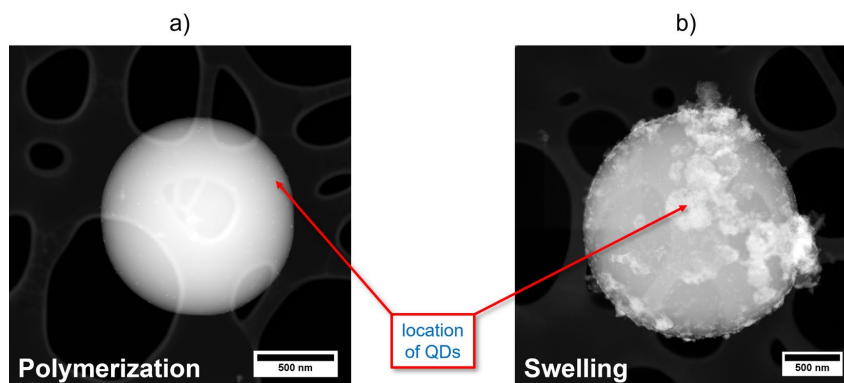


**Figure 4.** STEM images revealing the location of the CdSe/CdS-QDs (a) in QD-loaded PSMPs prepared by the polymerization procedure (route i) and (b) in QD-loaded PSMPs prepared by the post-synthetic swelling procedure (route ii). The differing amount of QDs visible (small, lighter particles on or close to the PSMP surface) is due to different QD concentrations used for the PSMP preparation.

oleic acid also underlines the affinity of the QD surface atoms to carboxylic acid groups. We assume that during the reaction, some of the initial QD ligands detach from the QD surface and make room for the binding of the COOH groups located at the PSMP surface, resulting in the binding of the QDs to the PSMP surface FGs. In the case of the PSMPs prepared by the polymerization procedure, the QDs are located either on the particle surface or underneath the bead surface. In a previous study on QD encoding of PSMPs, utilizing very similar polymerization conditions with additional crosslinking of the polymer network with divinylbenzene, yet not a surface functionalization with carboxyl groups, we observed a QD accumulation in the PSMP core region (no significant agglomeration of the QDs)<sup>31</sup>. This indicates that the presence of acrylic acid with its COOH groups, and possibly also the absence of the crosslinker, prevent QD migration into the PSMP core. This finding can also explain why the zeta potential of the PSMPs is modified in the case of the swelling procedure, leading to an increase in zeta potential, contrary to the zeta potential of the PSMPs prepared by the polymerization procedure. In addition, it explains the observed spectral shift of the emission maximum of the PSMPs prepared by the polymerization procedure compared to the free QDs, which also underlines a stronger interaction of the QDs with the polystyrene matrix in this case. Such a spectral shift does not occur for QD-encoded PSMPs prepared by the swelling procedure. Apparently, for the homogeneous encoding of such polymer beads suitable for subsequent surface modifications, a two-step procedure could be better suited, preparing first plain QD-stained beads followed by the subsequent introduction of surface FGs.

To study the potential influence of both QD staining approaches on the surface FGs of the resulting QD-encoded beads, the modified PSMPs were investigated with FTIR spectroscopy. This method should enable the semiquantitative determination of the amount of COOH FGs on the PSMPs. Therefore, the FTIR spectra of two different concentrations of both types of QD-loaded PSMPs and unstained, plain PSMPs (not functionalized with COOH FG, bead synthesis without acrylic acid), were measured. The IR spectra obtained for both concentrations are displayed in Fig. 5. From the spectra, we could determine whether the change in COOH amount can be detected by examining the vibrational bands caused by the carbonyl group. In this case, the OH band around  $3350\text{ cm}^{-1}$  could not be used for the comparison, because it was not strong enough to be visible in the spectra (see also SI, Figure S4). This could be caused by a broadening of the OH band, which is common especially in the presence of (traces of) water, and additionally by the much stronger signals from the (poly)styrene overriding the OH signals. Resulting from the monomer ratio, the amount of Poly-AA (containing the COOH FGs) in the beads is much smaller than that of PS. Apparently, for the different PSMPs, there is a clearly visible and reproducible change in the intensity of the peak at  $1744\text{ cm}^{-1}$ , which is ascribed to carbonyl vibrations. For the plain beads, there is also a small peak present at this wavelength. This peak is attributed to the underlying, aromatic benzene vibrations, but the intensity of this peak is much less pronounced than those of the bands resulting for the functionalized PSMPs. All other bands in the IR spectra match after normalization. The higher intensities of the peak at  $1744\text{ cm}^{-1}$  observed for both concentrations of the QD stained beads prepared by the two encoding methods indicate a higher amount of COOH surface groups for the PSMPs synthesized with the QDs present during bead formation.

Subsequently, the amount of surface FGs on the QD-loaded PSMPs and the similarly prepared unstained PSMPs was quantified by different analytical methods. For the quantification of the total number of COOH FGs, a conductometric acid/base titration was applied. As electrochemical titrations utilize the smallest possible reporters, namely protons ( $\text{H}^+$ ) and hydroxide ions ( $\text{OH}^-$ ), for signal generation, a maximum number of accessible FGs is detected with this approach. This number typically corresponds to the total number of (de)protonatable surface groups. This has been confirmed by us exemplarily for carboxylated polymer particles of different size by cross

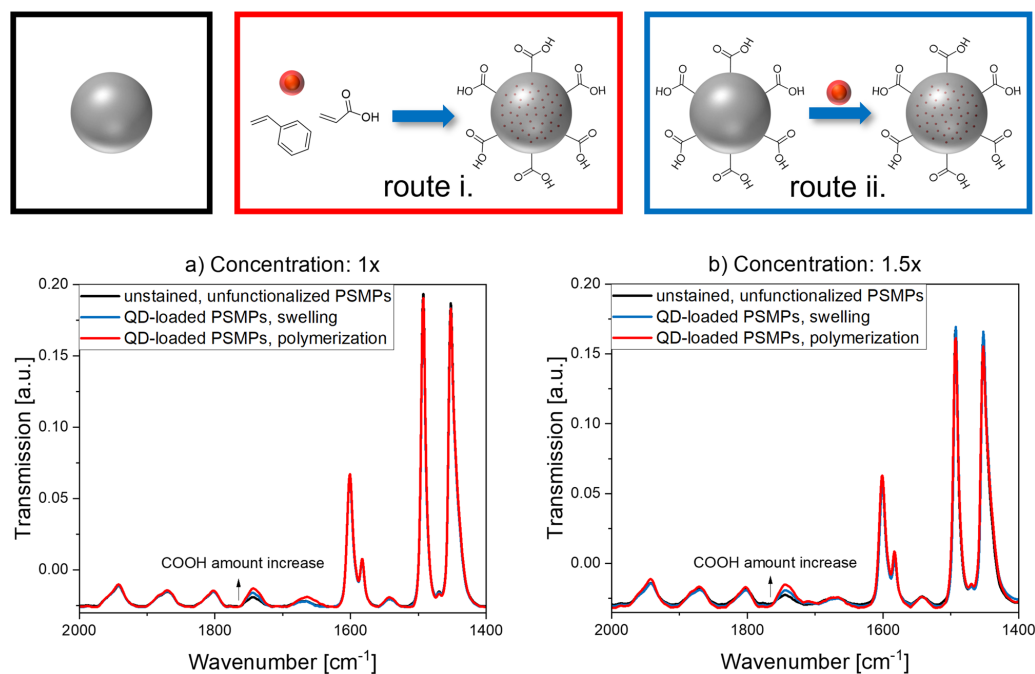


**Figure 5.** FTIR spectra (area of interest) of both QD-loaded PSMPs and unloaded, plain PSMPs, measured with two different PSMP concentrations, that reveal concentration and preparation-related changes in the intensity of the carbonyl peak at  $1744\text{ cm}^{-1}$ . The slight offset of the IR spectra (baseline value below 0) is caused by the normalization procedure. The complete IR spectra are provided in the SI (see Figure S4).

validation with  $^{13}\text{C}$  NMR measurements, i.e., by comparing the results of conductometric measurements and  $^{13}\text{C}$  NMR data<sup>40,56,57</sup>. As such, electrochemical titration methods are sensitive to the presence of (de)protonable and ionic contaminations present in the bead dispersion, remaining from particle synthesis like polymerization initiators, stabilizers, and salts, prior to conductometric measurements. Hence, all bead dispersions were purified by dialysis. The amount of COOH groups on the bead surface was determined to  $127 \pm 3\text{ nmol/mg}$  for the unstained PSMPs and to  $155 \pm 18\text{ nmol/mg}$  and  $177\text{ nmol/mg}$  for the PSMPs, QD-stained via the polymerization and swelling procedure, respectively. This indicates an increase in the amount of COOH FGs for both staining procedures, particularly for the swelling procedure. Considering the STEM results, the higher total amount of COOH groups can be ascribed to the oleic acid ligand shell of the CdSe/Cds QDs that are located on the PSMP surface. This also explains why the total COOH amount on the surface of the PSMPs prepared via the swelling procedure is higher than the amount of COOH FGs found for the PSMPs prepared with addition of the QDs present during bead formation, as more QDs were used for the swelling procedure. This assumption is further supported by the results obtained for beads stained with the dye RITC shown in the SI (Figure S5). For RITC staining, a decrease of the amount of COOH FGs compared to unstained beads was obtained, as the dye does not introduce more COOH groups, yet can bind to existing COOH FGs on the polymer beads.

Finally, the amount of accessible COOH groups on the unstained and the two types of QD-loaded PSMPs was determined (see Fig. 6 for results). Therefore, two optical assays were utilized that rely on the signal generation by optically detectable reporter molecules of different size and differ in the type of interaction/binding of the reporter to the particle surface. Both assays are versatile and allow for the quantification of the number of accessible surface groups on all types of transparent, scattering, absorbing and/or fluorescent particles as the actual optical quantification is performed in the supernatant after particle removal by centrifugation. Thereby, a distortion of the optical measurements by scattering is avoided. The colorimetric TBO assay exploits the adsorption/desorption of the positively charged dye TBO onto the surface of oppositely charged particles like negatively charged carboxylated beads. It yielded an amount of accessible COOH groups of  $15 \pm 4\text{ nmol/mg}$  COOH FGs and  $7 \pm 2\text{ nmol/mg}$  for the PSMPs stained with QDs by the polymerization and the swelling procedure, respectively. These numbers equal less than 20% of the total number of COOH groups found by conductometry. Please note here that the size of a TBO molecule with its three aromatic rings considerably exceeds the size of a COOH group. Hence, assuming a one-to-one binding stoichiometry of FG and dye considerably underestimates the accessible number of COOH surface groups. For a more reliable result, a stoichiometry factor must be used, which can be derived from a method comparison or cross validation. For example, in a previous study on the determination

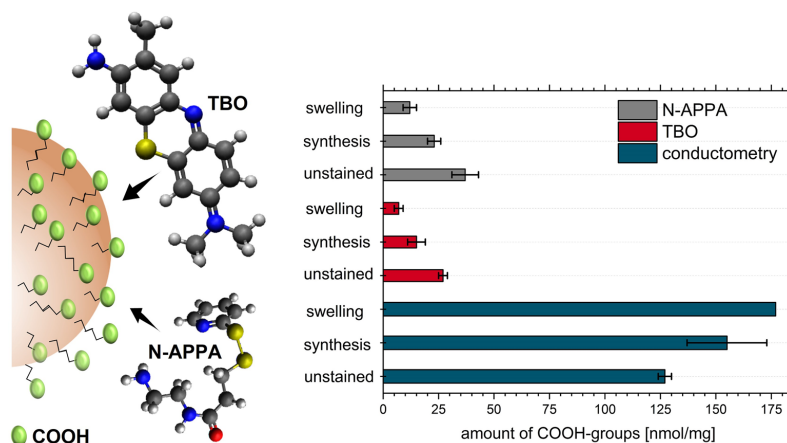


**Figure 6.** Quantification of the total and accessible amount of COOH groups on unstained and QD-loaded PSMPs (polymerization (here synthesis) and swelling procedure), using conductometry and optical assays with TBO and the cleavable reporter *N*-APPA. Both photometrically readout reporter molecules differ in size, shape, and steric demand with respect to the surface area and FGs to be detected.

of the amount of COOH groups on polymethylmethacrylate (PMMA) beads grafted with different amounts of polyacrylic acid, we obtained a stoichiometry factor of  $3.4 \pm 0.2$  by such a method cross validation<sup>40</sup>. An estimation of the theoretical steric demand of TBO on the particle surface (see Fig. 6, left, for molecule structures) indicates a maximum amount of about 6 nmol/mg PSMPs, depending on the assumption made on the binding/orientation of the TBO dye to the particle surface.

In addition, we performed a catch-and-release assay with the cleavable reporter *N*-APPA. *N*-APPA is first covalently bound to the COOH FGs to be quantified, followed by the reductive cleavage of the disulfide linker, yielding the photometrically detectable reporter 2-thiopyridone (2-TP). 2-TP is then photometrically quantified in the supernatant after particle removal by centrifugation. This versatile assay has been successfully used by us, e.g., for the quantification of different FGs on polymer and silica particles<sup>37,38</sup>. The size and hence the steric demand of *N*-APPA is smaller than that of TBO. Due to the less rigid molecular structure and smaller size, a higher number of accessible COOH groups should be found by this assay. As to be expected from these considerations, the data in Fig. 6 reveal 1.4–1.7 times higher values than obtained for the TBO assay. These results also underline the possible influence of the reporter size and shape on the quantification of the amount of accessible surface FGs and the importance of size and steric considerations for subsequent bead surface modifications with ligands or biomolecules<sup>38</sup>. The values of  $23 \pm 3$  nmol/mg,  $12 \pm 3$  nmol/mg, and  $37 \pm 6$  nmol/mg as found for the QD-loaded PSMPs obtained by the polymerization and the swelling procedure and the unstained PSMPs, respectively, also exceed the calculated amount of *N*-APPA molecules that can cover the bead surface (10 nmol/mg). This confirms the trend observed for the TBO assay. The observation can possibly be ascribed to a surface penetration of the two optically read out dyes through the somewhat porous PSMP surface, that differs between both dyes. Thereby, not only COOH groups present on the particle surface, but also COOH FGs near the PSMP surface are detected. In addition, the maximum calculated amount of attached dye relies on the assumption of a very smooth PSMP surface, which is not completely true. This can also lead to the higher values for the synthesized PSMPs compared to the theoretical, accessible COOH amount.

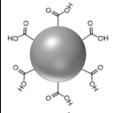
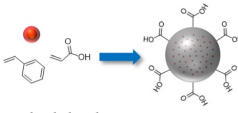
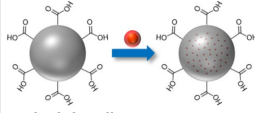
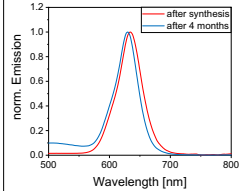
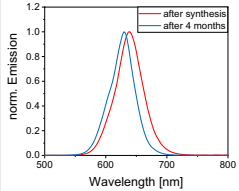
For the different PSMPs, the trend for the accessible amount of COOH groups determined from both assays, yielding the highest amount of accessible COOH groups for the unstained particles, is reversed compared to the total amount of COOH groups obtained by conductometric titration. This can also be ascribed to the presence of the QDs on the PSMP surface. Here, two effects need to be considered. First, the oleic acid ligands on the QD surface bear COOH groups. These are coordinatively bound to the QD surface, but can be still protonated, and thus can be detected by the conductometric titration, but not by the considerably larger dye/reporter molecules. Hence, for the QD-stained PSMPs, these molecules do not contribute to the COOH amount measured with the optical assays. In addition, the COOH FGs on the QD-loaded PSMPs are partly occupied by the QDs and are thus not available for the interaction or covalent binding of the colorimetric reporters TBO and *N*-APPA. This can explain why the accessible COOH amount determined by both assays is highest for the unstained particles. Moreover, this can also explain why the accessible COOH amount found for the PSMPs prepared by polymerization in the presence of QDs exceeds the amount of accessible COOH FGs determined for the PSMPs prepared via the swelling procedure, as for the polymerization approach, fewer QDs were employed.

**Stability of the QD-loaded PSMPs.** Subsequently, we performed first screening studies of the storage stability of both types of QD-loaded PSMPs and the unloaded PSMPs. The particles were all stored in ethanolic

dispersion at RT in the dark. As application-relevant readout parameter/particle properties, the most relevant functional properties size, surface charge, and photoluminescence were used. After a storage period of four months, the particles were characterized utilizing DLS and zeta potential measurements, which are routinely employed for characterizing the colloidal stability of all types of NPs and MPs. In addition, fluorescence measurements were performed, which provide information on changes in the performance parameters particle size, surface charge, emission band position, and PLQY. The results of these measurements were then compared to the result of the initially performed PSMP characterization. The data are summarized in Table 1.

As follows from the DLS measurements summarized in Table 1, the particle size decreased for all PSMPs within four months. With a 60% decrease, the size difference is most notable for the QD-loaded PSMPs prepared via the swelling procedure. The QD-loaded PSMPs fabricated by the polymerization procedure show a decrease by about 18% and the size of the unstained PSMP size decreased only by about 6%. The zeta potential of the QD-loaded PSMPs prepared by the swelling procedure barely changed over time. In contrast, the zeta potentials of the unstained and QD-loaded PSMPs prepared by the polymerization procedure slightly increased from values of  $-48/-49$  mV to  $-40$  mV. This still indicates a good colloidal stability. Apparently, not only the presence of the QDs has a significant influence on PSMP stability, but also the synthesis route. The decrease in PSMP size suggests a partial disintegration of the particles over time, and the chosen synthesis route seems to have a significant influence on this process. Possible reasons, that are currently assessed by us, could be related to different amounts of QDs and/or surface groups. In this respect, also other factors will be examined in the future such as the solvent chosen for PSMP dispersion, i.e., ethanol, ethanol/water mixtures and water, as well as the storage temperature. Other factors, that could be relevant for particle stability, include the degree of purification, i.e., whether the particles were purified after synthesis or stored in the reaction mixture, the amount of surface FG, and the usage of crosslinkers for the polymer matrix. Interestingly, up to now, there are only relatively few data available on systematic long-term stability studies of PSMPs. For commercial polymer particles of comparable composition and made from different polymers, commonly water is used for particle dispersion and storage, but also ethanol and ethanol/water mixtures are used for this purpose. Particle manufacturers typically recommend storage in the refrigerator. The findings of Wilkinson et al.<sup>39</sup>, who performed stability studies with latex micro-particles, reveal for example that the surfactant employed for particle synthesis can considerably affect particle stability. This is confirmed by first results from us regarding the deteriorating influence of the purification of the particles concerning polymer bead stability.

The luminescence properties of the QD-loaded PSMPs reveal a decrease in PLQY values from 24 to 15% and from 48 to 31% for the PSMPs prepared by the polymerization procedure and the swelling procedure, respectively. The emission spectra of both QD-loaded PSMPs underwent a hypsochromic shift. This shift is slightly more pronounced for the QD-loaded particles prepared via the swelling procedure. The decrease in PLQY and fluorescence intensity as well as the hypsochromic shift in fluorescence are attributed to time-dependent changes of the luminescence of surface-bound or near-surface located QDs, which were constantly exposed to ethanol used for PSMP dispersion and storage. Ethanol can initiate the quenching of the QD fluorescence, e.g., by

			
	Unstained PSMPs	QD-loaded, polymerization	QD-loaded, swelling
Particle size by DLS in $\mu\text{m}$			
After synthesis	$2.00 \pm 0.25$	$2.46 \pm 0.40$	$2.69 \pm 0.51$
After four months	$1.88 \pm 0.15$	$1.78 \pm 0.13$	$1.07 \pm 0.17$
Zeta potential by DLS in mV			
After synthesis	$-48 \pm 2$	$-49 \pm 1$	$-22 \pm 2$
After four months	$-40 \pm 4$	$-40 \pm 1$	$-24 \pm 3$
PLQY in %			
After synthesis	/	24%	48%
After four months	/	15%	31%
Emission spectra	/		

**Table 1.** Comparison of four months aged PSMPs with freshly prepared PSMPs, regarding particle size determined by DLS, zeta potential, emission spectra, and PLQY.

removal of the QD surface ligands and/or irreversible QD aggregation, as shown by us in a previous publication<sup>31</sup>, resulting in a time-dependent loss in emission. To investigate the occurrence of QD leakage, which would also lead to a diminution in fluorescence intensity, the QD-loaded PSMPs stored for four months were centrifuged (2000 rcf/3 min). Subsequently, an emission spectrum of the supernatant was recorded (see SI, Figure S10). The spectrum revealed only very minimal, barely detectable leakage of the QDs. This confirms that QD leakage does not predominantly account for the observed loss in fluorescence intensity.

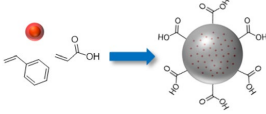
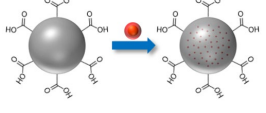
Please note that although both types of QD-loaded PSMPs show a significant decrease in QD fluorescence, they can still be used for many different life science applications after four months of storage under the here applied conditions. Moreover, the long-term stability of the PSMPs can most likely be considerably improved by optimized storage conditions, as described in the previous section.

### Conclusion and outlook

In summary, we prepared COOH surface-functionalized, quantum dot (QD)-loaded polymer microparticles (PSMPs) by two synthesis routes. These include QD addition during the polymerization procedure, and bead formation before QD loading via the postsynthetic swelling procedure. We utilized oleic acid and oleylamine stabilized CdSe/CdS-core/shell-QDs with a mean particle size of  $10.3 \pm 1.2$  nm and a strong red luminescence as representative QDs. Subsequently, the application-relevant or functional properties of both types of about 2  $\mu\text{m}$ -sized, QD-loaded PSMPs such particle size, amount of total and accessible surface functional groups (FGs), and photoluminescence were determined by different analytical and spectroscopic methods and compared. For this comparison, also unstained PSMPs as well as PSMPs stained with two differently charged molecular dyes were made and used as control samples. As revealed by this comparison, both synthetic approaches led to significant differences in the total and accessible amount of COOH groups on the surface of the PSMPs, as well as in the fluorescence properties of the PSMP-encoding CdSe/CdS QDs.

The main advantages and disadvantages of both synthesis routes are summarized in Table 2, also considering the suitability of the resulting carboxylated, QD-loaded PSMPs for future applications. Aside from the already mentioned differences in FG amount and luminescence properties, in terms of particle size, the chosen synthesis routes do not seem to have a significant effect on the PSMPs. With the polymerization procedure, however, the size can be more easily adjusted to specific needs, while for the swelling procedure, premanufactured PSMPs can be employed, which are commercially available. Another advantage of the former procedure is the higher yield of QD-encoded beads. Despite the differences in luminescence properties, FG amount, stability, and synthesis requirements/outcome, both QD-loaded PSMPs are suitable for a wide range of applications in the life sciences.

Overall, the results of our study highlight the possible influence of particle staining and loading, particularly on the number of accessible surface FGs, and hence on the subsequent conjugation of functional molecules. They provide a better understanding of the impact of the synthesis route on the application-relevant properties of the resulting luminophore-stained polymer particles. These insights can contribute to the reproducible preparation of safe(r) particles with an improved control of their surface functionalities. The surface functionalization largely determines the dispersibility, colloidal stability, and subsequent bioconjugation of these NP-loaded polymer

Synthesis approach	Advantages	Disadvantages
(i) QD addition during the polymerization procedure (route i) 	Large PSMP amounts (higher yield per synthesis batch)	More time consuming (in case of commercial particles)
	Higher amount of accessible FGs	No commercially available particles usable
	PSMP size easily adjustable	Less monodisperse
	Very versatile (size, crosslinking etc.)	Lower PLQY
	Better long-term stability	
(ii) QD-encoding by a post-synthetic swelling procedure of non-crosslinked, carboxylated particles (route ii) 	Facile and good transferability to other systems (matrix & staining species)	Low PSMP amounts (lower yield per synthesis batch)
	Use of commercial particles	Lower amount of accessible FGs
	Potentially better monodispersity (use of commercial PSMPs)	Size restriction (premanufactured beads)
	Very good luminescence properties (esp. PLQY)	Reduced long-term stability
	Less time consuming (when using commercial particles)	

**Table 2.** Comparison of the two synthesis routes: QD-stained carboxylated PSMP prepared i.) with the QDs present during the polymerization procedure, and ii.) by a post-synthetic swelling procedure of carboxylated PSMPs.

particles, as well as their performance in specific applications<sup>60,61</sup>. These findings are also of considerable relevance for safe(r)-by-design concepts for nanomaterials that often involve the encapsulation of potentially hazardous and toxic nanomaterials in other as safer or safe regarded materials, such as certain polymers or micelles. In the future, we plan to expand these studies also to differently sized, i.e., smaller as well as larger nanoparticles and different surface chemistries, thereby also addressing parameters such as surface or particle charge.

In addition, the presented FG characterization can also be applied to other particle systems made from different materials. This includes, e.g., different types of QDs of varying morphology, not only II/VI semiconductors such as CdSe cores with different passivation shells, and iron oxide nanoparticles encapsulated in crosslinked micelles utilizing polymers such as functionalized poly(isoprene) and poly(isoprene)-*block*-poly(ethylene oxide), which bear COOH and amino FGs and are currently examined by us and other groups<sup>12,62,63</sup>. First studies of such systems utilizing the Fluram assay for the quantification of primary amino FGs suggest that this approach can discriminate between the amino groups of the organic micelle shell, which point outwards from the QDs and are available for (bio)functionalization, and the amino groups which are involved in QD coordination within the micelles. The latter are not accessible for subsequent derivatization.

### Data availability

All data generated/analyzed during this study are included either in this article and its Supplementary Information files or are available upon request to the corresponding author (U. Resch-Genger, ute.resch@bam.de) or the first author (L. Scholtz, lena.scholtz@bam.de).

Received: 14 April 2023; Accepted: 10 July 2023

Published online: 24 July 2023

### References

- Wang, G. *et al.* Highly efficient preparation of multiscaled quantum dot barcodes for multiplexed hepatitis B detection. *ACS Nano* **7**, 471–481 (2013).
- Leng, Y. *et al.* Magnetic/fluorescent barcodes based on cadmium-free near-infrared-emitting quantum dots for multiplexed detection. *Adv. Funct. Mater.* **26**, 7581–7589 (2016).
- Mulvaney, S. P., Mattoussi, H. & Whitman, L. J. Incorporating fluorescent dyes and quantum dots into magnetic microbeads for immunoassays. *Biotechniques* **36**, 602–609 (2004).
- Kage, D., Hoffmann, K., Borcherding, H., Schedler, U. & Resch-Genger, U. Lifetime encoding in flow cytometry for bead-based sensing of biomolecular interaction. *Sci. Rep.* **10**, 19477 (2020).
- Li, J. & Zhang, J. Z. Optical properties and applications of hybrid semiconductor nanomaterials. *Coord. Chem. Rev.* **253**, 3015–3041 (2009).
- Talapin, D. V., Lee, J. S., Kovalenko, M. V. & Shevchenko, E. V. Prospects of colloidal nanocrystals for electronic and optoelectronic applications. *Chem. Rev.* **110**, 389–458 (2010).
- Ghosh Chaudhuri, R. & Paria, S. Core/shell nanoparticles: classes, properties, synthesis mechanisms, characterization, and applications. *Chem. Rev.* **112**, 2373–2433 (2011).
- Stark, W. J., Stoessel, P. R., Wohlleben, W. & Hafner, A. Industrial applications of nanoparticles. *Chem. Soc. Rev.* **44**, 5793–5805 (2015).
- Wolfbeis, O. S. An overview of nanoparticles commonly used in fluorescent bioimaging. *Chem. Soc. Rev.* **44**, 4743–4768 (2015).
- Pelaz, B. *et al.* Diverse applications of nanomedicine. *ACS Nano* **11**, 2313–2381 (2017).
- Oh, J. H., Park, D. H., Joo, J. H. & Lee, J. S. Recent advances in chemical functionalization of nanoparticles with biomolecules for analytical applications. *Anal. Bioanal. Chem.* **407**, 8627–8645 (2015).
- Schmidtko, C. *et al.* Amphiphilic, cross-linkable diblock copolymers for multifunctionalized nanoparticles as biological probes. *Nanoscale* **5**, 7433–7444 (2013).
- Lesnyak, V., Gaponik, N. & Eychmuller, A. Colloidal semiconductor nanocrystals: the aqueous approach. *Chem. Soc. Rev.* **42**, 2905–2929 (2013).
- Jing, L. H. *et al.* Aqueous based semiconductor nanocrystals. *Chem. Rev.* **116**, 10623–10730 (2016).
- Girma, W. M., Fahmi, M. Z., Permadi, A., Abate, M. A. & Chang, J. Y. Synthetic strategies and biomedical applications of I–III–VI ternary quantum dots. *J. Mater. Chem. B* **5**, 6193–6216 (2017).
- Wegner, K. D. *et al.* Influence of the core/shell structure of indium phosphide based quantum dots on their photostability and cytotoxicity. *Front. Chem.* **7**, 466 (2019).
- Bailey, R. E. & Nie, S. M. Alloyed semiconductor quantum dots: tuning the optical properties without changing the particle size. *J. Am. Chem. Soc.* **125**, 7100–7106 (2003).
- Chikan, V. Challenges and prospects of electronic doping of colloidal quantum dots: Case study of CdSe. *J. Phys. Chem. Lett.* **2**, 2783–2789 (2011).
- Reiss, P., Carriere, M., Lincheneau, C., Vaure, L. & Tamang, S. Synthesis of semiconductor nanocrystals, focusing on nontoxic and earth-abundant materials. *Chem. Rev.* **116**, 10731–10819 (2016).
- Yarema, O., Yarema, M. & Wood, V. Tuning the composition of multicomponent semiconductor nanocrystals: The case of I–III–VI materials. *Chem Mater* **30**, 1446–1461 (2018).
- Carbone, L. *et al.* Synthesis and micrometer-scale assembly of colloidal CdSe/CdS nanorods prepared by a seeded growth approach. *Nano Lett.* **7**, 2942–2950 (2007).
- Nightingale, A. M. *et al.* Large-scale synthesis of nanocrystals in a multichannel droplet reactor. *J. Mater. Chem. A* **1**, 4067–4076 (2013).
- Chen, O. *et al.* Compact high-quality CdSe–CdS core–shell nanocrystals with narrow emission linewidths and suppressed blinking. *Nat. Mater.* **12**, 445–451 (2013).
- Resch-Genger, U., Grabolle, M., Cavaliere-Jaricot, S., Nitschke, R. & Nann, T. Quantum dots versus organic dyes as fluorescent labels. *Nat. Methods* **5**, 763–775 (2008).
- Geißler, D. *et al.* Quantum dot biosensors for ultrasensitive multiplexed diagnostics. *Angew. Chem. Int. Ed.* **49**, 1396–1401 (2010).
- Hildebrandt, N., & Geißler, D. In *Advances in Experimental Medicine and Biology* 75–86 (2012).
- Geißler, D. & Hildebrandt, N. Recent developments in Förster resonance energy transfer (FRET) diagnostics using quantum dots. *Anal. Bioanal. Chem.* **408**, 4475–4483 (2016).
- Algar, W. R. *et al.* The controlled display of biomolecules on nanoparticles: a challenge suited to bioorthogonal chemistry. *Bioconjug. Chem.* **22**, 825–858 (2011).

29. Sapsford, K. E. *et al.* Functionalizing nanoparticles with biological molecules: developing chemistries that facilitate nanotechnology. *Chem. Rev.* **113**, 1904–2074 (2013).
30. Hines, D. A. & Kamat, P. V. Recent advances in quantum dot surface chemistry. *ACS Appl. Mater. Interfaces.* **6**, 3041–3057 (2014).
31. Scholtz, L. *et al.* Luminescence encoding of polymer microbeads with organic dyes and semiconductor quantum dots during polymerization. *Sci. Rep.* **12**, 12061 (2022).
32. Sheng, W. *et al.* In-situ encapsulation of quantum dots into polymer microspheres. *Langmuir* **22**, 3782–3790 (2006).
33. Sherman, R. L. & Ford, W. T. Semiconductor nanoparticle/polystyrene latex composite materials. *Langmuir* **21**, 5218–5222 (2005).
34. Rogach, A. *et al.* Nano- and Microengineering: 3-d colloidal photonic crystals prepared from sub- $\mu\text{m}$ -sized polystyrene latex spheres pre-coated with luminescent polyelectrolyte/nanocrystal shells. *Adv. Mater.* **12**, 333–337 (2000).
35. Sukhanova, A. *et al.* Nanocrystal-encoded fluorescent microbeads for proteomics: antibody profiling and diagnostics of autoimmune diseases. *Nano Lett.* **7**, 2322–2327 (2007).
36. Martynenko, I. V. *et al.* Magneto-fluorescent microbeads for bacteria detection constructed from superparamagnetic  $\text{Fe}_3\text{O}_4$  nanoparticles and AlS/ZnS quantum dots. *Anal. Chem.* **91**, 12661–12669 (2019).
37. Moser, M., Nirmalanathan, N., Behnke, T., Geißler, D. & Resch-Genger, U. Multimodal cleavable reporters versus conventional labels for optical quantification of accessible amino and carboxy groups on nano- and microparticles. *Anal. Chem.* **90**, 5887–5895 (2018).
38. Nirmalanathan-Budau, N. *et al.* Multimodal cleavable reporters for quantifying carboxy and amino groups on organic and inorganic nanoparticles. *Sci. Rep.* **9**, 17577 (2019).
39. Roloff, A. *et al.* Quantification of aldehydes on polymeric microbead surfaces via catch and release of reporter chromophores. *Anal. Chem.* **91**, 8827–8834 (2019).
40. Hennig, A. *et al.* Scope and limitations of surface functional group quantification methods: Exploratory study with poly (acrylic acid)-grafted micro- and nanoparticles. *J. Am. Chem. Soc.* **134**, 8268–8276 (2012).
41. Srivastava, P. *et al.* Multicolor polystyrene nanosensors for the monitoring of acidic, neutral, and basic pH values and cellular uptake studies. *Anal. Chem.* **94**, 9656–9664 (2022).
42. Meier, M. A. R., Aerts, S. N. H., Staal, B. B. P., Rasa, M. & Schubert, U. S. PEO-b-PCL block copolymers: Synthesis, detailed characterization, and selected micellar drug encapsulation behavior. *Macromol. Rapid Commun.* **26**, 1918–1924 (2005).
43. Kimura, F. *et al.* Dual luminophore polystyrene microspheres for pressure-sensitive luminescent imaging. *Meas. Sci. Technol.* **17**, 1254 (2006).
44. Hennig, A. *et al.* Simple colorimetric method for quantification of surface carboxy groups on polymer particles. *Anal. Chem.* **83**, 4970–4974 (2011).
45. Behnke, T. *et al.* Encapsulation of hydrophobic dyes in polystyrene micro- and nanoparticles via swelling procedures. *J. Fluoresc.* **21**, 937–944 (2011).
46. Behnke, T., Würth, C., Laux, E.-M., Hoffmann, K. & Resch-Genger, U. Simple strategies towards bright polymer particles via one-step staining procedures. *Dyes Pigm.* **94**, 247–257 (2012).
47. Huber, A., Behnke, T., Würth, C., Jaeger, C. & Resch-Genger, U. Spectroscopic characterization of coumarin-stained beads: quantification of the number of fluorophores per particle with solid-state  $^{19}\text{F}$ -NMR and measurement of absolute fluorescence quantum yields. *Anal. Chem.* **84**, 3654–3661 (2012).
48. Han, M., Gao, X., Su, J. Z. & Nie, S. Quantum-dot-tagged microbeads for multiplexed optical coding of biomolecules. *Nat. Biotechnol.* **19**, 631–635 (2001).
49. Gao, X. & Nie, S. Quantum dot-encoded mesoporous beads with high brightness and uniformity: Rapid readout using flow cytometry. *Anal. Chem.* **76**, 2406–2410 (2004).
50. Bradley, M., Bruno, N. & Vincent, B. Distribution of CdSe quantum dots within swollen polystyrene microgel particles using confocal microscopy. *Langmuir* **21**, 2750–2753 (2005).
51. Li, Z., Liu, Q., Li, Y., Yuan, W. & Li, F. One-step polymerized lanthanide-based polystyrene microsphere for sensitive lateral flow immunoassay. *J. Rare Earths* **39**, 11–18 (2021).
52. Yang, X., Zhang, P., Xing, X., lv, Q., Jiang, Y., Jiang, Y., Wang, Z. Improving the fluorescence intensity of lanthanide-doped microspheres via incorporation of lauryl methacrylate: Synthesis and their application in C-reactive protein detection. *Colloids Surf. A: Physicochem. Eng. Asp.* **2022**, 653, 130065.
53. Chung, T.-H. & Lee, W.-C. Preparation of styrene-based, magnetic polymer microspheres by a swelling and penetration process. *React. Funct. Polym.* **68**, 1441–1447 (2008).
54. Kromer, C. *et al.* Monitoring and imaging pH in biofilms utilizing a fluorescent polymeric nanosensor. *Sci. Rep.* **12**, 9823 (2022).
55. Mulvihill, M. J., Habas, S. E., Jen-La Plante, I., Wan, J. & Mokari, T. Influence of size, shape, and surface coating on the stability of aqueous suspensions of CdSe nanoparticles. *Chem. Mater.* **22**, 5251–5257 (2010).
56. Dietrich, P. M. *et al.* Surface analytical study of poly (acrylic acid)-grafted microparticles (beads): Characterization, chemical derivatization, and quantification of surface carboxyl groups. *J. Phys. Chem. C* **118**, 20393–20404 (2014).
57. Hennig, A. *et al.* En route to traceable reference standards for surface group quantifications by XPS, NMR and fluorescence spectroscopy. *Analyst* **140**, 1804–1808 (2015).
58. Geißler, D., Nirmalanathan-Budau, N., Scholtz, L., Tavernaro, I. & Resch-Genger, U. Analyzing the surface of functional nanomaterials—how to quantify the total and derivatizable number of functional groups and ligands. *Microchim. Acta* **188**, 321 (2021).
59. Wilkinson, M. C., Hearn, J., Karpowicz, F. H. & Chainey, M. The stability of latex particles in aqueous suspensions. *Part. Sci. Technol.* **5**, 65–82 (1987).
60. Tavernaro, I. *et al.* Safe-by-Design part II: A strategy for balancing safety and functionality in the different stages of the innovation process. *NanoImpact* **24**, 100354 (2021).
61. Soeteman-Hernandez, L. G. *et al.* Safe innovation approach: Towards an agile system for dealing with innovations. *Mater. Today Commun.* **20**, 100548 (2019).
62. Geißler, D. *et al.* An automatable platform for genotoxicity testing of nanomaterials based on the fluorometric  $\gamma\text{-H2AX}$  assay reveals no genotoxicity of properly surface-shielded cadmium-based quantum dots. *Nanoscale* **11**, 13458–13468 (2019).
63. Pösel, E. *et al.* Tailor-made quantum dot and iron oxide based contrast agents for in vitro and in vivo tumor imaging. *ACS Nano* **6**, 3346–3355 (2012).

### Acknowledgements

This research was carried out in part at the electron microscopy center at BAM. The authors would like to thank Ines Feldmann from BAM division 4.2 for the SEM measurements, Carsten Prinz from BAM division 6.3 for the STEM measurements (TEM owned by HU Berlin—Prof. Nicola Pinna), Dr. A. Schaefer from the Institute for Chemistry and Biochemistry, Free University Berlin for providing the NMR facilities (supported by DFG) and Toufiq Elahi from BAM division I.2/FU Berlin for excellent assistance in particle synthesis.

### Author contributions

L.S., I.T. and D.G. planned the study. L.S. planned and performed the polymer bead and *block*-copolymer syntheses and the DLS and zeta potential measurements as well as the fluorescence and integrating sphere spectroscopy studies, and analyzed these data. I.T. planned and carried out the post-synthetic swelling procedures for bead staining with QDs/dyes and the optical assays for FG quantification, including data analyses. J.G.E. performed the QD synthesis and the AAS measurements. M.L. performed the conductometry measurements and analyzed the conductometric data. A.H. and G.H. performed the FTIR measurements with help of L.S. and interpreted the corresponding data. L.S. and I.T. wrote the first drafts of the publication. U.R.-G. supervised the study and the writing of the manuscript and participated in writing the final version of the manuscript. N.C.B. also contributed significantly to the writing and revision of the manuscript. All authors approved the final version.

### Funding

Open Access funding enabled and organized by Projekt DEAL. L. S. acknowledges funding by the European Metrology Programme for Innovation and Research (EMPIR) as part of the project „AeroTox “ (18HLT02) and D. G. by project METVES II (18HLT01). The EMPIR initiative is co-funded by the European Union’s Horizon 2020 research and innovation programme and by the EMPIR participating states. I. T. acknowledges financial support from the WIPANO project AquaFunkNano (Federal Ministry for Economic Affairs and Climate Action (BmWK)) and the project MiGraGen (Novo Nordisk Fonden; Interdisciplinary Synergy Programme 2021). J. G. E. acknowledges funding by the MWK—School for Additive Manufacturing SAM. N.B. acknowledges funding by the Deutsche Forschungsgemeinschaft (DFG, German Research Foundation) under Germany’s Excellence Strategy within the Cluster of Excellence PhoenixD (EXC 2122, Project ID 390833453).

### Competing interests

The authors declare no competing interests.

### Additional information

**Supplementary Information** The online version contains supplementary material available at <https://doi.org/10.1038/s41598-023-38518-7>.

**Correspondence** and requests for materials should be addressed to U.R.-G.

**Reprints and permissions information** is available at [www.nature.com/reprints](http://www.nature.com/reprints).

**Publisher’s note** Springer Nature remains neutral with regard to jurisdictional claims in published maps and institutional affiliations.



**Open Access** This article is licensed under a Creative Commons Attribution 4.0 International License, which permits use, sharing, adaptation, distribution and reproduction in any medium or format, as long as you give appropriate credit to the original author(s) and the source, provide a link to the Creative Commons licence, and indicate if changes were made. The images or other third party material in this article are included in the article’s Creative Commons licence, unless indicated otherwise in a credit line to the material. If material is not included in the article’s Creative Commons licence and your intended use is not permitted by statutory regulation or exceeds the permitted use, you will need to obtain permission directly from the copyright holder. To view a copy of this licence, visit <http://creativecommons.org/licenses/by/4.0/>.

© The Author(s) 2023

Supplementary Information for:

**Influence of Nanoparticle Encapsulation and Encoding on the Surface Chemistry of Polymer Carrier Beads**

Lena Scholtz<sup>1,2</sup>, Isabella Tavernaro<sup>1</sup>, J. Gerrit Eckert<sup>3</sup>, Marc Lutowski<sup>1</sup>, Daniel Geißler<sup>1</sup>, Andreas Hertwig<sup>4</sup>, Gundula Hidde<sup>4</sup>, Nadja C. Bigall<sup>3,5</sup>, Ute Resch-Genger<sup>1,\*</sup>

<sup>1</sup>Federal Institute for Materials Research and Testing (BAM), Division 1.2 *Biophotonics*, Richard-Willstätter-Str. 11, 12489 Berlin, Germany.

<sup>2</sup>Free University Berlin, Institute for Chemistry and Biochemistry, Takustraße 3, 14195 Berlin, Germany.

<sup>3</sup>Leibniz University Hannover, Institute of Physical Chemistry and Electrochemistry, Callinstraße 3A, 30167 Hannover, Germany.

<sup>4</sup>Federal Institute for Materials Research and Testing (BAM), Division 6.1 *Surface Analysis and Interfacial Chemistry*, Unter den Eichen 87, 12205 Berlin, Germany.

<sup>5</sup>Cluster of Excellence PhoenixD (Photonics, Optics, and Engineering – Innovation Across Disciplines), 30167 Hannover, Germany.

\*ute.resch@bam.de, Phone: +49 (0)30 8104 1134

1. Synthesis of CdSe/CdS-core/shell-QDs .....	2
2. Preparation and <sup>1</sup> H-NMR spectrum of polyethylene glycol- <i>block</i> -poly( $\epsilon$ -caprolactone) .....	2
4. Size distribution of PSMPs .....	4
5. FTIR spectra of PSMPs.....	4
6. Dye-loading of PSMPs by postsynthetic swelling procedure with rhodamine B isothiocyanate (RITC) and Nile Red (NR).....	5
7. Conductometry.....	5
8. Investigation of QD leakage after four months of storage .....	7

### 1. Synthesis of CdSe/CdS-core/shell-QDs

The CdSe/CdS-QDs with a core/shell-architecture were prepared according to a previously described procedure<sup>1</sup> adapted from Carbone *et al.*, Nightingale *et al.* and Chen *et al.*.<sup>2-4</sup>

In the first step, CdSe cores with wurtzite structure were synthesised according to Carbone *et al.*<sup>2</sup> For this synthesis, 120 mg (0.93 mmol) CdO together with 560 mg (1.67 mmol) ODPa and 6 g (15.51 mmol) TOPO were degassed at 150 °C for 1 h. The mixture was then heated under argon flow to 300 °C. After the injection of 2 mL (4.48 mmol) of TOP, it was heated to 380 °C and, following a retention period of 10 min, 3.6 mL of a previously prepared TOP/Se solution (120 mg/3.6 mL) was swiftly injected. The temperature was allowed to rise to 380 °C again before the reaction was quenched by addition of 5 mL of ODE and cooled down to 70 °C in an air stream. During the cooldown period, 5 mL of toluene was added to prevent solidification. The resulting particles were precipitated by methanol/isopropanol (1:2), centrifuged at 6,000 rcf and redispersed in 2 mL of hexane.

A Cd(oleate)<sub>2</sub> precursor solution was synthesised according to Nightingale *et al.*<sup>3</sup> For this synthesis, a mixture of 1.284 g (1 mmol) CdO, 12.94 mL (40.77 mmol) of oleic acid and 7.04 mL of ODE was degassed for 10 min at 100 °C. The dispersion was heated to 180 °C under argon flow and kept there for 60 min under vigorous stirring. To remove water as a side product, the mixture was cooled to 120 °C and degassed for 45 min. The 0.5 M Cd(oleate)<sub>2</sub> solution was used as prepared for the next step.

The growth of the CdS surface passivation shell was performed according to an adapted synthesis by Chen *et al.*<sup>4</sup> For this, 100 nmol of the CdSe cores (60 – 100 µL) were dispersed in 3 mL of ODE and OLA, respectively. The mixture was carefully degassed for 30 min at 90 °C. In the meantime, the S and Cd precursor solutions were prepared. For the desired shell thickness of 10 monolayers, 3.191 mL of Cd(oleate)<sub>2</sub> and 286 µL of 1-octanethiol were diluted to a total volume of 7 mL with ODE, respectively. The flask was then heated under argon flow in two steps to 310 °C. When reaching 240 °C, the simultaneous injection of the previously prepared Cd(oleate)<sub>2</sub> and 1-octanethiol solutions via syringe pump (6 mL, 3 mL/h) was initiated. After two hours, 1 mL of oleic acid was injected, and the temperature was kept at 310 °C for another hour. Finally, the reaction mixture was cooled down to RT in an air flow, and the particles were precipitated by addition of acetone, centrifuged, and redispersed in hexane.

### 2. Preparation and <sup>1</sup>H-NMR spectrum of polyethylene glycol-*block*-poly(ε-caprolactone)

The *block*-copolymer polyethylene glycol-*block*-poly(ε-caprolactone) (PEG-*b*-PCL) was prepared according to a previously reported procedure<sup>1</sup> adapted from Meier *et al.*.<sup>5</sup>

For this, 800 mg of poly(ethylene glycol) was added to a dry flask together with 1536 µL (14.53 mmol) of ε-caprolactone. The mixture was placed in a preheated aluminium heating block and stirred for 5 min at 130 °C, followed by the addition of one drop of Sn(II) 2-ethylhexanoate as a catalyst and initiator. The mixture was then stirred at 130 °C for 3 h before it was rapidly cooled with an ice bath, leading to the precipitation of a white, solid product. The raw product was then recrystallized by first dissolving it in a small amount of dichloromethane, followed by precipitation with *n*-heptane. The such obtained *block*-copolymer was then filtered and washed several times with *n*-heptane before drying.

Characterization of the synthesized PEG-*b*-PCL was done by nuclear magnetic resonance spectroscopy (solution <sup>1</sup>H-NMR) at RT with a 400 MHz JEOL JNM-ECX400 spectrometer (Free University Berlin). The sample was prepared by dissolving 6 mg of PEG-*b*-PCL in 700 µL of CDCl<sub>3</sub>.

Chemical shifts: <sup>1</sup>H-NMR (CDCl<sub>3</sub>, 400 MHz): δ = 1.39 (m, 2H, γ), 1.63 (m, 4H, β & δ), 2.30 (m, 2H, α), 3.63 (s, 4H, a & b), 4.05 (t, 2H, ε), 4.22 (t, 2H, b).

The number-average molecular weight M<sub>n</sub> of the synthesized PEG-*b*-PCL was determined to be about 8024 g/mol according to Meier *et al.* from the ratio of protons corresponding to the PEG and PCL signals.<sup>5</sup>

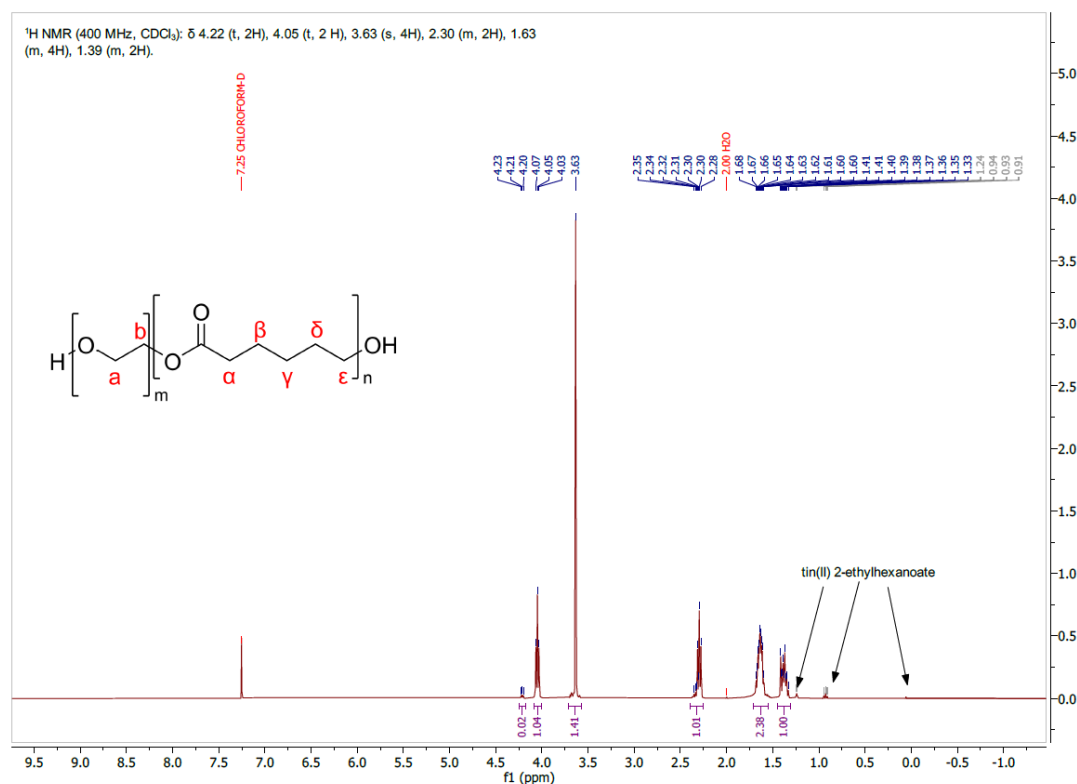


**Figure S1:** <sup>1</sup>H NMR spectrum (400 MHz, CDCl<sub>3</sub>) with structural formula of the synthesized PEG-*b*-PCL, including all compound peaks, solvent peaks and three impurity peaks that can be attributed to the catalyst Sn(II) 2-ethylhexanoate.

### 3. Electron microscopy of CdSe/CdS-QDs

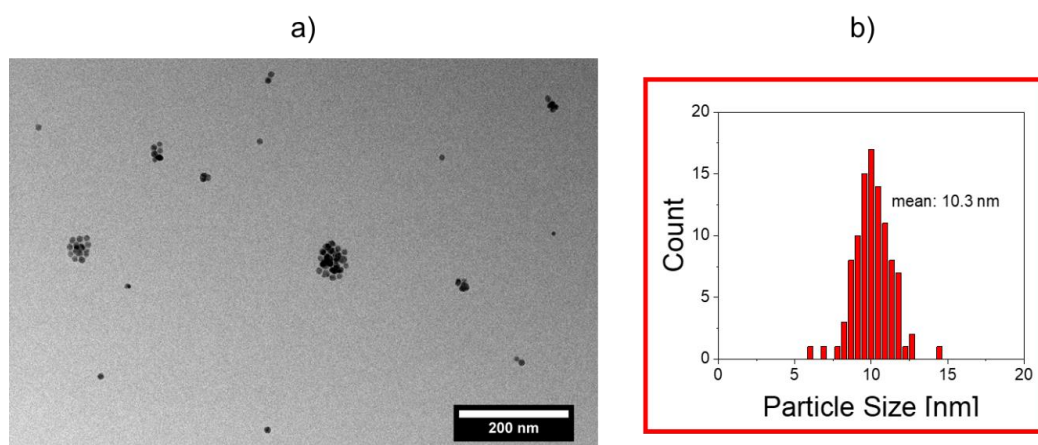


**Figure S2:** a) TEM image and b) corresponding histogram of the particle size distribution of the CdSe/CdS semiconductor core/shell-quantum dots (QDs).

The mean particle size of the QDs was calculated from TEM images to be  $10.3 \pm 1.2$  nm. The PLQY was determined to be 58% in hexane, and the Cd concentration of the QD dispersion was determined by atomic absorption spectroscopy (AAS) to be 32.85 mg/mL.

#### 4. Size distribution of PSMPs

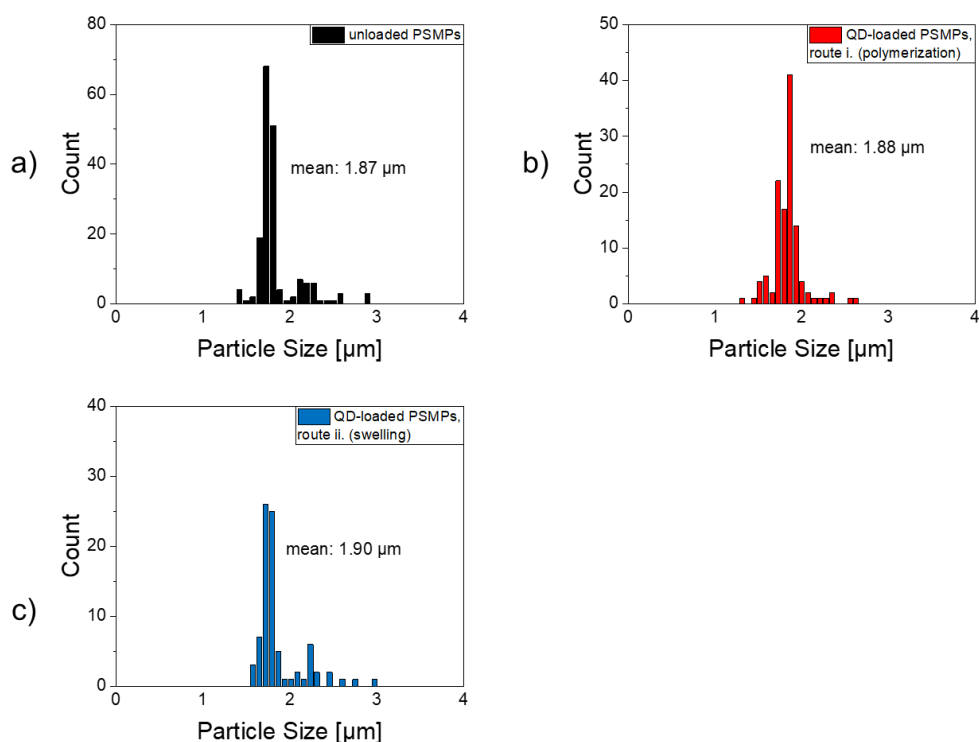


**Figure S3:** Histograms of the particle size distributions resulting from TEM micrographs of a) unloaded PSMPs, b) QD-loaded PSMPs prepared with QDs present during polymerization (route i.), and c) QD-loaded PSMPs prepared with a post-synthetic swelling procedure (route ii.).

#### 5. FTIR spectra of PSMPs

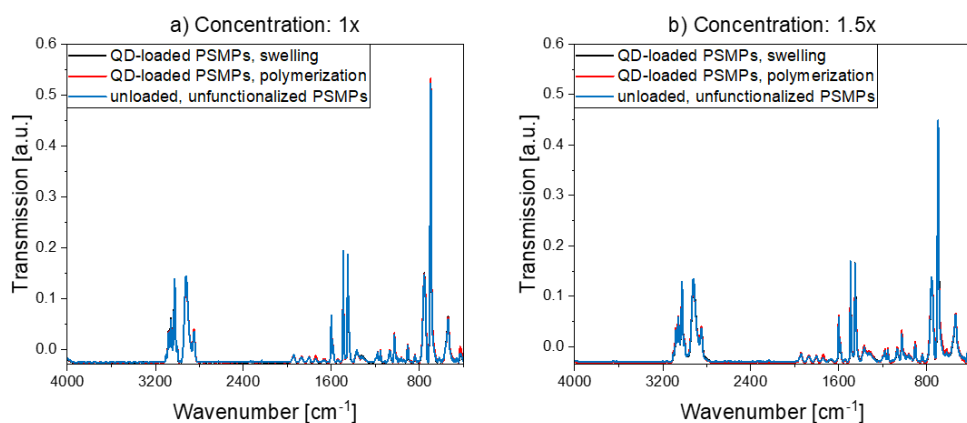


**Figure S4:** Full range FTIR spectra of both QD-loaded PSMPs and unloaded, unfunctionalized PSMPs with a change in carbonyl peak intensity, measured with two different PSMP concentrations. The slight offset of the spectra (baseline value below 0) is caused by the normalization procedure, the peak deviation at the right end of the spectra can be ascribed to impurities.

**6. Dye-loading of PSMPs by postsynthetic swelling procedure with rhodamine B isothiocyanate (RITC) and Nile Red (NR)**

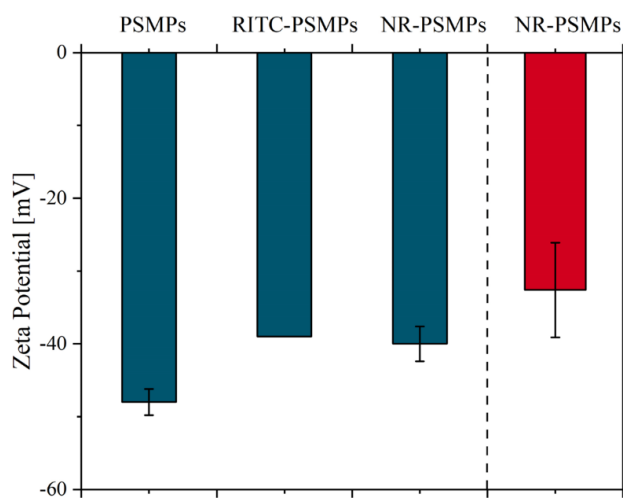


**Figure S5:** Comparison of zeta potentials of synthesized (blue) and commercially available 2  $\mu\text{m}$  PSMPs (red), loaded with RITC and NR in a postsynthetic swelling step.

**7. Conductometry**

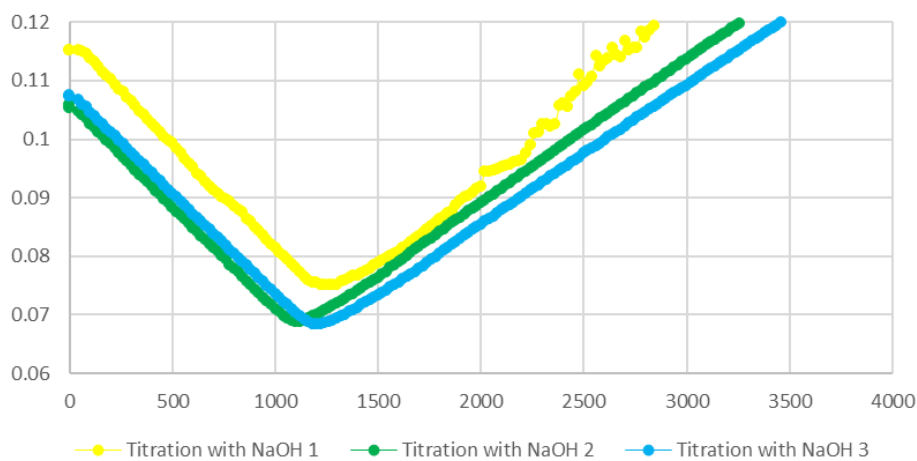


**Figure S6:** Results of conductivity measurements of unstained PSMPs.

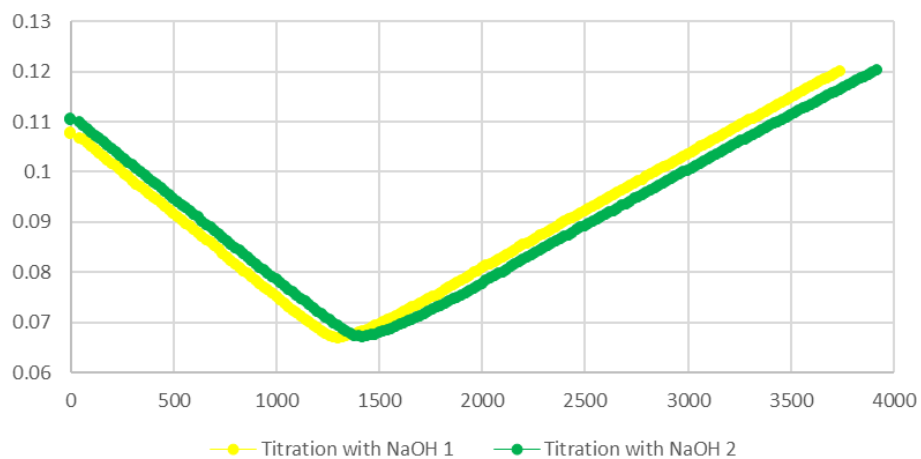


**Figure S7:** Results of conductivity measurements of QD-loaded PSMPs, prepared by the polymerization procedure.

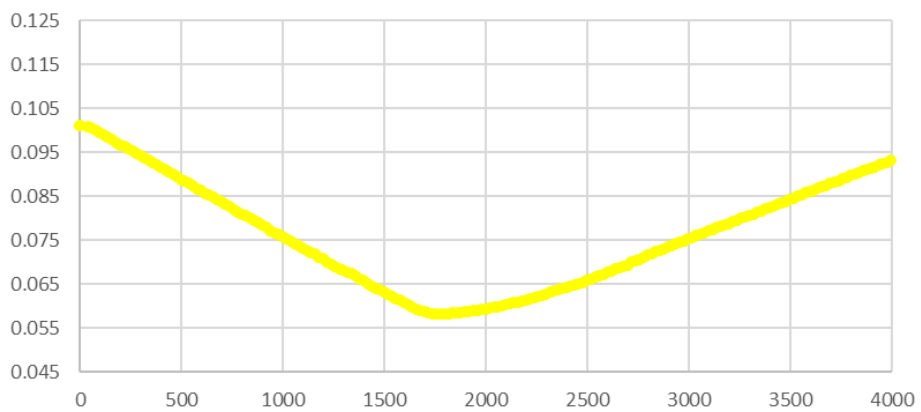


**Figure S8:** Results of conductivity measurements of QD-loaded PSMPs, synthesized by the postsynthetic swelling procedure.

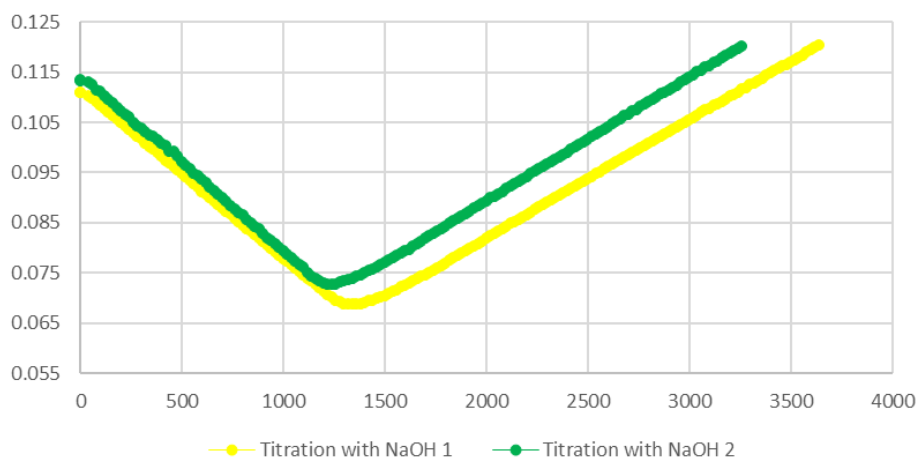


**Figure S9:** Results of conductivity measurements of RITC-loaded PSMPs, synthesized by the postsynthetic swelling procedure.

## 8. Investigation of QD leakage after four months of storage

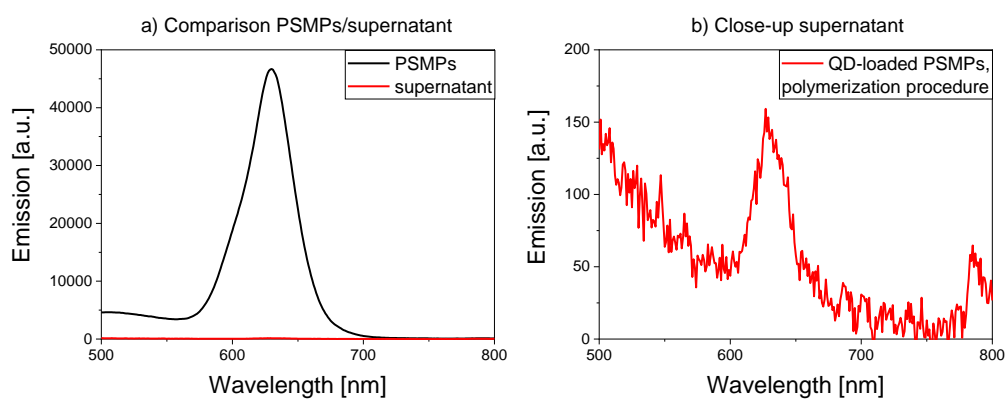


**Figure S10:** a) Emission spectra of QD-loaded PSMPs (prepared by the polymerization procedure) and their supernatant after centrifugation (2,000 rcf/3 min), with b) a close-up on the supernatant emission.

## References

- (1) Scholtz, L.; Eckert, J. G.; Elahi, T.; Lübke, F.; Hübner, O.; Bigall, N. C.; Resch-Genger, U. Luminescence encoding of polymer microbeads with organic dyes and semiconductor quantum dots during polymerization. *Scientific Reports* **2022**, *12* (1), 12061.
- (2) Carbone, L.; Nobile, C.; De Giorgi, M.; Sala, F. D.; Morello, G.; Pompa, P.; Hytch, M.; Snoeck, E.; Fiore, A.; Franchini, I. R. et al. Synthesis and Micrometer-Scale Assembly of Colloidal CdSe/CdS Nanorods Prepared by a Seeded Growth Approach. *Nano Letters* **2007**, *7* (10), 2942.
- (3) Nightingale, A. M.; Bannock, J. H.; Krishnadasan, S. H.; O'Mahony, F. T. F.; Haque, S. A.; Sloan, J.; Drury, C.; McIntyre, R.; deMello, J. C. Large-scale synthesis of nanocrystals in a multichannel droplet reactor. *Journal of Materials Chemistry A* **2013**, *1* (12), 4067.
- (4) Chen, O.; Zhao, J.; Chauhan, V. P.; Cui, J.; Wong, C.; Harris, D. K.; Wei, H.; Han, H.-S.; Fukumura, D.; Jain, R. K. et al. Compact high-quality CdSe–CdS core–shell nanocrystals with narrow emission linewidths and suppressed blinking. *Nature Materials* **2013**, *12* (5), 445.
- (5) Meier, M. A. R.; Aerts, S. N. H.; Staal, B. B. P.; Rasa, M.; Schubert, U. S. PEO-b-PCL Block Copolymers: Synthesis, Detailed Characterization, and Selected Micellar Drug Encapsulation Behavior. *Macromolecular Rapid Communications* **2005**, *26* (24), 1918.

### 5.1.3 | Correlating Semiconductor Nanoparticle Architecture and Applicability for the Controlled Encoding of Luminescent Polymer Microparticles

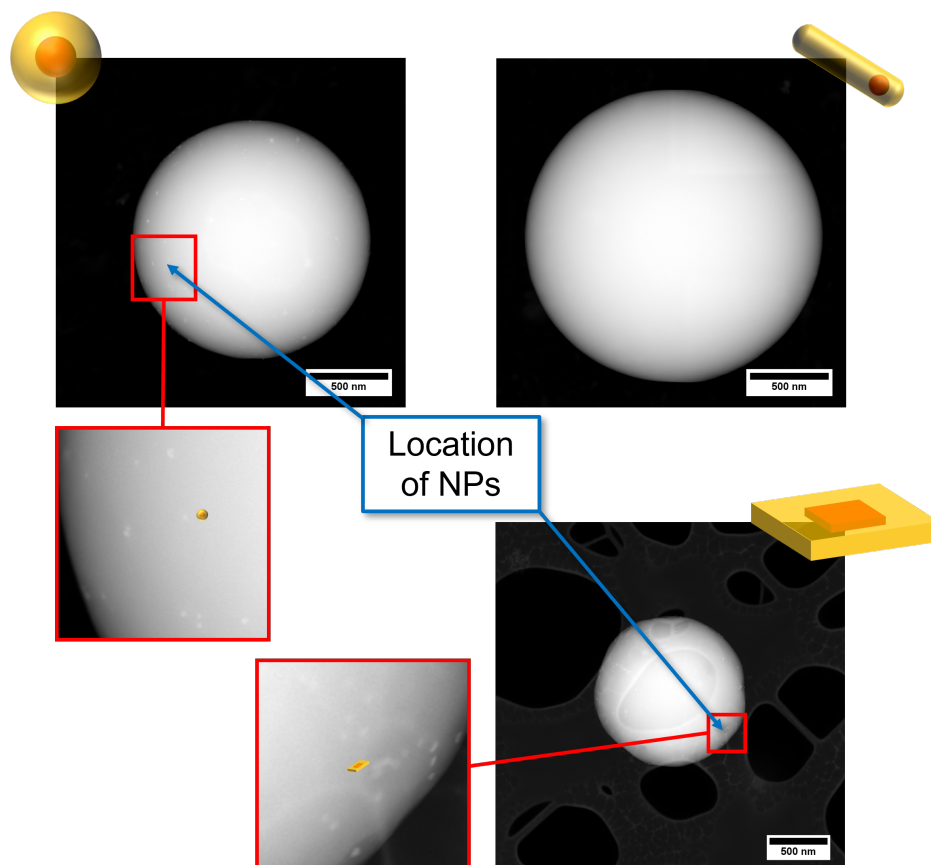


Figure 23: STEM images of NP-stained PSMPs, with location of the NPs in the beads highlighted. In case of the QRs, no particles could be detected in the PSMPs. This image was included in the manuscript (see above for title) submitted to *Chemistry of Materials*, 2023.

Authors: **Lena Scholtz**, J. Gerrit Eckert, Rebecca T. Graf, Alexandra Kunst, Karl-David Wegner, Nadja C. Bigall, Ute Resch-Genger\*

To this work, L. Scholtz contributed by planning the study and constructing the first draft of the manuscript, with help from U. Resch-Genger and K.-D. Wegner. L. Scholtz planned and performed all PSMP syntheses with help from A. Kunst, and carried out and interpreted all fluorescence and integrating sphere spectroscopy measurements. L. Scholtz also interpreted all TEM/STEM and SEM images recorded by the electron microscopy center at BAM. Further

contributions include the QD syntheses and corresponding AAS and TEM measurements performed by J. G. Eckert, the NPL synthesis and corresponding AAS and TEM measurements performed by R. T. Graf, and the help with writing the manuscript from U. Resch-Genger, K.-D. Wegner and N. C. Bigall.

**Estimated Contribution: 65%**

Work submitted to journal: Chemistry of Materials, 2023

# Correlating Semiconductor Nanoparticle Architecture and Applicability for the Controlled Encoding of Luminescent Polymer Microparticles

*Lena Scholtz*<sup>1,2</sup>, *J. Gerrit Eckert*<sup>3,4</sup>, *Rebecca T. Graf*<sup>3,4,5</sup>, *Alexandra Kunst*<sup>1,2</sup>, *K. David Wegner*<sup>1</sup>, *Nadja C. Bigall*<sup>3,4,5</sup>, *Ute Resch-Genger*<sup>1,\*</sup>

<sup>1</sup>Federal Institute for Materials Research and Testing (BAM), Division 1.2 *Biophotonics*,  
Richard-Willstätter-Str. 11, 12489 Berlin, Germany.

<sup>2</sup>Free University Berlin, Institute for Chemistry and Biochemistry, Takustraße 3, 14195 Berlin,  
Germany.

<sup>3</sup>Leibniz University Hannover, Institute of Physical Chemistry and Electrochemistry,  
Callinstraße 3A, 30167 Hannover, Germany.

<sup>4</sup>Cluster of Excellence PhoenixD (Photonics, Optics, and Engineering – Innovation Across  
Disciplines), 30167 Hannover, Germany.

<sup>5</sup>Leibniz University Hannover, Laboratory of Nano- and Quantum Engineering, Schneiderberg  
39, 30167 Hanover, Germany.

\*ute.resch@bam.de, Phone: +49 (0)30 8104 1134

**ORCID-IDs**

Lena Scholtz: 0000-0002-6869-3654

J. Gerrit Eckert: 0000-0001-5616-511X

Rebecca T. Graf: 0000-0003-3744-832X

Nadja C. Bigall: 0000-0003-0171-1106

Ute Resch-Genger: 0000-0002-0944-1115

Luminophore stained micro- and nanobeads made from organic polymers like polystyrene (PS) are broadly used in the life and material sciences as luminescent reporters, for bead-based assays, sensor arrays, printable barcodes, security inks, and the calibration of fluorescence microscopes and flow cytometers. Initially mostly prepared with organic fluorophores, meanwhile luminescent core/shell nanoparticles (NPs) like spherical semiconductor quantum dots (QDs) are increasingly employed for bead encoding due to their narrower emission spectra, tuneability of emission color, broad wavelength excitability, and better photostability. However, correlations between particle architecture, morphology, and photoluminescence (PL) of the encoding luminescent nanocrystals and the optical properties of the NP-stained beads have been barely explored, despite their importance for the tailored design of bright, NP-stained particles and the application-driven choice of optimum parameters for reproducible bead preparation. This encouraged us to perform a screening study on the incorporation of different types of luminescent core/shell semiconductor nanocrystals into polymer microparticles (PMPs) utilizing a previously optimized polymerization

reaction and explored the luminescence properties of the resulting NP-stained PMPs. Representatively assessed semiconductor nanomaterials included CdSe-based spherical QDs of different thickness and chemical composition of the inorganic surface passivation shell as well as quantum rods (QRs) and increasingly popular, two-dimensional nanoplatelets (NPLs). The results of this study provide new insights into structure-property relationships between the employed luminescent NPs and NP-stained-polymer beads and underline their importance for the performance optimization of NP-encoded beads.

## **Introduction**

Luminescent polymer microparticles (PMPs) are frequently utilized in bioanalysis and medical diagnostics.<sup>1-4</sup> Typical applications are multimodal and multicolor labels, luminescence sensing of specific targets, or biomolecular interactions,<sup>5, 6</sup> drug carriers, and calibration beads,<sup>5-11</sup> with optical signal read-out using fluorescence spectroscopy, fluorescence microscopy or flow cytometry.<sup>12, 13</sup> Combined with magnetic nanoparticles (NPs) like iron oxide NPs, such PMPs are also applied for immunoseparation.<sup>14-16</sup> For the preparation of such optically encoded beads, meanwhile different types of luminophores have been used such as organic dyes, semiconductor quantum dots (QDs), and lanthanide-based upconversion NPs (UCNPs).<sup>17-19</sup>

Luminescent polymer beads have been mostly fabricated from molecular luminophores such as organic dyes with sizes < 1 nm, utilizing either mild swelling procedures<sup>20,21,3</sup> or the incorporation of dye molecules during the polymerization reaction yielding the PMPs.<sup>20-22</sup> However, most organic dyes are prone to photobleaching, and concentration-dependent formation of non or barely emissive aggregates as well as spectral crosstalk.<sup>23</sup> The latter imposes considerable challenges for

bead encoding with multiple fluorophores of varying emission color and read out at a single excitation wavelength.<sup>24-26</sup> Principally better suited candidates are more photostable QDs and chemically inert UCNPs,<sup>4, 23, 27-33</sup> particularly for multiplexing applications.<sup>30, 33, 34</sup> The former reveal size-tunable absorption and emission features, large molar absorption cross sections, narrow and symmetric emission bands, and high photoluminescence (PL) quantum yields (PLQY), while the latter exhibit a multicolor emission.<sup>4, 23, 27-33</sup> However, the colloidal nature and larger size of luminescent NPs in the order of at least a few nanometers render bead staining more challenging. Nevertheless, there are an increasing number of reports on the staining of beads with luminescent NPs<sup>30,33</sup> like classical spherical II/VI semiconductor QDs with sizes of about 10 nm or less. Lately, also UCNPs with sizes of about 7–35 nm have been utilized.<sup>35, 36</sup> Procedures applied for PMP-encoding with NPs include simple swelling procedures,<sup>24, 26, 37</sup> the steric incorporation during bead formation by a polymerization reaction,<sup>20-22</sup> and layer-by-layer (LbL) approaches.<sup>16, 38, 39</sup> Challenging for the post-synthetic swelling of premanufactured polymer beads is the choice of the optimum solvent for bead swelling while simultaneously avoiding NP aggregation and fluorescence quenching.<sup>6, 12, 13, 33, 40</sup> Also, NP accumulation on the PMP surface can occur for beads bearing functional groups (FGs) as recently shown by us for carboxylated polymer beads and CdSe/CdS-core/shell QDs.<sup>41</sup> Thereby, FGs needed for subsequent functionalization steps with biomolecules or polyethylene glycol (PEG) ligands can be partly blocked and NP leaking could be encouraged. Luminophore addition during the polymerization reaction<sup>21, 42</sup> requires robust NPs which do not decompose during the harsh polymerization reactions commonly performed at elevated temperatures and implying the presence of thermally or photochemically formed radicals.<sup>43</sup> The less frequently applied LbL approach, which employs premanufactured beads as templates for the coating with alternating layers of oppositely charged polyelectrolytes<sup>13</sup> is tedious

and time- and material-consuming.<sup>39,44</sup> In addition, luminescence encoding is restricted to the bead surface area.<sup>16,38,39</sup> Until now, the vast majority of reports on NP-encoded PMPs was focused on bead preparation and their applications,<sup>18, 22, 33, 45</sup> yet not on establishing structure-property relationships for a high luminescence of the PMP-incorporated NPs.

Despite the increasing usage of beads stained with classical QDs made, e.g., from II/VI semiconductors, PMP encoding with more recently emerging luminescent semiconductor nanomaterials like doped QDs and broad band-emissive ternary and quaternary QDs<sup>46-48</sup> of similar size as classical QDs has been barely studied. Particularly the doping with semiconductor nanostructures of varying size and shape is underexplored. This includes dot-in-rod systems of varying aspect ratios (length divided by width of the rod) with a core or dot located within an elongated nanorod-shaped surface passivation shell,<sup>49-51</sup> also referred to as semiconductor quantum rods (QRs), and 2D-nanomaterials like semiconductor-based nanoplatelets (NPLs).<sup>52-54</sup> Favorable properties of QRs compared to classical QDs are their higher absorption cross sections and PLQY, especially for small aspect ratios.<sup>51</sup> NPLs have similarly advantageous size- and composition-dependent optical properties as QDs and QRs, yet exhibit more narrow emission bands and shorter luminescence lifetimes.<sup>52-54</sup> In addition, the spectral position of their emission maxima can be tuned nearly independently of the lateral NPL dimensions.<sup>55-57</sup> Since NPLs are chemically less stable than the more robust QDs and QRs, their incorporation into polymer beads, which has not been reported so far, is expected to be even more challenging, particularly the conservation of their attractive luminescence features (e.g., polarized/very narrow emission).

The tailored design of bright, NP-stained particles and the reproducible preparation of beads with controlled luminescence features can be eased by an experimentally derived structure-property relationship between particle architecture, morphology, and photoluminescence (PL) of

the encoding luminescent nanocrystals and the optical properties of the NP-stained beads. This is particularly relevant for QDs, QRs, and NPLs, where the chemical composition, thickness, and tightness of the surface passivation shell and the surface ligands largely control the optical properties of the NPs. This encouraged us to study the influence of the particle forming polymerization reaction on the incorporation and luminescence properties of representatively assessed CdSe-based nanostructures for polystyrene microparticles (PSMPs). NPs explored included CdSe QDs, made from the same CdSe core and surface passivated with CdS or ZnS shells of different thickness, CdSe/CdS QRs, and CdSe NPLs. To enable a comparison of the observed effects, always the same polymerization protocol and identical reaction parameters were employed, which had been previously established and optimized by us for CdSe/CdS QDs.<sup>20,41</sup> As measures for polymerization-induced changes in NP size and/or size distribution and quality of the core surface passivation, we utilized the spectral position and width of the PL band, and the PLQY as well as the PL decay kinetics. Electron microscopy was employed to determine the size and size distribution of the NP-stained PSMPs and the spatial location of the NPs within the beads. Based upon the results of this screening study, optimum NP particle architectures were identified that provided a high PL of the fabricated, luminescent microbeads for the polymerization protocol used.

## **Experimental Section**

### **Materials**

Styrene ( $\geq 99.0\%$ ), tin(II) 2-ethylhexanoate (92.5–100%),  $\epsilon$ -caprolactone (97%), poly(ethylene glycol) (PEG,  $M_w$  2,500), divinylbenzene (DVB, 80%), azobisisobutyronitrile (AIBN, 98%), trioctylphosphine oxide (TOPO, 99%), 1-octadecene (ODE, 90%), isopropanol ( $\geq 99.8\%$ ),

oleylamine (OLA, for QD synthesis, 70–80%), 1-octanethiol (98.5%), Na(myristate) ( $\geq 99\%$ ), *n*-hexane ( $\geq 99\%$ ), methanol ( $\geq 99.8\%$ ), ethanol ( $\geq 99.8\%$ ) and toluene ( $\geq 99.7\%$ ) were purchased from Sigma Aldrich Co. Cadmium oxide (CdO, 99.998%), Se powder (200 mesh, 99.999%), Cd(NO<sub>3</sub>)<sub>2</sub>·4 H<sub>2</sub>O (99.999%), polyvinylpyrrolidone (PVP, M<sub>w</sub> 40,000) and oleic acid (OA, 90%) were obtained from Alfa Aesar. Ethanol, *n*-heptane and toluene (all spectr. grade) as well as *n*-hexane ( $\geq 99\%$ ) were purchased from Merck KGaA. Dichloromethane (HPLC grade) and ethanol (abs., 99.9%) were obtained from Chemsolute, tri-*n*-octylphosphine (TOP, 99.7%), Cd(acetate)<sub>2</sub>·2 H<sub>2</sub>O (98%) and deuterated chloroform (99.8 atom%) as well as the CdSe/CdS QRs (CANdot quantum rods, 5 mg/mL, product nr. AB391053) from abcr GmbH. Benzyltrimethylammonium chloride (OBDAC, 98.9%) was obtained from HPC Standards GmbH, *n*-octadecylphosphonic acid (ODPA, >99%) from PCI Synthesis, and oleylamine (OLA, for NPL synthesis, 80–90%) from Acros Organics (now Thermo Scientific Chemicals). All chemicals were employed without further purification, all solvents used for optical measurements were of spectroscopic grade. All aqueous solutions were prepared with deionized water (0.055 μS·m<sup>-1</sup>; Milli-Q water, Millipore).

### **Synthesis of CdSe/CdS and CdSe/ZnS-core/shell QDs**

CdSe/CdS-core/shell QDs with shell thicknesses of about 3, 5, and 10 monolayers (ML) surface stabilized with oleic acid and oleylamine were prepared from the same CdSe core particles according to a modified synthesis adapted from Carbone *et al.*, Nightingale *et al.* and Chen *et al.*,<sup>58-60</sup> which was previously partly described by us.<sup>20, 41</sup> The same CdSe cores were also employed for the synthesis of CdSe/ZnS QDs with a ZnS shell thickness of approximately 3 ML. The shell

growth was carried out according to a self-developed procedure by J. G. Eckert, and the Zn precursor synthesis according to Boercker *et al.*<sup>61</sup>, respectively. The NP syntheses are described in detail in the Supporting Information (SI).

#### **Synthesis of CdSe/CdS-core/shell NPLs**

CdSe/CdS-core/shell-NPLs, surface stabilized with oleic acid and oleylamine, were synthesized according to a procedure adapted from Tessier *et al.*, Abécassis *et al.*, Miethe *et al.*, and Rossinelli *et al.*<sup>62-65</sup> The NPL synthesis is detailed in the SI.

#### **CdSe/CdS-dot-in-rod QRs**

The CdSe/CdS-dot-in-rod QRs surface stabilized with octadecylphosphonic and hexylphosphonic acid ligands were purchased from abcr GmbH (CANdot quantum rods, product nr. AB391053).

#### **Synthesis of polyethylene glycol-*block*-poly( $\epsilon$ -caprolactone)**

The synthesis of the *block*-copolymer polyethylene glycol-*block*-poly( $\epsilon$ -caprolactone) (PEG-*b*-PCL) was performed following a previously reported procedure<sup>20</sup> adapted from Meier *et al.*,<sup>66</sup> which is detailed in the SI. The chemical identity of the synthesized PEG-*b*-PCL was confirmed by solution <sup>1</sup>H-NMR spectroscopy (see SI, Figure S1).

### **Synthesis of NP-stained polystyrene microparticles (PSMPs)**

The synthesis of the NP-stained PSMPs was performed according to a procedure recently reported by us with minor modifications.<sup>20,41</sup> First, all luminescent NPs explored were coated with OBDAC to ensure a better compatibility with the polymer matrix of the PSMPs to be fabricated. Therefore, a spatula tip of OBDAC (about 2 mg) was added to 300  $\mu$ L of each NP solution. Ethanol was added until a volume of 1 mL was reached, and the mixture was placed on a shaker for 5 min. The precipitated NPs were then centrifuged at 6000 rcf for 5 min, the supernatant was discarded, the NPs were redispersed in fresh ethanol, centrifuged again using the same parameters as before, and the supernatant discarded. Finally, the resulting OBDAC-coated NPs were redispersed in 1.1 mL styrene, sealed, and stored in the refrigerator until use in the polymerization reaction.

For the synthesis of the NP-stained PSMPs, 45.75 mg PEG-*b*-PCL were added to 504  $\mu$ L toluene, and the mixture was placed on a shaker for 30 min. In the meantime, 400 mg PVP (M<sub>w</sub> 58,000) were dissolved in 45 mL of ethanol. A 100 mL two-neck flask was purged with argon for 5–10 min, and both solutions were combined in the flask under argon flow. The flask was sealed, equipped with an argon balloon, heated to 80 °C in an aluminum heating block, and the mixture was stirred for 30 min at 100 rpm. In parallel, 1 mL of the OBDAC-coated NP dispersion were combined with 4 mL styrene and 50  $\mu$ L DVB, and the mixture was briefly sonicated. Additionally, 180 mg AIBN were dissolved in 5 mL ethanol. The NP dispersion was added first to the PEG-*b*-PCL containing reaction mixture, followed by addition of the AIBN solution. The polymerization reaction was allowed to proceed for 4 h at 80 °C using a stirring speed of 100 rpm. After cooling, the polymerization mixture to RT, the formed NP-stained PSMPs were centrifuged for 2 min at

2000 rcf, and the supernatant was discarded. The PSMPs were then redispersed in ethanol, centrifuged under the same conditions as employed before, the supernatant was discarded, and the beads were redispersed in 45 mL ethanol. Before further application/characterization of this stock solution of NP-stained PSMPs, a defined amount of PSMPs was taken off the stock solution, centrifuged for 2 min at 1600 rcf, the supernatant was discarded, and the particles were redispersed in ethanol. This procedure was repeated two more times.

#### **Atomic absorption spectroscopy (AAS)**

AAS measurements were performed with an AA140 instrument from Varian Inc. with an air/acetylene flame atomizer to determine the cadmium ion (Cd(II)) concentration in the NP dispersions. Samples of the NP dispersions were prepared by dissolution of the particles with *aqua regia*. Six standard solutions with different Cd(II) concentration (0–2.5 ppm) were used to obtain a calibration curve for the subsequent quantification of the Cd(II) concentration.

#### **Scanning electron microscopy (SEM)**

The NP-stained PSMP samples were measured with a Philips XL30 ESEM using an acceleration voltage of 25 kV. The samples were prepared by drop-casting directly onto aluminum holders from diluted, ethanolic dispersions. The mean particle sizes and the corresponding size distribution of all PSMP samples were determined using the software ImageJ (Version: 1.52e, <https://imagej.nih.gov/ij/>).

### **Transmission electron microscopy (TEM)**

The TEM images of the CdSe/CdS QDs with a 5 ML thick surface passivation CdS shell and the CdSe/CdS-dot-rods, drop-casted onto carbon-coated copper grids (PELCO by Ted Pella, Inc., 400 mesh), were measured with a Thermo Fisher Scientific Talos F200S TEM at 200 kV. TEM measurements of all other NP dispersions were conducted with a JEOL JEM-2100F-UHR equipped with a field emission gun, operated at 200 kV. The NP samples were prepared on carbon-coated copper grids (Quantifoil, 400 mesh) via drop casting. The mean particle sizes and the size distributions of all NPs were determined with ImageJ as described above for the SEM samples.

### **High-angle annular dark-field scanning transmission electron microscopy (HAADF-STEM)**

For the HAADF-STEM measurements of the NP-stained PSMPs, the samples were drop-casted from diluted PSMP dispersions in ethanol onto carbon-coated copper grids (PELCO by Ted Pella, Inc., 400 mesh). For the NPL-stained PSMPs, lacey grids with otherwise the same specifications were used. Imaging was performed with a ThermoFisher Scientific Talos F200S TEM at 200 kV.

### **Fluorescence spectroscopy**

The emission spectra of the NPs in hexane and the emission spectra of the NP-stained PSMPs in ethanol were recorded with a calibrated FSP920 fluorescence spectrometer from Edinburgh

Instruments Ltd. at RT ( $(25\pm 2)$  °C) using (10 x 10) mm quartz glass cuvettes (Hellma GmbH). Excitation was always at 350 nm.

Fluorescence lifetime (FLT) measurements with these samples were performed with a calibrated FLS920 fluorescence spectrometer from Edinburgh Instruments Ltd. in (10 x 10) mm quartz glass cuvettes (Hellma GmbH) at RT. The samples were excited with a 375 nm EPL picosecond pulsed diode laser from Edinburgh Instruments Ltd.

### **Integrating sphere spectroscopy**

The PLQY values of the NP-stained PSMPs in ethanol and the semiconductor NP dispersion in toluene were determined with a stand-alone Quantaurus integrating sphere setup (Hamamatsu Photonics K.K.). The absolute PLQY measurements were performed in (10 x 10) mm long-neck quartz glass cuvettes (Hamamatsu Photonics K. K.) at RT using an excitation wavelength of 350 nm. As a blank for the transparent NP dispersions, the respective solvent was used. For the scattering NP-stained PSMPs, a blank containing a dispersion of unstained PSMPs of matching size and bead concentration was employed.

### **Results and Discussion**

We explored the polymerization- and environment-induced changes in the luminescence properties of representatively chosen CdSe-based QDs, QRs, and NPLs utilized for the preparation of nanoparticle (NP)-stained polystyrene microparticles (PSMPs). The representatively assessed

CdSe-based nanostructures employed for PSMP staining are displayed in Figure 1. The overall goal of this screening study is an in-depth understanding of the correlation between the particle architecture of these different types of core/shell semiconductor nanomaterials and the application-relevant physicochemical properties of the NP-stained PSMPs and the identification of optimum NP architectures for the encoding of PSMPs. As a prerequisite for the desired comparison of NP-specific effects, always the same polymerization protocol and identical reaction conditions were utilized, here a protocol previously developed by us for CdSe/CdS QDs<sup>20, 41</sup> and adapted for this work.

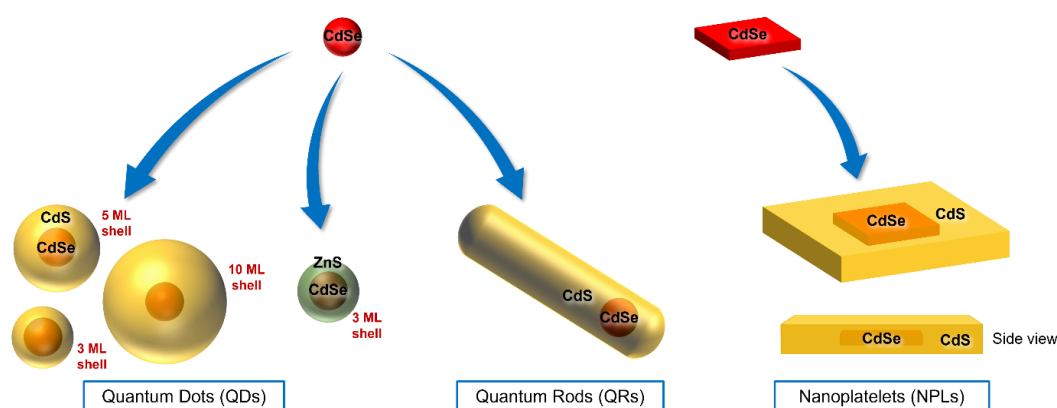


**Figure 1.** Schematic representation of the different types of semiconductor NPs used for the fabrication of NP-stained PSMPs. This included i.) spherical core/shell CdSe/CdS QDs of varying thickness of the surface passivation shell and ii.) spherical core/shell CdSe/ZnS QDs, as well as iii.) CdSe/CdS-dot-in-rod QRs, and iv.) CdSe/CdS-core/shell NPLs. All NPs bear OA and OLA surface ligands, except for the QRs that are surface stabilized with octadecylphosphonic acid and hexylphosphonic acid.

The synthesis of the NP-stained PSMPs and the different characterization steps performed with the NPs and NP-stained PSMPs are summarized in Figure 2. The luminescence properties were

derived from measurements of the emission spectra, PLQY, and fluorescence decay kinetics. In addition, other application-relevant bead parameters were assessed, such as the size and size distribution of the NP-stained PSMPs, and the NP distribution within the PSMPs. The determination of the dispersion concentration, the size and size distribution of the different NP systems was performed by AAS and TEM image analysis. The size and size distribution of the NP-stained PSMPs was obtained from SEM image analysis and the NP spatial distribution within the beads from HAADF-STEM measurements.

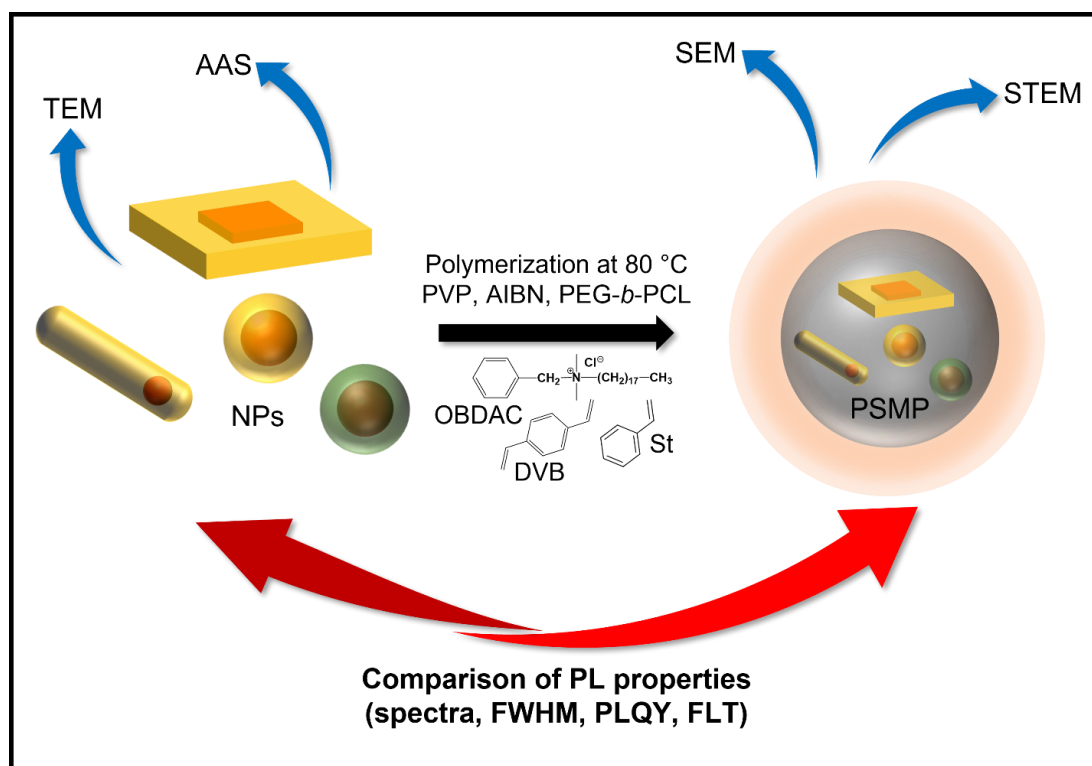


**Figure 2.** Overview of the synthesis and characterization of the NP-stained PSMPs, performed with different luminescent semiconductor nanostructures. The polymerization procedure was partly previously described by us for CdSe/CdS QDs with a thickness of the CdS shell of 5 ML

and adapted for this work.<sup>20, 41</sup> The polymer matrix is formed from styrene (St) and divinylbenzene (DVB), AIBN is used as an initiator, and PVP as a surfactant. The amphiphilic copolymer PEG-*b*-PCL is added to realize a narrower size distribution, and the additional ligand OBDAC provides a better NP compatibility with the polymer matrix. PL: photoluminescence, FWHM: full width at half maximum of the PL band, PLQY: photoluminescence quantum yield, FLTs: fluorescence lifetimes, determined from the measured and fitted photoluminescence (PL) decay kinetics (see SI, eq. SE1 and SE2).

### **Physicochemical and optical properties of the luminescent semiconductor NPs**

Table 1 and Figure 3 summarize the relevant physico-chemical properties of the QDs, QRs, and NPLs used for PSMP staining. These NPs reveal narrow and symmetric PL bands in the wavelength region of about 530 nm to 700 nm except for the CdSe/CdS QDs with a 10 monolayer (ML) CdS shell, which exhibits a broadened PL band. This indicates a ripening of the CdSe cores during the extended shelling procedure required to achieve a 10 ML CdS shell. The influence of the shell material employed for the surface passivation of the CdSe core is reflected by the spectral position of the emission band, PLQY value, and the PL decay kinetics, the fitting of which with equations SE1 and SE2 given in the SI yields the fluorescence lifetimes (FLTs). For the CdSe/CdS core/shell QDs, the increase in shell thickness leads to an increase in QD size and a bathochromic shift of the emission band as well as an increase in PLQY and FLTs as reported in the literature.<sup>67</sup> The latter is ascribed to the delocalization of the electron over a larger volume, thereby extending the time required for the radiative recombination of the exciton.<sup>68</sup> The ZnS surface shell introduces a hypsochromic shift of the emission band compared to the CdSe/CdS QDs. Moreover, a comparison of the CdSe QDs with a 3ML CdS and 3 ML ZnS shell reveals significantly longer

lifetimes for the CdSe/ZnS QDs and a significantly lower PLQY (see also Table 1). As follows from Table 1, the optical properties of semiconductor nanostructures are not only largely dependent on material composition, but also on particle shape as reported extensively in the literature.<sup>69,70</sup> The emission maximum of the QRs is directly linked to the aspect ratio ( $l/w$ ) of the rod. This equals 2.9 for the QRs used in this work. In the case of the NPLs, the shell growth procedure determines the type of the semiconductor heterostructure of the resulting NPL. The CdS shell shields the CdSe core in three dimensions for the CdSe/CdS core/shell QDs, yielding a quasi-type II semiconductor heterostructure,<sup>65</sup> protecting the emissive core from environmental effects, and enhancing the core fluorescence.

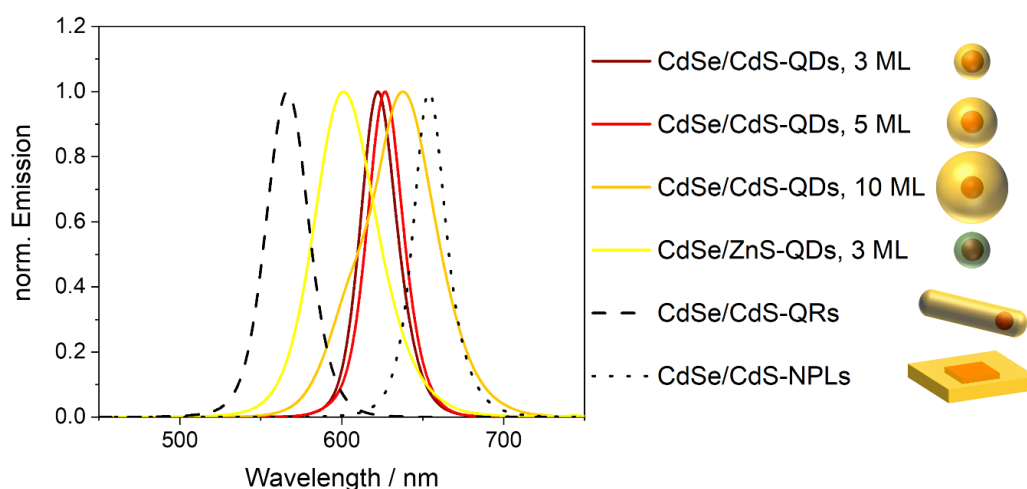


**Figure 3.** Emission spectra ( $\lambda_{exc} = 350$  nm) and a schematic representation of the different luminescent semiconductor nanostructures employed in this work, that were all dispersed in hexane. The absorption spectra of the NPs are provided in the SI (see Figure S2). All QDs were prepared from the same core particles, except for the CdSe/CdS QDs with a 5 ML CdS shell. Here, slightly smaller CdSe cores with a size of 3.6 nm compared to 3.9 nm were employed.

**Table 1.** Overview of the physico-chemical properties of the semiconductor NPs with a CdSe core and their application-relevant luminescence properties ( $\lambda_{em}$ : emission maximum). The different spherical CdSe-based QDs were prepared from the same CdSe core particle batch, except for the CdSe/CdS QDs with a 5 ML thick CdS shell. The similar size of the 3 ML and 5 ML QDs is attributed to the smaller CdSe core utilized for the synthesis of the latter core/shell CdSe/CdS QDs. The size distributions of the NPs and the multiexponential PL decay curves, from which the FLTs were obtained, are provided in the SI (see Figure S2 and equations SE1 and SE2). The emission spectra and TEM images of the NPs are displayed in Figure 3 and Figure 4.

Shape	Shell material thickness	Particle size / nm	$\lambda_{em}$ / nm	PLQY / %	FLT / ns
<b>Spherical</b>	CdS, 3 ML	$7.9 \pm 0.9$	622	78	12 & 32
	CdS, 5 ML	$7.9 \pm 0.7$	627	67	20 & 36
	CdS, 10 ML	$10.3 \pm 1.2$	638	59	73 & 184
	ZnS, 1 ML	$5.1 \pm 0.6$	601	45	20 & 60
<b>Elongated</b>	CdS	$4.0 \pm 0.5$	566	86	5 & 16 & 65
<b>Dot-in-rod</b>		$11.5 \pm 2.2$			
<b>2D Platelet</b>	CdS	$16.6 \pm 1.8$	654	34	2 & 10 & 44
		$17.2 \pm 2.2$			

**Structure-analytical characterization of the NP-stained PSMPs**

Figure 4 displays representative TEM and SEM images of the luminescent NPs (left panels) and the corresponding NP-stained PSMPs (right panels), shown here exemplarily for a CdSe/CdS QD sample (5 ML CdS shell), the QRs, and the NPLs.

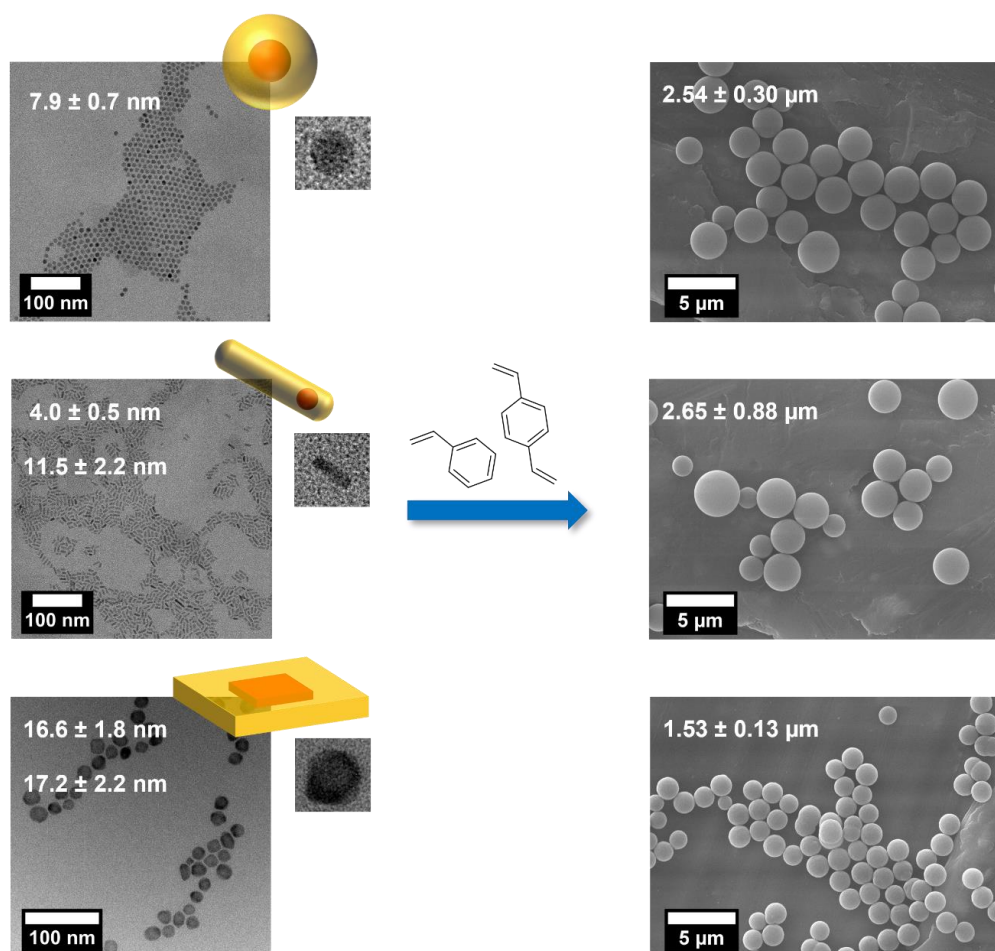


**Figure 4.** TEM images (left) of representative CdSe/CdS QDs (5 ML CdS shell), CdSe/CdS QRs, and CdSe/CdS NPLs, including the average particle sizes; and SEM images (right) of the resulting, NP-stained PSMPs. The histograms reflecting the size distribution of the NPs and PSMPs and the

TEM/SEM images of the other NPs and the NP-stained PSMPs studied are provided in the SI (see Figures S3-S5). The sizes of the single particle are provided as insets: 15x15 nm (QDs), 17x17 nm (QRs), and 23x23 nm (NPLs).

Apparently, the type of semiconductor nanostructure added to the polymerization reaction mixture can influence the size and size distribution of the resulting NP-stained PSMPs, and slightly also their surface morphology. Especially the anisotropic NPs, i.e., the QRs and particularly the NPLs, seem to have a significant influence on the size of the resulting NP-stained PSMPs. In a previous work, we showed that addition of CdSe/CdS QDs with a 5 ML thick CdS shell does not have a significant influence on the size of the PSMPs compared to unstained particles prepared under identical conditions of the polymerization reaction.<sup>20</sup> This suggests that the anisotropic shape of the NP as well as the material used for the surface passivation shell affect the size of the resulting PSMPs. As follows from the SEM images, all NP-stained PSMPs are spherical and have a very smooth surface, except for the NPL-stained PSMPs which have a slightly rough or textured surface structure. The size of the QD- and QR-stained PSMPs ranges between 2-3  $\mu\text{m}$ , while the size of the NPL-stained particles is significantly smaller with a value of about 1.5  $\mu\text{m}$ . The PSMP size distribution is relatively narrow for the NPL- and QD-stained PSMPs (8.5% and 11.1/11.8/10.4% variation for 3/5/10 ML QDs, respectively), except for the PSMPs stained with the CdSe/ZnS QDs (33.1% variation). It is also significantly broadened for the QR-stained PSMPs (33.2% variation). This suggests that the encoding NPs can significantly influence the polymerization process leading to PSMP formation. It also underlines the importance of the surface chemistry of the NPs applied for bead staining and incorporation into PSMPs.

### **Spatial distribution of the semiconductor NPs within the PSMPs**

The applicability of the PSMPs stained with luminophores can be also affected by the spatial location of the luminescent nanostructures utilized for bead encoding. Information on the homogeneity of PSMP staining of the particles and the distribution of the NPs within the PSMPs is especially relevant here as, e.g., NPs incorporated close to the PSMP surface could possibly affect further surface functionalization steps or favor NP leaking. In addition, the NP location can provide a hint at which step of the polymerization reaction the NPs are incorporated. This can contribute to a better understanding of the initial steps and propagation of this reaction. This information can be important for the optimization of the NP particle architecture and the polymerization reaction conditions, which is required to further improve the luminescence properties of the PSMP-encapsulated NPs, particularly the preservation of the luminescence features of the encoding NPs. Therefore, we determined the location of the different types of semiconductor nanostructures by recording STEM images of the NP-stained PSMPs. As illustrated in Figure 5, the CdSe/CdS QDs with the 3 ML, 5 ML, 10 ML thick CdS surface passivation shells and the CdSe/CdS NPLs are clearly detectable in the respective PSMPs and are preferentially located in the surface regions of the NP-stained PSMPs. These NPs as well as the CdSe/ZnS QDs (which have not been further analyzed by STEM) are stabilized with a mixture of oleic acid and oleylamine ligands. A near surface location of the staining QDs was observed by us before for QD-stained PSMPs, that were, however, surface functionalized with COOH groups by PSMP grafting with acrylic acid added to the polymerization mixture at a later stage of the polymerization, where the reaction mixture contained already preformed beads.<sup>41</sup> For these carboxylated PSMPs, we ascribed the near surface location of the oleic acid- and oleylamine-capped CdSe/CdS QDs to an interaction of the QDs with the carboxylic acid functionalities (see

also SI, Figure S8 for a STEM image). The observation of a similar spatial distribution of oleic acid- and oleylamine-capped CdSe/CdS QDs also for NP-encoded plain PSMPs suggests that the QD incorporation into the polymer beads occurs at a later stage of the polymerization reaction, i.e., during seed growth and not during the initial phase of seed formation. The fact that the differently shaped CdSe/CdS NPL, that bear the same surface capping ligands as the spherical CdSe/CdS QDs, are also preferentially located in the surface regions of the polymer beads suggest a considerable influence of NP surface chemistry on the incorporation of PSMPs formed by such a polymerization procedure. In contrast, the STEM images of the QR-stained PSMPs did not provide a hint for PSMP incorporation of the CdSe/CdS QRs surface stabilized with octadecylphosphonic and hexylphosphonic acid ligands. This finding agrees well with the lack of fluorescence of the PSMPs formed upon polymerization of the styrene and divinylbenzene monomers in the presence of the CdSe/CdS QRs (see Figure 8). One plausible explanation for the apparent difficulties of QR incorporation into the PSMPs could be the different surface capping ligands, i.e., octadecylphosphonic and hexylphosphonic acid ligands instead of oleic acid ligands employed for the core/shell QDs and NPLs. This different QR surface chemistry could affect the intercalation of OBDAC added to improve the polymer compatibility of all semiconductor NPs for the polymerization reaction. As follows from Figure 5, relevant parameters for the staining of PSMPs with semiconductor nanostructures and our polymerization protocol are NP size and particularly NP shape, which can affect the size of the resulting PSMPs, and NP surface chemistry, i.e., the interaction of the initially present NP surface ligands and OBDAC. Most likely, also the coverage of the NP surface capping organic ligand shell by OBDAC molecules comes here into play, that seems to be less optimum for octadecylphosphonic acid and hexylphosphonic acid surface ligands compared to oleic acid and oleylamine ligands.

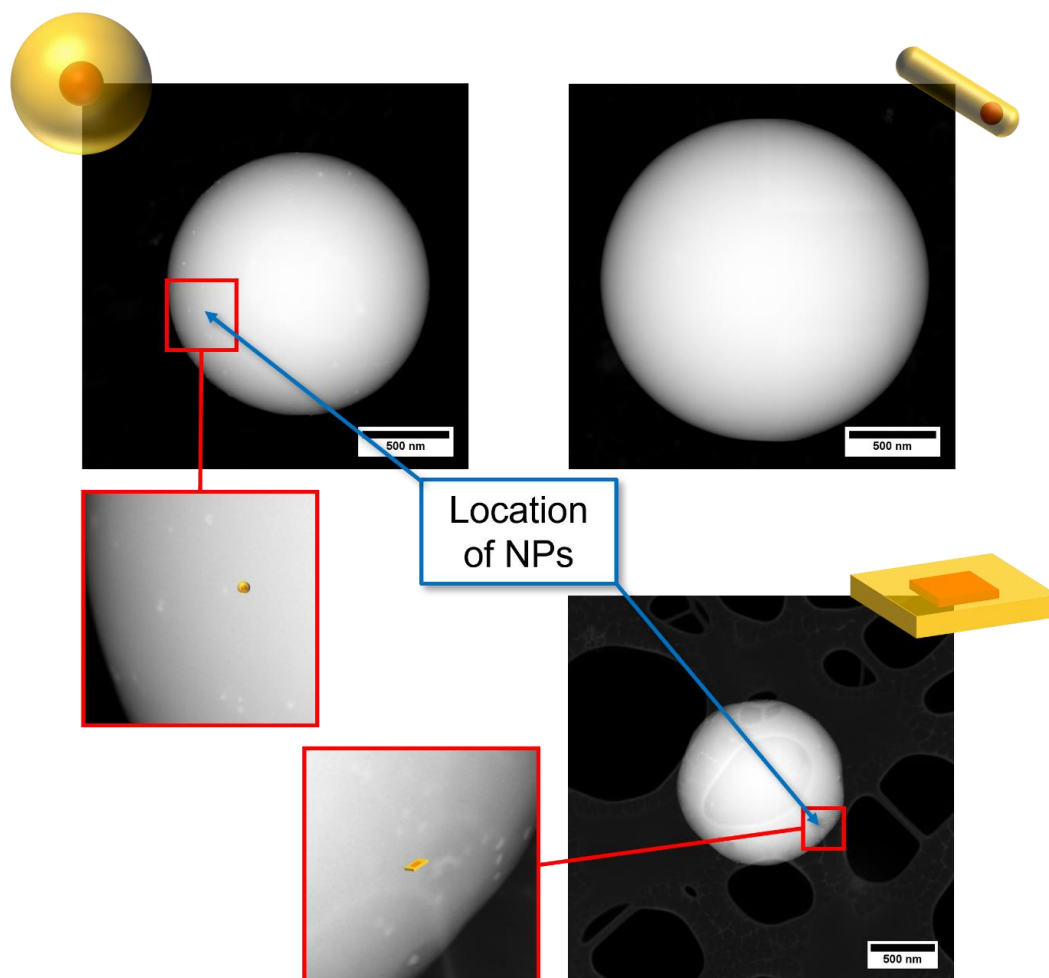


**Figure 5:** STEM images of NP-stained PSMPs, representatively shown for CdSe/CdS QDs with a 10 ML CdS surface passivation shell (top, left), CdSe/CdS QRs (top, right), and CdSe/CdS NPLs (bottom, right). The location of the semiconductor NPs is marked and displayed in more detail for smaller regions of the polymer particles. In the case of the QR-stained PSMPs, no QRs could be detected within the PSMPs. Comparative STEM images of COOH-functionalized PSMPs stained with CdSe/CdS QDs bearing a 10 ML CdS shell and plain PSMPs stained with CdSe/CdS QDs with a 5 ML CdS shell are displayed in the SI (see Figure S8).

To obtain a first hint on a possible influence of the polymerization reaction parameters on NP spatial distribution with the polymer particles, we compared the spatial distribution of oleic acid/oleylamine capped CdSe/CdS QDs (5 ML CdS shell) of PSMPs prepared with two different polymerization protocols. The first is a slightly different polymerization protocol published previously by us,<sup>20</sup> which was compared with the synthesis of QD stained PSMPs in this study. Interestingly, usage of this previously employed polymerization protocol, from which the optimized polymerization procedure employed in this study was derived, led to CdSe/CdS QDs preferably located in the bead core region. For both studies, closely matching CdSe/CdS QDs were used. Main differences between both polymerization protocols are the slightly higher stirring speed and temperature utilized in this work (100 rpm/80 °C vs. 70 rpm/70 °C previously used), the shorter reaction time (4 h compared to 24 h), and the smaller amount of the surfactant PVP used (400 mg compared to 1.465 g). Apparently, not only the type of NP, but also the performance of the polymerization reaction influence NP incorporation and NP spatial distribution within the PSMPs.

#### **Influence of bead synthesis on the luminescence properties of the NP-stained PSMPs**

For the screening study of the influence of the polymerization reaction mixture and the polymerization reaction on the luminescence properties of the different QDs, QRs, NPLs and the resulting NP-stained PSMPs, the polymerization conditions were kept identical. Therefore, for each NP, we spectroscopically characterized the following samples: i.) a sample of the freshly prepared polymerization mixture taken prior to the start of the polymerization reaction and the resulting NP-stained PSMPs after the synthesis ii.) without purification and iii.) after subsequent

washing steps. This included measurements of the PL spectra, PLQY values, and PL decay curves from which the intensity weighted FLTs of the different decay components were calculated (see SI, equation SE1). Thereby information on the application-relevant PL features at different stages of the preparation of the NP-stained PSMPs can be obtained. However, these data do not enable a distinction between the influence of the polymerization reaction and the changes in NP environment which was beyond the scope of this screening study. The obtained PL data are displayed in Figure 6 (CdSe/CdS QDs) and Figure 8 (CdSe/CdS QRs and CdSe/CdS NPLs). An overview of the PL properties, including the PLQY values, of all NPs explored and the respective NP-stained PSMPs subsequently discussed is given in the SI (see Table S1 and Figure S7).

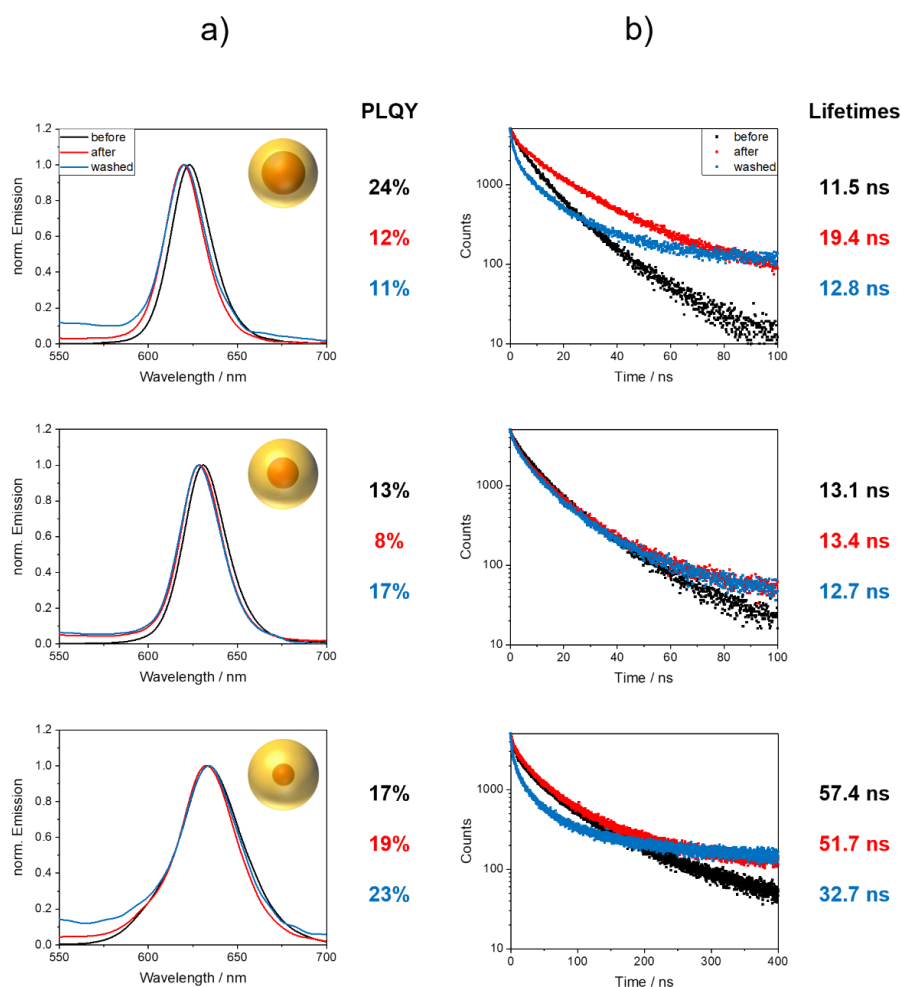


**Figure 6.** a) Normalized emission spectra with PLQY values, and b) PL decay curves with intensity weighted average FLT (FLT determination see SI, equation SE1) obtained for the NP-stained PSMPs prepared with CdSe/CdS-core/shell QDs of different shell thicknesses. The samples collected before (black) and after (red) bead synthesis were used for the measurements without purification. The “washed” (blue) sample was purified, involving five washing cycles with fresh ethanol. The particle concentration was kept identical by always using the same pipette to remove/add the identical amount of solvent. The higher background in the emission spectra of the

washed samples can be attributed to the polymer matrix and scattering effects. The luminescence properties of the analog assessed CdSe/ZnS QDs are displayed in the SI (see Figure S6).

At first, we explored the influence of the polymerization reaction on the luminescence properties of the resulting NP-stained PSMPs for CdSe QDs, surface passivated with differently thick CdS shells. As follows from Figure 6, the thickness of the CdS surface passivation shell plays a significant role in the preservation of the optical properties of the CdSe/CdS QDs, with a thicker CdS shell better protecting the emissive CdSe core. This is reflected by the emission spectra and PLQY data shown in the left panels of Figure 6, showing the highest PLQY for the QDs passivated with a 10 ML CdS shell (23% compared to 11% and 17% for CdSe/CdS QDs with 3 and 5 ML thick CdS shells, see Table 1), although these QDs exhibited the lowest PLQY values in hexane (59% compared to 78% and 67% for CdSe with 3 and 5 ML thick CdS shells, see Table 1). Time-resolved PL measurements of the different CdSe/CdS QD samples reveal that NP incorporation into the PSMPs results in the appearance of a long-lived component in the luminescence decay curves. This change in the PL decay kinetics becomes more pronounced with the progression of the polymerization reaction and bead formation. In the case of the CdSe QDs surface passivated with a 5 ML CdS shell, the observed small influence of the washing steps on the emission intensity and PL decay behavior together with the strong PLQY reduction suggest the presence of so-called “dark” QDs removed during this step, see also next section. This is significantly different from the behavior displayed by the other two CdSe/CdS QDs studied, where the PL measurements suggest the presence of free QDs, not incorporated into the formed PSMPs, which are still emissive.

The full width at half maximum (FWHM) of the PL bands of the CdSe/CdS QDs surface passivated with 3 ML and 5 ML CdS shells undergo only changes of maximum 5% (3 ML QDs: 5%; 5 ML QDs: 4%) during bead formation. In the case of the CdSe/CdS QDs with a 10 ML CdS shell, the FWHM is reduced by about 5% by the polymerization reaction. This suggests an incomplete PSMP incorporation of the 10 ML QDs, with the largest QDs of the particle batch remaining in solution; hence, these QDs do not contribute to the PL of the NP-stained PSMPs. This results in a narrowing of the size distribution of the PSMP-encapsulated QDs and in turn to a smaller FWHM. Combined with the only very small shift of the emission maximum, these findings do not provide a hint for a disintegration of the CdS shell. It is more likely that the surface chemistry of the QDs is altered upon incorporation into the polymer matrix, leading to the observed decrease in emission intensity and PLQY. These results underline the importance of QD surface passivation for the preservation of the PL property of the PSMP-incorporated NPs, at least for the polymerization conditions chosen for this study.

For a further in-depth study monitoring the luminescence properties of the CdSe QDs during the polymerization reaction, we chose CdSe QDs passivated with a 5 ML CdS shell. Thereby, QD samples were taken from the polymerization mixture with a syringe at different reaction times, diluted with fresh ethanol, and immediately measured to prevent a further influence of the polymerization reaction mixture on the optical properties of the QDs and to ensure sample comparability. The emission spectra and PLQY values of the CdSe/CdS QD samples recorded at different reaction times are summarized in Figure 7. As shown in this figure, the emission intensity and PLQY values of the QDs immediately decrease in the reaction mixture, followed first by a continuous diminution in the first minutes of the polymerization reaction. Between 5 to 20 min, the emission intensity and the PLQY values of the QDs increases again, reaching approximately

the start values of both PL parameters. Presumably, the QDs are incorporated into the PSMPs at this moment, leading to a change in QD environment and thus, PL properties. The continuous exposure to hot ethanol, and possibly also to the radicals formed from the initiator AIBN at longer reaction times then induces a diminution of the QD PL intensity and the PLQY values at longer until the polymerization reaction is completed. The size of the CdSe/CdS QDs does not seem to alter during the polymerization reaction since the FWHM of the QD PL band barely changed, varying between 26-27 nm as previously mentioned.

In addition to the samples continuously taken during the polymerization reaction, one sample was taken after completion of the polymerization reaction, washed five times with fresh ethanol, and then spectroscopically assessed. To keep the particle concentration constant during these successive washing steps, the same pipette was used to remove/add the identical amount of solvent. The exposure of the NP-stained PSMPs to ethanol during these washing steps was not expected to significantly affect the PL intensity of the QDs, as previously shown by us for a similar sample.<sup>20</sup> Apparently, while the subsequent washing steps do not significantly influence the sample's emission intensity, the PLQY of the NP-stained PSMPs is increased by more than 100%. This finding points to the presence of dark, i.e., non-emissive, but still light absorbing QDs at the outside of the formed PSMPs, which are removed by the washing steps.

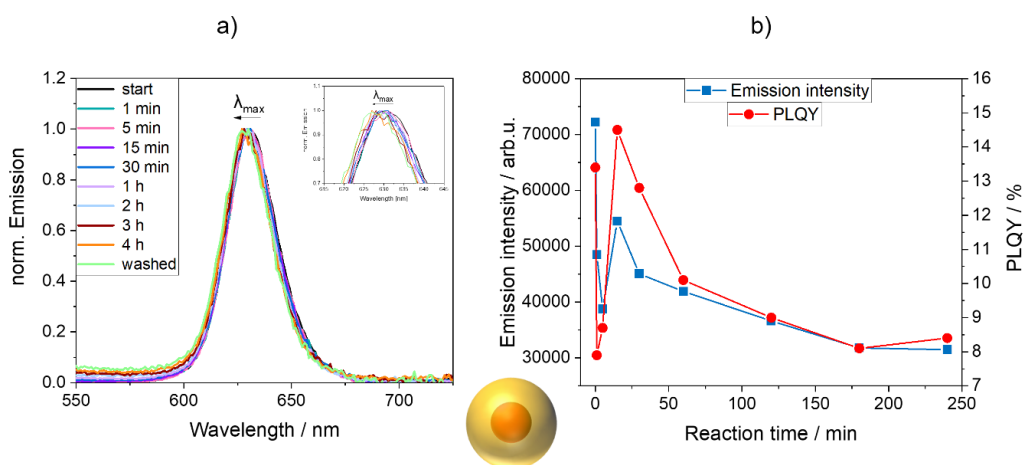


**Figure 7.** a) Normalized emission spectra of CdSe/CdS QDs passivated with a 5 ML CdS shell before, during, and after incorporation into PSMPs, and b) reaction time-dependent emission intensity and PLQY values of the QDs at the different stages of the PSMP-forming polymerization reaction and in the different microenvironments. Except for the washed QD-stained PSMPs, all samples were taken from the reaction mixture (always using the same amount of the reaction mixture), diluted with fresh ethanol without further purification, and measured immediately to preserve the luminescence properties. The last sample shown in this figure in the right panel was purified by five washing steps with fresh ethanol while keeping the particle concentration constant.

Subsequently, we explored the influence of the polymerization reaction and PSMP incorporation on the PL properties of the CdSe/ZnS QDs as well as the CdSe/CdS QRs and CdSe/CdS NPLs. The emission spectra, PLQY values, and PL decay curves of these semiconductor NPs employed for PSMP staining are displayed in Figure 8, and in the SI (see Figure S6). Apparently, in contrast to the CdSe QDs surface passivated with a 3 ML CdS shell, which remain emissive during the

polymerization reaction and within the formed PSMPs, the CdSe QDs coated with a 3 ML ZnS shell seem to decompose during the polymerization reaction. This is indicated by the complete loss in PL observed for the PSMPs stained with these QDs. This complete loss in fluorescence, which already occurred in the polymerization mixture before the initiation of the polymerization reaction, can be readily observed by utilizing a handheld UV flashlight (365 nm) as excitation light source as well as with a spectrometer. It can be speculated from the TEM images of the CdSe/ZnS QDs (see SI, Figure S5) and the deduced particle size of 5.1 nm, that the ZnS passivation shell is actually thinner than the intended 3 ML thickness. This relatively thin ZnS surface protecting shell could be the cause for the observed quenching of the CdSe/ZnS QD fluorescence or at least contribute to it.

Overall, these findings demonstrate the crucial influence of the shell material passivating and protecting the surface of the emissive QD core on the preservation of the initial QD PL utilizing a dispersion polymerization reaction and the reaction conditions previously optimized for CdSe/CdS QDs. For the luminescence staining of PSMPs with CdSe/ZnS QDs under the chosen reaction conditions, a further optimization of the ZnS shell seems to be necessary. However, although the use of CdSe QDs with a thicker ZnS shell could be attempted for a better protection of the emissive QD cores and their PL properties, this can lead to initially lower PLQY values of the CdSe/ZnS QDs used for PSMP staining.<sup>71</sup> Apparently, for this type of CdSe QDs, milder reaction conditions should be identified in screening studies for the preparation of luminescent NP-stained PSMPs.

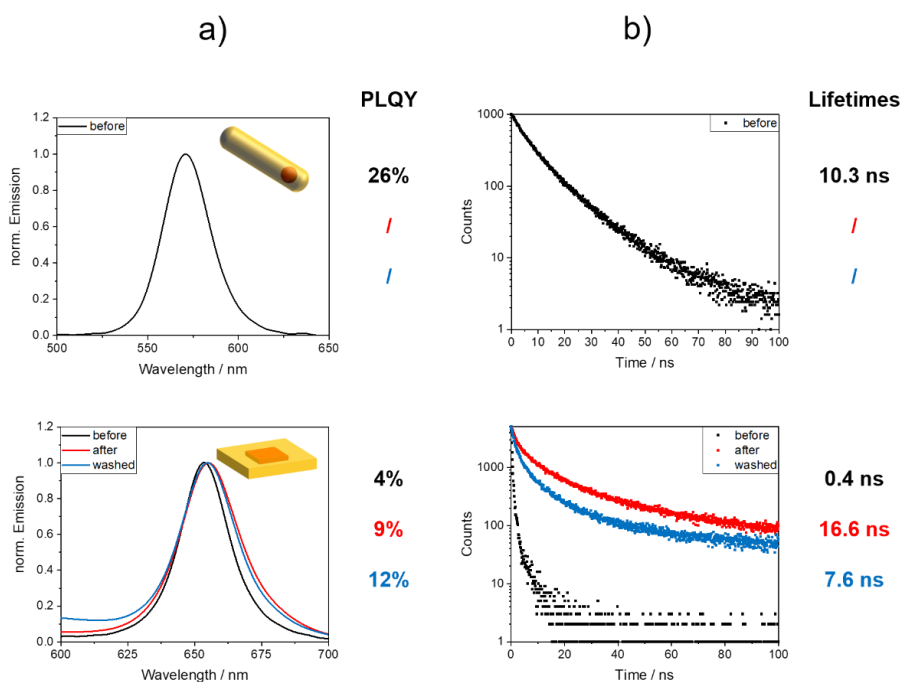


**Figure 8.** a) Normalized emission spectra of the CdSe/CdS QRs (top) and the CdSe/CdS core/shell NPLs (bottom) before and after the polymerization reaction yielding the respective NP-stained PSMPs, and after bead purification by washing with ethanol including the corresponding PLQY values (left), and b) the corresponding fluorescence decay curves with the intensity weighted average FLT (see SI, equation SE1). The samples collected before and after PSMP synthesis were employed for the spectroscopic measurements without purification. The purified samples were washed five times with fresh ethanol, thereby keeping the particle concentration constant. In the case of the QRs, only the purified QR sample exhibited a measurable fluorescence.

The CdSe/CdS QRs, that exhibit a moderate emission intensity and PLQY (see Table 1), became barely or non-emissive after the polymerization reaction and incorporation in the PSMPs.

Examination of the residue of the polymerization reaction revealed the presence of large, luminescent polymer agglomerates at the bottom of the flask, indicating an incomplete incorporation of the QRs into the beads. By STEM measurements shown in Figure 5 we could confirm that the QRs are not incorporated into the PSMPs. Also, for the CdSe/CdS core/shell NPLs, the polymerization reaction mixture has a significant influence on the PL properties of these semiconductor nanostructures, even before the initiation of the polymerization. This influence is, however, reduced upon incorporation of the NPLs into the PSMPs, although the decrease in emission intensity after the purifying washing steps suggests that not all NPLs present in the polymerization mixture are incorporated into the PSMPs formed. In addition, the polymerization reaction induces a slight broadening of the NPL emission band by about 17%. These findings, combined with the very small shift of the emission maximum, suggest that the NPL size/thickness is not affected by the polymerization reaction, but instead the surface chemistry and/or the number of surface defect states. The relatively high percentage of the preservation of the initial PLQY value of the NPLs in hexane (see Table 1, PLQY of 34%) of 35% for the NPL-stained PSMPs (see Figure 8, lower panel, PLQY of 12%) is very promising for these fragile semiconductor nanostructures. The PL decay kinetics of the PSMP-incorporated NPLs exhibit a longer decay component than previously observed for the initially prepared NPLs. A similar behavior was observed for the CdSe/CdS QDs. This points to defect emission of the NPLs. In addition, the faster FLT components of the PL decay kinetics of the CdSe/CdS NPLs also increase after PSMP incorporation. As the NPL luminescence is reduced, but still detectable, this suggests that most likely only the outside of the CdS shell is affected by the polymerization reaction.

## **Conclusion and Outlook**

We performed a screening study of the incorporation of different luminescent CdSe-based semiconductor nanoparticles (NPs) varying in size, shape, and particle architecture into polystyrene microparticles (PSMPs) by a polymerization reaction, thermally induced in the presence of the NPs. Nanostructures representatively explored included spherical core/shell CdSe quantum dots (QDs) surface passivated with differently thick CdS shells and for comparison, also with a ZnS shell, elongated core/shell CdSe/CdS dot-in-rod or so-called quantum rods (QRs), as well as core/shell CdSe/CdS nanoplatelets (NPLs), representing 2D-nanostructures. For the preparation of the NP-stained PSMPs, always the same polymerization conditions were employed, that were previously optimized for typical CdSe/CdS QDs. As readout parameters for an in-depth understanding of how the architectures and the thickness and chemical composition of the surface passivation shell of these CdSe-based nanostructures affect the application-relevant properties of the respective NP-encoded beads, we utilized the changes in the PL maximum, spectral width, PL quantum yield (PLQY), and PL decay kinetics of the initially prepared NPs introduced by the bead-forming polymerization reaction. In addition, the size, size distribution, and surface morphology of the NP-stained PSMPs and the spatial localization of the NPs within the polymer beads were determined with electron microscopy.

Based upon the spatial location and distribution of the different semiconductor nanostructures within the polymer beads determined by scanning transmission electron microscopy (STEM), we could identify NP size and particularly NP shape and NP surface chemistry as important parameters for NP incorporation for the polymerization protocol employed. This is suggested by the straightforward incorporation of spherical and platelet-shaped CdSe/CdS-core/shell NPs surface capped with oleic acid and oleylamine ligands while the incorporation of cylindrically

shaped NPs like QRs of the same core/shell composition but stabilized with octadecylphosphonic and hexylphosphonic acid failed for our polymerization protocol. The considerable influence of the NP surface ligand shell seems to be directly associated with the degree of the coverage of the organic ligand shell initially present from NP synthesis by OBDAC molecules, assuring the compatibility with the polymer matrix. The NP spatial distribution within the PSMPs suggests that for the polymerization protocol used, the NPs are not incorporated into the polymer particle seeds formed at the initial stage of the polymerization reaction, yet at a later stage of seed growth.

Our PL studies show that for the preservation of the initial QD PL of the semiconductor nanostructures during the thermally induced dispersion polymerization reaction and the reaction conditions employed in this study, the shell material and shell thickness passivating and protecting the surface of the emissive QD core is crucial. For core/shell CdSe QDs, a CdS surface protection shell is apparently superior to a ZnS shell for the preservation of the PL properties, with the latter resulting in a complete PL loss for the chosen polymerization conditions. For surface passivation with CdS shells, shell thickness is important, with a thicker protection shell being advantageous for high PLQY of the PSMP-incorporated QDs. Promisingly, the most sensitive nanostructures assessed, CdSe/CdS NPLs, survived the harsh polymerization conditions and were successfully encapsulated into polymer beads and remained emissive. Particularly favorable is the relatively high percentage of the preservation of the initial PLQY value of the NPLs of 35% observed for the PSMP-incorporated NPLs, equaling the changes in PLQY observed for the much more robust CdSe/CdS QDs.

Encouraged by the outcome of this first screening study, we are currently systematically assessing the influence of the polymerization reaction parameters on NP incorporation, NP distribution with PSMPs, and optimum PL features for semiconductor nanostructures with fine-

tuned surface chemistries, i.e., passivation and surface ligand shells. The ultimate goals are here a precise control of the spatial distribution within the resulting polymer beads and PL preservation for different sets of semiconductor nanostructures of fine-tuned surface chemistry.

#### AUTHOR INFORMATION

##### **Corresponding Author**

\*Ute Resch-Genger, ute.resch@bam.de

All correspondence should be addressed to U. Resch-Genger or the first author (Lena Scholtz, lena.scholtz@bam.de).

##### **Present Addresses**

May change for one of the authors during the submission process.

##### **Author Contributions**

L.S. and U.R.-G. planned this study with input from K.-D.W. The luminescent PSMP syntheses were performed by L.S. with help from A.K. All QD syntheses and the corresponding AAS measurements were carried out by J.G.E., who also performed the TEM measurements of the QDs (except CdSe/CdS QDs with 5 ML shell thickness). The NPL syntheses and corresponding AAS and TEM measurement were performed by R.G., and the *block*-copolymer synthesis was performed by L.S. LS also carried out the fluorescence and integrating sphere spectroscopy measurements and the analyses of the corresponding data. The first draft was written by L.S., while L.S., U.R.-G., N.C.B., and K.-D.W. contributed to the writing and revision of the manuscript. The

final manuscript was created by K.-D.W. and U.R.-G.. All authors have approved of the final version of the manuscript.

### **Funding Sources**

L. Scholtz and A. Kunst acknowledge funding by the SAFERA project ANOPSA and by BAM. J. G. Eckert acknowledges funding by the MWK – School for Additive Manufacturing SAM. R. T. Graf would like to thank the Hannover School for Nanotechnology (hsn) for funding. N. C. Bigall acknowledges funding by the Deutsche Forschungsgemeinschaft (DFG, German Research Foundation) under Germany’s Excellence Strategy within the Cluster of Excellence PhoenixD (EXC 2122, Project ID 390833453) and the grant BI 1708/4-3. U.R.G. acknowledges funding by DFG (grant RE 1203/23-2).

### **Notes**

### **ACKNOWLEDGMENT**

We thank C. Prinz (BAM, division 6.3) for the performance of the HAADF-STEM and TEM measurements (TEM owned by Prof. N. Pinna, HU Berlin), the Institute for Chemistry and Biochemistry, Free University Berlin (Dr. A. Schaefer) for providing the NMR facilities (supported by DFG), and I. Feldmann (BAM, division 4.2) for the SEM measurements. This research was carried out in part at the electron microscopy center at BAM.

## ASSOCIATED CONTENT

### Supporting Information

The following files are available free of charge. Supporting information with details of all QD syntheses and the NPL synthesis, as well as the synthesis and a  $^1\text{H-NMR}$  spectrum of PEG-b-PCL, confirming its chemical identity. In addition, fluorescence decay curves of all NPs and size distribution graphs of all NPs and NP-stained PSMPs are displayed. TEM and SEM images of the remaining NPs and NP stained PSMPs are included, as well as emission spectra of CdSe/ZnS QDs and the respective PSMPs, a comparison of STEM images of QD stained PSMPs from previous works and a summary of PSMP luminescence properties (including PLQY and emission intensity preservation). - (PDF file)

## REFERENCES

1. Pelaz, B.; Alexiou, C. H.; Alvarez -Puebla, R. A.; Alves, F.; Andrews, A. M.; Ashraf, S.; Balogh, L. P.; Ballerini, L.; Bestetti, A.; Brendel, C.; Bosi, S.; Carril, M.; Chan, W. C. W.; Chen, C. Y.; Chen, X. D.; Chen, X. Y.; Cheng, Z.; Cui, D. X.; Du, J. Z.; Dullin, C.; Escudero, A.; Feliu, N.; Gao, M. Y.; George, M.; Gogotsi, Y.; Grunweller, A.; Gu, Z. W.; Halas, N. J.; Hampp, N.; Hartmann, R. K.; Hersam, M. C.; Hunziker, P.; Jian, J.; Jiang, X. Y.; Jungebluth, P.; Kadhihsan, P.; Kataoka, K.; Khademhosseini, A.; Kopecek, J.; Kotov, N. A.; Krug, H. F.; Lee, D. S.; Lehr, C. M.; Leong, K. W.; Liang, X. J.; Lim, M. L.; Liz-Marzan, L. M.; Ma, X. M.; Macchiarini, P.; Meng, H.; Mohwald, H.; Mulvaney, P.; Nel, A. E.; Nie, S. M.; Nordlander, P.; Okano, T.; Oliveira, J.; Park, T. H.; Penner, R. M.; Prato, M.; Puentes, V.; Rotello, V. M.; Samarakoon, A.; Schaak, R. E.; Shen, Y. Q.; Sjoqvist, S.; Skirtach, A. G.; Soliman, M. G.;

Stevens, M. M.; Sung, H. W.; Tang, B. Z.; Tietze, R.; Udugama, B. N.; VanEpps, J. S.; Weil, T.; Weiss, P. S.; Willner, I.; Wu, Y. Z.; Yang, L. L.; Yue, Z.; Zhang, Q.; Zhang, Q.; Zhang, X. E.; Zhao, Y. L.; Zhou, X.; Parak, W. J. Diverse Applications of Nanomedicine. *ACS Nano* **2017**, *11* (3), 2313-2381.

2. Oh, J. H.; Park, D. H.; Joo, J. H.; Lee, J. S. Recent advances in chemical functionalization of nanoparticles with biomolecules for analytical applications. *Anal. Bioanal. Chem.* **2015**, *407* (29), 8627-8645.

3. Wolfbeis, O. S. An overview of nanoparticles commonly used in fluorescent bioimaging. *Chem. Soc. Rev.* **2015**, *44* (14), 4743-4768.

4. Geißler, D.; Hildebrandt, N. Recent developments in Förster resonance energy transfer (FRET) diagnostics using quantum dots. *Anal. Bioanal. Chem.* **2016**, *408* (17), 4475-4483.

5. Kage, D.; Hoffmann, K.; Borcherdig, H.; Schedler, U.; Resch-Genger, U. Lifetime encoding in flow cytometry for bead-based sensing of biomolecular interaction. *Scientific Reports* **2020**, *10* (1), 19477.

6. Li, Z.; Liu, Q.; Li, Y.; Yuan, W.; Y.Li, F. One-step polymerized lanthanide-based polystyrene microsphere for sensitive lateral flow immunoassay. *Journal of Rare Earths* **2021**, *39* (1), 11-18.

7. Mazetyte-Stasinskiene, R.; Köhler, J. M. Sensor Micro and Nanoparticles for Microfluidic Application. *Applied Sciences* **2020**, *10* (23), 8353.

8. Ming, K.; Kim, J.; Biondi, M. J.; Syed, A.; Chen, K.; Lam, A.; Ostrowski, M.; Rebbapragada, A.; Feld, J. J.; Chan, W. C. W. Integrated Quantum Dot Barcode Smartphone

Optical Device for Wireless Multiplexed Diagnosis of Infected Patients. *ACS Nano* **2015**, *9* (3), 3060-3074.

9. Hoffmann, K.; Nirmalanathan-Budau, N.; Resch-Genger, U. Fluorescence calibration standards made from broadband emitters encapsulated in polymer beads for fluorescence microscopy and flow cytometry. *Anal. Bioanal. Chem.* **2020**, *412* (24), 6499-6507.

10. Perfetto, S. P.; Ambrozak, D.; Nguyen, R.; Chattopadhyay, P.; Roederer, M. Quality assurance for polychromatic flow cytometry. *Nature protocols* **2006**, *1* (3), 1522-30.

11. DeRose, P.; Tian, L. H.; Elsheikh, E.; Urbas, A.; Zhang, Y. Z.; Wang, L. L. Expanding NIST Calibration of Fluorescent Microspheres for Flow Cytometry to More Fluorescence Channels and Smaller Particles. *Materials* **2020**, *13* (18).

12. Gao, X.; Nie, S. Quantum Dot-Encoded Mesoporous Beads with High Brightness and Uniformity: Rapid Readout Using Flow Cytometry. *Anal. Chem.* **2004**, *76* (8), 2406-2410.

13. Bradley, M.; Bruno, N.; Vincent, B. Distribution of CdSe Quantum Dots within Swollen Polystyrene Microgel Particles Using Confocal Microscopy. *Langmuir* **2005**, *21* (7), 2750-2753.

14. Leng, Y.; Wu, W.; Li, L.; Lin, K.; Sun, K.; Chen, X.; Li, W. Magnetic/Fluorescent Barcodes Based on Cadmium-Free Near-Infrared-Emitting Quantum Dots for Multiplexed Detection. *Advanced Functional Materials* **2016**, *26* (42), 7581-7589.

15. Mulvaney, S. P.; Mattoussi, H.; Whitman, L. J. Incorporating fluorescent dyes and quantum dots into magnetic microbeads for immunoassays. *BioTechniques* **2004**, *36* (4), 602-609.

16. Martynenko, I. V.; Kusić, D.; Weigert, F.; Stafford, S.; Donnelly, F. C.; Evstigneev, R.; Gromova, Y.; Baranov, A. V.; Rühle, B.; Kunte, H.-J.; Gun'ko, Y. K.; Resch-Genger, U.

Magneto-Fluorescent Microbeads for Bacteria Detection Constructed from Superparamagnetic Fe<sub>3</sub>O<sub>4</sub> Nanoparticles and AIS/ZnS Quantum Dots. *Anal. Chem.* **2019**, *91* (20), 12661-12669.

17. Kimura, F.; Khalil, G.; Zettsu, N.; Xia, Y.; Callis, J.; Gouterman, M.; Dalton, L.; Dabiri, D.; Rodriguez, M. Dual luminophore polystyrene microspheres for pressure-sensitive luminescent imaging. *Measurement Science and Technology* **2006**, *17* (6), 1254.

18. Vaidya, S. V.; Couzis, A.; Maldarelli, C. Reduction in Aggregation and Energy Transfer of Quantum Dots Incorporated in Polystyrene Beads by Kinetic Entrapment due to Cross-Linking during Polymerization. *Langmuir* **2015**, *31* (10), 3167-3179.

19. Cheng, Z.; Lin, J. Synthesis and Application of Nanohybrids Based on Upconverting Nanoparticles and Polymers. *Macromolecular Rapid Communications* **2015**, *36* (9), 790-827.

20. Scholtz, L.; Eckert, J. G.; Elahi, T.; Lübke, F.; Hübner, O.; Bigall, N. C.; Resch-Genger, U. Luminescence encoding of polymer microbeads with organic dyes and semiconductor quantum dots during polymerization. *Scientific Reports* **2022**, *12* (1), 12061.

21. Sherman, R. L.; Ford, W. T. Semiconductor Nanoparticle/Polystyrene Latex Composite Materials. *Langmuir* **2005**, *21* (11), 5218-5222.

22. Esteves, A. C. C.; Barros-Timmons, A.; Monteiro, T.; Trindade, T. Polymer Encapsulation of CdE (E = S, Se) Quantum Dot Ensembles via In-Situ Radical Polymerization in Miniemulsion. *Journal of Nanoscience and Nanotechnology* **2005**, *5* (5), 766-771.

23. Resch-Genger, U.; Grabolle, M.; Cavaliere-Jaricot, S.; Nitschke, R.; Nann, T. Quantum dots versus organic dyes as fluorescent labels. *Nature Methods* **2008**, *5* (9), 763-775.

24. Huber, A.; Behnke, T.; Würth, C.; Jaeger, C.; Resch-Genger, U. Spectroscopic Characterization of Coumarin-Stained Beads: Quantification of the Number of Fluorophores Per Particle with Solid-State  $^{19}\text{F}$ -NMR and Measurement of Absolute Fluorescence Quantum Yields. *Anal. Chem.* **2012**, *84* (8), 3654-3661.
25. Behnke, T.; Würth, C.; Hoffmann, K.; Hübner, M.; Panne, U.; Resch-Genger, U. Encapsulation of Hydrophobic Dyes in Polystyrene Micro- and Nanoparticles via Swelling Procedures. *Journal of Fluorescence* **2011**, *21* (3), 937-944.
26. Behnke, T.; Würth, C.; Laux, E.-M.; Hoffmann, K.; Resch-Genger, U. Simple strategies towards bright polymer particles via one-step staining procedures. *Dyes and Pigments* **2012**, *94* (2), 247-257.
27. Carbone, L.; Nobile, C.; De Giorgi, M.; Sala, F. D.; Morello, G.; Pompa, P.; Hytch, M.; Snoeck, E.; Fiore, A.; Franchini, I. R.; Nadasan, M.; Silvestre, A. F.; Chiodo, L.; Kudera, S.; Cingolani, R.; Krahn, R.; Manna, L. Synthesis and Micrometer-Scale Assembly of Colloidal CdSe/CdS Nanorods Prepared by a Seeded Growth Approach. *Nano Letters* **2007**, *7* (10), 2942-2950.
28. Chen, O.; Zhao, J.; Chauhan, V. P.; Cui, J.; Wong, C.; Harris, D. K.; Wei, H.; Han, H.-S.; Fukumura, D.; Jain, R. K.; Bawendi, M. G. Compact high-quality CdSe–CdS core–shell nanocrystals with narrow emission linewidths and suppressed blinking. *Nature Materials* **2013**, *12* (5), 445-451.
29. Geißler, D.; Charbonnière, L. J.; Ziessel, R. F.; Butlin, N. G.; Löhmansröben, H.-G.; Hildebrandt, N. Quantum Dot Biosensors for Ultrasensitive Multiplexed Diagnostics. *Angew. Chem. Int. Edit.* **2010**, *49* (8), 1396-1401.

30. Wang, G.; Leng, Y.; Dou, H.; Wang, L.; Li, W.; Wang, X.; Sun, K.; Shen, L.; Yuan, X.; Li, J.; Sun, K.; Han, J.; Xiao, H.; Li, Y. Highly Efficient Preparation of Multiscaled Quantum Dot Barcodes for Multiplexed Hepatitis B Detection. *ACS Nano* **2013**, *7* (1), 471-481.
31. Yarema, O.; Yarema, M.; Wood, V. Tuning the Composition of Multicomponent Semiconductor Nanocrystals: The Case of I-III-VI Materials. *Chem. Mater.* **2018**, *30* (5), 1446-1461.
32. Reiss, P.; Carriere, M.; Lincheneau, C.; Vaure, L.; Tamang, S. Synthesis of Semiconductor Nanocrystals, Focusing on Nontoxic and Earth-Abundant Materials. *Chem. Rev.* **2016**, *116* (18), 10731-10819.
33. Han, M.; Gao, X.; Su, J. Z.; Nie, S. Quantum-dot-tagged microbeads for multiplexed optical coding of biomolecules. *Nature Biotechnology* **2001**, *19* (7), 631-635.
34. Liu, S.; An, Z.; Zhou, B. Optical multiplexing of upconversion in nanoparticles towards emerging applications. *Chemical Engineering Journal* **2023**, *452*, 139649.
35. Gorris, H. H.; Wolfbeis, O. S. Photon-Upconverting Nanoparticles for Optical Encoding and Multiplexing of Cells, Biomolecules, and Microspheres. *Angewandte Chemie International Edition* **2013**, *52* (13), 3584-3600.
36. Zhang, Y.; Liao, Z.; Liu, Y.; Wan, Y.; Chang, J.; Wang, H. Flow cytometric immunoassay for aflatoxin B1 using magnetic microspheres encoded with upconverting fluorescent nanocrystals. *Microchimica Acta* **2017**, *184* (5), 1471-1479.
37. Borisov, S. M.; Mayr, T.; Karasyov, A. A.; Klimant, I.; Chojnacki, P.; Moser, C.; Nagl, S.; Schaeferling, M.; Stich, M. I.; Kocincova, A. S.; Wolfbeis, O. S. New Plastic Microparticles

and Nanoparticles for Fluorescent Sensing and Encoding. In *Fluorescence of Supramolecules, Polymers, and Nanosystems*, Berberan-Santos, M. N., Ed. Springer Berlin Heidelberg: Berlin, Heidelberg, 2008; pp 431-463.

38. Rogach, A.; Susha, A.; Caruso, F.; Sukhorukov, G.; Kornowski, A.; Kershaw, S.; Möhwald, H.; Eychmüller, A.; Weller, H. Nano- and Microengineering: 3-D Colloidal Photonic Crystals Prepared from Sub- $\mu\text{m}$ -sized Polystyrene Latex Spheres Pre-Coated with Luminescent Polyelectrolyte/Nanocrystal Shells. *Advanced Materials* **2000**, *12* (5), 333-337.

39. Sukhanova, A.; Susha, A. S.; Bek, A.; Mayilo, S.; Rogach, A. L.; Feldmann, J.; Oleinikov, V.; Reveil, B.; Donvito, B.; Cohen, J. H. M.; Nabiev, I. Nanocrystal-Encoded Fluorescent Microbeads for Proteomics: Antibody Profiling and Diagnostics of Autoimmune Diseases. *Nano Letters* **2007**, *7* (8), 2322-2327.

40. Chung, T.-H.; Lee, W.-C. Preparation of styrene-based, magnetic polymer microspheres by a swelling and penetration process. *Reactive and Functional Polymers* **2008**, *68* (10), 1441-1447.

41. Scholtz, L.; Tavernaro, I.; Eckert, J. G.; Lutowski, M.; Geißler, D.; Hertwig, A.; Hidde, G.; Bigall, N. C.; Resch-Genger, U. Influence of nanoparticle encapsulation and encoding on the surface chemistry of polymer carrier beads. *Scientific Reports* **2023**, *13* (1), 11957.

42. Sheng, W.; Kim, S.; Lee, J.; Kim, S.-W.; Jensen, K.; Bawendi, M. G. In-Situ Encapsulation of Quantum Dots into Polymer Microspheres. *Langmuir* **2006**, *22* (8), 3782-3790.

43. Kage, D.; Fischer, L.; Hoffmann, K.; Thiele, T.; Schedler, U.; Resch-Genger, U. Close Spectroscopic Look at Dye-Stained Polymer Microbeads. *The Journal of Physical Chemistry C* **2018**, *122* (24), 12782-12791.
44. Kage, D.; Hoffmann, K.; Nifontova, G.; Krivenkov, V.; Sukhanova, A.; Nabiev, I.; Resch-Genger, U. Tempo-spectral multiplexing in flow cytometry with lifetime detection using QD-encoded polymer beads. *Scientific Reports* **2020**, *10* (1), 653.
45. Yang, Y.; Tu, C.; Gao, M. A general approach for encapsulating aqueous colloidal particles into polymeric microbeads. *Journal of Materials Chemistry* **2007**, *17* (28), 2930-2935.
46. Makkar, M.; Viswanatha, R. Frontier challenges in doping quantum dots: synthesis and characterization. *RSC Advances* **2018**, *8* (39), 22103-22112.
47. Girma, W. M.; Fahmi, M. Z.; Permadi, A.; Abate, M. A.; Chang, J. Y. Synthetic strategies and biomedical applications of I-III-VI ternary quantum dots. *J. Mater. Chem. B* **2017**, *5* (31), 6193-6216.
48. Bai, X.; Purcell-Milton, F.; Gun'ko, Y. K. Optical Properties, Synthesis, and Potential Applications of Cu-Based Ternary or Quaternary Anisotropic Quantum Dots, Polytypic Nanocrystals, and Core/Shell Heterostructures. *Nanomaterials* **2019**, *9* (1), 85.
49. Geissler, D.; Wurth, C.; Wolter, C.; Weller, H.; Resch-Genger, U. Excitation wavelength dependence of the photoluminescence quantum yield and decay behavior of CdSe/CdS quantum dot/quantum rods with different aspect ratios. *Physical Chemistry Chemical Physics* **2017**, *19* (19), 12509-12516.

50. Hinsch, A.; Lohmann, S. H.; Strelow, C.; Kipp, T.; Wurth, C.; Geissler, D.; Kornowski, A.; Wolter, C.; Weller, H.; Resch-Genger, U.; Mews, A. Fluorescence Quantum Yield and Single-Particle Emission of CdSe Dot/CdS Rod Nanocrystals. *Journal of Physical Chemistry C* **2019**, *123* (39), 24338-24346.
51. Jia, G.; Xu, S.; Wang, A. Emerging strategies for the synthesis of monodisperse colloidal semiconductor quantum rods. *Journal of Materials Chemistry C* **2015**, *3* (32), 8284-8293.
52. Graf, R. T.; Schlosser, A.; Zámbo, D.; Schlenkrich, J.; Rusch, P.; Chatterjee, A.; Pfnür, H.; Bigall, N. C. Interparticle Distance Variation in Semiconductor Nanoplatelet Stacks. *Advanced Functional Materials* **2022**, *32* (24), 2112621.
53. Diroll, B. T.; Guzelturk, B.; Po, H.; Dabard, C.; Fu, N.; Makke, L.; Lhuillier, E.; Ithurria, S. 2D II–VI Semiconductor Nanoplatelets: From Material Synthesis to Optoelectronic Integration. *Chem. Rev.* **2023**, *123* (7), 3543-3624.
54. Bai, B.; Zhang, C.; Dou, Y.; Kong, L.; Wang, L.; Wang, S.; Li, J.; Zhou, Y.; Liu, L.; Liu, B.; Zhang, X.; Hadar, I.; Bekenstein, Y.; Wang, A.; Yin, Z.; Turyanska, L.; Feldmann, J.; Yang, X.; Jia, G. Atomically flat semiconductor nanoplatelets for light-emitting applications. *Chem. Soc. Rev.* **2023**, *52* (1), 318-360.
55. Ghosh Chaudhuri, R.; Paria, S. Core/Shell Nanoparticles: Classes, Properties, Synthesis Mechanisms, Characterization, and Applications. *Chem. Rev.* **2011**, *112* (4), 2373-2433.
56. Stark, W. J.; Stoessel, P. R.; Wohlleben, W.; Hafner, A. Industrial applications of nanoparticles. *Chem. Soc. Rev.* **2015**, *44* (16), 5793-5805.

57. Talapin, D. V.; Lee, J. S.; Kovalenko, M. V.; Shevchenko, E. V. Prospects of Colloidal Nanocrystals for Electronic and Optoelectronic Applications. *Chem. Rev.* **2010**, *110* (1), 389-458.
58. Carbone, L.; Nobile, C.; De Giorgi, M.; Sala, F. D.; Morello, G.; Pompa, P.; Hytch, M.; Snoeck, E.; Fiore, A.; Franchini, I. R. Synthesis and micrometer-scale assembly of colloidal CdSe/CdS nanorods prepared by a seeded growth approach. *Nano letters* **2007**, *7* (10), 2942-2950.
59. Nightingale, A. M.; Bannock, J. H.; Krishnadasan, S. H.; O'Mahony, F. T.; Haque, S. A.; Sloan, J.; Drury, C.; McIntyre, R.; deMello, J. C. Large-scale synthesis of nanocrystals in a multichannel droplet reactor. *Journal of Materials Chemistry A* **2013**, *1* (12), 4067-4076.
60. Chen, O.; Zhao, J.; Chauhan, V. P.; Cui, J.; Wong, C.; Harris, D. K.; Wei, H.; Han, H.-S.; Fukumura, D.; Jain, R. K. Compact high-quality CdSe–CdS core–shell nanocrystals with narrow emission linewidths and suppressed blinking. *Nature materials* **2013**, *12* (5), 445-451.
61. Boercker, J. E.; Woodall, D. L.; Cunningham, P. D.; Placencia, D.; Ellis, C. T.; Stewart, M. H.; Brintlinger, T. H.; Stroud, R. M.; Tischler, J. G. Synthesis and Characterization of PbS/ZnS Core/Shell Nanocrystals. *Chem. Mater.* **2018**, *30* (12), 4112-4123.
62. Tessier, M. D.; Spinicelli, P.; Dupont, D.; Patriarche, G.; Ithurria, S.; Dubertret, B. Efficient Exciton Concentrators Built from Colloidal Core/Crown CdSe/CdS Semiconductor Nanoplatelets. *Nano Letters* **2014**, *14* (1), 207-213.
63. Abécassis, B.; Tessier, M. D.; Davidson, P.; Dubertret, B. Self-Assembly of CdSe Nanoplatelets into Giant Micrometer-Scale Needles Emitting Polarized Light. *Nano Letters* **2014**, *14* (2), 710-715.

64. Miethe, J. F.; Schlosser, A.; Eckert, J. G.; Lübke, F.; Bigall, N. C. Electronic transport in CdSe nanoplatelet based polymer fibres. *Journal of Materials Chemistry C* **2018**, *6* (40), 10916-10923.
65. Rossinelli, A. A.; Riedinger, A.; Marqués-Gallego, P.; Knüsel, P. N.; Antolinez, F. V.; Norris, D. J. High-temperature growth of thick-shell CdSe/CdS core/shell nanoplatelets. *Chemical Communications* **2017**, *53* (71), 9938-9941.
66. Meier, M. A. R.; Aerts, S. N. H.; Staal, B. B. P.; Rasa, M.; Schubert, U. S. PEO-b-PCL Block Copolymers: Synthesis, Detailed Characterization, and Selected Micellar Drug Encapsulation Behavior. *Macromolecular Rapid Communications* **2005**, *26* (24), 1918-1924.
67. García-Santamaría, F.; Brovelli, S.; Viswanatha, R.; Hollingsworth, J. A.; Htoon, H.; Crooker, S. A.; Klimov, V. I. Breakdown of Volume Scaling in Auger Recombination in CdSe/CdS Heteronanocrystals: The Role of the Core–Shell Interface. *Nano Letters* **2011**, *11* (2), 687-693.
68. Sahu, A.; Kumar, D. Core-shell quantum dots: A review on classification, materials, application, and theoretical modeling. *Journal of Alloys and Compounds* **2022**, *924*, 166508.
69. Sitt, A.; Hadar, I.; Banin, U. Band-gap engineering, optoelectronic properties and applications of colloidal heterostructured semiconductor nanorods. *Nano Today* **2013**, *8* (5), 494-513.
70. Ithurria, S.; Dubertret, B. Quasi 2D Colloidal CdSe Platelets with Thicknesses Controlled at the Atomic Level. *J. Am. Chem. Soc.* **2008**, *130* (49), 16504-16505.

71. Grabolle, M.; Ziegler, J.; Merkulov, A.; Nann, T.; Resch-Genger, U. Stability and Fluorescence Quantum Yield of CdSe–ZnS Quantum Dots—Influence of the Thickness of the ZnS Shell. *Annals of the New York Academy of Sciences* **2008**, *1130* (1), 235-241.

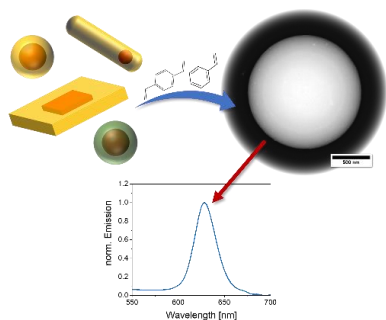


**Figure 9:** For Table of Contents Only.

Supplementary Information for:

**Correlating Semiconductor Nanoparticle Architecture and Applicability for the Controlled Encoding of Luminescent Polymer Microparticles**

Lena Scholtz<sup>1,2</sup>, J. Gerrit Eckert<sup>3,4</sup>, Rebecca T. Graf<sup>3,4,5</sup>, Alexandra Kunst<sup>1,2</sup>, K. David Wegner<sup>1</sup>, Nadja C. Bigall<sup>3,4,5</sup>, Ute Resch-Genger<sup>1,\*</sup>

<sup>1</sup>Federal Institute for Materials Research and Testing (BAM), Division 1.2 *Biophotonics*, Richard-Willstätter-Str. 11, 12489 Berlin, Germany.

<sup>2</sup>Free University Berlin, Institute for Chemistry and Biochemistry, Takustraße 3, 14195 Berlin, Germany.

<sup>3</sup>Leibniz University Hannover, Institute of Physical Chemistry and Electrochemistry, Callinstraße 3A, 30167 Hannover, Germany.

<sup>4</sup>Cluster of Excellence PhoenixD (Photonics, Optics, and Engineering – Innovation Across Disciplines), 30167 Hannover, Germany.

<sup>5</sup>Leibniz University Hannover, Laboratory of Nano- and Quantum Engineering, Schneiderberg 39, 30167 Hanover, Germany.

\*ute.resch@bam.de, Phone: +49 (0)30 8104 1134

<b>1. Synthesis of CdSe/CdS and CdSe/ZnS-core/shell-QDs .....</b>	<b>2</b>
<b>2. Synthesis of CdSe/CdS-core/shell-NPLs.....</b>	<b>2</b>
<b>3. Preparation and <sup>1</sup>H-NMR spectrum of polyethylene glycol-<i>block</i>-poly(<math>\epsilon</math>-caprolactone).....</b>	<b>3</b>
<b>4. Fluorescence lifetime decay curves of all NPs and calculation of FLTs .....</b>	<b>4</b>
<b>5. Size distribution graphs of NPs and NP-stained PSMPs .....</b>	<b>5</b>
<b>6. TEM and SEM images of remaining, employed QDs and respective PSMPs .....</b>	<b>7</b>
<b>6. Emission spectra of CdSe/ZnS QDs and the respective, stained PSMPs.....</b>	<b>7</b>
<b>7. Preservation of NP luminescence properties upon integration into the PSMPs.....</b>	<b>8</b>
<b>8. STEM images of PSMPs stained with QDs from previous works.....</b>	<b>9</b>

### 1. Synthesis of CdSe/CdS and CdSe/ZnS-core/shell-QDs

The CdSe/CdS-core/shell-QDs with shell thicknesses of about 3, 5, and 10 monolayers (ML) were prepared from the same CdSe core particles according to a modified synthesis adapted from Carbone *et al.*, Nightingale *et al.* and Chen *et al.*,<sup>1-3</sup> which was partly previously described by us.<sup>4,5</sup> The same CdSe cores were also employed for the synthesis of CdSe/ZnS-QDs with a ZnS shell thickness of approximately 3 ML. The shell growth was carried out according to a self-developed procedure by J. G. Eckert.

In the first step, CdSe cores with wurtzite structure were synthesised according to Carbone *et al.*<sup>6</sup> For this synthesis, 120 mg (0.93 mmol) CdO together with 560 mg (1.67 mmol) ODPa and 6 g (15.51 mmol) TOPO were degassed at 150 °C for 1 h. The mixture was then heated under argon flow to 300 °C. After the injection of 2 mL (4.48 mmol) of TOP, it was heated to 380 °C and, following a retention period of 10 min, 3.6 mL of a previously prepared TOP/Se solution (120 mg/3.6 mL) was swiftly injected. The temperature was allowed to rise to 380 °C again before the reaction was quenched by addition of 5 mL of ODE and cooled down to 70 °C in an air stream. During the cooldown period, 5 mL of toluene was added to prevent solidification. The resulting particles were precipitated by methanol/isopropanol (1:2), centrifuged at 6,000 rcf and redispersed in 2 mL of hexane.

A Cd(oleate)<sub>2</sub> precursor solution was synthesised according to Nightingale *et al.*<sup>7</sup> For this synthesis, a mixture of 1.284 g (1 mmol) CdO, 12.94 mL (40.77 mmol) of oleic acid and 7.04 mL of ODE was degassed for 10 min at 100 °C. The dispersion was heated to 180 °C under argon flow and kept there for 60 min under vigorous stirring. To remove water as a side product, the mixture was cooled to 120 °C and degassed for 45 min. The 0.5 M Cd(oleate)<sub>2</sub> solution was used as prepared for the shell growth step.

Zn(oleate)<sub>2</sub> was prepared by using a synthesis procedure described by Boercker *et al.*<sup>8</sup> For this, Zn(acetate)<sub>2</sub> and OA (molar ratio 1:4) were mixed in a flask and heated under vacuum to 110 °C while stirring. The reaction was allowed to proceed for 2 h before the mixture was left to cool to RT. The resulting solid was washed with acetone and centrifuged three times at 6000 rcf for 10 min. The final product was dried in a Schlenk flask and stored under argon until further use.

The growth of the CdS surface passivation shell was performed according to an adapted synthesis by Chen *et al.*<sup>9</sup> For this, 100 nmol of the CdSe cores (142.4 µL) were dispersed in 3 mL of ODE and OLA, respectively. The mixture was carefully degassed for 30 min at 90 °C. In the meantime, the S and Cd precursor solutions were prepared. For the different shell thickness of 3, 5 and 10 monolayers, 398/875/3101 µL of Cd(oleate)<sub>2</sub> were diluted to a total volume of 7 mL with ODE, respectively. Additionally, 35.7/78.4/278 µL of 1-octanethiol were similarly diluted to a total volume of 7 mL with ODE. The flask was then heated under argon flow in two steps to 310 °C. When reaching 240 °C, the simultaneous injection of the previously prepared Cd(oleate)<sub>2</sub> and 1-octanethiol solutions via syringe pump (6 mL, 3 mL/h) was initiated. After two hours, 1 mL (3 mL for 10 ML QDs) of oleic acid was injected, and the temperature was kept at 310 °C for another hour (3 h for 10 ML QDs). Finally, the reaction mixture was cooled down to RT in an air flow, and the particles were precipitated by addition of acetone, centrifuged, and redispersed in hexane.

The growth of the ZnS shell was performed similarly. The same amount of CdSe cores (142.4 µL) was employed, and all other synthesis parameters were kept the same apart from the amount of 1-octanethiol (40.2 µL, diluted with ODE to 7 mL) and Zn(oleate)<sub>2</sub> (140.9 mg, suspended in 7 mL ODE). The solubility of the Zn(oleate)<sub>2</sub> in ODE was poor, so the amount that was actually added to the synthesis was presumably slightly lower.

The concentrations of the resulting QD dispersion were determined by AAS (Cd content). They were determined to be 7.88/3.19/32.85 mg/mL for the CdSe/CdS QDs, and 1.30 mg/mL for the CdSe/ZnS QDs.

### 2. Synthesis of CdSe/CdS-core/shell-NPLs

The Cd(myristate)<sub>2</sub> precursor solution was prepared according to Tessier *et al.*<sup>10</sup> For this, Cd(NO<sub>3</sub>)<sub>2</sub>·4 H<sub>2</sub>O (3221 mg) was dissolved in methanol (80 mL). Simultaneously, Na(myristate) (6262 mg) was dissolved in methanol (500 mL) through stirring for 1.5 h. The Cd(NO<sub>3</sub>)<sub>2</sub> solution was slowly added to the Na(myristate) solution. The resulting Cd(myristate)<sub>2</sub> (white precipitate) was washed with 1.5 L methanol in a Buchner vacuum flask. Finally, the Cd(myristate)<sub>2</sub> was dried under vacuum for at least 12 h and stored in a glove box afterwards.

The synthesis of the quasi-quadratic CdSe core NPLs with a thickness of 4.5 ML were synthesized according to Abécassis *et al.* and Miethé *et al.*<sup>11, 12</sup> First, Cd(myristate)<sub>2</sub> (1360 mg), Se powder (108 mg) and ODE (120 mL) were mixed in a 250 mL three-neck round flask for 10 s in an ultrasonic bath. The flask was degassed for 30 min at 70 °C, purged with nitrogen and degassed again for 30 min at 70 °C. The temperature was set to 240 °C under a nitrogen flow. At 202 °C, the septum was withdrawn, and Cd(acetate)<sub>2</sub>·2 H<sub>2</sub>O (640 mg) was added swiftly to the reaction mixture. The reaction was held at 240 °C for 8 min before OA (4 mL) was injected. The solution was rapidly cooled with compressed air from the outside and OA (4 mL) was added a second time at around 160 °C.

The red dispersion was transferred to four centrifuge tubes. Ethanol (in total 50 mL) was added before centrifuging at 4226 rcf for 10 min. The precipitate was redispersed in hexane (in total 60 mL) and centrifuged again at 4226 rcf for 10 min. The supernatant was transferred to new centrifuge vials and precipitated with ethanol (20 mL in total). The dispersion was centrifuged a third time at 4226 rcf for 10 min. The resulting precipitate was redispersed in approximately 8 mL hexane.

To synthesize the CdSe/CdS-core/shell-NPLs, a procedure published by Rossinelli *et al.* was employed and slightly varied.<sup>13</sup> For this, Cd(oleate)<sub>2</sub> (270.3 mg), ODE (10 mL), and the CdSe core NPLs dispersed in hexane (438  $\mu$ L, c(Cd)=39.4 mmol/L) were combined and degassed for about 20 min at RT, 30 min at 60 °C and 3 h at 80 °C. After the addition of OLA (2 mL, directly from the glove box), the flask was heated to 300 °C under argon flow with about 15 °C/min. At 180 °C, 4.5 mL of a 1-octanethiol/ODE solution (77  $\mu$ L in 5.5 mL) was injected with a rate of 3 mL/h. Then, the reaction flask was cooled to RT. The reaction solution was transferred to a centrifuge vial, and hexane (5 mL) and ethanol (7.5 mL) were added. The mixture was centrifuged at 4226 rcf for 10 min. The precipitate was redispersed in hexane (6 mL) and centrifuged again at 4226 rcf for 10 min. The red supernatant was again centrifuged in a new vial to get rid of remaining CdO impurities.

Similar to the QDs, the concentration of the NPLs was determined by AAS to be 0.96 mg/mL (Cd content).

### 3. Preparation and <sup>1</sup>H-NMR spectrum of polyethylene glycol-*block*-poly( $\epsilon$ -caprolactone)

The *block*-copolymer polyethylene glycol-*block*-poly( $\epsilon$ -caprolactone) (PEG-*b*-PCL) was prepared according to a previously reported procedure<sup>4</sup> adapted from Meier *et al.*<sup>14</sup>

800 mg of poly(ethylene glycol) were placed in a dry flask with 1536  $\mu$ L (14.53 mmol) of  $\epsilon$ -caprolactone. The mixture was put in a preheated aluminium heating block and stirred for 5 min at 130 °C, before one drop of Sn(II) 2-ethylhexanoate was added as a catalyst and initiator. The reaction mixture was then stirred for 3 h at 130 °C before rapidly cooling it with an ice bath, which lead to the precipitation of a solid, white product. The raw product was recrystallized by dissolving it in a small amount of dichloromethane, followed by precipitation with *n*-heptane. The PEG-*b*-PCL was then filtered and washed several times with *n*-heptane before it was dried.

Characterization of the synthesized PEG-*b*-PCL was performed by nuclear magnetic resonance spectroscopy (solution <sup>1</sup>H-NMR) at RT with a 400 MHz JEOL JNM-ECX400 spectrometer (Free University Berlin), the resulting spectrum is displayed in Figure S1. The sample was prepared by dissolving 6 mg of PEG-*b*-PCL in 700  $\mu$ L of CDCl<sub>3</sub>.

Chemical shifts: <sup>1</sup>H-NMR (CDCl<sub>3</sub>, 400 MHz):  $\delta$  = 1.39 (m, 2H,  $\gamma$ ), 1.63 (m, 4H,  $\beta$  &  $\delta$ ), 2.30 (m, 2H,  $\alpha$ ), 3.63 (s, 4H, a & b), 4.05 (t, 2H,  $\epsilon$ ), 4.21 (t, 2H, b).

According to Meier *et al.*, the number-average molecular weight  $M_n$  of the synthesized PEG-*b*-PCL was determined to be about 10,050 g/mol (from the ratio of protons corresponding to the PEG and PCL signals).<sup>14</sup>

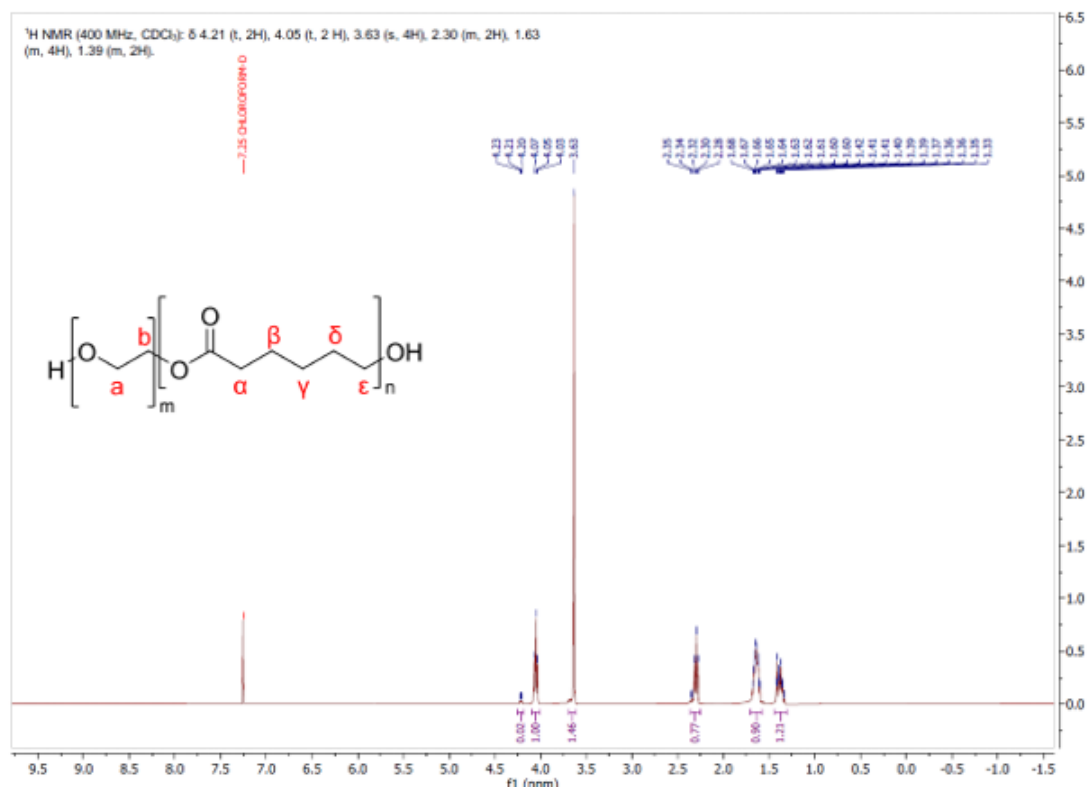


**Figure S1:** <sup>1</sup>H NMR spectrum (400 MHz, solvent CDCl<sub>3</sub>) with structural formula of PEG-*b*-PCL, including all compound peaks and the solvent peak.

#### 4. Fluorescence lifetime decay curves of all NPs and calculation of FLTs

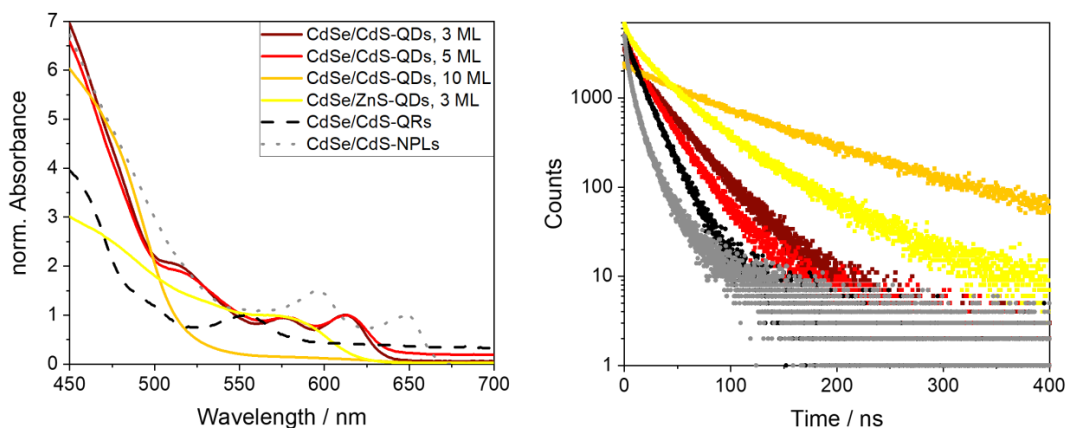


**Figure S2:** Normalized absorbance spectra (left) and fluorescence decay curves (right) of all employed NPs in hexane.

In the following equations, the intensity average FLT  $\tau_{int}$  (SE1) and the multi-exponential model (two or three exponents were chosen, depending on the measured NP) for the calculation of component FLTs  $\tau_i$  from multi-exponential decay curves (SE2) are specified. Here,  $B_i$  is the pre-exponential factor of the lifetime component  $i$ , and  $I(t)$  is the fluorescence intensity as a function of time  $t$ .

$$\langle \tau_{int} \rangle = \frac{\sum_{i=1}^n B_i \tau_i^2}{\sum_{i=1}^n B_i \tau_i} \quad (\text{SE1})$$

$$I(t) = \sum_{i=1}^n B_i \exp\left(\frac{-t}{\tau_i}\right) \quad (\text{SE2})$$

### 5. Size distribution graphs of NPs and NP-stained PSMPs

In Figure S3 and Figure S4, the size distribution graphs and mean particle sizes of all employed NPs and the resulting, NP-stained PSMPs are displayed.

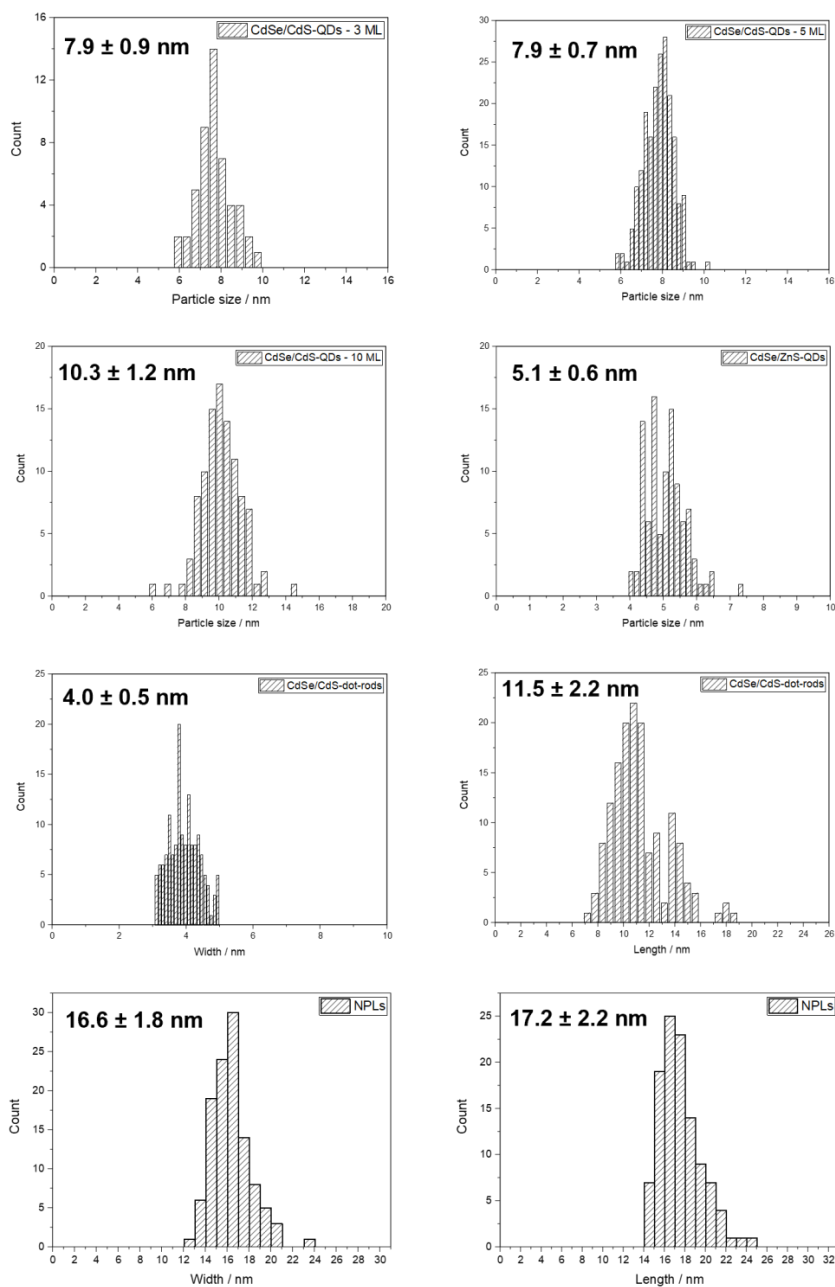


**Figure S3:** Size distribution histograms for all employed NPs with mean particle size and standard deviation, all sizes determined from TEM images.

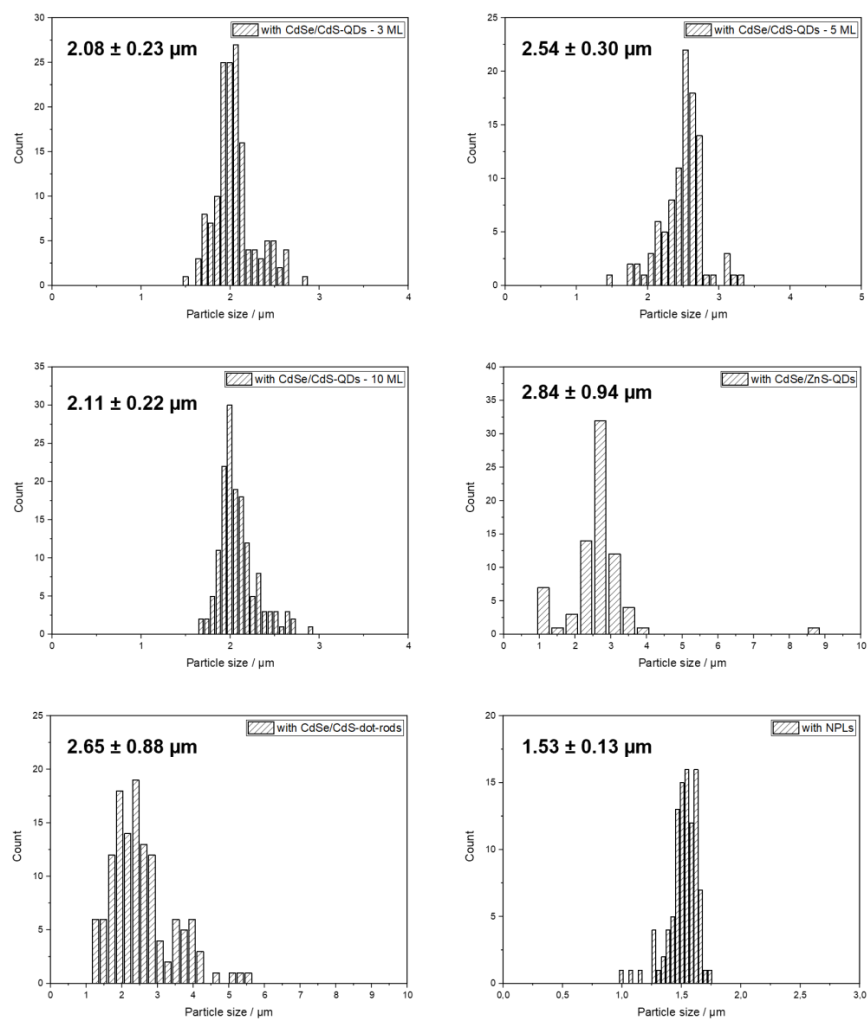


**Figure S4:** Size distribution histograms for all synthesized, NP-stained PSMPs with mean particle size and standard deviation, all sizes determined from SEM images.

## 6. TEM and SEM images of remaining, employed QDs and respective PSMPs

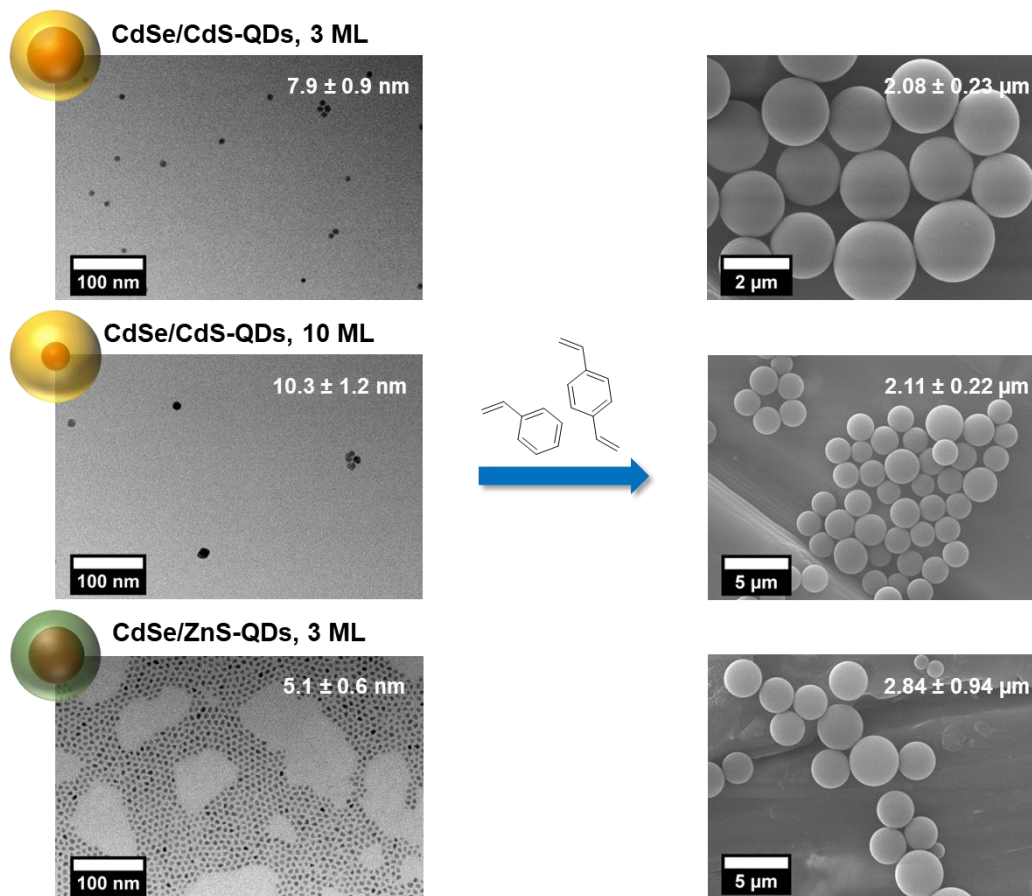


**Figure S5:** TEM images (left) of CdSe/CdS and CdSe/ZnS QDs, showing the average particle sizes; and the SEM images (right) of the resulting, NP-stained PSMPs with average particle sizes (right).

## 6. Emission spectra of CdSe/ZnS QDs and the respective, stained PSMPs

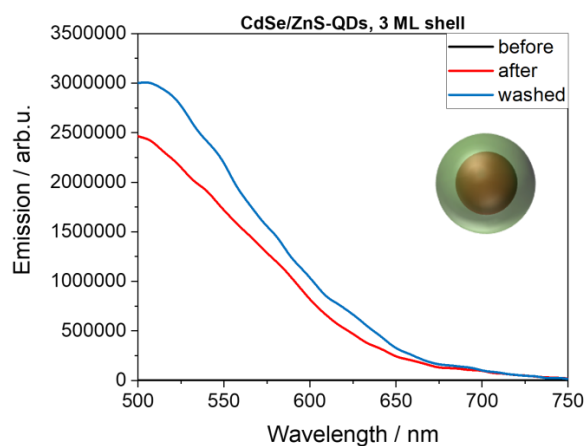


**Figure S6:** Emission spectra of CdSe/ZnS QDs before, during and after the incorporation into PSMPs. No emission bands of the QDs could be detected, even at the start of the reaction, which points to the destruction/quenching through the reaction mixture.

### 7. Preservation of NP luminescence properties upon integration into the PSMPs

In Table S1 and Figure S7, the position of the emission maxima, as well as the emission intensity and PLQY preservation of all NPs incorporated into the respective PSMPs are summarized. The preservation is specified as the percentage of emission intensity ( $P_{em}$ ) or PLQY ( $P_{PLQY}$ ) of the NPs retained, compared to the respective data before the start of the synthesis. The shift of the emission maximum, induced by the changed environment of the NPs in the polymer matrix, is typically very low (up to 7 nm).

**Table S1.** Emission maxima and intensity preservation ( $P_{em}$ ), as well as PLQY values and PLQY preservation ( $P_{PLQY}$ ), for the PSMPs stained with the different luminescent semiconductor NPs. For the CdSe/ZnS QDs, no remaining emission, and thus no PLQY and FLT, was detected.

Incorporated NPs	$\lambda_{em, max}$ / nm	$P_{em}$ / %	PLQY / %	$P_{PLQY}$ / %
CdSe/CdS QDs, 3 ML	Hexane: 622	/	78	/
	Start: 623	100	24	100
	End: 630	73	12	50
	Washed: 620	24	11	46
CdSe/CdS QDs, 5 ML	Hexane: 627	/	67	/
	Start: 631	100	13	100
	End: 627	44	8	62
	Washed: 627	38	17	131
CdSe/CdS QDs, 10 ML	Hexane: 638	/	59	/
	Start: 634	100	17	100
	End: 632	93	19	112
	Washed: 634	35	23	135
QRs	Hexane: 566	/	86	/
	Start: 571	100	26	100
	End: 573	2	2	8
	Washed: 566	3	2	8
NPLs	Hexane: 656	/	34	/
	Start: 653	100	4	100
	End: 655	1951	9	225
	Washed: 655	758	12	300

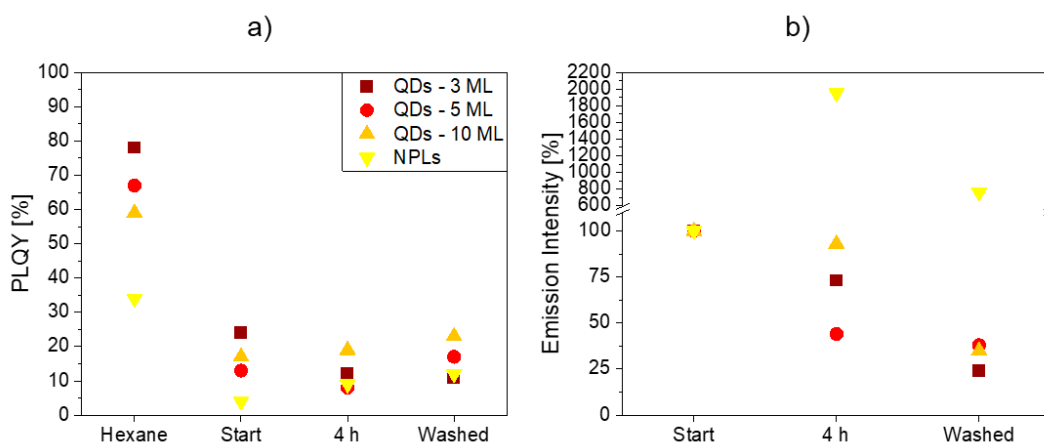


**Figure S7:** a) PLQY values and b) emission intensity of all NPs that showed sufficient PL properties in hexane and during the polymerization reaction. The emission intensity was defined as 100% at the start of the reaction. All values displayed here, as well as the shift in emission maxima, are also summarized in the SI (see Table S1).

### 8. STEM images of PSMPs stained with QDs from previous works

In Figure S8, STEM images of different, QD stained PSMPs are displayed. The images highlight the importance of not only NP type, but also the polymerization procedure parameters. The bead displayed in Figure S8 a) was synthesized with different polymerization parameters (e.g., slower stirring speed), and shows the CdSe/CdS QDs located in the bead core region, contrary to the QDs being located in the bead surface region which was observed for the PSMPs in this work. Figure S8 b) shows a COOH-functionalized PSMP stained with CdSe/CdS QDs (10 ML shell thickness) located in the bead surface region, which confirms that the QD location is very similar to plain PSMP stained with the same QDs.

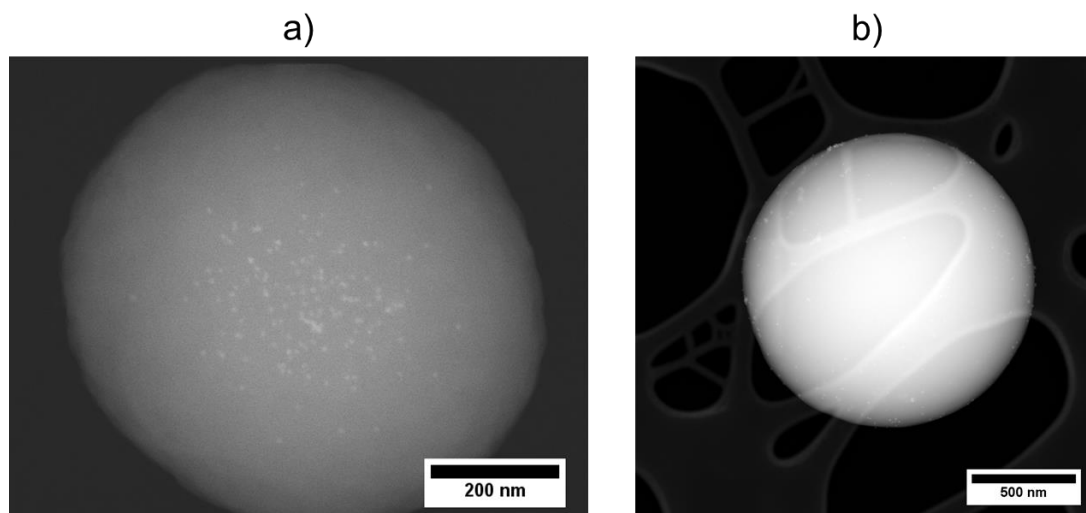


**Figure S8:** STEM images of QD stained PSMPs, with a) CdSe/CdS QDs (5 ML shell thickness) located in the bead core region, and b) CdSe/CdS QDs (10 ML shell thickness) located in (and even on) the bead surface region. The pictured particles were produced previously by us (see Scholtz *et al.* (2022)<sup>4</sup> for particles in a) and Scholtz *et al.* (2023)<sup>5</sup> for particles in b)).

## References

1. Carbone, L.; Nobile, C.; De Giorgi, M.; Sala, F. D.; Morello, G.; Pompa, P.; Hytch, M.; Snoeck, E.; Fiore, A.; Franchini, I. R. Synthesis and micrometer-scale assembly of colloidal CdSe/CdS nanorods prepared by a seeded growth approach. *Nano letters* **2007**, *7* (10), 2942-2950.
2. Nightingale, A. M.; Bannock, J. H.; Krishnadasan, S. H.; O'Mahony, F. T.; Haque, S. A.; Sloan, J.; Drury, C.; McIntyre, R.; deMello, J. C. Large-scale synthesis of nanocrystals in a multichannel droplet reactor. *Journal of Materials Chemistry A* **2013**, *1* (12), 4067-4076.
3. Chen, O.; Zhao, J.; Chauhan, V. P.; Cui, J.; Wong, C.; Harris, D. K.; Wei, H.; Han, H.-S.; Fukumura, D.; Jain, R. K. Compact high-quality CdSe–CdS core–shell nanocrystals with narrow emission linewidths and suppressed blinking. *Nature materials* **2013**, *12* (5), 445-451.
4. Scholtz, L.; Eckert, J. G.; Elahi, T.; Lübke, F.; Hübner, O.; Bigall, N. C.; Resch-Genger, U. Luminescence encoding of polymer microbeads with organic dyes and semiconductor quantum dots during polymerization. *Scientific Reports* **2022**, *12* (1), 12061.
5. Scholtz, L.; Tavernaro, I.; Eckert, J. G.; Lutowski, M.; Geißler, D.; Hertwig, A.; Hidde, G.; Bigall, N. C.; Resch-Genger, U. Influence of nanoparticle encapsulation and encoding on the surface chemistry of polymer carrier beads. *Scientific Reports* **2023**, *13* (1), 11957.
6. Carbone, L.; Nobile, C.; De Giorgi, M.; Sala, F. D.; Morello, G.; Pompa, P.; Hytch, M.; Snoeck, E.; Fiore, A.; Franchini, I. R.; Nadasan, M.; Silvestre, A. F.; Chiodo, L.; Kudera, S.; Cingolani, R.; Krahn, R.; Manna, L. Synthesis and Micrometer-Scale Assembly of Colloidal CdSe/CdS Nanorods Prepared by a Seeded Growth Approach. *Nano Letters* **2007**, *7* (10), 2942-2950.
7. Nightingale, A. M.; Bannock, J. H.; Krishnadasan, S. H.; O'Mahony, F. T. F.; Haque, S. A.; Sloan, J.; Drury, C.; McIntyre, R.; deMello, J. C. Large-scale synthesis of nanocrystals in a multichannel droplet reactor. *Journal of Materials Chemistry A* **2013**, *1* (12), 4067-4076.
8. Boercker, J. E.; Woodall, D. L.; Cunningham, P. D.; Placencia, D.; Ellis, C. T.; Stewart, M. H.; Brintlinger, T. H.; Stroud, R. M.; Tischler, J. G. Synthesis and Characterization of PbS/ZnS Core/Shell Nanocrystals. *Chem. Mater.* **2018**, *30* (12), 4112-4123.
9. Chen, O.; Zhao, J.; Chauhan, V. P.; Cui, J.; Wong, C.; Harris, D. K.; Wei, H.; Han, H.-S.; Fukumura, D.; Jain, R. K.; Bawendi, M. G., Compact high-quality CdSe–CdS core–shell nanocrystals with narrow emission linewidths and suppressed blinking. *Nature Materials* **2013**, *12* (5), 445-451.
10. Tessier, M. D.; Spinicelli, P.; Dupont, D.; Patriarche, G.; Ithurria, S.; Dubertret, B., Efficient Exciton Concentrators Built from Colloidal Core/Crown CdSe/CdS Semiconductor Nanoplatelets. *Nano Letters* **2014**, *14* (1), 207-213.
11. Abécassis, B.; Tessier, M. D.; Davidson, P.; Dubertret, B., Self-Assembly of CdSe Nanoplatelets into Giant Micrometer-Scale Needles Emitting Polarized Light. *Nano Letters* **2014**, *14* (2), 710-715.
12. Miethé, J. F.; Schlosser, A.; Eckert, J. G.; Lübke, F.; Bigall, N. C. Electronic transport in CdSe nanoplatelet based polymer fibres. *Journal of Materials Chemistry C* **2018**, *6* (40), 10916-10923.
13. Rossinelli, A. A.; Riedinger, A.; Marqués-Gallego, P.; Knüsel, P. N.; Antolinez, F. V.; Norris, D. J. High-temperature growth of thick-shell CdSe/CdS core/shell nanoplatelets. *Chemical Communications* **2017**, *53* (71), 9938-9941.
14. Meier, M. A. R.; Aerts, S. N. H.; Staal, B. B. P.; Rasa, M.; Schubert, U. S. PEO-b-PCL Block Copolymers: Synthesis, Detailed Characterization, and Selected Micellar Drug Encapsulation Behavior. *Macromolecular Rapid Communications* **2005**, *26* (24), 1918-1924.

## 5.2 | Minor Contributions

### 5.2.1 | Analyzing the Surface of Functional Nanomaterials - How to Quantify the Total and Derivatizable Number of Functional Groups and Ligands (Review Article)

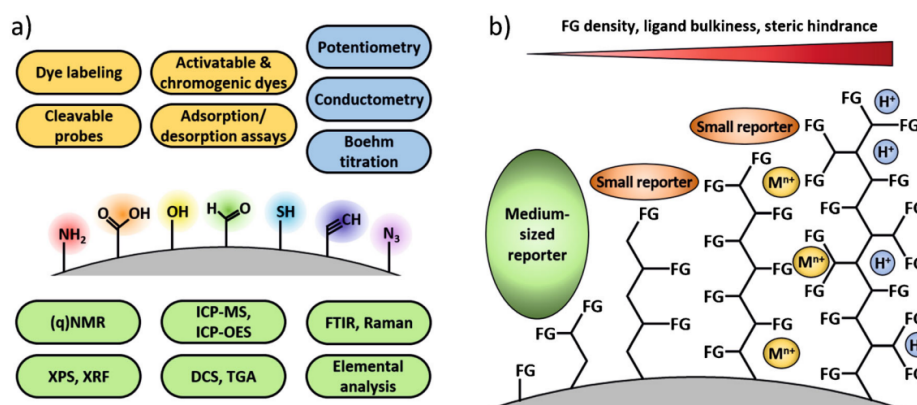


Figure 24: Schematic depiction of bioanalytically relevant FGs and corresponding characterization methods, taken with permission from D. Geißler *et al.*, copyright 2021 *Microchimica Acta*.<sup>[184]</sup>

Authors: Daniel Geißler, Nithiya Nirmalanathan-Budau, **Lena Scholtz**, Isabella Tavernaro, Ute Resch-Genger\*

To this work, L. Scholtz contributed by writing the section about "Electrochemical titrations for the quantification of (de)protonable FG on dispersed nanomaterials", including the corresponding literature research, with help from the other authors. L. Scholtz also assisted in the conceptual planning of the review and the composition and writing of abstract, introduction and conclusion. The other authors contributed by writing the remaining parts of the review.

**Estimated Contribution: 15%**

Work published in journal: *Microchimica Acta*, 2021

See online here: <https://link.springer.com/article/10.1007/s00604-021-04960-5>

DOI: <https://doi.org/10.1007/s00604-021-04960-5>

This article is licensed under a Creative Commons Attribution 4.0 International (CC BY 4.0, <https://creativecommons.org/licenses/by/4.0/>).

Microchimica Acta (2021) 188: 321  
https://doi.org/10.1007/s00604-021-04960-5

REVIEW ARTICLE



## Analyzing the surface of functional nanomaterials—how to quantify the total and derivatizable number of functional groups and ligands

Daniel Geißler<sup>1</sup> · Nithiya Nirmalanathan-Budau<sup>1</sup> · Lena Scholtz<sup>1</sup> · Isabella Tavernaro<sup>1</sup> · Ute Resch-Genger<sup>1</sup>

Received: 23 June 2021 / Accepted: 8 August 2021 / Published online: 4 September 2021  
© The Author(s) 2021

### Abstract

Functional nanomaterials (NM) of different size, shape, chemical composition, and surface chemistry are of increasing relevance for many key technologies of the twenty-first century. This includes polymer and silica or silica-coated nanoparticles (NP) with covalently bound surface groups, semiconductor quantum dots (QD), metal and metal oxide NP, and lanthanide-based NP with coordinatively or electrostatically bound ligands, as well as surface-coated nanostructures like micellar encapsulated NP. The surface chemistry can significantly affect the physicochemical properties of NM, their charge, their processability and performance, as well as their impact on human health and the environment. Thus, analytical methods for the characterization of NM surface chemistry regarding chemical identification, quantification, and accessibility of functional groups (FG) and surface ligands bearing such FG are of increasing importance for quality control of NM synthesis up to nanosafety. Here, we provide an overview of analytical methods for FG analysis and quantification with special emphasis on bioanalytically relevant FG broadly utilized for the covalent attachment of biomolecules like proteins, peptides, and oligonucleotides and address method- and material-related challenges and limitations. Analytical techniques reviewed include electrochemical titration methods, optical assays, nuclear magnetic resonance and vibrational spectroscopy, as well as X-ray based and thermal analysis methods, covering the last 5–10 years. Criteria for method classification and evaluation include the need for a signal-generating label, provision of either the total or derivatizable number of FG, need for expensive instrumentation, and suitability for process and production control during NM synthesis and functionalization.

**Keywords** Functional group quantification · Surface ligand · Nanomaterial · Nanoparticle · Bead · Dye-based assay · Optical detection · Electrochemical titration · Instrumental analysis · Nanosafety · Safe-by-design

### Introduction

#### Need for and importance of functional group quantification

Functionalized nanomaterials (NM) are of increasing industrial and economic importance in the life sciences and the health sector as well as for applications in nano(bio)technology, optical and sensor technologies, solid state lighting and photovoltaics, as well as opto-electronic and electronic devices and security applications. Nowadays, NM are used as catalysts,

hydrogen storage and energy conversion materials, contrast agents and drug carriers for imaging and therapy in medicine, signal-generating reporters in bioanalysis, molecular diagnostics and sensing, as additives for food and cosmetics, in textile industry, and as phosphors for lighting and display technologies [1–13]. This comprises all types of core and core/shell NM such as organic polymer and inorganic silica or silica-coated nanoparticles (NP) with covalently bound surface groups as well as other inorganic NP like metal and metal oxide NP, semiconductor quantum dots (QD), and lanthanide-based NP with coordinatively or electrostatically bound ligands [14–16]. It also includes different types of encapsulated nanostructures like inorganic NP with hydrophobic surface ligands wrapped with amphiphilic (co)polymers or lipid coatings that can also be crosslinked, yielding micellar-type systems, or coated with alternating layers of differently charged polyelectrolytes by the so-called layer-by-layer (LbL) approach [17–19].

✉ Ute Resch-Genger  
ute.resch@bam.de

<sup>1</sup> Bundesanstalt für Materialforschung und -prüfung (BAM), Division Biophotonics (BAM-1.2), Richard-Willstätter-Str. 11, 12489 Berlin, Germany

Decisive for most applications of NM are their specific surface properties, which are largely controlled by the chemical nature and number of ligands and functional group (FG) on the NM surface. The surface chemistry and surface FG determine the charge, dispersibility, and colloidal stability of NM, as well as their hydrophilicity/hydrophobicity, processability, and interaction with their environment [15, 18, 20–23]. In addition, FG enable the controlled modification and functionalization of NM by covalent binding of functional molecules such as hydrophilic ligands, anti-fouling agents, sensor dyes, and biomolecules like proteins, peptides, or oligonucleotides, e.g., for the preparation of nanosensors and targeted nanoprobe [5, 10, 24–26]. Control of the surface chemistry is also relevant for the minimization of unspecific adsorption, increase of colloidal and/or dissolution stability, and the design of drug carriers and triggered release systems [15, 22, 27–30]. For example, the reactivity and stability of NM can be altered intentionally and rationally by surface passivation strategies utilizing special coatings such as silica or polymeric shells, or via tailored modifications of the surface charge via the density of FG and ligands. This underlines the crucial importance of surface chemistry and surface functionalities for many NM applications in the life and material sciences and nano(bio)technology and their relevance for the rational design and tuning of the properties of functional NM. Knowledge of NM surface chemistry presents not only a key issue to understand the nano-bio interface largely controlling NM functionality and performance in (bio)applications, but is also relevant to assess the fate, exposure, dissolution, transformation, and accumulation of NM, and thus, NM toxicity and potential risks for human health and the environment [31–36]. This also includes the evaluation of risks associated with the application of engineered NM in consumer, food, and biomedical products [37–41]. Here, also unintentional changes and modifications in NM surface by time- and environment-dependent aging effects and transformations during the material's life-cycle must be considered, that can affect NM safety aspects [42]. This is addressed by the increasingly pursued safe-by-design (SbD) concept of NM, which integrates considerations of material safety and performance as early as possible into the innovation process [43–45], thereby balancing safety, functionality, and costs for the development of better nanotechnology-enabled products throughout their life-cycle [46].

The increasing importance of NM in fundamental research and technological applications makes the sustainable development of functional and safe(r) NM as well as a comprehensive understanding of the structure-function and structure-safety relationships mandatory [43, 47]. Reliable, robust, and simple methods for the adequate characterization of such materials are key requirements to overcome challenges associated with the rapidly diversifying development of NM and to address still existing uncertainties and knowledge gaps [48, 49]. This

is also essential for quality assurance and production control of engineered NM in support of the SbD concept [9, 18, 23, 50, 51]. In this context, the development of harmonized and standardized characterization methods not only simplifies to rank, prioritize, and choose safer alternatives during the innovation process of engineering NM, but is similarly beneficial for regulatory frameworks and the confidence in NM [41, 46, 52, 53]. Nevertheless, there is still a lack of normative measurement and characterization regulations, validated and standardized measurement protocols, reference materials of known surface chemistry for FG quantification, and reference data on application-relevant NM. Together with the often contradictorily literature in this field, this presents growing technological and economic challenges for manufacturers and users of NM. This has been increasingly recognized not only by scientists from different disciplines all over the world, but also by European legislation as well as national and international standardization organizations like ISO, IEC, and OECD [50, 54]. This makes the assessment of analytical methods for FG analysis on NM, including the determination of method-inherent limitations and NM-specific requirements and limitations as well as achievable method uncertainties, an increasingly important topic for NM-based technologies and NM risk assessment and regulation.

#### Nanomaterial surface functionalization and bioanalytically relevant FG

The reactive FG and surface ligands relevant for NM-based (bio)analytical applications typically correspond with the complementary FG on the functional molecules utilized in typical (bio)conjugation reactions, e.g., biomolecules used as target-specific recognition moieties [24, 26, 55]. For biomolecules like peptides and proteins including antibodies and enzymes, this includes amino groups ( $-NH_2$ ) at the N-terminus of the polyamide backbone and at the side chains of the amino acids arginine, histidine, lysine, and tryptophan, carboxy groups ( $-COOH$ ) at the C-terminus of the polyamide backbone and at the side chains of aspartic acid and glutamic acid, the hydroxyl and phenol groups ( $-OH$ ) of serine, threonine, and tyrosine, the thiol ( $-SH$ ) and thioether groups of cysteine and methionine, as well as chemically introduced thiol groups, e.g., via reductive cleavage of disulfide bridges [56, 57]. For carbohydrates like mono- and disaccharides, oligo- and polysaccharides, and as part of glycolipids and glycoproteins, the most abundant native FG are hydroxyl groups. Some monosaccharide derivatives such as non-acetylated amino sugars provide additional reactive FG for bioconjugation. Also, vicinal diols can be oxidized to aldehyde groups ( $-CHO$ ). Oligonucleotides like DNA and RNA consist of a sugar-phosphate polymer backbone with a reactive phosphate group at the 5'-terminus and a OH group in the case of DNA or a vicinal diol for RNA at the 3'-terminus, respectively. The

native nucleic acids cannot be chemically modified as easily as the amino acids in proteins. However, synthetic oligonucleotides can be prepared via solid-phase synthesis with aminoalkyl- or thioalkyl-containing linkers attached to the nucleobases, the phosphate backbone, or the 3'- or 5'-terminus, which allow for further modifications and labeling [58]. Besides native FG, there are several FG which can also be chemically introduced into biomolecules that are suitable for chemoselective labeling and bio-orthogonal chemistry such as azide ( $-N_3$ ), alkyne ( $-C\equiv CH$ ), or maleimide groups for cycloaddition reactions [26, 57–59]. Other interesting FG for (bio)analytical applications are silanol ( $\equiv Si-OH$ ,  $\equiv Si(OH)_2$ ) and siloxane ( $\equiv Si-O-Si\equiv$ ) groups present on silica particles and silica-based surface modifications and coatings used for all types of NM to improve or tune their stability and dispersibility in aqueous media, for SbD concepts and the supply of surface FG for further functionalization reactions [60–62].

#### Quantifying total vs. derivatizable FG on nanomaterials

For the quantification of FG on NM, it needs to be distinguished between methods that provide the total number of FG present on the NM surface, and methods that determine the number of derivatizable FG [63, 64]. The total FG number largely determines NM charge (zeta potential), and thus, colloidal stability, dispersibility, and hydrophobicity/ hydrophilicity, and is therefore an important and application-relevant parameter for all types of NM in addition to size, size distribution, and shape/morphology. The number of derivatizable FG, in turn, controls the number of groups available for covalent attachment of functional molecules such as hydrophilic ligands, anti-fouling agents, or biomolecules. Hence, the number of derivatizable FG is important for all (bio)labeling reactions as well as the functionality and performance of the resulting surface-modified NP and NP (bio)conjugates.

Relevant for the selection of suitable analytical methods for FG and surface ligand quantification is the signal generation principle, i.e., whether these methods can quantify FG directly without a signal generating reporter (label-free methods), or whether they require a reporter for readout (label-based methods) that is covalently bound or interacts with the FG via electrostatic or adsorptive interactions [51]. In Fig. 1a, the analytical methods for FG quantification covered by this review are displayed and highlighted according to the principle of signal generation including electrochemical methods, dye-based optical methods, and other instrumental analytical techniques. For label-based methods, reporter properties such as molecule size, shape, and charge as well as the coupling efficiency and yield of the chemical reaction used for reporter conjugation can influence the analytical result. Especially the size and shape of the reporter utilized to determine the number

of derivatizable FG can play an important role, as the obtained labeling density, and hence, number of derivatizable FG can be affected by the bulkiness of the label and steric effects [63], as shown in Fig. 1b. This, however, is also the case for any other covalently bound (bio)molecule of interest, so that the results can be correlated if a suitable reporter is applied, or can at least be estimated from the size and shape of the reporter and the (bio)molecule of interest. Moreover, it must be distinguished between absolute, i.e., calibration-free analytical methods and methods that require a calibration for analyte quantification. The latter is by far more common but can introduce additional challenges and uncertainties due to the need of a suitable reference material or standards, particularly for optical methods like absorption and fluorescence that yield signals which are affected by reporter environment. Depending on the method used, this can also determine whether the whole nanoobject can be analyzed as prepared, or whether the NM has to be dissolved prior to FG quantification.

Also, the type of bond between the NM and the FG-bearing ligand must be considered. For FG tightly bound to NP via covalently attached ligands, only steric effects affect the accessibility of the FG. For silica NP, it must be kept in mind that not all hydroxy groups are quantitatively involved in the grafting procedure and free ethoxy or methoxy groups remain on the silica NM. For electrostatically or coordinatively bound ligands, in turn, excess ligands must be removed and potential influences of NP concentration and dilution steps that can shift the ligand adsorption/desorption equilibrium must be excluded or properly considered for FG analysis [65]. For NP encapsulated in micellar structures, as often utilized for inorganic NP like iron oxide, semiconductor QD, and lanthanide-based upconversion NP [17, 18, 66, 67], even the orientation of the FG can play a role for FG analysis, depending on the chemical nature of the respective organic coating. Such systems can consist of buried FG pointing inwards that interact with the surface atoms of the encapsulated NP, and FG pointing outwards to the NP microenvironment. Only the latter ones are relevant for the covalent attachment of functional molecules. For such nanostructures, the information provided by the applied analytical method must be carefully evaluated regarding its information content to decide whether the whole nanoobject should be analyzed as prepared or whether the encapsulated NM should be dissolved prior to FG quantification.

Besides FG/ligand concentration, also the NM number concentration and surface area of the NM are of importance, as they determine the number of FG or ligands per particle as well as the FG or ligand density on the NM. Typically, the measured number of FG/ligands is divided by the number of particles or their total surface area. The NP number concentration can be determined via counting methods such as resistive pulse sensing (Coulter counter), nanoparticle tracking

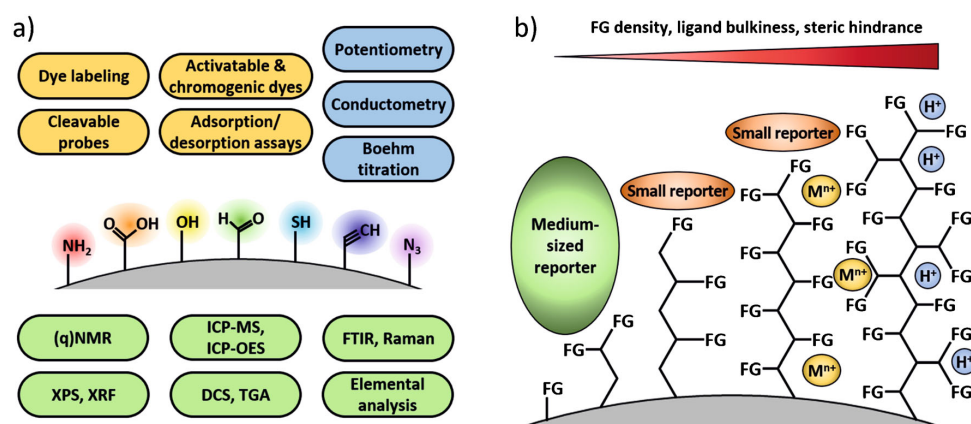


**Fig. 1** Brief overview of the bioanalytically relevant FG and the analytical methods covered by this review including typical reporters. **a** Method classification according to the principle of signal generation, i.e., electrochemical methods (blue), dye-based optical methods (yellow), and other instrumental analytical techniques (green). **b** Schematic presentation of the influence of the reporter size used to determine the number of

FG depending on FG density or ligand bulkiness (steric hindrance) on the NP surface. The sizes of the labels can range from very small reporters like protons ( $\text{H}^+$ ) and metal ( $\text{M}^{n+}$ ) ions, to small and medium-sized reporters like organic dyes, that are still smaller than large biomolecules

analysis (NTA), flow cytometry (FCM), as well as by absorption spectroscopy (if the molar absorption coefficient or the molar absorption cross section is known). The mean particle concentration can also be calculated indirectly from the NM mass (dry weight) or the concentration of certain NM-specific elements that can be quantified, e.g., with inductively coupled plasma mass spectrometry (ICP-MS) or optical emission spectroscopy (ICP-OES). The surface area, in turn, can be directly measured using gas sorption methods, or can be calculated from the NP concentration and the particle dimensions, obtained by sizing techniques such as transmission or scanning electron microscopy (TEM/SEM), small-angle X-ray scattering (SAXS), NTA, or dynamic light scattering (DLS). All these NM characterization techniques regarding NP size and concentration are well-known and have been reviewed in the literature [68–72], and we will focus here solely on methods for FG and ligand quantification.

For the determination of the total and derivatizable number of FG or ligands per particle, always another parameter needs to be considered, namely the distribution of NM size (and shape) and the corresponding variations of the surface-to-volume ratios within one particle batch, which directly influence the total surface area of the NM, and thus, the determined FG/ligand density (number of FG/ligands per particle). A perfect FG quantification method should be able to count the groups/ligands of interest per particle for a large number of individual particles to yield a histogram of FG or ligands per NM independent of particle size/size distribution and shape. A few sophisticated analytical techniques such as single-particle ICP-MS (sp-ICP-MS) or flow methods like FCM are in principle capable of measuring NM properties like elemental composition (for suited elements) and scattering and fluorescence

(intensity) features on a particle-by-particle basis. These methods, however, still face limitations in NM surface characterization, e.g., related to the lack of sensitivity or influences of labeling chemistries (vide infra). Even if FG/ligand counting on single particles was possible, different morphological features (i.e., exposed crystal facets, local curvature radii of the surface) that can be present even at various surface areas of a single particle will still impact the ligand density on the NM surface. Thus, most analytical techniques applied for FG/ligand quantification and described here are ensemble techniques that yield only a mean value of FG/ligands for a given (mean) particle size and shape. As smaller particles have a smaller surface area, but a larger surface-to-volume ratio compared with larger particles, the distribution of FG/ligands per (individual) particles can strongly differ for particles with the same (mean) size but different size distributions. However, as the particle size has to be determined to calculate the surface area (vide supra), the obtained number-based size distribution can also be used to calculate the distribution of FG/ligands (assuming a similar surface morphology) and even to consider the size- and shape-dependent curvature of the NM surface.

In this review, typical methods for FG quantification on NM are presented (cf. Fig. 1a), and their working principles, advantages, and limitations are described, focusing on publications from the last 5–10 years and selected, representative examples to underline the versatility of the respective methods. Analytical techniques covered include electrochemical titration methods, optical assays, nuclear magnetic resonance (NMR), ICP-MS and ICP-OES, infrared (IR) and Raman spectroscopy, X-ray photoelectron spectroscopy (XPS) and X-ray fluorescence spectroscopy (XRF), as well

as thermal analysis methods and elemental analysis. Other mass spectrometry techniques like laser ablation ICP-MS (LA-ICP-MS) or time-of-flight secondary ion mass spectrometry (ToF-SIMS) are not considered here, as these techniques are commonly used for the surface analysis of 2D-supports. Parameters addressed and used for method classification and evaluation include whether the respective analytical method (i) provides the total or derivatizable number of FG and (ii) is label-free or requires a signal-generating reporter; (iii) whether the reporter is covalently bound to the FG, giving rise to a possible influence of the efficiency of the conjugation reaction; (iv) the influence of reporter size; and (v) the need for method calibration. Special emphasis is dedicated to simple FG quantification methods with inexpensive instrumentation that are broadly accessible and can be used for routine analysis and process control during NM production and surface functionalization, like electrochemical and optical methods. We do not intend to cover NM bioconjugation strategies utilized for preparing nano-bioconjugates nor methods to quantify NM-bound biomolecules or to assess biomolecule functionality, which have already been excellently described in other review articles [56, 57].

### Electrochemical titrations for the quantification of (de)protonable FG on dispersed nanomaterials

Electrochemical titrations methods like potentiometric titrations (measurement of the electrochemical potential(s) of the sample), conductometric titrations (measurement of the sample conductivity), and the so-called Boehm titration that is specifically employed for carbon materials are commonly used as inexpensive and precise methods for the quantification of (de)protonable surface FG such as carboxylic acids, amines, or thiols. Closely related Zeta potential measurements that provide NM surface charge, which presents a measure for colloidal stability and can be used for the monitoring of reactions on nano- and microparticles [73], are not further detailed here.

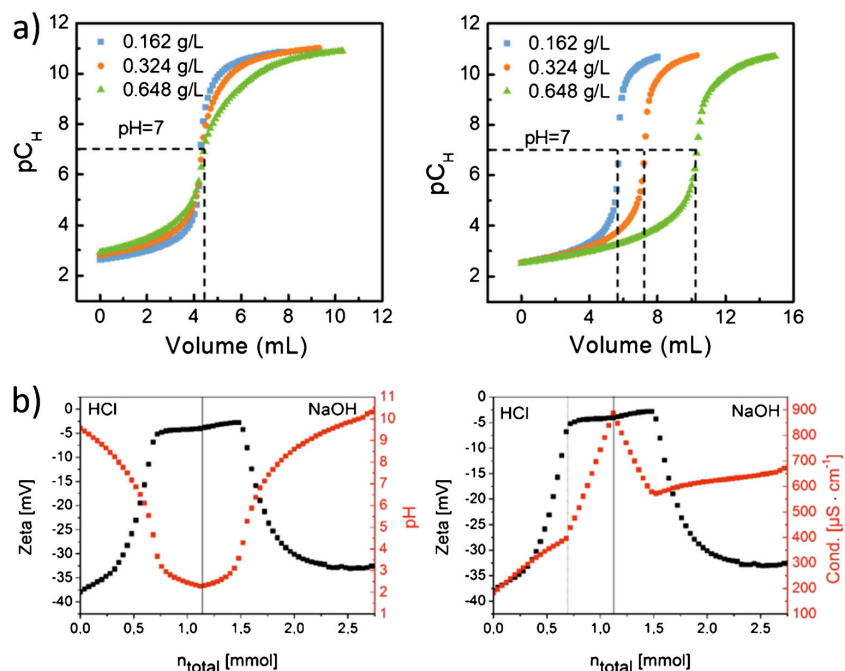
During the course of an electrochemical titration, defined amounts of a titrant (typically acids or bases) are added to the sample, and the resulting changes in the electrochemical properties of the sample are monitored. As electrochemical acid-base titrations are typically carried out over a broad pH range, often including the isoelectric point of the sample (i.e., the pH value at which the net surface charge is zero), they can only be applied for NM that are stable under the given pH conditions. For example, the determination of amino groups ( $pK_a$  about 9–11) on silica-based NM can be challenging as silica dissolves at basic pH values, and some metal oxide and other chalcogenide-based NM can dissolve at acidic pH values where carboxylic groups ( $pK_a$  about 5) are typically detected.

Nevertheless, for many other NM like carbon-based and polymeric particles, electrochemical titrations are well suited for FG and ligand quantification. Another limitation of electrochemical methods is their lack of specificity and selectivity, as all (de)protonable species with comparable  $pK_a$  values are detected which can distort the obtained results. This can include surfactants, initiators, or stabilizers from the NM synthesis, excess ligands with the (de)protonable group of interest, or the presence of other (de)protonable FG having a similar  $pK_a$  value. In addition, electrochemical titration methods require a relatively large amount of sample (typically about 10–20 mg/mL of NM sample).

### Potentiometric titration

In a potentiometric titration, the electrochemical potential(s) of the analyte solution is measured with two electrodes, normally in the form of pH measurements, upon addition of defined amounts of acid or base as titrant which yields a pH titration curve. The equivalence points of the titration curves provide the amount and the  $pK_a$  values of the (de)protonable FG of the analyzed sample. Also, the use of other ion-selective electrodes is possible [74, 75]. Potentiometric titrations have been used for characterizing the surface chemistry of different types of organic and inorganic NM with various FG, and have been applied to determine the number and nature of acidic sites (carboxy, lactone, phenol, and ester groups) on carbon-based materials like carbon dots (CD), nanocellulose/nanobentonite composites, biochar particles, multi-walled carbon nanotubes, or cellulose nanocrystals [76–80], or to quantify hydroxy (silanol) and thiol groups on hybrid silica particles [81]. Potentiometric titrations have also been used to determine the total number of acidic sites on different catalyst materials like phosphotungstic acid-functionalized Sn-TiO<sub>2</sub> and organic-inorganic polyoxometalate NP, SrTiO<sub>3</sub> particles used to catalyze condensation, hydrogenation, and amination reactions, functionalized silica particles employed as catalysts for the esterification of linoleic acid, and photocatalytic TiO<sub>2</sub>/S-doped carbon hybrids [82–86]. For example, Wang et al. potentiometrically quantified carboxy and amino groups on fluorescent CD prepared with different amounts of L-arginine or L-glycine (see Fig. 2a) [87]. By addition of Fe(III) ions before the titration and comparison of the results with measurements done without metal ions, the authors could also derive information on metal ion-CD interactions. Renner et al. compared potentiometric pH titrations with Zeta potential and conductivity measurements to quantify the number of hydroxy groups on silica and iron oxide NP [88]. The results obtained for silica particles, shown in Fig. 2b, demonstrate that Zeta potential values are closely linked to pH and conductivity of a sample, which is reflected by the respective curves changing at the same titrant volumes added. The titration with HCl used to protonate surface hydroxy groups was

**Fig. 2** Representative examples for the FG quantification on NM using potentiometric titrations. **a** Results for the potentiometric FG quantification for carbon dots functionalized with different concentrations of either L-arginine (left) or L-glycine (right) using NaOH as titrant. Adapted with permission from ref. [87]. Copyright 2019, American Chemical Society. **b** Reversible deprotonation of a colloidal silica dispersion using HCl/NaOH titrants as detected by zeta potential (black) and pH (red, left) or conductivity (red, right) measurements. Adapted with author permission from ref. [88] (CC BY-NC 4.0)



reversed by back titration with NaOH to ensure the reversibility of the process. The slightly negative zeta potential at full protonation was attributed to non-accessible hydroxy groups.

### Conductometric titration

In a conductometric titration, the conductivity of a sample is measured as a function of the added amount of acid or base. Typical examples present the quantification of the total amount of amino and carboxy groups on polystyrene (PS) particles [64, 89, 90]. The suitability of conductometry for carboxy group quantification on polymeric particles has been validated for polymethylmethacrylate (PMMA) particles grafted with polyacrylic acid (PAA) by comparison with quantitative NMR spectroscopy (qNMR) [63] and for PS particles by comparison with Zeta potential measurements [90]. Conductometric titrations are also commonly used for quantifying sulfate half-esters as well as carboxy and amino groups on cellulose nanocrystals (CNC), e.g., to achieve a tailored surface charge and to control CNC surface modification, or to study the effect of surface treatment on the dispersion rheology of CNC [91–95]. Other groups applied conductometric titrations to characterize CNC regarding their applicability for acid-base organo-catalysis [96, 97], or to determine the hydroxy group content on the surface of hydrogels consisting of modified cellulose nanofibrils suitable for controlled and pH-

responsive release of a chemotherapeutic agent [98]. A general procedure for the determination of the sulfate half-ester content on CNC via conductometric titration, consisting of dialysis followed by treatment with a strong acid to ensure full protonation, was developed by Beck et al. [99], and a protocol to for the conductometric quantification of the sulfur and sulfate half-ester content on CNC was validated in an interlaboratory comparison [100]. The difference in the sulfur content determined by conductometry and by ICP-OES was attributed to sulfur in the CNC interior that is not conductometrically accessible.

### Boehm titration

Boehm titration is a method developed by Boehm et al. in 1964 [101] suitable for the quantification of acidic, oxygen-containing surface groups on various carbon-based materials such as graphene, carbon nanotubes (CNT), CD, and carbon-coated particles. This method allows not only to quantify common FG relevant for biolabeling and bioanalytical applications, but also other FG such as lactone or phenol groups [101–104]. The Boehm method is based on the treatment of a dispersed carbon sample with titration bases of different pK<sub>a</sub> values like NaOH, Na<sub>2</sub>CO<sub>3</sub>, and NaHCO<sub>3</sub> [101, 105], followed by the back titration of the unconsumed amount of the titrant. It is assumed that each base only neutralizes FG that

are more acidic than the respective base, and the ratios of the amounts of the different oxygen-containing FG can then be calculated directly from the base consumption. Boehm titration has been utilized to characterize the FG on different kinds of CNT [106–108] as well as on other carbon-based materials like ozone-treated nanodiamonds, carbon NP derived from organic resin, graphite-decorated  $\text{MnFe}_2\text{O}_4$  nanocomposites, and natural char nano- and microparticles [109–112]. To evaluate and standardize Boehm titration regarding accuracy, robustness, repeatability, and precision, Schönherr et al. investigated the FG on oxidized multi-walled CNT using different reaction bases, treatment times, and amounts of carbon material [105, 113]. A major concern of these studies was the dissolution of  $\text{CO}_2$  from air which leads to the formation of  $\text{HCO}_3^-$  and  $\text{CO}_3^{2-}$ , that can considerably influence the titration results. To quantify this effect, a direct and an indirect approach to the Boehm titration procedure were compared. The results, shown in Fig. 3, underline the influence of  $\text{CO}_2$  particularly for the direct titration curve with NaOH. To circumvent such distortions, a medium-strong base like  $\text{Na}_2\text{CO}_3$  was proposed and a protocol for an indirect titration approach with this base using an autotitrator was developed. Schönherr et al. also compared Boehm titration to other analytical techniques suitable for the quantification of oxygen-containing FG like XPS or temperature-programmed desorption mass spectrometry (TPD-MS), underlining its superior precision [105, 113].

Boehm titration is presently the only electrochemical titration method considered by international standardization organizations like IEC TC 113: *Nanotechnology for Electrotechnical Products and Systems* for surface FG analysis and quantification in the currently evaluated standardization document 62607-6-13: *Nanomanufacturing – Key control characteristics – Part 6-13: Determination of Oxygen Functional Groups Content of Graphene Materials with*

*Boehm titration method*. The main purpose of this document is to provide a standardized method for the determination of surface oxygen FG on graphene materials prepared by, e.g., oxidation-reduction method, solution-phase exfoliation, micro mechanical exfoliation, and organic synthesis using the Boehm titration method and to obtain quantitative information about the acidic oxides at the surface of graphene materials, including carboxy groups (also in the form of their cyclic anhydrides), lactone groups, hydroxyl groups and reactive carbonyl groups.

### FG quantification with photometric and fluorometric assays and different optical reporters

FG quantification with optical spectroscopy relies on the measurement of the absorption (spectrophotometry; photometric or colorimetric assay) or emission (fluorometry; fluorometric assay) of a dye label (also called reporter or probe). Typically, fluorometric measurements are considered more sensitive than photometric measurements, as emission can in principle be detected down to the single molecule level, while absorption measurements utilizing the Beer-Lambert law for quantification commonly require a higher reporter concentration, depending on the reporter's molar absorption coefficient. The dye label is either covalently bound to the FG on the NM surface requiring a reporter with a complementary reactive group, or interacts with the FG electrostatically in the case of adsorption/desorption assays [63]. In all cases, only the number of derivatizable FG is obtained (see also Fig. 1), which can considerably differ from the total amount of FG particularly for higher FG densities or concentrations, as most dye labels are much larger than the FG to be quantified. To correlate the measured optical properties with label

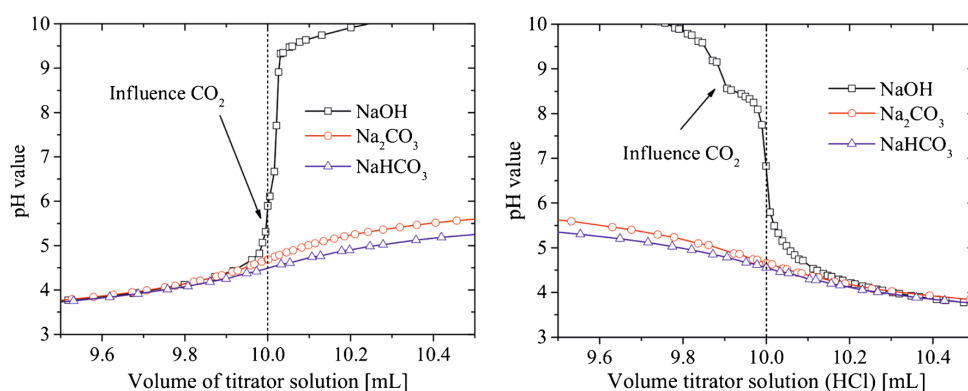


**Fig. 3** Boehm titration curves (potentiometric detection) obtained for the direct titration (**left**) and indirect titration (**right**) with HCl as analyte solution and  $\text{NaHCO}_3$ ,  $\text{Na}_2\text{CO}_3$ , or NaOH as titrant solutions,

underlining the strong impact of  $\text{CO}_2$  from air on the results of the direct approach. Adapted from ref. [105] (CC BY 4.0)

concentration, optical quantification always requires a calibration with a dye closely matching the optical reporter used for FG quantification since the signal relevant optical properties of most reporters are influenced by reporter environment. Calibration can be carried out either with the free (unbound) dye itself, the reacted (bound) dye, or with a model system consisting of the optical label bound to a molecule mimicking the NM surface chemistry, given that the absorption and emission features are closely matching those of the sample.

Optical assays for FG quantification on NM can be distorted by interferences originating from light scattering by the NM, which in turn depends on NM size, excitation wavelength, and the difference in refractive index between the NM and its environment, as well as from NM absorption and/or emission. Only for very small NM (< 25 nm), light scattering is negligible and optical reporters bound to the NM surface can be quantified directly, if the NM does not absorb/emit at the same wavelengths as the dye reporter (spectral discrimination) and if dye-dye interactions at the NM surface can be excluded. For larger particles, light scattering can hamper a reliable and accurate quantification in the presence of the NM. In these cases, the NM has to be removed prior to optical dye quantification by either filtration or centrifugation. Alternatively, the particles must be dissolved, so that only the reporter dyes present in the transparent solution are detected. Also, FG determination via optical reporters can be done by an indirect quantification of unbound labels, or with the aid of cleavable probes and catch-and-release assays where the optical reporter is readout in a transparent solution as detailed in the following sections.

A broad variety of optical assays for different FG on NM and 2D-supports has been developed which utilize different types of absorbing or fluorescent labels. As summarized in Fig. 4, this includes (i) conventional (“always ON”) dyes, (ii) chromogenic/fluorogenic (“chameleon”-type) dyes and activatable (“turn-ON”) dye reporters that change either the spectral position of their absorption and/or emission bands upon reaction with the respective FG or become absorptive (colored) or emissive upon the binding event [64, 114, 115], and (iii) cleavable probes that can be quantitatively cleaved off from the NM surface and subsequently quantified in solution [64, 89]. In addition, (iv) adsorption/desorption assays relying on negatively or positively charged reporters and electrostatic interactions with oppositely charged FG are utilized [116]. These different types of optical assays are subsequently described and compared including representative examples.

### FG quantification with conventional “always ON” dyes

Conventional dyes used for FG quantification on NM are fluorophores with a reactive group that allow for the covalent coupling of the label to the FG on the NM surface. Due to the large toolbox of commercial dyes available from different

fluorophore classes bearing different reactive groups, that were developed for bioconjugation reactions ranging from simple NHS chemistry to biorthogonal reactions and Click chemistry, this approach can be utilized for all types of bioanalytically relevant FG. The optical properties of conventional dye labels such as the spectral position of their absorption and emission bands as well as their absorption and emission intensities, determined by their molar absorption coefficients and photoluminescence quantum yields ( $QY_{PL}$ ) commonly change only slightly upon NM conjugation. The size of such changes, particularly in  $QY_{PL}$ , depend on dye class, the optical transitions involved, and on the length of the linker between the reactive group of the reporter binding to the NM surface and the dye’s chromophore system. This is advantageous and disadvantageous at the same time. As NM-bound dyes and unbound (free) dyes cannot be spectroscopically distinguished, a separation of bound and unbound dye molecules is necessary prior to optical quantification [64].

Conventional dyes have been applied for the quantification of derivatizable FG on various kinds of inorganic, organic, and hybrid NM, e.g., amino groups on a silane surface using a self-made BODIPY dye and a commercial Rhodamine B dye [117], or aldehyde and azide-containing ligands on the surface of CdSe-ZnS QD using 2-hydrozinoipyridine (forming a stable hydrazone chromophore with aldehydes) or an NHS-activated Cy3 dye in conjunction with amino-dibenzocyclooctyne crosslinkers, respectively [118]. Felbeck et al. utilized various NHS-activated conventional dyes to quantify amino groups on the surface of laponite nanoclays modified with 3-(aminopropyl)triethoxysilane (APTES), as shown in Fig. 5 [114]. The authors compared dyes of different charge like the negatively charged hemi-cyanine DY681, the zwitterionic BODIPY 581/591, a neutral dansyl derivative, and the positively charged pyrylium dye Chromeo P503. While charged dyes were prone to aggregation or did not react with the FG on the laponite surface due to electrostatic repulsion, the neutral dansyl dye enabled efficient labeling of the amino groups of APTES.

For conventional dye labels, an indirect quantification, i.e., the quantification of the amount of unbound dye molecules, is recommended as the most effective and reliable way to determine the number of accessible FG [64]. Depending on the NM, alternatively, the dye-functionalized sample can be dissolved after removal of unbound label, followed by optical quantification of the residual reporter molecules. Only if light scattering is negligible (e.g., due to a small NP size) and dye-dye interactions can be excluded (e.g., due to a low FG density on the NM surface), a direct quantification of the particle-bound reporters leads to reliable and accurate results [119]. A strategy to circumvent dye-dye interactions for higher FG densities presents NM labeling with a mixture of dye molecules and non-functional molecules bearing the same reactive group, thereby diluting the dye reporters at the NM surface

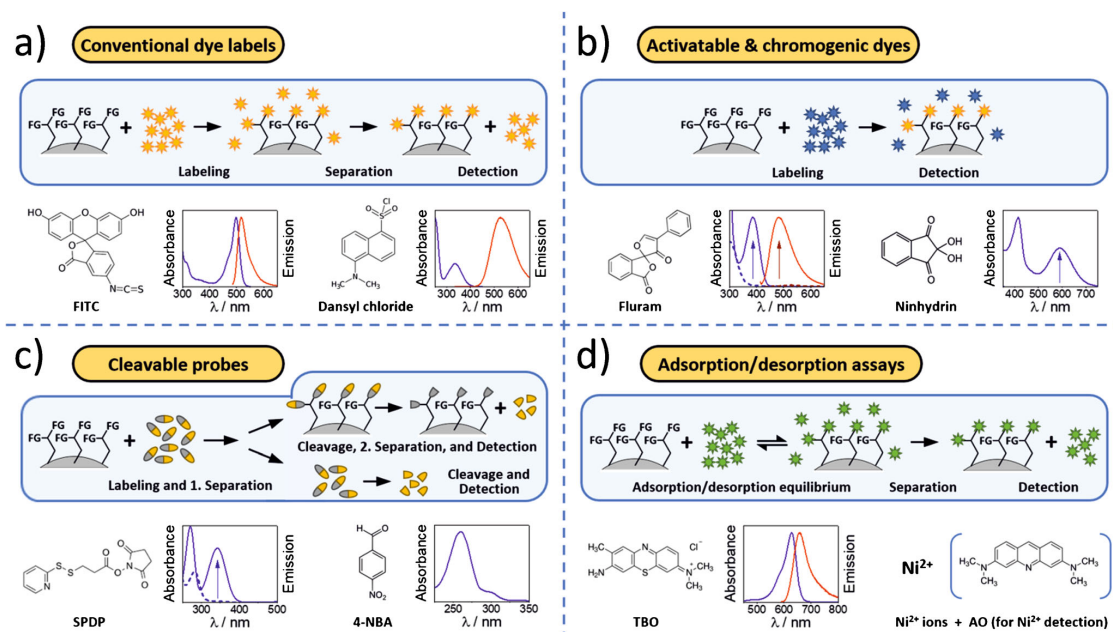


**Fig. 4** Schematic presentation of the working principles of different photometric and/or fluorometric assays for FG quantification on NM using different optical reporters including typical examples for respective dye-based reporters and their absorption and/or emission spectra

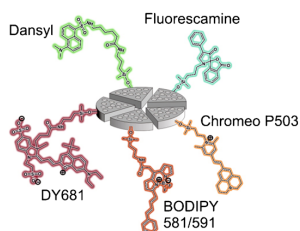
[63]. In this case, FG quantification relies on the assumption of identical coupling efficiencies of both reactants, which needs to be validated individually.

### Activatable (“turn-ON”) and chromogenic (“chameleon”) reporter dyes

Activatable reporters are dye precursors that become strongly absorbing (“colored”) or emissive (so-called turn-ON dyes) after covalent coupling to the respective FG on the NM surface, while chromogenic dyes display significant spectral shifts in their absorption and/or emission bands upon the covalent attachment to FG. The latter dyes are sometimes also referred to as “chameleon dyes.” Well-known examples for activatable dyes utilized as reporters in photometric and fluorometric assays are Ninhydrin (2,2-dihydroxyindane-1,3-

dione) and Fluram (4'-phenylspiro[2-benzofuran-3,2'-furan]-1,3'-dione) that both form optically detectable products upon reaction with primary amino groups.

Ninhydrin, that has been initially used in protein assays, forms the dye Ruhemann's Purple with primary amino groups, absorbing at about 570 nm [120]. The photometrically detectable colored species is released and the absorption measurement is done in the supernatant, thereby circumventing interferences from possible scattering of the excitation light by the NM. As the Ninhydrin reaction is an equilibrium reaction, Ruhemann's Purple is continuously generated in the presence of primary amino groups reacting to aldehyde functionalities, which reduces the impact of steric crowding of multiple Ninhydrin molecules occupying neighboring FG. Ninhydrin was, e.g., used to monitor the reproducibility of silica particle synthesis and their modification with APTES



sample	-NH <sub>2</sub> per disk [disk <sup>-1</sup> ] <sup>a,c</sup>	no. of coupled fluorophores (dye <sub>cou</sub> ) per disk [disk <sup>-1</sup> ] <sup>b</sup>								
		dansyl		fluorescamine		BODIPY		DY681		
		abs	em	abs	em	abs	em	abs	em	
1 L-NH <sub>2</sub>	66	28	23	20	23	2	5	2	<1	nd
2 L-NH <sub>2</sub>	94	39	48	28	35	7	7	3	<1	nd
3 L-NH <sub>2</sub>	115	57	67	29	42	3	7	3	<1	nd
4 L-NH <sub>2</sub>	132	64	74	33	47	4	10	3	<1	nd
5 L-NH <sub>2</sub>	159	64	78	38	55	6	8	3	<1	nd
6 L-NH <sub>2</sub>	420	nd	nd	nd	nd	nd	nd	nd	nd	nd

<sup>a</sup>Adsorbed dyes on unmodified laponite (Figure 3b) were used for the calibration of the optical measurements. <sup>b</sup>Calculated with the assumption of  $5.2 \times 10^{17}$  disks/g; silanization only at the rim of the clay sheets ( $78.5 \text{ nm}^2$ ). <sup>c</sup>Data derived from elemental analysis, i.e., carbon determination ( $n = 3$ ).

**Fig. 5** Quantification of the derivatizable amino groups on APTES-modified laponite disks using differently charged NHS-activated conventional dyes. Reprinted with permission from ref. [114]. Copyright 2015, American Chemical Society

in comparison to NMR measurements [121], and to study the FG density and colloidal stability of surface functionalized silica NP over a period of time of 30 days [122]. Sun et al. compared the quantification potential of two optical assays (Ninhydrin and 4-nitrobenzaldehyde) with  $^{19}\text{F}$  solid state NMR measurements to quantify FG on amino-modified silica NP of different sizes (see Fig. 6) [123].

Fluram, that is also referred to as Fluorescamine, is a colorless dye precursor that forms a yellow product with primary amines with a strong emission between 400 and 600 nm. As the amino group is integrated into the fluorophore in a ring-formation mechanism, the emissive Fluram product needs to be measured directly bound to the NM surface. As unreacted Fluram itself is not emissive, no washing or purification steps are required to remove the unreacted precursor dye prior to assay readout. As the emissive dye product is of limited stability, the assay should be read out at a constant time point after the reaction with Fluram. Moreover, particle light scattering and dye-dye interactions can interfere with the Fluram assay, as has been demonstrated in comparison to the results obtained with the cleavable fluorenylmethyloxycarbonyl protecting group (Fmoc, vide infra) [124]. Fluram was applied to study the influence of the FG density on the biocompatibility of aminated silica NP [125], and to quantify primary amino groups on nanoclays (see Fig. 5) as well as on PS nano- and microparticles [64, 114]. In the latter case, a reliable and accurate FG quantification with the Fluram assay involved the dissolution of the polymer particles in an organic solvent and a correlation of the subsequently detected dye signal with a calibration curve obtained with a suitable model system consisting of the dye bound to a small molecule such as propylamine bearing a primary amino group.

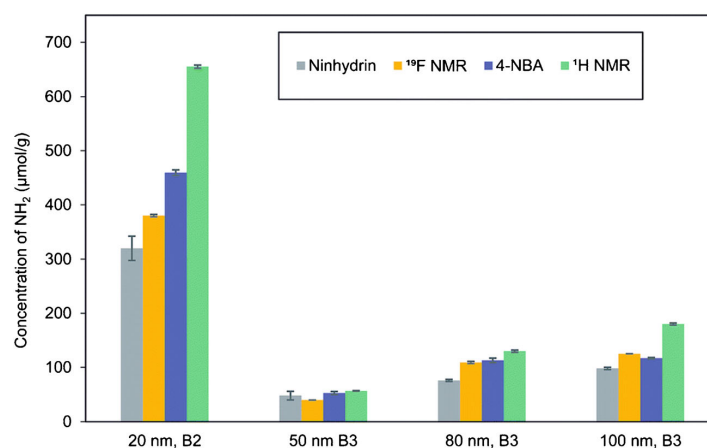
A related method, here for the quantification of thiol groups, is the Ellman's assay which exploits the reaction of 5,5'-dithiobis-2-nitrobenzoic acid (DTNB, also called Ellman's reagent) with thiolate anions to a mixed disulfide

and 2-nitro-5-thiobenzoic acid, which can be detected photometrically at about 410 nm. The Ellman's assay, which has been initially developed for the quantification of thiol groups on proteins, has been used to quantify thiol groups (directly) or maleimide groups (indirectly after reaction with L-cysteine) on functionalized PS particles [126, 127], and to determine the number of thiol ligands like mercaptopropionic acid (MPA) or dithiol dihydrolipoic acid (DHLA) on semiconductor QD and noble metal particles [65, 127].

Chameleon dyes possess an electron-withdrawing group conjugated with the chromophore  $\pi$ -system (e.g., a halogen atom such as -Cl) that is transformed upon the reaction with a FG, e.g., a primary amino group, into an electron-donating group, resulting in strong blue shifts in absorption and emission. The spectral shifts as well as the changes in the molar absorption coefficients and  $QY_{\text{PL}}$  values are considerably influenced by the exact chemical structure of the analyte or FG (i.e., the electron donating amino group-containing ligand) substituting the electron-withdrawing group. Cyanine-based chameleon dyes have been utilized for the labeling and subsequent detection of biomolecules containing primary amino groups [128] and to confirm the amino modification of silica and PS NP both photometrically and fluorometrically [129]. The chameleon dye IR797 was used by us to quantify the amount of accessible amino groups on PS nano- and microbeads [64]. As for activatable reporters, a reliable and accurate FG quantification required the dissolution of the dye-bound particles and a thorough calibration with a suitable model system. Another class of chameleon dyes also suited for FG quantification are pyrylium reporters that react with primary amino groups to form pyridinium dyes with strongly blue shifted absorption and emission bands [115].

The advantage of activatable and chromogenic dye reporters compared to conventional dye labels are the different optical properties of the NM-bound and free dyes, allowing for a straightforward spectroscopic discrimination between

**Fig. 6** Comparison of two optical assays utilizing dye reporters (Ninhydrin, 4-nitrobenzaldehyde) and quantitative  $^{19}\text{F}$  NMR using the F-containing label trifluoromethyl benzaldehyde for FG quantification on amino-modified silica NP of different sizes. Reprinted from ref. [123] with permission from the authors (CC BY-NC 3.0)



these species. For activatable dyes, only a quantification of the NM-bound reporters is possible, which can be hampered by particle light scattering, while for chromogenic labels a spectroscopic quantification of both the NM-bound dyes and the unreacted free dyes is feasible. Moreover, some NM such as metal particles or semiconductor QD exhibit strong absorption and/or emission bands that can interfere with the dye spectra. As for conventional labels, FG quantification requires a calibration curve from a model system with absorption and/or emission properties that closely match those of the NM-bound activatable or chromogenic dyes to consider the environment dependence of the absorption and emission features of the reporter, particularly its  $QY_{PL}$ .

### Labeling with cleavable probes, catch-and-release assays, and indicator displacement assays

Modularly built cleavable probes consist of a reactive group that can be coupled to the FG of interest, a cleavable linker that can be cleaved fast and quantitatively after the conjugation reaction, and a reporter unit subsequently released which can be quantified photometrically or fluorometrically. Suitable cleavable linkers can be taken from established drug release concepts like pH-cleavable hydrazone bonds or reductively cleavable disulfide bridges. Another type of cleavable probes are optically detectable protection groups like Fmoc, which is frequently used to determine resin substitution in solid-phase peptide synthesis. Fmoc can be used for the quantification of amino groups on NM by cleaving off the NM-bound Fmoc protecting groups with piperidine in DMF followed by photometric or fluorometric detection of the released dibenzofulvene-piperidine adduct [130–136]. Meanwhile, variations of the reaction solvent [137] and other suitable detection wavelengths [138] have been reported. To increase the sensitivity of the assays, that was initially read out photometrically, a Fmoc-Cl fluorescence assay was developed that can be performed in aqueous solution. This assay is approximately 50–200-fold more sensitive than the photometric method, but the separation of excess Fmoc-Cl and its strongly fluorescent reaction products is still challenging [124, 139].

We rationally designed the cleavable probes *N*-succinimidyl-3-(2-pyridyldithio) propionate (SPDP) and *N*-(aminoethyl)-3-(pyridin-2-yl)disulfanyl-propane amide (*N*-APPA) by combining a reactive NHS- or amino group, a reductively cleavable disulfide linker, and a simple 2-thiopyridone reporter unit. [64] To demonstrate the advantages of these cleavable probes, we compared their performance with that of conventional dye labels and activatable/chromogenic reporter dyes (vide supra) for the quantification of amino and carboxy groups on PS nano- and microparticles, as shown in Fig. 7. This comparison confirmed the advantages of SPDP and *N*-APPA for FG quantification, i.e., the possibility for determining mass balances and a straightforward

method validation with other analytical methods like  $^{32}S$  ICP-OES. These cleavable probes are also suited for quantifying amino and carboxy groups at various FG densities and even on absorbing and fluorescent NM like dye-stained fluorescent particles.[89]. Moreover, this design principle can be easily adapted to other FG. For example, we developed the SPDP derivative 3-(2-pyridyldithio)propionyl hydrazide (PDPH) bearing a reactive hydrazide group for the quantification of aldehyde groups on a set of PMMA microparticles [140]. Validation was done by comparison with another catch-and-release assay utilizing a hydrazide-functionalized fluorescent BODIPY dye (BDP-hzd) as reporter that proved to be even more sensitive due to the fluorometric readout.

Other examples for optical assays utilizing cleavable probes present the use of 7-methoxycoumarin-3-carboxylic acid conjugated to an alkyne group for the fluorometric quantification of azide groups on solid substrates, silica particles, and biomolecules after cleaving off the dye under basic conditions [141], and the use of 4-nitrobenzaldehyde (4-NBA) for the photometric quantification of amino groups on silica particles of different sizes (see Fig. 6) after dye hydrolysis [123]. A similar type of assay that also relies on reporter detection in solution after particle removal is the so-called indicator displacement assay that exploits supramolecular host-guest chemistry, e.g., the competitive binding of the reporter dye acridine orange (AO) and the high affinity guest aminomethyladamantane (AMADA) to the macrocycle host cucurbit[7]uril (CB7) for the optical quantification of azide groups on PMMA particles [142].

Cleavable probes and catch-and-release assays are ideally suited for FG quantification on NM, since quantification of both the unbound (unreacted) dye and the initially particle-bound reporter (after cleavage) can be performed in solution after removal of the NM. Hence, these methods allow for FG quantification without interferences from light scattering, absorbing and/or emitting NM, or dye-dye interactions of surface-bound reporters. The cleavable reporter approach enables to generate a mass balance from the known amount of applied label and the measured amount of unbound and bound reporters, which increases the accuracy and reliability of this FG quantification method and simplifies method validation. In addition, the modular design of the cleavable probes offers the opportunity to specifically choose the reactive group, the cleavable linker, and the reporter unit according to the desired application and sample-specific requirements (specific type of target FG, limitations due to particle material-related properties, etc.).

### Optical adsorption/desorption assays

Alternatives to optical assays involving covalent labeling are adsorption/desorption assays with photometric or fluorometric readout. In an adsorption/desorption assay, optically

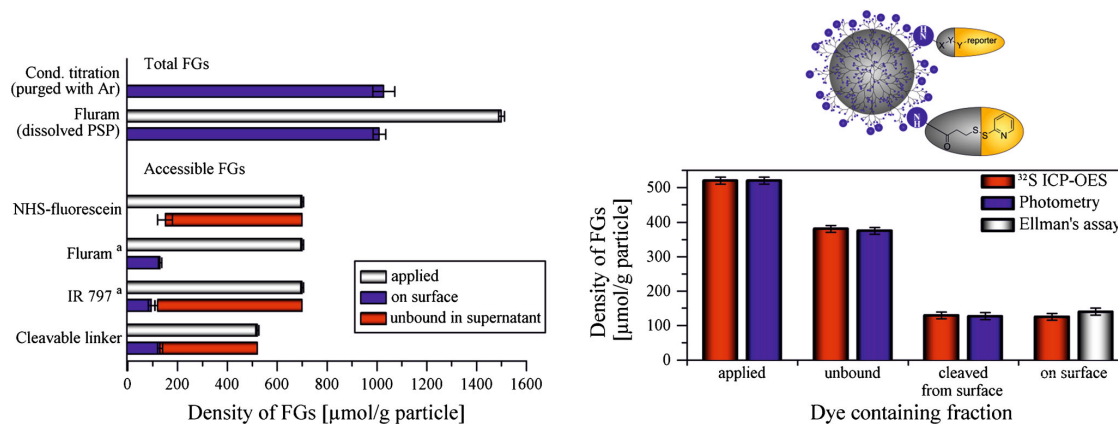


**Fig. 7** Comparison of optical FG quantification using cleavable probes, conventional dyes, and activatable/chromogenic reporters. Validation of the former approach was done with ICP-OES and the Ellman's assay.

detectable reporter dyes or, less common, small metal ions with charges complementary to that of the FG of interest, are allowed to adsorb at the charged NM surface. The reporters must not bear a reactive group and should not penetrate the particle matrix. Subsequently, non-adsorbed probe molecules are removed by several washing steps, followed by quantitative desorption of the adsorbed reporter by addition of a surfactant. Then, the desorbed reporter is quantified photometrically or fluorometrically in the supernatant after removal of the NM by centrifugation or filtration. In the case of metal ions, with few exceptions [143], optical detection is achieved by addition of an indicator dye that forms a colored or fluorescent product of defined stoichiometry with the metal ion. Alternatively, the non-adsorbed amount of the reporter can be quantified after removal of the NM containing the fraction of the adsorbed reporter. In conjunction with a fluorescent dye and readout with fluorescence microscopy or flow cytometry, also the amount of particle-adsorbed fluorophore can be measured directly [144]. The use of metal ions as reporters in adsorption/desorption assays for charged FG like carboxy and amino groups exploits the much smaller size of metal ions compared to organic dyes which is expected to provide a reporter-to-FG stoichiometry close to 1, and thus, a number of (accessible) FG approaching the total number of FG.

A popular dye-based adsorption/desorption assay for the photometric quantification of carboxy groups is based on the cationic dye toluidine blue (TBO) that displays an intense blue color with an absorption maximum at around 630 nm [63]. An example for a dye-based adsorption/desorption assay with fluorometric detection utilizes the red emissive cyanine-type nucleic acid stain SYTO-62 [144]. Metal ion-based adsorption/desorption assays have been reported by several research groups, e.g., using  $Mg^{2+}$  ions to quantify tryptophan

ligands on gold NP [143], or  $Ni^{2+}$  ions to quantify carboxy groups on polymeric microparticles [116, 145].

Advantages of adsorption/desorption assays are their simplicity, as they are in principle suitable for all types of NM bearing charged FG independent of their chemical composition, if dye penetration into the NM matrix can be excluded. Thus, such assays are not suited for porous materials like mesoporous silica NP. They are very versatile and require only one calibration for different NM samples. A drawback presents the time-consuming washing steps needed for quantitative dye desorption. Moreover, as typically more than one FG interacts with one reporter molecule, FG quantification requires the determination of a stoichiometry factor by comparison with the results obtained by another method yielding the total number of FG [63]. This stoichiometry factor is most likely NM-specific, which can affect the reliability of FG quantification with this type of assay without a thorough validation. Adsorption/desorption assays are well suited for quality assurance and process control (including control of product reproducibility) of NM bearing charged FG as well as the monitoring of aging effects affecting surface FG, as such conclusions can be drawn based upon relative comparisons.

### Other methods for FG quantification on nanomaterials

Other analytical techniques used for FG analysis and quantification on NM surfaces include NMR spectroscopy, ICP-MS and ICP-OES, IR and Raman spectroscopy, X-ray-based methods such as XPS and XRF, as well as thermal analysis methods and elemental analysis [18, 23, 51]. Depending on the chemical nature of the NM and the FG of interest, these

analytical techniques can either utilize intrinsically present moieties (label-free methods) or specific reporters (label-based methods) for signal generation and quantification, and thereby, provide the total or derivatizable number of FG. These analytical methods are very valuable tools for FG quantification and for validation of the results obtained with simpler methods (method validation). A straightforward approach to simplify method comparisons for method validation and calibration is the utilization of multimodal labels and reporters that are designed for the readout by different analytical techniques relying on different signal generation principles. Multimodal reporters can be realized, e.g., by including heteroatoms like sulfur, nitrogen, fluorine, or certain metal ions into molecular labels like organic dyes used for chemical derivatization reactions or reporters utilized for the design of cleavable probes. In the following, also examples for this strategy including its use to provide a traceability chain of FG quantification to the SI unit mole are highlighted.

### Nuclear magnetic resonance spectroscopy

Nuclear magnetic resonance (NMR) spectroscopy measures the intrinsic magnetic moments of certain nuclei such as hydrogen ( $^1\text{H}$ ), carbon ( $^{13}\text{C}$ ), fluorine ( $^{19}\text{F}$ ), or phosphorus ( $^{31}\text{P}$ ) in the presence of a strong magnetic field. NMR spectroscopy can provide chemical, physical, and structural information about the NM, its organic ligand shell and surface FG, as well as information on dynamic interactions with the environment [146]. Moreover, it can distinguish between surface bound and free (excess) ligands which has been exploited to gain a deeper understanding of the NM-ligand interface including ligand binding sites and dynamics, particularly for semiconductor QD with their surface-dependent luminescence properties [29, 147–150].

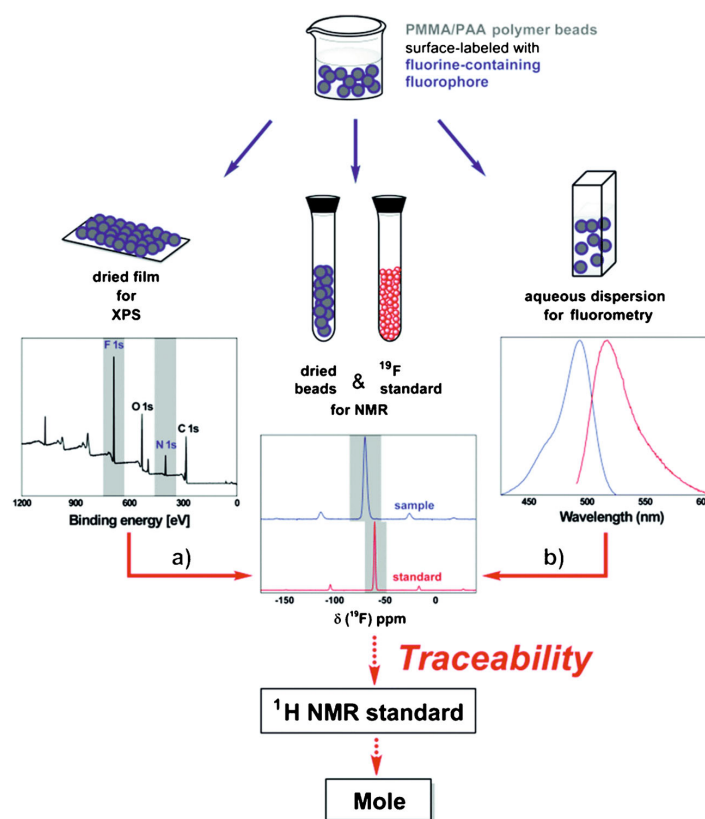
The quantification of FG and ligands on NM surfaces can be carried out by solution phase NMR techniques and by solid-state NMR. It typically involves the addition of an internal standard of known concentration and known, high purity, that is chosen to reveal NMR signals (chemical shift) well separated from the NMR signals originating from the FG or ligands of interest and the matrix [51, 89]. Particularly for solution NMR, it must also be considered that the NMR signals of the FG or ligands bound to a NM surface can significantly change compared to the signals of the free molecule or FG in solution. The NMR signals obtained typically show differences in both chemical shift and linewidth due to homogeneous and/or inhomogeneous line broadening, which can hamper peak assignment and integration [151]. The size of such effects depends on NM size. Since the percent weight of the bound surface ligands decreases with increasing particle size, quantification of larger size NM can require a relatively large amount of sample compared to other analytical methods. To overcome these limitations,

dissolution methods for FG and ligand quantification prior to NMR analysis have been developed [121, 152]. Particularly for organic polymer particles, the distinction of NMR signals originating from surface FG and the NM matrix can present a challenge, which can be met by using isotope-enriched reagents for surface functionalization [63], or by applying a multi-Lorentzian-splitting algorithm [153]. Also, combinations of multinuclear and multidimensional NMR techniques are a promising approach to identify and quantify FG/ligands, and to study their interaction with and binding to the NM surface [154–156].

Quantitative NMR (qNMR) is particularly attractive for FG quantification, due to its potential for an absolute quantification. Moreover, it can provide traceability to the SI unit mole if suitable calibration materials of very high and known purity are available [157, 158]. For instance, qNMR was used to study the FG or ligand density on gold NP [159, 160], semiconductor QDs [161], and silica NPs [123, 162]. However, qNMR requires special measurement conditions. Prior to collecting NMR spectra, the  $T_1$  relaxation times of the components must be determined with a series of inversion-recovery experiments. These  $T_1$  times then have to be considered for the recording of the NMR spectra used for signal quantification which commonly requires a relatively high number of scans, and thus, elongated measurement times. For data evaluation, the integral values of the evaluated signals must be baseline-corrected and the purity of the internal standard added in a precisely known amount must be determined, for example by comparing its NMR signals to that of a reference material of certified purity. Despite the need for expensive equipment operated by well-trained scientists, qNMR has become increasingly popular for the quantification of FG on NM due to its inherent chemical selectivity and the provision of the total number of FG without the need for a calibration curve. Also, this technique is increasingly used for the calibration and validation of other more simple analytical methods, particularly for NM where electrochemical titrations cannot be utilized due to interferences from the NM matrix, or for the quantification of FG that are electrochemically not accessible. For example, the quantification of carboxylate and amino functionalities on silica NM is not feasible by electrochemical titrations as the  $\text{pK}_a$  values of the inherently present silanol groups and carboxylate groups cannot be well separated and as silica NM dissolve at alkaline pH. Here, qNMR is the method of choice for the quantification of the total amount of carboxylate and amino groups [89, 123, 156, 163, 164].

An example for a possible traceability chain for FG analysis with different analytical methods including NMR is shown in Fig. 8, using multimodal reporters that can be read out by different analytical techniques, here solid-state  $^{19}\text{F}$  NMR, emission spectroscopy, and XPS, and a certified NMR reference standard containing both  $^{19}\text{F}$  and  $^1\text{H}$  [157, 158].

**Fig. 8** Example for a traceability chain for FG quantification, linking measurements (blue arrows) of XPS (a) and fluorometry (b) to quantitative solid-state  $^{19}\text{F}$  NMR (solid red arrows). The use of a certified NMR reference standard containing both  $^{19}\text{F}$  and  $^1\text{H}$  provides the link to the SI unit mole (dotted red arrows). Reprinted from Ref. [158] (CC BY 3.0 unported)



### Mass spectrometry and atomic spectroscopy

Mass spectrometry (MS) and optical emission spectroscopy (OES; also referred to as atomic emission spectroscopy, AES) can quantitatively measure the total number of atoms of certain elements within a sample. This can be utilized for the quantification of surface FG and ligands on NM as well as for the determination of NP concentration. Typically, both techniques use inductively coupled plasma (ICP) to produce excited atoms and ions, which are then identified based upon their characteristic mass-to-charge ratios (ICP-MS) or atomic spectral emission lines (ICP-OES). ICP-MS and ICP-OES directly measure the element concentration with unparalleled sensitivity over a wide linear dynamic range regardless of NM size or surface chemistry down to the parts-per-trillion level. However, the achievable detection limits (LOD) depend on the element(s) of interest, instrument, experimental conditions, and possible spectroscopic interferences between the analyte elements. For NM analysis, ICP-MS and ICP-OES are often used in connection with an upstream particle separation method like high performance liquid chromatography

(HPLC) or asymmetric flow field-flow fractionation (AF4) [165–170].

ICP-MS and ICP-OES are often applied to determine the NM concentration from the measured element concentration of the sample in combination with the known NM dimensions, typically determined with sizing techniques such as TEM, SAXS, DLS, or NTA [166, 171, 172]. However, both methods can also be applied to detect elements that directly correspond to ligands and FG native on the NM surface, and thus, the total amount of FG, or to detect specific labels conjugated or associated to the FG, and hence, the number of derivatizable FG. Examples for the latter case present the quantification of elements such as sulfur present in certain dyes or cleavable probes [64, 89, 127], or the use of metal ion containing reporters [173]. ICP-OES has been used to quantify FG on various NM such as carbon-based NM, noble metal NP, polymer beads, and lanthanide-based NP [127, 174–177]. ICP-MS has been frequently used to quantify FG-bearing ligands on gold NP [169, 173, 178–180], but has also been applied to quantify FG and ligands on other NM such as silica NP, polymeric beads, and semiconductor QD [126,

166–168]. Particularly single-particle ICP-MS (sp-ICP-MS) is a promising technique as in principle it allows to simultaneously measure the particle number concentration and the number of FG/ligands on the surface of individual particles. However, especially for light elements often present in commonly used organic FG and ligands, that are difficult to ionize (large ionization potential) and are prone to a high background, quantification is very challenging and detection limits are higher compared to other heavier elements. Further instrument improvements and methodological advances can make sp-ICP-MS a very well-suited method for NM characterization [181–183].

In principle, atomic absorption spectroscopy (AAS) with either flame-based or electrothermal (graphite tube) atomizers can also be used to quantify FG and ligands, but as AAS is mostly limited to metallic and semi-metallic elements that are typically not present in organic ligands and surface groups, this technique is of very limited use for FG analysis [184]. However, there exists a special AAS technique that is very sensitive to fluorine [185], which can be utilized for the quantification of FG derivatized with fluorine-containing labels, such as BODIPY dyes for the validation of optical assays or other elemental tags bearing  $\text{CF}_3$  groups for the comparison with XPS measurements or  $^{19}\text{F}$ -NMR (see Fig. 8).

Other MS methods that can also be used for NM surface characterization, but are not further detailed here, are time-of-flight secondary ion mass spectrometry (ToF-SIMS) and matrix-assisted laser desorption/ionization (MALDI) in combination with time-of-flight (ToF) analysis of the released ions by mass spectrometry (MALDI-ToF-MS). These methods can provide molecular information of FG and surface bound molecules [186–188], but up to now, have been rarely utilized for NP analysis.

### Vibrational spectroscopy

Vibrational spectroscopy measures the absorption or (inelastic) scattering of incident light due to vibrational stretching and/or bending modes of molecules within a sample. Infrared (IR) spectroscopy relies on the absorption of IR radiation, typically in a wavelength region between 2500 nm and 25  $\mu\text{m}$  (4000–400  $\text{cm}^{-1}$  on the wavenumber scale). The fundamental vibrations of most chemical bonds occur within this spectral region. IR spectroscopy is frequently being used for qualitative and quantitative analysis of organic compounds in agriculture, food products, polymers, pharmaceuticals, cosmetics and the petroleum industry as well as for the monitoring of chemical reactions in process analysis [189–191]. Nowadays, commonly Fourier-transform infrared (FTIR) spectroscopy is used, allowing for the simultaneous detection of all vibrational frequencies [192, 193]. Raman spectroscopy is a complimentary vibrational spectroscopic technique, which detects inelastically scattered photons (Raman

scattering) from a monochromatic light source (usually a laser) in the near-UV to near-IR range. Due to the different selection rules valid for both methods, Raman spectroscopy yields similar—yet complementary—information compared to IR spectroscopy [194]. Both methods are relatively fast and non-destructive, and can be coupled with other analysis methods. For FG and ligand analysis on NM, surface-sensitive variants of these techniques are of particular importance like attenuated total reflection (ATR-) FTIR [195, 196], diffuse reflectance infrared Fourier transform spectroscopy (DRIFTS) [197, 198], and surface-enhanced Raman spectroscopy (SERS) [199–201]. While SERS is limited to electrically conducting materials such as graphene or noble metals, FTIR spectroscopy is frequently employed to study a wide range of NM. Both DRIFTS and ATR-FTIR overcome the shortcomings of sample preparation complexity in classical FTIR spectroscopy, and ATR-FTIR further allows in situ characterization of particle surfaces in biologically and environmentally relevant media [196]. Although vibrational spectroscopy is widely accepted for qualitative analysis of NM surfaces [202–205], there are only few literature reports on the application of these methods for quantitative analysis. Nevertheless, with modern instrumentation and combined approaches, the quantitative determination of FG and ligands at the nano- to picogram level should be feasible [206, 207]. Examples for FG determination with ATR-FTIR spectroscopy include the measurement of the density of thiol and bromoalkyl FG on silica particles [208] and the amount of APTES on silica-coated iron oxide NP [209]. Furthermore, ATR-FTIR can be applied to characterize and (semi-)quantify the chemical composition of mixed ligand layers at NM surfaces [210, 211]. To quantify FG and surface ligands with FTIR spectroscopy, a calibration curve is generally required and samples that obey the Beer-Lambert law. A combined use of chemometric tools such as convolutional neural networks and ensemble learning, with different vibrational spectroscopy techniques, might contribute to an increased accuracy of quantitative FG analysis in the future [212].

### X-ray-based methods

X-ray photoelectron spectroscopy (XPS) measures the number and kinetic energy of electrons that escape from the near-surface region of a sample, like a planar substrate or particles deposited on a substrate, up to an information depth of 5–10 nm upon irradiation with an X-ray beam in vacuum. In laboratories, typically Mg  $\text{K}\alpha$  or Al  $\text{K}\alpha$  sources with photon energies of 1253.6 eV or 1486.6 eV are used. The information depth of XPS is determined by the inelastic mean free path (IMFP) of the photo-excited electrons in solid matter. Using higher photon energies between 3 and 15 keV as in hard X-ray photoelectron spectroscopy (HAXPES) can extend the information depth up to about 100 nm [213]. XPS measurements

provide information on surface composition, the enrichment or depletion of elements at the surface, the presence and/or thickness of coatings, and the chemical states of the elements [23, 214, 215]. Therefore, information on the chemical composition and amount of FG or certain chemical species at the particle surface can be obtained [216]. Due to the sensitivity of XPS for all elements except H and He, not only inorganic surface coatings, passivation shells, and surface modifications by chemical processes like oxidation or etching can be determined [217–219], but also organic coatings, ligands, and surface-bound biomolecules [220, 221]. Depending on the chemical composition of the sample and the surface ligands or FG, XPS can be done without the need for a label. A reliable quantification requires calibration with suitable reference material or standards [222]. Alternatively, theoretically derived values for the cross sections (Scofield factors), the IMFP and the transmission function of the spectrometer can be used [214, 223–225]. It must be noted that all these quantification procedures are only valid to homogeneous planar surfaces; however, there are different approaches which can be used for NP [214]. To enhance the sensitivity and selectivity of XPS and/or to enable the comparison with other more quantitative methods like NMR for method calibration and validation, for example fluorine-containing reactive labels like 3,5-bis(trifluoromethyl)phenyl isothiocyanate [226], trifluoroacetic anhydride (TFAA) [227], and 2,2,2-trifluoroethylamine (TFEA) [158] can be employed for the chemical derivatization of specific surface FG like amino, hydroxyl, and carboxy FG, respectively. The use of TFEA to quantify the amount of carboxy groups on PMMA particles with a grafted shell of PAA also provides a link to the SI unit mole, as shown in Fig. 8 [157, 158].

In the last years, an increasing number of examples for the applicability of XPS to determine the elemental distribution of small inorganic NM and the chemical surface modification of various NP by light-induced chemical changes, ligand exchange, or the presence of certain species like chloride ions has been reported [23, 28, 219, 228]. XPS was also used to derive the thickness of inorganic passivation shells, e.g., on semiconductor QD like CdSe/CdS by simulation of the spectra [214]. As the size of many NM is larger than the XPS information depth, and as NP size, shape, and morphology determine the fraction of surface elements accessible within this information depth, the use of XPS for the quantification of NM ligand shells and FG is challenging and requires mathematical modeling of the measured data, e.g., with a software like SESSA (Simulation of Electron Spectra for Surface Analysis) [229], thereby also considering the size- and shape-dependent curvature of the NM surface. New approaches for the quantification of XPS at nanostructured materials take these effects into account, but further developments are necessary for more complex materials [214, 230–233]. Another challenge of XPS measurements is the

need of an appropriate sample preparation and handling to prevent changes of the NM due to undesired influences from the surrounding of the particles [23]. Also, NM agglomeration and aggregation as well as decomposition or changes induced by the X-ray beam can influence the reliability of the obtained results.

Another X-ray based analytical technique that is in principle capable of quantitatively measuring the elemental composition of a sample presents X-ray fluorescence (XRF) spectroscopy, which detects the secondary (“fluorescent”) X-rays emitted from a material after excitation with high-energy X-rays (or sometimes gamma rays) using either energy-dispersive (EDXRF) or wavelength-dispersive (WDXRF) spectroscopy [234]. As the secondary radiation from lighter elements (with  $Z < 12$ ) is of relatively low energy ( $< 3$  keV) and has a low penetration depth, it is often reabsorbed by the sample and severely attenuated by any matter between the sample and the detector. Hence, XRF is usually only applied to characterize the chemical composition or impurities on inorganic materials such as metal, glass, ceramic, and semiconductor surfaces, films, or layers. However, using vacuum technique, synchrotron radiation, and/or special detector windows also lighter elements such as carbon, nitrogen, oxygen, and fluorine can be detected [234–236]. Particularly the surface-sensitive methods total reflection X-ray fluorescence (TXRF) and grazing-incidence X-ray fluorescence (GIXRF) spectroscopy using X-ray standing waves (XSW) are principally well suited for a reference-free quantification of FG on NM [237–239], but for particle samples additional corrections are necessary to account for absorption and shadowing effects occurring on the nanostructured surfaces [240].

#### Other techniques to determine the total number of FG

Other techniques that can be applied for FG and ligand characterization and are more or less well suited for a quantitative analysis include elemental analysis (EA), thermal analysis methods such as thermogravimetric analysis (TGA) and differential scanning calorimetry (DSC), and separation techniques like asymmetrical flow field-flow fractionation (AF4).

EA is an inexpensive method to determine the elemental composition of a material by combusting the sample under controlled conditions and analyzing the combustion products quantitatively. Particularly the so-called CHNS analysis, that provides the mass fractions of carbon, hydrogen, nitrogen, and sulfur via their combustion gases under high temperature and high oxygen conditions (converting these elements to their oxidized form, i.e., to  $\text{CO}_2$ ,  $\text{H}_2\text{O}$ ,  $\text{NO}$  or  $\text{NO}_2$ , and  $\text{SO}_2$ , or reducing, e.g.,  $\text{NO}$  or  $\text{NO}_2$  to  $\text{N}_2$ ), is in principle well suited for FG or ligand quantification on NM, as long as the NM matrix does not contain the FG-specific element(s). These gases are then detected by a thermal conductivity detector that typically is calibrated daily with suitable standards or reference

materials. However, CHNS analysis has only rarely been used for FG quantification, e.g., for carboxy groups on alumina particles, [241] or amino groups on graphene oxide [242] as well as silica particles [243, 244], due to relatively large amounts of sample needed and the relatively low detection sensitivity compared to other methods like ICP-MS [126]. For NM characterization, CHNS analysis is often used only in conjunction with other analytical methods such as FTIR, TGA, or XPS [126, 242, 243, 245].

TGA and DSC are typically used to obtain information on the thermal stability, chemical composition, and purity of a sample as well as on kinetic parameters. DSC can also be employed to determine phase transitions, e.g., of liquid crystals. TGA detects the resulting mass changes as a function of temperature under defined conditions, while DSC measures the difference in the amount of heat required to increase the temperature of the sample [246]. Recent results of the EU funded project *ProSafe* identified TGA as a very useful, simple, and reliable method to study the surface chemistry particularly of inorganic NM like silica, metal, and lanthanide-based NP as well as QD [247]. For TGA measurements, no complex sample preparation is needed. However, due to the underlying measurement principle, all contaminants present in the sample such as remaining dispersion media/solvents, impurities originating from NM synthesis, and free ligands/molecules can contribute to the mass changes, and thus, influence the results. Therefore, a careful work-up and clean-up procedure of the NM sample to be analyzed is mandatory. Also control samples and precise heating steps at lower temperatures are often included to overcome the inherent challenge of undesired mass contributions from matters other than the organic surface ligand/FG [164, 248]. Another drawback is the amount of NM needed for a single TGA analysis, i.e., commonly several milligrams, which can make TGA less suitable for small-scale samples of functionalized NM used in biomedical applications. Modern TGA methods address these limitations by a higher sensitivity. Mansfield et al. [246] developed a micro-scale TGA method ( $\mu$ -TGA) using a quartz crystal microbalance, that needs a 1000-fold reduced amount of sample. With this method, the authors could obtain results for commercial CNT, polymer-coated gold NP as well as polymer-modified gold/silica NP which were comparable with those determined by conventional TGA [246, 249, 250]. They also used  $\mu$ -TGA to quantify the amount of surface-bound poly-L-lysine and DNA on gold NP intended for potential use in biomedical applications [250]. Another advanced TGA approach presents the coupling with mass spectrometry (TGA-MS) or FTIR spectroscopy (TGA-FTIR) to enable the identification of the species responsible for the observed mass loss upon heating. For example, TGA-MS has been used to determine the amount of aromatic molecules adsorbed on CNT [251] and to identify the organic compounds extractable from various NM [252]. Moreover, TGA has been used in multi-method

approaches for quantitative analysis to enhance the reliability of the results by comparing them with information from FTIR, NMR, ICP-MS/OES, and XPS measurements [164, 175, 186, 253–256]. And just recently, TGA has been applied to quantify adsorbed citrate molecules on the surface of gold NP, which provided new insights into mechanistic details of the well-known *Turkevich* gold NP synthesis method [257].

As the density of FG/ligands on the NM surface determines its charge and hydrophilicity/hydrophobicity, also NP separation techniques like AF4, a fractionation method that is used for the characterization of polymers, proteins, and NP, coupled with capillary electrophoresis (CE) can be used for FG quantification. Combining AF4 and CE provides separation by size and surface charge. The correlation of these parameters requires a calibration curve with similarly sized particles of known FG density to correlate the CE retention times with FG density [258]. This method is, however, only suited for surface FG that control particle charge, e.g., for (de)protonable functionalities such as carboxylic acids and amines. Moreover, in addition to the method-inherent limitation of AF4, this method combination faces the same limitations as electrochemical titration methods, except for signal contributions from the presence of other (de)protonable molecules due to the coupling with a NP separation technique.

## Conclusion and future challenges

All analytical techniques presented here for the analysis and quantification of functional groups (FG) and ligands on nanomaterial (NM) surfaces possess specific method- and material-related requirements and limitations. For a straightforward, efficient, and reliable quantification of FG and ligands on NM, these parameters need to be considered. Also, the distribution of NM size, shape, and surface morphology must be taken into account for a thorough determination of the FG/ligand density (number of FG/ligands per particle or surface area), which can vary from particle to particle in a NM population. In addition, it must be kept in mind whether the total number or the derivatizable number of FG is desired for which purpose/application and with which uncertainty. For example, quality control during NM fabrication and surface modification or the bioconjugation of NM reporters to bioligands for fluorescence assays do not necessarily require the knowledge of the total number of FG. For the production and characterization of nanoscale reference materials, e.g. as negative and/or positive controls in toxicity tests or for the application in the health sector or as food additives can impose more stringent requirements on NM characterization. To provide guidelines for the choice of the optimum method(s), an overview of the most relevant criteria for the choice of suitable methods for FG and ligand quantification on NM is summarized in Table 1.

**Table 1** Overview of the analytical methods for FG and ligand quantification on NM covered by FG or derivatizable FG). Important parameters such as the necessity of a label, sample this review, classified according to their signal generation principle and utilized reporters, with requirements, and the need for method calibration are also summarized

Analytical method	Description/reporter (Examples)	Functional groups/Ligands		Requirements		Ref.
		Target	Type	Label	Calibration	
Electrochemical titration	Electrochemical potential as function of added $H^+/OH^-$	All (de)protonable FG (e.g., -COOH, -NH <sub>2</sub> , -SH)	Total FG	Label-free	Aqueous dispersion, free of (de)protonable contaminants	[75–88]
Conductometric titration	Conductivity as function of added $H^+/OH^-$	All (de)protonable FG (e.g., -COOH, -NH <sub>2</sub> , -SO <sub>3</sub> )				[63, 64, 89–100]
Boehm titration	Potent. titration with bases of different $pK_{in}$ , back titration of residual titrant	Oxygen containing, acidic FG				[101–113]
Optical spectroscopy	Labeling with conventional dyes	Corresponds to reactive group of the label (e.g., -NH <sub>2</sub> , -COOH, -N <sub>3</sub> )	Derivatizable FG	Dye labeling	Aqueous dispersion, free of contaminants bearing the same FG	[63, 64, 114, 117–119]
	Activatable or chromogenic dyes	Corresponds to reactive group of the dye (e.g., -NH <sub>2</sub> , -SH)		Dye formation upon reaction	Calibration required: Knowledge of the reporter's optical properties used for quantification ( $\epsilon_\lambda$ and/or $\Phi_{rel}$ ) needed	[64, 65, 114, 115, 120–129]
	Cleavable reporter	Fluorim, Ninhydrin, Ellman's reagent		Labeling and release of dye reporter		[64, 89, 123, 124, 130–142]
	Adsorptive reporter	Fmoc, SPDP, 4-NBA	Total FG or derivatizable FG <sup>a</sup>	Adsorption/desorption equilibrium	Aqueous dispersion	[63, 116, 143–145]
Other analytical techniques	NMR	Toluidine Blue, Ni <sup>2+</sup>	Total FG or derivatizable FG <sup>a</sup>	Label-free or reporter-based <sup>b</sup>	Dispersion in deuterated solvent, or solid state	[29, 51, 63, 89, 121, 123, 146–164]
	ICP-MS/OES/AAS	Incl. quantitative solid-state NMR	FG containing elements with intrinsic magnetic moment ( <sup>1</sup> H, <sup>13</sup> C, <sup>19</sup> F, <sup>31</sup> P)	Label-free or reporter-based <sup>b</sup>	Any physical state	[64, 89, 126, 127, 165–188]
	FTIR/Raman	Incl. coupled techniques and single particle ICP-MS	Most elements, but not H, C, N, O; is often used to determine NM conc.	Label-free or reporter-based <sup>b</sup>	Any physical state, free of contaminants	[189–212]
	XPS/XRF	Incl. ATR-FTIR, DRIFTS, and SERS	All FG with IR/Raman-active transition bands	Label-free or reporter-based <sup>b</sup>	Calibration or chemometric tools required	
	TGA/DSC	Incl. HAXPES and TXRF/GIXRF	All elements except H, He, Li	Label-free or reporter-based <sup>b</sup>	Sample deposited on planar substrate	[23, 28, 157, 158, 213–240]
	EA	Thermal analysis (mass change or heat quantity)	In principle all organic FG/ligands	Label-free	Powder, dispersion, film (TGA), or gel (DSC); free of contaminants	[164, 175, 186, 246–257]
		Quantitatively analysis of combustion products	C/H/N/S-containing FG, O and F also possible	Label-free	Any physical state	[126, 241–245]

<sup>a</sup> Depending on the size of the adsorptive reporter: small metal ion reporters will yield the total number of FG (or a value very close to this number), while larger dye reporters will yield a lower number of derivatizable FG

<sup>b</sup> Depending on the chemical nature of the NM and the FG of interest, either intrinsically present moieties (label-free) or specific reporters (label-based methods) can be utilized for signal generation and quantification, yielding either the total or the derivatizable number of FG

Electrochemical titration methods are inexpensive, rapid, require only simple and widely available laboratory instrumentation, and can be performed by technical staff under ambient conditions at constant temperature. Also, data interpretation is comparatively easy and straightforward. This makes these methods well suited for routine analysis as well as production and quality control of synthesized or functionalized NM. Sometimes the removal of CO<sub>2</sub> from air is mandatory by purging sample solutions and dispersions with nitrogen or argon. Moreover, it must be assured that complete (de)protonation has been reached after each titration step. All electrochemical methods provide the total amount of the FG of interest present in the sample, i.e., on the NM surface, as the reporters used for signal generation, namely protons or hydroxide ions, are very small [64, 89]. This has been verified, e.g., by comparing the results from conductometry and quantitative solid state NMR measurements [63]. In principle, also the number of derivatizable FG can be obtained via electrochemical measurements by comparing the results prior to and after FG derivatization, combining electrochemical titrations with other quantification methods such as optical spectroscopy utilizing dye reporters. A general drawback of electrochemical methods is their lack of specificity and selectivity, as they measure all (de)protonable species with comparable  $pK_a$  values present in the sample, and hence, not necessarily only the number of FG on the NM surface. As previously mentioned, other species remaining from NM synthesis like surfactants, initiators, stabilizers, or excess ligands with (de)protonable groups can also contribute to the measured signals, and thus, can distort the obtained results if not removed prior to analysis. Also, other (de)protonable FG on NM can interfere with the signals originating from the target. For example, for NM bearing a mixture of different types of FG like carboxy and amino groups, the simultaneous quantification of the total amount of both types of FG is very challenging if not impossible [64]. This implies also, that certain particle matrices can interfere with electrochemical titrations like mesoporous silica where the close match of the  $pK_a$  values of the silanol groups ( $pK_a$  4.5–5.5) and carboxy groups  $pK_a$  (about 4.8) prevents a discrimination between these FG. Moreover, the NM needs to be colloidal stable during the course of the acid-base titration, i.e., at the pH conditions necessary for (de)protonation of the FG/ligand of interest. For example, the dissolution of the silica matrix at alkaline pH values required for the determination of amino groups ( $pK_a$  about 9–11) renders the electrochemical quantification of amino FG on silica not feasible [89]. In addition, electrochemical titration methods like conductometry require a relatively large amount of sample (about 10–20 mg/mL of the surface functionalized NM), which renders these methods suitable only for relatively simple and self-made particles that are either not expensive or can be easily prepared in larger quantities. For expensive NM that are difficult to obtain on a

large scale or for surface ligands which are either costly or difficult to synthesize, other methods that require less amount of sample present a better choice like optical assays.

Optical assays, particularly fluorometric assays, are very sensitive, require only small amounts of sample, and can be performed by technical staff with standard bench-top instrumentation available in most laboratories. This makes them ideal for routine process monitoring during particle manufacturing and for quality control of surface functionalization. Moreover, optical measurements are simple and fast, and the chemical derivatization step necessary for labeling-based assays can provide an additional selectivity. Meanwhile, there is a large toolbox of differently sized optical reporters with various reactive groups commercially available including the different types of reporters introduced in the section on optical assays. However, for all optical assays as well as for other analytical methods relying on labeling reactions, only the number of derivatizable FG is obtained and the result can be affected by a combination of the reactivity of the label or reporter, the underlying reaction mechanism, the reaction yield, and particularly for crowded surfaces, also by reporter size, shape, and charge. Depending on the NM application, the influence of reporter size and shape must not be a disadvantage but can provide a more realistic estimate of the number of FG that can be derivatized with the molecule of interest. For bioconjugation reactions involving large biomolecules, commonly, the number of derivatizable FG determined with a reporter such as an organic dye provides an upper limit of the FG on the NM surface that can be coupled to the respective biomolecule. A general drawback of optical methods is the need for a suitable calibration to correlate the intensity of the measured optical signal to the analyte concentration, i.e., the amount of FG or ligands. The calibration needs to consider the sensitivity of the reporter's optical properties to its microenvironment, which can change the spectroscopic properties relevant for quantification, i.e., the reporter's molar absorption coefficient and especially its  $QY_{PL}$  values. This can be accomplished by choosing a standard for assay calibration that closely matches the reporter and its environment in the optical assay. This can make an accurate calibration (i.e., measurement uncertainties < 5%) tedious and can render the calibration sample specific. However, if larger uncertainties exceeding 20% are acceptable, a universal calibration could be sufficient. Also, optical signals can be distorted by interferences from the sample material like size- and wavelength-dependent light scattering as well as NM absorption and/or emission. For fluorescent labels that are detected when bound to the NM surface, quantification can also be hampered by reporter-specific and labeling density-dependent dye-dye interactions resulting in fluorescence quenching. Such sources of uncertainty can be elegantly circumvented with the aid of cleavable probes and catch-and-release assays.

Analytical techniques like NMR spectroscopy, ICP-MS, and XPS are very valuable tools for FG quantification and can yield the number of total and/or derivatizable FG depending on the respective surface-modified NM and the reporter used for signal generation. As detailed before, utilizing intrinsically present moieties provides the total amount of a certain FG, while the use of specific reporters in conjunction with chemical derivatization/labeling reactions yields the number of derivatizable FG. Moreover, particularly NMR and XPS can simultaneously provide information on mixed ligand shells and different FG. Drawbacks of these methods are, however, the need for expensive and sophisticated instrumentation, well-trained scientific staff, and elaborated data analysis. Therefore, such methods are often not the optimum choice for routine analysis and quality control; here, simple electrochemical methods and optical assays are better suited. However, these analytical methods are essential for validating the results obtained with simpler methods. Elegant tools for method validation present multimodal reporters that can be read out with different analytical techniques varying in the principle of signal generation, as summarized in the previous sections. Also, methods like NMR are mandatory to establish a traceability chain to the SI unit mole.

In the future, the increasingly recognized importance of FG and ligand quantification on NM and its direct correlation with the safe(r) use of NM will require more interlaboratory comparisons using different analytical methods to determine accomplishable uncertainties for broadly used NM and typical surface modifications. This is particularly relevant for applications of NM in the life sciences, health sector, and as food additives, and the corresponding quality control of NM production and long-term stability. Due to the application-specific importance of information on the total and derivatizable number of FG/ligands, analytical methods for both types of surface functionalities are needed. For the latter, the information obtained is influenced by the size, shape, and charge of the applied reporter, also in comparison to the respective properties of the molecule(s) of interest that are to be attached to the FG/ligands on the NM surface. Thus, models are desired that enable to consider these features. A relatively simple approach would be to calculate or estimate the steric demand (footprint) of the reporter label and the molecule of interest, which, however, needs to be verified at least for a set of commonly used reporters and application-relevant target (bio)molecules such as typical peptides, oligonucleotides, and proteins including antibodies and enzymes. In any case, the overall aim should be to establish protocols for surface FG/ligand analysis and quantification (with known uncertainties) for commonly employed methods, and to eventually standardize these methods. Such activities are currently being pushed

forward, e.g., by ISO/TC 229 *Nanotechnologies*, the Nanomaterials Study Group of ISO TC201 SG1, and ISO TC 201 *Surface Chemical Analysis* as well as different working groups of IEC. Other activities are being pursued by national standardization organizations, e.g., by the XPS community. Particularly attractive and efficient tools for surface group analysis are multimodal reporters, which enable to correlate the results obtained with different analytical methods, thereby simplifying method comparison, validation, and traceability, as exemplarily shown in Fig. 8.

Protocols and recommended methods for surface analysis are also needed for establishing nanoscale reference materials for method calibration and/or validation, as reliable control for toxicity tests, and the supply of reference data of NM. Other properties of NM, that are closely linked to surface chemistry and will be of increasing importance for nanotechnology and nanobiotechnology in the future, are NM hydrophobicity/hydrophilicity, NM stability (including the possible release of potentially toxic constituents), and environment-induced changes in NM surface chemistry (including adsorption of (bio)molecules, (bio)corona formation, etc.) for representative and application-relevant test scenarios. Here, also overall accepted methods are needed. Although these needs have been meanwhile recognized by metrological institutes, standardization organizations, and regulatory agencies worldwide, the constantly increasing number of new and more advanced NM developed make it difficult to keep track. A categorization or classification of NM could present an appropriate tool that has been addressed by different EU consortia, and stronger requirements on the quality of the analytical data to be provided for scientific publications involving NM could be beneficial to improve the overall confidence in “nano” data [31, 32, 41, 247, 259].

**Acknowledgements** The authors would like to thank Dr. Jörg Radnik (BAM, Division 6.1 - Surface Analysis and Interfacial Chemistry) for his valuable input to the XPS part.

**Author contribution** Not applicable.

**Funding** Open Access funding enabled and organized by Projekt DEAL. This work was financially supported by the Federal Institute for Materials Research and Testing (BAM) through an MI type 3 project, by the German Federal Ministry for Economic Affairs and Energy (BMWi) through the WIPANO project “AquaFunkNano” (03TNK005A), and by the European Metrology Programme for Innovation and Research (EMPIR) as part of the projects 18HLT01 “MetVes II” and 18HLT02 “AeroTox”. The EMPIR initiative is co-funded by the European Union’s Horizon 2020 research and innovation programme and by the EMPIR participating states.

**Data availability** Not applicable.

**Code availability** Not applicable.

## Declarations

**Ethics approval and consent to participate** Not applicable.

**Consent for publication** Not applicable.

**Competing interests** The authors declare no competing interests.

**Conflict of interest** The authors declare that they have no competing of interests.

**Open Access** This article is licensed under a Creative Commons Attribution 4.0 International License, which permits use, sharing, adaptation, distribution and reproduction in any medium or format, as long as you give appropriate credit to the original author(s) and the source, provide a link to the Creative Commons licence, and indicate if changes were made. The images or other third party material in this article are included in the article's Creative Commons licence, unless indicated otherwise in a credit line to the material. If material is not included in the article's Creative Commons licence and your intended use is not permitted by statutory regulation or exceeds the permitted use, you will need to obtain permission directly from the copyright holder. To view a copy of this licence, visit <http://creativecommons.org/licenses/by/4.0/>.

## References

- Shin SJ, Beech JR, Kelly KA (2013) Targeted nanoparticles in imaging: paving the way for personalized medicine in the battle against cancer. *Integr Biol* 5(1):29–42
- Pelaz B, Alexiou CH, Alvarez-Puebla RA et al (2017) Diverse applications of nanomedicine. *ACS Nano* 11(3):2313–2381
- Farka Z, Juriik T, Kovaar D, Trnkova L, Sklaadal P (2017) Nanoparticle-based immunochemical biosensors and assays: recent advances and challenges. *Chem Rev* 117(15):9973–10042
- Giner-Casares JJ, Henriksen-Lacey M, Coronado-Puchau M, Liz-Marzan LM (2016) Inorganic nanoparticles for biomedicine: where materials scientists meet medical research. *Mater Today* 19(1):19–28
- Howes PD, Chandrawati R, Stevens MM (2014) Colloidal nanoparticles as advanced biological sensors. *Science* 346(6205):1247390
- Kim D, Kim J, Park YI, Lee N, Hyeon T (2018) Recent development of inorganic nanoparticles for biomedical imaging. *ACS Cent Sci* 4(3):324–336
- Peng HS, Chiu DT (2015) Soft fluorescent nanomaterials for biological and biomedical imaging. *Chem Soc Rev* 44(14):4699–4722
- Petryayeva E, Algar WR (2015) Toward point-of-care diagnostics with consumer electronic devices: the expanding role of nanoparticles. *RSC Adv* 5(28):22256–22282
- Stark WJ, Stoessel PR, Wohleben W, Hafner A (2015) Industrial applications of nanoparticles. *Chem Soc Rev* 44(16):5793–5805
- Wolfbeis OS (2015) An overview of nanoparticles commonly used in fluorescent bioimaging. *Chem Soc Rev* 44(14):4743–4768
- Bobo D, Robinson KJ, Islam J, Thurecht KJ, Corrie SR (2016) Nanoparticle-based medicines: a review of FDA-approved materials and clinical trials to date. *Pharm Res* 33(10):2373–2387
- Pietryga JM, Park YS, Lim JH, Fidler AF, Bae WK, Brovelli S, Klimov VI (2016) Spectroscopic and device aspects of nanocrystal quantum dots. *Chem Rev* 116(18):10513–10622
- Geißler D, Hildebrandt N (2016) Recent developments in Förster resonance energy transfer (FRET) diagnostics using quantum dots. *Anal Bioanal Chem* 408(17):4475–4483
- Andresen E, Resch-Genger U, Schaferling M (2019) Surface modifications for photon-upconversion-based energy-transfer nanoprobes. *Langmuir* 35(15):5093–5113
- Heuer-Jungemann A, Feliu N, Bakaimi I, Hamaly M, Alkilany A, Chakraborty I, Masood A, Casula MF, Kostopoulou A, Oh E, Susumu K, Stewart MH, Medintz IL, Stratakis E, Parak WJ, Kanaras AG (2019) The role of ligands in the chemical synthesis and applications of inorganic nanoparticles. *Chem Rev* 119(8):4819–4880
- Ghosh Chaudhuri R, Paria S (2011) Core/shell nanoparticles: classes, properties, synthesis mechanisms, characterization, and applications. *Chem Rev* 112(4):2373–2433
- Wilhelm S, Kaiser M, Würth C, Heiland J, Carrillo-Carrion C, Muhr V, Wolfbeis OS, Parak WJ, Resch-Genger U, Hirsch T (2015) Water dispersible upconverting nanoparticles: effects of surface modification on their luminescence and colloidal stability. *Nanoscale* 7(4):1403–1410
- Hühn J, Carrillo-Carrion C, Soliman MG, Pfeiffer C, Valdeperez D, Masood A, Chakraborty I, Zhu L, Gallego M, Yue Z, Carril M, Feliu N, Escudero A, Alkilany AM, Pelaz B, del Pino P, Parak WJ (2017) Selected standard protocols for the synthesis, phase transfer, and characterization of inorganic colloidal nanoparticles. *Chem Mater* 29(1):399–461
- Zhao S, Caruso F, Dahne L et al (2019) The future of layer-by-layer assembly: a tribute to ACS Nano associate editor Helmut Mohwald. *ACS Nano* 13(6):6151–6169
- Hildebrandt N, Spillmann CM, Algar WR, Pons T, Stewart MH, Oh E, Susumu K, Diaz SA, Delehanty JB, Medintz IL (2017) Energy transfer with semiconductor quantum dot bioconjugates: a versatile platform for biosensing, energy harvesting, and other developing applications. *Chem Rev* 117(2):536–711
- Soenen SJ, Parak WJ, Rejman J, Manshian B (2015) (intra)cellular stability of inorganic nanoparticles: effects on cytotoxicity, particle functionality, and biomedical applications. *Chem Rev* 115(5):2109–2135
- Gagner JE, Shrivastava S, Qian X, Dordick JS, Siegel RW (2012) Engineering nanomaterials for biomedical applications requires understanding the Nano-bio Interface: a perspective. *J Phys Chem Lett* 3(21):3149–3158
- Baer DR, Engelhard MH, Johnson GE, Laskin J, Lai J, Mueller K, Munusamy P, Thevuthasan S, Wang H, Washton N, Elder A, Baisch BL, Karakoti A, Kuchibhatla SVNT, Moon DW (2013) Surface characterization of nanomaterials and nanoparticles: important needs and challenging opportunities. *J Vac Sci Technol A* 31(5):050820
- Silvi S, Baroncini M, La Rosa M, Credi A (2016) Interfacing luminescent quantum dots with functional molecules for optical sensing applications. *Top Curr Chem* 374(5):65
- Steichen SD, Calderera-Moore M, Peppas NA (2013) A review of current nanoparticle and targeting moieties for the delivery of cancer therapeutics. *Eur J Pharm Sci* 48(3):416–427
- Algar WR, Prasuhn DE, Stewart MH, Jennings TL, Blanco-Canosa JB, Dawson PE, Medintz IL (2011) The controlled display of biomolecules on nanoparticles: a challenge suited to bioorthogonal chemistry. *Bioconjug Chem* 22(5):825–858
- Zhou J, Liu Y, Tang J, Tang WH (2017) Surface ligands engineering of semiconductor quantum dots for chemosensory and biological applications. *Mater Today* 20(7):360–376
- Lim SJ, Ma L, Schleife A, Smith AM (2016) Quantum dot surface engineering: toward inert fluorophores with compact size and bright, stable emission. *Coord Chem Rev* 320:216–237
- Boles MA, Ling D, Hyeon T, Talapin DV (2016) The surface science of nanocrystals. *Nat Mater* 15(2):141–153

30. Alkilany AM, Zhu L, Weller H, Mews A, Parak WJ, Barz M, Feliu N (2019) Ligand density on nanoparticles: a parameter with critical impact on nanomedicine. *Adv Drug Deliv Rev* 143:22–36
31. Dekkers S, Oomen AG, Bleeker EA et al (2016) Towards a nanospecific approach for risk assessment. *Regul Toxicol Pharmacol* 80:46–59
32. Oomen AG, Bleeker EA, Bos PM, van Broekhuizen F, Gottardo S, Groenewold M, Hristozov D, Hund-Rinke K, Irfan MA, Marcomini A, Peijnenburg W, Rasmussen K, Jiménez A, Scott-Fordsmand J, van Tongeren M, Wiench K, Wohlleben W, Landsiedel R (2015) Grouping and read-across approaches for risk assessment of nanomaterials. *Int J Environ Res Public Health* 12(10):13415–13434
33. Zielinska A, Costa B, Ferreira MV et al (2020) Nanotoxicology and nanosafety: safety-by-design and testing at a glance. *Int J Environ Res Public Health* 17(13):4657
34. Lead JR, Batley GE, Alvarez PJJ, Croteau MN, Handy RD, McLaughlin MJ, Judy JD, Schirmer K (2018) Nanomaterials in the environment: behavior, fate, bioavailability, and effects—an updated review. *Environ Toxicol Chem* 37(8):2029–2063
35. Geißler D, Wegmann M, Jochum T, Somma V, Sowa M, Scholz J, Fröhlich E, Hoffmann K, Niehaus J, Roggenbuck D, Resch-Genger U (2019) An automatable platform for genotoxicity testing of nanomaterials based on the fluorometric gamma-H2AX assay reveals no genotoxicity of properly surface-shielded cadmium-based quantum dots. *Nanoscale* 11(28):13458–13468
36. Fubini B (1997) Surface reactivity in the pathogenic response to particulates. *Environ Health Perspect* 105:1013–1020
37. del Pino P, Yang F, Pelaz B et al (2016) Basic physicochemical properties of polyethylene glycol coated gold nanoparticles that determine their interaction with cells. *Angew Chem Int Edit* 55(18):5483–5487
38. Henriksen-Lacey M, Carregal-Romero S, Liz-Marzan LM (2017) Current challenges toward in vitro cellular validation of inorganic nanoparticles. *Bioconjug Chem* 28(1):212–221
39. Lewinski N, Colvin V, Drezek R (2008) Cytotoxicity of nanoparticles. *Small* 4(1):26–49
40. Rivera-Gil P, De Aberasturi DJ, Wulf V et al (2013) The challenge to relate the physicochemical properties of colloidal nanoparticles to their cytotoxicity. *Acc Chem Res* 46(3):743–749
41. Isgonis P, Afantitis A, Antunes P, Bartonova A, Beitollahi A, Bohmer N, Bouman E, Chaudhry Q, Cimpan MR, Cimpan E, Doak S, Dupin D, Fedrigo D, Fessard V, Gromelski M, Gutleb AC, Halappanavar S, Hoet P, Jeliazkova N et al (2020) Risk governance of emerging technologies demonstrated in terms of its applicability to nanomaterials. *Small* 16(36):2003303
42. Lin S, Yu T, Yu Z, Hu X, Yin D (2018) Nanomaterials safer-by-design: an environmental safety perspective. *Adv Mater* 30(17):1705691
43. Tavernaro I, Dekkers S, Soeteman-Hernandez LG et al. (2021) Safe-by-design part II: a strategy for balancing safety and functionality in the different stages of the innovation process. *NanoImpact* (accepted for publication)
44. Dekkers S, Wijnhoven SWP, Braakhuis HM, Soeteman-Hernandez LG, Sips AJAM, Tavernaro I, Kraegeloh A, Noorlander CW (2020) Safe-by-design part I: proposal for nanospecific human health safety aspects needed along the innovation process. *NanoImpact* 18:100227
45. Sánchez Jiménez A, Puelles R, Pérez-Fernández M, Gómez-Fernández P, Barruetaña L, Jacobsen NR, Suarez-Merino B, Micheletti C, Manier N, Trouiller B, Navas JM, Kalman J, Salieri B, Hischier R, Handzhiyski Y, Apostolova MD, Hadrup N, Bouillard J, Oudart Y et al (2020) Safe(r) by design implementation in the nanotechnology industry. *NanoImpact* 20:100267
46. Kraegeloh A, Suarez-Merino B, Sluijters T, Micheletti C (2018) Implementation of safe-by-design for nanomaterial development and safe innovation: why we need a comprehensive approach. *Nanomaterials* 8(4):239
47. Gilbertson LM, Zimmerman JB, Plata DL, Hutchison JE, Anastas PT (2015) Designing nanomaterials to maximize performance and minimize undesirable implications guided by the principles of green chemistry. *Chem Soc Rev* 44(16):5758–5777
48. Johnston LJ, Gonzalez-Rojano N, Wilkinson KJ, Xing B (2020) Key challenges for evaluation of the safety of engineered nanomaterials. *NanoImpact* 18:100219
49. Comandella D, Gottardo S, Rio-Echevarria IM, Rauscher H (2020) Quality of physicochemical data on nanomaterials: an assessment of data completeness and variability. *Nanoscale* 12(7):4695–4708
50. Lopez-Serrano A, Olivas RM, Landaluze JS, Camara C (2014) Nanoparticles: a global vision. Characterization, separation, and quantification methods. Potential environmental and health impact. *Anal Methods* 6(1):38–56
51. Smith AM, Johnston KA, Crawford SE, Marbella LE, Millstone JE (2017) Ligand density quantification on colloidal inorganic nanoparticles. *Analyst* 142(1):11–29
52. Soeteman-Hernandez LG, Apostolova MD, Bekker C, Dekkers S, Grafström RC, Groenewold M, Handzhiyski Y, Herbeck-Engel P, Hoehener K, Karagkiozaki V, Kelly S, Kraegeloh A, Logothetidis S, Micheletti C, Nymark P, Oomen A, Oosterwijk T, Rodríguez-Llopis I, Sabella S et al (2019) Safe innovation approach: towards an agile system for dealing with innovations. *Mater Today Commun* 20:100548
53. Miernicki M, Hofmann T, Eisenberger I, von der Kammer F, Praetorius A (2019) Legal and practical challenges in classifying nanomaterials according to regulatory definitions. *Nat Nanotechnol* 14(3):208–216
54. Modena MM, Rühle B, Burg TP, Wuttke S (2019) Nanoparticle characterization: what to measure? *Adv Mater* 31(32):1901556
55. Palui G, Aldeek F, Wang WT, Mattoussi H (2015) Strategies for interfacing inorganic nanocrystals with biological systems based on polymer-coating. *Chem Soc Rev* 44(1):193–227
56. Sapsford KE, Tyner KM, Dair BJ, Deschamps JR, Medintz IL (2011) Analyzing nanomaterial bioconjugates: a review of current and emerging purification and characterization techniques. *Anal Chem* 83(12):4453–4488
57. Sapsford KE, Algar WR, Berti L, Gemmill KB, Casey BJ, Oh E, Stewart MH, Medintz IL (2013) Functionalizing nanoparticles with biological molecules: developing chemistries that facilitate nanotechnology. *Chem Rev* 113(3):1904–2074
58. Algar WR (2017) A brief introduction to traditional bioconjugate chemistry. In: Algar WR, Dawson P, Medintz IL (eds) *Chemoselective and bioorthogonal ligation reactions - concepts and applications*, 1st edn. Wiley-VCH, Weinheim. <https://doi.org/10.1002/9783527683451>
59. Devaraj NK (2018) The future of bioorthogonal chemistry. *ACS Cent Sci* 4(8):952–959
60. Rubio L, Pyrgiotakis G, Beltran-Huarac J, Zhang Y, Gaurav J, Deloid G, Spyrogianni A, Sarosiek KA, Bello D, Demokritou P (2019) Safer-by-design flame-sprayed silicon dioxide nanoparticles: the role of silanol content on ROS generation, surface activity and cytotoxicity. *Part Fibre Toxicol* 16(1):40
61. Pavan C, Delle Piane M, Gullo M, Filippi F, Fubini B, Hoet P, Horwell CJ, Huaux F, Lison D, Lo Giudice C, Martra G, Montfort E, Schins R, Sulpizi M, Wegner K, Wyart-Remy M, Ziemann C, Turci F (2019) The puzzling issue of silica toxicity: are silanols bridging the gaps between surface states and pathogenicity? *Part Fibre Toxicol* 16(1):32
62. Pavan C, Santalucia R, Leinardi R, Fabbiani M, Yakoub Y, Uwambayinema F, Ugliengo P, Tomatis M, Martra G, Turci F, Lison D, Fubini B (2020) Nearly free surface silanols are the

- critical molecular moieties that initiate the toxicity of silica particles. *Proc Natl Acad Sci U S A* 117(45):27836–27846
63. Hennig A, Borcherding H, Jaeger C, Hatami S, Würth C, Hoffmann A, Hoffmann K, Thiele T, Schedler U, Resch-Genger U (2012) Scope and limitations of surface functional group quantification methods: exploratory study with poly(acrylic acid)-grafted Micro- and nanoparticles. *J Am Chem Soc* 134(19):8268–8276
  64. Moser M, Nirmalanathan N, Behnke T, Geißler D, Resch-Genger U (2018) Multimodal cleavable reporters versus conventional labels for optical quantification of accessible amino and Carboxy groups on Nano- and Microparticles. *Anal Chem* 90(9):5887–5895
  65. Leubner S, Hatami S, Esendemir N, Lorenz T, Joswig JO, Lesnyak V, Recknagel S, Gaponik N, Resch-Genger U, Eychmüller A (2013) Experimental and theoretical investigations of the ligand structure of water-soluble CdTe nanocrystals. *Dalton Trans* 42(35):12733–12740
  66. Poselt E, Schmidtke C, Fischer S et al (2012) Tailor-made quantum dot and Iron oxide based contrast agents for in vitro and in vivo tumor imaging. *ACS Nano* 6(4):3346–3355
  67. Schmidtke C, Poselt E, Ostermann J et al (2013) Amphiphilic, cross-linkable diblock copolymers for multifunctionalized nanoparticles as biological probes. *Nanoscale* 5(16):7433–7444
  68. Mahmood S, Mandal UK, Chatterjee B, Taher M (2017) Advanced characterizations of nanoparticles for drug delivery: investigating their properties through the techniques used in their evaluations. *Nanotechnol Rev* 6(4):355–372
  69. Mourdikoudis S, Pallares RM, Thanh NTK (2018) Characterization techniques for nanoparticles: comparison and complementarity upon studying nanoparticle properties. *Nanoscale* 10(27):12871–12934
  70. Maguire CM, Rosslein M, Wick P, Prina-Mello A (2018) Characterisation of particles in solution—a perspective on light scattering and comparative technologies. *Sci Technol Adv Mater* 19(1):732–745
  71. Shang J, Gao XH (2014) Nanoparticle counting: towards accurate determination of the molar concentration. *Chem Soc Rev* 43(21):7267–7278
  72. Varga Z, Yuana Y, Grootemaat AE, van der Pol E, Gollwitzer C, Krumrey M, Nieuwland R (2014) Towards traceable size determination of extracellular vesicles. *J Extracell Vesicles* 3(1):23298
  73. Thielbeer F, Donaldson K, Bradley M (2011) Zeta potential mediated reaction monitoring on Nano and Microparticles. *Bioconjug Chem* 22(2):144–150
  74. Charron G, Huhn D, Perrier A et al (2012) On the use of pH titration to quantitatively characterize colloidal nanoparticles. *Langmuir* 28(43):15141–15149
  75. Fedin I, Talapin DV (2014) Probing the surface of colloidal nanomaterials with Potentiometry in situ. *J Am Chem Soc* 136(32):11228–11231
  76. Alves LA, de Castro AH, de Mendonca FG, de Mesquita JP (2016) Characterization of acid functional groups of carbon dots by nonlinear regression data fitting of potentiometric titration curves. *Appl Surf Sci* 370:486–495
  77. Anirudhan TS, Deepa JR, Christa J (2016) Nanocellulose/nanobentonite composite anchored with multi-carboxyl functional groups as an adsorbent for the effective removal of cobalt(II) from nuclear industry wastewater samples. *J Colloid Interface Sci* 467:307–320
  78. Chen ZM, Xiao X, Chen BL, Zhu LZ (2015) Quantification of chemical states, dissociation constants and contents of oxygen-containing groups on the surface of biochars produced at different temperatures. *Environ Sci Technol* 49(1):309–317
  79. Castro VG, Costa IB, Medeiros FS et al (2019) Improved functionalization of multiwalled carbon nanotubes in ultra-low acid volume: effect of solid/liquid Interface. *J Braz Chem Soc* 30(11):2477–2487
  80. Torlopov MA, Martakov IS, Mikhaylov VI, Legki PV, Golubev YA, Krivoshapkina EF, Tracey C, Sitnikov PA, Udoratina EV (2019) Manipulating the colloidal properties of (non-)sulfated cellulose nanocrystals via stepwise surface cyanoethylation/carboxylation. *Eur Polym J* 115:225–233
  81. Nedeljko P, Turel M, Kosak A, Lobnik A (2016) Synthesis of hybrid thiol-functionalized SiO<sub>2</sub> particles used for agmatine determination. *J Sol-Gel Sci Technol* 79(3):487–496
  82. Hassan SM, Ahmed AI, Mannaa MA (2019) Surface acidity, catalytic and photocatalytic activities of new type H3PW12O40/Sn-TiO<sub>2</sub> nanoparticles. *Colloid Surf A* 577:147–157
  83. Khoshnavazi R, Bahrami L, Havasi F, Naseri E (2017) H3PW12O40 supported on functionalized polyoxometalate organic-inorganic hybrid nanoparticles as efficient catalysts for three-component Mannich-type reactions in water. *RSC Adv* 7(19):11510–11521
  84. Srilakshmi C, Saraf R, Shivakumara C (2018) Structural studies of multifunctional SrTiO<sub>3</sub> nanocatalyst synthesized by microwave and oxalate methods: its catalytic application for condensation, hydrogenation, and amination reactions. *ACS Omega* 3(9):10503–10512
  85. Aboelhasan MM, Peixoto AF, Freire C (2017) Sulfonic acid functionalized silica nanoparticles as catalysts for the esterification of linoleic acid. *New J Chem* 41(9):3595–3605
  86. Bandosz TJ, Policicchio A, Florent M, Poon PS, Matos J (2019) TiO<sub>2</sub>/S-doped carbons hybrids: analysis of their interfacial and surface features. *Molecules* 24(19):3585
  87. Wang Z, Xie Y, Lei Z, Lu Y, Wei G, Liu S, Xu C, Zhang Z, Wang X, Rao L, Chen J (2019) Quantitative analysis of surface sites on carbon dots and their interaction with metal ions by a potentiometric titration method. *Anal Chem* 91(15):9690–9697
  88. Renner AM, Schutz MB, Moog D, Fischer T, Mathur S (2019) Electroacoustic quantification of surface bound ligands in functionalized silica and Iron oxide nanoparticles. *Chemistryselect* 4(40):11959–11964
  89. Nirmalanathan-Budau N, Rühle B, Geißler D, Moser M, Kläber C, Schäfer A, Resch-Genger U (2019) Multimodal cleavable reporters for quantifying carboxy and amino groups on organic and inorganic nanoparticles. *Sci Rep* 9(1):17577
  90. Zhu SC, Panne U, Rurack K (2013) A rapid method for the assessment of the surface group density of carboxylic acid-functionalized polystyrene microparticles. *Analyst* 138(10):2924–2930
  91. Spinella S, Maiorana A, Qian Q, Dawson NJ, Hepworth V, McCallum SA, Ganesh M, Singer KD, Gross RA (2016) Concurrent cellulose hydrolysis and esterification to prepare a surface-modified cellulose nanocrystal decorated with carboxylic acid moieties. *ACS Sustain Chem Eng* 4(3):1538–1550
  92. Zhao FP, Repo E, Song Y, Yin D, Hammouda SB, Chen L, Kalliola S, Tang J, Tam KC, Sillanpää M (2017) Polyethylenimine-cross-linked cellulose nanocrystals for highly efficient recovery of rare earth elements from water and a mechanism study. *Green Chem* 19(20):4816–4828
  93. Sahlin K, Forsgren L, Moberg T, Bernin D, Rigdahl M, Westman G (2018) Surface treatment of cellulose nanocrystals (CNC): effects on dispersion rheology. *Cellulose* 25(1):331–345
  94. Jordan JH, Easson MW, Condon BD (2019) Alkali hydrolysis of sulfated cellulose nanocrystals: optimization of reaction conditions and tailored surface charge. *Nanomaterials* 9(9):1232
  95. Trache D, Tarchoun AF, Derradji M, Hamidon TS, Masruchin N, Brosse N, Hussin MH (2020) Nanocellulose: from fundamentals to advanced applications. *Front Chem* 8:392
  96. Ellebracht NC, Jones CW (2018) Amine functionalization of cellulose nanocrystals for acid-base organocatalysis: surface

- chemistry, cross-linking, and solvent effects. *Cellulose* 25(11): 6495–6512
97. Ellebracht NC, Jones CW (2019) Optimized cellulose nanocrystal organocatalysts outperform silica-supported analogues: cooperativity, selectivity, and bifunctionality in acid-base aldol condensation reactions. *ACS Catal* 9(4):3266–3277
98. Hujaya SD, Lorite GS, Vainio SJ, Liimatainen H (2018) Polyion complex hydrogels from chemically modified cellulose nanofibrils: structure-function relationship and potential for controlled and pH-responsive release of doxorubicin. *Acta Biomater* 75:346–357
99. Beck S, Methot M, Bouchard J (2015) General procedure for determining cellulose nanocrystal sulfate half-ester content by conductometric titration (vol 22, pg 101, 2015). *Cellulose* 22(1): 117
100. Johnston LJ, Jakubek ZJ, Beck S, Araki J, Cranston ED, Danumah C, Fox D, Li H, Wang J, Mester Z, Moores A, Murphy K, Rabb SA, Rudie A, Stephan C (2018) Determination of sulfur and sulfate half-ester content in cellulose nanocrystals: an interlaboratory comparison. *Metrologia* 55(6):872–882
101. Boehm HP, Heck W, Sappok R, Diehl E (1964) Surface oxides of carbon. *Angew Chem Int Edit* 3(10):669
102. Boehm HP (1966) Chemical identification of surface groups. *Adv Catal* 16:179–274
103. Boehm HP, Voll M (1968) Studies on basic surface oxides of carbon. *Carbon* 6(2):226
104. Voll M, Boehm HP (1971) Basic surface oxides on carbon .4. Chemical Reactions for Identification of Surface Groups. *Carbon* 9(4):481
105. Schönherr J, Buchheim JR, Scholz P, Adelhelm P (2018) Boehm titration revisited (part I): practical aspects for achieving a high precision in quantifying oxygen-containing surface groups on carbon materials. *Carbon* 4(2):21
106. Hou JF, Xu LX, Han YX, Tang Y, Wan H, Xu Z, Zheng S (2019) Deactivation and regeneration of carbon nanotubes and nitrogen-doped carbon nanotubes in catalytic peroxymonosulfate activation for phenol degradation: variation of surface functionalities. *RSC Adv* 9(2):974–983
107. Tang ZC, Boer DG, Syariati A, Enache M, Rudolf P, Heeres HJ, Pescarmona PP (2019) Base-free conversion of glycerol to methyl lactate using a multifunctional catalytic system consisting of Au-Pd nanoparticles on carbon nanotubes and Sn-MCM-41-XS. *Green Chem* 21(15):4115–4126
108. Kolanowska A, Wasik P, Zieba W, Terzyk AP, Boncel S (2019) Selective carboxylation versus layer-by-layer unsheathing of multi-walled carbon nanotubes: new insights from the reaction with boiling nitrating mixture. *RSC Adv* 9(64):37608–37613
109. Ackermann J, Krueger A (2019) Efficient surface functionalization of detonation nanodiamond using ozone under ambient conditions. *Nanoscale* 11(16):8012–8019
110. Bergaoui M, Aguir C, Khalfouli M, Enciso E, Duclaux L, Reinert L, Fierro JLG (2017) New insights in the adsorption of bovine serum albumin onto carbon nanoparticles derived from organic resin: experimental and theoretical studies. *Microporous Mesoporous Mater* 241:418–428
111. Pham V, Nguyen HTT, Nguyen DTC et al (2019) Process optimization by a response surface methodology for adsorption of Congo red dye onto exfoliated graphite-decorated MnFe<sub>2</sub>O<sub>4</sub> nanocomposite: the pivotal role of surface chemistry. *Processes* 7(5):305
112. Motamedi E, Moteszarezedeh B, Shirinfekr A, Samar SM (2020) Synthesis and swelling behavior of environmentally friendly starch-based superabsorbent hydrogels reinforced with natural char nano/micro particles. *J Environ Chem Eng* 8(1):103583
113. Schönherr J, Buchheim JR, Scholz P, Adelhelm P (2018) Boehm titration revisited (part II): a comparison of Boehm titration with other analytical techniques on the quantification of oxygen-containing surface groups for a variety of carbon materials. *Carbon* 4(2):22
114. Felbeck T, Hoffmann K, Lezhnina MM, Kynast UH, Resch-Genger U (2015) Fluorescent Nanoclays: covalent functionalization with amine reactive dyes from different fluorophore classes and surface group quantification. *J Phys Chem C* 119(23):12978–12987
115. Hoffmann K, Mix R, Resch-Genger U, Friedrich JF (2007) Monitoring of amino functionalities on plasma-chemically modified polypropylene supports with a chromogenic and Fluorogenic Pyrylium reporter. *Langmuir* 23(16):8411–8416
116. Hennig A, Hoffmann A, Borcharding H, Thiele T, Schedler U, Resch-Genger U (2011) Simple colorimetric method for quantification of surface Carboxy groups on polymer particles. *Anal Chem* 83(12):4970–4974
117. Fischer T, Dietrich PM, Unger WES, Rurack K (2016) Multimode surface functional group determination: combining steady-state and time-resolved fluorescence with X-ray photoelectron spectroscopy and absorption measurements for absolute quantification. *Anal Chem* 88(2):1210–1217
118. Zhan NQ, Palui G, Merkl JP, Mattoussi H (2016) Bio-orthogonal coupling as a means of quantifying the ligand density on hydrophilic quantum dots. *J Am Chem Soc* 138(9):3190–3201
119. Laux EM, Behnke T, Hoffmann K, Resch-Genger U (2012) Keeping particles brilliant—simple methods for the determination of the dye content of fluorophore-loaded polymeric particles. *Anal Methods* 4(6):1759–1768
120. Cisneros-Covarrubias CA, Palestino G, Gomez-Duran CFA, Rosales-Mendoza S, Betancourt-Mendiola ML (2021) Optimized microwave-assisted functionalization and quantification of superficial amino groups on porous silicon nanostructured microparticles. *Anal Methods* 13(4):516–525
121. Hristov DR, Rocks L, Kelly PM, Thomas SS, Pitek AS, Verderio P, Mahon E, Dawson KA (2015) Tuning of nanoparticle biological functionality through controlled surface chemistry and characterisation at the bioconjugated nanoparticle surface. *Sci Rep* 5: 17040
122. Miller PJ, Shantz DF (2020) Covalently functionalized uniform amino-silica nanoparticles. Synthesis and validation of amine group accessibility and stability. *Nanoscale Adv* 2(2):860–868
123. Sun Y, Kunc F, Balhara V, Coleman B, Kodra O, Raza M, Chen M, Brinkmann A, Lopinski GP, Johnston LJ (2019) Quantification of amine functional groups on silica nanoparticles: a multi-method approach. *Nanoscale Adv* 1(4):1598–1607
124. Zhang Y, Chen Y (2012) Fmoc-Cl fluorescent determination for amino groups of nanomaterial science. *IET Nanobiotechnol* 6(2): 76–80
125. Hsiao IL, Fritsch-Decker S, Leidner A et al (2019) Biocompatibility of amine-functionalized silica nanoparticles: the role of surface coverage. *Small* 15(10):1805400
126. Moser M, Behnke T, Hamers-Allin C, Klein-Hartwig K, Falkenhagen J, Resch-Genger U (2015) Quantification of PEG-Maleimide ligands and coupling efficiencies on nanoparticles with Ellman's reagent. *Anal Chem* 87(18):9376–9383
127. Moser M, Schneider R, Behnke T, Schneider T, Falkenhagen J, Resch-Genger U (2016) Ellman's and Aldrithiol assay as versatile and complementary tools for the quantification of thiol groups and ligands on nanomaterials. *Anal Chem* 88(17):8624–8631
128. Gorris HH, Saleh SM, Groegel DBM, Ernst S, Reiner K, Mustroph H, Wolfbeis OS (2011) Long-wavelength absorbing and fluorescent chameleon labels for proteins, peptides, and amines. *Bioconjug Chem* 22(7):1433–1437
129. Saleh SM, Ali R, Wolfbeis OS (2011) New silica and polystyrene nanoparticles labeled with longwave absorbing and fluorescent chameleon dyes. *Microchim Acta* 174(3–4):429–434

130. Behrendt R, White P, Offer J (2016) Advances in Fmoc solid-phase peptide synthesis. *J Pept Sci* 22(1):4–27
131. Eissler S, Kley M, Bachle D et al (2017) Substitution determination of Fmoc-substituted resins at different wavelengths. *J Pept Sci* 23(10):757–762
132. Yoon TJ, Yu KN, Kim E et al (2006) Specific targeting, cell sorting, and bioimaging with smart magnetic silica core-shell nanomaterials. *Small* 2(2):209–215
133. Yang H, Zhuang Y, Hu H, du X, Zhang C, Shi X, Wu H, Yang S (2010) Silica-coated manganese oxide nanoparticles as a platform for targeted magnetic resonance and fluorescence imaging of Cancer cells. *Adv Funct Mater* 20(11):1733–1741
134. Cao T, Yang Y, Gao Y, Zhou J, Li Z, Li F (2011) High-quality water-soluble and surface-functionalized upconversion nanocrystals as luminescent probes for bioimaging. *Biomaterials* 32(11):2959–2968
135. Liu Y, Zhou S, Tu D, Chen Z, Huang M, Zhu H, Ma E, Chen X (2012) Amine-functionalized lanthanide-doped zirconia nanoparticles: optical spectroscopy, time-resolved fluorescence resonance energy transfer biodetection, and targeted imaging. *J Am Chem Soc* 134(36):15083–15090
136. Paris JL, Manzano M, Cabanas MV, Vallet-Regi M (2018) Mesoporous silica nanoparticles engineered for ultrasound-induced uptake by cancer cells. *Nanoscale* 10(14):6402–6408
137. Fidecka K, Giacoboni J, Picconi P, Vago R, Licandro E (2020) Quantification of amino groups on halloysite surfaces using the Fmoc-method. *RSC Adv* 10(24):13944–13948
138. Szczepanska E, Grobelna B, Ryl J et al (2020) Efficient method for the concentration determination of Fmoc groups incorporated in the core-shell materials by Fmoc-Glycine. *Molecules* 25(17):3983
139. Chen Y, Zhang Y (2011) Fluorescent quantification of amino groups on silica nanoparticle surfaces. *Anal Bioanal Chem* 399(7):2503–2509
140. Roloff A, Nirmalanathan-Budau N, Rühle B, Borchering H, Thiele T, Schedler U, Resch-Genger U (2019) Quantification of aldehydes on polymeric microbead surfaces via catch and release of reporter chromophores. *Anal Chem* 91(14):8827–8834
141. Sakai R, Iguchi H, Maruyama T (2019) Quantification of azide groups on a material surface and a biomolecule using a clickable and cleavable fluorescent compound. *RSC Adv* 9(8):4621–4625
142. Zhang S, Dominguez Z, Assaf KI et al (2018) Precise supramolecular control of surface coverage densities on polymer micro- and nanoparticles. *Chem Sci* 9(45):8575–8581
143. Kim DY, Shinde S, Ghodake G (2017) Colorimetric detection of magnesium (II) ions using tryptophan functionalized gold nanoparticles. *Sci Rep* 7:3966
144. Rodiger S, Ruhland M, Schmidt C et al (2011) Fluorescence dye adsorption assay to quantify carboxyl groups on the surface of poly(methyl methacrylate) microbeads. *Anal Chem* 83(9):3379–3385
145. Stelmach E, Maksymiuk K, Michalska A (2016) Copolymeric hexyl acrylate-methacrylic acid microspheres—surface vs. bulk reactive carboxyl groups. Coulometric and colorimetric determination and analytical applications for heterogeneous microtitration. *Talanta* 159:248–254
146. Marbella LE, Millstone JE (2015) NMR techniques for noble metal nanoparticles. *Chem Mater* 27(8):2721–2739
147. Hines DA, Kamat PV (2014) Recent advances in quantum dot surface chemistry. *ACS Appl Mater Interfaces* 6(5):3041–3057
148. Kopping JT, Patten TE (2008) Identification of acidic phosphorus-containing ligands involved in the surface chemistry of CdSe nanoparticles prepared in tri-n-octylphosphine oxide solvents. *J Am Chem Soc* 130(17):5689–5698
149. Ji XH, Copenhaver D, Sichmeller C, Peng XG (2008) Ligand bonding and dynamics on colloidal nanocrystals at room temperature: the case of alkylamines on CdSe nanocrystals. *J Am Chem Soc* 130(17):5726–5735
150. Morris-Cohen AJ, Malicki M, Peterson MD, Slavin JWJ, Weiss EA (2013) Chemical, structural, and quantitative analysis of the ligand shells of colloidal quantum dots. *Chem Mater* 25(8):1155–1165
151. De Roo J, Yazdani N, Drijvers E et al (2018) Probing solvent-ligand interactions in colloidal nanocrystals by the NMR line broadening. *Chem Mater* 30(15):5485–5492
152. Crucho CIC, Baleizao C, Farinha JPS (2017) Functional group coverage and conversion quantification in nanostructured silica by H-1 NMR. *Anal Chem* 89(1):681–687
153. Lu J, Xue Y, Shi R, Kang J, Zhao CY, Zhang NN, Wang CY, Lu ZY, Liu K (2019) A non-sacrificial method for the quantification of poly(ethylene glycol) grafting density on gold nanoparticles for applications in nanomedicine. *Chem Sci* 10(7):2067–2074
154. Davidowski SK, Holland GP (2016) Solid-state NMR characterization of mixed phosphonic acid ligand binding and organization on silica nanoparticles. *Langmuir* 32(13):3253–3261
155. Hens Z, Martins JC (2013) A solution NMR toolbox for characterizing the surface chemistry of colloidal nanocrystals. *Chem Mater* 25(8):1211–1221
156. Lehman SE, Tataurova Y, Mueller PS, Mariappan SVS, Larsen SC (2014) Ligand characterization of covalently functionalized mesoporous silica nanoparticles: an NMR toolbox approach. *J Phys Chem C* 118(51):29943–29951
157. Huber A, Behnke T, Würth C, Jaeger C, Resch-Genger U (2012) Spectroscopic characterization of coumarin-stained beads: quantification of the number of fluorophores per particle with solid-state 19F-NMR and measurement of absolute fluorescence quantum yields. *Anal Chem* 84(8):3654–3661
158. Hennig A, Dietrich PM, Hemmann F, Thiele T, Borchering H, Hoffmann A, Schedler U, Jäger C, Resch-Genger U, Unger WES (2015) En route to traceable reference standards for surface group quantifications by XPS, NMR and fluorescence spectroscopy. *Analyst* 140(6):1804–1808
159. Guo C, Yarger JL (2018) Characterizing gold nanoparticles by NMR spectroscopy. *Magn Reson Chem* 56(11):1074–1082
160. Wu M, Vartanian AM, Chong G, Pandiakumar AK, Hamers RJ, Hernandez R, Murphy CJ (2019) Solution NMR analysis of ligand environment in quaternary ammonium-terminated self-assembled monolayers on gold nanoparticles: the effect of surface curvature and ligand structure. *J Am Chem Soc* 141(10):4316–4327
161. Chen Y, Ripka EG, Franck JM, Maye MM (2019) Ligand surface density decreases with quantum rod aspect ratio. *J Phys Chem C* 123(38):23682–23690
162. Kong N, Zhou J, Park J, Xie S, Ramström O, Yan M (2015) Quantitative fluorine NMR to determine carbohydrate density on glyconanomaterials synthesized from perfluorophenyl azide-functionalized silica nanoparticles by click reaction. *Anal Chem* 87(18):9451–9458
163. Kunc F, Balhara V, Brinkmann A, Sun Y, Leek DM, Johnston LJ (2018) Quantification and stability determination of surface amine groups on silica nanoparticles using solution NMR. *Anal Chem* 90(22):13322–13330
164. Kunc F, Balhara V, Sun Y, Daroszevska M, Jakubek ZJ, Hill M, Brinkmann A, Johnston LJ (2019) Quantification of surface functional groups on silica nanoparticles: comparison of thermogravimetric analysis and quantitative NMR. *Analyst* 144(18):5589–5599
165. Galazzi RM, Chacon-Madrid K, Freitas DC, da Costa LF, Arruda MAZ (2020) Inductively coupled plasma mass spectrometry based platforms for studies involving nanoparticle effects in biological samples. *Rapid Commun Mass Spectrom* 34:8726
166. Bartczak D, Vincent P, Goenaga-Infante H (2015) Determination of size- and number-based concentration of silica nanoparticles in

- a complex biological matrix by online techniques. *Anal Chem* 87(11):5482–5485
167. Bouzas-Ramos D, Menendez-Miranda M, Costa-Fernandez JM, Encinar JR, Sanz-Medel A (2016) Precise determination of the nanoparticle concentration and ligand density of engineered water-soluble HgSe fluorescent nanoparticles. *RSC Adv* 6(24):19964–19972
168. Garcia-Cortes M, Gonzalez ES, Fernandez-Arguelles MT et al (2017) Capping of Mn-doped ZnS quantum dots with DHLA for their stabilization in aqueous media: determination of the nanoparticle number concentration and surface ligand density. *Langmuir* 33(25):6333–6341
169. Zhou HY, Li X, Lemoff A, Zhang B, Yan B (2010) Structural confirmation and quantification of individual ligands from the surface of multi-functionalized gold nanoparticles. *Analyst* 135(6):1210–1213
170. Wilschefska SC, Baxter MR (2019) Inductively coupled plasma mass spectrometry: introduction to analytical aspects. *Clin Biochem Rev* 40(3):115–133
171. Fabricius AL, Duyster L, Meermann B, Temes TA (2014) ICP-MS-based characterization of inorganic nanoparticles-sample preparation and off-line fractionation strategies. *Anal Bioanal Chem* 406(2):467–479
172. Costo R, Heinke D, Gruttner C et al (2019) Improving the reliability of the iron concentration quantification for iron oxide nanoparticle suspensions: a two-institutions study. *Anal Bioanal Chem* 411(9):1895–1903
173. Xia XH, Yang MX, Wang YC, Zheng Y, Li Q, Chen J, Xia Y (2012) Quantifying the coverage density of poly(ethylene glycol) chains on the surface of gold nanostructures. *ACS Nano* 6(1):512–522
174. Elzey S, Tsai DH, Rabb SA, Yu LL, Winchester MR, Hackley VA (2012) Quantification of ligand packing density on gold nanoparticles using ICP-OES. *Anal Bioanal Chem* 403(1):145–149
175. Tong L, Lu E, Pichaandi J, Cao P, Nitz M, Winnik MA (2015) Quantification of surface ligands on NaYF<sub>4</sub> nanoparticles by three independent analytical techniques. *Chem Mater* 27(13):4899–4910
176. Vargas KM, San KA, Shon YS (2019) Isolated effects of surface ligand density on the catalytic activity and selectivity of palladium nanoparticles. *ACS Appl Nano Mater* 2(11):7188–7196
177. Yang R, Lin Y, Liu BY, Su Y, Tian Y, Hou X, Zheng C (2020) Simple universal strategy for quantification of carboxyl groups on carbon nanomaterials: carbon dioxide vapor generation coupled to microplasma for optical emission spectrometric detection. *Anal Chem* 92(5):3528–3534
178. Hinterwirth H, Kappel S, Waitz T, Prohaska T, Lindner W, Lämmerhofer M (2013) Quantifying thiol ligand density of self-assembled monolayers on gold nanoparticles by inductively coupled plasma-mass spectrometry. *ACS Nano* 7(2):1129–1136
179. Nicolardi S, van der Burgt YEM, Codee JDC et al (2017) Structural characterization of biofunctionalized gold nanoparticles by ultrahigh-resolution mass spectrometry. *ACS Nano* 11(8):8257–8264
180. Tsai DH, Shelton MP, DelRio FW et al (2012) Quantifying dithiothreitol displacement of functional ligands from gold nanoparticles. *Anal Bioanal Chem* 404(10):3015–3023
181. Goenaga-Infante H, Bartczak D (2020) Single particle inductively coupled plasma mass spectrometry (spICP-MS). In: characterization of nanoparticles: measurement processes for nanoparticles. Pp 65–77. <https://doi.org/10.1016/B978-0-12-814182-3.00003-1>
182. Mozhayeva D, Engelhard C (2020) A critical review of single particle inductively coupled plasma mass spectrometry—a step towards an ideal method for nanomaterial characterization. *J Anal At Spectrom* 35(9):1740–1783
183. Peters R, Herrera-Rivera Z, Undas A, van der Lee M, Marvin H, Bouwmeester H, Weigel S (2015) Single particle ICP-MS combined with a data evaluation tool as a routine technique for the analysis of nanoparticles in complex matrices. *J Anal At Spectrom* 30(6):1274–1285
184. Bings NH, Bogaerts A, Broekaert JAC (2010) Atomic spectroscopy: a review. *Anal Chem* 82(12):4653–4681
185. Abad C, Florek S, Becker-Ross H, Huang MD, Buzanich AG, Radtke M, Lippitz A, Hodoroaba VD, Schmid T, Heinrich HJ, Recknagel S, Jakubowski N, Panne U (2018) Zirconium permanent modifiers for graphite furnaces used in absorption spectrometry: understanding their structure and mechanism of action. *J Anal At Spectrom* 33(12):2034–2042
186. Aslund AKO, Sulheim E, Snipstad S et al (2017) Quantification and qualitative effects of different PEGylations on poly(butyl cyanoacrylate) nanoparticles. *Mol Pharm* 14(8):2560–2569
187. Ju S, Yeo WS (2012) Quantification of proteins on gold nanoparticles by combining MALDI-TOF MS and proteolysis. *Nanotechnology* 23(13):135701
188. Kim YP, Shon HK, Shin SK, Lee TG (2015) Probing nanoparticles and nanoparticle-conjugated biomolecules using time-of-flight secondary ion mass spectrometry. *Mass Spectrom Rev* 34(2):237–247
189. Cozzolino D (2015) Infrared spectroscopy as a versatile analytical tool for the quantitative determination of antioxidants in agricultural products, foods and plants. *Antioxidants* 4(3):482–497
190. Deidda R, Sacre P-Y, Clavaud M, Coïc L, Avohou H, Hubert P, Ziemons E (2019) Vibrational spectroscopy in analysis of pharmaceuticals: critical review of innovative portable and handheld NIR and Raman spectrophotometers. *Trac-Trends Anal Chem* 114:251–259
191. Kiefer J (2015) Recent advances in the characterization of gaseous and liquid fuels by vibrational spectroscopy. *Energies* 8(4):3165–3197
192. Berthomieu C, Hienerwadel R (2009) Fourier transform infrared (FTIR) spectroscopy. *Photosynth Res* 101(2–3):157–170
193. Lopez-Lorente AI, Mizaikoff B (2016) Recent advances on the characterization of nanoparticles using infrared spectroscopy. *Trac-Trends Anal Chem* 84:97–106
194. Gouadec G, Colombari P (2007) Raman spectroscopy of nanomaterials: how spectra relate to disorder, particle size and mechanical properties. *Prog Cryst Growth Ch* 53(1):1–56
195. Rytwo G, Zakai R, Wicklein B (2015) The use of ATR-FTIR spectroscopy for quantification of adsorbed compounds. *J Spectrosc* 2015:1–8
196. Mudunkotuwa IA, Al Minshid A, Grassian VH (2014) ATR-FTIR spectroscopy as a tool to probe surface adsorption on nanoparticles at the liquid-solid interface in environmentally and biologically relevant media. *Analyst* 139(5):870–881
197. Dengo N, Vittadini A, Natile MM, Gross S (2020) In-depth study of ZnS nanoparticle surface properties with a combined experimental and theoretical approach. *J Phys Chem C* 124(14):7777–7789
198. Altmann L, Kunz S, Bäumer M (2014) Influence of organic amino and thiol ligands on the geometric and electronic surface properties of Colloidally prepared platinum nanoparticles. *J Phys Chem C* 118(17):8925–8932
199. Garcia-Rico E, Alvarez-Puebla RA, Guerrini L (2018) Direct surface-enhanced Raman scattering (SERS) spectroscopy of nucleic acids: from fundamental studies to real-life applications. *Chem Soc Rev* 47(13):4909–4923
200. Feliu N, Hassan M, Garcia Rico E, Cui D, Parak W, Alvarez-Puebla R (2017) SERS quantification and characterization of proteins and other biomolecules. *Langmuir* 33(38):9711–9730

201. Zou S, Ma L, Li J, Xie Z, Zhao D, Ling Y, Zhang Z (2018) Quantification of trace chemicals in unknown complex systems by SERS. *Talanta* 186:452–458
202. Wang Y, Li P, Kong L (2013) Chitosan-modified PLGA nanoparticles with versatile surface for improved drug delivery. *AAPS PharmSciTech* 14(2):585–592
203. Palo E, Lahtinen S, Pakkila H et al (2018) Effective shielding of NaYF<sub>4</sub>:Yb(3+),Er(3+) upconverting nanoparticles in aqueous environments using layer-by-layer assembly. *Langmuir* 34(26):7759–7766
204. Podila R, Chacón-Torres J, Spear JT, Pichler T, Ayala P, Rao AM (2012) Spectroscopic investigation of nitrogen doped graphene. *Appl Phys Lett* 101(12):123108
205. Jaramillo AF, Baez-Cruz R, Montoya LF, Medinam C, Pérez-Tijerina E, Salazar F, Rojas D, Melendrez MF (2017) Estimation of the surface interaction mechanism of ZnO nanoparticles modified with organosilane groups by Raman spectroscopy. *Ceram Int* 43(15):11838–11847
206. Joshi AS, Gahane A, Thakur AK (2016) Deciphering the mechanism and structural features of polysorbate 80 during adsorption on PLGA nanoparticles by attenuated total reflectance—Fourier transform infrared spectroscopy. *RSC Adv* 6(110):108545–108557
207. Andersen AJ, Yamada S, Pramodkumar EK, Andresen TL, Boisen A, Schmid S (2016) Nanomechanical IR spectroscopy for fast analysis of liquid-dispersed engineered nanomaterials. *Sensors Actuators B Chem* 233:667–673
208. Mangos DN, Nakanishi T, Lewis DA (2014) A simple method for the quantification of molecular decorations on silica particles. *Sci Technol Adv Mater* 15(1):015002
209. Demin AM, Koryakova OV, Krasnov VP (2014) Quantitative determination of 3-aminopropylsilane on the surface of Fe<sub>3</sub>O<sub>4</sub> nanoparticles by attenuated total reflection infrared spectroscopy. *J Appl Spectrosc* 81(4):565–569
210. Valkenier H, Malyskiy V, Blond P, Retout M, Mattiuzzi A, Goole J, Raussens V, Jabin I, Bruylants G (2017) Controlled functionalization of gold nanoparticles with mixtures of calix[4]arenes revealed by infrared spectroscopy. *Langmuir* 33(33):8253–8259
211. Tsai DH, Davila-Morris M, DelRio FW et al (2011) Quantitative determination of competitive molecular adsorption on gold nanoparticles using attenuated total reflectance-Fourier transform infrared spectroscopy. *Langmuir* 27(15):9302–9313
212. Yuanyuan C, Zhibin W (2018) Quantitative analysis modeling of infrared spectroscopy based on ensemble convolutional neural networks. *Chemom Intell Lab Syst* 181:1–10
213. Hard X-ray photoelectron spectroscopy (HAXPES) (2016). In: Woicik JC (ed) Springer series in surface sciences. vol 59. Springer. doi:<https://doi.org/10.1007/978-3-319-24043-5>
214. Weigert F, Müller A, Häusler I, Geißler D, Skrobilin D, Krumrey M, Unger W, Radnik J, Resch-Genger U (2020) Combining HR-TEM and XPS to elucidate the core-shell structure of ultrabright CdSe/CdS semiconductor quantum dots. *Sci Rep* 10(1):20712
215. Saleh MI, Rühle B, Wang S, Radnik J, You Y, Resch-Genger U (2020) Assessing the protective effects of different surface coatings on NaYF<sub>4</sub>:Yb<sup>3+</sup>, Er<sup>3+</sup> upconverting nanoparticles in buffer and DMEM. *Sci Rep* 10(1):19318
216. Dietrich PM, Hennig A, Holzweber M, Thiele T, Borchering H, Lippitz A, Schedler U, Resch-Genger U, Unger WES (2014) Surface analytical study of poly(acrylic acid)-grafted microparticles (beads): characterization, chemical derivatization, and quantification of surface carboxyl groups. *J Phys Chem C* 118(35):20393–20404
217. Fairclough SM, Tyrrell EJ, Graham DM, Lunt PJB, Hardman SJO, Pietzsch A, Hennies F, Moghal J, Flavell WR, Watt AAR, Smith JM (2012) Growth and characterization of strained and alloyed type-II ZnTe/ZnSe Core-shell nanocrystals. *J Phys Chem C* 116(51):26898–26907
218. Hardman SJO, Graham DM, Stubbs SK, Spencer BF, Seddon EA, Fung HT, Gardonio S, Sirotti F, Silly MG, Akhtar J, O'Brien P, Binks DJ, Flavell WR (2011) Electronic and surface properties of PbS nanoparticles exhibiting efficient multiple exciton generation. *Phys Chem Chem Phys* 13(45):20275–20283
219. Page RC, Espinobarro-Velazquez D, Leontiadou MA, Smith C, Lewis EA, Haigh SJ, Li C, Radtke H, Pengpad A, Bondino F, Magnano E, Pis I, Flavell WR, O'Brien P, Binks DJ (2015) Near-unity quantum yields from chloride treated CdTe colloidal quantum dots. *Small* 11(13):1548–1554
220. Wang Y-C, Engelhard MH, Baer DR, Castner DG (2016) Quantifying the impact of nanoparticle coatings and nonuniformities on XPS analysis: gold/silver core-shell nanoparticles. *Anal Chem* 88(7):3917–3925
221. Torelli MD, Putans RA, Tan YZ, Lohse SE, Murphy CJ, Hamers RJ (2015) Quantitative determination of ligand densities on nanomaterials by X-ray photoelectron spectroscopy. *ACS Appl Mater Interfaces* 7(3):1720–1725
222. ISO 18118:2015(en) Surface chemical analysis—Auger electron spectroscopy and X-ray photoelectron spectroscopy - Guide to the use of experimentally determined relative sensitivity factors for the quantitative analysis of homogeneous materials (2015). International Organization for Standardization (ISO)
223. Seah MP (1995) A system for the intensity calibration of electron spectrometers. *J Electron Spectros* 71(3):191–204
224. Hesse R, Streubel P, Szargan R (2005) Improved accuracy of quantitative XPS analysis using predetermined spectrometer transmission functions with UNIFIT 2004. *Surf Interface Anal* 37(7):589–607
225. Walton J, Fairley N (2006) A traceable quantification procedure for a multi-mode X-ray photoelectron spectrometer. *J Electron Spectros* 150(1):15–20
226. Graf N, Lippitz A, Gross T, Pippig F, Holländer A, Unger WES (2010) Determination of accessible amino groups on surfaces by chemical derivatization with 3,5-bis(trifluoromethyl)phenyl isothiocyanate and XPS/NEXAFS analysis. *Anal Bioanal Chem* 396(2):725–738
227. Gross T, Pippig F, Merz B, Merz R, Vohrer U, Mix R, Steffen H, Bremser W, Unger WES (2010) Determination of OH groups at plasma oxidised poly(propylene) by TFAA chemical derivatisation XPS: an inter-laboratory comparison. *Plasma Process Polym* 7(6):494–503
228. Jasieniak J, Smith L, van Embden J, Mulvaney P, Califano M (2009) Re-examination of the size-dependent absorption properties of CdSe quantum dots. *J Phys Chem C* 113(45):19468–19474
229. Smekal W, Werner WSM, Powell CJ (2005) Simulation of electron spectra for surface analysis (SESSA): a novel software tool for quantitative Auger-electron spectroscopy and X-ray photoelectron spectroscopy. *Surf Interface Anal* 37(11):1059–1067
230. Chudzicki M, Werner WSM, Shard AG, Wang YC, Castner DG, Powell CJ (2015) Evaluating the internal structure of Core-Shell nanoparticles using X-ray photoelectron intensities and simulated spectra. *J Phys Chem C* 119(31):17687–17696
231. Kalbe H, Rades S, Unger WES Determining shell thicknesses in stabilised CdSe@ZnS core-shell nanoparticles by quantitative XPS analysis using an infinitesimal columns model. *J Electron Spectros* 2016, 212:34–43
232. Powell CJ, Werner WSM, Kalbe H, Shard AG, Castner DG (2018) Comparisons of analytical approaches for determining shell thicknesses of core-shell nanoparticles by X-ray photoelectron spectroscopy. *J Phys Chem C* 122(7):4073–4082
233. Sarma DD, Santra PK, Mukherjee S, Nag A (2013) X-ray photoelectron spectroscopy: a unique tool to determine the internal Heterostructure of nanoparticles. *Chem Mater* 25(8):1222–1232

234. Acquafredda P (2019) XRF technique. *Phys Sci Rev* 4(8): 20180171
235. Adams C, Brand C, Dentith M, Fiorentini M, Caruso S, Mehta M (2020) The use of pXRF for light element geochemical analysis: a review of hardware design limitations and an empirical investigation of air, vacuum, helium flush and detector window technologies. *Geochem-Explor Env A* 20(3):366–380
236. Lai MS, Xiang LW, Lin JM, Li HF (2013) Quantitative analysis of elements (C, N, O, Al, Si and Fe) in polyamide with wavelength dispersive X-ray fluorescence spectrometry. *Sci China Chem* 56(8):1164–1170
237. Dietrich PM, Streeck C, Glamsch S, Ehler C, Lippitz A, Nutsch A, Kulak N, Beckhoff B, Unger WES (2015) Quantification of Silane molecules on oxidized silicon: are there options for a traceable and absolute determination? *Anal Chem* 87(19):10117–10124
238. Fischer T, Dietrich PM, Streeck C, Ray S, Nutsch A, Shard A, Beckhoff B, Unger WES, Rurack K (2015) Quantification of variable functional-group densities of mixed-silane monolayers on surfaces via a dual-mode fluorescence and XPS label. *Anal Chem* 87(5):2685–2692
239. Reinhardt F, Osan J, Torok S et al (2012) Reference-free quantification of particle-like surface contaminations by grazing incidence X-ray fluorescence analysis. *J Anal At Spectrom* 27(2): 248–255
240. Nowak SH, Reinhardt F, Beckhoff B, Dousse JC, Szlachetko J (2013) Geometrical optics modelling of grazing incidence X-ray fluorescence of nanoscaled objects. *J Anal At Spectrom* 28(5): 689–696
241. Meder F, Kaur S, Treccani L, Rezwan K (2013) Controlling mixed-protein adsorption layers on colloidal alumina particles by tailoring carboxyl and hydroxyl surface group densities. *Langmuir* 29(40):12502–12510
242. Ederer J, Janos P, Ecorchard P et al (2017) Determination of amino groups on functionalized graphene oxide for polyurethane nanomaterials: XPS quantitation vs. functional speciation. *RSC Adv* 7(21):12464–12473
243. Huynh J, Palacio R, Safizadeh F, Lefèvre G, Descostes M, Eloy L, Guignard N, Rousseau J, Royer S, Tertre E, Batonneau-Gener I (2017) Adsorption of uranium over NH<sub>2</sub>-functionalized ordered silica in aqueous solutions. *ACS Appl Mater Interfaces* 9(18): 15672–15684
244. van de Waterbeemd M, Sen T, Biagini S, Bruce IJ (2010) Surface functionalisation of magnetic nanoparticles: quantification of surface to bulk amine density. *Micro Nano Lett* 5(5):282–285
245. Bakhshaei S, Kamboh MA, Nodeh HR, Md Zain S, Mahmud Rozi SK, Mohamad S, Mohammed Mohialdeen IA (2016) Magnetic solid phase extraction of polycyclic aromatic hydrocarbons and chlorophenols based on cyano-ionic liquid functionalized magnetic nanoparticles and their determination by HPLC-DAD. *RSC Adv* 6(80):77047–77058
246. Mansfield E (2015) Recent advances in thermal analysis of nanoparticles: Methods, models and kinetics. In: Tewary VK, Zhang Y (eds) *Modeling, characterization, and production of Nanomaterials - Electronics, Photonics and Energy Applications*. Woodhead Publishing, pp 167–178. <https://doi.org/10.1016/b978-1-78242-228-0.00006-5>
247. Steinhäuser KG, Sayre PG (2017) Reliability of methods and data for regulatory assessment of nanomaterial risks. *NanoImpact* 7: 66–74
248. Das D, Yang Y, O'Brien JS et al (2014) Synthesis and physicochemical characterization of mesoporous SiO<sub>2</sub> nanoparticles. *J Nanomater* 2014:176015
249. Seby KB, Mansfield E (2015) Determination of the surface density of polyethylene glycol on gold nanoparticles by use of micro-scale thermogravimetric analysis. *Anal Bioanal Chem* 407(10): 2913–2922
250. Mansfield E, Tyner KM, Poling CM, Blacklock JL (2014) Determination of nanoparticle surface coatings and nanoparticle purity using microscale thermogravimetric analysis. *Anal Chem* 86(3):1478–1484
251. Schirowski M, Hauke F, Hirsch A (2019) Controlling the degree of functionalization: in-depth quantification and side-product analysis of Diazonium chemistry on SWCNTs. *Chemistry* 25(55): 12761–12768
252. Clausen PA, Kofoed-Sorensen V, Norgaard AW, Sahlgren NM, Jensen KA (2019) Thermogravimetry and mass spectrometry of extractable organics from manufactured nanomaterials for identification of potential coating components. *Materials* 12(22):3657
253. Lagarrigue P, Soulié J, Grossin D, Dupret-Bories A, Combes C, Darcos V (2020) Well-defined polyester-grafted silica nanoparticles for biomedical applications: synthesis and quantitative characterization. *Polymer* 211:123048
254. Demin AM, Mekhaev AV, Kandarakov OF et al (2020) L-lysine-modified Fe<sub>3</sub>O<sub>4</sub> nanoparticles for magnetic cell labeling. *Colloid Surface B* 190:110879
255. Kunc F, Kodra O, Brinkmann A, Lopinski GP, Johnston LJ (2020) A multi-method approach for quantification of surface coatings on commercial zinc oxide nanomaterials. *Nanomaterials* 10(4):678
256. Jang E, Kim Y, Won YH, Jang H, Choi SM (2020) Environmentally friendly InP-based quantum dots for efficient wide color gamut displays. *ACS Energy Lett* 5(4):1316–1327
257. Bajaj M, Wangoo N, Jain DVS, Sharma RK (2020) Quantification of adsorbed and dangling citrate ions on gold nanoparticle surface using thermogravimetric analysis. *Sci Rep* 10(1):8213
258. You Z, Nirmalanathan-Budau N, Resch-Genger U, Panne U, Weidner SM (2020) Separation of polystyrene nanoparticles bearing different carboxyl group densities and functional groups quantification with capillary electrophoresis and asymmetrical flow field flow fractionation. *J Chromatogr A* 1626:461392
259. Giusti A, Atluri R, Tsekovska R, Gajewicz A, Apostolova MD, Battistelli CL, Bleeker EAJ, Bossa C, Bouillard J, Dusinska M, Gómez-Fernández P, Grafström R, Gromelski M, Handzhiyski Y, Jacobsen NR, Jantunen P, Jensen KA, Mech A, Navas JM et al (2019) Nanomaterial grouping: existing approaches and future recommendations. *NanoImpact* 16:100182

**Publisher's note** Springer Nature remains neutral with regard to jurisdictional claims in published maps and institutional affiliations.

## 5.2.2 | Dual Color pH Probes Made From Silica and Polystyrene Nanoparticles and Their Performance in Cell Studies

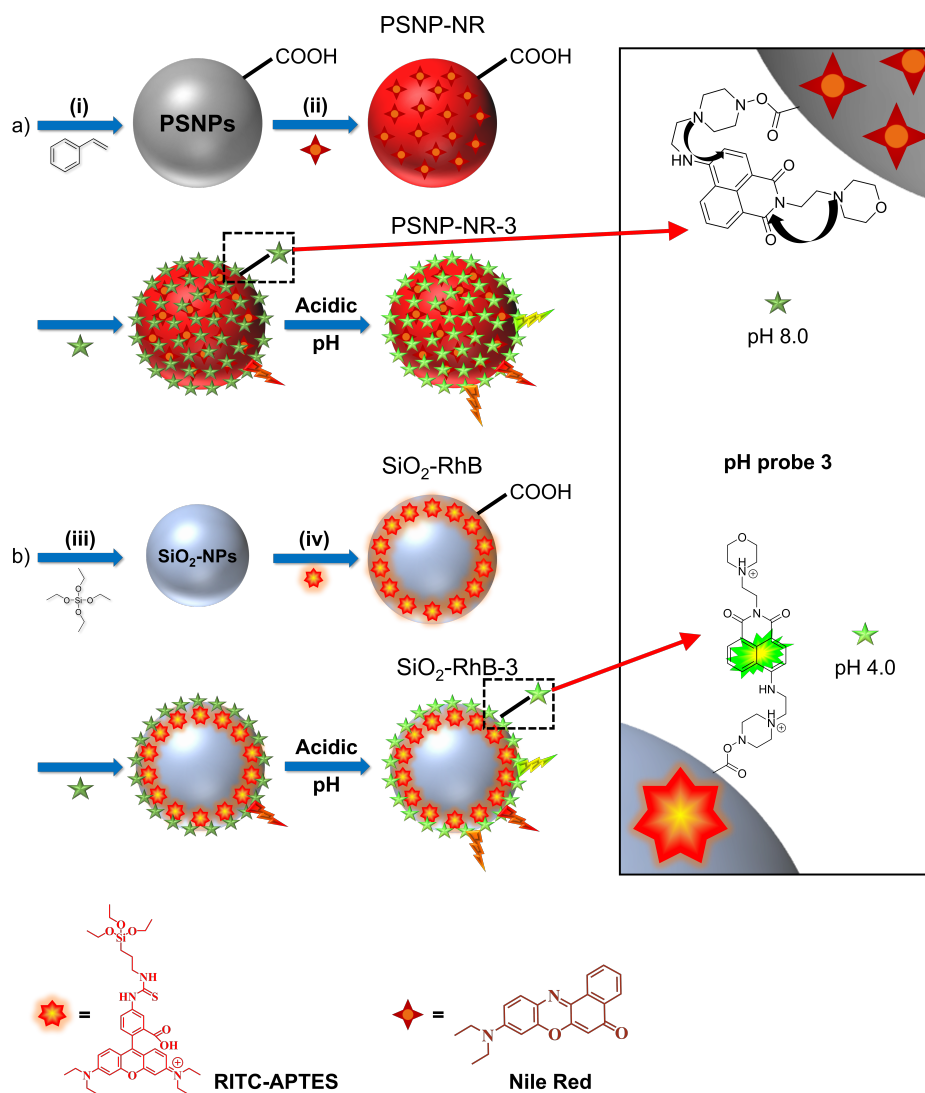


Figure 25: Schematic depiction of the synthesis of dye-stained polystyrene and silica nanoparticles surface modified with a pH-sensitive optical probe, taken with permission from P. Srivastava *et al.*, copyright 2023 Scientific Reports.<sup>[11]</sup>

Authors: Priyanka Srivastava, Isabella Tavernaro, **Lena Scholtz**, Claudia Genger, Pia Welker, Frank Schreiber, Klas Meyer, Ute Resch-Genger\*

To this work, L. Scholtz contributed by synthesizing the unstained and NR-stained PSNPs. Together with I. Tavernaro, L. Scholtz performed the colloidal stability study of these particles, the quantification of the accessible FGs on their surface, and the physico-chemical particle

characterization. P. Srivastava and I. Tavernaro planned the study, with the former synthesizing the pH-responsive optical probe and attaching it to both polystyrene and silica particles, and the latter synthesizing the silica NPs and performing the corresponding characterization. The pH-dependent NMR measurements were performed by K. Meyer, the spectroscopic studies by P. Srivastava with help from I. Tavernaro. The cellular uptake studies were planned by C. Genger, with P. Welker conducting the epifluorescence measurements, and P. Srivastava and F. Schreiber performing the confocal measurements. The manuscript text was written by P. Srivastava, and largely edited by U. Resch-Genger with help from I. Tavernaro, L. Scholtz and C. Genger. The corresponding figures were prepared by I. Tavernaro and L. Scholtz with help from P. Srivastava and P. Welker.

**Estimated Contribution: 20%**

Work published in journal: Scientific Reports, 2023

See online here: <https://www.nature.com/articles/s41598-023-28203-0>

DOI: <https://doi.org/10.1038/s41598-023-28203-0>

This article is licensed under a Creative Commons Attribution 4.0 International (CC BY 4.0, <https://creativecommons.org/licenses/by/4.0/>).



# OPEN Dual color pH probes made from silica and polystyrene nanoparticles and their performance in cell studies

Priyanka Srivastava<sup>1,7</sup>, Isabella Tavernaro<sup>1,7</sup>, Lena Scholtz<sup>1,2</sup>, Claudia Genger<sup>3,4</sup>, Pia Welker<sup>3,4</sup>, Frank Schreiber<sup>5</sup>, Klas Meyer<sup>6</sup> & Ute Resch-Genger<sup>1✉</sup>

Ratiometric green–red fluorescent nanosensors for fluorometrically monitoring pH in the acidic range were designed from 80 nm-sized polystyrene (PS) and silica (SiO<sub>2</sub>) nanoparticles (NPs), red emissive reference dyes, and a green emissive naphthalimide pH probe, analytically and spectroscopically characterized, and compared regarding their sensing performance in aqueous dispersion and in cellular uptake studies. Preparation of these optical probes, which are excitable by 405 nm laser or LED light sources, involved the encapsulation of the pH-inert red-fluorescent dye Nile Red (NR) in the core of self-made carboxylated PSNPs by a simple swelling procedure and the fabrication of rhodamine B (RhB)-stained SiO<sub>2</sub>-NPs from a silane derivative of pH-insensitive RhB. Subsequently, the custom-made naphthalimide pH probe, that utilizes a protonation-controlled photoinduced electron transfer process, was covalently attached to the carboxylic acid groups at the surface of both types of NPs. Fluorescence microscopy studies with the molecular and nanoscale optical probes and A549 lung cancer cells confirmed the cellular uptake of all probes and their penetration into acidic cell compartments, i.e., the lysosomes, indicated by the switching ON of the green naphthalimide fluorescence. This underlines their suitability for intracellular pH sensing, with the SiO<sub>2</sub>-based nanosensor revealing the best performance regarding uptake speed and stability.

One of the most frequently measured environmental parameters in the life sciences using fluorescent probes is pH<sup>1–7</sup>. This is related to its importance for proper cell function and its potential to act as an indicator for inflammatory diseases and cancer. Although the pH value in the cytoplasm of tumour cells is not very different to healthy cells, the pH value of their microenvironment is significantly altered and is a potential target for cancer therapy<sup>8</sup>. Moreover, the determination and monitoring of pH values in different cell compartments allows, e.g., to localize vesicular structures of the endosomal-lysosomal apparatus in cells. The lowest pH values of about 4.5 are reached in the lysosomes involved in autophagy, protein degradation, apoptosis, and cell defence mechanism<sup>9,10</sup>. The interest in measuring pH in biological systems together with the general advantages offered by fluorescence methods such as relatively simple and inexpensive instrumentation<sup>11,12</sup>, minimal invasiveness, and suitability for the in situ online monitoring of local pH using, e.g., optical microscopy, and remote sensing<sup>11,12</sup> has triggered the development of pH-responsive organic fluorophores from different dye classes. This includes BODIPY and BF<sub>2</sub>-chelated tetraarylazadipyrromethene dyes<sup>13–18</sup>, as well as xanthene<sup>19–24</sup>, cyanine<sup>25–29</sup>, squaraine<sup>23</sup>, and naphthalimide fluorophores<sup>30–33</sup>, which exploit intramolecular photoinduced electron transfer (PET), intramolecular charge transfer (ICT), and fluorescence energy transfer processes for the signaling of pH. Optical parameters utilized for the determination and monitoring of pH are pH-induced changes in the spectral position and/or intensity of the dye's absorption and/or emission bands or fluorescence lifetime<sup>31,34–37</sup>. In addition,

<sup>1</sup>Division Biophotonics, Federal Institute for Materials Research and Testing (BAM), Richard-Willstaetter-Str. 11, 12489 Berlin, Germany. <sup>2</sup>Institut für Chemie und Biochemie, Freie Universität Berlin, Takustr. 3, 14195 Berlin, Germany. <sup>3</sup>nanoPET Pharma GmbH, Robert-Koch-Platz 4, 10115 Berlin, Germany. <sup>4</sup>Charité-Universitätsmedizin Berlin, Charitéplatz 1, 10117 Berlin, Germany. <sup>5</sup>Division Biodeterioration and Reference Organisms, Federal Institute for Materials Research and Testing (BAM), Unter den Eichen 87, 12205 Berlin, Germany. <sup>6</sup>Division Process Analytical Technology, Federal Institute for Materials Research and Testing (BAM), Richard-Willstaetter-Str. 11, 12489 Berlin, Germany. <sup>7</sup>These authors contributed equally: Priyanka Srivastava and Isabella Tavernaro. ✉email: ute.resch@bam.de

protonation-induced ring opening and closing mechanisms accompanied by characteristic modifications in the absorption and emission properties have been employed for pH sensing<sup>4,38</sup>.

In the last decades, also an increasing number of modularly built nanoparticle (NP)-based sensors has been reported, utilizing, e.g., silica and polymer NPs, lanthanide-based upconversion NPs, and semiconductor quantum dots in combination with organic sensor dyes<sup>4,19,39–46</sup>. Nanomaterials which have been the most frequently employed for the preparation of nanosensors for bioimaging applications are organic polymeric particles such as biocompatible polystyrene (PS) NPs (PSNPs), and inorganic silica (SiO<sub>2</sub>) NPs (SiO<sub>2</sub>-NPs) that can be prepared in a variety of sizes with different surface functionalities<sup>47–51</sup>. Advantages of dye-based polymer and silica nanosensors compared to molecular sensors are a straightforward signal amplification, the possibility to apply hydrophobic fluorophores for analyte sensing in aqueous environments, and the ease of combining two or more different fluorophores for realizing ratiometric or self-referenced sensors<sup>52</sup>, which read out the quotient of a spectrally distinguishable analyte responsive and an analyte insensitive (reference) fluorescence signal at a single excitation wavelength. With this sensor design, fluctuations of the excitation light source can be elegantly considered, which would otherwise directly affect and distort the fluorescence output of the sensor<sup>52,53</sup>. In the case of polymer and silica nanomaterials, ratiometric nanosensors are commonly obtained by either incorporating a sensor dye and a reference dye into the particle core or by the staining of the particle core with a reference dye followed by the covalent attachment of the sensor molecules to functional groups at the particle surface<sup>49,54</sup>. These surface groups can be also utilized for the binding of recognition moieties such as (bio)molecules, proteins, and antibodies<sup>55,56</sup>, yielding targeted nanostructures. Core encapsulation enables the utilization of hydrophobic fluorophores without reactive groups and can increase the stability particularly of near infrared (NIR)-emissive chromophores. For sensor dyes, core encapsulation is only suitable if the target analyte can penetrate the particle matrix. In the case of polymer particles such as PSNPs, core staining with hydrophobic organic dyes can be easily achieved with a simple swelling procedure, utilizing premanufactured NPs that bear surface functionalities such as carboxyl or amino groups<sup>57,58</sup>. SiO<sub>2</sub>-NPs can be encoded with dyes by covalently coupling reactive dyes to the silica precursors, forming the silica matrix of the core or shells surrounding the core. Alternatively, physisorption during PSNP or SiO<sub>2</sub>-NP formation can be exploited, thereby sterically incorporating the dye molecules into the polymer or silica network. This requires fluorophores that are sufficiently stable under the reaction conditions employed for NP formation.

In the following, we present a comparative screening study of the sensing potential of two sets of closely matching ratiometric pH nanosensors made from PSNPs and SiO<sub>2</sub>-NPs of comparable size which were core stained with a red emissive reference dye and surface-functionalized with a novel hydrophilic neutral PET-operated naphthalimide dye that exhibits a pH-responsive green fluorescence. This includes the synthesis and spectroscopic characterization of the pH-sensitive naphthalimide dye and the analytical and optical characterization of the different nanosensors, providing application-relevant particle properties such as size, size distribution, surface charge / zeta potential, sensor dye labeling density, and fluorescence quantum yields, as well as reversibility and stability studies. Subsequently, cellular uptake and imaging studies were performed with both types of nanosensors. As we aimed for a comparison of both types of nanosensors and not a complete characterization of their sensor parameters and performance, we kept as many nanosensor properties as closely matching as possible including particle size, sensor dye, spectroscopic properties of the reference dyes, nanosensor surface chemistry, and number of surface-bound sensor dyes. In addition, all experiments were performed with the same NP concentration to enable a comparison of the pH sensing potential of the polymer and silica nanosensors.

## Results and discussion

As a prerequisite for the fabrication of green–red emissive pH nanosensors utilizing custom made PSNPs and SiO<sub>2</sub>-NPs, we developed the hydrophilic PET-operated, naphthalimide-based fluorescent pH probe **3** shown in Fig. 1, intended for the signaling of acidic pH values by the protonation-induced switching ON of its green fluorescence and allow for lysosomal targeting<sup>31,59,60</sup>. Compared to other pH sensitive dyes such as fluorescein, the incorporated lysosomal targeting morpholine group was expected to be beneficial for the intended cell studies. The synthesis of optical probe **3**, which is summarized in Fig. 1 and detailed in the Supporting Information (SI; Figs. S1–S10), involved the covalent linking of a morpholine unit to 4-bromo-1,8-naphthalic anhydride **1** for the selective lysosomal targeting and the incorporation of a piperazine moiety to improve the water solubility and induce a pH sensitivity of the chromophore's fluorescence. Subsequently, the optical properties of **3** were characterized by absorption and emission spectroscopy and fluorescence quantum yield measurements at different pH values.

As shown in Fig. 2, fluorescent probe **3** has a broad absorption band at 405 nm ( $\epsilon = 4,920 \text{ M}^{-1} \text{ cm}^{-1}$ ) that is attributed to an ICT from the unprotonated nitrogen atoms of the piperazine and morpholine units to the naphthalimide chromophore. **3** exhibits a very weak emission centered at 530 nm upon excitation ( $\lambda_{\text{EX}}$ ) at 405 nm in Britton Robinson (B–R) buffer at a pH of 8.1. The low fluorescence intensity at neutral and basic pH values is ascribed to PET-induced quenching of the naphthalimide fluorescence by the nitrogen atoms of the morpholine and piperazine moiety, that can be reversibly blocked at acidic pH values as was observed for other naphthalimide-based fluorescent probes<sup>30–33</sup>. The ICT and PET processes controlling the photophysics of **3** were confirmed by nuclear magnetic resonance spectrometry (NMR) measurements in D<sub>2</sub>O in the pH range of 8.5 to 2.5 (SI, Fig. S11). As revealed by this NMR study, the amine group at the 4th position acts as a donor and the naphthalimide chromophore as an acceptor for the ICT process determining the absorption features of **3**. Protonation of the nitrogen atoms of the morpholine and piperazine moiety at acidic pH values, indicated by a downfield shift of the aromatic and some aliphatic signals of the morpholine and piperazine unit in the NMR spectrum, prevents PET, thereby turning ON the green naphthalimide fluorescence. This provides the basis for the pH-dependent reversible ON–OFF switching of probe **3**.

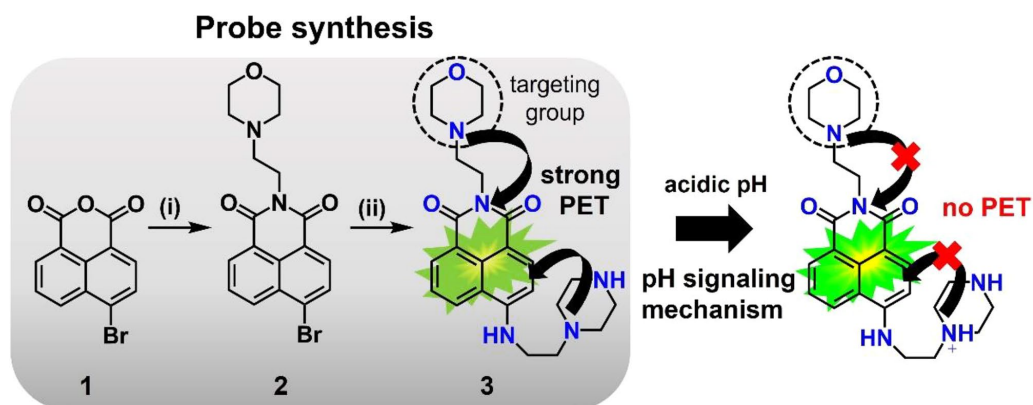


**Figure 1.** Synthesis of the hydrophilic neutral optical pH probe **3** designed for lysosomal targeting and its pH signaling mechanism; (i) 4-(2-Aminoethyl) morpholine, ethanol, 50 °C, 5 h; (ii) 1-(2-Aminoethyl) piperazine, triethylamine, pyridine, reflux, overnight. The pH signaling mechanism of **3** relies on an intramolecular photoinduced electron transfer (PET) from the unprotonated nitrogen atoms of the piperazine and morpholine units to the naphthalimide chromophore. Nitrogen protonation results in the blocking of these fluorescence quenching PET processes leading to the appearance of the chromophore's green fluorescence at acidic pH values as confirmed in the following sections.

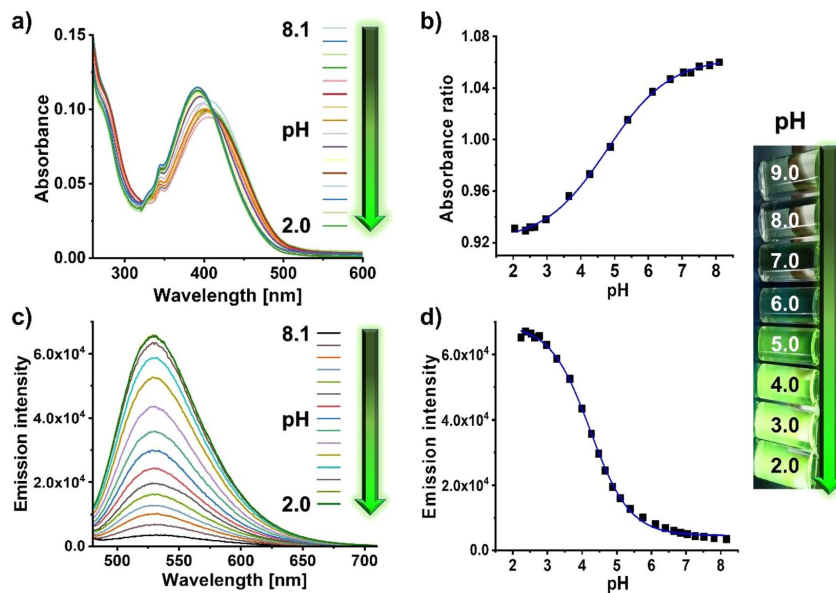


**Figure 2.** pH-dependent spectroscopic properties of fluorescent probe **3**; (a) absorption spectra (25  $\mu\text{M}$ ) at different pH values; (b) plot of the absorbance ratio (405 nm/390 nm) at different pH values; (c) emission spectra (0.13  $\mu\text{M}$ ) at different pH values; and (d) emission intensity ( $\lambda_{\text{ex}} = 405 \text{ nm}$ ) at different pH values used to calculate the  $\text{pK}_a$  of the optical probe. The inset shows a photograph of the color changes of the emission of **3** under UV light at different pH values that can be detected by naked eye.

A more detailed spectroscopic study of the pH sensing behavior of **3** in the pH range of 8.1 to 2.0 in B-R buffer revealed a hypsochromic shift of the ICT absorption band from 405 to 392 nm for pH < 5 and a decrease in absorbance for further decreasing pH values (Fig. 2 and SI, Fig. S12). These pH-induced spectral and intensity changes in absorption were subsequently considered for the calculation of the probe's pK<sub>a</sub> and the fluorescence measurements. Fluorescence measurements confirmed a gradual increase in the intensity of the naphthalimide fluorescence at 530 nm that remained eventually constant at a pH value of 2.5. A sigmoidal fit of the plot of the pH-dependent fluorescence intensity at 530 nm gave a pK<sub>a</sub> = 4.23 ± 0.02. The pK<sub>a</sub> value of **3** is suitable for lysosomal targeting as the lysosomes exhibit pH values of about 4.5<sup>61</sup>. In the inset of Fig. 2, the visual changes in the emission color under ultraviolet (UV) light in the pH range of 9.0 (colorless) to 2.0 (green) are displayed that can be detected by naked eye. The fluorescence quantum yield of **3**, which was absolutely measured in B-R buffer in the pH range of 8.1 to 2.0, revealed a constant increase for decreasing pH values (SI, Fig. S13 and Table S1) and amounted to 37% for fully protonated probe **3**.

**Reversibility and photostability studies with optical probe 3.** Reversibility studies with **3** performed at pH values varied between 8.1 and 4.8 showed no loss in fluorescence. This is a prerequisite for the applicability of **3** as a pH sensor (SI, Fig. S14). Photostability studies of **3** at pH 4.0 in B-R buffer at an illumination wavelength of λ<sub>ex</sub> = 405 nm utilizing the 450 W xenon lamp of the spectrofluorometer revealed only small changes in the fluorescence spectrum and fluorescence intensity of **3** for illumination times of up to 8 h (SI, Fig. S15).

**Dual color emissive ratiometric PSNP- and SiO<sub>2</sub>-NP based nanosensors.** In the next step, we prepared two sets of ratiometric pH nanosensors by combining our lysosomal targeting pH probe with dye-stained PSNPs and SiO<sub>2</sub>-NPs of closely matching size. Therefore, pristine carboxylated PSNPs with an average particle size of about 80 nm were synthesized by an emulsion polymerization approach<sup>57</sup>. For core staining, the hydrophobic and neutral dye Nile Red (NR) was chosen as pH-inert reference dye and encapsulated in the polymer matrix by a simple swelling procedure (Fig. 3a<sup>41,57</sup>). The synthesis of the amorphous SiO<sub>2</sub>-NPs of similar size involved multistep hydrolysis and condensation reactions of the silicon precursor in a biphasic cyclohexane/water system (SI, Fig. S17) and different dye staining approaches. The initially pursued attempt to also use NR as a reference dye for the SiO<sub>2</sub>-NPs failed because the incorporation of NR into the SiO<sub>2</sub> matrix by adsorptive interactions led to an increase in particle size (SI, Fig. S21), and the dye molecules were washed out during NP purification (data not shown), as has been reported before for other dyes<sup>62</sup>. The synthesis of a NR silane derivative (SI, Fig. S18–S20), that should enable the covalent attachment of NR to the SiO<sub>2</sub> matrix to prevent dye leaking also did not yield a higher number of encapsulated dye molecules per particle. Therefore, we modified our preparation strategy and synthesized first amorphous SiO<sub>2</sub>-NPs with a size of 60 nm (SI, Fig. S17) followed by the shelling of the resulting SiO<sub>2</sub> core with a 20 nm thick rhodamine B isothiocyanate (RhB)-stained silica layer made from a dye-silane derivative obtained by reacting RhB with an amino silane (SI, Fig. S18b)<sup>63,64</sup>. With this approach, the size of both types of nanosensors could be kept identical and dye leaking was prevented (Fig. 3b). Subsequent surface functionalization of the 80 nm red emissive SiO<sub>2</sub>-NPs with carboxylic acid groups was achieved by a two-step post-synthetic grafting reaction (Fig. 3b). Dye leakage experiments performed after each grafting reaction showed no influence of the functional groups grafted onto the particle surface (SI, Fig. S24). Thereby, the particle surface chemistry and the conjugation chemistry used for the covalent attachment of **3** to the PSNPs and SiO<sub>2</sub>-NPs could also be kept identical as a prerequisite for the intended nanosensor comparison.

The PSNPs and SiO<sub>2</sub>-NPs were characterized by dynamic light scattering (DLS) and zeta potential measurements before and after the loading with the reference dyes, as well as after the surface modification with carboxylic acid groups (Fig. 4b,c, and SI, Figs. S22 and S23). The observed increase in z-average after dye loading of the PSNPs (177 ± 7 nm) compared to the pristine particles (96 ± 0.2 nm) is attributed to the influence of the swelling procedure. However, the hydrodynamic diameter of the particles, determined from the number distribution, showed a smaller increase in particle size from 68 ± 14 to 74 ± 26 nm. While the z-average of pristine SiO<sub>2</sub>-NPs (69 ± 1 nm) only increased by about 20 nm during the cladding of the dyed silica shell (SiO<sub>2</sub>-RhB), the particle size significantly increased after the two-step surface modification to 164 ± 3 nm and 176 ± 1 nm for SiO<sub>2</sub>-RhB-NH<sub>2</sub> and SiO<sub>2</sub>-RhB-COOH, respectively. Transmission electron microscopy (TEM) measurements of the PSNPs and SiO<sub>2</sub>-NPs performed to determine the size of the particle cores and the particle morphology gave particle sizes of 77.4 ± 6.5 nm (pristine PSNPs), 60.5 ± 1.6 nm (pristine SiO<sub>2</sub>-NPs, Fig. 4a, and SI, Fig. S21d), and 79.3 ± 2.4 nm (SiO<sub>2</sub>-RhB-COOH, after surface modification with COOH groups; Fig. 4a). The PSNPs exhibited a nearly spherical shape with a smooth particle surface while the SiO<sub>2</sub>-NPs showed a rougher surface due to their synthesis in multiple steps. Zeta potential measurements of the carboxylated PSNPs and SiO<sub>2</sub>-NPs gave negative zeta potentials of -58 ± 14 mV and -23.9 ± 0.7 mV, indicative of a high colloidal stability of both particles. The number of reference dye molecules per NP was determined spectroscopically to 130 NR molecules for the PSNPs and to 223 RhB-APTES molecules (APTES: 3-aminopropyltriethoxysilane) for the SiO<sub>2</sub>-NPs (SI, Figs. S25–S28), after particle dissolution. For the fluorometric quantification, calibration curves of solutions of known concentrations of NR in tetrahydrofuran (THF) and RhB-APTES in aqueous B-R buffer were utilized and the emission spectra of previously dried amounts of PSNP-NR-COOH and SiO<sub>2</sub>-RhB-COOH of known mass dissolved in an aqueous B-R buffer were measured.

Subsequently, the number of accessible COOH groups on the surface of the PSNP-NR-COOH and SiO<sub>2</sub>-RhB-COOH systems was determined by an optical toluidine blue (TBO) assay previously assessed by us for the characterization of the number of carboxylic acid groups on carboxylated polymethylmethacrylate particles<sup>65</sup>. This assay relies on the adsorption of the positively charged dye TBO onto the surface of the negatively charged particles and electrostatic interactions and requires the determination of a stoichiometry factor to consider the



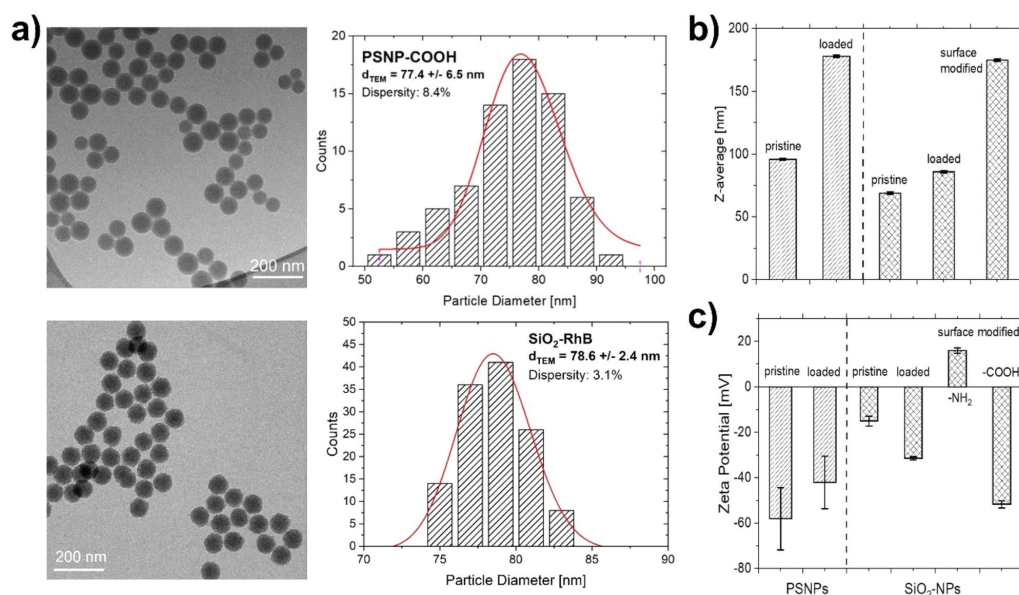


**Figure 4.** (a) TEM images and histograms of the pristine PSNPs and the surface modified SiO<sub>2</sub>-NPs; (b) hydrodynamic diameters (z-average) measured by DLS; (c) zeta potential measurements after different synthesis steps.

with a fluorophore such as optical probe **3**, the appropriate amount of **3** was covalently attached to the carboxylated particles by EDC/NHS coupling chemistry, resulting in the green–red emissive pH nanosensors PS-NR-**3** and SiO<sub>2</sub>-RhB-**3**. This is displayed in Fig. 3. The photometric quantification of **3** on the surface of the PSNPs and SiO<sub>2</sub>-NPs (SI, Figs. S16 and S32) revealed a comparable number of surface-bound probe molecules, i.e., 0.4 molecules/nm of **3** for PSNP-NR-**3** (equaling a dye conjugation of 76% of the accessible COOH groups) and 0.4 molecules/nm of **3** for SiO<sub>2</sub>-RhB-**3** (equaling a nearly quantitative functionalization of the accessible COOH groups). The NP surface modification was additionally confirmed by FT-IR spectroscopy (SI, Fig. S31).

**pH-dependent optical properties of the nanosensors.** The pH sensitivity of the nanosensors PSNP-NR-**3** and SiO<sub>2</sub>-RhB-**3** was fluorometrically examined under similar conditions as used for molecular probe **3** (absorption spectra, see SI, Figs. S33 and S34). At pH 8.1, excitation of the nanosensors at  $\lambda_{EX}$  of 405 nm led to emission bands at 578 nm originating from the reference dyes NR and RhB (Fig. 5a; and SI, Fig. S35). At more acidic pH values, a new fluorescence band appeared at about 530 nm corresponding to the emission of surface bound probe **3** switched ON under these conditions. This green fluorescence became more prominent with decreasing pH. The normalized emission spectra of the nanosensors obtained at different excitation wavelengths of the reference dyes NR ( $\lambda_{EX}$  = 510 nm), RhB-APTES ( $\lambda_{EX}$  = 540 nm), and **3** ( $\lambda_{EX}$  = 405 nm) at pH 4.0 are displayed in the SI in Fig. S36. Measurements of the fluorescence quantum yields of both nanosensors at different pH values between 8.1 and 2.0 revealed maximum fluorescence quantum yields of 14% for both PSNP-NR-**3** and SiO<sub>2</sub>-RhB-**3** (Fig. 5b). This reduction of the fluorescence quantum yield of probe **3** from initially 37% is attributed to surface effects caused by the relatively short distance between the pH-responsive dye and the particle surface and was not further examined. Finally, the reversibility of the pH-sensitivity of PSNP-NR-**3** and SiO<sub>2</sub>-RhB-**3** was assessed by varying the pH between 8.1 and 3.0/4.0 in cycles as well as possible interferences. We deliberately chose a broad pH range for this reversibility study although pH values below 4.2 (lysosomes) are not observed in cells to pave the road for other applications such as corrosion studies. The results shown in Fig. 5c,d, and in the SI (Fig. S35c,d) confirmed the reversibility of the switching ON and OFF of the green naphthalimide fluorescence of both nanosensors.

**Stability studies at different pH and in different environments.** As a prerequisite for the intended cell studies, the colloidal stability of PSNP-NR-**3** and SiO<sub>2</sub>-RhB-**3** and their particle precursors were investigated at pH values between 7.0 and 2.0 in MilliQ water, PBS, and the cell culture medium DMEM, and evaluated by DLS and zeta potential measurements. The zeta potential measurements at different pH values (Fig. 6a) showed a decreased colloidal stability of PSNP-NR-COOH NPs for pH values between pH 2–3, while the SiO<sub>2</sub>-RhB-COOH NPs exhibited a good colloidal stability at all pH values examined. The particle size (Fig. 6b) varied slightly for both types of NPs at the different pH values. The stability studies of both nanosensors at 37 °C

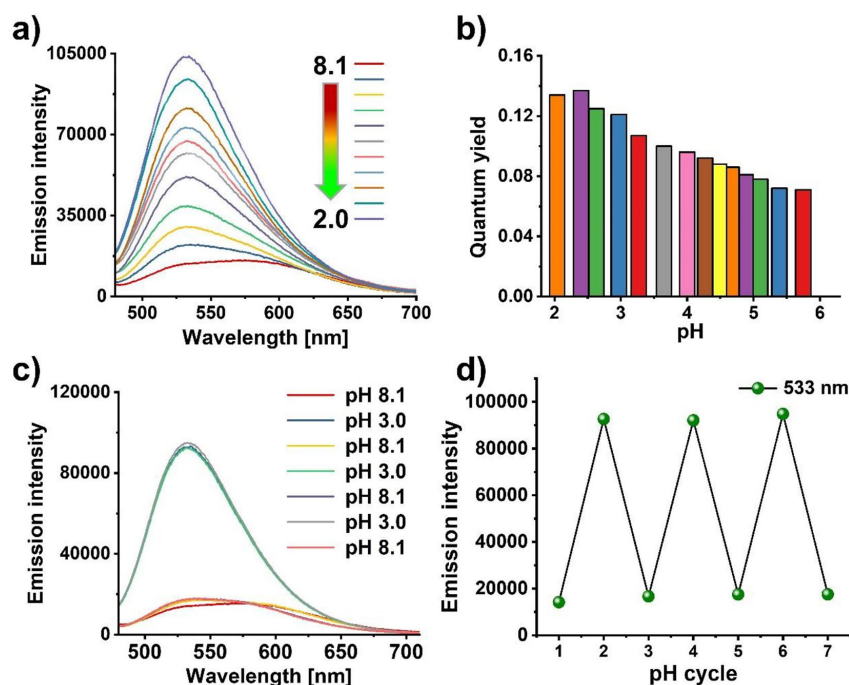


**Figure 5.** pH-dependent fluorescence of PSNP-NR-3. (a) Emission spectra at different pH values; (b) bar diagram of the pH-dependence of the fluorescence quantum yields in the pH range of 8.1–2.0; (c,d) reversibility study of PSNP-NR-3 involving the measurement of the emission spectra and the fluorescence intensity obtained by varying the pH from 8.1 to 3.0 in cycles in an aqueous B-R buffer (25 mM). Excitation was at  $\lambda_{Ex}$  of 405 nm.

in MilliQ water, PBS, and DMEM revealed no significant changes of the particle size and only slight changes of the zeta potential (Fig. 6c,d).

**Intracellular pH imaging with green–red emissive PSNP- and SiO<sub>2</sub>-NPs based nanosensors.** To assess the suitability of both pH nanosensors for bioimaging studies, we performed in vitro uptake studies with molecular probe 3 and the pH nanosensors PSNP-NR-3 and SiO<sub>2</sub>-RhB-3 using the cell line A549. This cell line presents a model for human alveolar epithelial type II cells. The A549 cells were incubated with 1:10 diluted stock solutions of 3 (containing 37  $\mu$ g) or 100  $\mu$ g of each of the two nanosensors for 30 min up to 24 h. Cellular uptake was then examined by epifluorescence measurements (Fig. 7). To visualize the cells and to localize optical probe 3 and both pH nanosensors, the cell nuclei were co-stained with 4,6-diamidino-2-phenylindole (DAPI, see Fig. 7, blue) and the actin filaments of the cytoskeleton were co-stained with phalloidin-Alexa 488 (Fig. 7a,d-red; b,c,e,f-green). Qualitative image analysis indicated the cellular uptake of 3 after 30 min (SI, Fig. S37) and its subsequent accumulation at longer incubation times (Fig. 7a,d, and SI, Fig. S37). The exposure of the cells to both types of pH nanosensors led to the internalization of both nanomaterials. After 3 h, the cellular uptake of the SiO<sub>2</sub>-RhB-3 particles was slightly higher than that of the PSNP-NR-3 particles, yet a similar uptake was observed for both nanosensors after 24 h (Fig. 7b,c,e,f, and SI, Fig. S37 and S38)<sup>66</sup>. The appearance of the green naphthalimide fluorescence indicated cellular uptake and the localization of the naphthalimide-based sensors in an acidic microenvironment, as the green emission of the naphthalimide-based PET probe is only switched ON at acidic pH values below 6. This provides a clear hint for the localization of the probes near or in acidic organelles such as the lysosomes involved in autophagy, protein degradation, apoptosis, and cell defence mechanism<sup>9,10</sup>. Figure 7 and Fig. S38 in the SI also highlight the advantages of dual color emissive nanosensors, that are detectable in the merged blue-green channel and additionally in the red channel, compared to single color fluorescent molecular probe 3.

To study the influence of intracellular pH changes on the fluorescence response of the two nanosensors in more detail, the H<sup>+</sup>/K<sup>+</sup> ionophore nigericin was used to homogenize the intracellular pH and the external pH of the culture media<sup>67,68</sup>, employing a literature protocol<sup>69</sup>. Subsequently, living cells were incubated with optical probe 3 and both nanosensors dispersed in sterile PBS solution of varying pH values (pH 4.5, pH 5.5, and pH 7.5), in the presence of this ionophore. After 30 min the cells were fixed with PFA to maintain the fluorescence

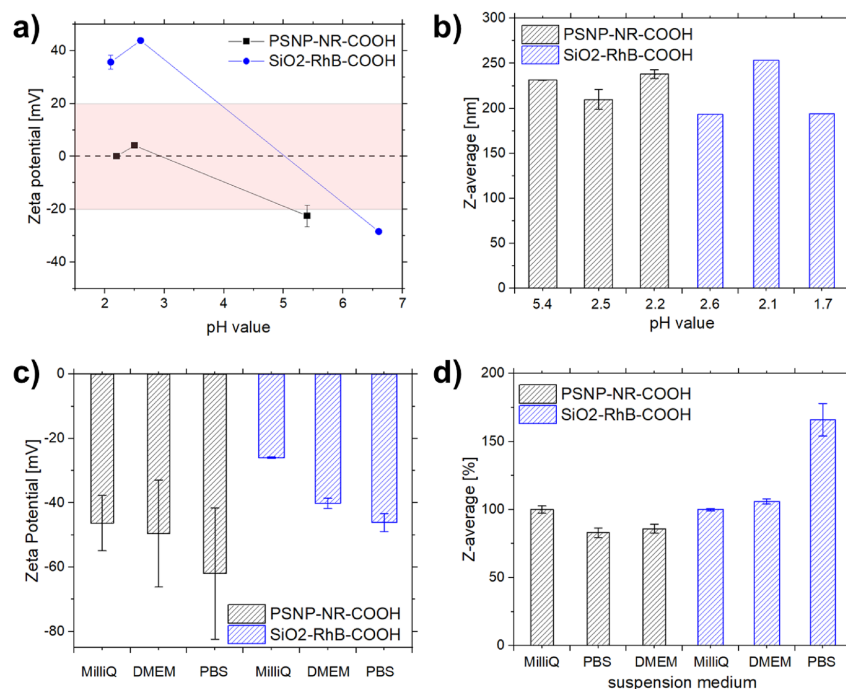


**Figure 6.** Overview of the results of the stability studies with carboxylated and dye stained PSNPs and SiO<sub>2</sub>-NPs utilizing zeta potential and DLS measurements at various pH values (a,b) and in different dispersion media (c,d).

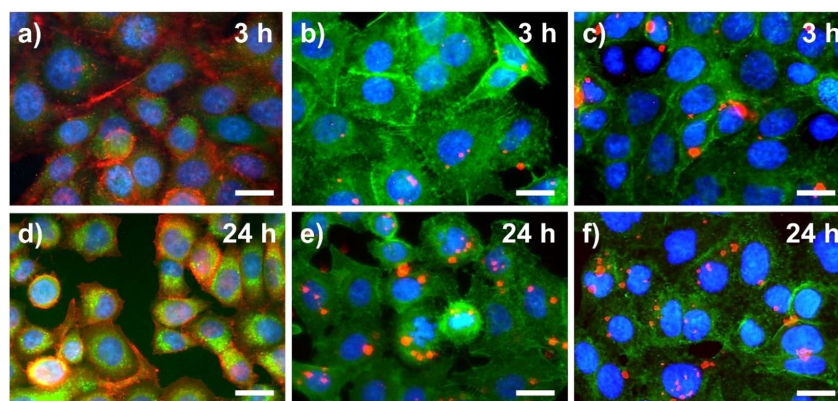


**Figure 7.** Epifluorescence images of the uptake of optical probe 3 (a,d) and the pH nanosensors PSNP-NR-3 (b,e) and SiO<sub>2</sub>-RhB-3 (c,f) by A549 cells measured after different incubation times, 3 h and 24 h, respectively. Prior to the fluorescence microscopy studies, the cells were incubated alive, fixed with 4% paraformaldehyde (PFA), and then co-stained with DAPI (cell nuclei, blue) and partly phalloidin-Alexa 488 (actin filaments, shown in red for (a,d) and in green for (b,c,e,f)) 1:10 dilution of probes dispersed in MilliQ water with PBS buffer. Excitation was carried out with an Osram 50 W/ACL1 Cz HBO Mercury vapor short-arc lamp and the fluorescence was monitored with emission filters set to  $\lambda_{Em} = 470$  nm (green channel) and to  $\lambda_{Em} = 560$  nm (red channel). For the detection of the fluorescence of DAPI Leica filter cube A ( $\lambda_{Em} = 340/380$  nm (blue channel)) was used. All images show a scale bar of 10  $\mu$ m.

signal intensities. While the cells cultivated with a physiological culture medium (pH 7.4) only have an acidic pH value of approximately 4.5 in the lysosomal compartment, the pH value changed during incubation with the ionophore and culture medium, yielding different pH values also in the cytoplasm. To enable a comparison of the intensities of the fluorescence signals measured with the epifluorescence microscope, all images were recorded with the same exposure times. As shown in Fig. 8, the fluorescence signals of both nanosensors increased with decreasing pH values. At pH 7.5, fluorescence signals could be observed only the acidic lysosomal compartment, while at pH 4.5, fluorescence signals also originated from the now acidic cytoplasm. With the instrument settings applied for the epifluorescence microscope measurements, i.e., excitation with a mercury vapor short-arc lamp and a 470 nm (“green”) and a 560 nm (“red”) filter in the emission channel, fluorescence signals could be detected in both the 470 nm and 560 nm channel (Fig. 8). In the case of the PSNP-NR-3 particles, the fluorescence intensity increase under acidic conditions was more pronounced in the red fluorescence channel, while for the SiO<sub>2</sub>-RhB-3 particles, the fluorescence enhancement was stronger in the green channel. This dual emission can open variable application possibilities for the use of these green–red emissive nanosensors in biological models, e.g., the detection of acidic environments in tumor tissues. These possibilities can be expanded through the utilization of other filter settings or other measurement conditions in conjunction with a confocal laser scanning microscope (CLSM) enabling laser excitation at defined excitation wavelengths and more choices of emission filter settings and thereby a better spectral discrimination of the two fluorescence signals.

Subsequently, we performed first CLSM studies with fixed A549 cells incubated with the optical probe 3 and both nanosensors at pH values of 4.5 and pH 7.5 to confirm the epifluorescence imaging results (Fig. 9 and SI, Fig. S39). These measurements enable a better morphological assignment. In addition, the more specific choice of the excitation wavelength and the emission filter settings allows a more selective recording of the green and red fluorescence. The disadvantage is, however, the lower sensitivity and the increased risk of bleaching effects. Depending on their location within the cells, the nanosensor emission could be detected in the red and green channel of the CLSM, while 3 was only visible in the green channel at pH 4.5 and not fluorometrically detectable at pH 7.5 (SI, Fig. S39h), as to be expected. To support the internalization of the NPs by the cells, a z-stack was measured (SI, Fig. S40) which confirmed the cellular uptake of the two nanosensors. The fluorescence detected in the green channel in the absence of nigericin at pH 7.5 in the medium (SI, Fig. S40) indicates that some nanosensor particles already entered acidic cell compartments, most likely the lysosomes. For a better co-localization assignment of the endosomes and lysosomes, however, live cell imaging studies are needed that were beyond the scope of this comparative screening study.

### Conclusion and outlook

We developed a set of dual color emissive ratiometric pH nanosensors utilizing polystyrene (PS) and silica (SiO<sub>2</sub>) nanoparticles (NPs) core stained with a red emissive pH-inert reference dye with an always ON fluorescence and surface functionalized with a green-fluorescent pH-responsive naphthalimide probe bearing a piperazine and a morpholine unit favoring lysosomal targeting. The ICT emission of this water-soluble pH probe, designed

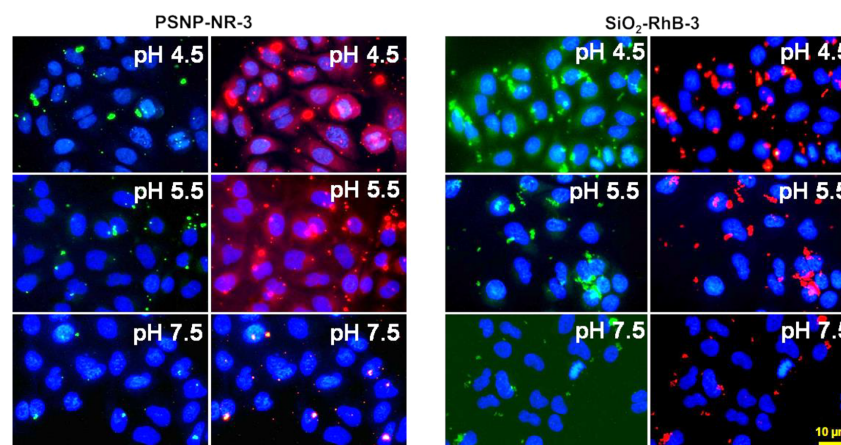


**Figure 8.** Epifluorescence images of fixed A549 cells incubated with solutions of pH nanosensors PSNP-NR-3, and SiO<sub>2</sub>-RhB-3 in the presence of the ionophore nigericin for 30 min at different pH values; co-staining with DAPI, fixation with PFA. Excitation was carried out with an Osram 50 W/ACL1 Cz HBO Mercury vapor short-arc lamp and the fluorescence was monitored with emission filters set to  $\lambda_{Em} = 470$  nm (green channel) and to  $\lambda_{Em} = 560$  nm (red channel). For the detection of the fluorescence of DAPI Leica filter cube A ( $\lambda_{Em} = 340/380$  nm (blue channel)) was used. All images show a scale bar of 10  $\mu$ m. For all images the autofluorescence of the cells was subtracted by using images of a control measurement done under identical conditions without the addition of particles.

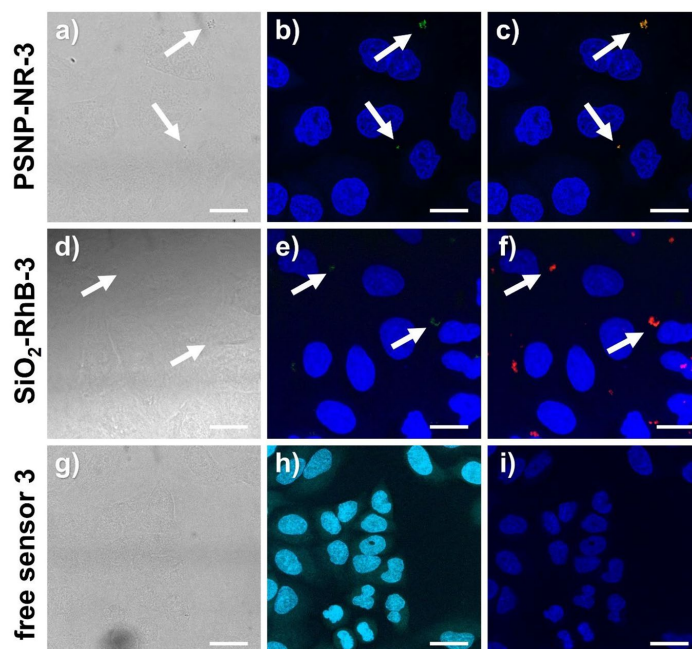


**Figure 9.** CLSM images of the fixed A549 cells (PFA) that were previously incubated with PSNP-NR-3 (a–c, particle concentration 100 µg/mL), SiO<sub>2</sub>-RhB-3 (d–f, particle concentration 100 µg/mL), and 3 (g–i, dye concentration 35 µg/mL) for 30 min at a pH 4.5 in the presence of the H<sup>+</sup>/K<sup>+</sup> ionophore nigericin. The nuclei were stained with DAPI. Transmitted light (a,d,g); merged blue (DAPI) and green (pH probe 3) channels: (b,e,h); and merged blue (DAPI), green (pH probe 3) and red (reference dyes, NR or RhB) channels: (c,f,i). The following measurements conditions were used:  $\lambda_{Ex}$  = 405 nm,  $\lambda_{Em1}$  = 420–480 nm and  $\lambda_{Em2}$  = 520–560 nm for DAPI and 3, and  $\lambda_{Ex}$  = 560 nm and  $\lambda_{Em}$  = 570–660 nm for the red reference dyes. All images show a scale bar of 10 µm.

for lysosomal targeting, is quenched by PET from the unprotonated nitrogen atoms of the piperazine and morpholine moieties at basic and neutral pH values and switched ON at pH values < 6. This was confirmed by pH titrations monitored optically and by NMR spectroscopy. Aiming for a comparative screening of the performance of inorganic and organic matrices typically used for nanosensors such as PS and SiO<sub>2</sub>, the nanosensor design and preparation were performed to provide closely matching physico-chemical and optical properties relevant for life sciences applications. This included the particle size, choice of the sensor dye, spectroscopic properties of the reference dyes, nanosensor surface chemistry, and number of surface-bound sensor dyes as supported by the subsequent nanosensor characterization, as well as the nanosensor concentration used for all characterization and cell uptake studies.

A comparison of the cellular uptake and sensing potential of both nanosensors using A549 cancer cells and epifluorescence and confocal fluorescence microscopy confirmed the cellular uptake of both types of nanosensors. Dual color emission was observed under acidic conditions required to switch ON the green fluorescence of the naphthalimide pH probe and suggested nanosensor penetration into acidic cell compartments. This underlines the suitability of both nanosensors for the fluorescence imaging of intracellular pH and lysosomal tracking. Cellular uptake of the SiO<sub>2</sub>-based nanosensor particles was slightly more efficient than that of the PS-based nanosensor particles. The silica nanosensors also revealed an improved stability. This provides clear evidence of the importance of the carrier matrix for nanosensor performance. Our results also underline the relevance of the choice of filter settings for the optimum read out of dual emissive probes and nanosensors.

In the future, we plan to further perform similar studies with analogously designed PS and SiO<sub>2</sub> nanosensors of different size to gain a better insight in the influence of the nanosensor matrix on nanosensor performance in cellular imaging studies. In addition, we will also assess different dye combinations such as the combination of our green emissive naphthalimide PET probe with a reference dye revealing a longer-wavelength emission than Nile Red or rhodamine B or the substitution of our neutral naphthalimide probe for a pH-responsive zwitterionic Bodipy dye with a green LE-type PET-operated fluorescence.

## Materials and methods

**Materials.** All chemicals used for the particle syntheses were obtained in the highest purity available, while all solvents used for the optical measurements were of spectroscopic grade. The chemicals, reagents, and solvents were employed as received, unless otherwise stated. For all syntheses and purification steps, ultrapure water was used (18.2 M $\Omega$ , MilliQ water). Tetraethoxysilane (TEOS, 99%), acrylic acid (AA, 99%), rhodamine B isothiocyanate ( $\geq 95\%$ ), anhydrous sodium hydroxide ( $\geq 98\%$ ), anhydrous potassium carbonate ( $\geq 99\%$ ) and *N,N'*-dimethylformamide (DMF, anhydrous, 99.8%) were purchased from Sigma Aldrich. 4-(2-aminoethyl) morpholine, triethylamine (NEt<sub>3</sub>), toluene (spectr. grade), styrene ( $\geq 99.0\%$ ), succinic anhydride (98%) and potassium persulfate (PPS,  $\geq 99.0\%$ , p.a.) were obtained from Merck KGaA. Ethanol (abs., 99.9%), cyclohexane (99.5%), dichloromethane (DCM), methanol (MeOH), DMF, ethyl acetate (EtOAc), acetonitrile (MeCN), hexane, glacial acetic acid and tetrahydrofuran (THF, 99.9%, p.a.) were obtained from Labsolute, and pyridine, Na<sub>2</sub>CO<sub>3</sub> were acquired from Chemsolute. 1-(2-aminoethyl)piperazine and phosphoric acid (85%) were purchased from Alfa Aesar, while 1-ethyl-3-(3-dimethylaminopropyl)carbodiimide (EDC) and sodium dodecyl sulfate (SDS,  $\geq 97\%$ , p.a.) were purchased from Carl Roth GmbH + Co. KG. 4-bromo, 1–8 naphthalic anhydride, *N*-hydroxy-sulfosuccinimide sodium salt (sulfo-NHS), 3-aminopropyltriethoxysilane (APTES) were purchased from abcr. Nile Red was purchased from Fluka Analytical.

**Synthesis of the water-soluble pH probe 3.** *Step 1: Synthesis of 4-bromo-N-4-(2-Aminoethyl) morpholine-1-8 naphthalimide (2).* 4-bromo, 1–8 naphthalic anhydride (277 mg, 1 mmol) and 4-(2-Aminoethyl) morpholine (131  $\mu$ L, 1 mmol) were taken in EtOH and heated at 50° C for 5 h. After complete reaction monitored by thin layer chromatography (tlc) the reaction mixture was concentrated and added to ice-cold water. The obtained precipitate was filtered and washed with 10% Na<sub>2</sub>CO<sub>3</sub> solution and dried. The pure product was obtained by column chromatography using ethyl acetate and hexane as eluents as an off-white shining powder. 311 mg; Yield: 80%. <sup>1</sup>H NMR (CDCl<sub>3</sub>; 500 MHz):  $\delta$  (ppm) 8.64–8.62 (dd, 1H), 8.56–8.54 (dd, 2H), 8.39–8.38 (d, 1H), 8.03–8.02 (d, 1H), 7.85–7.82 (m, 1H), 4.36–4.34 (m, 2H), 3.71 (b, 4H), 2.67–2.66 (b, 6H); <sup>13</sup>C NMR (125 MHz, CDCl<sub>3</sub>)  $\delta$  (ppm) 163.7, 133.4, 132.1, 131.3, 131.2, 130.7, 130.4, 129.1, 128.1, 123.1, 122.2, 66.7, 56.0, 53.7, 37.07; ESI-MS *m/z* calculated for C<sub>18</sub>H<sub>17</sub>BrN<sub>2</sub>O<sub>3</sub>; [M + H]<sup>+</sup> 389.2490, found 389.0541.

*Step 2: Synthesis of Lysosomal targeting water soluble pH sensor; 4-Amino (2-aminoethyl)piperazine-N-4-(2-aminoethyl) morpholine-1,8 naphthalimide (3).* **3** (194 mg, 0.5 mmol), 1-(2-aminoethyl)piperazine (78.7  $\mu$ L, 0.6 mmol) and a few drops of triethylamine (NEt<sub>3</sub>) were dissolved in pyridine. The reaction mixture was stirred under reflux overnight. After completed reaction as monitored by thin layer chromatography (TLC), the reaction mixture was concentrated and purified by column chromatography with dichloromethane and methanol mixture to obtain a dark yellow solid. <sup>1</sup>H NMR (CD<sub>3</sub>OD; 500 MHz):  $\delta$  (ppm) 8.45–8.42 (m, 2H), 8.39–8.37 (m, 1H), 7.73 (m, 1H), 7.30–7.29 (m, 2H), 4.29–4.27 (m, 2H), 3.70 (m, 4H), 3.36 (m, 4H), 3.20 (m, 2H), 2.91–2.84 (m, 6H), 2.70–2.69 (m, 2H), 2.63 (m, 4H); <sup>13</sup>C NMR (125 MHz, CD<sub>3</sub>OD)  $\delta$  (ppm) 168.3, 167.9, 160.1, 136.3, 136.2, 134.2, 134.6, 133.5, 129.7, 129.4, 126.5, 119.7, 118.7, 70.3, 59.8, 58.6, 57.5, 56.7, 40.4, 40.2; ESI-MS *m/z* calculated for C<sub>24</sub>H<sub>31</sub>N<sub>5</sub>O<sub>3</sub>; [M + H]<sup>+</sup> 438.2460, found 438.2554.

**Synthesis of the PS and SiO<sub>2</sub> particles and surface modifications.** *Synthesis of Nile Red loaded and carboxy functionalized PSNP (PSNP-NR).* The spherical, carboxy functionalized PSNPs (PSNP-COOH) were synthesized by an emulsion polymerization under argon atmosphere and loaded with Nile Red (NR) according to a procedure adapted from Nirmalanathan-Budau et al.<sup>55</sup> For the synthesis, 400  $\mu$ L of an aqueous solution of the radical initiator PPS (0.148 mM) was added to a mixture of 5.2 mL of an aqueous solution of the surfactant SDS (0.042 mM) and 1.3 mL styrene monomer at 70 °C. After 1 h of stirring, 30  $\mu$ L AA in 470  $\mu$ L of water were added dropwise. The mixture was kept at 70 °C and stirred for three more hours before cooled to r.t.. The resulting particle solution was diluted fivefold and centrifuged two times for 2 min at 13,500 rcf, the supernatants were collected and combined to create a stock solution with a particle concentration of 28 mg/mL (determined by weighing).

For PSNP swelling and dye staining, 100  $\mu$ L of NR in THF (2 mM) were quickly added to 3 mg of PSNP-COOH stock particles in 600  $\mu$ L of MilliQ water and placed in a plate shaker at 300 rpm and r.t. for 30 min. 300  $\mu$ L of MilliQ water were added, and the NPs were redispersed and centrifuged two times for 40 min at 16,000 rcf followed by discarding the supernatants. The PSNP dispersions were combined and centrifuged again to yield a dispersion of NR-stained PSNPs in MilliQ water with a particle concentration of 10 mg/mL.

*Synthesis of RhB-APTES loaded SiO<sub>2</sub>-NP (SiO<sub>2</sub>-RhB).* SiO<sub>2</sub>-NPs were synthesized as described in the literature, using a L-arginine controlled hydrolysis of TEOS in a biphasic water/cyclohexane system<sup>63,64</sup>. 91 mg (0.522 mmol) of L-arginine were dissolved in 69 mL of MilliQ water and 4.5 mL of cyclohexane was added. After heating the biphasic water / cyclohexane system to 60 °C, 5.5 mL (0.025 mmol) of TEOS were added to the upper layer and the reaction mixture was stirred for an additional 20 h at 150 rpm. To purify the obtained SiO<sub>2</sub> seeds with an average size of 25 nm, a dialysis step against water (4 L, water exchange after 30 min, 1 h, 2 h, and 4 h) with a dialysis membrane (Nadir, Carl Roth GmbH, molecular weight cut-off: 10–20 kDa) was performed. Subsequently, the obtained SiO<sub>2</sub> seeds were used to grow larger SiO<sub>2</sub>-NPs. 10 mL of the SiO<sub>2</sub> seeds were mixed with 36 mL of MilliQ water and 14 mg (0.08 mmol) of L-arginine, before 5 mL of cyclohexane was added. After heating to 60 °C, 3.52 mL (0.016 mmol) of TEOS were added and the reaction mixture was stirred for 20 h at 150 rpm. Purification of the SiO<sub>2</sub>-NPs was performed as described for the SiO<sub>2</sub> seeds. To obtain 80 nm large SiO<sub>2</sub>-NPs loaded with RhB-APTES, the regrowth step was performed three times. In the last regrowth step,

0.05 mL (0.9  $\mu\text{mol}$ ) of RhB-APTES in ethanol was injected into the aqueous phase 20 min after the addition of TEOS.

**Surface modification of  $\text{SiO}_2$ -RhB ( $\text{SiO}_2$ -RhB-COOH).** The particle surface of the  $\text{SiO}_2$ -RhB was modified by a two-step post-synthetic reaction. In the first step, amino groups were grafted onto the particle surface using APTES. Therefore 10 mg (20.56 nmol/L of particles) of  $\text{SiO}_2$ -RhB were diluted in 10 mL of ethanol and stirred at r.t. under a continuous argon flow. Next, 13.6  $\mu\text{L}$  (0.058 mmol) of APTES was added under constant stirring and the reaction mixture was allowed to stir at 400 rpm for another 20 h. To purify the obtained aminated  $\text{SiO}_2$ -NPs, they were centrifuged at 15,000 rcf and washed three times with ethanol. After the last washing step, the particles were redispersed in 5 mL of anhydrous DMF. In the second surface modification step, succinic anhydride reacted with the amino groups on the ligand periphery of the aminated  $\text{SiO}_2$ -NPs. Therefore, succinic anhydride (1.25 equiv. of the mol of APTES used in the amination process) was added dropwise to the particle suspension in DMF at 45  $^\circ\text{C}$  and stirred at 400 rpm overnight under an Ar atmosphere. Purification of the particles was performed by centrifugation at 15,000 rcf and washing with MilliQ water thrice. Finally, the particles were redispersed in 5 mL of MilliQ water.

**Labeling of  $\text{SiO}_2$ -RhB-COOH and PS-NR-COOH with probe 3.** pH probe 3 was covalently attached to the surface of the silica and polystyrene particles using the same reaction conditions. 3 mg each of  $\text{SiO}_2$ -RhB-COOH and PS-NR-COOH were taken with *N*-hydroxy sulfo succinimide (s-NHS, 5 mg, 0.023 mmol) and *N*-(3-Dimethylaminopropyl)-*N*-ethylcarbodiimide hydrochloride (EDC, 4.5 mg, 0.023 mmol) in 500  $\mu\text{L}$  of MilliQ water and stirred at r.t. for 1 h. pH probe 3 was dissolved in 100  $\mu\text{L}$  of MilliQ water and then added to the particle suspension. Then, 400  $\mu\text{L}$  of PBS buffer (pH 8) were added to the reaction mixture and stirred overnight at r.t. The resulting PSNP-NR-3 and  $\text{SiO}_2$ -RhB-3 nanosensors were centrifuged for 10 min at 20,000 g and washed one time with PBS buffer and three times with MilliQ water and finally redispersed in 3 mL of MilliQ water.

**Particle characterization. Dynamic light scattering (DLS) and zeta potential measurements.** DLS and zeta potential measurements of the PSNPs and  $\text{SiO}_2$ -NPs with and without dyes and sensors were carried out with a Zetasizer Nano ZS from Malvern Panalytical Ltd. at  $T = 25$   $^\circ\text{C}$  in disposable folded capillary cells (DTS1070), also from Malvern Panalytical Ltd. or disposable cuvettes (Sarstedt). All particles were dispersed in MilliQ water for these measurements. Three independent measurements including several runs were performed for each sample during the DLS measurement (back scattering angle 173 $^\circ$ , total time 10 min; only one measurement with three runs for the PSNP-COOH and PSNP-NR-COOH particles as well as the PSNP-NR-3 sensor particles directly after the synthesis) and zeta potential (total time 5 min, five measurements for PSNPs) measurements. The zeta potential was calculated from the nanoparticle electrophoretic mobility using the Einstein-Smoluchowski theory, while for DLS measurements the hydrodynamic diameter based on the z-average and number distribution was used. A refractive index of 1.4649 for  $\text{SiO}_2$  and 1.4600 for PS was used, respectively.

**Transmission electron microscopy (TEM).** The particle shape, average particle diameter, and agglomeration state were determined using a Tecnai G2 20 S-Twin from FEI. The particles were ultrasonicated for the measurements, diluted and added onto a TEM grid. The grids were dried overnight, measured, and the particle size distribution was determined representatively for a randomly chosen sample of 50–150 particles using the X-ImageJ software (Version: 1.52 e, winPenPack X-ImageJ) Launcher from the National Institute of Health (<http://rsb.info.nih.gov/ij/>).

**Conductometric titration.** The total amount of (de)protonable COOH groups on the surface of the PSNPs was determined by a conductometric titration with a Modul 856 conductometer from Metrohm at r.t., following a slightly modified procedure previously described<sup>19</sup>. Samples containing at least 20 mg of PSNP-COOH in 80 mL of MilliQ water were titrated with 0.01 M NaOH in 20  $\mu\text{L}/5$  s steps under argon atmosphere until a final conductivity of 0.12 mS/cm was reached. Prior to the titration of the particle dispersion, the conductivity was adjusted to 0.1 mS/cm with HCl (0.01 M) and NaBr (30 mM).

**Dye leaking studies.** To determine possible dye leakage from the nanosensor core, leaking studies in different application-relevant microenvironments were performed. For this, 150  $\mu\text{L}$  of the particle suspension was filtered through filter units (Ultracel, MWCO: 30 KDa, Merck) and centrifuged for 10 minutes at 12,000 rcf. After centrifugation, the filtrate and particles were diluted in 3 mL of MilliQ water and the emission intensity was measured.

**Absorption and emission studies.** The absorption spectra of the 3 and particles (PSNPs and  $\text{SiO}_2$ -NPs) were measured with a Specord 21 spectrometer from Analytik Jena using quartz cuvettes from Hellma. Fluorescence measurements were performed with a calibrated FluoroMax-4 Spectrofluorometer, HORIBA Jobin Yvon with excitation and emission slit widths of 5 nm. The fluorescence quantum yields were absolutely measured with a calibrated stand-alone Quantaurus Hamamatsu integrating sphere setup using an excitation wavelength  $\lambda_{\text{ex}}$  of 405 nm. Photostability studies of the nanosensors at pH 4.0 were done with the spectrofluorometer FSP920 from Edinburgh Instruments equipped with a xenon lamp and  $\lambda_{\text{ex}} = 405$  nm, with monochromator slit widths set to 4 nm and 6 nm in excitation and emission, respectively.

For the spectroscopic studies, the dye solutions were prepared from a 1 mM stock solution in DMF. For the experiments in aqueous environments, then a solution of the dye (0.1 mM) in MilliQ water was prepared by

dilution of this stock solution. 4  $\mu\text{L}$  of this aqueous solution were used for the fluorescence measurement of **3** and 7.5  $\mu\text{L}$  of the 1 mM stock solution for the absorption measurements.

The different pH solutions were made in B-R buffer using acidic solutions containing phosphoric acid, boric acid, and acetic acid and a basic solution of sodium hydroxide. Solutions of different pH were obtained by the mixing of different acid and base solutions. All pH solutions were prepared using MilliQ water. Reversibility experiments were performed by the addition of HCl and NaOH, subsequently to adjust pH values of 4.8 and 8.1 for pH sensor, 4.0 and 8.1 for SiO<sub>2</sub>-RhB-**3** and 3.0 and 8.1 for PSNP-NR-**3** nanoparticles.

The dose/response Eq. (1) was used to calculate the pK<sub>a</sub> values of the free pH sensor **3** and covalently linked on the surface of silica and polystyrene nanoparticles by sigmoidal curve fitting of the emission intensities with respect to different pH values.

$$y = I_1 + \frac{I_2 - I_1}{1 + 10^{(\text{LOG}x_0 - x)p}} \quad (1)$$

All aqueous solutions were prepared with MilliQ water (0.055  $\mu\text{S m}^{-1}$ ; Merck Milli-Q® IQ 700 device). <sup>1</sup>H NMR and <sup>13</sup>C NMR spectra of the final sensor dye **3** preparation steps were measured on a Bruker AVANCE III 500 instrument employing CDCl<sub>3</sub> and CD<sub>3</sub>OD (Deutero GmbH) as solvents and tetramethylsilane (TMS) as an internal reference. The <sup>1</sup>H NMR titration was performed in D<sub>2</sub>O using a Varian VNMR500 type NMR spectrometer operating at 499.9 MHz equipped with a Varian OneNMR probe. Optical probe **3** was also measured in DMSO-*d*<sub>6</sub> solution followed by exchange by D<sub>2</sub>O to determine the exact structure of the sensor. An Agilent 6210 ESI-TOF mass spectrometer from Agilent Technologies, Santa Clara, CA, USA was used to obtain the mass spectra. All pH measurements of dye **3** and the PSNPs and SiO<sub>2</sub>-NPs were performed with a Mettler Toledo pH-meter Seven Compact Advanced, Gießen, Germany and the calibrated pH electrode Mettler Toledo InLab® Micro. The pH-meter was calibrated with standard buffers of pH 10.00, 7.01, 4.01, and 2.00.

**Cell culture.** The human lung cancer cell line A549 were routinely propagated as follows: DMEM medium, with 10% fetal calf serum (FCS), 2% glutamine, and penicillin/streptomycin (all from PAN Biotech) added. Cells were seeded into medium at a concentration of  $1 \times 10^5$  cells/mL, cultured at 37 °C with 5% CO<sub>2</sub>, and split twice in a ratio of 1:5 per week. For cytochemistry, the cells were seeded at a concentration of  $5 \times 10^5$  cells/mL in a 24-well culture plate on glass coverslips (Sigma Aldrich), and cultured for 48 h at 37 °C. Thereafter, cells were incubated with normal culture medium or medium containing test substances as optical probes and nanosensors for different times at 37 °C. Afterwards, the cells were fixed with 4% PFA, rinsed and 4,6-diamidino-2-phenylindole (DAPI, Abcam) was used for nuclear counterstaining.

**Microscopy studies.** *Epifluorescence microscopy.* Image acquisition of live cells was performed with a Leica DMRB microscope (Leica, Wetzlar, Germany). The images were taken with a digital camera (Spot 32, Diagnostic Instruments) with the same exposure time for all images. Excitation was carried out with an Osram 50 W/ACL1 Cz HBO Mercury vapor short-arc lamp and commercially available filter settings from Leica were used for the detection of the fluorescence of DAPI (blue channel: Leica Filter Cube A ( $\lambda_{\text{Emx}} = 340/380$  nm) and the green and red emission of the pH-responsive and pH-inert fluorophores (green channel:  $\lambda_{\text{Em}} = 470$  nm; red channel:  $\lambda_{\text{Em}} = 560$  nm).

*CLSM.* Confocal laser scanning microscopy (CLSM) imaging was done on a confocal laser scanning microscope Leica SP8 equipped with a white light laser (Superk Extreme EXW-9 NIM, NKT Photonics, Denmark) and a 405 nm laser diode (LASOS, VLK 0550 T01) using a  $100\times$  oil immersion objective with a numerical aperture of 1.4 (HC PC APO CS2 100x/1.40 OIL). The following sequential measurement conditions were used:  $\lambda_{\text{Ex}} = 405$  nm,  $\lambda_{\text{Em1}} = 420\text{--}480$  nm and  $\lambda_{\text{Em2}} = 520\text{--}560$  nm for DAPI and **3**, and  $\lambda_{\text{Em}} = 560$  nm and  $\lambda_{\text{Em}} = 570\text{--}660$  nm for the red reference dyes. The images and z-scans (step size = 0.3 micrometer) were deconvoluted with the software Huygens Essential (Version 17.04, Scientific Volume Imaging B.V., The Netherlands) with default settings and a maximum intensity projection of the deconvoluted z-stacks was created.

### Data availability

All data generated or analyzed during this study are included in this published article (and its Supplementary Information files) or are available upon request from the corresponding author.

Received: 9 November 2022; Accepted: 13 January 2023

Published online: 24 January 2023

### References

1. Tantama, M., Hung, Y. P. & Yellen, G. Imaging intracellular pH in live cells with a genetically encoded red fluorescent protein sensor. *J. Am. Chem. Soc.* **133**, 10034–10037. <https://doi.org/10.1021/ja202902d> (2011).
2. Steinegger, A., Wolfbeis, O. S. & Borisov, S. M. Optical sensing and imaging of pH values: Spectroscopies, materials, and applications. *Chem. Rev.* **120**, 12357–12489. <https://doi.org/10.1021/acs.chemrev.0c00451> (2020).
3. Wencel, D., Abel, T. & McDonagh, C. Optical chemical pH sensors. *Anal. Chem.* **86**, 15–29. <https://doi.org/10.1021/ac4035168> (2014).
4. Clark, H. A., Kopelman, R., Tjalkens, R. & Philbert, M. A. Optical nanosensors for chemical analysis inside single living cells. 2. Sensors for pH and calcium and the intracellular application of PEBBLE sensors. *Anal. Chem.* **71**, 4837–4843. <https://doi.org/10.1021/ac990630n> (1999).
5. Schäferling, M. Nanoparticle-based luminescent probes for intracellular sensing and imaging of pH. *Wiley Interdiscip. Rev. Nanomed. Nanobiotechnol.* **8**, 378–413. <https://doi.org/10.1002/wnan.1366> (2016).

6. Sondergaard, R. V., Henriksen, J. R. & Andresen, T. L. Design, calibration and application of broad-range optical nanosensors for determining intracellular pH. *Nat. Protoc.* **9**, 2841–2858. <https://doi.org/10.1038/nprot.2014.196> (2014).
7. Bartoš, D., Rewers, M., Wang, L. & Sørensen, T. J. Incorporating fluorescent nanomaterials in organically modified sol–gel materials—creating single composite optical pH sensors. *Sens. Diagn.* **1**, 185–192. <https://doi.org/10.1039/d1sd00002k> (2022).
8. Yang, K.-N. *et al.* pH-responsive mesoporous silica nanoparticles employed in controlled drug delivery systems for cancer treatment. *Cancer Biol. Med.* **11**, 34–43. <https://doi.org/10.7497/j.issn.2095-3941.2014.01.003> (2014).
9. Ohkuma, S. & Poole, B. Fluorescence probe measurement of the intralysosomal pH in living. *Proc. Natl. Acad. Sci. USA* **75**, 3327–3331. <https://doi.org/10.1073/pnas.75.7.3327> (1978).
10. Han, J. & Burgess, K. Fluorescent indicators for intracellular pH. *Chem. Rev.* **110**, 2709–2728. <https://doi.org/10.1021/cr900249z> (2010).
11. Aylott, J. W. Optical nanosensors—an enabling technology for intracellular measurements. *Analyst* **128**, 309–312. <https://doi.org/10.1039/b302174m> (2003).
12. Holzinger, M., Le Goff, A. & Cosnier, S. Nanomaterials for biosensing applications: A review. *Front. Chem.* **2**, 63. <https://doi.org/10.3389/fchem.2014.00063> (2014).
13. Radunz, S. *et al.* Simple self-referenced luminescent pH sensors based on upconversion nanocrystals and pH-sensitive fluorescent BODIPY dyes. *Anal. Chem.* **91**, 7756–7764. <https://doi.org/10.1021/acs.analchem.9b01174> (2019).
14. Jokic, T. *et al.* Highly photostable near-infrared fluorescent pH indicators and sensors based on BF<sub>2</sub>-chelated tetraarylazadipyromethene dyes. *Anal. Chem.* **84**, 6723–6730. <https://doi.org/10.1021/ac3011796> (2012).
15. Han, J., Loudet, A., Barhoumi, R., Burghardt, R. C. & Burgess, K. A Ratiometric pH reporter for imaging protein-dye conjugates in living cells. *J. Am. Chem. Soc.* **131**, 1642. <https://doi.org/10.1021/ja8073374> (2009).
16. Hoogendoorn, S., Blom, A. E. M., Willems, L. I., van der Marel, G. A. & Overkleef, H. S. Synthesis of pH-activatable red fluorescent BODIPY dyes with distinct functionalities. *Org. Lett.* **13**, 5656–5659. <https://doi.org/10.1021/ol202379w> (2011).
17. Kowada, T. *et al.* In vivo fluorescence imaging of bone-resorbing osteoclasts. *J. Am. Chem. Soc.* **133**, 17772–17776. <https://doi.org/10.1021/ja2064582> (2011).
18. Xiong, H. *et al.* Activatable water-soluble probes enhance tumor imaging by responding to dysregulated pH and exhibiting high tumor-to-liver fluorescence emission contrast. *Bioconjug. Chem.* **27**, 1737–1744. <https://doi.org/10.1021/acs.bioconjchem.6b00242> (2016).
19. Srivastava, P. *et al.* Multicolor polystyrene nanosensors for the monitoring of acidic, neutral, and basic pH values and cellular uptake studies. *Anal. Chem.* **94**, 9656–9664. <https://doi.org/10.1021/acs.analchem.2c00944> (2022).
20. Srivastava, P., Fürstenwerth, P. C., Witte, J. F. & Resch-Genger, U. Synthesis and spectroscopic characterization of a fluorescent phenanthrene-rhodamine dyad for ratiometric measurements of acid pH values. *New J. Chem.* **45**, 13755–13762. <https://doi.org/10.1039/d1nj01573g> (2021).
21. Andresen, E., Radunz, S. & Resch-Genger, U. Novel PET-pperedated rosamine pH-sensor dyes with substitution pattern-tunable pK(a) values and temperature sensitivity. *New J. Chem.* **45**, 13934–13940. <https://doi.org/10.1039/d1nj02505h> (2021).
22. Longmire, M. R. *et al.* Determination of optimal rhodamine fluorophore for in vivo optical imaging. *Bioconjug. Chem.* **19**, 1735–1742. <https://doi.org/10.1021/bc800140c> (2008).
23. Nakata, E. *et al.* A novel strategy to design latent ratiometric fluorescent pH probes based on self-assembled SNARF derivatives. *RSC Adv.* **4**, 348–357. <https://doi.org/10.1039/c3ra43928c> (2014).
24. Wang, Y. *et al.* Recent developments in rhodamine-based chemosensors: A review of the years 2018–2022. *Chemosensors* **10**, 399. <https://doi.org/10.3390/chemosensors10100399> (2022).
25. Lee, H. *et al.* Near-infrared pH-activatable fluorescent probes for imaging primary and metastatic breast tumors. *Bioconjug. Chem.* **22**, 777–784. <https://doi.org/10.1021/bc100584d> (2011).
26. Lee, H., Berezin, M. Y., Tang, R., Zhegalova, N. & Achilefu, S. Pyrazole-substituted near-infrared cyanine dyes exhibit pH-dependent fluorescence lifetime properties. *Photochem. Photobiol.* **89**, 326–331. <https://doi.org/10.1111/php.12009> (2013).
27. Mu, H. *et al.* pH-activatable cyanine dyes for selective tumor imaging using near-infrared fluorescence and photoacoustic modalities. *ACS Sensors* <https://doi.org/10.1021/acssensors.0c01926> (2020).
28. Yue, X. *et al.* DNA-based pH nanosensor with adjustable FRET responses to track lysosomes and pH fluctuations. *Anal. Chem.* **93**, 7250–7257. <https://doi.org/10.1021/acs.analchem.1c00436> (2021).
29. Mathejczyk, J. E. *et al.* High-sensitivity detection of breast tumors in vivo by use of a pH-sensitive near-infrared fluorescence probe. *J. Biomed. Opt.* **17**, 076028–076028–076029. <https://doi.org/10.1117/1.jbo.17.7.076028> (2012).
30. Srivastava, P., Srivastava, P. & Patra, A. K. Biological perspectives of a FRET based pH-probe exhibiting molecular logic gate operation with altering pH. *New J. Chem.* **42**, 9543–9549. <https://doi.org/10.1039/c8nj01318g> (2018).
31. Dong, B. *et al.* Dual site-controlled and lysosome-targeted intramolecular charge transfer-photoinduced electron transfer-fluorescence resonance energy transfer fluorescent probe for monitoring pH changes in living cells. *Anal. Chem.* **88**, 4085–4091. <https://doi.org/10.1021/acs.analchem.6b00422> (2016).
32. Stewart, W. W. Synthesis of 3,6-disulfonated 4-aminonaphthalimides. *J. Am. Chem. Soc.* **103**, 7615–7620. <https://doi.org/10.1021/ja00415a033> (1981).
33. Dong, H.-Q. *et al.* 1,8-Naphthalimide-based fluorescent chemosensors: Recent advances and perspectives. *J. Mater. Chem. C* **8**, 13501–13529. <https://doi.org/10.1039/d0tc03681a> (2020).
34. Gao, P., Pan, W., Li, N. & Tang, B. Fluorescent probes for organelle-targeted bioactive species imaging. *Chem. Sci.* **10**, 6035–6071. <https://doi.org/10.1039/c9sc01652j> (2019).
35. Resch-Genger, U. & Licha, K. Probes for optical imaging: New developments. *Drug Discovery Today* **8**, e87–e94. <https://doi.org/10.1016/j.ddtec.2011.11.003> (2011).
36. Berezin, M., Y. & Achilefu, S. Fluorescence lifetime measurements and biological imaging. *Chem. Rev.* **110**, 2641–2684. <https://doi.org/10.1021/cr900343z> (2010).
37. Rurack, K. & Resch-Genger, U. Rigidization, preorientation and electronic decoupling - the “magic triangle” for the design of highly efficient fluorescent sensors and switches. *Chem. Soc. Rev.* **31**, 116–127. <https://doi.org/10.1039/B100604P> (2002).
38. Yang, Y., Zhao, Q., Feng, W. & Li, F. Luminescent chemodosimeters for bioimaging. *Chem. Rev.* **113**, 192–270. <https://doi.org/10.1021/cr2004103> (2012).
39. Wolfbeis, O. S. An overview of nanoparticles commonly used in fluorescent bioimaging. *Chem. Soc. Rev.* **44**, 4743–4768. <https://doi.org/10.1039/c4cs00392f> (2015).
40. Carrillo-Carrion, C., Escudero, A. & Parak, W. J. Optical sensing by integration of analyte-sensitive fluorophore to particles. *Trac-Trends Anal. Chem.* **84**, 84–96. <https://doi.org/10.1016/j.trac.2016.05.001> (2016).
41. Kromer, C. *et al.* Monitoring and imaging pH in biofilms utilizing a fluorescent polymeric nanosensor. *Sci. Rep.* **12**. <https://doi.org/10.1038/s41598-022-13518-1> (2022).
42. Cheng, S. *et al.* Reversible ratiometric probe combined with the time-gated method for accurate in vivo gastrointestinal pH sensing. *ACS Appl. Mater. Interfaces.* **12**, 25557–25564. <https://doi.org/10.1021/acsmi.0c04237> (2020).
43. Ding, C. *et al.* Ratiometric upconversion luminescence nanoprobe with near-infrared Ag<sub>2</sub>S nanodots as the energy acceptor for sensing and imaging of pH in vivo. *Anal. Chem.* **91**, 7181–7188. <https://doi.org/10.1021/acs.analchem.9b00404> (2019).
44. Andresen, E., Resch-Genger, U. & Schaferling, M. Surface Modifications for Photon-Upconversion-Based Energy-Transfer Nanoprobes. *Langmuir* **35**, 5093–5113. <https://doi.org/10.1021/acs.langmuir.9b00238> (2019).

45. Bruni, F. *et al.* Two-color emitting colloidal nanocrystals as single-particle ratiometric probes of intracellular pH. *Adv. Funct. Mater.* **27**. <https://doi.org/10.1002/adfm.201605533> (2017).
46. Silvi, S., Baroncini, M., La Rosa, M. & Credi, A. Interfacing luminescent quantum dots with functional molecules for optical sensing applications. *Top. Curr. Chem.* **374**. <https://doi.org/10.1007/s41061-016-0066-7> (2016).
47. Reisch, A. & Klymchenko, A. S. Fluorescent polymer nanoparticles based on dyes: Seeking brighter tools for bioimaging. *Small* **12**, 1968–1992. <https://doi.org/10.1002/sml.201503396> (2016).
48. Holländer, A. Labelling techniques for the chemical analysis of polymer surfaces. *Surf. Interface Anal.* **36**, 1023–1026. <https://doi.org/10.1002/sia.1828> (2004).
49. Banik, B. L., Fattahi, P. & Brown, J. L. Polymeric nanoparticles: The future of nanomedicine. *WIREs Nanomed. Nanobiotechnol.* **8**, 271–299. <https://doi.org/10.1002/wnan.1364> (2016).
50. Zhang, X. *et al.* Fabrication of aggregation induced emission dye-based fluorescent organic nanoparticles via emulsion polymerization and their cell imaging applications. *Polym. Chem.* **5**, 399–404. <https://doi.org/10.1039/C3PY00984J> (2014).
51. Li, K. & Liu, B. Polymer-encapsulated organic nanoparticles for fluorescence and photoacoustic imaging. *Chem. Soc. Rev.* **43**, 6570–6597. <https://doi.org/10.1039/c4cs00014e> (2014).
52. Schäferling, M. The art of fluorescence imaging with chemical sensors. *Angew. Chem. Int. Ed.* **51**, 2–25. <https://doi.org/10.1002/anie.201105459> (2012).
53. Wang, C., Otto, S., Dorn, M., Heinze, K. & Resch-Genger, U. Luminescent TOP nanosensors for simultaneously measuring temperature, oxygen, and pH at a single excitation wavelength. *Anal. Chem.* **91**, 2337–2344. <https://doi.org/10.1021/acs.analchem.8b05060> (2019).
54. Huang, X. *et al.* Ratiometric optical nanoprobes enable accurate molecular detection and imaging. *Chem. Soc. Rev.* **47**, 2873–2920. <https://doi.org/10.1039/C7CS00612H> (2018).
55. Nirmalanathan-Budau, N. *et al.* Multimodal cleavable reporters for quantifying carboxy and amino groups on organic and inorganic nanoparticles. *Sci. Rep.* **9**, 17577. <https://doi.org/10.1038/s41598-019-53773-3> (2019).
56. Hetemi, D. & Pinson, J. Surface functionalisation of polymers. *Chem. Soc. Rev.* **46**, 5701–5713. <https://doi.org/10.1039/C7CS00150A> (2017).
57. Behnke, T. *et al.* Encapsulation of hydrophobic dyes in polystyrene micro- and nanoparticles via swelling procedures. *J. Fluoresc.* **21**, 937–944. <https://doi.org/10.1007/s10895-010-0632-2> (2011).
58. Behnke, T., Würth, C., Laux, E.-M., Hoffmann, K. & Resch-Genger, U. Simple strategies towards bright polymer particles via one-step staining procedures. *Dyes Pigm.* **94**, 247–257. <https://doi.org/10.1016/j.dyepig.2012.01.021> (2012).
59. Gupta, K., Verma, M., Srivastava, P., Sivakumar, S. & Patra, A. K. A luminescent pH-sensitive lysosome targeting Eu(III) probe. *New J. Chem.* **44**, 3570–3573. <https://doi.org/10.1039/c9nj05561d> (2020).
60. Ma, Q. *et al.* A lysosome-targetable and ratiometric fluorescent probe for hypochlorous acid in living cells based on a 1,8-naphthalimide derivative. *Spectrochim. Acta Part A Mol. Biomol. Spectrosc.* **223**, 117334. <https://doi.org/10.1016/j.saa.2019.117334> (2019).
61. Li, S.-S. *et al.* Monitoring the changes of pH in lysosomes during autophagy and apoptosis by plasmon enhanced Raman imaging. *Anal. Chem.* **91**, 8398–8405. <https://doi.org/10.1021/acs.analchem.9b01250> (2019).
62. Klippel, N., Jung, G. & Kickelbick, G. Hybrid inorganic-organic fluorescent silica nanoparticles—influence of dye binding modes on dye leaching. *J. Sol-Gel Sci. Technol.* <https://doi.org/10.1007/s10971-021-05578-y> (2021).
63. Tavernaro, I., Cavelius, C., Peuschel, H. & Kraegeloh, A. Bright fluorescent silica-nanoparticle probes for high-resolution STED and confocal microscopy. *Beilstein J. Nanotechnol.* **8**, 1283–1296. <https://doi.org/10.3762/bjnano.8.130> (2017).
64. Clasen, A. *et al.* Kinetic and spectroscopic responses of pH-sensitive nanoparticles: Influence of the silica matrix. *RSC Adv.* **9**, 35695–35705. <https://doi.org/10.1039/c9ra06047b> (2019).
65. Hennig, A. *et al.* Scope and limitations of surface functional group quantification methods: Exploratory study with poly(acrylic acid)-grafted micro- and nanoparticles. *J. Am. Chem. Soc.* **134**, 8268–8276. <https://doi.org/10.1021/ja302649g> (2012).
66. Saftig, P. & Klumperman, J. Lysosome biogenesis and lysosomal membrane proteins: Trafficking meets function. *Nat. Rev. Mol. Cell Biol.* **10**, 623–635. <https://doi.org/10.1038/nrm2745> (2009).
67. Orte, A., Alvarez-Pez, J. M. & Ruedas-Rama, M. J. Fluorescence lifetime imaging microscopy for the detection of intracellular pH with quantum dot nanosensors. *ACS Nano* **7**, 6387–6395. <https://doi.org/10.1021/nn402581q> (2013).
68. Varnes, M. E., Bayne, M. T., Menegay, H. J. & Tuttle, S. W. Effect of the K<sup>+</sup>/H<sup>+</sup> ionophore nigericin on response of A549 cells to photodynamic therapy and Tert-butylhydroperoxide. *Free Radical. Biol. Med.* **15**, 395–405. [https://doi.org/10.1016/0891-5849\(93\)90039-W](https://doi.org/10.1016/0891-5849(93)90039-W) (1993).
69. Lucien, F., Harper, K., Pelletier, P.-P., Volkov, L. & Dubois, C. M. Simultaneous pH measurement in endocytic and cytosolic compartments in living cells using confocal microscopy. *JoVE* **1**, e51395. <https://doi.org/10.3791/51395> (2014).

### Acknowledgements

The authors express their gratitude to Carsten Prinz from Division *Structure Analysis*, Federal Institute for Materials Research and Testing (BAM) for TEM measurements, and Dr. Andreas Hertwig and Gundula Hidde from Division *Surface Analysis and Interfacial Chemistry*, BAM, for FT-IR measurements. We thank Lora Friesen from Division *Biophotonics*, BAM, for the performance of the conductometry measurements.

### Author contributions

P.S. and I.T. planned the study, P.S. designed the pH-responsive molecular optical probes and synthesized the naphthalimide molecules, I.T. prepared the different silica nanoparticles and nanosensors, L.S. prepared the unstained and Nile Red stained polymer particles, and P.S. coupled the naphthalimide probe to the Nile Red-stained polymer nanoparticles yielding the corresponding pH-nanosensor. K.M. performed the pH-dependent NMR measurements. I.T. and L.S. performed the physico-chemical particle characterization, the colloidal stability study, and the determination of the accessible number of the functional, i.e., carboxylic groups. The optical-spectroscopic studies were done by P.S. with help from I.T. C.G. developed the protocol for the cellular uptake studies at different pH, P.W. performed the epifluorescence measurements, and P.S. and F.S. performed the confocal fluorescence measurements. The first draft was written by P.S. and revised and largely rewritten by U.R.-G. with the language brush-up done by C.G.: The figures were prepared by I.T. with help from P.S., L.S., and P.W. U.R.-G. was responsible for organizing external funding from the WIPANO program (Federal Ministry for Economic Affairs and Climate Action (BMWK)), the European Metrology program for Innovation and Research (EMPIR), the Novo Nordisk Fonden; Interdisciplinary Synergy Program 2021, and the program “Central Innovation Program for small and medium-sized enterprises (SMEs)” / “Zentrales Innovationsprogramm Mittelstand” (ZIM), BMWK, the latter jointly with P.W. All authors were involved in discussing the results as well as proofreading, reviewing, and editing, and approved the final manuscript.

### Funding

Open Access funding enabled and organized by Projekt DEAL. P.S. acknowledges funding by an Adolf Marten fellowship of the Federal Institute for Material Research and Testing (BAM) and the ZIM project *FluoSon* (program ZIM, BMWK) and L.S. funding by the European Metrology program for Innovation and Research (EMPIR) as part of the project 18HLT02 *AeroTox*. The EMPIR initiative is co-funded by the European Union's Horizon 2020 research and innovation programme and by the EMPIR participating states. I.T. acknowledges financial support from the WIPANO project *AquaFunkNano* (Federal Ministry for Economic Affairs and Climate Action (BmWK)) and the project *MiGraGen* (Novo Nordisk Fonden; Interdisciplinary Synergy Program 2021).

### Competing interests

The authors declare no competing interests.

### Additional information

**Supplementary Information** The online version contains supplementary material available at <https://doi.org/10.1038/s41598-023-28203-0>.

**Correspondence** and requests for materials should be addressed to U.R.-G.

**Reprints and permissions information** is available at [www.nature.com/reprints](http://www.nature.com/reprints).

**Publisher's note** Springer Nature remains neutral with regard to jurisdictional claims in published maps and institutional affiliations.



**Open Access** This article is licensed under a Creative Commons Attribution 4.0 International License, which permits use, sharing, adaptation, distribution and reproduction in any medium or format, as long as you give appropriate credit to the original author(s) and the source, provide a link to the Creative Commons licence, and indicate if changes were made. The images or other third party material in this article are included in the article's Creative Commons licence, unless indicated otherwise in a credit line to the material. If material is not included in the article's Creative Commons licence and your intended use is not permitted by statutory regulation or exceeds the permitted use, you will need to obtain permission directly from the copyright holder. To view a copy of this licence, visit <http://creativecommons.org/licenses/by/4.0/>.

© The Author(s) 2023

## Dual color pH probes made from silica and polystyrene nanoparticles and their performance in cell studies

Priyanka Srivastava<sup>a,‡</sup>, Isabella Tavernaro<sup>a,‡</sup>, Lena Scholtz<sup>a,b</sup>, Claudia Genger<sup>c,d</sup>, Pia Welker<sup>c,d</sup>, Frank Schreiber<sup>e</sup>, Klas Meyer<sup>f</sup> and Ute Resch-Genger<sup>a\*</sup>

<sup>a</sup>Division *Biophotonics*, Federal Institute for Materials Research and Testing (BAM), Richard-Willstaetter-Str. 11, 12489 Berlin, Germany.

<sup>b</sup>Institut für Chemie und Biochemie, Freie Universität Berlin, Takustr. 3, 14195 Berlin, Germany.

<sup>c</sup>nanoPET Pharma GmbH, Robert-Koch-Platz 4, 10115 Berlin, Germany.

<sup>d</sup>Charité-Universitätsmedizin Berlin, Charitéplatz 1, 10117 Berlin, Germany.

<sup>e</sup>Division *Biodeterioration and Reference Organisms*, Federal Institute for Materials Research and Testing (BAM), Unter den Eichen 87, 12205 Berlin, Germany.

<sup>f</sup>Division *Process Analytical Technology*, Federal Institute for Materials Research and Testing (BAM), Richard-Willstaetter-Str. 11, 12489 Berlin, Germany.

‡ The authors contributed equally.

\*ute.resch@bam.de, Phone: +49 (0)30 8104 1134

### ORCID-IDs

Lena Scholtz: 0000-0002-6869-3654

Ute Resch-Genger: 0000-0002-0944-1115

Klas Meyer 0000-0003-1837-3801

<b>1. Characterization of pH probe 3</b> .....	2
<b>2. Optical spectroscopy of pH probe 3</b> .....	8
<b>3. Characterization of PSNPs and SiO<sub>2</sub>-NPs</b> .....	11
3.1 <i>Synthesis of reference dyes: Silane derivatives of Nile Red (NR-Silane) and rhodamine B (RhB-APTES) and their embedding into the SiO<sub>2</sub>-NPs</i> .....	12
3.2 <i>Determination of the amount of reference dyes in the particle cores</i> .....	15
3.3 <i>Determination of the number of total and accessible COOH groups on the particle surface of PSNP-NR-COOH and SiO<sub>2</sub>-RhB-COOH</i> .....	18
3.4 <i>Surface modification of carboxylated PSNPs and SiO<sub>2</sub>-NPs with 3</i> .....	19
<b>4. Optical spectroscopy of nanosensors</b> .....	20
<b>5. Fluorescence cell microscopy</b> .....	24

### 1. Characterization of pH probe 3

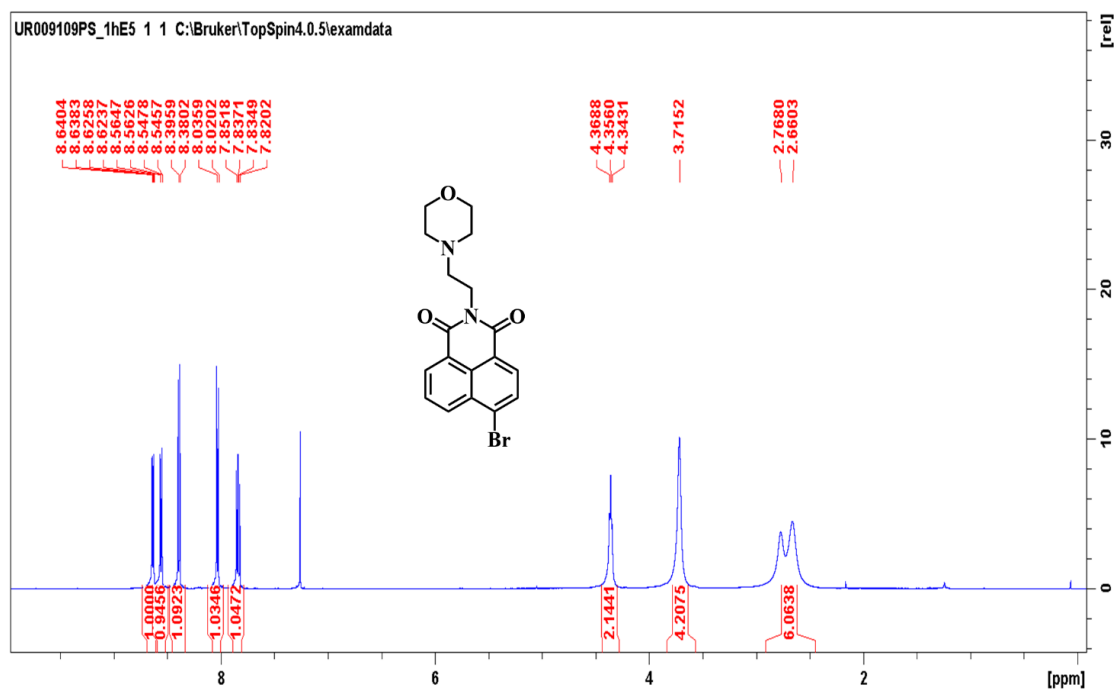


Figure S 1. <sup>1</sup>H NMR spectra of compound 2 in CDCl<sub>3</sub>.

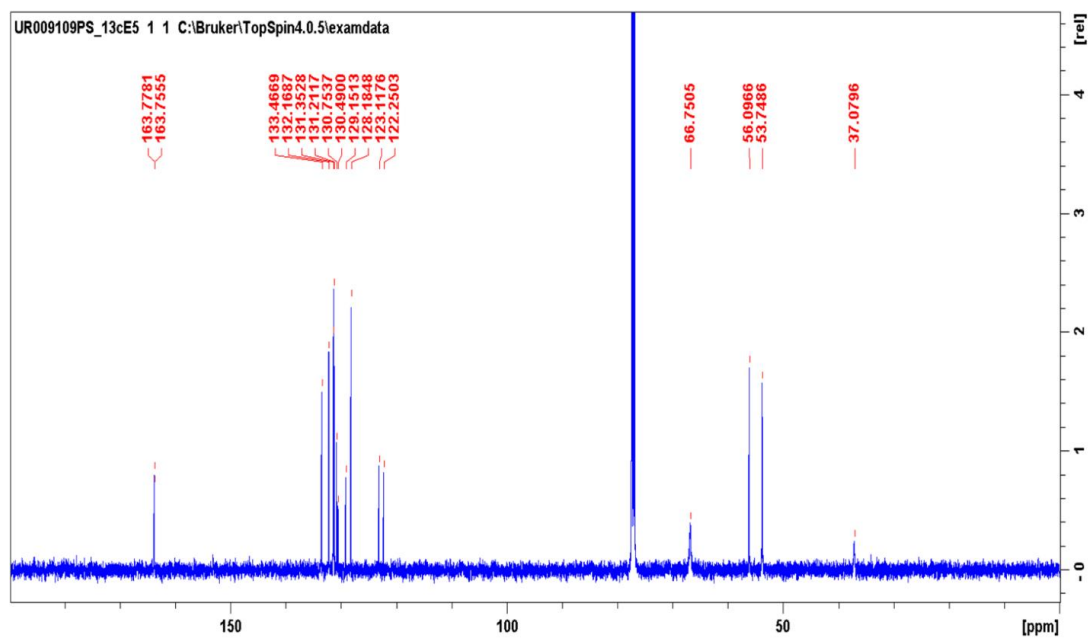


Figure S 2. <sup>13</sup>C NMR spectra of compound 2 in CDCl<sub>3</sub>.

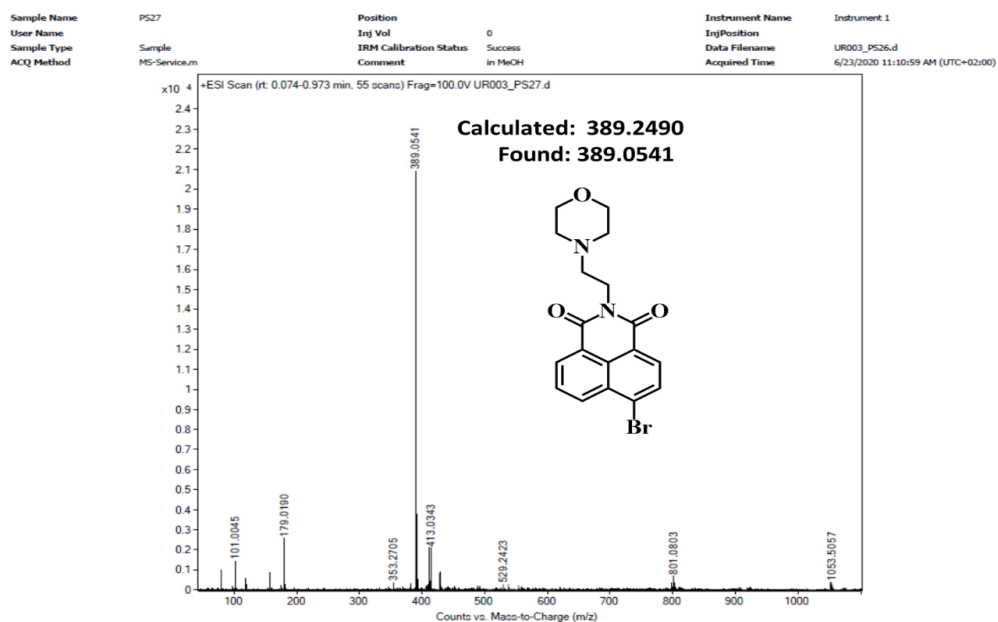
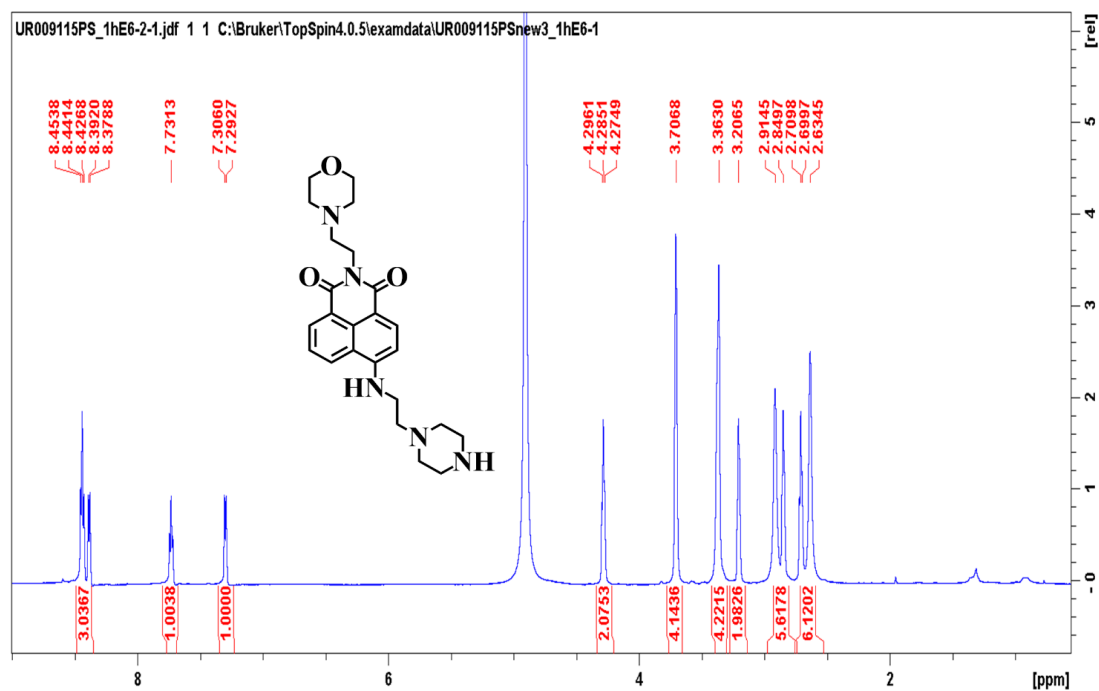


Figure S 3. ESI-MS spectra of compound 2 in methanol.

Figure S 4.  $^1\text{H}$  NMR spectra of pH probe 3 in  $\text{CD}_3\text{OD}$ .

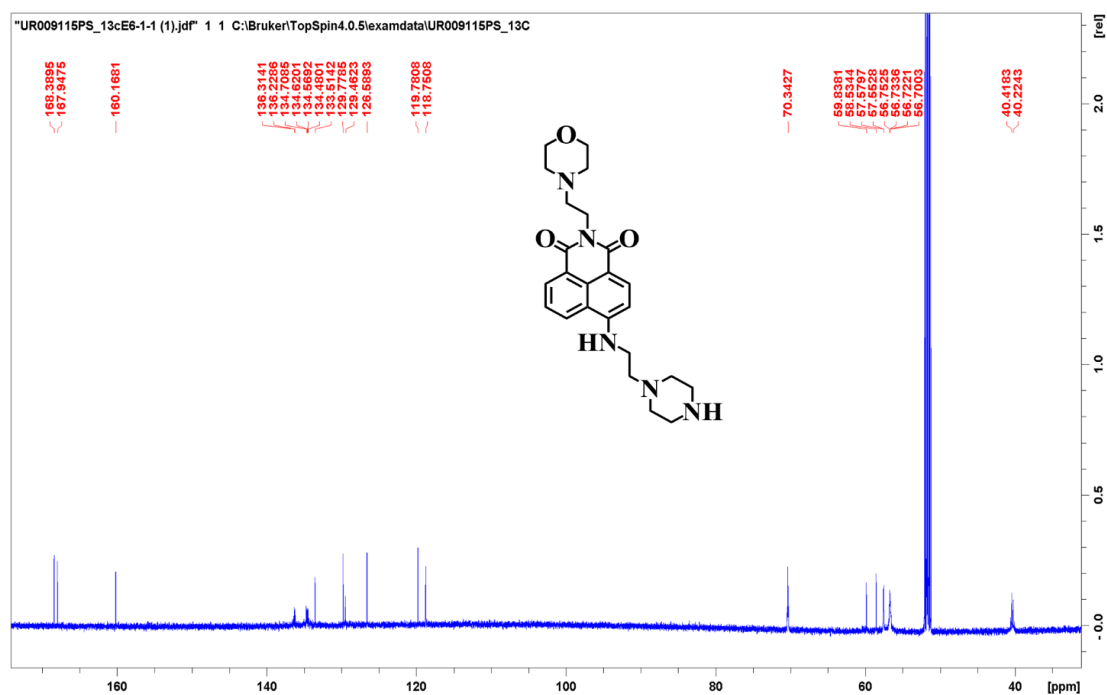


Figure S 5.  $^{13}\text{C}$  NMR spectra of **3** in  $\text{CD}_3\text{OD}$ .

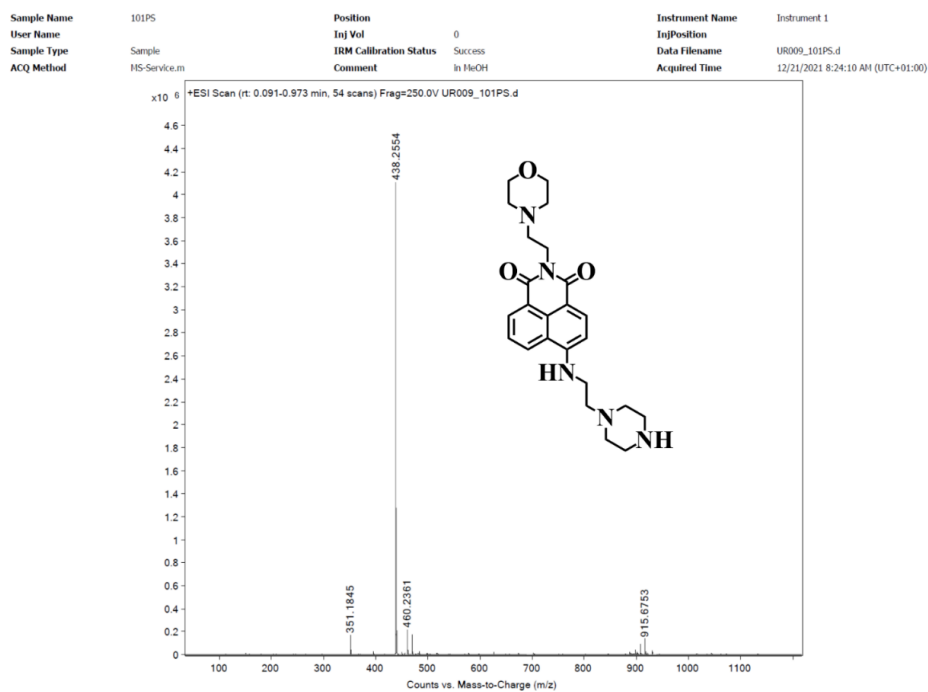


Figure S 6. ESI-MS spectra of **3** in methanol.

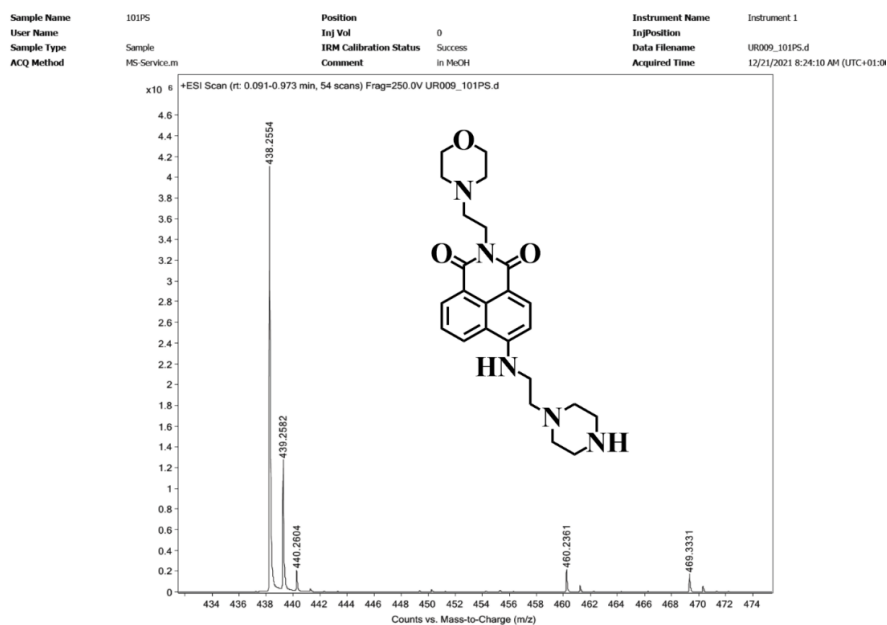


Figure S 7. Magnified ESI-MS spectra of **3** in methanol.

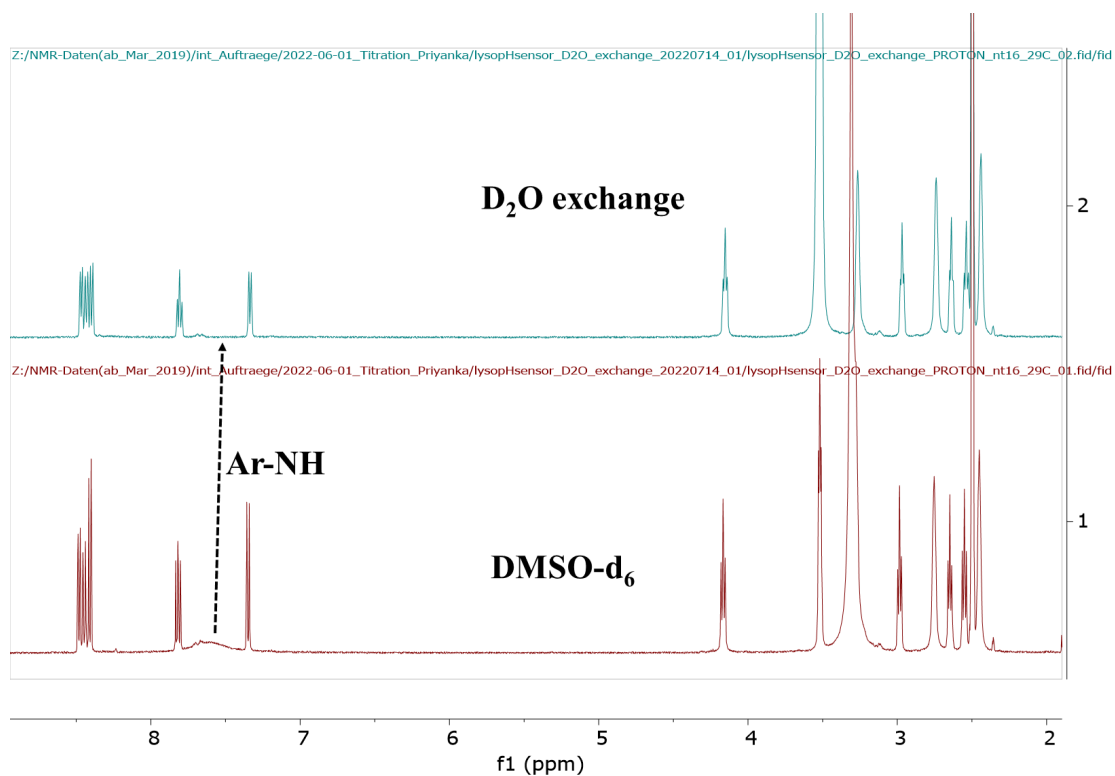
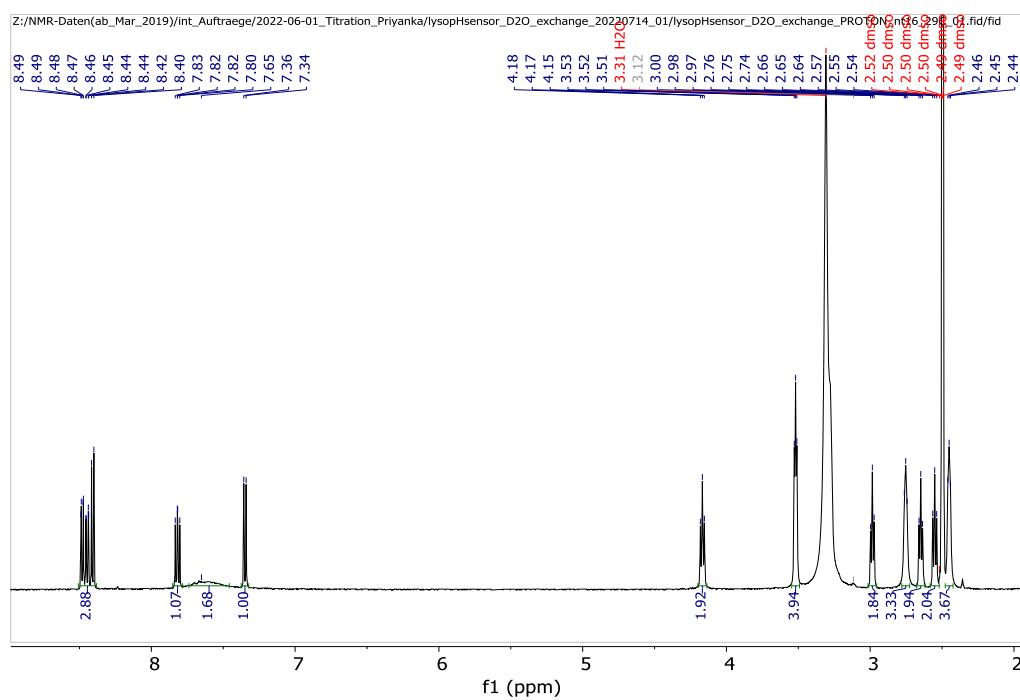
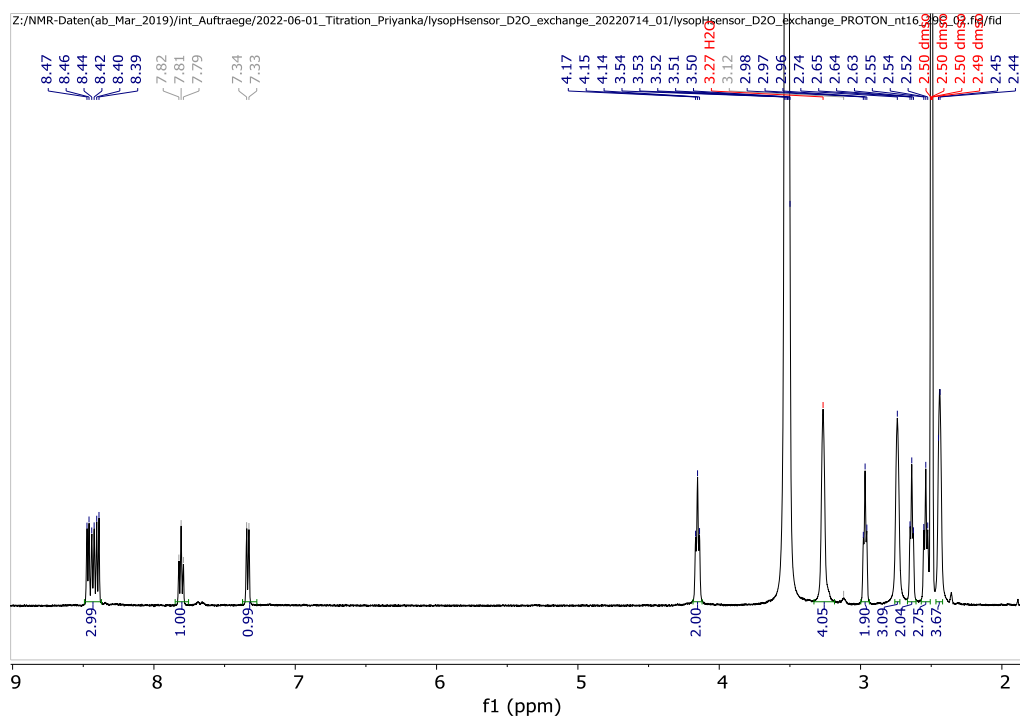


Figure S 8.  $^1H$  NMR spectra of **3** in  $DMSO-d_6$  and followed by  $D_2O$  exchange.



**Figure S 9.**  $^1\text{H}$  NMR spectra of **3** in  $\text{DMSO-d}_6$  (Figure S8 lower spectra).



**Figure S 10.**  $^1\text{H}$  NMR spectra of **3** in  $\text{DMSO-d}_6$  and followed by  $\text{D}_2\text{O}$  exchange (Figure S8 upper spectra).

To study the pH signaling mechanism of **3** in more detail, pH titration by NMR measurements in D<sub>2</sub>O was performed. The pH probe was dissolved in D<sub>2</sub>O and measured by addition of varying amounts of HCl, to change the pH from 8.5 to 2.5 (Figure S 11).

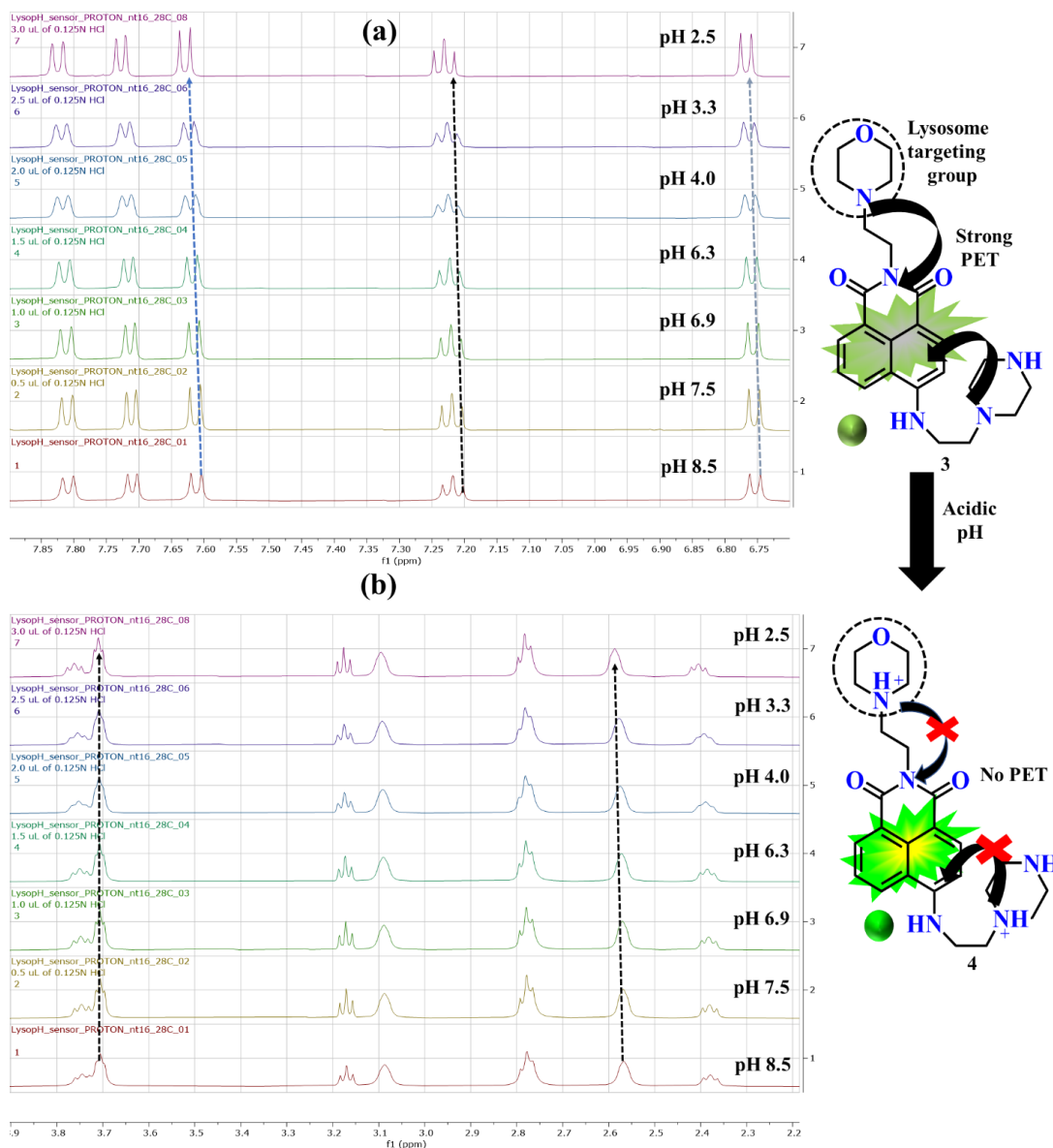


**Figure S 11.** NMR titration spectra of pH probe **3** performed in D<sub>2</sub>O solvent and over a pH range of pH 8.5 to pH 2.5; (a) aromatic region (b) aliphatic region.

## 2. Optical spectroscopy of pH probe 3

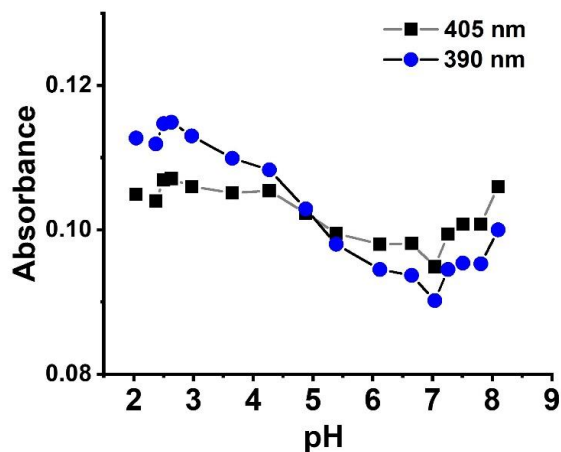


**Figure S 12.** Variation of absorbance ( $\lambda_{\max}$  405 nm and 392 nm) with different pH values of **3** in the pH range of 3.0 to 8.5 in water (Britton-Robinson buffer (B-R buffer)).

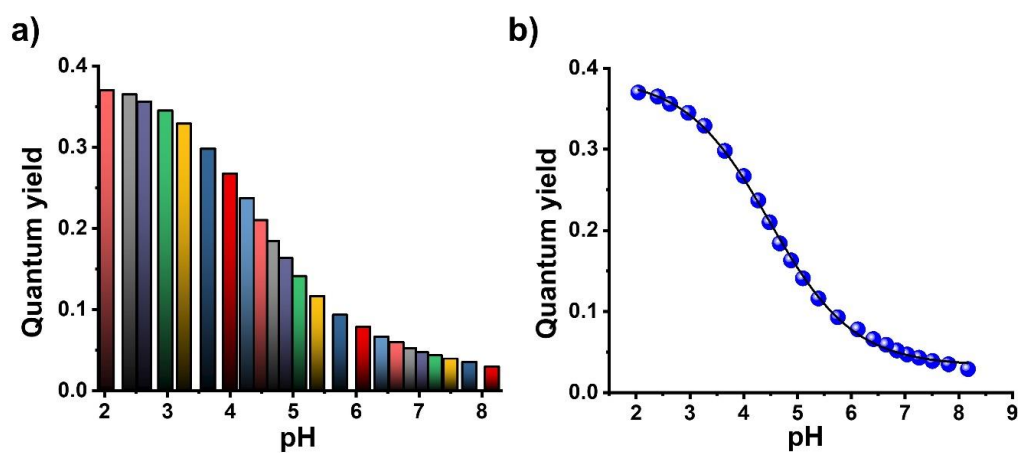


**Figure S 13.** Quantum yield of pH probe **3**; a) Bar diagram and b) plot of quantum yield at respective pH in the pH region 8.1 to 2.0 in an aqueous buffer (B-R buffer 25 mM).

**Table S1.** Quantum yield of **3** at different pH values; absorption maxima ( $\lambda_{\max}$ , Abs), emission maxima ( $\lambda_{\max}$ , Em), and fluorescence quantum yields ( $\Phi$ ).

Sample	Solvent	Buffer	$\lambda_{\max}/\text{Abs}$ [nm]	$\lambda_{\max}/\text{Em}$ [nm]	pH	$\Phi$	pH	$\Phi$
<b>3</b>	MilliQ-water	B-R buffer	405	530	8.1	0.029	4.8	0.163
					7.8	0.035	4.6	0.184
					7.5	0.039	4.4	0.210
					7.2	0.043	4.2	0.237
					7.0	0.047	4.0	0.267
					6.8	0.052	3.6	0.298
					6.6	0.059	3.2	0.329
					6.4	0.066	2.9	0.345
					6.1	0.078	2.6	0.356
					5.7	0.093	2.4	0.365
					5.3	0.116	2.0	0.370
				5.1	0.141			

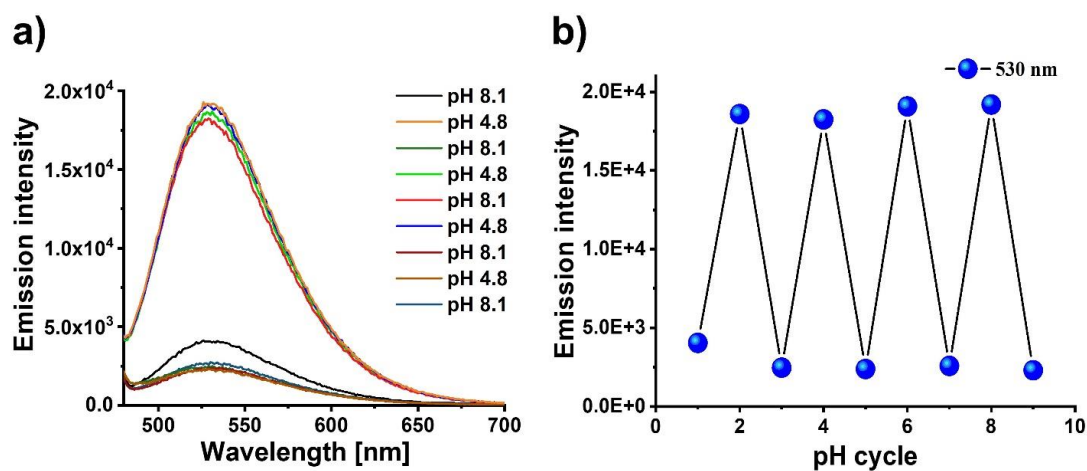


**Figure S 14.** Reversibility experiment of **3**; a) emission spectra and b) plot of emission intensity at 530 nm with varying pH upto three cycles from pH 8.1 to pH 4.8 in an aqueous buffer (B-R buffer 25 mM).

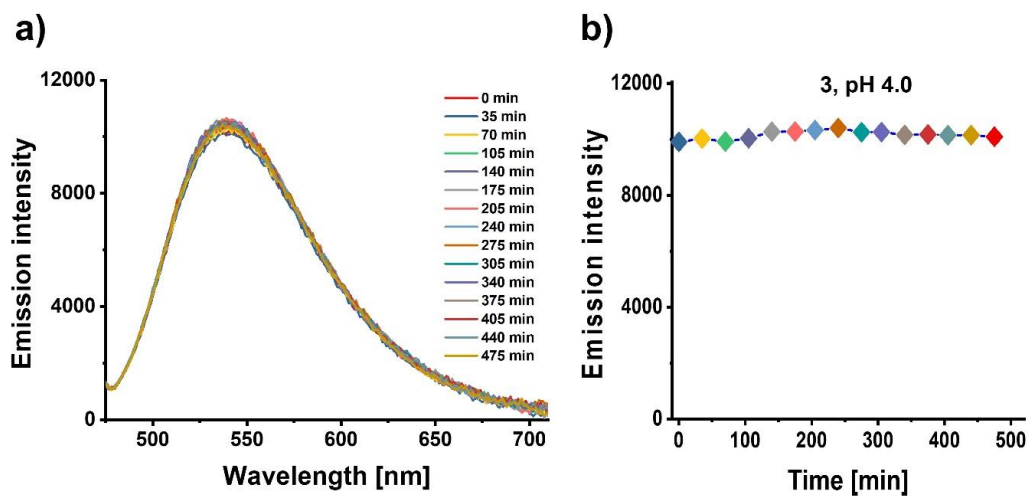


**Figure S 15.** Photostability experiment of **3** at pH 4.0; a) emission spectra and b) plot of emission intensity at 530 nm with increasing time upto 475 min (measured after every 35 min) in an aqueous buffer (B-R buffer 25 mM).

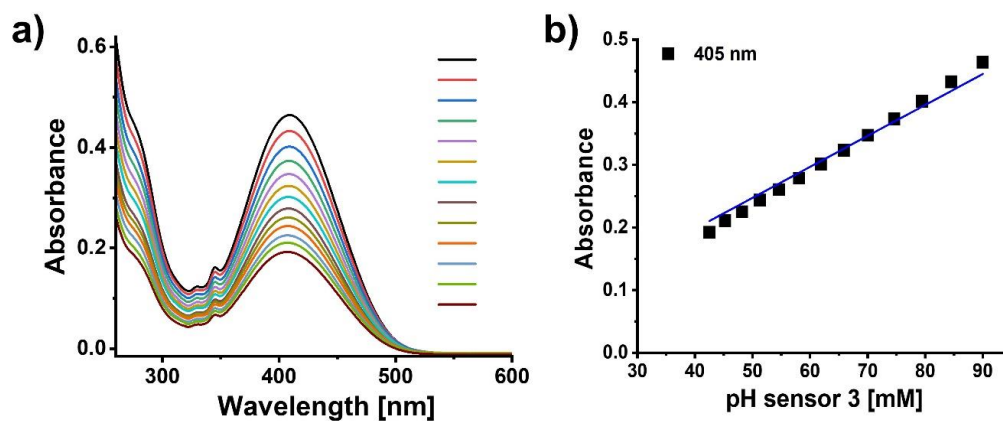


**Figure S 16.** a) Absorption spectra and b) calibration curve of **3** in water at different concentrations.

### 3. Characterization of PSNPs and SiO<sub>2</sub>-NPs

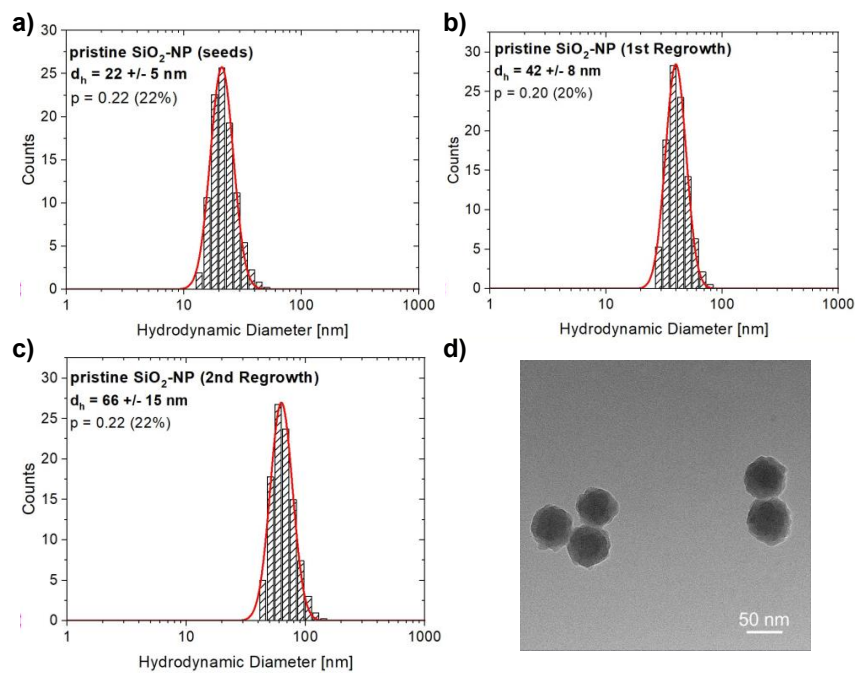


**Figure S 17.** Results of DLS measurements by number distribution of pristine SiO<sub>2</sub>-NPs, after the formation of the seeds (a), after the first regrowth step (b), and after the second regrowth step (c), indicating a particle growth of around 20 nm in each step. TEM micrograph of pristine SiO<sub>2</sub>-NPs after the second regrowth step showing spherical particles with a particle diameter of  $d_{\text{TEM}} = 60.5 \pm 1.6$  nm (d).

### 3.1 Synthesis of reference dyes: Silane derivatives of Nile Red (NR-Silane) and rhodamine B (RhB-APTES) and their embedding into the SiO<sub>2</sub>-NPs

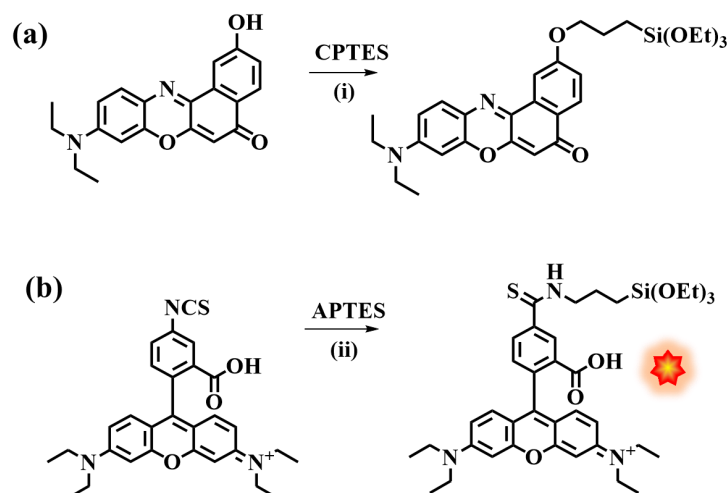


**Figure S 18.** Synthesis of NR-Silane derivative a) and RhB-APTES b); (i) K<sub>2</sub>CO<sub>3</sub>, DMF, 80 °C; (ii) ethanol, Ar, 2 d, room temperature (r.t.).

**Synthesis of 9-Diethylamino-2-(triethoxysilyl-3-propyloxy)-5H-benzo[*a*]phenoxazin-5-one NR-Silane derivative (NR-Silane):** 9-Diethylamino-2-hydroxy-5H-benzo[*a*]phenoxazin-5-one (Hydroxy Nile Red) was synthesized as reported in the literature (**Fehler! Verweisquelle konnte nicht gefunden werden. a)**).<sup>1</sup> Hydroxy Nile Red (20 mg, 0.05 mmol), K<sub>2</sub>CO<sub>3</sub> (8.2 mg, 0.05 mmol) and 3-Chloropropylmethoxysilane (CPTES, 17.2  $\mu$ L, 0.07 mmol) were taken in DMF. The reaction mixture was heated at 80 °C overnight. After complete reaction the solvent was removed and precipitate obtained was washed with hexane, dried and used without further purification.

**Synthesis of reference dye RhB-APTES.** The synthesis of RhB-APTES was adopted from the literature (**Fehler! Verweisquelle konnte nicht gefunden werden. b)**).<sup>2</sup> 9.97 mg (0.019 mmol) of RITC was dissolved in 1 mL of ethanol (absolute), followed by the addition of 13.2  $\mu$ L (0.056 mmol, 2.9 equiv.) of 3-Aminopropyltriethoxysilane (APTES) under a strict argon atmosphere; the resulting mixture was then allowed to stir for 2 d at room temperature (r.t.). Finally, the prepared RhB-APTES was stored under light exclusion at 4 °C, to be utilized later in dye embedding experiments.

**Loading of SiO<sub>2</sub>-NP with NR and NR-Silane.** To obtain 80 nm large SiO<sub>2</sub>-NPs loaded with NR or NR-Silane, the synthesis of the particles was performed as described for RhB-APTES loaded NPs, only in the last regrowth step 0.15 mL (6.4·10<sup>-7</sup> mol) of NR or 0.15 mL (6.4·10<sup>-7</sup> mol) of NR-APTES in DMSO was injected into the aqueous phase 20 min after the addition of TEOS.

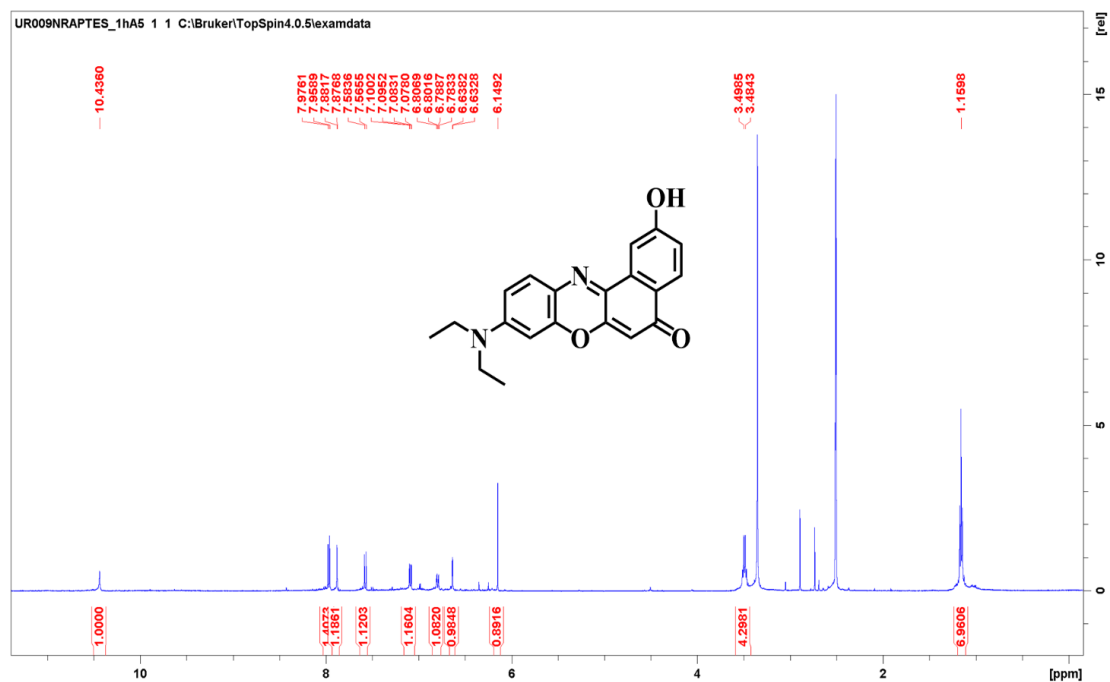
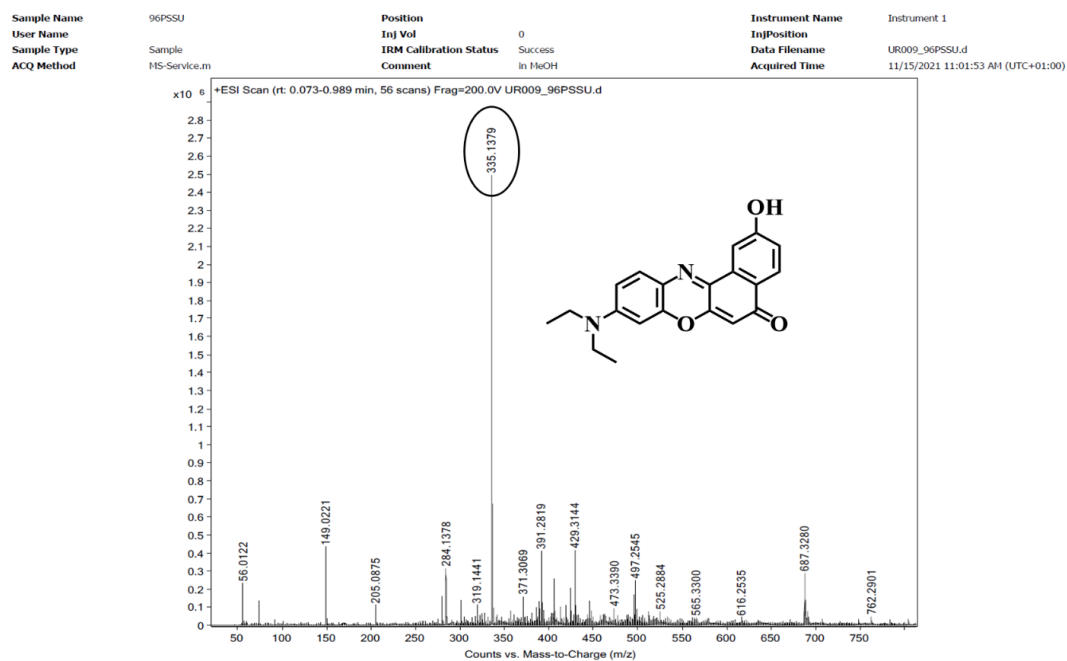
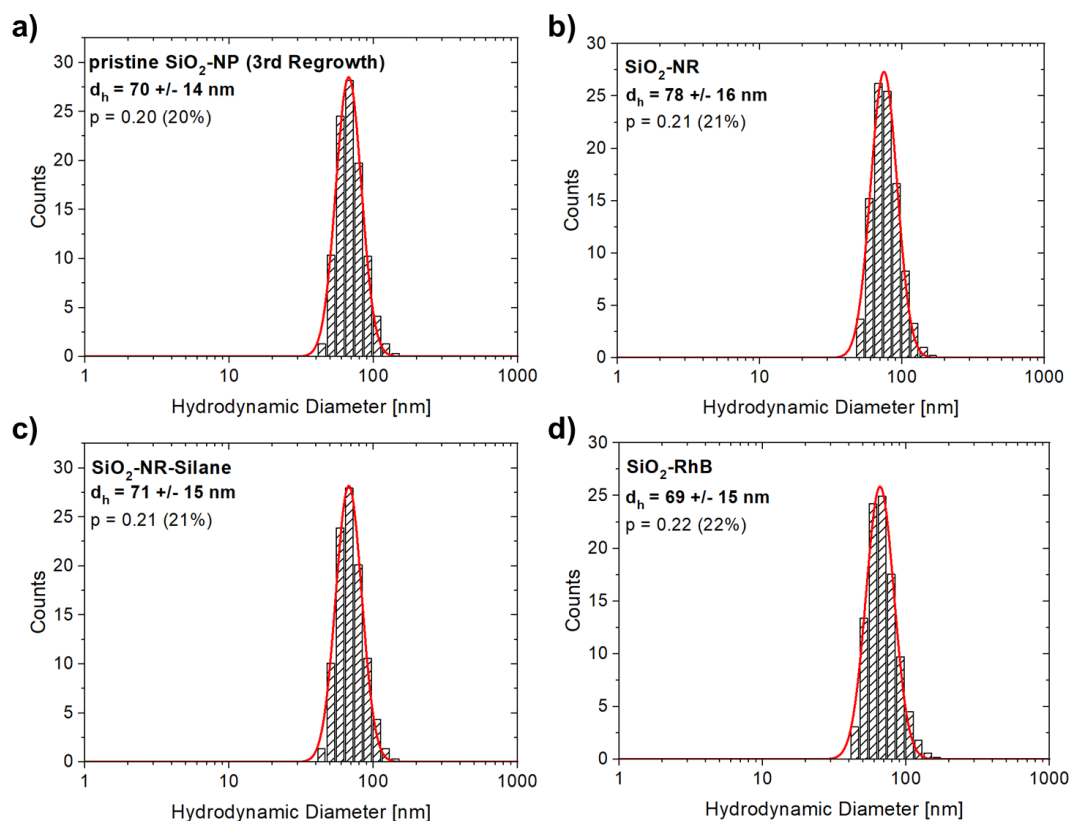
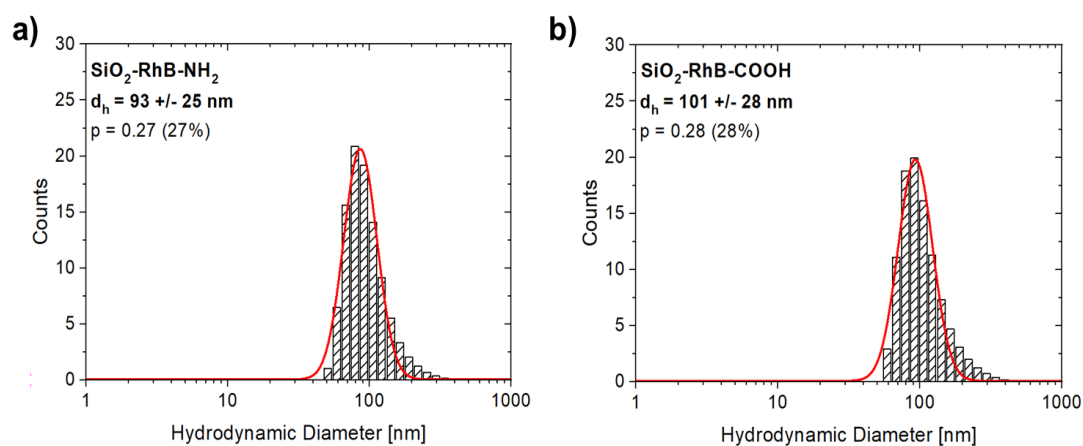
Figure S 19.  $^1\text{H}$  NMR of Hydroxy derivative of Nile Red in  $\text{DMSO-d}_6$ .

Figure S 20. ESI-MS spectra of Hydroxy derivative of Nile Red in MeOH.

S13



**Figure S 21.** Results of DLS measurements by number distribution of dye stained SiO<sub>2</sub>-NPs, using Nile Red (NR) b), NR-Silane c), and RhB-APTES d).



**Figure S 22.** Results of DLS measurements by number distribution of RhB-APTES stained SiO<sub>2</sub>-NPs after surface modification with APTES a) and succinic anhydride b). The measured z-average are  $164 \pm 3$  nm (SiO<sub>2</sub>-RhB-NH<sub>2</sub>) and  $176 \pm 1$  nm (SiO<sub>2</sub>-RhB-COOH), respectively.

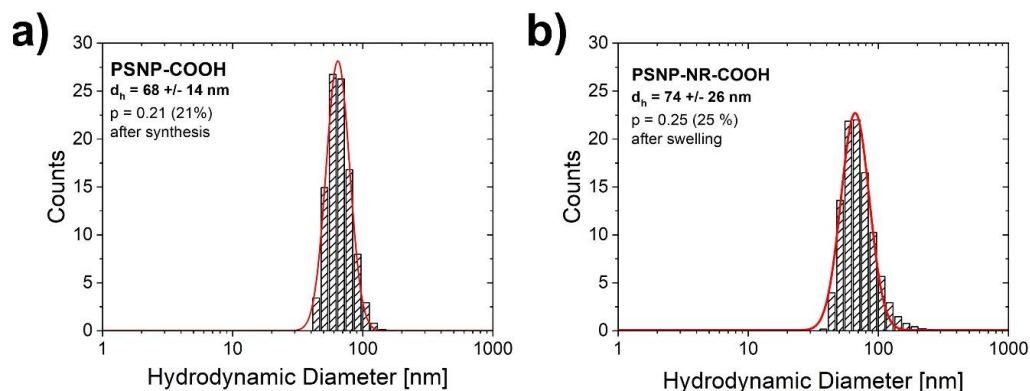


**Figure S 23.** Results of DLS measurements by number distribution of the pristine PSNPs after their synthesis a) and after the embedding of the NR dye by a swelling step (PSNP-NR-COOH, b)). The measured z-average are  $96 \pm 0.2$  nm (PS-COOH) and  $177 \pm 7$  nm (PSNP-NR-COOH), respectively.

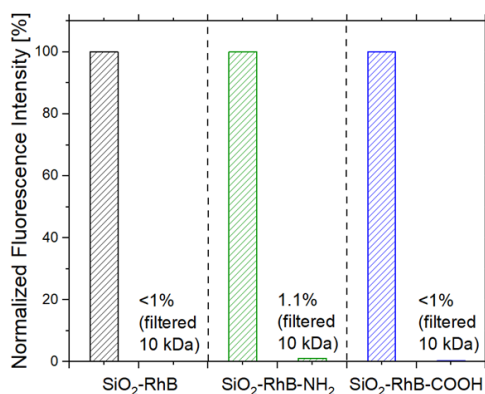


**Figure S 24.** Dye leaking experiments after encapsulation of RhB into the SiO<sub>2</sub> matrix and the influence of surface modification ( $\lambda_{ex} = 520$  nm).

### 3.2 Determination of the amount of reference dyes in the particle cores

To determine the amount of loaded reference dye molecules per particle a dissolution method was used. Different concentrations of NR in THF and RhB-APTES in aqueous B-R buffer were dissolved and the emission spectra (Figure S 25 and Figure S.27) and calibration curves were recorded. In addition, a previously dried amount of PSNP-NR-COOH of known mass was dissolved in 2.5 mL of THF and the emission spectrum was measured (Figure S 26), while SiO<sub>2</sub>-RhB-COOH were dissolved in aqueous B-R buffer at pH 12. The amount of reference dye molecules per particle was then calculated from the experimentally determined (average) amount of incorporated dye and the number of particles in the dispersion, using the number-based hydrodynamic diameters and a density of  $\rho(\text{PS}) = 1.06$  g/cm<sup>3</sup> and  $\rho(\text{SiO}_2) = 2.09$  g/cm<sup>3</sup>.

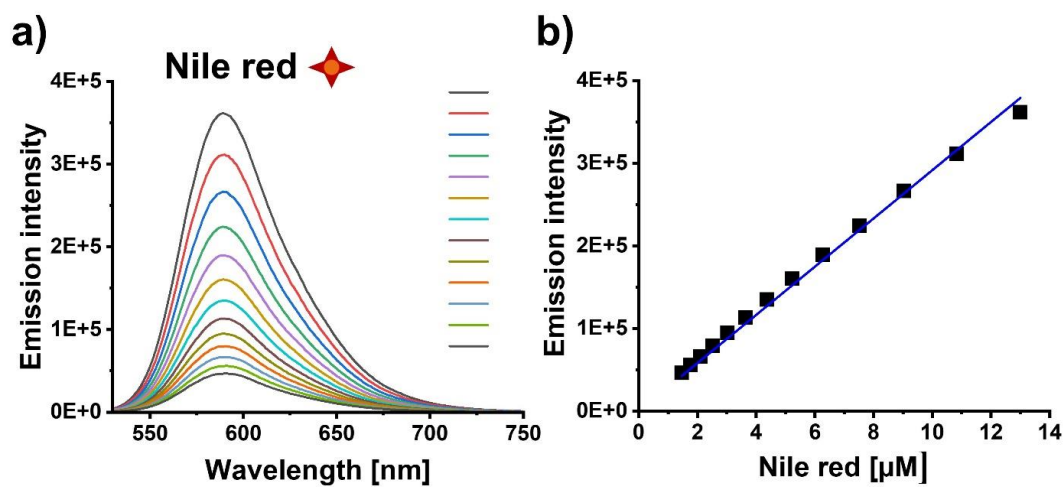


Figure S 25. a) Emission spectra and b) calibration curve of NR in THF at different concentrations.

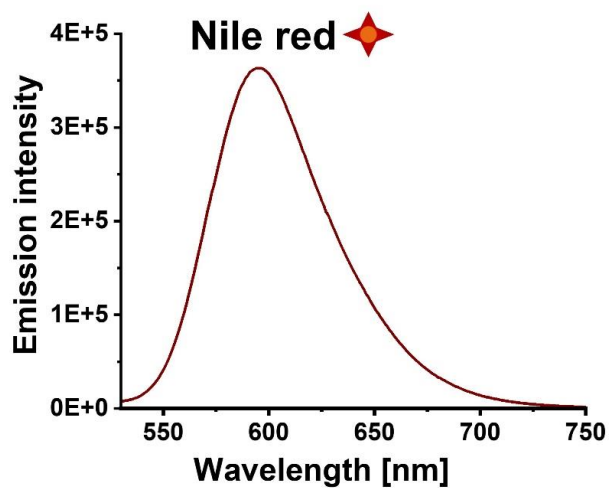


Figure S 26. Emission spectra of PSNP-NR-COOH after dissolving them in THF.

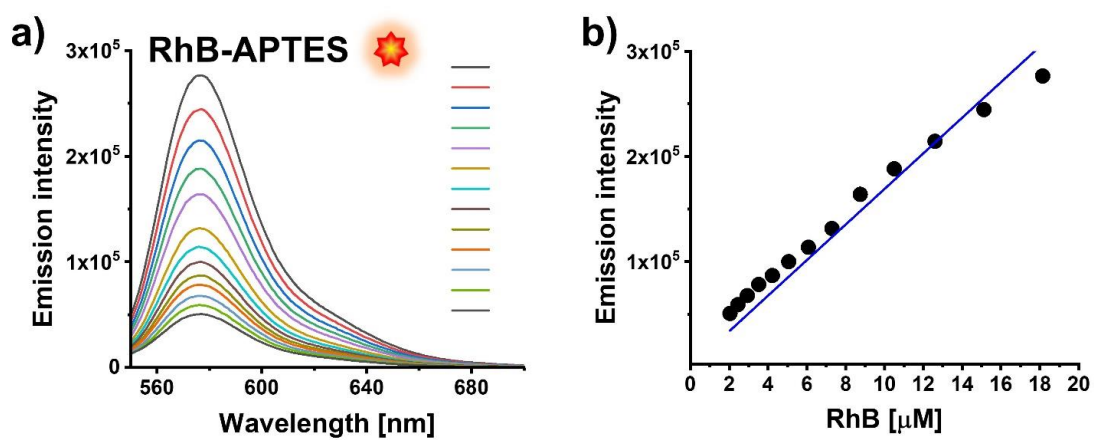


Figure S 27. a) Emission spectra and b) calibration curve of RhB-APTES at pH 12 in aqueous B-R buffer.

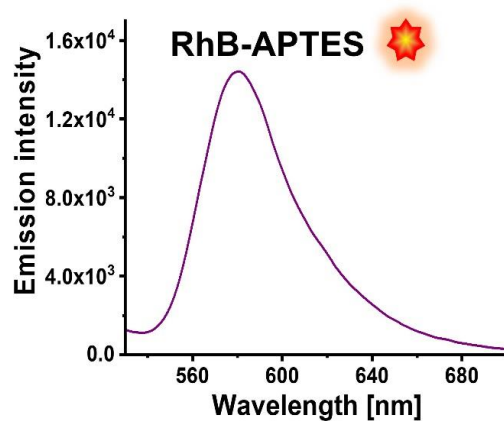
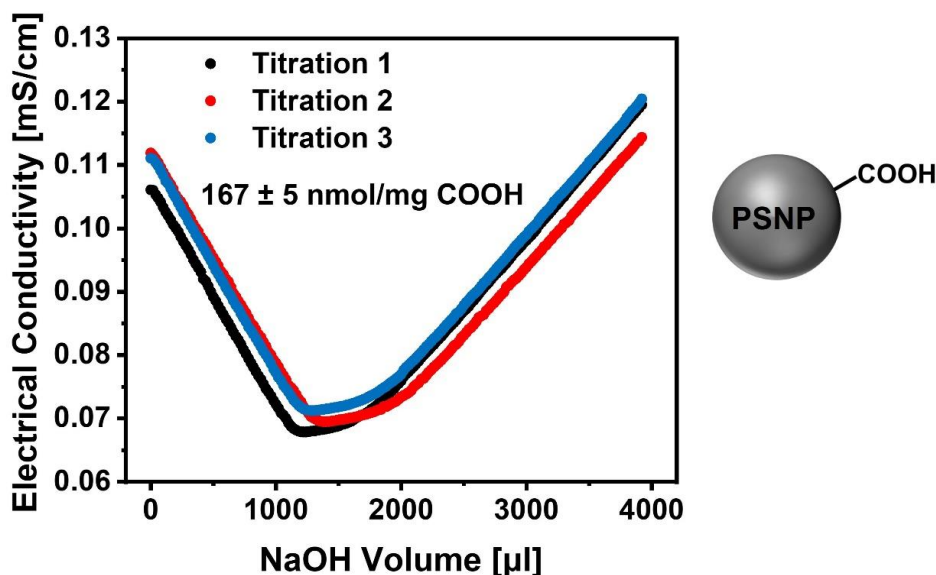


Figure S 28. Emission spectra of SiO<sub>2</sub>-RhB-COOH at pH 12 in aqueous B-R buffer.

### 3.3 Determination of the number of total and accessible COOH groups on the particle surface of PSNP-NR-COOH and SiO<sub>2</sub>-RhB-COOH



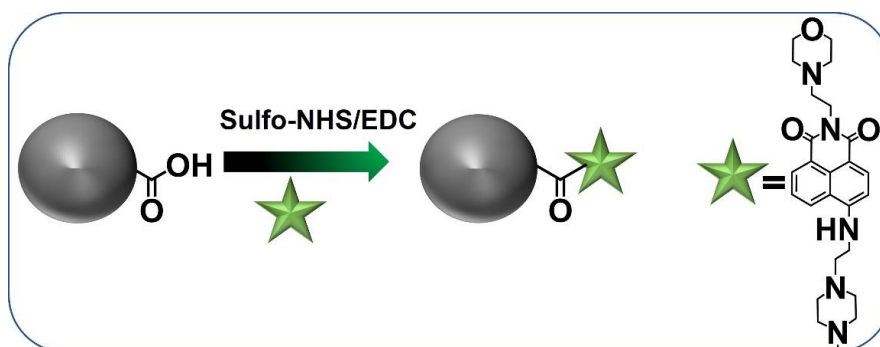
**Figure S 29.** Results of conductivity measurements of PSNPs.

To determine the accessible number of COOH groups on the particle surface a toluidine blue assay was performed.<sup>3</sup> Therefore, 0.2 mL of toluidine blue O in MilliQ water, containing 3.2  $\mu\text{mol}$  of the dye, were added to 0.8 mL of the PSNP-NR-COOH in MilliQ water. After 15 min of gentle shaking, the particles were centrifuged (16,000 rcf/15 min) and the supernatant was collected. The absorbance spectra of the supernatant (175  $\mu\text{L}$  & 1.325  $\mu\text{L}$  of MilliQ water) and of a toluidine blue O solution with 3.2  $\mu\text{mol}/1\text{ mL}$  (10  $\mu\text{L}$  & 1.49  $\mu\text{L}$  of MilliQ water) were recorded, and the absorbance values at the maximum (633 nm) were used in equation (1). The particle mass was determined to be 2.49 mg after the assay.

$$\begin{aligned} \text{accessible COOH groups (PSNP - COOH)} &= \frac{\text{abs}(\text{supernatant}) \cdot n(\text{TB solution})}{\text{abs}(\text{TB solution}) \cdot m(\text{particles})} \\ &= \frac{0.3584 \cdot 3.2 \mu\text{mol}}{17.5 \cdot 0.7493 \cdot 2.49 \text{ mg}} = 35 \frac{\text{nmol}}{\text{mg}} \quad (1) \end{aligned}$$

**Equation S1.** Calculation of the number of accessible COOH groups on the surface of PSNP-NR-COOH, obtained by an optical toluidine blue O assay, leading to a functional group density of 35 nmol/mg.

In comparison, 0.2  $\mu\text{L}$  (3.2  $\mu\text{mol}$ ) of toluidine blue O in MilliQ water were added to 0.4 mg of SiO<sub>2</sub>-RhB-COOH in MilliQ water. After 15 min of incubation, the particles were washed by several cycles of centrifugation (15,000 rcf/20 min), removal of supernatant and addition of MilliQ water. The supernatants of all washing steps were collected. When the supernatant was clear, 1 mL of 1% SDS was added and the particles were incubated for another 30 min with gentle shaking. After centrifugation, an absorption spectrum (633 nm) of the supernatant was measured to determine the amount of desorbed toluidine blue O. Finally, the particles were extensively washed to remove SDS, dried *in vacuo* and the weight of the remaining particles was determined.

3.4 Surface modification of carboxylated PSNPs and SiO<sub>2</sub>-NPs with **3**

**Figure S 30.** Reaction scheme of the surface modification of plain, carboxylated PSNPs (no red reference dye in the particle core) with **3**.

*IR measurements*

FT-IR measurements were measured on Vertex 70 instrument from Bruker with MCT (N<sub>2</sub>(l) cooled) detector. To confirm the binding of the synthesized optical probe **3** on the surface of the particles, PSNP-COOH with only **3** on the particle surface is synthesized as shown in Figure S 30 and compared by measuring the FT-IR spectra of PSNP-COOH, free **3** and PSNP-**3** in KBr pellets. pH sensor **3** showed bands at 2923 cm<sup>-1</sup>, 1692 cm<sup>-1</sup>, 1614 cm<sup>-1</sup>, 1513 cm<sup>-1</sup>, 1383 cm<sup>-1</sup>, 1234 cm<sup>-1</sup> and 1040 cm<sup>-1</sup> corresponding to the stretching vibrations of CH, CO, aromatic -C=C, C-C-O, -C-N in the IR spectra. The spectra of carboxylated PSNPs showed bands at 3024 cm<sup>-1</sup>, 2922 cm<sup>-1</sup> and 2847 cm<sup>-1</sup>, corresponding to the stretching vibrations of aromatic CH, and CH/CH<sub>2</sub>, respectively. The bands at 1599 cm<sup>-1</sup>, 1492 cm<sup>-1</sup>, 1068 cm<sup>-1</sup> and 1027 cm<sup>-1</sup> are due to the stretching vibration of aromatic C=C, CH<sub>2</sub>, C-C respectively. The PSNP-**3** showed 1027 cm<sup>-1</sup>, 1218 cm<sup>-1</sup>, 1741 cm<sup>-1</sup>, 1661 cm<sup>-1</sup>, 1371 cm<sup>-1</sup> bands corresponding to the C-O and C-N stretching similar to **3** besides the stretching observed in the PSNPs indicating the binding of the sensor on the surface of the particles.

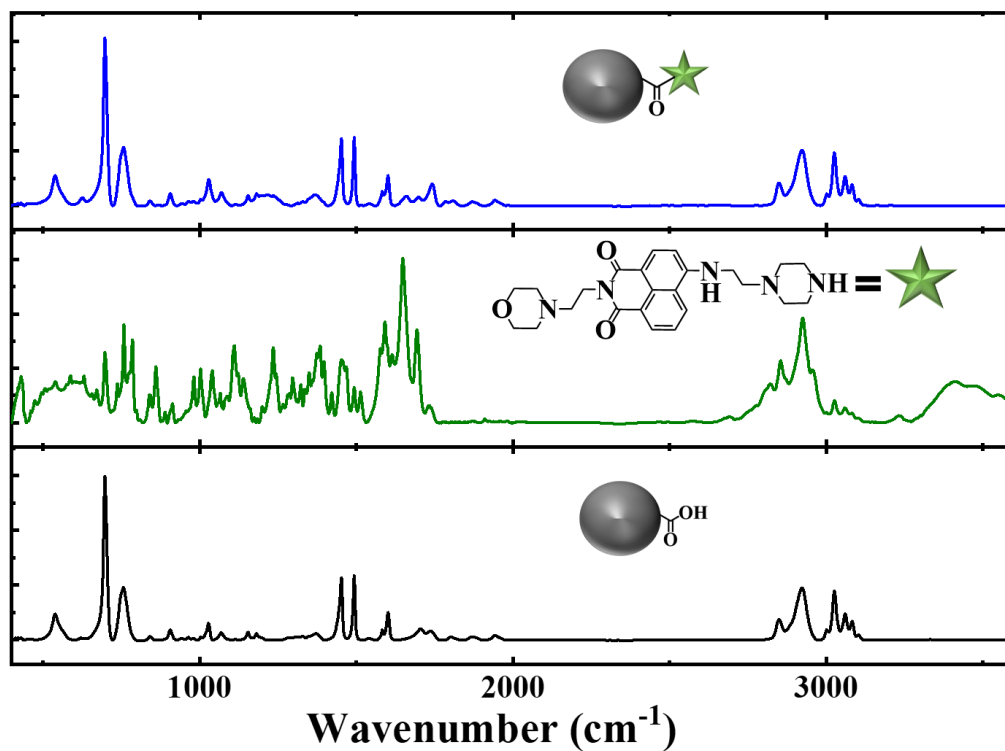


**Figure S 31.** FT-IR spectra of PSNP-COOH (black), free **3** (green) and PSNP-**3** (blue) measured on KBr pellets.

#### 4. Optical spectroscopy of nanosensors

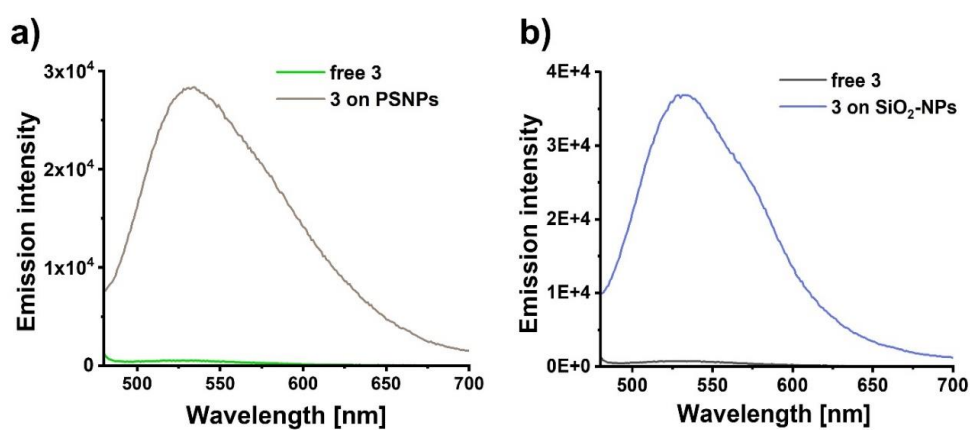


**Figure S 32.** Emission spectra of free **3** in the supernatant and bound **3** on the particles surface of PSNPs (a) and SiO<sub>2</sub>-NPs (b) after dialysis.

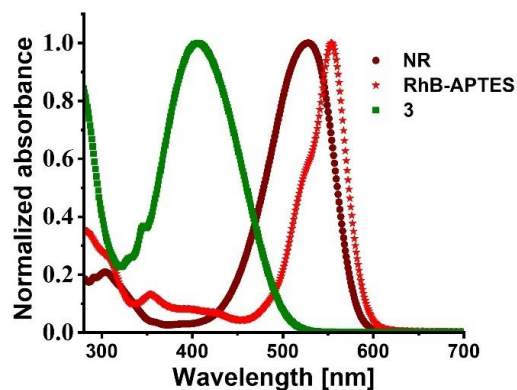


**Figure S 33.** Normalized absorbance spectra of the reference dyes NR and RhB-APTES as well as the free optical probe 3 in THF (NR) or an aqueous buffer (B-R buffer 25 mM, RhB-APTES, 3).

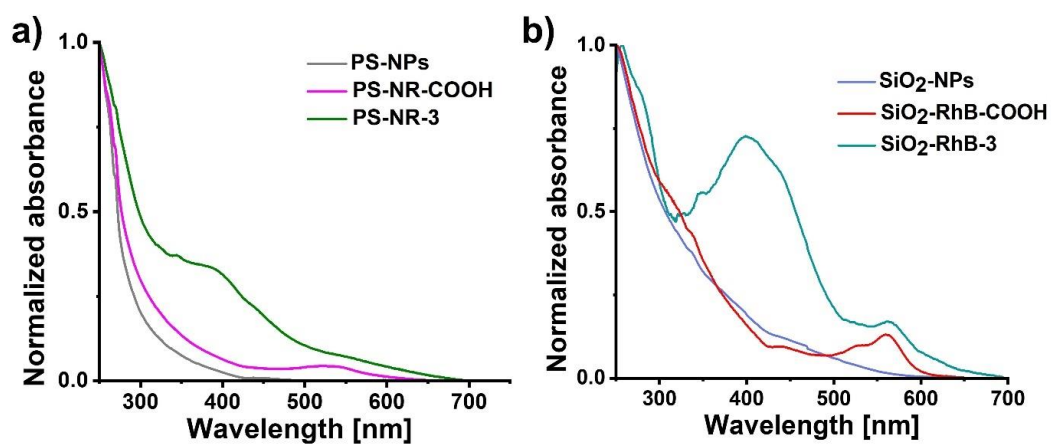


**Figure S 34.** Normalized absorption spectra of a) PSNPs (plain polystyrene particles with COOH groups), PSNP-NR-COOH (PSNPs with encapsulated NR) and PSNP-NR-3; b) pristine SiO<sub>2</sub>-NPs, SiO<sub>2</sub>-RhB-COOH (silica particles with encapsulated RhB and COOH groups on the particle surface) and SiO<sub>2</sub>-RhB-3 in an aqueous buffer (B-R buffer 25 mM).

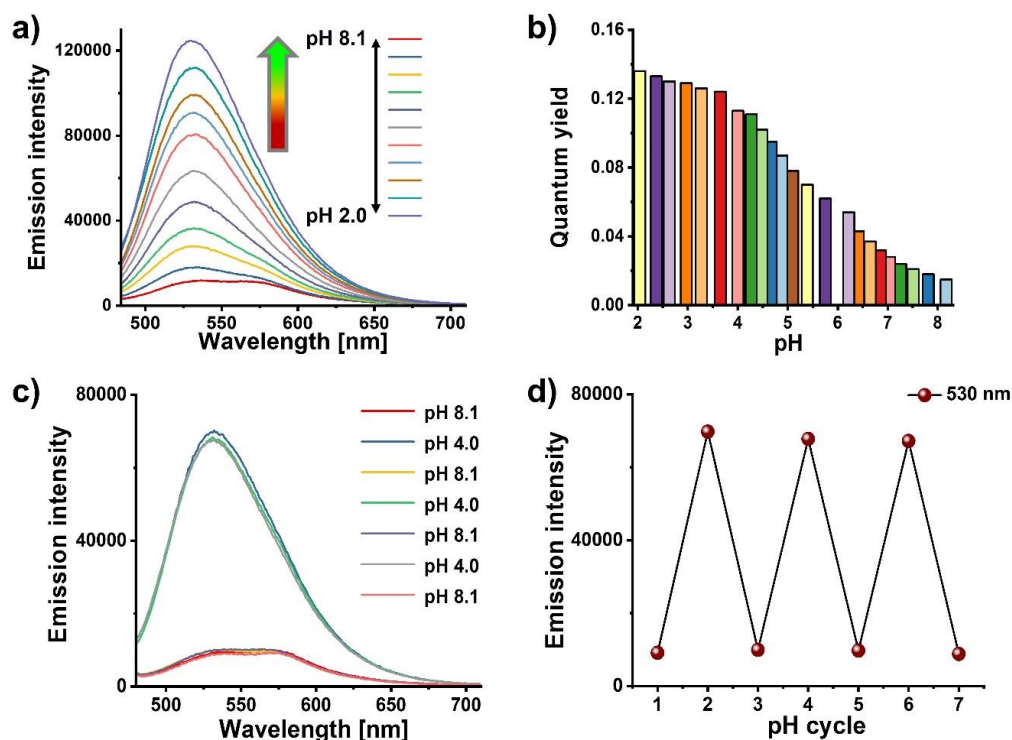


**Figure S 35.** pH-dependent fluorescence of SiO<sub>2</sub>-RhB-3. a) Emission spectra at different pH values; b) bar diagram of the pH-dependence of quantum yields in the pH range of 8.1 to 2.0; c) and d) Reversibility study of SiO<sub>2</sub>-RhB-3 involving the measurement of the emission spectra and the fluorescence intensity by varying the pH from 8.1 to 4.0 in cycles in an aqueous B-R buffer (25 mM).

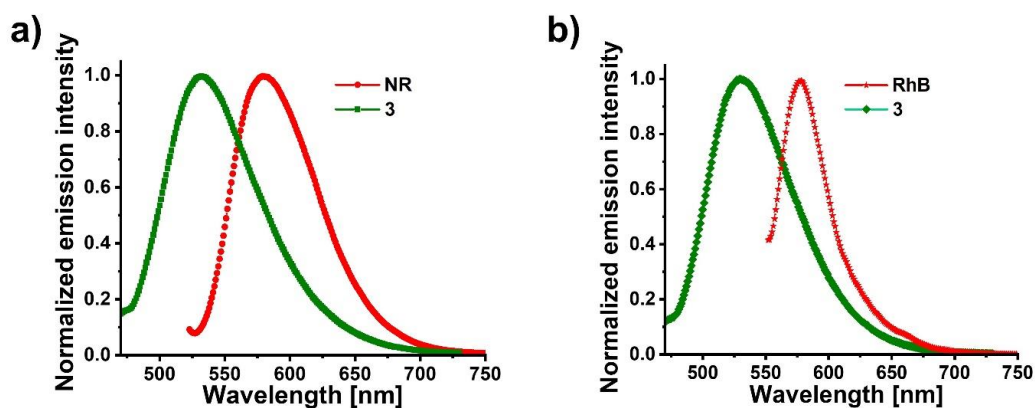


**Figure S 36.** Normalized emission spectra of particles with **3** and reference dyes NR and RhB-APTES at pH 4; a) NR ( $\lambda_{\text{Ex}}$  510 nm) and **3** ( $\lambda_{\text{Ex}}$  405 nm) in PS-NR-3; b) RhB-APTES ( $\lambda_{\text{Ex}}$  540 nm) and **3** ( $\lambda_{\text{Ex}}$  405 nm) in SiO<sub>2</sub>-RhB-3 in an aqueous B-R buffer (25 mM).

**Table S2.** Quantum yield of PSNP-NR-3, at different pH values, absorption maxima ( $\lambda_{\max}$ , Abs), emission maxima ( $\lambda_{\max}$ , Em), and fluorescence quantum yields  $\Phi$  in an aqueous B-R buffer.

Sample	Solvent	Buffer	$\lambda_{\max}/\text{Abs}$ [nm]	$\lambda_{\max}/\text{Em}$ [nm]	pHs	$\Phi$	pHs	$\Phi$
PS-NR-3	MilliQ water	B-R buffer	400 and 538	533 and 578	8.1	0.032	4.8	0.081
					7.8	0.036	4.6	0.086
					7.5	0.038	4.4	0.088
					7.2	0.044	4.2	0.092
					7.0	0.049	4	0.096
					6.8	0.052	3.6	0.1
					6.6	0.055	3.2	0.107
					6.4	0.062	2.9	0.121
					6.1	0.064	2.6	0.125
					5.7	0.071	2.4	0.137
					5.3	0.072	2.0	0.134
					5.1	0.078		

**Table S3.** Quantum yield of SiO<sub>2</sub>-RhB-3, at different pH values, absorption maxima ( $\lambda_{\max}$ , Abs), emission maxima ( $\lambda_{\max}$ , Em), and fluorescence quantum yields  $\Phi$  in an aqueous B-R buffer.

Sample	Solvent	Buffer	$\lambda_{\max}/\text{Abs}$ [nm]	$\lambda_{\max}/\text{Em}$ [nm]	pHs	$\Phi$	pHs	$\Phi$
Si-RhB-3	MilliQ water	B-R buffer	400 and 560	530 and 577	8.1	0.015	4.8	0.087
					7.8	0.018	4.6	0.095
					7.5	0.021	4.4	0.102
					7.2	0.024	4.2	0.111
					7.0	0.028	4	0.113
					6.8	0.032	3.6	0.124
					6.6	0.037	3.2	0.126
					6.4	0.043	2.9	0.129
					6.1	0.054	2.6	0.13
					5.7	0.062	2.4	0.133
					5.3	0.07	2.0	0.136
					5.1	0.078		

## 5. Fluorescence cell microscopy

### *Cellular fluorescence microscopy*

The human lung cancer cell line A549 were routinely propagated as described in the literature.<sup>4</sup> In short, the A549 cells were cultivated in DMEM medium, to which 10% fetal calf serum (FCS), 2% glutamine, and penicillin / streptomycin (purchased from PAN Biotech) were added. Cells were disseminated into medium at a concentration of  $1 \times 10^5$  cells/mL, cultivated at 37 °C with 5% CO<sub>2</sub>, and split 1:5 twice per week. Using a 24-well culture plate prepared with glass cover slips (Sigma Aldrich), cells were disseminated at a concentration of  $1 \times 10^5$  cells/mL in 1 mL of medium and cultured at 37 °C and 5% CO<sub>2</sub> for 48 h. Cells were rinsed with sterile PBS, after which cell pH was adjusted following the protocol by Lucien *et al.*<sup>5</sup>, with pH values of 4.5, 5.5, and 7.5 being used over time periods of 30 min, 1 h, 3 h, or 24 h. Nanoparticle samples (100 µg/mL) and free pH probe **3** (35 µg/mL) in sterile PBS were added to the cells and incubated for 30 min at 37 °C and 5% CO<sub>2</sub>. Cells were rinsed again using sterile PBS and fixed with cold PFA solution. 4,6-diamidino-2-phenylindole (DAPI, Abcam) was used for nuclear counterstain. The cytoskeleton was stained with phalloidin-Alexa 488 (Cell Signaling). Image acquisition was performed using a Leica DMRB microscope (Leica) Images were taken with a digital camera (Spot 32, Diagnostic Instruments) with the same exposure time for all pictures.

Confocal laser scanning microscopy was done with fixed cells on a Leica SP8 equipped with a white light laser (Superk Extreme EXW-9 NIM, NKT Photonics, Denmark) and a 405 nm laser diode (LASOS, VLK 0550 T01), using a 100x oil immersion objective with a numerical aperture of 1.4 (HC PL APO 100x/1.40 OIL CS2). The fluorescence of DAPI was excited at 405 nm and its emission was recorded in the spectral window of 420 – 480 nm. The pH sensor dye was excited at 405 nm and its emission was detected in the spectral window of 520 – 560 nm. The reference dye was excited at 560 nm and its emission was detected in the spectral window of 570 – 660 nm. All channels were sequentially excited to minimize spectral bleed through. The pixel size of the recorded images was 29.36 nm. A z-stack over the height of the cells with a step size of 0.3 µm was recorded. All images were acquired with the same imaging settings. Adjustments of the intensity histograms of the images to improve the visibility of the fluorescence signal were equally applied to all images.

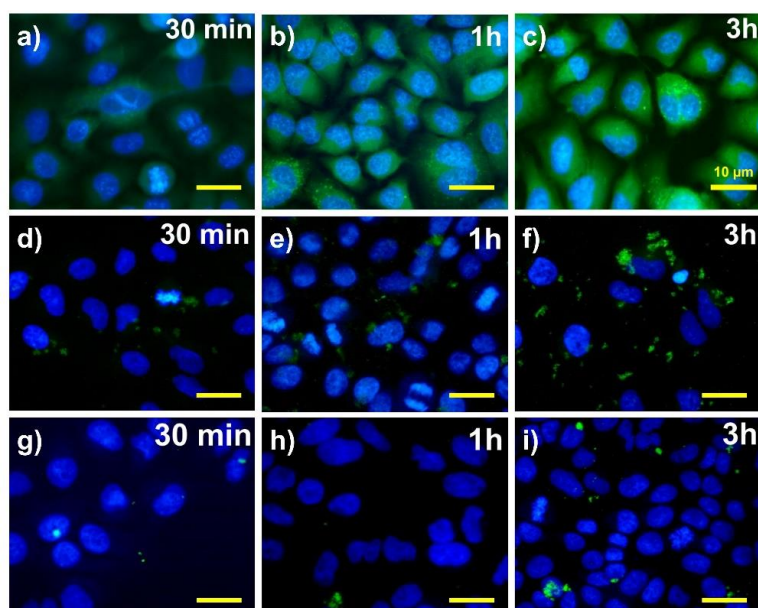


**Figure S 37.** Epifluorescence images at neutral pH of the uptake of free optical probe 3 (a-c), dye concentration 35  $\mu\text{g/mL}$ ,  $\lambda_{\text{em}} = 470 \text{ nm}$ , and the pH nanosensors PSNP-NR-3 (d-f), particle concentration 100  $\mu\text{g/mL}$ ,  $\lambda_{\text{em}} = 470 \text{ nm}$  and  $\text{SiO}_2\text{-RhB-3}$  (g-f), particle concentration 100  $\mu\text{g/mL}$ ,  $\lambda_{\text{em}} = 470 \text{ nm}$ ) by A549 cells measured after different incubation times, 30 min, 1 h and 3 h, respectively. Prior to the fluorescence microscopy studies, the cells were incubated alive, fixed with 4% paraformaldehyde (PFA), and then co-stained with DAPI (cell nuclei, blue channel:  $\lambda_{\text{em}} = 340/380 \text{ nm}$ ). Excitation was carried out with an Osram 50W/ACL1 Cz HBO Mercury vapor short-arc lamp. All images show a scale bar of 10  $\mu\text{m}$ .

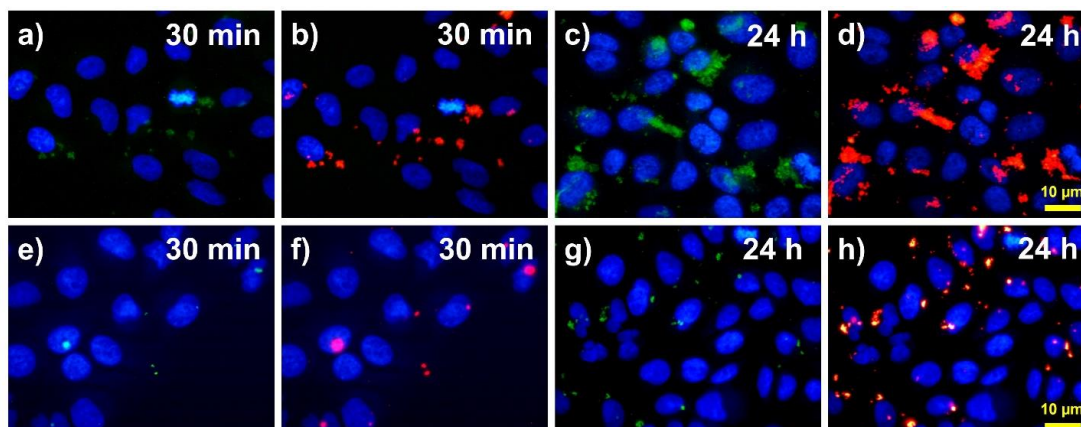


**Figure S 38.** Epifluorescence images of the pH nanosensors PSNP-NR-3 (a-d), particle concentration 100  $\mu\text{g/mL}$ ) and  $\text{SiO}_2\text{-RhB-3}$  (e-h), particle concentration 100  $\mu\text{g/mL}$ ) by A549 cells measured after incubation times of 30 min, and 24 h, respectively. Prior to the fluorescence microscopy studies, the cells were incubated alive, fixed with 4% paraformaldehyde (PFA), and then co-stained with DAPI (cell nuclei, blue channel). Excitation was carried out with an Osram 50W/ACL1 Cz HBO Mercury vapor short-arc lamp and the fluorescence was monitored with emission filters set to  $\lambda_{\text{Em}} = 470 \text{ nm}$  (green channel) and to  $\lambda_{\text{Em}} = 560 \text{ nm}$  (red channel). For the detection of the fluorescence of DAPI Leica filter cube A ( $\lambda_{\text{Em}} = 340/380 \text{ nm}$  (blue channel) was used. All images show a scale bar of 10  $\mu\text{m}$ .

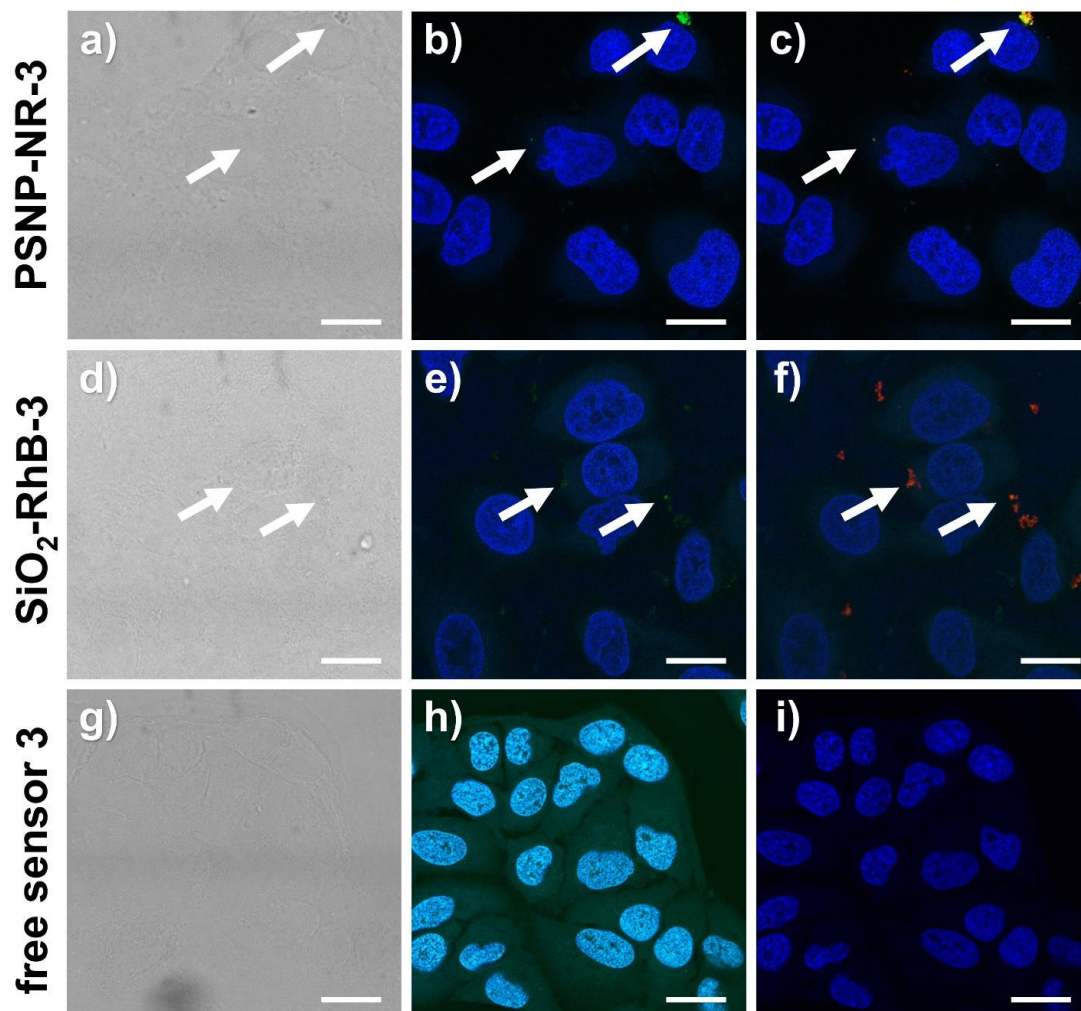


**Figure S 39.** Confocal laser scanning microscope (CLSM) images of fixed A549 cells (PFA) incubated for 30 min with PSNP-NR-3 (a-c, particle concentration 100  $\mu\text{g}/\text{mL}$ ), SiO<sub>2</sub>-RhB-3 (d-f, particle concentration 100  $\mu\text{g}/\text{mL}$ ), and free pH sensor **3**, (g-i, sensor concentration 35  $\mu\text{g}/\text{mL}$ ) at pH 7.5 in PBS buffer. The nuclei were stained with DAPI. Transmitted light a), d), g); merged blue (DAPI) and green (pH sensor **3**) channels: b), e), h); and merged blue (DAPI), green (pH sensor **3**) and red (reference dyes, NR or RhB) channels: c), f), i).  $\lambda_{\text{Ex}} = 405 \text{ nm}$ ,  $\lambda_{\text{Em1}} = 420 - 480 \text{ nm}$  and  $\lambda_{\text{Em2}} = 520 - 560 \text{ nm}$  for DAPI and **3** respectively. and  $\lambda_{\text{Ex}} = 560 \text{ nm}$  and  $\lambda_{\text{Em}}$  range 570 – 660 nm for the reference dyes. Scale bar 10  $\mu\text{M}$ .

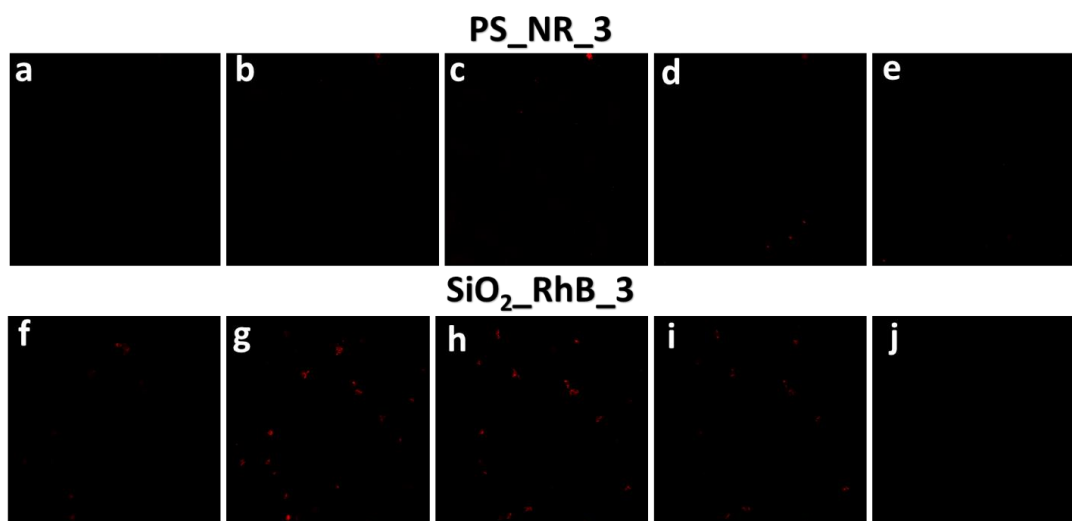


**Figure S 40.** CLSM z-stack images of A549 cells incubated 30 min and 3 h with PSNP-NR-3 (a-e, particle concentration 100  $\mu\text{g/mL}$ ), and SiO<sub>2</sub>-RhB-3 (f-j, particle concentration 100  $\mu\text{g/mL}$ ) at pH 7.5 (z step size 1.5  $\mu\text{m}$ ; a -e and f-j top to bottom)  $\lambda_{\text{Ex}} = 560 \text{ nm}$ ,  $\lambda_{\text{Em}}$  of 570 - 660 nm).

## 6. References

- 1 Martin-Brown, S. A., Fu, Y., Saroja, G., Collinson, M. M. & Higgins, D. A. Single-Molecule Studies of Diffusion by Oligomer-Bound Dyes in Organically Modified Sol-Gel-Derived Silicate Films. *Anal. Chem* **77**, 486-494 (2005).
- 2 Jiang, Z. *et al.* Multifunctional Au@mSiO<sub>2</sub>/Rhodamine B Isothiocyanate Nanocomposites: Cell Imaging, Photocontrolled Drug Release, and Photothermal Therapy for Cancer Cells. *Small* **9**, 604-612, doi:<https://doi.org/10.1002/sml.201201558> (2013).
- 3 Hennig, A. *et al.* Scope and Limitations of Surface Functional Group Quantification Methods: Exploratory Study with Poly(acrylic acid)-Grafted Micro- and Nanoparticles. *Journal of the American Chemical Society* **134**, 8268-8276, doi:10.1021/ja302649g (2012).
- 4 Srivastava, P. *et al.* Multicolor Polystyrene Nanosensors for the Monitoring of Acidic, Neutral, and Basic pH Values and Cellular Uptake Studies. *Analytical Chemistry* **94**, 9656-9664, doi:10.1021/acs.analchem.2c00944 (2022).
- 5 Lucien, F., Harper, K., Pelletier, P.-P., Volkov, L. & Dubois, C. M. Simultaneous pH Measurement in Endocytic and Cytosolic Compartments in Living Cells using Confocal Microscopy. *JoVE*, e51395, doi:doi:10.3791/51395 (2014).



---

## 6 | Synopsis of Results

The main goal of this thesis was to develop and optimize a facile and reproducible synthesis of luminescent PSMPs, stained with semiconductor NPs and/or organic dyes. For this purpose, the performance of a dispersion polymerization reaction in the presence of the NPs was chosen as a low-cost, simple and still very effective approach. Therefore, control over the application relevant particle properties is of considerable importance, as they determine the suitability of the synthesized PSMPs for applications as fluorescent sensors, labels or carrier beads for bead-based assays and immuno-separation. Application-relevant properties of luminophore-stained PSMPs include PSMP size, size distribution and luminescence, as well as the type and amount of the total and accessible surface FGs. The luminescence properties, e.g., a sufficient emission intensity and brightness, are important for the optical readout of the luminescent PSMPs with methods such as fluorescence spectroscopy or microscopy. The surface chemistry controls the colloidal stability of the PSMPs and determines their interaction with biological systems and subsequent (bio)functionalization steps. A systematic study of the influence of the polymerization reaction on the preservation of the luminescence for different types of luminescent NPs is thus of considerable importance for the selection of suitable fit-for-purpose nanoscale luminophores for staining.

### 6.1 | Optimized Synthesis of PSMPs Stained with Luminophores

In subsection 5.1.1 (see also Scholtz *et al.*, *Scientific Reports* 2022<sup>[22]</sup>), the synthesis of PSMPs stained with CdSe/CdS-core/shell-QDs or an organic dye (NR) via a dispersion polymerization procedure was established and optimized. The synthesis was first performed with NR to demonstrate its general suitability to produce optimized, luminophore-stained PSMPs, before QDs were employed for bead staining. Due to the gradual introduction of an additional ligand for the QDs, namely the polymer-compatible molecule OBDAc, and DVB as a second monomer and crosslinker, we could efficiently incorporate QDs in the formed beads and significantly improve the preservation of the QD luminescence properties (emission intensity

and PLQY). For the optimized synthesis, about 80–90% of the initial QD emission intensity could be preserved during PSMP incorporation. These numbers are quite high. In the existing literature, the PL properties (especially the PLQY) of luminescent PSMPs are rarely compared to those of the initial QDs, which renders this work an important starting point for the further optimization and comparison of protocols for the synthesis of luminescent PSMPs. Addition of the *block*-copolymer PEG-*b*-PCL lead to a significantly narrower size distribution of the PSMPs ( $768 \pm 57$  nm, 7.4% variation) compared to the synthesis without copolymer ( $872 \pm 150$  nm, 17% variation). The achieved, optimized size distribution is in the reported range for PSMPs synthesized by free-radical dispersion polymerization, which typically lies between 3–10%.

The influence of various synthesis parameters like temperature, reaction time, stirring speed and the amount of radical starter (AIBN) on the application relevant physico-chemical properties of the formed PSMPs was investigated and used to gain precise control over the size of the beads in a range of 0.5–2.5  $\mu$ m. Furthermore, the distribution of the QDs in the PSMPs was determined by CLSM and STEM with energy-dispersive X-ray spectroscopy (EDXS). Both methods confirmed the location of the QDs in the core region of the PSMPs without any signs for a severe aggregation visible. We presume that this finding is connected with the stable incorporation of the QDs at a very early stage of the polymerization reaction, which also shields the NPs from the harsh environment and helps the QDs to retain their fluorescence properties. QD location in the bead core, and PS crosslinking with DVB, largely prevent the QDs (and dye) leaking from the PSMPs even upon incubation in application relevant media at 37 °C for one hour. This was revealed by photometric studies of the respective supernatants after the centrifugation of the dye- and QD-stained PSMPs, which yielded a leakage of <2% in all cases. Photostability studies of QD- and dye-stained PSMPs demonstrated a better photostability of the former compared to the latter for short- and long-term illumination (seconds and days, respectively). In summary, the work in this subsection sets the ground for the facile synthesis of QD- or dye-stained PSMPs with a variety of different molecular or nanoscale luminophores, narrow size distribution, and good luminescence properties.

---

## 6.2 | Influence of Synthesis Routes on the Preparation of QD-stained PSMPs and Their Surface FGs

The subsection 5.1.2 (see also Scholtz *et al.*, *Scientific Reports* 2023<sup>[26]</sup>) describes and summarizes the preparation of QD-stained PSMPs via different synthesis routes and the observed differences. We specifically investigated the influence of two different reaction procedures on the surface functional group density and the luminescence properties of the employed QDs, both being very important characteristics for later applications of the PSMPs. The first procedure was adapted from the synthesis described in subsection 5.1.1, with the QDs present during the polymerization reaction, while the second approach includes the synthesis of unstained PSMPs, followed by a swelling procedure to stain the beads by QD diffusion into the polymer matrix. The swelling procedure utilizes an organic solvent compatible with both PSMPs and QDs to preserve their luminescence. The size of the unstained and both types of QD-stained PSMPs was determined to be nearly identical, but significant differences in zeta potential (-48/-49/-22 mV for unstained/polymerization procedure/swelling procedure), COOH surface group quantity (37/23/12 nmol/mg, determined by *N*-APPA assay) and PLQY (-/24/48%) were found. While the luminescence properties of the employed QDs (CdSe/CdS-core/shell, with about 10 monolayer (ML) shell thickness) were retained much better in the case of the post-synthetic swelling procedure, the accessible amount of COOH groups, determined by two independent colorimetric assays, was higher for the PSMPs obtained by the polymerization procedure.

Closer examination of the QD location within the PSMPs using STEM imaging revealed that the QDs were attached to the PSMP surface, especially for the swelling procedure. This can be understood when looking at the different interactions between the QDs, the PSMP matrix and the COOH groups introduced by acrylic acid grafting during the polymerization reaction/QD staining. The QDs are surface capped with OA ligands, which contain COOH groups, confirming their affinity for COOH groups. During the swelling procedure, the QDs have to pass through the COOH surface groups on the PSMPs to reach the bead interior, which apparently is not possible. In the case of the QD staining during polymerization, the QDs are already partly incorporated into the PSMPs before the COOH surface groups are introduced to the particles by addition of acrylic acid. This favors QD incorporation into the

polymer matrix. These findings explain the lower amount of accessible COOH surface FGs for the PSMPs prepared via the swelling procedure, as a significant number of COOH surface FGs is blocked by the QDs. The total COOH amount, however, is higher for these PSMPs, as the QDs introduce new COOH groups through their OA ligands. These OA ligands can be reached by protons acting as reporters for the conductometric measurements of the total amount of COOH groups, but they are not accessible for the larger dyes used for signal generation in the colorimetric assays.

The PLQY value of the QDs used for the PSMPs prepared by the swelling procedure of 48% exceeded the PLQY of the QDs incorporated during the polymerization reaction amounting to 24% by 100%. There is a balance between a high PLQY of the staining QDs and a high amount of COOH groups accessible for subsequent functionalization steps that must be considered for the application-specific choice of the optimum procedure for the preparation of QD-stained PSMPs. Nevertheless, there are other relevant factors to be considered which were not further explored in this thesis. This includes a potentially higher toxicity of PSMPs stained with QDs via swelling, due to the presence of surface-bound QDs. The fact that the QDs are located on or near the PSMPs surface also potentially means that the leaking of QDs from the beads is favored. When employing other, also Cd-free, QDs for the PSMPs staining via swelling, their affinity to COOH groups should be considered, as a high affinity could lead to the same outcome as for the here employed CdSe/CdS-QDs.

Further knowledge about surface FG quantification was gained and demonstrated by taking part in the writing of a review summarizing and evaluating analytical methods for the quantification of surface FGs on nanomaterials presented in subsection 5.2.1 (see also Geißler *et al.*, *Microchim Acta* 2021<sup>[184]</sup>), particularly the chapter about "electrochemical titrations for the quantification of (de)protonable FG on dispersed nanomaterials". Here, electrochemical FG quantification methods such as potentiometric and conductometric titrations are discussed and compared, with the latter also being employed in subsection 5.1.2 for the quantification of COOH surface FGs on unstained and QD-stained PSMPs. This review also includes photometric and fluorometric assays, as well as NMR, Raman and IR spectroscopy, and X-ray based methods.

---

## 6.3 | Correlation Between NP Architecture and Their Applicability for Controlled PSMP Staining

In subsection 5.1.3 (see also Scholtz *et al.*, submitted to *Chemistry of Materials* 2023<sup>[27]</sup>), the synthesis of QD-stained PSMPs developed in the previous subsections and publications is further developed and applied to different types of CdSe-based core/shell nanostructures. Here, the focus is set on the investigation of the influence of the polymerization reaction on the incorporation and PL properties of core/shell-type, luminescent NPs with different shell materials, thickness and particle architecture. A systematic study of this topic, that has not been reported before, provides important knowledge on the applicability of different NPs for the incorporation into PSMPs and a first derivatization of structure-property relations. For this purpose, CdSe/CdS- and CdSe/ZnS-core/shell-QDs, the former with three different shell thicknesses, CdSe/CdS-dot-in-rod-QRs, and CdSe/CdS-core/shell-NPLs were employed for the synthesis of luminescent PSMPs following a procedure adjusted from a previously optimized synthesis discussed in subsection 5.1.1. Fluorescence and integrating spectroscopy before, during, and after the synthesis of the PSMPs revealed that a thicker passivation shell improves the preservation of the QD luminescence properties such as emission intensity and PLQY during the polymerization. With a thicker shell, the CdSe core of the QDs is better protected from the harsh reaction environment containing ethanol and radicals formed from the polymerization starter AIBN. The shell material also strongly influences the stability and luminescence preservation of the QDs, which is demonstrated by the CdSe/ZnS-QDs PL being completely quenched, while the CdSe/CdS-QDs retained their luminescence properties to varying degrees. Furthermore, we demonstrate that CdSe/CdS-NPLs, which are known to generally be much more fragile and react more drastically to changes in their environment than QDs, can still be used for this synthesis. While these NPLs become less emissive and show a significant reduction in PLQY, they still show sufficient luminescence to be suitable for applications in NPL-stained PSMPs. In contrast, the CdSe/CdS-QRs are not incorporated into the PSMPs with the chosen polymerization procedure. The QRs bear different surface ligands, i.e., octadecylphosphonic acid and hexylphosphonic acid, than the QDs and NPLs stabilized with OA and OIA ligands. STEM images show that the NPs are generally located in the surface region of the PSMPs.

## 6.4 | Synthesis of pH-responsive PSNPs Stained with NR and Their Application as Ratiometric Sensors

In the work presented in subsection 5.2.2 (see also Srivastava *et al.*, *Scientific Reports* 2023<sup>[11]</sup>), ratiometric pH nanosensors based on PSNPs and silica NPs were synthesized and tested regarding their suitability for the penetration into acidic cell components such as lysosomes and the signaling of pH changes in the different microenvironments. My proprietary contribution to this work included the preparation of NR-stained and unstained PSNPs, their physico-chemical characterization, stability studies, and the quantification of the accessible FGs (COOH) on the particle surface. The polystyrene and silica particles were prepared with matching optical and physico-chemical properties (e.g., size, surface chemistry, spectroscopic properties) to enable a comparative study of the sensor performances. Both types of NPs were core-stained with an analyte-inert organic dye and surface functionalized with COOH FGs, to which a pH-sensitive compound could be attached. A post-synthetic swelling procedure was applied to stain the COOH functionalized PSNPs with NR. The silica NPs were prepared by a seeded growth approach, with a Rhodamine B (RhB) derivate incorporated into the outermost layer. A custom-made naphthalimide compound was then attached to both particle surfaces, allowing ratiometric sensing through protonation-controlled photoinduced electron transfer (PET) that switches ON or OFF the luminescence of the molecule at different pH values. Fluorescence microscopy studies confirmed the cellular uptake of both sensor particles and the staining of acidic cell components, and thus their suitability for intracellular pH sensing. The silica-based sensors showed a slightly more efficient cellular uptake and a better stability. These findings underline the importance of the matrix material for sensor performance.

## 6.5 | Summary of Generated Knowledge and Outlook

In summary, a facile, low-cost, and effective dispersion polymerization procedure for the synthesis of luminescent, dye- and NP-stained PSMPs with or without surface functionalization has been developed and further optimized. The synthesis was first demonstrated for dye (NR) staining to confirm its suitability for luminescent PSMP production, before attempting the more challenging incorporation of more complex nanostructures like QDs. Thereby, knowl-

edge about the influence of synthesis parameters like temperature, stirring speed, reaction time, and the amount of radical initiator on the size of the resulting PSMPs was generated. For representatively chosen CdSe/CdS-core/shell-QDs, it was shown that the preservation of QD PL can be improved significantly through the addition of a polymer-compatible ligand like OBDAC to the QD surface, and a second monomer acting as a crosslinker for the polymer matrix. This polymerization procedure resulted in the QDs being located in the core region of the PSMPs, as determined by electron microscopy.

Subsequently, it was demonstrated for the incorporation of CdSe/CdS-QDs with a 10 ML shell that the synthesis route has a significant influence on the PL properties of the QDs in the formed beads. This particularly concerns the QD PLQY, and unexpectedly also the amount of surface FGs present at the surface as published in Scholtz *et al.* (2023).<sup>[26]</sup> Apparently, the QD incorporation during polymerization leads to a higher amount of accessible surface FGs, while QD incorporation with a post-synthetic swelling procedure results in a better preservation of the PL properties of the QDs. By a thorough analytical characterization of the QD-stained PSMPs, it was demonstrated that the employed, OA/OIA stabilized CdSe/CdS-QDs tend to attach to the COOH surface FGs of the PSMPs in the case of the swelling procedure. This leaves the QDs exposed to the bead microenvironment and could lead to an accelerated QD release or leakage, raising possible toxicity concerns, and a decrease of the PL intensity of the QD-stained PSMPs.

The subsequent, successful usage of different semiconductor NPs with core/shell-architecture for the synthesis of luminescent PSMPs builds on the previously established synthesis procedure. A systematic study of the NP luminescence preservation after incorporation into PSMPs, which was not reported before in the literature, was conducted to evaluate the correlation of NP architecture with PL preservation. Employed NPs include CdSe/CdS-core/shell-QDs with three different shell thicknesses, CdSe/ZnS-core/shell-QDs, CdSe/CdS-dot-in-rod-QRs and CdSe/CdS-core/shell-NPLs surface stabilized with OA/OIA (QDs and NPLs) or octadecylphosphonic acid/hexylphosphonic acid (QRs). In addition, a correlation between NP size, shape, and surface chemistry was attempted by exploring the spatial distribution of the different core/shell semiconductor nanostructures in the beads. Thereby, a clear correlation was found between QD shell thickness and preservation of the PL properties, with

a thicker CdS shell protecting the QDs core more efficiently from environmental factors and allowing better PL preservation in terms of emission intensity and PLQY. The importance of QD shell material was demonstrated by employing CdSe/ZnS-QDs, which lost their PL during the polymerization reaction. Moreover, the successful incorporation of NPLs into PSMPs was achieved, which has not been reported before. The lack of incorporation of CdSe/CdS-QRs stabilized with different organic surface ligands than the QDs and NPLs suggests an influence of shape, and most likely also surface chemistry, which was not further assessed in this study. The versatility of the developed polymerization reaction for the preparation of luminescent polymer beads from molecular and nanoscale emitters was demonstrated with the synthesis of dye-stained PSNPs, which were subsequently converted into ratiometric pH sensors for intracellular sensing by the covalent attachment of sensor molecules to the FGs on the PSMP surface. Fluorescence microscopy studies confirmed the cellular uptake of these nanosensors and their applicability for the monitoring of pH changes during processing in the cells, and the fluorescence staining of acidic cell compartments such as lysosomes. However, the comparison with corresponding sensors prepared from silica NPs showed a less efficient cell uptake and inferior stability of the PSNP sensors.

All successfully synthesized, NP-stained PSMPs show promising characteristics regarding future applications, including both PL properties and colloidal stability of the produced particles. The initially developed PSMP synthesis with the QDs located in the bead core region potentially yields NP-stained beads that are less prone to NP leaking, and thus have a reduced (cyto)toxicity potential. This renders them interesting candidates for bioanalytical and chemical studies. For many applications in this field, a PSMP surface functionalization is required for the covalent attachment of targeting or recognition moieties to the bead surface. Here, the COOH-functionalized PSMPs prepared with the QDs present during the polymerization can be used as a starting point to e.g., develop selective sensor particles. Finally, the NPL-stained PSMPs are promising candidates for multiplexing applications, with the potential of including differently colored NPLs to create a barcode.

In the future, the already demonstrated versatility of the developed synthesis should be extended to other, also non-luminescent NPs of different size, shape and surface chemistry. We are currently working on PSMP staining with upconversion nanoparticles (UCNPs) and mag-

netic FeO<sub>x</sub> NPs, the latter of which could be combined with QDs to create multifunctional beads for immuno-separation applications. The use of less toxic QDs, such as Ag<sub>2</sub>S, could be a step towards imaging. The staining of the PSMPs with mixtures of NPs and dyes varying in their PL properties, such as emission color and decay kinetics, should be attempted to explore the full potential of this PSMP synthesis for NP staining.



---

# References

- [1] E. Campos et al. “Designing polymeric microparticles for biomedical and industrial applications”. In: *European Polymer Journal* 49.8 (2013), pp. 2005–2021. DOI: <https://doi.org/10.1016/j.eurpolymj.2013.04.033>.
- [2] R. Mazetyte-Stasinskiene and J. M. Köhler. “Sensor Micro and Nanoparticles for Microfluidic Application”. In: *Applied Sciences* 10.23 (2020), p. 8353. DOI: <https://doi.org/10.3390/app10238353>.
- [3] O. S. Wolfbeis. “An overview of nanoparticles commonly used in fluorescent bioimaging”. In: *Chemical Society Reviews* 44.14 (2015), pp. 4743–4768. DOI: <https://doi.org/10.1039/C4CS00392F>.
- [4] B. Pelaz et al. “Diverse Applications of Nanomedicine”. In: *ACS Nano* 11.3 (2017), pp. 2313–2381. DOI: [10.1021/acsnano.6b06040](https://doi.org/10.1021/acsnano.6b06040).
- [5] J. H. Oh, D. H. Park, J. H. Joo, and J. S. Lee. “Recent advances in chemical functionalization of nanoparticles with biomolecules for analytical applications”. In: *Analytical and Bioanalytical Chemistry* 407.29 (2015), pp. 8627–8645. DOI: [10.1007/s00216-015-8981-y](https://doi.org/10.1007/s00216-015-8981-y).
- [6] S. Kawaguchi and K. Ito. “Dispersion Polymerization”. In: *Polymer Particles*. Ed. by M. Okubo. 2005, pp. 299–328. DOI: <https://doi.org/10.1007/b100118>.
- [7] R. van Roij, M. Dijkstra, and J.-P. Hansen. “Phase diagram of charge-stabilized colloidal suspensions: van der Waals instability without attractive forces”. In: *Phys. Rev. E* 59 (2 1999), pp. 2010–2025. DOI: <https://link.aps.org/doi/10.1103/PhysRevE.59.2010>.
- [8] G. Charron et al. “On the Use of pH Titration to Quantitatively Characterize Colloidal Nanoparticles”. In: *Langmuir* 28.43 (2012), pp. 15141–15149. DOI: <https://doi.org/10.1021/la302570s>.
- [9] S. A. Kulkarni and S.-S. Feng. “Effects of Particle Size and Surface Modification on Cellular Uptake and Biodistribution of Polymeric Nanoparticles for Drug Delivery”.

- In: *Pharmaceutical Research* 30.10 (2013), pp. 2512–2522. DOI: <https://doi.org/10.1007/s11095-012-0958-3>.
- [10] P. Srivastava et al. “Multicolor Polystyrene Nanosensors for the Monitoring of Acidic, Neutral, and Basic pH Values and Cellular Uptake Studies”. In: *Analytical Chemistry* 94.27 (2022), pp. 9656–9664. DOI: <https://doi.org/10.1021/acs.analchem.2c00944>.
- [11] P. Srivastava et al. “Dual color pH probes made from silica and polystyrene nanoparticles and their performance in cell studies”. In: *Scientific Reports* 13.1 (2023), p. 1321. DOI: <https://doi.org/10.1038/s41598-023-28203-0>.
- [12] J. Goddard and J. Hotchkiss. “Polymer surface modification for the attachment of bioactive compounds”. In: *Progress in Polymer Science* 32.7 (2007), pp. 698–725. DOI: <https://doi.org/10.1016/j.progpolymsci.2007.04.002>.
- [13] C. Zhou et al. “Fluorescent QDs-polystyrene composite nanospheres for highly efficient and rapid protein antigen detection”. In: *Journal of Nanoparticle Research* 15.9 (2013), p. 1901. DOI: <https://doi.org/10.1007/s11051-013-1901-1>.
- [14] X. Yang et al. “Improving the fluorescence intensity of lanthanide-doped microspheres via incorporation of lauryl methacrylate: Synthesis and their application in C-reactive protein detection”. In: *Colloids and Surfaces A: Physicochemical and Engineering Aspects* 653 (2022), p. 130065. DOI: <https://doi.org/10.1016/j.colsurfa.2022.130065>.
- [15] K. Ming et al. “Integrated Quantum Dot Barcode Smartphone Optical Device for Wireless Multiplexed Diagnosis of Infected Patients”. In: *ACS Nano* 9.3 (2015), pp. 3060–3074. DOI: <https://doi.org/10.1021/nm5072792>.
- [16] L. Liu, W. Li, and Q. Liu. “Recent development of antifouling polymers: structure, evaluation, and biomedical applications in nano/micro-structures”. In: *WIREs Nanomedicine and Nanobiotechnology* 6.6 (2014), pp. 599–614. DOI: <https://doi.org/10.1002/wnan.1278>.
- [17] Z. Zhang, P.-C. Tsai, T. Ramezanli, and B. B. Michniak-Kohn. “Polymeric nanoparticles-based topical delivery systems for the treatment of dermatological diseases”. In: *WIREs Nanomedicine and Nanobiotechnology* 5.3 (2013), pp. 205–218. DOI: <https://doi.org/10.1002/wnan.1211>.

- 
- [18] V. Vijayan, K. R. Reddy, S. Sakthivel, and C. Swetha. “Optimization and characterization of repaglinide biodegradable polymeric nanoparticle loaded transdermal patches: In vitro and in vivo studies”. In: *Colloids and Surfaces B: Biointerfaces* 111 (2013), pp. 150–155. DOI: <https://doi.org/10.1016/j.colsurfb.2013.05.020>.
- [19] J. P. Rao and K. E. Geckeler. “Polymer nanoparticles: Preparation techniques and size-control parameters”. In: *Progress in Polymer Science* 36.7 (2011). Special Issue on Composites, pp. 887–913. DOI: <https://doi.org/10.1016/j.progpolymsci.2011.01.001>.
- [20] J. A. Champion, Y. K. Katare, and S. Mitragotri. “Making polymeric micro- and nanoparticles of complex shapes”. In: *Proceedings of the National Academy of Sciences* 104.29 (2007), pp. 11901–11904. DOI: <https://www.pnas.org/doi/abs/10.1073/pnas.0705326104>.
- [21] J. A. Champion and S. Mitragotri. “Shape Induced Inhibition of Phagocytosis of Polymer Particles”. In: *Pharmaceutical Research* 26.1 (2009), pp. 244–249. DOI: <https://doi.org/10.1007/s11095-008-9626-z>.
- [22] L. Scholtz et al. “Luminescence encoding of polymer microbeads with organic dyes and semiconductor quantum dots during polymerization”. In: *Scientific Reports* 12.1 (2022), p. 12061. DOI: <https://doi.org/10.1038/s41598-022-16065-x>.
- [23] J. Stetefeld, S. A. McKenna, and T. R. Patel. “Dynamic light scattering: a practical guide and applications in biomedical sciences”. In: *Biophysical Reviews* 8 (4 2016), pp. 409–427. DOI: <https://doi.org/10.1007/s12551-016-0218-6>.
- [24] X. Gao and S. Nie. “Quantum Dot-Encoded Mesoporous Beads with High Brightness and Uniformity: Rapid Readout Using Flow Cytometry”. In: *Analytical Chemistry* 76.8 (2004), pp. 2406–2410. DOI: <https://doi.org/10.1021/ac0354600>.
- [25] D. Kage et al. “Tempo-spectral multiplexing in flow cytometry with lifetime detection using QD-encoded polymer beads”. In: *Scientific Reports* 10.1 (2020), p. 653. DOI: <https://doi.org/10.1038/s41598-019-56938-2>.
- [26] L. Scholtz et al. “Influence of nanoparticle encapsulation and encoding on the surface chemistry of polymer carrier beads”. In: *Scientific Reports* 13.1 (2023), p. 11957. DOI: <https://doi.org/10.1038/s41598-023-38518-7>.

- [27] L. Scholtz et al. “Correlating Semiconductor Nanoparticle Architecture and Applicability for the Controlled Encoding of Luminescent Polymer Microparticles”. In: *Chemistry of Materials* (2023). submitted.
- [28] M. T. Gokmen and F. E. Du Prez. “Porous polymer particles—A comprehensive guide to synthesis, characterization, functionalization and applications”. In: *Progress in Polymer Science* 37.3 (2012). Topical Issue on Nanomaterials, pp. 365–405. DOI: <https://doi.org/10.1016/j.progpolymsci.2011.07.006>.
- [29] I. M. Huxham, L. Tetley, B. Rowatt, and D. C. Sherrington. “Comparison of porosity characteristics of macroporous poly(styrene–divinylbenzene) resins determined from mercury intrusion data and image analysis of transmission electron micrographs”. In: *J. Mater. Chem.* 4 (2 1994), pp. 253–255. DOI: <http://dx.doi.org/10.1039/JM9940400253>.
- [30] S. Podzimek. “The use of GPC coupled with a multiangle laser light scattering photometer for the characterization of polymers. On the determination of molecular weight, size and branching”. In: *Journal of Applied Polymer Science* 54.1 (1994), pp. 91–103. DOI: <https://doi.org/10.1002/app.1994.070540110>.
- [31] H. Räder and W. Schrepp. “MALDI-TOF mass spectrometry in the analysis of synthetic polymers”. In: *Acta Polymerica* 49.6 (1998), pp. 272–293. DOI: [https://doi.org/10.1002/\(SICI\)1521-4044\(199806\)49:6<272::AID-APOL272>3.0.CO;2-1](https://doi.org/10.1002/(SICI)1521-4044(199806)49:6<272::AID-APOL272>3.0.CO;2-1).
- [32] D. M. Meunier et al. “Determination of Particle Size Distributions, Molecular Weight Distributions, Swelling, Conformation, and Morphology of Dilute Suspensions of Cross-Linked Polymeric Nanoparticles via Size-Exclusion Chromatography/Differential Viscometry”. In: *Macromolecules* 47.19 (2014), pp. 6715–6729. DOI: <https://doi.org/10.1021/ma501420z>.
- [33] J. U. Izunobi and C. L. Higginbotham. “Polymer Molecular Weight Analysis by  $^1\text{H}$  NMR Spectroscopy”. In: *Journal of Chemical Education* 88.8 (2011), pp. 1098–1104. DOI: <https://doi.org/10.1021/ed100461v>.
- [34] R. Arshady. “Suspension, emulsion, and dispersion polymerization: A methodological survey”. In: *Colloid and Polymer Science* 270 (1992), pp. 717–732. DOI: <https://doi.org/10.1007/BF00776142>.

- 
- [35] M. Ramezanpour, E. Nikzad, and A. Rezaee Shirin-Abadi. “Making particle size library of polystyrene latexes prepared through surfactant-free emulsion polymerization: from nano to microns size”. In: *Journal of Polymer Research* 30 (6 2023), p. 208. DOI: <https://doi.org/10.1007/s10965-023-03582-0>.
- [36] G. Moad, E. Rizzardo, and S. H. Thang. “RAFT Polymerization and Some of its Applications”. In: *Chemistry – An Asian Journal* 8.8 (2013), pp. 1634–1644. DOI: <https://doi.org/10.1002/asia.201300262>.
- [37] J. Chiefari et al. “Living Free-Radical Polymerization by Reversible Addition-Fragmentation Chain Transfer: The RAFT Process”. In: *Macromolecules* 31.16 (1998), pp. 5559–5562. DOI: <https://doi.org/10.1021/ma9804951>.
- [38] P. A. Lovell and F. J. Schork. “Fundamentals of Emulsion Polymerization”. In: *Biomacromolecules* 21.11 (2020), pp. 4396–4441. DOI: <https://doi.org/10.1021/acs.biomac.0c00769>.
- [39] Y. Yamashita and K. Sakamoto. “Hydrophilic–Lipophilic Balance (HLB): Classical Indexation and Novel Indexation of Surfactant”. In: *Encyclopedia of Biocolloid and Biointerface Science 2V Set*. John Wiley & Sons, 2016. Chap. 45, pp. 570–574. DOI: <https://doi.org/10.1002/9781119075691.ch45>.
- [40] R. Lewarchik. The Fundamentals of Emulsion Polymerization. 2016. URL: <https://www.ulprospector.com/knowledge/4911/pc-fundamentals-emulsion-polymerization/> (visited on 06/28/2023).
- [41] W. Li, T. S. H. Leong, M. Ashokkumar, and G. J. O. Martin. “A study of the effectiveness and energy efficiency of ultrasonic emulsification”. In: *Phys. Chem. Chem. Phys.* 20 (1 2018), pp. 86–96. DOI: <http://dx.doi.org/10.1039/C7CP07133G>.
- [42] A. Sood. “Particle size distribution control in emulsion polymerization”. In: *Journal of Applied Polymer Science* 92.5 (2004), pp. 2884–2902. DOI: <https://doi.org/10.1002/app.20231>.
- [43] J. W. Vanderhoff. “Mechanism of emulsion polymerization”. In: *Journal of Polymer Science: Polymer Symposia* 72.1 (1985), pp. 161–198. DOI: <https://doi.org/10.1002/polc.5070720121>.

- [44] A. M. van Herk and K. Landfester. Hybrid latex particles: preparation with (mini) emulsion polymerization. Vol. 233. *Advances in Polymer Science*. Springer, 2010. DOI: 10.1007/978-3-642-16060-8.
- [45] V. Chaudhary and S. Sharma. “Effect of various synthesis parameters on styrene–divinylbenzene copolymer properties”. In: *Journal of Porous Materials* 26.6 (2019), pp. 1559–1571. DOI: <https://doi.org/10.1007/s10934-019-00753-7>.
- [46] W. J. Duncanson et al. “Microfluidic synthesis of advanced microparticles for encapsulation and controlled release”. In: *Lab Chip* 12 (12 2012), pp. 2135–2145. DOI: <http://dx.doi.org/10.1039/C2LC21164E>.
- [47] D. Dendukuri and P. S. Doyle. “The Synthesis and Assembly of Polymeric Microparticles Using Microfluidics”. In: *Advanced Materials* 21.41 (2009), pp. 4071–4086. DOI: <https://doi.org/10.1002/adma.200803386>.
- [48] The European Commission. Commission Recommendation of 10 June 2022 on the definition of nanomaterial. The European Commission, 2022. URL: [https://eur-lex.europa.eu/legal-content/EN/TXT/?uri=CELEX:32022H0614\(01\)](https://eur-lex.europa.eu/legal-content/EN/TXT/?uri=CELEX:32022H0614(01)).
- [49] F. J. Heiligtag and M. Niederberger. “The fascinating world of nanoparticle research”. In: *Materials Today* 16.7 (2013), pp. 262–271. DOI: <https://doi.org/10.1016/j.mattod.2013.07.004>.
- [50] W. R. Algar et al. “The Controlled Display of Biomolecules on Nanoparticles: A Challenge Suited to Bioorthogonal Chemistry”. In: *Bioconjugate Chemistry* 22.5 (2011), pp. 825–858. DOI: <https://doi.org/10.1021/bc200065z>.
- [51] H. Weller. “Colloidal Semiconductor Q-Particles: Chemistry in the Transition Region Between Solid State and Molecules”. In: *Angewandte Chemie International Edition in English* 32.1 (1993), pp. 41–53. DOI: <https://doi.org/10.1002/anie.199300411>.
- [52] D. Bimberg and U. W. Pohl. “Quantum dots: promises and accomplishments”. In: *Materials Today* 14.9 (2011), pp. 388–397. DOI: [https://doi.org/10.1016/S1369-7021\(11\)70183-3](https://doi.org/10.1016/S1369-7021(11)70183-3).
- [53] W. R. Algar, K. Susumu, J. B. Delehanty, and I. L. Medintz. “Semiconductor Quantum Dots in Bioanalysis: Crossing the Valley of Death”. In: *Analytical Chemistry* 83.23 (2011), pp. 8826–8837. DOI: <https://doi.org/10.1021/ac201331r>.

- 
- [54] E. Petryayeva, W. R. Algar, and I. L. Medintz. “Quantum Dots in Bioanalysis: A Review of Applications across Various Platforms for Fluorescence Spectroscopy and Imaging”. In: *Applied Spectroscopy* 67.3 (2013), pp. 215–252. DOI: <https://doi.org/10.1366/12-06948>.
- [55] H. Born. “Rekombination und Relaxation in nulldimensionalen Strukturen”. PhD thesis. Technische Universität Berlin, 2003. URL: [https://depositonce.tu-berlin.de/bitstream/11303/978/1/Dokument\\_38.pdf](https://depositonce.tu-berlin.de/bitstream/11303/978/1/Dokument_38.pdf).
- [56] C. Pu and X. Peng. “To Battle Surface Traps on CdSe/CdS Core/Shell Nanocrystals: Shell Isolation versus Surface Treatment”. In: *Journal of the American Chemical Society* 138.26 (2016), pp. 8134–8142. DOI: <https://doi.org/10.1021/jacs.6b02909>.
- [57] W. R. Algar, A. J. Tavares, and U. J. Krull. “Beyond labels: A review of the application of quantum dots as integrated components of assays, bioprobes, and biosensors utilizing optical transduction”. In: *Analytica Chimica Acta* 673.1 (2010), pp. 1–25. DOI: <https://doi.org/10.1016/j.aca.2010.05.026>.
- [58] U. Resch-Genger, M. Grabolle, S. Cavaliere-Jaricot, R. Nitschke, and T. Nann. “Quantum dots versus organic dyes as fluorescent labels”. In: *Nature Methods* 5.9 (2008), pp. 763–775. DOI: <https://doi.org/10.1038/nmeth.1248>.
- [59] E. Petryayeva, W. R. Algar, and I. L. Medintz. “Quantum Dots in Bioanalysis: A Review of Applications Across Various Platforms for Fluorescence Spectroscopy and Imaging”. In: *Applied Spectroscopy* 67.3 (2013), pp. 215–252. DOI: <https://doi.org/10.1366/12-06948>.
- [60] W. M. Girma, M. Z. Fahmi, A. Permadi, M. A. Abate, and J.-Y. Chang. “Synthetic strategies and biomedical applications of I–III–VI ternary quantum dots”. In: *J. Mater. Chem. B* 5 (31 2017), pp. 6193–6216. DOI: <http://dx.doi.org/10.1039/C7TB01156C>.
- [61] M. E. Khan, A. Mohammad, and T. Yoon. “State-of-the-art developments in carbon quantum dots (CQDs): Photo-catalysis, bio-imaging, and bio-sensing applications”. In: *Chemosphere* 302 (2022), p. 134815. DOI: <https://doi.org/10.1016/j.chemosphere.2022.134815>.
- [62] L. Yang et al. “I–III–VI Quantum Dots and Derivatives: Design, Synthesis, and Properties for Light-Emitting Diodes”. In: *Nano Letters* 23.7 (2023), pp. 2443–2453. DOI: <https://doi.org/10.1021/acs.nanolett.2c03138>.

- [63] M. V. Kovalenko. “Opportunities and challenges for quantum dot photovoltaics”. In: *Nature Nanotechnology* 10 (12 2015), pp. 994–997. DOI: <https://doi.org/10.1038/nnano.2015.284>.
- [64] J. A. Caputo et al. “General and Efficient C–C Bond Forming Photoredox Catalysis with Semiconductor Quantum Dots”. In: *Journal of the American Chemical Society* 139.12 (2017), pp. 4250–4253. DOI: <https://doi.org/10.1021/jacs.6b13379>.
- [65] B. Chen, D. Li, and F. Wang. “InP Quantum Dots: Synthesis and Lighting Applications”. In: *Small* 16.32 (2020), p. 2002454. DOI: <https://doi.org/10.1002/sml1.202002454>.
- [66] S. I. Sadovnikov and A. I. Gusev. “Recent progress in nanostructured silver sulfide: from synthesis and nonstoichiometry to properties”. In: *J. Mater. Chem. A* 5 (34 2017), pp. 17676–17704. DOI: <http://dx.doi.org/10.1039/C7TA04949H>.
- [67] Y. Hu et al. “Polarity, intramolecular charge transfer, and hydrogen bond co-mediated solvent effects on the optical properties of graphene quantum dots”. In: *Nano Research* 16 (1 2023), pp. 45–52. DOI: <https://doi.org/10.1007/s12274-022-4752-1>.
- [68] K. Dohnalová, T. Gregorkiewicz, and K. Kůsová. “Silicon quantum dots: surface matters”. In: *Journal of Physics: Condensed Matter* 26.17 (2014), p. 173201. DOI: <https://dx.doi.org/10.1088/0953-8984/26/17/173201>.
- [69] D. Mo et al. “Cadmium-containing quantum dots: properties, applications, and toxicity”. In: *Applied Microbiology and Biotechnology* 101 (7 2017), pp. 2713–2733. DOI: <https://doi.org/10.1016/j.chemosphere.2022.134815>.
- [70] H. Zhu, N. Song, W. Rodríguez-Córdoba, and T. Lian. “Wave Function Engineering for Efficient Extraction of up to Nineteen Electrons from One CdSe/CdS Quasi-Type II Quantum Dot”. In: *Journal of the American Chemical Society* 134.9 (2012), pp. 4250–4257. DOI: <https://doi.org/10.1021/ja210312s>.
- [71] K. Agarwal, H. Rai, and S. Mondal. “Quantum dots: an overview of synthesis, properties, and applications”. In: *Materials Research Express* 10.6 (2023), p. 062001. DOI: <https://doi.org/10.1088/2053-1591/acda17>.
- [72] W. Zhou and J. J. Coleman. “Semiconductor quantum dots”. In: *Current Opinion in Solid State and Materials Science* 20.6 (2016), pp. 352–360. DOI: <https://doi.org/10.1016/j.cossms.2016.06.006>.

- 
- [73] C. B. Murray, D. J. Norris, and M. G. Bawendi. “Synthesis and characterization of nearly monodisperse CdE (E= sulfur, selenium, tellurium) semiconductor nanocrystallites”. In: *Journal of the American Chemical Society* 115.19 (1993), pp. 8706–8715. DOI: <https://doi.org/10.1021/ja00072a025>.
- [74] C. de Mello Donegá, P. Liljeroth, and D. Vanmaekelbergh. “Physicochemical Evaluation of the Hot-Injection Method, a Synthesis Route for Monodisperse Nanocrystals”. In: *Small* 1.12 (2005), pp. 1152–1162. DOI: <https://doi.org/10.1002/sml1.200500239>.
- [75] J. J. Li et al. “Large-Scale Synthesis of Nearly Monodisperse CdSe/CdS Core/Shell Nanocrystals Using Air-Stable Reagents via Successive Ion Layer Adsorption and Reaction”. In: *Journal of the American Chemical Society* 125.41 (2003), pp. 12567–12575. DOI: [10.1021/ja0363563](https://doi.org/10.1021/ja0363563).
- [76] O. Chen et al. “Compact high-quality CdSe-CdS core-shell nanocrystals with narrow emission linewidths and suppressed blinking”. In: *Nature Materials* 12.5 (2013), pp. 445–451. DOI: <https://doi.org/10.1038/nmat3539>.
- [77] R. Singh, S. Akhil, V. G. V. Dutt, and N. Mishra. “Study of Shell Thickness-Dependent Charge Transfer Dynamics in Green-Emitting Core/Shell Giant Quantum Dots”. In: *Inorganic Chemistry* 61.2 (2022), pp. 1059–1066. DOI: <https://doi.org/10.1021/acs.inorgchem.1c03185>.
- [78] B. M. I. van der Zande, M. R. Böhmer, L. G. J. Fokkink, and C. Schönenberger. “Aqueous Gold Sols of Rod-Shaped Particles”. In: *The Journal of Physical Chemistry B* 101.6 (1997), pp. 852–854. DOI: <https://doi.org/10.1021/jp963348i>.
- [79] L. Carbone et al. “Synthesis and Micrometer-Scale Assembly of Colloidal CdSe/CdS Nanorods Prepared by a Seeded Growth Approach”. In: *Nano Letters* 7.10 (2007), pp. 2942–2950. DOI: <https://doi.org/10.1021/nl0717661>.
- [80] A. Sitt, I. Hadar, and U. Banin. “Band-gap engineering, optoelectronic properties and applications of colloidal heterostructured semiconductor nanorods”. In: *Nano Today* 8.5 (2013), pp. 494–513. DOI: <https://doi.org/10.1016/j.nantod.2013.08.002>.
- [81] S. Ithurria and B. Dubertret. “Quasi 2D Colloidal CdSe Platelets with Thicknesses Controlled at the Atomic Level”. In: *Journal of the American Chemical Society* 130.49 (2008), pp. 16504–16505. DOI: <https://doi.org/10.1021/ja807724e>.

- [82] S. Ithurria, G. Bousquet, and B. Dubertret. “Continuous Transition from 3D to 1D Confinement Observed during the Formation of CdSe Nanoplatelets”. In: *Journal of the American Chemical Society* 133.9 (2011), pp. 3070–3077. DOI: <https://doi.org/10.1021/ja110046d>.
- [83] M. D. Tessier et al. “Efficient Exciton Concentrators Built from Colloidal Core/Crown CdSe/CdS Semiconductor Nanoplatelets”. In: *Nano Letters* 14.1 (2014), pp. 207–213. DOI: <https://doi.org/10.1021/nl403746p>.
- [84] A. A. Rossinelli et al. “High-temperature growth of thick-shell CdSe/CdS core/shell nanoplatelets”. In: *Chem. Commun.* 53 (71 2017), pp. 9938–9941. DOI: <http://dx.doi.org/10.1039/C7CC04503D>.
- [85] N. Petersen, M. Girard, A. Riedinger, and O. Valsson. “The Crucial Role of Solvation Forces in the Steric Stabilization of Nanoplatelets”. In: *Nano Letters* 22.24 (2022), pp. 9847–9853. DOI: <https://doi.org/10.1021/acs.nanolett.2c02848>.
- [86] R. T. Graf et al. “Interparticle Distance Variation in Semiconductor Nanoplatelet Stacks”. In: *Advanced Functional Materials* 32.24 (2022), p. 2112621. DOI: <https://doi.org/10.1002/adfm.202112621>.
- [87] D. Kage, K. Hoffmann, H. Borchering, U. Schedler, and U. Resch-Genger. “Lifetime encoding in flow cytometry for bead-based sensing of biomolecular interaction”. In: *Scientific Reports* 10.1 (2020), p. 19477. DOI: <https://doi.org/10.1038/s41598-020-76150-x>.
- [88] Z. Li, Q. Liu, Y. Li, W. Yuan, and F. Y. Li. “One-step polymerized lanthanide-based polystyrene microsphere for sensitive lateral flow immunoassay”. In: *Journal of Rare Earths* 39.1 (2021), pp. 11–18. DOI: <https://doi.org/10.1016/j.jre.2020.06.020>.
- [89] S. Shikha, T. Salafi, J. Cheng, and Y. Zhang. “Versatile design and synthesis of nano-barcode”. In: *Chem. Soc. Rev.* 46 (22 2017), pp. 7054–7093. DOI: <http://dx.doi.org/10.1039/C7CS00271H>.
- [90] K. A. White et al. “Near-Infrared Luminescent Lanthanide MOF Barcodes”. In: *Journal of the American Chemical Society* 131.50 (2009), pp. 18069–18071. DOI: <https://doi.org/10.1021/ja907885m>.

- 
- [91] G. Wang et al. “Highly Efficient Preparation of Multiscaled Quantum Dot Barcodes for Multiplexed Hepatitis B Detection”. In: *ACS Nano* 7.1 (2013), pp. 471–481. DOI: <https://doi.org/10.1021/nn3045215>.
- [92] Y. Leng et al. “Magnetic/Fluorescent Barcodes Based on Cadmium-Free Near-Infrared-Emitting Quantum Dots for Multiplexed Detection”. In: *Advanced Functional Materials* 26.42 (2016), pp. 7581–7589. DOI: <https://doi.org/10.1002/adfm.201602900>.
- [93] M. Bradley, N. Bruno, and B. Vincent. “Distribution of CdSe Quantum Dots within Swollen Polystyrene Microgel Particles Using Confocal Microscopy”. In: *Langmuir* 21.7 (2005), pp. 2750–2753. DOI: <https://doi.org/10.1021/la047322r>.
- [94] S. P. Mulvaney, H. Mattoussi, and L. J. Whitman. “Incorporating fluorescent dyes and quantum dots into magnetic microbeads for immunoassays”. In: *BioTechniques* 36.4 (2004), pp. 602–609. DOI: <https://doi.org/10.2144/04364BI01>.
- [95] I. V. Martynenko et al. “Magneto-Fluorescent Microbeads for Bacteria Detection Constructed from Superparamagnetic Fe<sub>3</sub>O<sub>4</sub> Nanoparticles and AIS/ZnS Quantum Dots”. In: *Analytical Chemistry* 91.20 (2019), pp. 12661–12669. DOI: <https://doi.org/10.1021/acs.analchem.9b01812>.
- [96] S. L. Sonawane and S. K. Asha. “Fluorescent Polystyrene Microbeads as Invisible Security Ink and Optical Vapor Sensor for 4-Nitrotoluene”. In: *ACS Applied Materials & Interfaces* 8.16 (2016), pp. 10590–10599. DOI: <https://doi.org/10.1021/acsami.5b12325>.
- [97] F. Kimura et al. “Dual luminophore polystyrene microspheres for pressure-sensitive luminescent imaging”. In: *Measurement Science and Technology* 17.6 (2006), p. 1254. DOI: <https://dx.doi.org/10.1088/0957-0233/17/6/S04>.
- [98] X. Wang, S. Xu, and W. Xu. “Luminescent properties of dye-PMMA composite nanospheres”. In: *Phys. Chem. Chem. Phys.* 13 (4 2011), pp. 1560–1567. DOI: <http://dx.doi.org/10.1039/C0CP00929F>.
- [99] X. Zhang et al. “Fabrication of aggregation induced emission dye-based fluorescent organic nanoparticles via emulsion polymerization and their cell imaging applications”. In: *Polym. Chem.* 5 (2 2014), pp. 399–404. DOI: <http://dx.doi.org/10.1039/C3PY00984J>.

- [100] J. Chen et al. "Design and Synthesis of FRET-Mediated Multicolor and Photoswitchable Fluorescent Polymer Nanoparticles with Tunable Emission Properties". In: *The Journal of Physical Chemistry B* 116.14 (2012), pp. 4354–4362. DOI: <https://doi.org/10.1021/jp2110659>.
- [101] Yang and Y. Zhang. "Encapsulation of Quantum Nanodots in Polystyrene and Silica Micro-/Nanoparticles". In: *Langmuir* 20.14 (2004), pp. 6071–6073. DOI: <https://doi.org/10.1021/la049610t>.
- [102] P. O'Brien et al. "Quantum dot-labelled polymer beads by suspension polymerisation". In: *Chem. Commun.* (20 2003), pp. 2532–2533. DOI: <http://dx.doi.org/10.1039/B307500A>.
- [103] A. C. C. Esteves, A. Barros-Timmons, T. Monteiro, and T. Trindade. "Polymer Encapsulation of CdE (E = S, Se) Quantum Dot Ensembles via In-Situ Radical Polymerization in Miniemulsion". In: *Journal of Nanoscience and Nanotechnology* 5.5 (2005), pp. 766–771. DOI: <https://doi.org/10.1166/jnn.2005.090>.
- [104] Y. Li et al. "Synthesis and characterization of CdS quantum dots in polystyrene microbeads". In: *J. Mater. Chem.* 15 (12 2005), pp. 1238–1243. DOI: <http://dx.doi.org/10.1039/B412317D>.
- [105] Y. Yang, Z. Wen, Y. Dong, and M. Gao. "Incorporating CdTe Nanocrystals into Polystyrene Microspheres: Towards Robust Fluorescent Beads". In: *Small* 2.7 (2006), pp. 898–901. DOI: <https://doi.org/10.1002/sml1.200600086>.
- [106] Y. Yang, C. Tu, and M. Gao. "A general approach for encapsulating aqueous colloidal particles into polymeric microbeads". In: *J. Mater. Chem.* 17 (28 2007), pp. 2930–2935. DOI: <http://dx.doi.org/10.1039/B703060F>.
- [107] C. Tu, Y. Yang, and M. Gao. "Preparations of bifunctional polymeric beads simultaneously incorporated with fluorescent quantum dots and magnetic nanocrystals". In: *Nanotechnology* 19.10 (2008), p. 105601. DOI: <https://dx.doi.org/10.1088/0957-4484/19/10/105601>.
- [108] S. V. Vaidya, A. Couzis, and C. Maldarelli. "Reduction in Aggregation and Energy Transfer of Quantum Dots Incorporated in Polystyrene Beads by Kinetic Entrapment due to Cross-Linking during Polymerization". In: *Langmuir* 31.10 (2015), pp. 3167–3179. DOI: <https://doi.org/10.1021/la503251s>.

- 
- [109] D. Kage et al. “Close Spectroscopic Look at Dye-Stained Polymer Microbeads”. In: *The Journal of Physical Chemistry C* 122.24 (2018), pp. 12782–12791. DOI: <https://doi.org/10.1021/acs.jpcc.8b02546>.
- [110] W. Sheng et al. “In-Situ Encapsulation of Quantum Dots into Polymer Microspheres”. In: *Langmuir* 22.8 (2006), pp. 3782–3790. DOI: <https://doi.org/10.1021/la051973l>.
- [111] N. Joumaa et al. “Synthesis of Quantum Dot-Tagged Submicrometer Polystyrene Particles by Miniemulsion Polymerization”. In: *Langmuir* 22.4 (2006), pp. 1810–1816. DOI: <https://doi.org/10.1021/la052197k>.
- [112] R. L. Sherman and W. T. Ford. “Semiconductor Nanoparticle/Polystyrene Latex Composite Materials”. In: *Langmuir* 21.11 (2005), pp. 5218–5222. DOI: <https://doi.org/10.1021/la0468139>.
- [113] F. Fleischhaker and R. Zentel. “Photonic Crystals from Core-Shell Colloids with Incorporated Highly Fluorescent Quantum Dots”. In: *Chemistry of Materials* 17.6 (2005), pp. 1346–1351. DOI: <https://doi.org/10.1021/cm0481022>.
- [114] A. Rubio-Ríos et al. “Effect of synthesis variables on the fluorescence properties of CdSe-polystyrene latexes”. In: *Journal of Polymer Research* 19.3 (2012), p. 9833. DOI: <https://doi.org/10.1007/s10965-012-9833-5>.
- [115] H. Zhang et al. “Fluorescent Nanocrystal-Polymer Composites from Aqueous Nanocrystals: Methods without Ligand Exchange”. In: *Chemistry of Materials* 17.19 (2005), pp. 4783–4788. DOI: <https://doi.org/10.1021/cm0502601>.
- [116] X. Yu, G. Cheng, M.-D. Zhou, and S.-Y. Zheng. “On-Demand One-Step Synthesis of Monodisperse Functional Polymeric Microspheres with Droplet Microfluidics”. In: *Langmuir* 31.13 (2015), pp. 3982–3992. DOI: <https://doi.org/10.1021/acs.langmuir.5b00617>.
- [117] J. S. Kim et al. “In vivo NIR imaging with CdTe/CdSe quantum dots entrapped in PLGA nanospheres”. In: *Journal of Colloid and Interface Science* 353.2 (2011), pp. 363–371. DOI: <https://doi.org/10.1016/j.jcis.2010.08.053>.
- [118] W. Yin et al. “Fluorescent Quantum Dot-Polymer Nanocomposite Particles by Emulsification/Solvent Evaporation”. In: *Chemistry of Materials* 19.12 (2007), pp. 2930–2936. DOI: <https://doi.org/10.1021/cm070214g>.

- [119] M. M. Abdel-Mottaleb, A. Beduneau, Y. Pellequer, and A. Lamprecht. “Stability of fluorescent labels in PLGA polymeric nanoparticles: Quantum dots versus organic dyes”. In: *International Journal of Pharmaceutics* 494.1 (2015), pp. 471–478. DOI: <https://doi.org/10.1016/j.ijpharm.2015.08.050>.
- [120] M. Bradley, N. Bruno, and B. Vincent. “Distribution of CdSe Quantum Dots within Swollen Polystyrene Microgel Particles Using Confocal Microscopy”. In: *Langmuir* 21.7 (2005), pp. 2750–2753. DOI: <https://doi.org/10.1021/la047322r>.
- [121] F. Bian, H. Wang, L. Sun, Y. Liu, and Y. Zhao. “Quantum-dot-encapsulated core-shell barcode particles from droplet microfluidics”. In: *J. Mater. Chem. B* 6 (44 2018), pp. 7257–7262. DOI: <http://dx.doi.org/10.1039/C8TB00946E>.
- [122] Y. Chen, P.-F. Dong, J.-H. Xu, and G.-S. Luo. “Microfluidic Generation of Multicolor Quantum-Dot-Encoded Core-Shell Microparticles with Precise Coding and Enhanced Stability”. In: *Langmuir* 30.28 (2014), pp. 8538–8542. DOI: <https://doi.org/10.1021/la501692h>.
- [123] Y. Zhao et al. “Microfluidic Generation of Multifunctional Quantum Dot Barcode Particles”. In: *Journal of the American Chemical Society* 133.23 (2011), pp. 8790–8793. DOI: <https://doi.org/10.1021/ja200729w>.
- [124] Y. Zhao et al. “Microfluidic Synthesis of Barcode Particles for Multiplex Assays”. In: *Small* 11.2 (2015), pp. 151–174. DOI: <https://doi.org/10.1002/smll.201401600>.
- [125] H. Liu et al. “Microfluidic synthesis of QD-encoded PEGDA microspheres for suspension assay”. In: *J. Mater. Chem. B* 4 (3 2016), pp. 482–488. DOI: <http://dx.doi.org/10.1039/C5TB02209F>.
- [126] A. Riedinger et al. “An intrinsic growth instability in isotropic materials leads to quasi-two-dimensional nanoplatelets”. In: *Nature Materials* 16 (7 2017), pp. 743–748. DOI: <https://doi.org/10.1038/nmat4889>.
- [127] T. Behnke et al. “Encapsulation of Hydrophobic Dyes in Polystyrene Micro- and Nanoparticles via Swelling Procedures”. In: *Journal of Fluorescence* 21 (3 2011), pp. 937–944. DOI: <https://doi.org/10.1007/s10895-010-0632-2>.
- [128] M. Han, X. Gao, J. Z. Su, and S. Nie. “Quantum-dot-tagged microbeads for multiplexed optical coding of biomolecules”. In: *Nature Biotechnology* 19.7 (2001), pp. 631–635. DOI: <https://doi.org/10.1038/90228>.

- 
- [129] T.-H. Chung and W.-C. Lee. “Preparation of styrene-based, magnetic polymer microspheres by a swelling and penetration process”. In: *Reactive and Functional Polymers* 68.10 (2008), pp. 1441–1447. DOI: <https://doi.org/10.1016/j.reactfunctpolym.2008.07.003>.
- [130] M. Han, X. Gao, J. Z. Su, and S. Nie. “Quantum-dot-tagged microbeads for multiplexed optical coding of biomolecules”. In: *Nature Biotechnology* 19.7 (2001), pp. 631–635. DOI: <https://doi.org/10.1038/90228>.
- [131] G. B. Sukhorukov et al. “Layer-by-layer self assembly of polyelectrolytes on colloidal particles”. In: *Colloids and Surfaces A: Physicochemical and Engineering Aspects* 137.1 (1998), pp. 253–266. DOI: [https://doi.org/10.1016/S0927-7757\(98\)00213-1](https://doi.org/10.1016/S0927-7757(98)00213-1).
- [132] A. Rogach et al. “Nano- and Microengineering: 3-D Colloidal Photonic Crystals Prepared from Sub- $\mu\text{m}$ -sized Polystyrene Latex Spheres Pre-Coated with Luminescent Polyelectrolyte/Nanocrystal Shells”. In: *Advanced Materials* 12.5 (2000), pp. 333–337. DOI: [https://doi.org/10.1002/\(SICI\)1521-4095\(200003\)12:5<333::AID-ADMA333>3.0.CO;2-X](https://doi.org/10.1002/(SICI)1521-4095(200003)12:5<333::AID-ADMA333>3.0.CO;2-X).
- [133] A. Sukhanova et al. “Nanocrystal-Encoded Fluorescent Microbeads for Proteomics: Antibody Profiling and Diagnostics of Autoimmune Diseases”. In: *Nano Letters* 7.8 (2007), pp. 2322–2327. DOI: <https://doi.org/10.1021/nl070966+>.
- [134] Y. Yan, M. Björnalm, and F. Caruso. “Assembly of Layer-by-Layer Particles and Their Interactions with Biological Systems”. In: *Chemistry of Materials* 26.1 (2014), pp. 452–460. DOI: <https://doi.org/10.1021/cm402126n>.
- [135] Q. Wang, Y. Liu, C. Lin, and H. Yan. “Layer-by-layer growth of superparamagnetic, fluorescent barcode nanospheres”. In: *Nanotechnology* 18.40 (2007), p. 405604. DOI: <https://dx.doi.org/10.1088/0957-4484/18/40/405604>.
- [136] N. R. Visaveliya and J. M. Köhler. “Softness Meets with Brightness: Dye-Doped Multifunctional Fluorescent Polymer Particles via Microfluidics for Labeling”. In: *Advanced Optical Materials* 9.13 (2021), p. 2002219. DOI: <https://doi.org/10.1002/adom.202002219>.
- [137] M. C. Mancini, B. A. Kairdolf, A. M. Smith, and S. Nie. “Oxidative Quenching and Degradation of Polymer-Encapsulated Quantum Dots: New Insights into the Long-

- Term Fate and Toxicity of Nanocrystals in Vivo”. In: *Journal of the American Chemical Society* 130.33 (2008), pp. 10836–10837. DOI: <https://doi.org/10.1021/ja8040477>.
- [138] C.-T. Kuo et al. “Optically Encoded Semiconducting Polymer Dots with Single-Wavelength Excitation for Barcoding and Tracking of Single Cells”. In: *Analytical Chemistry* 89.11 (2017), pp. 6232–6238. DOI: <https://doi.org/10.1021/acs.analchem.7b01214>.
- [139] A. A. Saei et al. “Nanoparticle Surface Functionality Dictates Cellular and Systemic Toxicity”. In: *Chemistry of Materials* 29.16 (2017), pp. 6578–6595. DOI: <https://doi.org/10.1021/acs.chemmater.7b01979>.
- [140] G. Sun et al. “Facile, Efficient Approach to Accomplish Tunable Chemistries and Variable Biodistributions for Shell Cross-Linked Nanoparticles”. In: *Biomacromolecules* 9.7 (2008), pp. 1997–2006. DOI: <https://doi.org/10.1021/bm800246x>.
- [141] K.-i. Fukukawa et al. “Synthesis and Characterization of Core–Shell Star Copolymers for In Vivo PET Imaging Applications”. In: *Biomacromolecules* 9.4 (2008), pp. 1329–1339. DOI: <https://doi.org/10.1021/bm7014152>.
- [142] N. Nirmalananthan-Budau. “Synthesis, Characterization and Surface Group Quantification of Functionalized Polymer Particles for Signal Amplification Strategies”. Dissertation. 2019. URL: <http://dx.doi.org/10.17169/refubium-26041>.
- [143] T. Xia et al. “Comparison of the Abilities of Ambient and Manufactured Nanoparticles To Induce Cellular Toxicity According to an Oxidative Stress Paradigm”. In: *Nano Letters* 6.8 (2006), pp. 1794–1807. DOI: <https://doi.org/10.1021/nl061025k>.
- [144] E. Fröhlich. “The role of surface charge in cellular uptake and cytotoxicity of medical nanoparticles”. In: *International Journal of Nanomedicine* 7 (2012), pp. 5577–5591. DOI: 10.2147/IJN.S36111.
- [145] W. R. Algar et al. “The Controlled Display of Biomolecules on Nanoparticles: A Challenge Suited to Bioorthogonal Chemistry”. In: *Bioconjugate Chemistry* 22.5 (2011), pp. 825–858. DOI: <https://doi.org/10.1021/bc200065z>.
- [146] P. D. Quevedo, T. Behnke, and U. Resch-Genger. “Streptavidin conjugation and quantification—a method evaluation for nanoparticles”. In: *Analytical and Bioanalytical Chemistry* 408.15 (2016), pp. 4133–4149. DOI: <https://doi.org/10.1007/s00216-016-9510-3>.

- [147] V. B. Ivanov, J. Behnisch, A. Holländer, F. Mehdorn, and H. Zimmermann. “Determination of Functional Groups on Polymer Surfaces Using Fluorescence Labelling”. In: *Surface and Interface Analysis* 24.4 (1996), pp. 257–262. DOI: [https://doi.org/10.1002/\(SICI\)1096-9918\(199604\)24:4<257::AID-SIA107>3.0.CO;2-1](https://doi.org/10.1002/(SICI)1096-9918(199604)24:4<257::AID-SIA107>3.0.CO;2-1).
- [148] M. R. Lockett, M. F. Phillips, J. L. Jarecki, D. Peelen, and L. M. Smith. “A Tetrafluorophenyl Activated Ester Self-Assembled Monolayer for the Immobilization of Amine-Modified Oligonucleotides”. In: *Langmuir* 24.1 (2008), pp. 69–75. DOI: <https://doi.org/10.1021/1a702493u>.
- [149] E. Valeur and M. Bradley. “Amide bond formation: beyond the myth of coupling reagents”. In: *Chem. Soc. Rev.* 38 (2 2009), pp. 606–631. DOI: <http://dx.doi.org/10.1039/B701677H>.
- [150] K. E. Sapsford et al. “Functionalizing Nanoparticles with Biological Molecules: Developing Chemistries that Facilitate Nanotechnology”. In: *Chemical Reviews* 113.3 (2013), pp. 1904–2074. DOI: <https://doi.org/10.1021/cr300143v>.
- [151] T. Felbeck, K. Hoffmann, M. M. Lezhnina, U. H. Kynast, and U. Resch-Genger. “Fluorescent Nanoclays: Covalent Functionalization with Amine Reactive Dyes from Different Fluorophore Classes and Surface Group Quantification”. In: *The Journal of Physical Chemistry C* 119.23 (2015), pp. 12978–12987. DOI: <https://doi.org/10.1021/acs.jpcc.5b01482>.
- [152] M. Moser et al. “Quantification of PEG-Maleimide Ligands and Coupling Efficiencies on Nanoparticles with Ellman’s Reagent”. In: *Analytical Chemistry* 87.18 (2015), pp. 9376–9383. DOI: <https://doi.org/10.1021/acs.analchem.5b02173>.
- [153] G. M. Whitesides, J. E. Lilburn, and R. P. Szajewski. “Rates of thiol-disulfide interchange reactions between mono- and dithiols and Ellman’s reagent”. In: *The Journal of Organic Chemistry* 42.2 (1977), pp. 332–338. DOI: <https://doi.org/10.1021/jo00422a034>.
- [154] K. R. West and S. Otto. “Reversible Covalent Chemistry in Drug Delivery”. In: *Current Drug Discovery Technologies* 2.3 (2005), pp. 123–160. DOI: <https://doi.org/10.2174/1570163054866882>.

- [155] I. S. Carrico, B. L. Carlson, and C. R. Bertozzi. “Introducing genetically encoded aldehydes into proteins”. In: *Nature Chemical Biology* 3.6 (2007), pp. 321–322. DOI: [doi:10.2174/1570163054866882](https://doi.org/10.2174/1570163054866882).
- [156] A. Dirksen and P. E. Dawson. “Rapid Oxime and Hydrazone Ligations with Aromatic Aldehydes for Biomolecular Labeling”. In: *Bioconjugate Chemistry* 19.12 (2008), pp. 2543–2548. DOI: <https://doi.org/10.1021/bc800310p>.
- [157] M. Albuszis, P. J. Roth, W. Pauer, and H.-U. Moritz. “Two in one: use of azide functionality for controlled photo-crosslinking and click-modification of polymer microspheres”. In: *Polym. Chem.* 7 (34 2016), pp. 5414–5425. DOI: <http://dx.doi.org/10.1039/C6PY00937A>.
- [158] L. Carbone et al. “Synthesis and Micrometer-Scale Assembly of Colloidal CdSe/CdS Nanorods Prepared by a Seeded Growth Approach”. In: *Nano Letters* 7.10 (2007), pp. 2942–2950. DOI: [10.1021/nl0717661](https://doi.org/10.1021/nl0717661).
- [159] A. M. Nightingale et al. “Large-scale synthesis of nanocrystals in a multichannel droplet reactor”. In: *J. Mater. Chem. A* 1 (12 2013), pp. 4067–4076. DOI: [10.1039/C3TA10458C](https://doi.org/10.1039/C3TA10458C).
- [160] A. Einstein. “Über die von der molekularkinetischen Theorie der Wärme geforderte Bewegung von in ruhenden Flüssigkeiten suspendierten Teilchen”. In: *Annalen der Physik* 322.8 (1905), pp. 549–560. DOI: <https://doi.org/10.1002/andp.19053220806>.
- [161] M. von Smoluchowski. “Zur kinetischen Theorie der Brownschen Molekularbewegung und der Suspensionen”. In: *Annalen der Physik* 326.14 (1906), pp. 756–780. DOI: <https://doi.org/10.1002/andp.19063261405>.
- [162] D. J. Stokes. Principles and practice of variable pressure/environmental scanning electron microscopy (VP-ESEM). 1st ed. ISBN: 978-0-470-06540-2. John Wiley & Sons, 2008.
- [163] R. F. Egerton. Physical principles of electron microscopy. 1st ed. Vol. 56. Springer, 2005. DOI: <https://doi.org/10.1007/978-3-319-39877-8>.
- [164] J. C. H. Spence. High-resolution electron microscopy. 4th ed. OUP Oxford, 2013. DOI: <https://doi.org/10.1093/acprof:oso/9780199668632.001.0001>.
- [165] N. Tanaka. “Present status and future prospects of spherical aberration corrected TEM/STEM for study of nanomaterials\*”. In: *Sci Technol Adv Mater* 9 (1 2008), p. 014111. DOI: <https://doi.org/10.1088%2F1468-6996%2F9%2F1%2F014111>.

- 
- [166] M. T. Otten. “High-Angle annular dark-field imaging on a tem/stem system”. In: *Journal of Electron Microscopy Technique* 17.2 (1991), pp. 221–230. DOI: <https://doi.org/10.1002/jemt.1060170209>.
- [167] J. B. Pawley. Handbook of biological confocal microscopy. 3rd ed. Vol. 236. Springer Science & Business Media, 2006. DOI: <https://doi.org/10.1007/978-0-387-45524-2>.
- [168] G. Cox. Optical imaging techniques in cell biology. 1st ed. CRC Press, 2006, pp. 57–75. DOI: <https://doi.org/10.1201/9781420005615>.
- [169] W. Schmidt. Optische Spektroskopie: Eine Einführung. 2nd ed. ISBN: 978-3-527-29828-0. John Wiley & Sons, 2000.
- [170] D. J. Dahm and K. D. Dahm. Interpreting Diffuse Reflectance and Transmittance: A Theoretical Introduction to Absorption Spectroscopy of Scattering Materials. 1st ed. NIR Publications, 2007. DOI: 10.1255/978-1-901019-05-6.
- [171] B. Valeur and M. N. Berberan-Santos. Molecular fluorescence: principles and applications. 2nd ed. ISBN: 978-3-527-32837-6. John Wiley & Sons, 2012.
- [172] “Introduction to Fluorescence”. In: *Principles of Fluorescence Spectroscopy*. Ed. by J. R. Lakowicz. Springer US, 2006, pp. 1–26. DOI: [https://doi.org/10.1007/978-0-387-46312-4\\_2](https://doi.org/10.1007/978-0-387-46312-4_2).
- [173] C. Würth, M. Grabolle, J. Pauli, M. Spieles, and U. Resch-Genger. “Comparison of Methods and Achievable Uncertainties for the Relative and Absolute Measurement of Photoluminescence Quantum Yields”. In: *Analytical Chemistry* 83.9 (2011), pp. 3431–3439. DOI: <https://doi.org/10.1021/ac2000303>.
- [174] “Instrumentation for Fluorescence Spectroscopy”. In: *Principles of Fluorescence Spectroscopy*. Ed. by J. R. Lakowicz. Springer US, 2006, pp. 27–61. DOI: [https://doi.org/10.1007/978-0-387-46312-4\\_2](https://doi.org/10.1007/978-0-387-46312-4_2).
- [175] A. Sillen and Y. Engelborghs. “The Correct Use of “Average” Fluorescence Parameters”. In: *Photochemistry and Photobiology* 67.5 (1998), pp. 475–486. DOI: <https://doi.org/10.1111/j.1751-1097.1998.tb09082.x>.
- [176] J. Keeler. Understanding NMR spectroscopy. 2nd ed. ISBN: 978-0-470-74608-0. John Wiley & Sons, 2010.

- [177] C. P. Slichter. Principles of magnetic resonance. 3rd ed. Springer Science & Business Media, 1990. DOI: <https://doi.org/10.1007/978-3-662-09441-9>.
- [178] B. Welz and M. Sperling. Atomabsorptionsspektrometrie. 4th ed. John Wiley & Sons, 2012. DOI: [10.1002/3527603204](https://doi.org/10.1002/3527603204).
- [179] A. Walsh. “The application of atomic absorption spectra to chemical analysis”. In: *Spectrochimica Acta* 7 (1955), pp. 108–117. DOI: [https://doi.org/10.1016/0371-1951\(55\)80013-6](https://doi.org/10.1016/0371-1951(55)80013-6).
- [180] S. R. Koirtyohann. “A History of Atomic Absorption Spectrometry”. In: *Analytical Chemistry* 63.21 (1991), 1024A–1031A. DOI: <https://doi.org/10.1021/ac00021a716>.
- [181] P. R. Griffiths and J. A. De Haseth. Fourier Transform Infrared Spectrometry. 2nd ed. John Wiley & Sons, 2007. DOI: [10.1002/047010631X](https://doi.org/10.1002/047010631X).
- [182] H. Günzler and H.-U. Gremlich. IR-Spektroskopie: Eine Einführung. 4th ed. John Wiley & Sons, 2012. DOI: [10.1002/9783527662852](https://doi.org/10.1002/9783527662852).
- [183] E. J. Cho et al. “Nanoparticle Characterization: State of the Art, Challenges, and Emerging Technologies”. In: *Molecular Pharmaceutics* 10.6 (2013), pp. 2093–2110. DOI: <https://doi.org/10.1021/mp300697h>.
- [184] D. Geißler, N. Nirmalanathan-Budau, L. Scholtz, I. Tavernaro, and U. Resch-Genger. “Analyzing the surface of functional nanomaterials—how to quantify the total and derivatizable number of functional groups and ligands”. In: *Microchimica Acta* 188.10 (2021), p. 321. DOI: <https://doi.org/10.1007/s00604-021-04960-5>.
- [185] A. Hennig et al. “Scope and Limitations of Surface Functional Group Quantification Methods: Exploratory Study with Poly(acrylic acid)-Grafted Micro- and Nanoparticles”. In: *Journal of the American Chemical Society* 134.19 (2012), pp. 8268–8276. DOI: <https://doi.org/10.1021/ja302649g>.
- [186] S. Zhu, U. Panne, and K. Rurack. “A rapid method for the assessment of the surface group density of carboxylic acid-functionalized polystyrene microparticles”. In: *Analyt* 138 (10 2013), pp. 2924–2930. DOI: <http://dx.doi.org/10.1039/C3AN36578F>.

- 
- [187] M. Randelović, M. Momčilović, M. Purenović, A. Zarubica, and A. Bojić. “The acid-base, morphological and structural properties of new biosorbent obtained by oxidative hydrothermal treatment of peat”. In: *Environmental Earth Sciences* 75 (9 2016), p. 764. DOI: <https://doi.org/10.1007/s12665-016-5242-0>.
- [188] L. Frás et al. “Determination of dissociable groups in natural and regenerated cellulose fibers by different titration methods”. In: *Journal of Applied Polymer Science* 92.5 (2004), pp. 3186–3195. DOI: <https://doi.org/10.1002/app.20294>.
- [189] A. V. Selitrenikov and Y. E. Zevatskii. “Study of acid-base properties of weak electrolytes by conductometric titration”. In: *Russian Journal of General Chemistry* 85 (1 2015), pp. 7–13. DOI: <https://doi.org/10.1134/S1070363215010028>.
- [190] B. K. Wetzl, S. M. Yarmoluk, D. B. Craig, and O. S. Wolfbeis. “Chameleon Labels for Staining and Quantifying Proteins”. In: *Angewandte Chemie International Edition* 43.40 (2004), pp. 5400–5402. DOI: <https://doi.org/10.1002/anie.200460508>.
- [191] Y. Yang and S. H. L. Verhelst. “Cleavable trifunctional biotin reagents for protein labelling, capture and release”. In: *Chem. Commun.* 49 (47 2013), pp. 5366–5368. DOI: <http://dx.doi.org/10.1039/C3CC42076K>.
- [192] N. Nirmalananthan-Budau et al. “Multimodal Cleavable Reporters for Quantifying Carboxy and Amino Groups on Organic and Inorganic Nanoparticles”. In: *Scientific Reports* 9.1 (2019), p. 17577. DOI: <https://doi.org/10.1038/s41598-019-53773-3>.



---

# A | Appendix

## A.1 | List of Publications

- 1) B. von Boehn, L. Scholtz, R. Imbihl, "Reactivity and Stability of Ultrathin VO<sub>x</sub> Films on Pt(111) in Catalytic Methanol Oxidation", *Top. Catal.* **2020**, *63*, 1545–1556. (not included in this thesis)
  
- 2) D. Geißler, N. Nirmalananthan-Budau, L. Scholtz, I. Tavernaro, U. Resch-Genger, "Analyzing the surface of functional nanomaterials—how to quantify the total and derivatizable number of functional groups and ligands", *Microchim. Acta* **2021**, *188*, 321. (included in this thesis)
  
- 3) L. Scholtz, J. G. Eckert, T. Elahi, F. Lübke, O. Hübner, N. C. Bigall, U. Resch-Genger, "Luminescence encoding of polymer microbeads with organic dyes and semiconductor quantum dots during polymerization", *Sci. Rep.* **2022**, *12*, 12061. (included in this thesis)
  
- 4) Y. Hu, C. Neumann, L. Scholtz, A. Turchanin, U. Resch-Genger, S. Eigler, "Polarity, intramolecular charge transfer, and hydrogen bond co-mediated solvent effects on the optical properties of graphene quantum dots", *Nano Res.* **2023**, *16* (1), 45–52. (not included in this thesis)
  
- 5) P. Srivastava, I. Tavernaro, L. Scholtz, C. Genger, P. Welker, F. Schreiber, K. Meyer, U. Resch-Genger, "Dual color pH probes made from silica and polystyrene nanoparticles and their performance in cell studies", *Sci. Rep.* **2023**, *13*, 1321. (included in this thesis)
  
- 6) L. Scholtz, I. Tavernaro, J. G. Eckert, M. Lutowski, D. Geißler, A. Hertwig, G. Hidde, Nadja C. Bigall, Ute Resch-Genger, "Influence of Nanoparticle Encapsulation and Encoding on the Surface Chemistry of Polymer Carrier Beads", *Sci. Rep.* **2023**, *13*, 11957. (included in this thesis)

7) L. Scholtz, J. G. Eckert, R. T. Graf, A. Kunst, K.-D. Wegner, N. C. Bigall, U. Resch-Genger, "Correlating Semiconductor Nanoparticle Architecture and Applicability for the Controlled Encoding of Luminescent Polymer Microparticles", submitted to *Chem. Mater.* **2023**. (included in this thesis)

## A.2 | Conference Contributions

The posters were presented/the talks held by the first author mentioned.

1) L. Scholtz, J. G. Eckert, N. C. Bigall, U. Resch-Genger, "Luminescence Encoding of Polymer Microbeads during Polymerization", **Poster Presentation** at Bad Honnef Physics School, Bad Honnef, Germany, **2021**.

2) S. Orell, N. Faruqui, J. Rissler, N. Marek, D. Kalbermatter, L. Scholtz, U. Resch-Genger, L. Elowsson Rendin, K. Vasilatou, M. Shaw, M. Kåredal, A.-K. Larsson-Callerfelt, "Differential toxicities of particulate matter components linked to air pollution and adverse health effects", **Poster Presentation and Conference Paper** at ERS International Congress, Online Conference, **2021**.

3) L. Scholtz, J. G. Eckert, N. C. Bigall, U. Resch-Genger, "Luminescence Encoding of Polymer Microbeads during Polymerization", **Poster Presentation** at JCF Frühjahrssymposium, Hannover, Germany, **2022**.

4) L. Scholtz, J. G. Eckert, T. Elahi, F. Lübke, O. Hübner, N. C. Bigall, U. Resch-Genger, "Luminescence Encoding of Polymer Microbeads during Polymerization" (updated version), **Poster Presentation** at Frontiers of Polymer Colloids, Prague, Czech Republic, **2022**.

5) L. Scholtz, J. G. Eckert, T. Elahi, F. Lübke, O. Hübner, N. C. Bigall, U. Resch-Genger, "Luminescence Encoding of Polymer Microbeads during Polymerization" (updated version), **Poster Presentation** at BAM PhD Day, Berlin, Germany, **2022**.

- 6) C. Dondi, S. Rey, L. Scholtz, I. Taverno, U. Resch-Genger, A.-K. Larsson-Callerfelt, M. Shaw, "Advances in high-resolution imaging of cell cultures and tissues exposed to airborne particles", **Poster Presentation** at International Aerosol Conference, Athens, Greece, **2022**.
- 7) I. Tavernaro, P. Srivastava, L. Scholtz, O. Hübner, U. Resch-Genger, "Optical micro- and nanosensors for versatile use in biomedical applications", **Poster Presentation** at 5. Münchner POCT Symposium, Munich, Germany, **2022**.
- 8) L. Scholtz, J. G. Eckert, F. Lübkekmann, R. Graf, A. Schlosser, O. Hübner, N. C. Bigall, U. Resch-Genger, "Luminescence Encoding of Polymer Microbeads with Nanocrystals During Polymerization", **Oral Presentation** at GrK Nanohybrid Conference, Hamburg, Germany, **2022**.
- 9) L. Scholtz, J. G. Eckert, F. Lübkekmann-Warwas, O. Hübner, N. C. Bigall, U. Resch-Genger, "Luminescent Polymer Microbeads – Synthesis & Applications", **Poster Presentation** at Future WiNS Conference, Berlin, Germany, **2022**.
- 10) L. Scholtz, J. G. Eckert, F. Lübkekmann, R. Graf, A. Schlosser, O. Hübner, N. C. Bigall, U. Resch-Genger, "Luminescent Polymer Microbeads – Why and How?", **Pitch Talk** at JCF Frühjahrssymposium, Gießen, Germany, **2023**.
- 11) I. Tavernaro, N. Nirmalanathan-Budau, L. Scholtz, U. Resch-Genger, "Development of multimodal methods to quantify the total & accessible number of functional groups & ligands on nanomaterials", **Poster Presentation** at ANAKON, Vienna, Austria, **2023**.
- 12) L. Scholtz, I. Tavernaro, J. G. Eckert, M. Lutowski, A. Hertwig, G. Hidde, N. C. Bigall, U. Resch-Genger, "Luminescent, Nanoparticle-Loaded Polymer Microparticles – Comparing Synthesis Routes", **Poster Presentation** at Bunsen-Tagung, Berlin, Germany, **2023**.
- 13) I. Tavernaro, N. Nirmalanathan-Budau, L. Scholtz, U. Resch-Genger, "A Multimodal Approach to Quantify Surface Functional Groups on Nanomaterials for Safe and Sustainable

by Design", **Oral Presentation** at nanoSAFE & NanoSafety Cluster 2023, Grenoble, France, **2023**.

14) I. Tavernaro, P. Srivastava, L. Scholtz, N. Nirmalanathan-Budau, U. Resch-Genger, "Multicolored sensors based on silica and polymeric particles for ratiometric monitoring of pH, oxygen and saccharides", **Oral Presentation** at 4<sup>th</sup> European Biosensor Symposium 2023, Aachen, Germany, **2023**.